Structure-Directing Influence of Hydrogen on the Formation of Hydrides of Palladium and Rhodium Compounds Based on *In Situ* Studies

Von der Fakultät für Chemie und Mineralogie
der Universität Leipzig
genehmigte
DISSERTATION
zur Erlangung des akademischen Grades
DOCTOR RERUM NATURALIUM
(Dr. rer. nat.)
vorgelegt

von M.Sc. André Götze
geboren am 08.03.1989 in Eilenburg

Angenommen aufgrund der Gutachten von:
  Prof. Dr. Holger Kohlmann, Universität Leipzig
  Prof. Dr. Rainer Pöttgen, Universität Münster

Tag der Verleihung 07.08.2018

Die vorliegende Arbeit wurde in der Zeit von März 2014 bis Juni 2018 am Institut für anorganische Chemie an der Fakultät für Chemie und Mineralogie der Universität Leipzig unter Leitung von Herrn Prof. Dr. Kohlmann angefertigt.

Bibliographische Beschreibung

André Götze:

Structure-Directing Influence of Hydrogen on the Formation of Hydrides of Palladium and Rhodium Compounds Based on *In Situ* Studies, Universität Leipzig, Fakultät für Chemie und Mineralogie, Institut für Anorganische Chemie, Dissertation, 2018, 263 Seiten, 141 Abbildungen, 73 Tabellen, 686 Referenzen.

Abstract

Palladium and palladium-rich compounds are well known to take up hydrogen and form interstitial hydrides. Hydrogen is preferred to occupy $[Pd_6]$ octahedral voids in binary $M Pd_3$ (M: metal atom) compounds which show often a rearrangement from one superstructure of the cubic closed packing (ccp) to another. A possible hydride formation and the incorporated hydrogen amount is affected by electronic and geometric aspects of the metal atom M. Main group elements with an electronegativity similar to and an atomic radius greater than palladium promote hydride formation. Therefore, $SnPd_3H_{0.14}$, $PbPd_3H_{0.13}$ and $BiPd_3H_{0.2}$ absorb less hydrogen than for example the known $TlPd_3H$. *In situ* methods, like neutron powder diffraction, thermal analysis and hydrogen sorption experiments, enable us to follow these solid-gas reactions. The hydrogen position and its occupation can be determined during the whole hydrogenation process based *in situ* neutron powder diffraction data. In addition, intermediates that are invisible to *ex situ* methods are characterized. During the hydrogenation of $MgPd_3$, firstly $[Pd_6]$ and $[MgPd_5]$ and then $[Mg_2Pd_4]$ octahedral sites are occupied by hydrogen. A hydrogen induced rearrangement from double hexagonal closed packing (dhcp) to ccp is observed during the hydrogenation of $BiPd_3$. A neglible hydrogen amount is sufficient for the direct change of structures without intermediates. Similarly, $MgPd_2$ shows a considerable volume expansion with only low occupied interstices during first-time hydrogenation. $MgPd_2$ is the only Co_2Si-type palladium-rich compound which takes up hydrogen. $MgPd_2H$ releases hydrogen at hydrogen pressure and increasing temperatures forming $MgPd_2H_{0.2}$ before the decomposition to cubic $MgPd_3H_x$ and MgH_2 takes place. The reaction enthalpy for the hydride formation of $MgPd_2H_{0.9}$ is -37.3 kJ (mol H_2)$^{-1}$ resulting in hydrogenations at mild conditions.

Further palladium-containing compounds were synthesized and investigated regarding their hydrogenation properties. However, the binary Pd_2Zn, $PdCd$, $PdHg$, Pd_2Sn, $Pd_{13}Pb_9$, Pd_5Pb_3, Pd_3As, $PdSb$, Pd_5Sb_2, Pd_8Sb_3, $Pd_{20}Sb_7$, Pd_5Bi_2, $Pd_{17}Se_{15}$ and Pd_4Se as well as the ternary compounds Pd_5CdSe, Pd_5HgSe, Pd_5CdAs, Pd_5InAs, Pd_5TlAs, Pd_5InP and $Pd_3Bi_2Se_2$ do not absorb a significant amount of hydrogen. The increase in valence electron concentration (VEC) by the insertion of electron-rich semimetals in palladium-rich compounds hinders a hydrogenation of them. In addition, their structures include often voids with an ordered distribution. Pd_5InSe as precursor shows a hydrogen uptake. At high temperatures it decomposes to palladium selenides and $InPd_3$, the latter is subsequently hydrogenated. $Pd_{11}Bi_2Se_2$ is related to W type and also does not show a reaction with hydrogen. Therefore, this compound attracts interests in catalysis. $Pd_{11}Bi_2Se_2$ as catalyst material shows a high selectivity to ethylene in the semi-hydrogenation of acetylene with a small conversion.

Besides palladium-rich compounds, the Laves phase $CaRh_2$ takes up hydrogen and forms cubic α-$CaRh_2H_{0.05}$ and orthorhombic β-$CaRh_2H_{3.9}$. γ-$CaRh_2H_{3.2}$ is formed during the dehydrogenation. The Laves phase hydrides are intermediates during the kinetically controlled decompostion into the perovskite-type hydride $CaRhH_3$ and rhodium with a small crystallite size. $CaRhH_3$ is not accessible through direct synthesis of rhodium and calcium hydride.

These results shed light into the hydrogenation processess of palladium-rich and calcium-rhodium compounds and show the potential of *in situ* studies. The abscense of hydride formation in electron-richer compounds shows the possibility for application in hydrogenation catalysis.

Zusammenfassung

Palladium und palladiumreiche Verbindungen sind dafür bekannt, dass sie Wasserstoff aufnehmen und interstitielle Hydride bilden. Wasserstoff besetzt bevorzugt $[Pd_6]$-Oktaederlücken in MPd$_3$-Verbindungen (M: Metall), die häufig von einer Überstruktur der kubisch dichtesten Packung (ccp) in eine andere umgelagert werden. Eine mögliche Hydridbildung und der eingelagerte Wasserstoffgehalt werden durch elektronische und geometrische Aspekte des Metals M beeinflusst. Hauptgruppenelemente mit einer ähnlichen Elektronegativität und einem größerem Atomradius als Palladium fördern eine Hydridbildung. $SnPd_3H_{0.14}$, $PbPd_3H_{0.13}$ und $BiPd_3H_{0.2}$ absorbieren deshalb weniger Wasserstoff als zum Beispiel das bekannte $TlPd_3H$. *In situ*-Methoden, wie Neutronenpulverbeugung, thermische Analyse und Wasserstoffsorptionsexperimente, ermöglichen es, solche Feststoff-Gas-Reaktionen zu untersuchen. Die Wasserstoffposition und dessen Besetzung kann während des gesamten Hydrierungsprozesses basierend auf *in situ*-Neutronenpulverbeugungsdaten bestimmt werden. Zusätzlich können Intermediate, die für *ex situ*-Methoden nicht detektierbar sind, charkterisiert werden. Während der Hydrierung von $MgPd_3$ werden zuerst $[Pd_6]$- und $[MgPd_5]$- und erst dann $[Mg_2Pd_4]$-Oktaederlücken von Wasserstoff besetzt. Bei der Hydrierung von $BiPd_3$ findet eine wasserstoffinduzierte Umlagerung von der doppelt-hexagonalen-dichtesten Packung (dhcp) zur kubisch-dichtesten Packung statt. Ein sehr geringer Wasserstoffgehalt reicht dabei aus, um die direkte Veränderung der Strukturen zu ermöglichen, ohne Intermediate zu bilden. Ähnlich dazu ist $MgPd_2$, das trotz geringer Wasserstoffbesetzung eine beachtliche Volumenzunahme während der ersten Hydrierung zeigt. $MgPd_2$ ist das einzige der im Co_2Si-Typ kristallisierenden palladiumreichen Verbindungen, das Wasserstoff aufnimmt. Unter Wasserstoffdruck bei steigenden Temperaturen gibt $MgPd_2H$ Wasserstoff ab und bildet $MgPd_2H_{0.2}$, bevor es sich zum kubischen $MgPd_3H_x$ und MgH_2 zersetzt. Die Reaktionsenthalpie für die Hydridbildung beträgt -37.3 kJ (mol H_2)$^{-1}$, das in einer Hydrierung unter milden Bedigungen resultiert.

Weitere palladiumenthaltene Verbindungen wurden synthetisiert und auf deren Hydriereigenschaften getested. Die binären Verbindungen Pd_2Zn, $PdCd$, $PdHg$, Pd_2Sn, $Pd_{13}Pb_9$, Pd_5Pb_3, Pd_3As, $PdSb$, Pd_5Sb_2, Pd_8Sb_3, $Pd_{20}Sb_7$, Pd_5Bi_2, $Pd_{17}Se_{15}$ und Pd_4Se sowie die tenären Verbindungen Pd_5CdSe, Pd_5HgSe, Pd_5CdAs, Pd_5InAs, Pd_5TlAs, Pd_5InP and $Pd_3Bi_2Se_2$ zeigen jedoch keine signifikante Wasserstoffabsorption. Die Erhöhung der Valenzelektronenkonzentration (VEC) durch Einbringen von elektronenreichen Halbmetallen in palladiumreiche Verbindungen hemmt eine Wasserstoffaufnahme. Zusätzlich enthalten deren Strukturen häufig Lücken mit geordneter Verteilung. Pd_5InSe als Vorläuferverbindung zeigt eine Wasserstoffaufnahme. Es zersetzt sich bei hohen Temperaturen zu Palladiumseleniden und $InPd_3$, das anschließend hydriert wird. $Pd_{11}Bi_2Se_2$ ist mit dem W-Typ verwandt und nimmt keinen Wasserstoff auf. Deshalb ist diese Verbindung interessant für die Katalyse. $Pd_{11}Bi_2Se_2$ als Katalysatormaterial zeigt bei der Semihydrierung von Acetylen eine hohe Selektivität zu Ethylen, bei einem geringem Umsatz.

Neben den palladiumreichen Hydriden, nimmt auch die Laves-Phase $CaRh_2$ Wasserstoff auf und bildet kubisches α-$CaRh_2H_{0.05}$ und orthorhombisches β-$CaRh_2H_{3.9}$. Während der Dehydrierung wird γ-$CaRh_2H_{3.2}$ gebildet. Die Laves-Phasen-Hydride sind Zwischenprodukte bei der kinetisch gesteuerten Zersetzung zu dem Perowskit-Typ-Hydrid $CaRhH_3$ und Rhodium mit sehr kleiner Kristallitgröße. $CaRhH_3$ ist nicht über die Direktsynthese von Rhodium und Calciumhydrid zugänglich.

Diese Ergebnisse beleuchten Hydrierungprozesse von palladiumreichen und Calcium-Rhodium-Verbindungen und zeigen das Potential von *in situ*-Studien. Elektronenreichere Verbindungen, die keine Hydride bilden, zeigen die Möglichkeit als Anwendung in der katalytischen Hydrierung.

Contents

Contents

Part I.

Overview

This work is a publication based thesis. This first part gives an overview of intermetallic and palladium-rich compounds and an introduction to metal hydrides. Furthermore, used methods and materials are described and results within the publications are summarized and discussed.

The second part includes all publications within this thesis, beginning with a review about palladium and palladium-rich hydrides [1] followed by articles about the *in situ* neutron powder diffraction method including the hydrogenation of $MgPd_3$ [2] and further *in situ* studies of $BiPd_3$ [3] and $MgPd_2$ [4]. This is followed by publications of the hydrogenation properties of binary and ternary palladium-rich compounds [5], [6] and in particular $Pd_{11}Bi_2Se_2$ [7]. At the end of this part, an article describing the access to the perovskite $CaRhH_3$ via hydrogenation of the Laves phase $CaRh_2$ [8] is presented.

The third part contains further, not yet published results within this thesis as hydrogen sorption experiments of $MgPd_2$, calculations and neutron powder diffraction of MPd_3 compounds and catalytic experiments of $Pd_{11}Bi_2Se_2$.

1. Introduction

In 1766 Henry Cavendish was the first who investigated properties of hydrogen and found out that "only three metallic substances, namely, zinc, iron and tin [...] generate inflammable air [(hydrogen), note from the autor] by solution in acids; and those only by solution in the diluted vitriolic acid [(sulphuric acid), note from the autor], or spirit of salt [(hydrochloric acid), note from the autor]" (Henry Cavendish in [9], p. 144). Hydrogen is known to be the most abundant chemical element in the universe. Hydrogen is known to be in the liquid or solid state at low temperatures, however, diverse calculations predict transitions from molecular hydrogen to metallic hydrogen under high pressures [10–13]. It was discovered that this metallic hydrogen might be a component of the planets Jupiter and Saturn [14, 15]. Ranga Dias and Isaac Silvera reported recently that they have observed metallic hydrogen in laboratory [16] which is highly controversial [17].

From another point of view compounds of metals like palladium and solved hydrogen will behave metallic. Thomas Graham discovered in 1866 that "palladium has taken up a large volume of [hydrogen, note from the autor] gas [...] 1 vol. palladium held 526 vols. hydrogen" (Thomas Graham in [18], p. 426). After this discovery further hydrogen containing compounds, designated as hydrides, have been studied and palladium as catalyst became also of growing interest. In 2010 Richard F. Heck, Ei-ichi Negishi and Akira Suzuki were even awarded with the Nobel Prize in Chemistry for their work on "Palladium-catalyzed Cross Coupling in Organic Synthesis" [19].

However, the research of new materials with useful properties for application represent a difficult challenge in solid state chemistry. Three different strategies can be a solution approach for solid state research. The easiest way are so-called "shake and bake", "stone baking" or hard chemistry. Solid substances are thermally treated to create new compounds or structures. Solid state chemistry was based on this method up to the middle of the 20th century. Another strategy for new, and also metastable materials is "chimie douce" (soft chemistry) that describes reactions under mild conditions [20] to make kinetic stabilized materials accessible. Some known representatives are synthesis by sol-gel processes [21, 22] or topotactic reactions to modify precursor materials and retain structural motifs [23, 24]. The way to get new functional materials is similar for both, synthesis at high temperatures and soft chemistry. New compounds are synthesized and afterwards their structures characterized to optimize the reaction conditions. Thus, the synthesis is systematically improved with the goal to get phase pure compounds within this process. The third strategy is linked to another part of the process. By unraveling reactions pathways with *in situ* methods, intermediates can be investigated that are not stable at ambient conditions. Furthermore, the gained knowledge about the reaction pathway can also be used for synthesis improvements.

In this work all three strategies are taken into account to form palladium-rich intermetallic compounds and hydrides of noble metals with metallic to covalent bonding behavior.

1.1. Intermetallics and palladium-rich compounds

Chemical compounds containing only metals, which could have a phase width and crystallize mainly in ordered structures that are different from the metal structures, are referred to as intermetallic compounds (intermetallics) in this work. The importance of intermetallic compounds has been recognized

since the Bronze Age about 4000 years ago. It was found that bronze is harder and melts at lower temperatures compared to cupper. A high tin bronze (20-50 wt-% tin) mirror that was made in the Han dynasty about the first years before Christ [25] is a still preserved example. Nowadays, inter-metallics are important for application like magnets (e. g. $SmCo_5$ [26–28]), turbines (high temperature and fire as well as oxidation resistant materials, e. g. TiAl [29]) and metal hydride batteries (e. g. $LaNi_5$ [30, 31]). Some platinum containing intermetallics are used in catalysis, e. g. for fuel cells applications [32]. Additional, intermetallic palladium-rich compounds are also interesting for catalysis, e. g. $PbPd_3$ for direct synthesis of methyl methacrylate from methacrolein, methanol and oxygen [33]. In the following, palladium-rich intermetallics or compounds are understood as compounds containing $2/3$ or more palladium which results in $MPd_{\geq 2}$ in the case of binary compounds. Main group element representatives of them are shown in Table 1.1.1. In the case of MPd_3 compounds, IUPACs rule for nomenclature is not apllied in this work. Instead, MPd_3 compounds are named in the same order as their structure types, e. g., $AuCu_3$ type or $ZrAl_3$ type.

Most of these compounds are available through high temperatures and long annealing times (hard chemistry). However, soft chemistry is also of importance to get ordered metastable compounds, e. g. $MgPd_2$ [45] and $AlPd_5$ [48] by iodine catalyzed synthesis. Typically, small amounts of iodine are added to solid state reaction mixtures. Iodine lowers the activation barrier of the reaction of metals with palladium by forming gasous metal iodides resulting in lower reaction temperatures and annealing time. In some cases, the iodine catalyzed method is a transport reaction through formed

Table 1.1.1.: Overview of known ordered binary palladium-rich (definition see text above) compounds with main group elements of stoichiometric compositions.

period	group 1	group 2	group 13	group 14	group 15	group 16
2	$LiPd_2$ [34], $LiPd_7$ [35]	$BePd_2$ [36], $BePd_3$ [36]	Pd_2B [37], Pd_5B_2 [38], Pd_3B [39], Pd_5B [40], $Pd_{16}B_3$ [41], Pd_6B [42]		Pd_2N [43]	Pd_2O [44]
3		$MgPd_2$ [45], $MgPd_3$ [45, 46]	Pd_2Al [47], Pd_3Al [48], Pd_5Al [48]	Pd_2Si [49], Pd_3Si [50], Pd_9Si_2 [51]	Pd_7P_3 [52], Pd_3P [53], Pd_6P [54], $Pd_{15}P_2$ [55]	$Pd_{16}S_7$ [56], Pd_3S [57], Pd_4S [58]
4		$CaPd_2$ [59], $CaPd_5$ [60]	Pd_2Ga [61], Pd_7Ga_3 [61], Pd_5Ga_2 [62], $Pd_{13}Ga_5$ [63]	Pd_2Ge [64], $Pd_{21}Ge_8$ [65], $Pd_{25}Ge_9$ [66], Pd_5Ge [67]	Pd_2As [68, 69], Pd_5As_2 [70], Pd_3As paper, Pd_5As [71]	$Pd_{34}Se_{11}$ [72], Pd_7Se_2 [72], Pd_4Se [58]
5		$SrPd_2$ [59], $SrPd_5$ [73]	Pd_2In [74], $InPd_3$ [75, 76]	Pd_2Sn [77], $SnPd_3$ [78]	Pd_2Sb [69], Pd_5Sb_2 [79], Pd_8Sb_3 [80, 81], $Pd_{20}Sb_7$ [82]	Pd_9Te_4 [83], Pd_5Te_2 [84], Pd_8Te_3 [84], $Pd_{20}Te_7$ [82], $Pd_{13}Te_3$ [85]
6		$BaPd_2$ [59], $BaPd_5$ [86]	Pd_2Tl [87], $TlPd_3$ [88, 89]	$PbPd_3$ [78]	Pd_5Bi_2 [90], Pd_8Bi_3 [90], $BiPd_3$ [87]	

gaseous complexes [91,92]. Further incidental benefits of this method are phase purity or single crystal growing [48,61,93]. Additional soft chemistry methods, which play no role in this work, are syntheses from organometallic compounds to get new intermetallics with nano-sized particles by wet chemical or electrochemical methods [94], e. g. the formation of nanoscale $BiPd_3$ [95].

Palladium-rich intermetallics mainly show metallic behavior and the electronic states below the Fermi level are often dominated by Pd-d states [96, 97]). Multi centered metal-metal bonds were calculated, e. g. in $InPd_3$ [98], and charge transfer from metal to palladium is not unusual in these systems [96–98]. Paramagnetic to negligible paramagnetic behavior is usually observed for palladium-rich intermetallics [99, 100] as well as palladium itself. Another property of some palladium-rich intermetallics that is essential for this work, is their hydrogenation behavior. New or known palladium-rich compounds, which are possible candidates for hydride formation or catalysts for hydrogenation reactions, were investigated for this thesis.

1.2. Hydrogen and hydrides

Hydrogen occurs at ambient conditions as the diatomic molecule H_2 in gaseous state. Special properties of hydrogen are its high diffusivity ($D_{12} = 0.668$ cm^2 s^{-1} in air at ambient conditions [101]), high thermal conductivity ($\kappa = 0.1844$ W m^{-1} K^{-1} at 300 K [102]) and small density ($\rho = 0.08988$ g l^{-1} [103]). A considerable gravimetric energy density attracts hydrogen as application for energy storage e. g. in pressure tanks [104]. Hydrogen has a medium electronegativity ($\chi = 2.2$ after ALLRED and RO-CHOW [105]) and, therefore, is well known either as reducing or oxidizing agent. The more commonly used reductive properties of hydrogen are applied for hydrogenation reactions in organic chemistry, e. g. hydrogenation of alkenes or alkynes [106,107], as well as for synthesis of pure metals from oxides, e. g., nickel from NiO [108, 109] or iron from Fe_2O_3 [110]. Furthermore, hydrogen can also be used to form intermetallics by reducing base metals oxides in a coupled reaction with noble metals like platinum [111].

More interesting for this work is the oxidative character of hydrogen to form metal hydrides. They are typically prepared by solid gas reactions of hydrogen with a less electronegative metal or intermetallic compound. In rare cases solution methods for hydride synthesis are used, e. g. CuH_x from cupper sulfate and hypophosphorous acid in aqueous solution [112]. Metal hydrides can roughly be ordered by their bonding situations in the range of ionic via covalent to metallic. Therefore, hydrogen takes an oxidation state between -1 and 0. The series of the hydrides of europium with increasing amount of palladium are a textbook example for the different bonding situations [113]. The range of ionic towards covalent to metallic hydrogen bonds are observed in the sequence EuH_2 - Eu_2PdH_4 - $EuPdH_3$ - $EuPd_2H_x$ - PdH_y (Fig. 1.2.1) and, thus, the composition changes from stoichiometric to nonstoichiometric [113]. The reported hydrides in this work are located in the area between metallic and covalent bonding characters.

1.2.1. Interstitial hydrides

Interstitial hydrides are compounds with hydrogen incorporated typically in tetrahedral or octahedral voids and mainly metallic bonding character. Palladium hydride was the first known representative. As mentioned in the beginning of Chapter 1, the hydrogen uptake of palladium was firstly reported by THOMAS GRAHAM in 1866 [18]. Since then palladium hydride was investigated regarding its phase diagram [114], diffusion of hydrogen [115], superconductivity [116], magnetism [117], isotope effects of hydrogen [114, 118], electronic structure [119] and applications [19, 120]. PdH_x crystallizes in a defect NaCl type structure [121] with a miscibility gap (hydrogen occupation of 0.02 to 0.6 at room
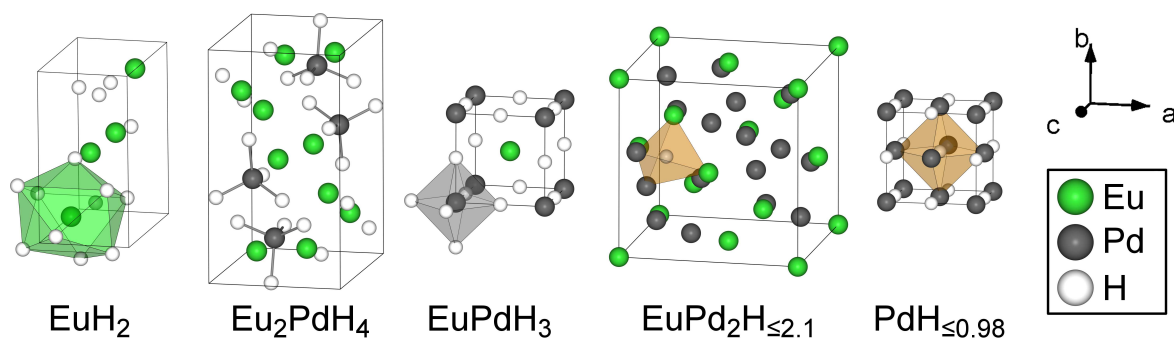
Figure 1.2.1.: Crystal structures of the hydrides in the system Eu-Pd, hydrogen bonding behavior ranges from ionic (left) to metallic (right) [113]. Only one representative H-site of the Laves-phase hydride $EuPd_2H_x$ is shown.

temperature) resulting in an α-phase and a β-phase differing only by their hydrogen amount [114]. A large quantity of known palladium-rich disordered compounds form hydrides. The solubility of a metal in palladium can be quite negligible as in Li_xPd_{1-x} ($x \leq 0.04$) or up to complete solid solutions as for all eight metals surrounding palladium in the periodic table of the elements and iron [122]. It should be noted that with increasing unit cell volume, $Pd_{1-x}M_x$ dissolves more hydrogen in the α-phase than palladium [114]. However, only rhodium as minor metal enables a higher dissolvability of hydrogen in the β-phase [123] compared to palladium.

Moreover, ordered palladium-rich intermetallic compounds are forming hydrides as well for example the Laves phases hydrides $SrPd_2H$ [124] and $EuPd_2H_x$ ($x = 0.1, 1.5, 2.1$) [113]. There is no intermetallic precursor compound available for $CaPd_3H_x$ crystallizing in filled $TiNi_3$ type [125]. Further MPd_3 (M = Mg [46,126], In [127], Tl [88], Y [128], Mn [129], Ce [130]) compounds are forming hydrides that are related to the cubic closed packing (ccp). A rearrangement from one to another superstructure of ccp is often observed in these systems. Hydrogen occupies preferably $[Pd_6]$ octahedral voids. The number of $[Pd_6]$ voids increases in the series $TiAl_3$ type - $ZrAl_3$ type - $AuCu_3$ type from 0 to 1 per formula unit that might be the driving force [131], e. g., for the rearrangement of $InPd_3$ from $TiAl_3$ or $ZrAl_3$ type to $AuCu_3$ type during hydrogenation [75]. On the one hand, $InPd_3$ [127] and $TlPd_3$ [88] form hydrides and, on the other hand, for aluminum or gallium no hydrides were found, yet [76]. The size of the metal M seems to have a strongly influence on hydride formation, but why are no palladium-rich hydrides with the contiguous metals like lead, tin or bismuth reported? To shed more light on the phenomena of hydrogenation of palladium-rich intermetallics, additional compounds were investigated regarding their hydrogenation properties within this thesis. A more comprehensive overview of the behaviors and properties of palladium hydride and palladium-rich disordered and ordered hydrides as stated above is given in the review in Chapter 8, [1].

1.2.2. Covalent and complex hydrides

Late main group elements with an electronegativity similar to hydrogen tends to form covalent hydrides, e. g., solid alane (AlH_3 crystallizing in FeF_3 type [132]) and gaseous stannane (SnH_4). A special kind of covalent hydrides are complex hydrides with hydrogen ligands bound covalently to a transition metal which is stabilized by a less electronegative metal as cation. Ternary compounds typically consists of mono- or bivalent cations A^{n+}, and a hydrido complex $[T_yH_z]^{nx-}$ that takes up n valence electrons per cation resulting in the general formula $A_xT_yH_z$. A common structure type of these complex hydrides is the K_2PtCl_6 type. The transition metal is coordinated octahedrally by six hydrogen atoms forming hydrido complexes, e. g., $[Fe^{II}H_6]^{4-}$ [133,134] or $[Pt^{IV}H_6]^{2-}$ [135]. Complexes

of rhodium as transition metal crystallize either in Na_3RhH_6 type containing $[Rh^{III}H_6]^{3-}$ hydrido complexes [135, 136] or in defect K_2PtCl_6 type containing $[Rh^I H_{6.5/6}]^{4-}$ units their anion site is occupied by only $5/6$ with hydrogen. [137,138].

The transition from covalent to metallic hydrides is smooth as well as to ionic hydrides. Therefore, compounds exsist which can not be classified either one or the other. As an example, Li_3RhH_4 is no typical 16 valence electron complex, because weak Rh-Rh bonds (d = 3.865 Å) between square planar $[RhH_4]^{3-}$ units were observed [139]. $MgRhH_{1-x}$, as another example, also contains weak Rh-Rh interactions (d = 2.980 Å) between tetrameric $[Rh_4H_4]$ units with strong Rh-H bonds (d = 1.708 Å) [140, 141]. The hypothetical higher homologue CaRhH was attempted to be calculated by density functional theory (DFT) methods, however, no convergence within the model of MgRhH was achieved [141]. Despite that, the question arises, whether a hydride of the compostion $CaRhH_x$ exsist and how it is accessible.

1.2.3. Ionic hydrides

Ionic bonds are formed in salt-like alkaline or alkaline earth hydrides, though, the ionic character decreases in series from barium to beryllium hydride. The ionic hydrogen radii of ionic hydrides depend strongly on the polarizing effect of the metal cation, they increase with number of period e. g. from LiH to CsH [142].

The bonding character in lanthanide hydrides depends on the composition that changes with pressure and temperature [143]. The hydrides undergo a transition from LnH_2 ($Ln^{3+}(H^-)_2e^-$) to LnH_3 and show covalent-metallic behaviors. In contrast, the exceptions YbH_2 and EuH_2 are primary ionic [142, 144, 145]. These hydrides scarcely play a role for this work, but they are listed for completeness.

2. Methods and Materials

This chapter deals with synthesis and characterization by determination of crystal structures as well as physical properties of the investigated compounds. Besides the descriptions of used methods and devices, their limitations are presented in some cases.

2.1. Synthesis

The palladium-rich compounds were synthesized from elements in sealed quartz glass ampules (about 100 mm length, 10 mm inside diameter and 0.5 mm wall thickness) under vacuum or argon atmosphere. Elements that are not stable in air were weighed in an argon filled glove box. The reaction mixtures were typically melted and annealed subsequently for a long time at temperatures just below melting points. The more similar the elements in electronegativity and radii compared to palladium the more annealing time is required for ordering. To reduce this annealing time and to increase the reactivity of the mixtures, a few crystals of iodine were added as mineralizing agent. During vacuum application or just before sealing the ampules with oxy-hydrogen flame, the sublimation of iodine was prevented by cooling the lower end of the ampules with liquid nitrogen. Mixtures containing elements that react with quartz glass, e. g. alkaline earth metals, were placed inside a niobium tube closed on one side and welded under reduced pressure argon atmosphere.

For *ex situ* hydrogenation experiments the intermetallic compounds were placed inside of Inconel (Böhler L718, nickel chromium alloy) crucibles and transferred into an autoclave made from the same alloy. The autoclaves were flushed several times with hydrogen or deuterium gas and the required starting pressures (0.1 MPa $\leq p \leq 30$ MPa) of hydrogen or deuterium were adjusted. The autoclaves were placed inside a vertical tube furnaces and heated up to 823 K.

2.2. Elemental analysis

The purity of samples was checked by chemical analysis with energy dispersive X-ray spectroscopy (EDX) performed by an EDX INCA SYSTEM from Oxford Instruments mounted on a Zeiss LEO 1530 scanning electron microscope (SEM) with a working distance of 15 mm. A few particles of the samples were sprinkled on conductive carbon adhesive tabs (PLANO) and vaporized with carbon to improve the conductivity on the surface. The samples were placed in the sample chamber and subsequently vacuum was applied. Electrons of the tungsten hot cathode are accelerated with an acceleration voltage of 20 kV and focused with electromagnetic lenses on the sample surface. Ions in energetically excited states are formed by ejecting electrons from the inner shell during the interaction with the accelerated focused electrons. Thereby generated 'holes' are filled by electrons from outer shells resulting in emitted X-ray quanta. Consequently characteristic X-ray spectra and integration of the intensity of emission lines enable a quantitative chemical analysis with about 5 % uncertainty. This method is suitable for the determination of compositions of samples containing elements with greater atomic numbers ($Z \geq 11$) like the synthesized intermetallic compounds within this thesis. However, hydrogen or deuterium can not be detected with this method.

Table 2.2.1.: Hydrogen content of hydrides within this thesis and difficulties regarding gas-hot extraction elemental analysis

compound	theoretical hydrogen content	difficulties
$MgPd_2H$	0.42 weight-%	release hydrogen at ambient conditions
$MgPd_3H$	0.29 weight-%	
$SnPd_3H_{0.1}$	0.023 weight-%	
$PbPd_3H_{0.13}$	0.025 weight-%	
$BiPd_3H_{0.19}$	0.036 weight-%	
$CaRh_2H_{3.9}$	1.574 weight-%	release hydrogen at ambient conditions
$CaRhH_3 + Rh$	1.215 weight-%	release hydrogen at ambient conditions

For the determination of hydrogen contents an elemental analysis (elementar vario EL, Elementar Analysensysteme GmbH) using the carrier gas-hot extraction method in triplicate repetition can be used, though, the detection limit for standard weight ($\approx$ 20 mg) are by approxximately 0.1 wt-%. Therefore, this method is not suitable because the hydrogen content of some hydrides within this thesis is too small or the hydrides are not stable at ambient conditions and release hydrogen (see Table 2.2.1).

2.3. Diffraction

Diffraction is the most important method for structure determination and likewise for crystalline solid state characterization. X-ray, synchrotron, electron or neutron radiation is used for structural analysis. Single crystal X-ray diffraction and X-ray and neutron powder diffraction performed *ex* as well as *in situ* are used in this work as described below.

2.3.1. Single crystal X-ray diffraction

Single crystals of hydrides are hardly available, but the formation of single crystals of palladium-rich compounds is possible. The presence of gaseous reactants through required temperatures or the usage of mineralizing agents like iodine, promotes the formation of large single crystals. Crystals were fixed with nail polish on the top of a glass thread and adjusted in a STOE IDPS-I diffractometer with Ag-$K_{\alpha 1}$ radiation (λ = 0.56085 Å, graphite monochromator). The crystal surfaces were measured by an integrated camera and optimized with X-SHAPE [146]. A numerical absorption correction was necessary due to absorption problems of the used heavy elements, and carried out with X-RED [147]. The structure was solved by direct methods and subsequently refined with SHELX [148]. The quality of the refinement is defined by residual factors (R values). The mean deviation between observed (F_0) and calculated structure amplitude (F_c) results in R_1 value and in consideration of a weighting factor w including minimum sums of squares of the errors results in wR_2 value (Eq. (1)) [149].

$$R_1 = \frac{\sum_{\text{hkl}} ||F_0| - |F_c||}{\sum_{\text{hkl}} |F_0|} \qquad wR_2 = \sqrt{\frac{\sum_{\text{hkl}} w(F_0{}^2 - F_c{}^2)^2}{\sum_{\text{hkl}} w(F_0{}^2)^2}} \qquad w = \frac{1}{\sigma^2(|F_0|)} \quad (1)$$
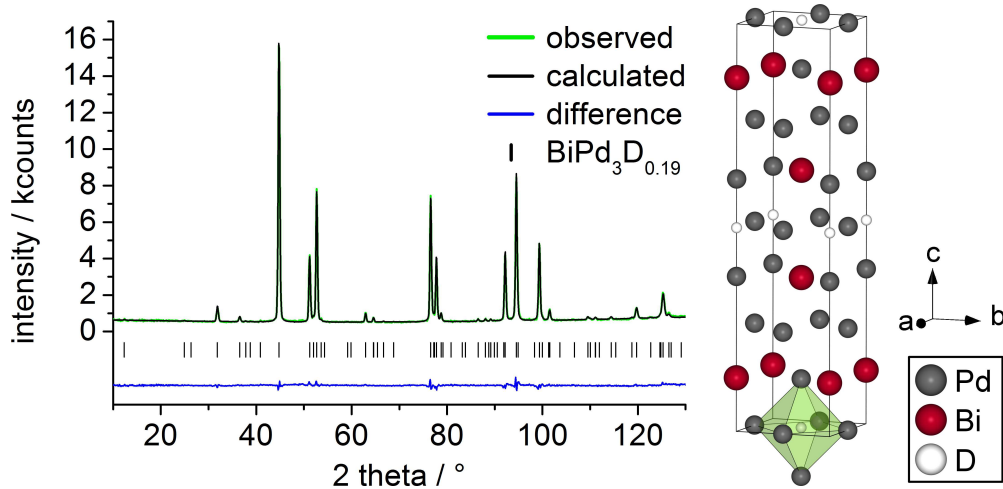
Figure 2.3.1.: Rietveld refinement of the crystal structure of tetragonal $BiPd_3D_{0.19(1)}$ (anti-Ba_2ZnF_6-type, $I4/mmm$, $a = 4.0452(2)$ Å, $c = 16.6158(8)$ Å, $R_{Bragg} = 0.055$) based on neutron powder diffraction ($\lambda = 1.79725(2)$ Å, E9, HZB Berlin, $R_p = 0.032$, $R_{wp} = 0.041$, $\chi^2 = 2.4$).

2.3.2. X-ray and neutron powder diffraction

The formation of suitable large single crystals of metal hydrides is usually not possible. Powder diffraction is most commonly used and for the analysis of hydrides indispensable. Crystal structures of palladium-rich compounds and of the metal atoms in hydrides are determined by X-ray powder diffraction (XRPD). For flat sample measurements, powders were fixed on Kapton® foils with Apiezon® grease, placed on a flat sample holder and clamped on a G670 diffractometer with Guinier geometry and $CuK_{\alpha1}$ or $MoK_{\alpha1}$ radiation. Capillary samples were measured on a STOE STADI P diffractometer with a $CuK_{\alpha1}$ radiation.

The detection of hydrogen atoms of hydrides is practically impossible with X-ray diffraction, because of the low number of electrons compared to the heavy atoms. For localizing hydrogen or other light atoms like lithium or oxygen, neutron powder diffraction is used. In contrast to X-ray diffraction, neutrons are scattered at nuclei and penetrate deeper into samples due to about four orders of magnitudes smaller absorption coefficients for most elements. Samples sizes are larger compared to X-ray diffraction because of smaller scattering cross sections and weaker neutron sources [150]. Further advantages of neutron diffraction are the possibility to determine and refine magnetic structures as well as to differentiate neighboring atoms of the periodic table, e. g., sodium, magnesium and aluminum. For hydrogen determination in crystalline compounds, deuterium was used due to the less bound incoherent scattering length ($b_i = 4.04(3)$ fm) compared to hydrogen ($b_i = 25.274(9)$ fm) [151]. The isotpe effect of hydrogen with regards to crystal structures is negligible. However, unit cells of deuterides are typically smaller compared to hydrides because deuterium atoms has the doubled mass, and thus an apparent smaller size due to vibrational isotope effects [114].

Samples for neutron diffraction experiments were placed in vanadium cylinders that barely scatter neutrons coherently, and sealed with indium wire in the case of air sensitive samples. Neutron diffraction data were collected at the high-flux diffractometer D20 at Institut Laue-Langevin (ILL, Grenoble, France) in high resolution mode (120° take-off angle, Ge (115) monochromator, $\lambda \approx 1.88$ Å) [152], at the fine resolution powder diffractometer E9 (FIREPOD) at Helmholtz-Zentrum Berlin (HZB, Berlin, Germany) in default mode (111.7° take-off angle, Ge (115) monochromator, $\lambda = 1.79725(2)$ Å) [153] or at high-resolution powder diffractometer for thermal neutrons (HRPT) at Paul Scherrer Institut

(PSI, Viligen, Switzerland) in high intensity mode (120° take-off angle, Ge (335) monochromator, $\lambda = 1.494$ Å) [154].

The crystal structures were refined by the Rietveld method [155, 156] using the programs Fullprof [157] or Topas [158]. One representative result of an Rietveld refinement is shown in Fig. 2.3.1. Cif-files of known structures were imported from the data bases Pearson's Crystal Data (PCD) [159] and Inorganic Crystal Structure Database (ICSD) [160]. The reflection shapes were modeled with a pseudo-Voigt-function by Fullprof or semi-empiric fundamental parameter approach by Topas. The quality of a model compared to measured data is expressed by R values for powder diffraction refinements comparable to for single crystal diffraction. The commonly used χ^2 value is calculated by the ratio of the weighted profile R value (R_{wp}) to the expected R value (R_{exp}) squared [161]. The weighting includes the errors of observed intensities squared ($\frac{1}{\sigma^2[y_i(obs)]}$) similar to single crystal diffraction, however, the intensities (y_i) over all data points (i) are used. The number of data points (n) is far grater than the varied parameters (p), thus p can be ignored (Eq. (2)).

$$\chi^2 = \left(\frac{R_{\mathrm{wp}}}{R_{\mathrm{exp}}}\right)^2 \qquad R_{\mathrm{wp}} = \sqrt{\frac{\sum_i w_i[y_i(obs) - y_i(calc)]^2}{\sum_i w_i[y_i(obs)]^2}} \qquad R_{\mathrm{exp}} = \sqrt{\frac{n - p}{\sum_i w_i[y_i(obs)]^2}} \qquad (2)$$

In situ powder diffraction

Reaction pathways and mechanisms of many organic syntheses are known. However, following solid-gas reactions are often technically challenging due to hard conditions, but the knowledge of reaction pathways is very helpful for synthesis planning and improvement. *In situ* diffraction is a very suitable method to follow solid-gas reactions, detect metastable intermediates and understand the reaction pathways. *In situ*, the Latin word for "on site", means time-resolved hydrogenation reactions on the diffractometer with changes of external parameters, e. g. temperature and hydrogen pressure. Gas pressure cells for XRPD and neutron diffraction were constructed and investigated [2, 162, 163]. A quartz capillary can be attached to a gas supply system by glueing it into a fitting of a Swagelok connection. The temperature of the capillary can be varied by a resistivity heater. This setup enables hydrogen pressures up to 10 MPa at 700 K during an XRPD experiment (Huber G670, Mo$K_{\alpha 1}$ radiation) [162]. For the analysis of the measured *in situ* XRPD data attention was paid to poor statistics because a capillary rotation is not possible in this setup. Thus, *in situ* XRPD were used to folllow hydrogenations with regards to formation of intermediates, lattice parameter trends and as preliminary studies for *in situ* neutron powder diffraction experiments, e. g. Fig. 2.3.2.

For *in situ* powder diffraction, a leuco-sapphire single crystal cell was used [163]. The big advantage of this sample cell is a well defined diffraction background with no reflection peaks from the single crystal. This is achieved by a special orientation of the single crystal towards the beam. In addition, the optical transparency allows heating by a contactless laser system. The cell is attached to a gas supply system. This setup allows simultaneously temperature and hydrogen gas pressure control during the neutron diffraction experiment. However, the cell is limited at high temperatures. Mechanical failure is likely at temperatures above 700 K [2]. Further information and the detailed design of the cell are described in Chapter 9, [2].

In situ diffraction experiments are a key element of this thesis. The hydrogenations of MgPd$_3$ (see [2] in Chapter 9), BiPd$_3$ (see [3] in Chapter 10), MgPd$_2$ (see [4] in Chapter 11), CaRh$_2$ (see [8] in Chapter 15) were investigated by this method. The hydrogen position and amount at any step of these reactions can be determined and intermediates that are invisible to *ex situ* diffraction were detected and characterized. *In situ* neutron powder diffraction experiments were conducted at diffractometer D20 (ILL, Grenoble) under various deuterium pressures (isotopic purity, 99.8 %) with a typically time resolution of 2 min per pattern.
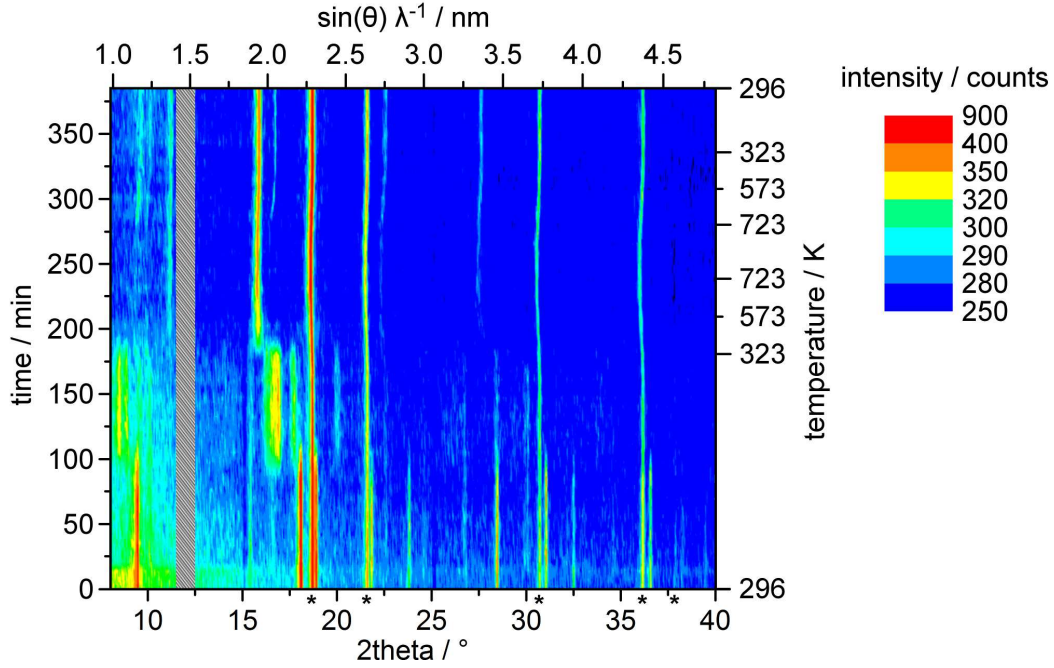
Figure 2.3.2.: *In situ* XRPD diffraction data of the hydrogenation of CaRh$_2$ at various temperatures and 5.0 MPa hydrogen pressure. It shows the reaction of CaRh$_2$ (bottom) via CaRh$_2$H$_x$ (middle) to CaRhH$_3$ and rhodium (top). The reflections of the second phase rhodium are marked with asterisks. The region around 12° is excluded due to reflections from the heating element. The results of this study were used to find the optimal conditions for later *in situ* neutron powder diffraction experiments.

2.4. Thermal analysis

In situ differential scanning calorimetry (DSC) was used to monitor hydrogenation reactions. It was performed on a Q1000 DSC (TA Instruments) equipped with a gas pressure chamber. 10-40 mg of powdered samples or reaction mixtures were put in aluminum crucibles which were closed with aluminum lids. Samples which are sensitive to air were handled in an argon filled glove box and crucibles were crimped to be sealed against air but not to hydrogen. The crucibles were placed inside the pressure chamber which was flushed several times with hydrogen gas before filling it to the desired hydrogen gas pressure (0.1 MPa $\leq p(\mathrm{H}_2) \leq$ 7.0 MPa). The samples were heated at a typical rate of 10 K min^{-1} up to 703 K and a few runs can be performed to check the possible reversibility of reactions. The reaction of samples with hydrogen but also phase transitions were detected through differences in heat flow ($\dot{Q}$, see Eq. (3), where κ is the thermal conductivity factor, A the surface area, ΔT the difference in temperature and d the thickness of the material) between the sample crucible and an empty reference crucible. The heat flow per gram as function of temperature was plotted for graphic evaluation. The onset points of measured peaks were determined as reaction temperatures with the software Universal Analysis [164]. This method is convenient in combination with X-ray powder diffraction to investigate hydrogenation reactions. Furthermore, metastable intermediates can be detected and reaction temperatures determined, therefore this method is an essential part of *in situ* investigation of hydrides.

$$\dot{Q} \; = \; \frac{dQ}{dt} \; \approx \; \frac{\Delta Q}{\Delta t} \; = \; \frac{\kappa A \Delta T}{d} \tag{3}$$

Phase transitions, melting or decomposition points of intermetallics were determined by differential thermal analysis (DTA) with incorporated thermogravimetric analysis (TGA) in helium atmosphere on a Netzsch F1 Jupiter device. 20-50 mg sample were put in a sintered alumina crucible which was placed together with an empty reference crucible on sample holders with integrated thermocouples and coupled scale. The sample compartment was closed and flushed a few minutes with helium until the sample was heated at small gas flow with a typically heating rate of 10 K min^{-1}.

2.5. Volumetric and gravimetric analysis

The hydrogen analysis by gravimetric and volumetric sorption measurements are more suitable for the hydrides of this thesis than the determination by elemental analysis. However, hydrides with a hydrogen amount below 0.1 wt-% are not suitable (see Table 2.2.1). Hydrogen sorption experiments have the advantage to analyze metastable intermediate hydrides. Volumetric sorption experiments are proved as the method of choice for isothermal measurements and gravimetric experiments were used for isobaric conditions. Furthermore, reaction enthalpies and entropies can be determined on the basis of sorption isotherms.

Samples for hydrogenation sorption experiments (about 200 mg) were activated at 393 K and under applied vacuum to remove sorbed impurities like oxygen before starting the measurement. For volumetric sorption experiments, the remaining volume of the measuring cell excluding the sample was determined with helium gas (Air Products, 99.9992 %) at the measuring temperature. The experiments were executed with the Quantachrome volumetric sorption analyzer AUTOSORB-iQ and the temperature was controlled with a Julabo F12-ED thermostat. The cell was evacuated before the sorption experiment with hydrogen gas (Air Products, 99.9992 %) started. The equilibrium was reached when the final value of the pressure did not change more than 0.3 % within 300 s. The output of these experiments are loading of hydrogen per gram of activated intermetallic based on a function of the detected absolute pressure at a constant temperature. Further details of the volumetric sorption method are described in the experimental part of the respective publication (see [8] in Chapter 15). Gravimetric sorption experiments were executed with a Rubotherm magnetic suspension balance IsoSORP (type E10). For isobaric conditions the temperature was controlled by the device and the hydrogen pressure was kept constant by manual pressure regulation. The buoyancy of the sample was also measured for corrections.

Additional, the hydrogen amount can roughly be determined by weighing large size of samples before and after hydrogenation. The size of difference in mass will be about twice as big, if deuterium is used for hydrogenation instead of hydrogen.

2.6. Electronic structure by first principles calculations

Density functional theory (DFT) calculations were performed with the Vienna Ab-initio Simulation Package (VASP) [165–167], using projector augmented wave (PAW) pseudopotentials [168, 169] and the Perdew-Burke-Ernzerhof (PBE) exchange-correlation functional [170]. Further details of the calculation methods are described in the experimental parts of the respective publications (see [4] in Section 11.6 and [7] in Section 14.4.5).

2.7. Molar volume increments of hydrogen atoms

The volume increments of hydrogen in hydrides are different depending on their bonding situation and due to the extraordinary polarizability of hydrogen atoms. The volume increment of hydrogen can be calculated from the unit cell volume of the hydrides (Eq. (4)). For the calculations, ionic increments of metal cations are used from the table after BILTZ [171] and atomic increments are taken from [142], calculated from elemental structures or the hydrogen free intermetallics.

$$V_{(\text{H})} = \frac{V_{\text{unit cell}} \, N_A - \sum_{\text{atom}}[V_{(\text{atom})} \, \text{multiplicity}_{(\text{atom})}]}{\text{multiplicity}_{(\text{H})}} \tag{4}$$

2.8. Magnetism

The magnetism of selected compounds was investigated by temperature dependent magnetic susceptibility measurements. The sample was placed in a gelatin capsule and inserted in a MPMS 7XL SQUID magnetometer (QUANTUM DESIGN). The measurement was executed with applied magnetic fields of 0.01, 0.02 and 0.05 T and temperatures from 2 to 330 K. The diamagentic contribution of the sample holder was corrected with the program package DAVE [172]. The reciprocal molar suszeptibility (χ_{M}^{-1}) was plotted against the temperature (T) and the magnetic parameters (Curie temperature θ_{C} and Curie constant C) were calculated by a linear regression according to the Curie-Weiss-law (Eq. (5)) in the case of paramagnetic samples. In addition, the effective magnetic moment (μ_{eff}) is calculated from the Curie constant.

$$\chi_{\text{M}}^{-1} = \frac{1}{C} \, T - \frac{\theta_{\text{C}}}{C} \qquad \qquad \mu_{\text{eff}} = \sqrt{\frac{3 \, k_{\text{B}} \, C}{\mu_0 \, N_{\text{A}}}} \tag{5}$$

2.9. Chemical stability

The stability of hydrides against air was investigated by additional X-ray diffraction after storing time in air for days to months. The stability of compounds against organic solvents, water and acids or rather their solubility was tested in micro test tubes. Additional XRPD was carried out on poorly soluble compounds to exclude that they react with the liquids.

2.10. Catalytical experiments

Catalytical invesigations were perfomed on $Pd_{11}Bi_2Se_2$, which is a phase pure sample without contaminants from the synthesis, e. g. no iodine additives were used, and which does not form hydrides. The catalysis of the semi-hydrogenation of acetylene was tested. Catalytic experiments were conducted in a plug flow reactor consisting of a quartz glass tube (7 mm inner diameter, 300 mm length) and a sintered glass frit as catalyst bed with the flow conditons of 14 ml min^{-1} helium gas, 20 ml min^{-1} ethen, 1.4 ml min^{-1} acetylene and 2 ml min^{-1} hydrogen gas. This yields in a total flow of 0.5 % C_2H_2, 5 % H_2 and 50 % C_2H_4. A pill of the catalysator material ($\approx$ 0.6 g) was transferred into the reactor. The temperature during the catalysis was 473 K. The conversion of acetylene and the selectivity to ethylene were calculated (Eq. (6)) and plotted against time.

$$X_{C_2H_2} = \frac{c_{\text{feed}} - c_x}{c_{\text{feed}}} \qquad \qquad S_{C_2H_4} = \frac{c_{C_2H_4}}{c_{C_2H_4} + c_{C_2H_6} + c_{C_4H_x}} \tag{6}$$

3. Hydrogenation of binary palladium-rich compounds

This chapter deals with the hydrogenation properties of binary palladium-rich compounds. In the beginning, hydrides of $M\mathrm{Pd_3}$ compounds are described focusing on the diversity of their structures. Special attention is given to their derivation from close packings and the investigation of hydrogenation pathways by *in situ* methods. Afterwards, the hydrogenation behavior of $M\mathrm{Pd_2}$ compounds of the $\mathrm{Co_2Si}$ type structure is discussed. Special emphasis is put on the hydrogenation process of $\mathrm{MgPd_2}$. At the end of this chapter, further binary palladium-rich and other palladium containing compounds, that were tested for hydrogenation, are taken into account. An overview of ternary ordered palladium-rich hydrides are given in Section 8.6 (review [1]).

Compounds $M\mathrm{Pd_3}$ (M = Mg [46, 126], In [127], Tl [88], Y [128], Mn [129], Ce [130]) and $M\mathrm{Pd_2}$ (M = Sr [124], Eu [113]) are known to form hydrides, whereas $M\mathrm{Pd_2}$ (M = Al, Ga, In), $\mathrm{Pd_3Al}$, $\mathrm{Pd_{13}Ga_5}$, $\mathrm{Pd_5In_3}$ [76], and $\mathrm{Pd_5As}$ do not show a significant hydrogen uptake. This work reports on further compounds whose hydrogenation behavior is investigated (Table 3.0.1).

The Laves phase $\mathrm{EuPd_2}$ with 2.1 hydrogen atoms per formula unit absorbs the most hydrogen [113]. Hydrogen occupies tetrahedral interstices. The majority of the reported ternary palladium-rich hydrides crystallize in stacking variants of the cubic closed packing (ccp). $\mathrm{MgPd_3}$ crystallizing in $\mathrm{ZrAl_3}$ type has the second highest hydrogen uptake [2]. In contrast to Laves phase hydrides, hydrogen occupies $[\mathrm{Pd_6}]$ and in specific cases $[M\mathrm{Pd_5}]$ (M = Mg, Mn) as well as $[\mathrm{Mg_2Pd_4}]$ octahedral voids (Fig. 3.0.1). Solely palladium consisting octahedral sites are preferred to the other interstices. Binding states at low energies were calculated to be dominated almost exclusively by palladium and hydrogen through hydrogen uptake. The increase of the number of $[\mathrm{Pd_6}]$ octahedral sites from $\mathrm{TiAl_3}$

Table 3.0.1.: Section of the periodic table's main group elements of palladium containing compounds that were observed to form hydrides (green from literature, blue from own work) or show no significant hydrogen uptake (red from literature, orange from own work).

period	group 2	group 13	group 14	group 15	group 16
3	$\mathrm{MgPd_2D_{0.97}}$ [4], $\mathrm{MgPd_3D_{1.18}}$ [2], $\mathrm{MgPd_3D_{0.67}}$ [46]	$\mathrm{Pd_2Al}$ [76], $\mathrm{Pd_3Al}$ [76]		$\mathrm{Pd_3P_{0.8}D_{0.15}}$ [173], $\mathrm{Pd_6PD_{0.26}}$ [54], $\mathrm{Pd_{15}P_2D_{0.46}}$ [174]	
4	$\mathrm{CaPd_3H_x}$ [125]	$\mathrm{Pd_2Ga}$ [76], $\mathrm{Pd_{13}Ga_5}$ [76]		$\mathrm{Pd_3As}$ [5], $\mathrm{Pd_5As}$ [71]	$\mathrm{Pd_{17}Se_{15}}$ [5], $\mathrm{Pd_4Se}$ [5]
5	$\mathrm{SrPd_2H}$ [124]	$\mathrm{Pd_2In}$ [76], $\mathrm{InPd_3D_{0.89}}$ [127]	$\mathrm{Pd_2Sn}$ [5], $\mathrm{SnPd_3D_{0.138(7)}}$	PdSb [5], $\mathrm{Pd_5Sb_2}$ [5], $\mathrm{Pd_8Sb_3}$ [5], $\mathrm{Pd_{20}Sb_7}$ [5]	
6		$\mathrm{TlPd_3H}$ [88]	$\mathrm{Pd_{13}Pb_9}$ [5], $\mathrm{Pd_5Pb_3}$ [5], $\mathrm{PbPd_3D_{0.13}}$ [3]	$\mathrm{Pd_5Bi_2}$ [5], $\mathrm{BiPd_3D_{0.23}}$ [3]	
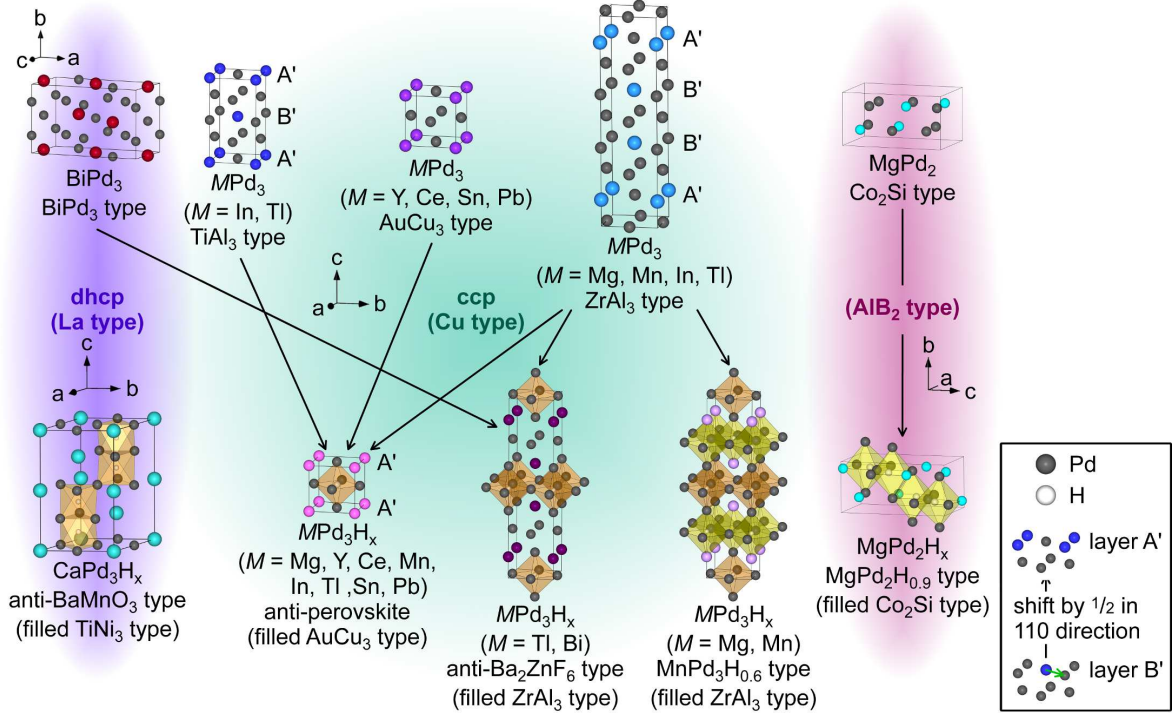
Figure 3.0.1.: Structures of palladium-rich hydrides with hydrogen occupying $[Pd_6]$ (orange polyhedra) and $[MPd_5]$ (yellow polyhedra) octahedral sites. $BiPd_3$ and $CaPd_3H_x$ (no intermetallic starting material known, [125]) are related to double hexagonal closed packing (dhcp, La type, purple background, [3]); MPd_3 and MPd_3H_x (M = Mg [46, 126], Y [128], Ce [130], Mn [129], In [127], Tl [88], Sn, Pb [3], Bi [3]) are related to ccp (Cu type, turquoise background, [75]) and rearrange from $TiAl_3$ or $ZrAl_3$ type to $AuCu_3$ type trough a gliding mechanism of plane B' shifted by $^1/_2$ in 110 direction [75]; $MgPd_2$ and $MgPd_2H_x$ are related to AlB_2 type (pink background, [4]).

type or $ZrAl_3$ type to $AuCu_3$ type and the preference of Pd-H bonding reveals the thermodynamic driving force of the rearrangement between these ccp related MPd_3 compounds [126, 131].

The interatomic Pd-H distances range from 1.94 - 2.11 Å for $[Pd_6]$ and 1.84 - 2.11 Å for $[MPd_5]$ sites (Table 3.0.2), which are in agreement to 2.017 Å of $PdD_{0.66}$ [175]. As the M atoms are usually not in the first coordinations sphere, the M-H distances are markedly larger than 3 Å, except for M = Mg, Mn ($d(M\text{-H})$ = 1.56 -2.27 Å) that are involved in the octahedral surrounding. The minimum H-H distances are about 4 Å for corner sharing, hydrogen-centered octahedra. That corresponds to the lattice parameters a of the hydrides. For edge sharing octahedra the minimum H-H distances are about 3 Å. In the case of $CaPd_3H_x$ ($d(\text{H-H})$ = 2.45 Å), its HPd_6 octahedra are face sharing. The M-Pd and Pd-Pd distances of the hydrides are all in same range as those observed in the intermetallic starting materials and, therefore, in the order of interatomic distances of pure palladium.

The amount of hydrogen atoms occupying these octahedral interstices depends on geometric and even more on electronic aspects of the element M. Thallium and indium or lead and tin have the same number of valence electrons, but in each case the larger atom by means of atomic or metallic radii allows a higher hydrogen incorporation in MPd_3 compounds. Another example for the geometric influence are manganese and lead (as element M) that are similar in electronegativities, though $MnPd_3$ absorbs considerably more hydrogen than $PbPd_3$. However, the geometric factors do not describe the whole phenomenon, as e. g., manganese and tin are of similar atomic radius, but $SnPd_3$ absorbs only negligible amounts of hydrogen. Looking now at the valence electrons, M of group 13 (In,

Table 3.0.2.: Interatomic distances of intermetallics and their hydrides

compound	structure type	d(Pd-H) / Å	d(M-H) / Å	d(H-H) / Å	d(M-Pd) / Å	d(Pd-Pd) / Å
$MgPd_2$ [a] [4]	Co_2Si				2.573 - 2.871	2.682 - 2.941
$MgPd_2D_{0.86}$ [a] [4]	$MgPd_2H_{0.9}$	1.837 - 2.106	2.271	3.083	2.708 - 2.886	2.812 - 2.987
$MgPd_3$ [46]	$ZrAl_3$				2.702 - 2.837	2.768 - 2.776
$MgPd_3D_{1.18}$ [a] [2]	$MgPd_3H_{0.9}$	1.994 - 2.112	1.757 - 2.08	2.819	2.657 - 3.015	2.819 - 2.904
$MgPd_3D_{0.67}$ [46]	anti-perovskite	1.991	3.449	3.982	2.816	2.816
$CaPd_3H_x$ [125]	anti-$BaMnO_3$	2.028 - 2.088 [b]	3.598 [b]	2.445 [b]	2.931 - 3.016	2.802 - 3.060
$InPd_3$ [76]	$ZrAl_3$				2.721 - 2.877	2.783 - 2.876
$InPd_3$ [76]	$TiAl_3$				2.775 - 2.899	2.775 - 2.899
$InPd_3D_{0.89}$ [127]	anti-perovskite	2.011	3.484	4.023	2.844	2.844
$TlPd_3$ [88]	$ZrAl_3$				2.796 - 2.904	2.777 - 2.904
$TlPd_3$ [89]	$TiAl_3$				2.795 - 2.932	2.795 - 2.932
$TlPd_3H_{\approx0.2}$ [c] [88]	anti-Ba_2ZnF_6	2.017 - 2.057	3.531	4.114	2.757 - 2.909	2.747 - 2.909
$TlPd_3H$ [88]	anti-perovskite	2.032	3.519	4.063	2.873	2.873
$SnPd_3$ [a] [5]	$AuCu_3$				2.813	2.813
$SnPd_3H_{\approx0.1}$ [a] [5]	anti-perovskite	1.990	3.448	3.981	2.815	2.815
$PbPd_3$ [a] [3]	$AuCu_3$				2.853	2.853
$PbPd_3D_{0.13}$ [a] [3]	anti-perovskite	2.020	3.499	4.040	2.857	2.857
$BiPd_3$ [a] [3]	$BiPd_3$				2.716 - 3.041	2.485 - 3.252
$BiPd_3D_{0.23}$ [a] [3]	anti-Ba_2ZnF_6	2.000 - 2.024	3.606	4.047	2.819 - 2.985	2.845 - 2.957
YPd_3 [176]	$AuCu_3$				2.881	2.881
$YPd_3H_{0.3}$ [176]	anti-perovskite	2.040	3.533	4.080	2.885	2.885
$CePd_3$ [130]	$AuCu_3$				2.917	2.917
$CePd_3H$ [130]	anti-perovskite	2.068	3.581	4.135	2.924	2.924
$MnPd_3$ [d] [129]	$ZrAl_3$				2.757	2.752 - 2.763
$MnPd_3D_{0.61}$ [d] [129]	$MnPd_3H_{0.6}$	1.900 - 1.976	1.952	2.798	2.711 - 2.866	2.769 - 2.806
$MnPd_3D_{0.7}$ [d] [177]	anti-perovskite	1.963	3.400	3.926	2.776	2.776

[a] part of this thesis

[b] distances calculated by assuming occupation of [Pd_6] octahedral sites (Wyckoff position 4f: $2/3$, $1/3$, $1/8$) by hydrogen.

[c] distances determined by refinement of data "5-phase mixture, 730 °C, 12 h, 7.5% H_2/Ar, 1bar" of [88]

[d] metal atoms are slightly disordered (0.077 - 0.156 Pd on Mn site and 0.026 - 0.052 Mn on Pd sites) [129, 177]

Tl) results in a higher hydrogen uptake compared to M of group 14 (Sn, Pb). By contrast, $BiPd_3$ absorbs almost twice as much hydrogen as $SnPd_3$ or $PbPd_3$. A general trend based on valence electron concentration can therefore not be identified. The electronegativities of the elements M seem to affect the hydrogenation properties more than geometry. Electronegativities of M similar to palladium promote a hydrogen uptake. Thus, the electronic and the geometric aspects were associated by a structure map (Fig. 8.6.4 of Section 8.6.2 in [1]). However, this map does not apply to transition metals, e. g. zirconium is very similar in electronegativity and atomic radius to magnesium, but $ZrPd_3$ does not take up hydrogen in contrast to $MgPd_3$ (see Section 3.1.5). Quantum-mechanical calculation show the hydrogenation to be exergonic for $MgPd_3$, weak exergonic for $ScPd_3$ and endergonic for $ZrPd_3$ Chapter 16.

A series of bonding properties as for the hydrides of the system Eu-Pd (Section 1.2) can be established also for hydrides of the system Mg-Pd. The magnesium amount and, therefore, the valence electron concentration (VEC, after SCHUBERT [178]) decreases in the series MgH_2 - Mg_2PdH_4 - $MgPd_2H$ - $MgPd_3H$ - PdH. The hydrogen atoms in MgH_2 have besides ionic already strong covalent bonding characters [179, 180]. Calculations of Mg_2PdH_4 [180, 181] in the well known Mg_2NiH_4 type [182] yields a complex hydride. It is a typical 18 valence electron complex. The compound was not found experimentally yet, but a cubic Mg_2PdH_4 (a = 12.047 Å, structure only indexed) was observed by decomposition of Mg_4Pd at 9 MPa hydrogen pressure and temperatures of 650 K with MgH_2 as side product [183]. A closer look on the hydrogen bonding behavior in the system Mg-Pd results in the order MgH_2 - Mg_2PdH_4 - PdH - $MgPd_2H$ - $MgPd_3H$, though the number of hydrogen per palladium atoms and the interatomic Pd-Pd decrease whereas the minimum H-H distances increases (Table 3.0.3). The Pd-Pd distances of Mg_2PdH_4 are larger than 4 Å [181]. That makes Pd-Pd interactions very unlikely, and their Pd-H bonding is of covalent nature. In contrast, metallic Pd-Pd and Pd-H interactions

Table 3.0.3.: Comparison of properties with regard to bonding behavior of the hydrides in the system Mg-Pd based on *ab initio* calculations [4, 97, 131, 179–181, 184–186]

compound	MgH$_2$	Mg$_2$PdH$_4$	PdH	MgPd$_2$H	MgPd$_3$H
structure type	rutile	Mg$_2$NiH$_4$	NaCl	MgPd$_2$H	anti-perovskite
VEC after Schubert	1.33	1.14	0.50	0.75	0.60
VEC [a]	1.33	2.57	5.5	5.75	6.6
N_{EF} / states eV^{-1} atom^{-1}	-	-	0.06 [184, 185]	0.23 [4]	0.59 [97]
E_g / eV	3.8 [179, 180]	1.72 [180]	-	-	-
d(Pd-Pd) / Å	-	$\geq$ 4.35 [181]	2.88 [185] - 2.96 [186]	2.85 - 3.01 [4]	2.78 [131] - 2.84 [97]
d(H-Pd) / Å	-	1.70 - 1.76 [180, 181]	2.04 [185] - 2.09 [186]	1.86 - 2.15 [4]	1.97 [131] - 2.01 [97]
d_{min}(H-H) / Å	-	2.42 [181]	2.88 [185]	3.10 [4]	3.93 [131]
$V_{(H)}$ / cm^3 mol^{-1}	8.28 [b]	8.18 [181] [b]	1.33 [185] - 2.01 [186] [b]	1.86 [4] [c]	1.46 [97] - 1.63 [131] [c]

[a] each Pd atom introduces ten valence electrons for VEC calculation

[b] calculated with $V_{(Mg2+)}$ = 2.0 cm^3 mol^{-1} and $V_{(Pd)}$ = 8.9 cm^3 mol^{-1} [142]

[c] calculated by difference between volume of hydride and intermetallic compound (see Section 2.7)

are observed for the palladium-rich representatives. Additionally, the density of states (DOS) at the Fermi level (N_{EF}) increases from PdH via MgPd$_2$H to MgPd$_3$H. That indicates an improvement of the electrical conductivity. For MgPd$_3$H$_{0.5}$ in ZrAl$_3$ type with fully occupied [Pd$_6$] octahedral sites, an even greater DOS at the Fermi level (N_{EF} = 0.64 states eV^{-1} atom^{-1}) was calculated [97]. MgH$_2$ and Mg$_2$PdH$_4$ show a band gap (E_g) of 3.8 [180, 181] and 1.72 eV [180], respectively. The trend of the bonding behavior of hydrogen is also supported by the calculation of molar volume increments ($V_{(H)}$ [142]), with the exception of PdH, which differs strongly by the different calculations. For the calculation of the molar volume of the H atoms of MgPd$_2$H and MgPd$_3$H, the volume increment of the ion Mg^{2+} ($V_{(Mg^{2+})}$) can not be used, because Mg atoms show mainly metallic behavior. The calculated value obtained from the elemental structure of magnesium can also not be used, because the volume increment of Mg is too large resulting in negative values for $V_{(H)}$. Therefore, the molar volume of the H atoms was calculated by the difference of the unit cell volume between the hydrides (MgPd$_2$H and MgPd$_3$H) and the hydrogen free intermetallics (MgPd$_2$ and MgPd$_3$). Alternatively, the volume increment of a Mg atom in the intermetallics can be calculated and used subsequently for the calculation of $V_{(H)}$. The former values do not differ significantly to the latter. The greater the molar volume of the hydrogen atoms, the more ionic is the bonding. Lower values indicate more metallic bonding character.

3.1. *M*Pd$_3$ compounds

Most structures of the *M*Pd$_3$ compounds are related to the ccp (Fig. 3.0.1). Firstly, MgPd$_3$, MnPd$_3$ crystallizing in ZrAl$_3$ type, and forming hydrides in filled ZrAl$_3$ as well as AuCu$_3$ type, are discussed, followed by InPd$_3$ and TlPd$_3$ crystallizing in ZrAl$_3$ and TiAl$_3$ type. Afterwards, hydrides of palladium-rich compounds of the AuCu$_3$ type and / or with transition metals are described, followed by BiPd$_3$ and CaPd$_3$H with relations to dhcp. Finally, Pd$_3$As that does not form a hydride, is listed for completeness.

3.1.1. MgPd$_3$

MgPd$_3$ crystallizes in tetragonal ZrAl$_3$ type structure [45] and incorporates hydrogen in [Pd$_6$] as well as in [MgPd$_5$] and [Mg$_2$Pd$_4$] octahedral voids [126]. The structures of these metastable tetragonal α-MgPd$_3$H$_x$ phases and the occupation by hydrogen of these various octahedral sites were determined by sequential Rietveld refinement based on *in situ* neutron powder diffraction at isothermal conditions (see Chapter 9, [2]). During the isothermal hydrogenation (297 K, 1.0 MPa deuterium pressure), at first, [Pd$_6$] and [MgPd$_5$] octahedral sites were occupied by about one half and one quarter, respectively (Fig. 3.1.1). This hydrogen uptake results in a characteristic volume expansion. Lattice parameter a expands more than c caused by the occupation of [MgPd$_5$] octahedral sites that are edge sharing within a-b plane. The size of [Mg$_2$Pd$_4$] octahedral voids increases with the lattice expansion and a noticeable occcupation (site occupancy factor SOF(D) > 2 σ(SOF)) begins only when Mg-D distances became larger than 1.96(3) Å. However, the SOF of hydrogen on [Mg$_2$Pd$_4$] octahedral sites are always less than one quarter under hydrogen pressures up to 1.0 MPa. At higher temperatures ($T \approx 550$ K) under 0.5 MPa hydrogen pressure MgPd$_3$H$_x$ rearranges to the AuCu$_3$ type with hydrogen occupying only [Pd$_6$] octahedral sites [126]. This transition can be formally understood as a gliding of the atomic layers B' by $^1/_2$ in **[110]** direction resulting in the layers A' (Fig. 3.0.1). This transition is irreversible [46]. The formed β-MgPd$_3$H$_x$ is more stable than α-MgPd$_3$H$_x$ due to stronger Pd-H interactions [97]. As a result another MgPd$_3$ polymorph crystallizing in AuCu$_3$ type, called β-MgPd$_3$, can be formed by dehydrogenation of the cubic β-MgPd$_3$H$_x$.
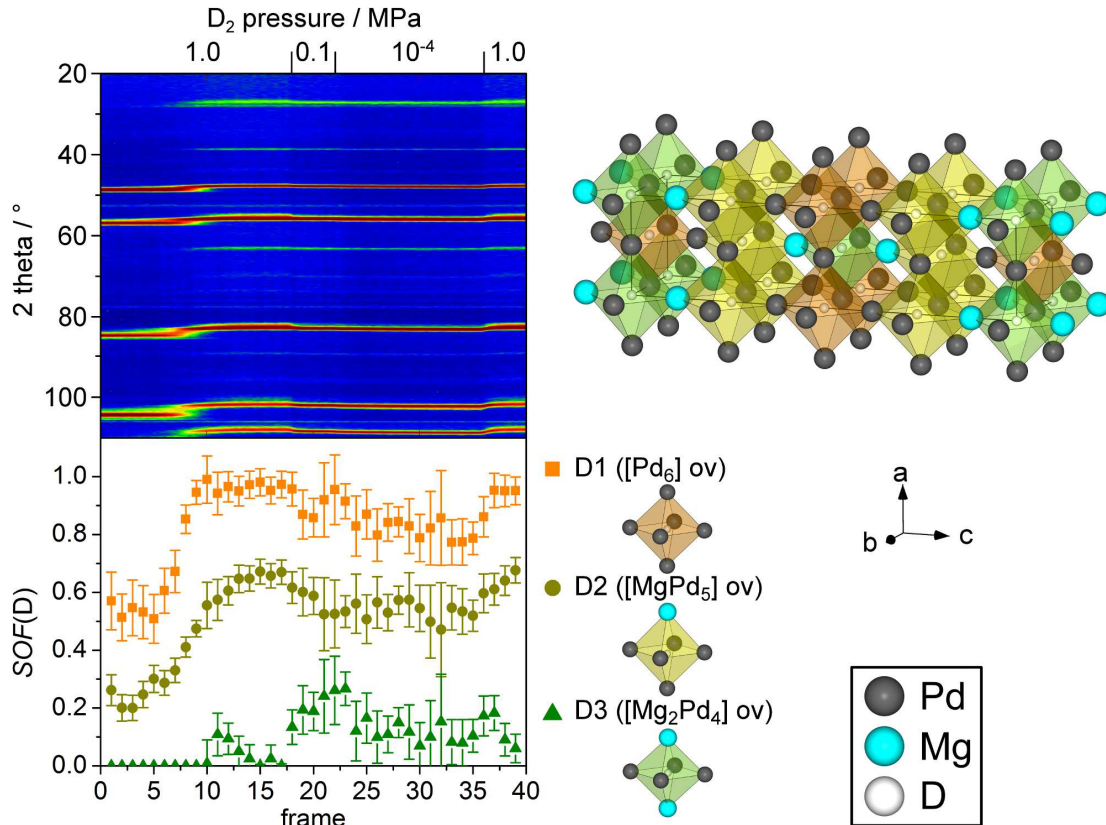
Figure 3.1.1.: *In situ* neutron powder diffraction data of the hydrogenation of tetragonal MgPd$_3$ at 297 K taken on diffractometer D20 (ILL, Grenoble, $\lambda = 1.86786(3)$Å) in a leuco-sapphire single crystal cell. The site occupancy factors (SOF) of the deuterium atoms were refined based on diffraction data of each frame (6 min data collection time).

Table 3.1.1.: Degree of disorder in mostly ordered MnPd$_3$ compound and its hydrides. Site occupancy factors (SOF) of the minority component is shown.

compound	structure type	SOF(Pd) at Mn site	SOF(Mn) at Pd site	literature
MnPd$_3$	ZrAl$_3$	0.156	0.052	[129]
MnPd$_3$D$_{0.61}$	MnPd$_3$H$_{0.6}$	0.141	0.047	[129]
MnPd$_3$D$_{0.7}$	anti-perovskite	0.077	0.026	[177]

3.1.2. MnPd$_3$

The hydrides of MnPd$_3$ were among the first known, mostly ordered, palladium-rich hydrides. Mostly ordered means, that Mn and Pd atoms are occupying separate crystallographic sites, though with a slight mixed occupation of about 15 % (Table 3.1.1). This phenomenon is caused by the similarities in size and electronegativity of Mn and Pd atoms and leads to a relatively large phase width from MnPd$_3$ up to Mn$_{1.2}$Pd$_{2.8}$ for the tetragonal structure [187]. In the interest of clarity, MnPd$_3$ compounds with a high degree of atomic order are labeled as ordered in the following. Disordered MnPd$_3$ crystallizes in Cu type. By annealing at temperatures below 800 K it changes to ZrAl$_3$ type [188]. Both phases can take up hydrogen [129]. The disordered phase (Cu type) absorbs hydrogen with a subsequent formation of ordered AuCu$_3$ type. This transition is reversible by removing incorporated hydrogen [189]. The disordered MnPd$_3$ can take up less hydrogen in comparison to the ordered hydrides (filled ZrAl$_3$ and AuCu$_3$ type) [129, 177, 189].

The magnetic properties of MnPd$_3$ are especially interesting, because Pd atoms are determined to have no ordered magnetic moment [188] on the one hand. On the other hand, magnetic moments on Mn atoms were found to be 7.3 μ_B in disordered cubic Pd$_{0.75}$Mn$_{0.25}$ [190, 191] (corrected by [192]), 5.2 μ_B in tetragonal MnPd$_3$ [188], 4.8 μ_B at 4 K in tetragonal MnPd$_3$D$_{0.53}$ [193] and 4.1 μ_B at 1.5 K in tetragonal MnPd$_3$D$_{0.6}$ [177]. The magnetic moments of the disordered Mn atoms at Pd sites agree with them on the Mn sites [188]. The tetragonal structures show a collinear antiferromagnetic ordering of the type $+--+$ [188, 193].

3.1.3. InPd$_3$

InPd$_3$ crystallizes in ZrAl$_3$ type and TiAl$_3$ type. During the hydrogenation both tetragonal structures rearrange to the cubic AuCu$_3$ type. For the TiAl$_3$ type the same gliding mechanism can be utilized as for ZrAl$_3$ type, however, only one B' layer per unit cell is gliding during hydrogenation [75, 76] (Fig. 3.0.1). A deuterium amount of 0.89 per formula unit was determined for cubic InPd$_3$ [127]. Interestingly, no hydrogen uptake of the tetragonal structures, especially of ZrAl$_3$ type containing [Pd$_6$] octahedral voids, was observed by neutron diffraction. Only a very small exothermic peak at about 350 K of *in situ* DSC indicates a hydrogen uptake [76]. InPd$_3$H$_x$ can alternatively be formed by decomposition at hydrogen pressure and subsequent hydrogenation of the tetragonal compounds Pd$_5$InSe and Pd$_8$In$_2$Se (see Chapter 4 and Chapter 12, [5]).

3.1.4. TlPd$_3$

There are also two tetragonal modification of TlPd$_3$, ZrAl$_3$ and TiAl$_3$ type, are known [89,194]. In contrast to InPd$_3$, α-TlPd$_3$ (ZrAl$_3$ type) takes up hydrogen, before it rearranges to cubic AuCu$_3$ type. This two step reaction was also observed by *in situ* DSC sharing two broad exothermic signals. The hydrogenation of TlPd$_3$ in TiAl$_3$ type was not investigated, yet. In cubic TlPd$_3$H, the [Pd$_6$] octahedral site is fully occupied by hydrogen. This is currently the only known hydride of MPd$_3$ compounds, that forms a fully occupied anti-perovskite type structure. As an alternative synthesis of this hydride, the reduction under hydrogen pressure of TlPd$_3$O$_4$ is reported [88].

3.1.5. AuCu$_3$ type and transition metal compounds

The binary compounds YPd$_3$ and CePd$_3$ crystallize in AuCu$_3$ type structure. The pre-existing [Pd$_6$] octahedral voids are occupied by hydrogen during hydrogenation and the unit cell expands by 0.4 % for YPd$_3$H$_{0.3}$ and 0.7 % for CePd$_3$H$_x$. A filled AuCu$_3$ type, better described as defect anti-perovskite is formed. Further isotypic compounds were investigated towards their hydrogenation properties. SnPd$_3$ and PbPd$_3$ as candidates showed similar volume expansions of 0.4 % and 0.6 % after hydrogenation. The composition of SnPd$_3$D$_{0.138(7)}$ (see Chapter 16) and PbPd$_3$D$_{0.13(1)}$ (see [3] inChapter 10) was refined based on *ex situ* neutron powder diffraction data. The hydrogenation reaction of PbPd$_3$ and SnPd$_3$ is not detectable with *in situ* DSC under the tested conditions, because of slow kinetics and only a small hydrogen uptake (see [5] in Chapter 12).

Further palladium-rich compounds TPd$_3$ (T = Sc, Zr, V, Nb, Fe) were tested regarding their hydrogenation behavior [195]. FePd$_3$, crystallizing in ordered AuCu$_3$ type or disordered Cu type, was found to be the only one, which can take up hydrogen. It was also previously reported that the level of order affects the hydrogen uptake. A significantly higher hydrogen absorption is observed by compounds with a higher level of order [196]. ScPd$_3$ crystallizing in AuCu$_3$ type and ZrPd$_3$, VPd$_3$ and NbPd$_3$ crystallizing in TiNi$_3$ type did not show any reaction towards hydrogen [195]. The TiNi$_3$ structure is related to the double hexagonal closed packing (dhcp, La type, [3] in Chapter 10) and contains [Pd$_6$] octahedral voids, that are most likely occupied by hydrogen in the case of CaPd$_3$H$_x$ (see Section 3.1.7), but did not get experimentally verified, yet. We proposed a structure map that associates the electronegativities and the atomic radii of the minor elements with the incorporated hydrogen amount in MPd$_3$H$_x$ (Fig. 8.6.4 of Section 8.6.2 in [1]). This structure map does not hold for transition metals. Although magnesium, scandium and zirconium are very similar in electronegativity and atomic radius, MgPd$_3$ takes up a considerably higher amount of hydrogen compared to ScPd$_3$ and ZrPd$_3$, that absorbs only a little hydrogen to zero. Quantum-mechanical calculations support this Chapter 16. ScPd$_3$H and ZrPd$_3$H are less stable than MgPd$_3$.

3.1.6. BiPd$_3$

Orthorhombic BiPd$_3$ is different from the other MPd$_3$ compounds. It crystallizes in its own structure type [87, 194] derived from double hexagonal closed packing (dhcp, La type) and forms ZrAl$_3$ type during hydrogenation (see [3] in Chapter 10). BiPd$_3$ has the highest valence electron concentration (VEC = 1.25 after SCHUBERT [178]) of MPd$_3$ compounds. The coordination spheres of the atoms are not only cuboctahedra like for ccp related MPd$_3$, but also disheptahedra, which is also called anticuboctahedron. *In situ* investigations of BiPd$_3$ shows a weak, broad and irreversible exothermic DSC-signal at 580 K (5.0 MPa hydrogen pressure) and a structure transition to the ZrAl$_3$ type with hydrogen occupying [Pd$_6$] octahedral sites based on neutron powder diffraction. For example, BiPd$_3$D$_{0.19(1)}$ (defect anti-BaZnF$_6$ type) was refined (see Fig. 2.3.1 in Section 2.3.2). The rearrange-
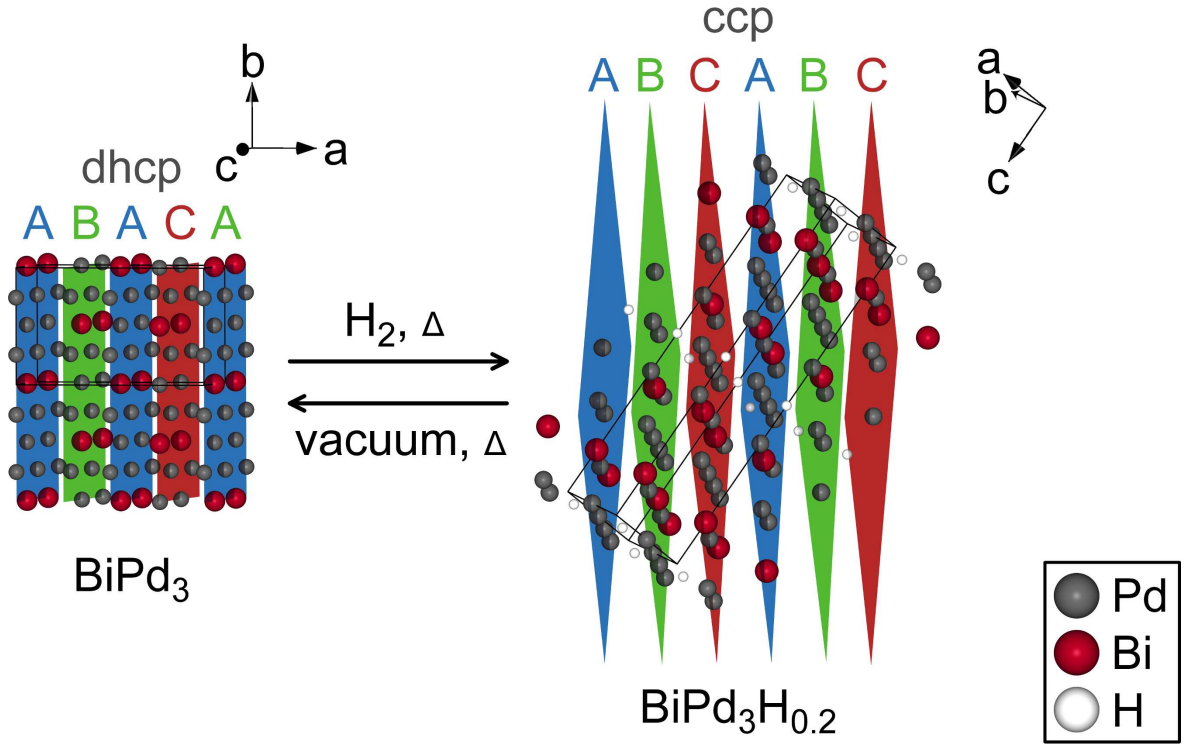
Figure 3.1.2.: Crystal structure of orthorhombic BiPd$_3$ (related to dhcp) and its reversible hydrogen induced rearrangement to BiPd$_3$H$_{0.2}$ (related to ccp).

ment from dhcp (ABAC,A . . .) to ccp (ABC,A . . .) can be described by gliding mechanism of the hexagonal layers (Fig. 3.1.2). However, a short range diffusion of the metal atoms is more likely, because of slow kinetics and high required temperatures (T > 550 K).

It is interesting to note that only a negligibly low hydrogen amount is sufficient for the change of structures. Quantum chemical calculations of BiPd$_3$ showed similarities in energy of BiPd$_3$ type (-20.631 eV formula unit^{-1}) to ZrAl$_3$ type (-20.633 eV formula unit^{-1}) [197] which enables us to understand this phenomena. The rearrangement is accompanied by a volume expansion, whereby the unit cell volume increases more at higher hydrogen pressures. This is a consequence of an increased hydrogen amount incorporated by the intermetallic. The hydrogenation of BiPd$_3$ is reversible at high temperatures (T > 450 K) and applied vacuum with comparable slow kinetics.

3.1.7. CaPd$_3$

The intermetallic compound CaPd$_3$ does not exist, but the hydride CaPd$_3$H$_x$ is formed by the reaction of the binary hydrides CaH$_2$ and PdH$_x$. It crystallizes in a filled TiNi$_3$ type and hydrogen is most-likely occupying the [Pd$_6$] octahedral sites [125]. CaPd$_3$H$_x$ is the only yet known TiNi$_3$ type hydride.
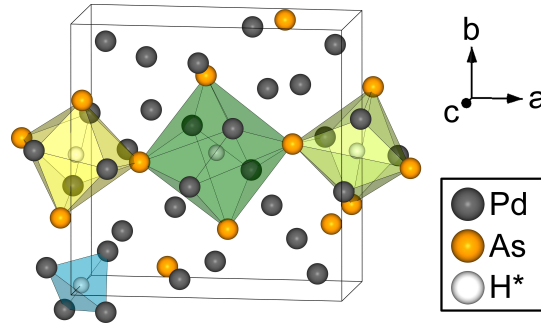
Figure 3.1.3.: Crystal structure of Pd_3As with suitable hydrogen positions (H*) and their coordination polyhedra at Wyckoff positions $2a$ (0, 0, 0, dark green polyhedra), $2b$ (0, 0, $^1/_2$, blue tetrahedra), $2c$ (0, $^1/_2$, $^1/_4$, light green polyhedra) and $2d$ (0, $^1/_2$, $^3/_4$, yellow polyhedra).

3.1.8. Pd_3As

Although Pd_3As does not belong to intermetallics (see Section 1.1 for definition), its crystal structure and hydrogenation properties were still determined (see [5] in Chapter 12). Pd_3As crystallizes in Ni_3P type. Interesting for a possible hydrogen incorporation are several $[Pd_4]$ tetrahedral voids (Wyckoff positions $2a$, b, c, d, see Fig. 3.1.3). The void at Wyckoff position $2b$ (0, 0, $^1/_2$) is solely surrounded by four Pd atoms with a □-Pd distance of 1.788 Å. The remaining $[Pd_4]$ tetrahedral sites are slightly larger (d(□-Pd) = 1.778 - 1.892 Å), but they are surrounded by additional four As atoms (d(□-As) = 2.472 - 2.847 Å) forming a second tetrahedron. The distances between palladium and the hypothetical hydrogen sites are comparable to those observed in $Pd_{15}P_2D_{0.46}$ (d(D-Pd) = 1.515 - 1.953 Å) [174], however, no hydrogenation of Pd_3As was observed [5].

3.2. Hydrogenation of MPd$_2$ compounds of Co$_2$Si type

Compounds of the composition MPd$_2$ (M = Mg, Zn, Al, Ga, In, Sn) crystallize in the Co_2Si type which belongs to the anti-PbCl$_2$ family. Both structures are not isotypic due to their diffrent axial ratios [198, 199]. The M atom of these compounds is coordinated by ten palladium atoms. The coordination polyhedron can be described as a distorted tetragonal prism that is capped on two faces. However, it can be alternatively seen as a trigonal prism that is capped by four additional palladium atoms in a plane, but the magnesium atom is not located in the center of the prism [45]. The latter demonstrates better the similarity to TiNiSi compounds, which contain corrugated layers of capped trigonal prisms within ab plane (Fig. 3.2.1). Several TiNiSi type compounds like LnTSn are known to incorporate hydrogen into $[Ln_3 T]$ tetrahedral interstices [200–202]. The unit cell of for example TbNiSn [202] expands anistropically during the hydrogenation. The distorted tetrahedral voids between the trigonal SnTb$_4$Ni$_2$ prisms are occupied by hydrogen. The HTb$_3$Ni tetrahedra are forming zigzag chains by edge-sharing in **[010]** direction (Fig. 3.2.1, bottom left). Therefore, the angles between the edge-sharing prisms decrease from 104° to 100° and the tin atoms in the prisms get off-centered resulting in lattice parameter c increases whereby b decreases and a decreases slightly (Fig. 3.2.1, left).

In contrast to TiNiSi compounds, MPd$_2$ (M = Zn [4], Al [76], Ga [76], In [76], Sn [5]) do not show a significant hydrogen absorption. Only MgPd$_2$ takes up hydrogen, though not in $[Pd_4]$ tetrahedral voids, but in distorted $[MgPd_5]$ octahedral voids (see [4] in Chapter 11). The main reason for the different hydrogenation behaviors of MPd$_2$ compounds is of thermodynamic nature shown by *ab initio* calculations. The hydrogenation of MgPd$_2$ shows a similar anisotropically lattice expansion compared
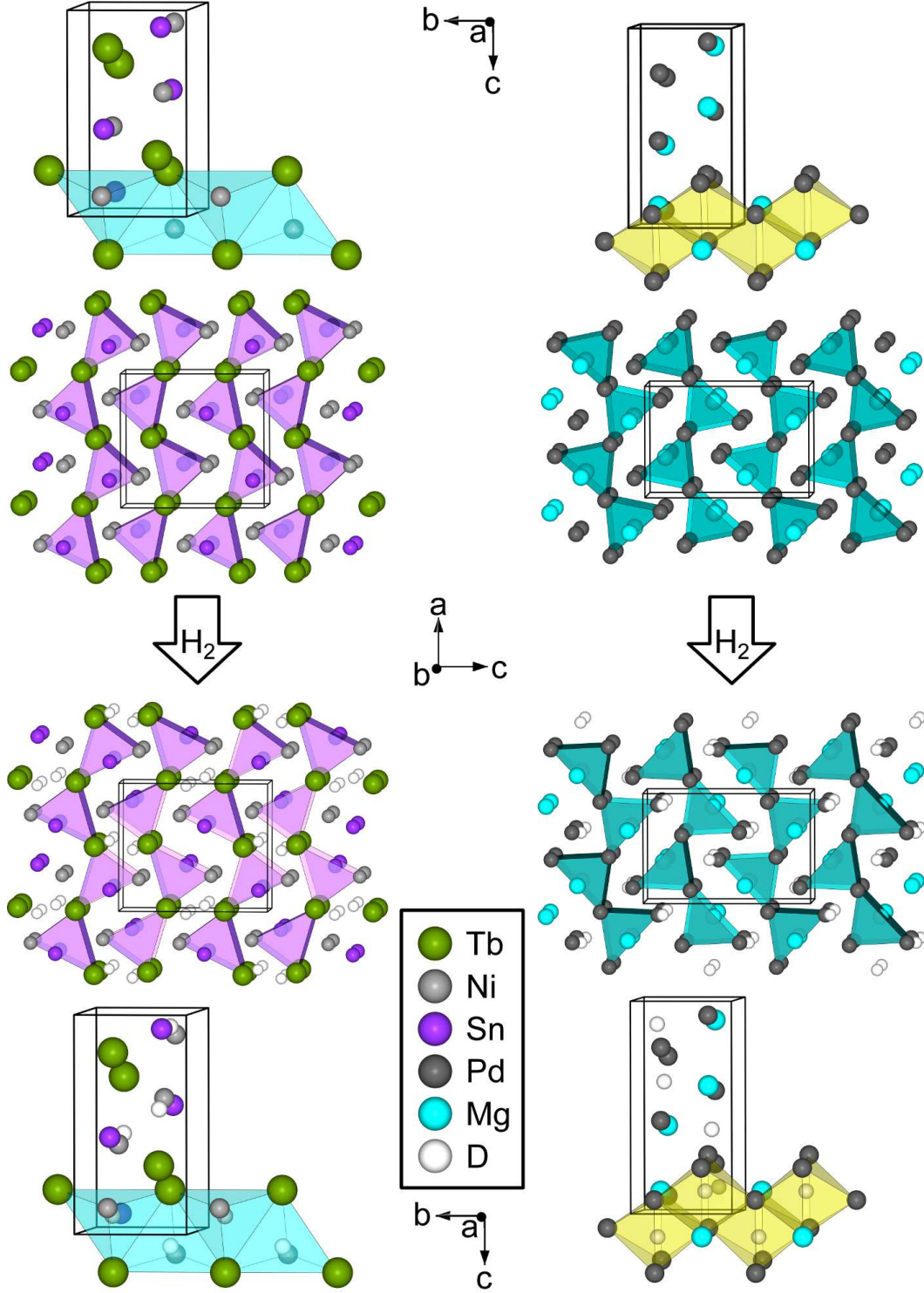
Figure 3.2.1.: Comparison of the structures of TbNiSn [203] (TiNiSi type, left) and MgPd₂ [45] (Co₂Si type, right) and their hydrides [4, 202]. Intermetallics (top) with empty and hydrides (bottom) with occupied distorted tetrahedral (light blue polyhedra) and octahedral sites (yellow polyhedra) with viewing direction perpendicular to *bc* plane and currugated layers of distorted trigonal SnTb₄Ni₂ (purple polyhedra) and MgPd₆ (blue polyhedra) prisms of the intermetallics (top middle) and their hydrides (bottom middle) with viewing direction perpendicular to *ac* plane (offset by ¹/₂ in **[010]** direction of neighboring layers).

to TiNiSi compounds. However, hydrogen occupies the distorted octahedral voids along the edges of the trigonal prism that are not linked. Therefore, the Mg-Pd distance around the hydrogen atom increases and the angles between the edge-sharing prisms decrease from 96° to 84°(Fig. 3.2.1, right). Thus, the lattice parameters c and a increase whereby b decreases. The HMgPd$_5$ octahedra form also zigzag chains by edge-sharing in **[010]** direction and they are additionally linked by corners (Fig. 3.2.1, bottom right). The edge-sharing of HMgPd$_5$ octahedra is also observed in α-MgPd$_3$H$_x$ [2,126].

The hydrogenation pathway of MgPd$_2$ was followed by *in situ* DSC (Fig. 3.2.2), *in situ* neutron powder diffraction (see [4] in Chapter 11) as well as gravimetric and volumetric sorption experiments (Chapter 17). The hydrogenation of MgPd$_2$ takes place at a hydrogen pressure of several hundred kPa and is reversible due to hydrogen release at applied vacuum. The hydrogen amount of the hydride can be almost one, which means the distorted octahedral site is fully occupied. The composition MgPd$_2$H$_{0.97(1)}$ was determined by *in situ* neutron diffraction ($T = 308$ K, p(H$_2$) = 2.56 MPa), MgPd$_2$H$_{1.0(1)}$ by gravimetric analysis and MgPd$_2$H$_{0.87(4)}$ by hydrogen sorption experiments. At the beginning of the hydrogenation, octahedral interstisies are occupied by 20 to 30 % with a considerable volume expension resulting in lattice parameters that are similar to those of the hydride with nearly fully occupied octahedral sites. A similar observation was made by the *in situ* hydrogenation studies of BiPd$_3$ (see Section 3.1.6). During the dehydrogenation under applied vacuum, the lattice parameters of the compound do not reach those from the intermetallic starting material. This is an indication of remaning hydrogen, although, sorption experiments did not confirm this. Subsequent hydrogenations show an almost complete filled octahedral site from the beginning of hydride formation. This observation is in contrast to the first hydrogenation of the starting material and supports the presumption of remainig hydrogen during dehydrogenation. MgPd$_2$H$_{\approx 1}$ releases hydrogen and forms MgPd$_2$H$_{\approx 0.2}$ at about 413 K under isobaric conditions (2.5 MPa H$_2$). This release is also reversible by cooling. The hydrides MgPd$_2$H$_x$ can decompose irreversible at higher temperatures ($T \geq 641$ K, p(H$_2$) = 2.5 MPa) into MgH$_2$ and the anti-perovskite type hydride MgPd$_3$H$_x$. The hydrogenation properties of MgPd$_2$ suggest a sorption enthalpy near to benchmark value of -38.9 kJ (mol H$_2$)$^{-1}$ at 298 K (Calculation of Gibbs energy with change of hydrogen sorption is solely standard entropy of molecular hydrogen). Hydrogen sorption experiments at 283, 298 and 313 K result in a sorption enthalpy of -37.3 kJ (mol H$_2$)$^{-1}$ and an entropy of -110.7 (mol H$_2$)$^{-1}$ K^{-1} (Chapter 17). A hysteresis in pressure-composition (p-c) isotherm was observed, which is well known in intermetallic compound-hydrogen systems [204]. The magnitude of enthalpy explains the hydrogen release at ambient and the hydrogenation under mild conditions. In addition, the enthalpy is similar to the reaction enthalpy of hydrogen with elemental palladium (-38.2 kJ (mol H$_2$)$^{-1}$) [205]. Furthermore, the results of the sorption experiments are in accordance with those of the *in situ* DSC and neutron powder diffraction experiments.

3.3. Further palladium-rich and palladium containing compounds

During this work, Pd$_5$Sb$_2$ [206], Pd$_8$Sb$_3$ [81], Pd$_{20}$Sb$_7$ [82], Pd$_5$Bi$_2$ [90] and Pd$_4$Se [207] were tested for hydrogenation by *in situ* DSC under 5.0 MPa hydrogen pressure and temperatures up to 703 K (see [5] in Chapter 12). None of them shows a significant hydrogen uptake under the tested conditions, however suitable interstices can be found in their structures (Fig. 3.3.1). All investigated compounds with pnictogen (Pn = Sb, Bi) posses [PnPd$_3$] tetrahedral voids with distances from atoms to the void (d(A-□)$\approx$ 1.7 to 1.9 Å) similar to those of MPd$_2$H$_x$ (M = Sr, Eu; d = 1.73 and 1,74 Å) [113,124].

$$3\ MgPd_2 + 2\ H_2 \longrightarrow 3\ MgPd_2H + \tfrac{1}{2}\ H_2 \;\underset{\longleftarrow}{\overset{437\ K}{\longrightarrow}}\; 3\ MgPd_2H_{0.2} + 1.7\ H_2 \;\xrightarrow{641\ K}\; MgH_2 + 2\ MgPd_3H$$
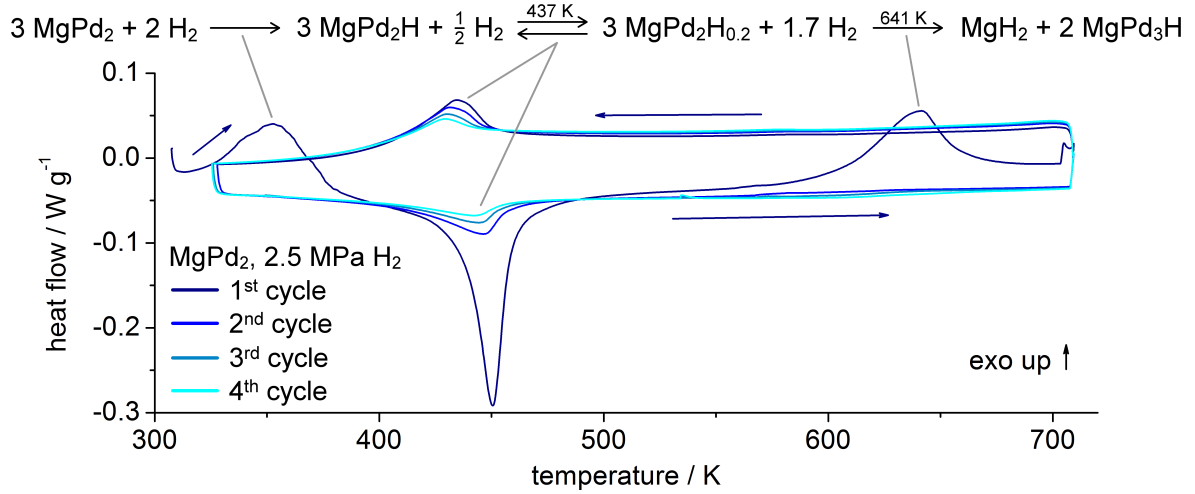
Figure 3.2.2.: *In situ* thermal analysis (DSC) of the hydrogenation of $MgPd_2$ at 2.5 MPa hydrogen pressure (starting pressure at 303 K, increasing during heating process up to 3.4 MPa). The intensity of the reversible signal at 437 K decreases with the number of cycles due to the irreversible decomposition at 641 K.

Furthermore, distorted $[Pn Pd_5]$ octahedral voids ($d(\text{Pd-}\square) \approx 1.9$ to 2.3 Å, $d(\text{Sb-}\square) \approx 1.7$ Å or $d(\text{Bi-}\square) \approx 2.0$ Å) can be found in these structures. The short distances to the pentel atom inhibite a hydrogen incorporation. The antimony containing structures with increasing palladium amount form additional attractive voids. A $[Pd_4]$ tetrahedral void ($d(\text{Pd-}\square) \approx 2.02$ Å) that is capped by a trigonal $[Sb_4]$ pyramid ($d(\text{Sb-}\square) \approx 2.07$ and 2.82Å (3x)) can be found in Pd_8Sb_3. An $[Pd_4]$ tetrahedral void ($d(\text{Pd-}\square) \approx 1.83$ Å) that is capped by two antimony atoms ($d(\text{Sb-}\square) \approx 2.6$ Å) is observed in $Pd_{20}Sb_7$. Pd_4Se contains interesting interstices surrounded by strongly distorted cubes ($d(\text{Pd-}\square) \approx 1.98$ (2x) and 2.43 Å (4x), $d(\text{Se-}\square) \approx 2.67$ Å) as well as twofold edge-capped tetrahedra ($d(\text{Pd-}\square) \approx 1.78$ Å, $d(\text{Se-}\square) \approx 2.82$ Å (2x)).

Even if a formation of hydrides seems very unlikely, the palladium containing compounds PdCd [208], PdHg [209], Pd_5Pb_3 [210], $Pd_{13}Pb_9$ [211], PdSb [212] and $Pd_{17}Se_{15}$ [213] were also investigated on their reaction behavior towards hydrogen as they are easily available or gained as by-products during other palladium-rich synthesis. As expected, none of them shows a reaction towards hydrogen.
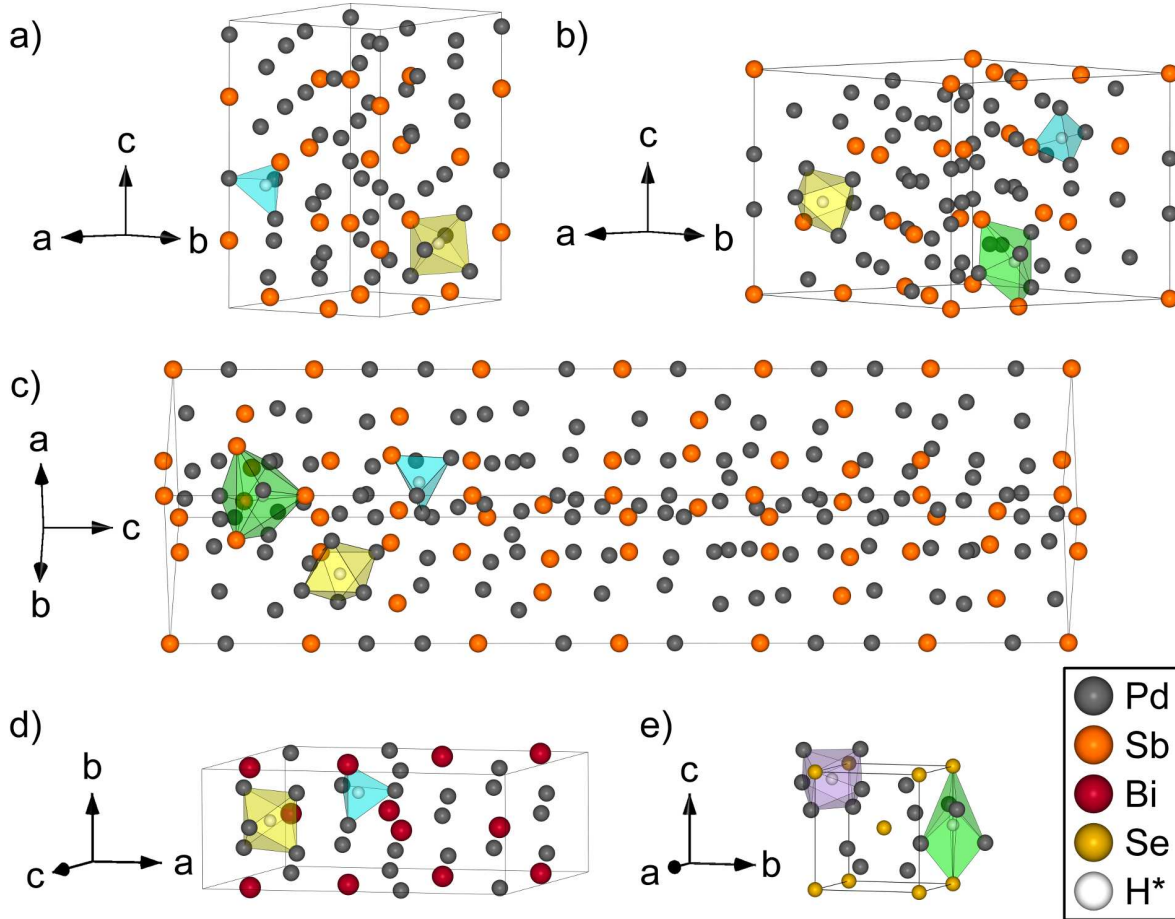
Figure 3.3.1.: Structures of palladium-rich compounds [a) Pd_5Sb_2, b) $Pd_{20}Sb_7$, c) Pd_8Sb_3, d) Pd_5Bi_2, e) Pd_4Se] with suitable voids [distorted [PnPd$_5$] octahedra (yellow polyhedra: a) at Wyckoff position $12d$ (0.17 0.477 0.21), b) at $18f$ (0.83 0.16 0.413), c) at $36f$ (0.347 0.854 0.19), d) at $4i$ (0.115 $^1/_2$ 0.603)); [PnPd$_3$] tetrahedra (blue polyhedra: a) at $12d$ (0.105 0.263 0.426), b) at $18f$ (0.303 0.789 0.714), c) at $36f$ (0.85 0.72 0.28), d) at $8j$ (0.105 0.24 0.44)); capped [Pd$_4$] tetrahedra (green polyhedra: b) at $18f$ (0.454 0.717 0.167), c) at $12c$ (0 0 0.109), e) at $2b$ (0 0 $^1/_2$)); and distorted cube (lilac polyhedron: e) at $4d$ ($^1/_2$ 0 0.904))] for potential hydrogen uptake (H*).

4. Ternary palladium-rich intermetallics as possible precursor for metal hydrides

In the search of further candidates for hydrogenation and to understand the influence of the electronic phenomena, ternary palladium-rich compounds were investigated. The number of electrons and, thus, the VEC were increased by substitution with semimetals like arsenic, selenium or phosphorous. This chapter includes the hydrogenation properties of palladium-rich compounds of the Pt_5TlAs type structure, the new compound $Pd_{11}Bi_2Se_2$ and the half-antiperovskite $Pd_3Bi_2Se_2$. None of the tested compounds can take up significant amounts of hydrogen. Consequently, the insertion of electron-rich semimetals like selenium and arsenic, and an increase in VEC relating thereto, inhibits a hydrogenation of these compounds. Solely Pd_5InSe forms a hydride, but only by decomposition into palladium selenides and $InPd_3$ that is subsequently hydrogenated.

Furthermore, the catalytic properties of $Pd_{11}Bi_2Se_2$ for the semi-hydrogenation of acetylene to ethylene are covered.

4.1. Pt_5TlAs type compounds

The isotypic compounds Pd_5CdSe, Pd_5HgSe, Pd_5CdAs, Pd_5InAs, Pd_5TlAs and Pd_5InP do not show any reaction towards hydrogen (see [5] in Chapter 12 and [6] in Chapter 13) despite the relation of Pt_5TlAs type structures to ccp [93]. These structures consit of alternating layers of face-sharing MPd_{12} cuboctahedra and layers of selenium, arsenic or phosphorus atoms (Fig. 4.1.1, left). Hence, only $[MPd_5]$ octahedral voids exist, which are less suitable for hydrogen incorporation (see Section 3.1). A change of structure for Pd_5CdSe, Pd_5HgSe, Pd_5CdAs, Pd_5InAs, Pd_5TlAs and Pd_5InP was not observed, however, Pd_5InSe forms $InPd_3H_x$ during hydrogenation.

This hydride formation was indirectly proven by the investigation of thermal decompostion of Pd_5InSe by DTA and temperature-resolved XRPD (see [5] in Chapter 12). Pd_5InSe reacts at 798 K to Pd_8In_2Se and a liquid phase $(2Pd + Se)_{(l)}$ due to the eutectic (see Pd-Se phase diagram [214]). The stacking sequence in Pd_8In_2Se is different to Pt_5TlAs isotypes with double layers of face linked MPd_{12} cuboctahedra between the selenium layers (Fig. 4.1.1). Pd_8In_2Se decomposes further at 849 K to $InPd_3$ and an additional amount of $(2Pd + Se)_{(l)}$. This liquid phase can be indirectly evidenced by crystallizing $Pd_{34}Se_{11}$, Pd_7Se_4 and $Pd_{17}Se_{15}$ due to quenching according to the Pd-Se phase diagram [122]. Hysteresis for both reactions are observed upon cooling, where the reverse reaction from $InPd_3$ to Pd_8In_2Se takes place at 852 K and to Pd_5InSe at 624 K. These reactions clarify the formation of $InPd_3H_x$ from Pd_5InSe or Pd_8In_2Se at moderate temperatures under hydrogen pressure.

4.2. $Pd_{11}Bi_2Se_2$

Reaction mixtures with the molar ratio 5:1:1 of palladium to bismuth to selenium were investigated to maximize the VEC in ternary palladium-rich systems with a metal and a semimetal. Phase analysis of measured XRPD data show that the reflections of most intensity match with the previously reported
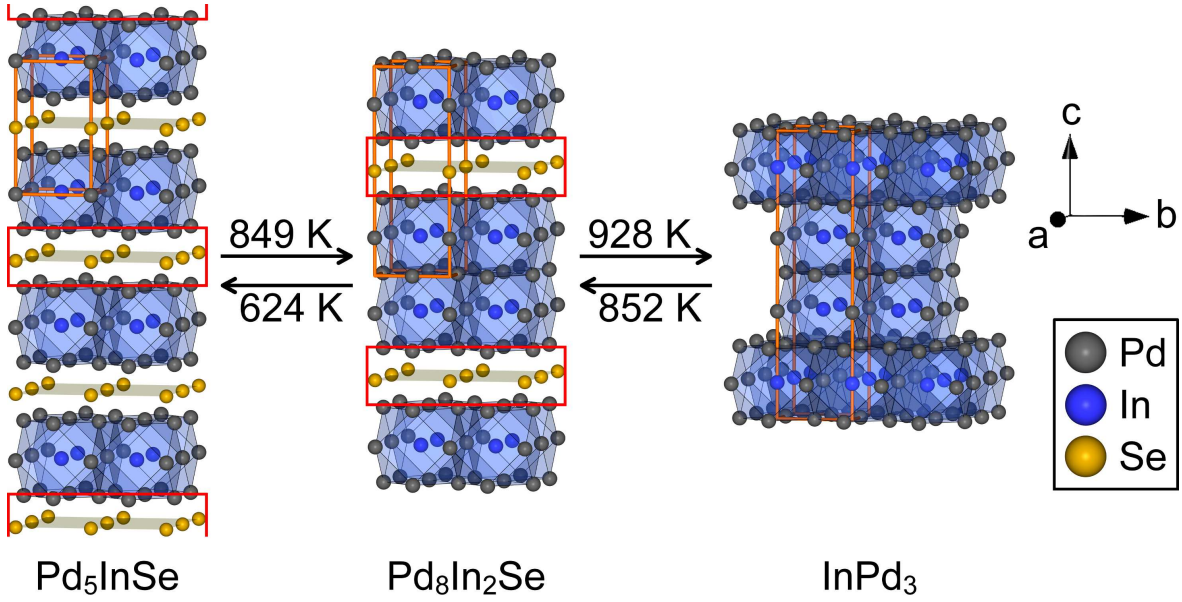
Figure 4.1.1.: Reaction from Pd_5InSe to Pd_8In_2Se to $InPd_3$ by heating. One unit cell of each structure is displayed (orange cell edges). Blocks of selenium layers and adjacent Pd atoms ($2Pd + Se$) are eluted (red boxes) in series from Pd_5InSe to $InPd_3$ and $InPd_{12}$ cuboctahedra (blue polyhedra) are stacked.

$Pd_3Bi_{0.6}Se_{0.4}$ (BiF_3 type) [215]. However, superstructure reflections were observed, which cannot be explained with this model. The formation of single crystals enabled the structure solution of $Pd_{11}Bi_2Se_2$ by single crystal X-ray diffraction (see [7] in Chapter 14). Samples with high phase purity of this compound can be yielded by synthesis with stoichiometric amounts of the elements. $Pd_{11}Bi_2Se_2$ crystallizes in a 4 x 4 x 4 superstructure of the W type and is similar to the $Li_{13}In_3$ type. One crystallographic site of $Li_{13}In_3$ type (Wyckoff position $8b$) is empty in $Pd_{11}Bi_2Se_2$ and, as a consequence, the sourrounding atoms shift towards the void. Therefore, this compound is not isotypic to $Li_{13}In_3$ type. Furthermore, $Pd_{11}Bi_2Se_2$ is also a 2 x 2 x 2 superstructure of the BiF_3 type which was suggested for $Pd_3Bi_{0.6}Se_{0.4}$. In contrast to Bi and Se atoms of $Pd_3Bi_{0.6}Se_{0.4}$ forming a ccp with statistical distribution, Bi and Se atoms of $Pd_{11}Bi_2Se_2$ are ordered. The octahedral and tetrahedral sites of these ccp of Bi and Se atoms are occupied by palladium, but in the case of $Pd_{11}Bi_2Se_2$ only $5/8$ of tetrahedral sites are occupied generating voids with an ordered distribution. The crystal chemical formula $(Pd3)[o]_4(Pd1)[t]_6(Pd2)[t]\square[t]Bi_2Se_2$ describes the structure in detail. Alternatively, the structure can be described by the classical ABC notation of close-packed structures. The atoms of $Pd_{11}Bi_2Se_2$ are stacked as $A\beta_{3/4}\gamma\alpha B\gamma\alpha'\beta_{3/4}C\alpha_{3/4}\beta\gamma A\beta\gamma'\alpha_{3/4}B\gamma_{3/4}\alpha\beta C\alpha\beta'\gamma_{3/4}$ where the packing is made by Bi and Se atoms (Roman letters). The octahedral voids (middle Greek letters) are occupied by Pd3 atoms that are shifted to the upper or lower layer. The latter is marked with quote. The tetrahedral voids (outer Greek letters) are either occupied by $1/4$ Pd2 and $3/4$ Pd1 atoms or only by $3/4$ Pd1 atoms. This stacking is similar to them of the BiF_3 type ($A\beta\gamma\alpha B\gamma\alpha\beta C\alpha\beta\gamma$). Therefore it is likely, that $Pd_{11}Bi_2Se_2$ was mistaken for the proposed $Pd_3Bi_{0.6}Se_{0.4}$ (BiF_3 type) [215] and the ordering in the crystal structure was overseen.

This compound is stable against air, water, many organic solvents and even concentrated hydrochloric acid. Furthermore, $Pd_{11}Bi_2Se_2$ has a negligible effective magnetic moment of 0.01 μ_B per palladium atom and is quite likely a poor metal, inferred by a pseudo-gap at the Fermi level in the density of states. The region close to the Fermi level is dominated by almost filled Pd 4d-states, which is also known for other palladium-rich compounds. The hydrogenation properties of $Pd_{11}Bi_2Se_2$ were tested
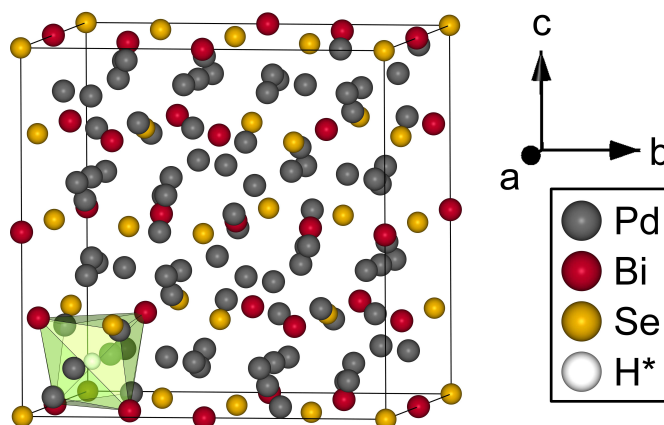
Figure 4.2.1.: The ordered void (green polyhedra) in the structure of Pd$_{11}$Bi$_2$Se$_2$ as a suitable hydrogen position (H*).

by *in situ* DSC and afterwards XRPD. No hydrogen uptake was detected despite of the high proportion of palladium and promising voids in the structure (Fig. 4.2.1). An assumed site for hydrogen incorporation was the ordered interstice of the structure, which is tetrahedrally surrounded by palladium atoms ($d(\square$-Pd) = 1.974 Å) and additional surrounded by four Bi atoms ($d(\square$-Bi) = 2.704 Å) forming a second tetrahedron.

4.2.1. Catalytic investigations of the semi-hydrogenation of acetylen

Pd$_{11}$Bi$_2$Se$_2$ is interesting for hydrogenation catalysis, because of the absence of hydride formation under hydrogen pressure and heating. Therefore, catalytical investigation on the semi-hydrogenation of acetylene to ethylene with Pd$_{11}$Bi$_2$Se$_2$ as catalyst were executed Chapter 18. The catalysis at 437 K with Pd$_{11}$Bi$_2$Se$_2$ is very selective to ethylene with 90 to 95 %, whereby the selectivity to ethane is below 10 % and to C$_4$H$_x$ below 5 %. This high selectivity to ethylene is comparable with them of PdZn (90 %) [216] and even higher as them of PdGa (75 %) [217] and Pd$_2$Ga (74 %) [218] as catalyst materials. However, the catalysis with Pd$_{11}$Bi$_2$Se$_2$ has only a maximum conversion of 46 % (after 24.5 h) which is much lower as those of the mentioned materials (> 85 %), [216–218] and starts only after 7.5 h. X-ray photoelectron spectroscopy (XPS) measurements before and after the catalytic investigation show that a bismuth oxide phase on the surface is reduced during the catalytic experiment. The reduction of the bismuth oxide phase on the compound has a long duration, due to low hydrogen diffusion processes. In comparison, the complete reduction of pure α-Bi$_2$O$_3$ by hydrogen has a duration of 18 h at 523 K [219].

4.3. Half-antiperovskites

$Pd_3Bi_2Se_2$ is not a palladium-rich compound, however, strongly distorted $[BiPd_5]$ octahedral voids in its structure attract interest for hydrogenation investigations. $Pd_3Bi_2Se_2$ crystallizes in $Ni_3Bi_2S_2$ (parkerite) type [220], which is a 2 x 2 x 2 superstructure of the anti-perovskite type. Only half of the Pd sites of a cubic anti-perovskite type are orderly occupied forming stair like layers of edge-sharing square planar $[PdBi_4]$ units (Fig. 4.3.1). Thus, strongly distorted $[BiPd_5]$ octahedral voids are formed, that are capped by two selenium atoms and edge-sharing within the layers. Although strongly compressed octahedral interstices (d(Bi-Pd) = 3.059 Å, perpendicular to the layers [221]) make a hydrogen uptake unlikely, an imaginable elongation by hydrogenation was a reason for investigating the hydrogenation properties of $Pd_3Bi_2Se_2$. However, no reaction of this half-antiperovskite towards hydrogen was observed using *in situ* DSC and afterwards XRPD (see [5] in Chapter 12).
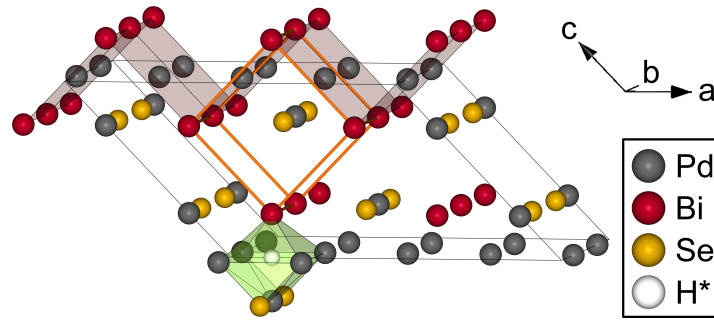
Figure 4.3.1.: Structure of the half-antiperovskite $Pd_3Bi_2Se_2$ containing stair like layers of edge-sharing square planar $[PdBi_4]$ units (light pink planes) and strongly distorted twofold capped $[BiPd_5Se_2]$ octahedral voids along the layers (green polyhedra), which are suitable hydrogen positions (H*). A cubic perovskite unit is highlighted with orange edges.

5. Hydrides of the calcium-rhodium system

This chapter deals with ternary calcium-rhodium hydrides and the extension to representatives with increasing rhodium content. The hydrogenation pathway of the Laves phase $CaRh_2$ is discussed and the related access to the perovskite $CaRhH_3$ is shown.

Besides palladium containg hydrides, further noble metal containing hydrides are known. In contrast to palladium, iridium, platinum or rhodium do not form binary hydrides. However, ternary hydrides, especially complex transition metal hydrides are interesting, e. g., for catalysis [222], received attention recently [223]. Hydrogen has a covalent bonding behavior in many noble metal hydrides, e. g., ternary rhodium hydrides. A_3RhH_6 (A = Li [135], Na [136]) or M_2RhH_5 (M = Ca [137], Sr [137], Eu [138]) form the 18 valence electron complexes $[Rh^{III}H_6]^{3-}$ and $[Rh^IH_{6.5/6}]^{4-}$, respectively. The rhodium atom is coordinated to six hydrogen atoms forming an isolated octahedron, but only $^5/_6$ of the hydrogen sites of $[Rh^IH_{6.5/6}]^{4-}$ are occupied statistically. The hydrogen bonding behavior can be switched to be more metallic with increasing content of the transition metal, as shown for ternary palladium hydrides. WELF BRONGER and LUDGER BREIL showed such as transition of hydrides in the Ca-Rh system with the hydrides $Ca_2RhH_{5.5}$, $Ca_8Rh_5H_{25}$ and $Ca_6Rh_8H_{24}$ [224]. The RhH_6 octahedra get connected with increasing rhodium content and a maximum connection is reached in the perovskite type structure (Fig. 5.0.1). However, no hydride $CaRhH_x$ was known, yet, despite of existing perovskite-type hydrides with other noble metals like $CaNiH_3$ [225] or the defect perovskite-type hydride $CaPdH_2$ [226]. $CaRhH_x$ is not accessible with rhodium and calcium hydride under hydrogen pressure [224]. Furthermore, calculations of CaRhH in a distorted orthorhombic structure isotypic to MgRhH reached no convergence [141]. However, $CaRhH_3$ is accessible through the hydrogenation of the Laves phase $CaRh_2$ (see Chapter 15 in [8]).

In situ investigations show that the hydrogenation of the Laves phase $CaRh_2$ results in three different hydride phases. Firstly, the cubic Laves phase α-$CaRh_2H_{0.05}$ ($ZrCr_2H_{3.08}$ type), then the orthorhombic β-$CaRh_2H_{3.9}$ (own structure type) is formed and finally, γ-$CaRh_2H_{3.2}$ (β-$CaRh_2H_{3.9}$ type) is observed during the dehydrogenation of the β-phase. β-$CaRh_2H_{3.9}$ decomposes at 480 K under 5.0 MPa hydrogen pressure to the perovskite-type $CaRhH_3$ and nano-crystalline rhodium. This exothermic reaction is kinetically controlled. A direct synthesis from α-$CaRh_2H_{0.05}$ to the perovskite-type hydride and rhodium is kinetically hindered, and was only observed at 723 K.

The interatomic Rh-H distances of hydrides in the calcium-rhodium system are consistent with each other and range from 1.55 - 1.91 Å. However the interatomic Rh-Rh-distances decrease with increasing rhodium content. $Ca_2RhH_{5.5}$ has mostly covalent Rh-H bonds and long Rh-Rh distances (d = 5.129 Å) [227] that makes interaction very unlikely. The other hydrides in the calcium rhodium system contain shorter Rh-Rh distances (d(Rh-RH) < 3.65 Å) [8, 224] indicating a more metallic bonding character. Furthermore, the VEC and the molar volume increment $V_{(H)}$ decreases in the series CaH_2 - $Ca_2RhH_{5.5}$ - $Ca_8Rh_5H_{25}$ - $Ca_6Rh_8H_{24}$ - $CaRhH_3$ - β-$CaRh_2H_{3.9}$ - γ-$CaRh_2H_{3.2}$ from 1.33 to 0.84 and 7.58 to 2.78 cm^3 mol^{-1}, respectively. Thus, the hydrogen bonding character can be affected by variation of the noble metal content as observed for the hydrides of the europium-palladium and magnesium-palladium systems (see Section 1.2 and Chapter 3, respectively).
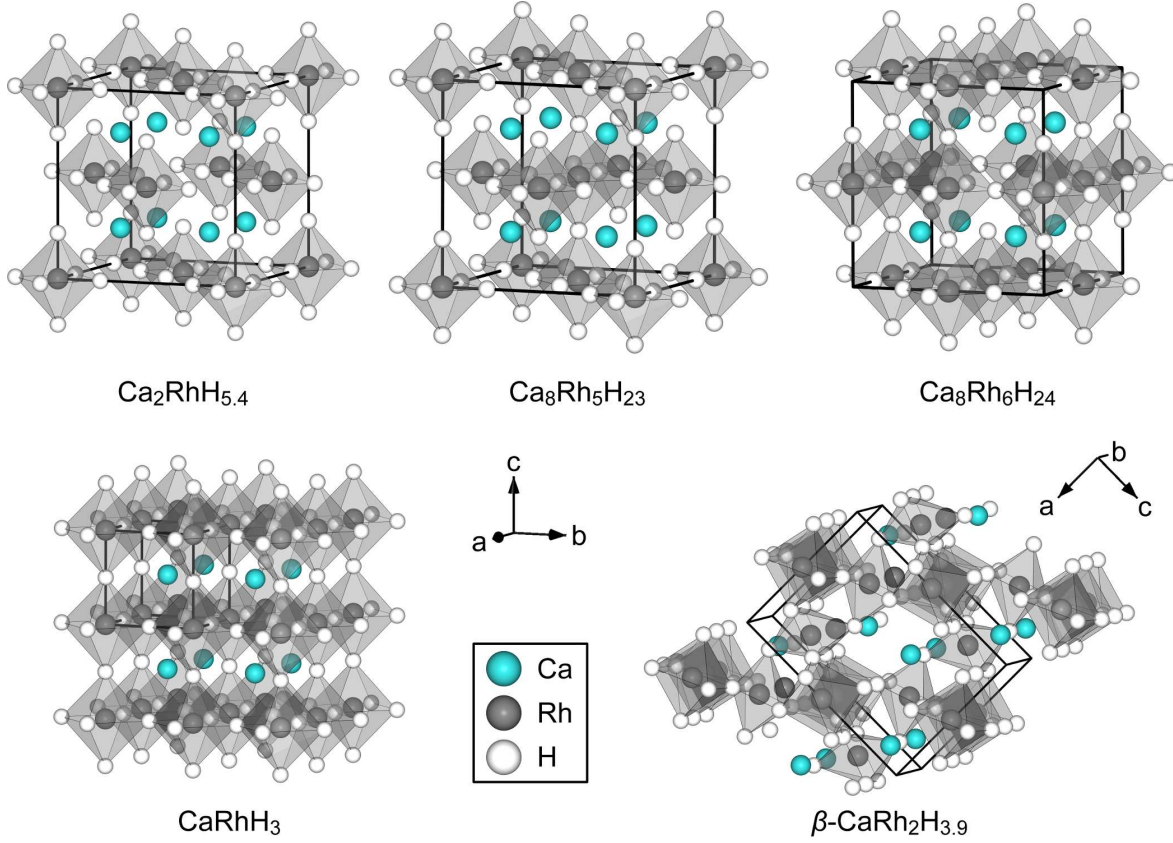
Figure 5.0.1.: Hydrides of the calcium rhodium system with RhH_6 units (grey polyhedra) [8, 224, 227]. The level of corner connectivity (*lcc*) of RhH_6 units increase with increasing rhodium amount (from left to right: $lcc_{Ca_2RhH_{5.5}}=0$, $lcc_{Ca_8Rh_5H_{25}} = 2.67$, $lcc_{Ca_6Rh_8H_{24}} = 4$, $lcc_{CaRhH_3} = lcc_{\beta\text{-}CaRh_2H_{3.9}} = 6$). The RhH_6 octahedra of β-$CaRh_2H_{3.9}$ are strongly distorted (bottom, right)

5.1. Laves phase hydrides CaRh$_2$H$_x$

During the hydrogenation and dehydrogenation of the Laves phase $CaRh_2$ three phases are observed (see [8] in Chapter 15). The cubic α-$CaRh_2H_{0.05}$ crytallizes in the $ZrCr_2H_{3.08}$ type structure. The hydrogen content was estimated by the assumption that the volume expands by 5 % per incorporated hydrogen atom [113]. The position of the hydrogen atom is not determined by neutron diffraction due to the low hydrogen content, but the lattice parameter of α-$CaRh_2H_{0.05}$ ($a = 7.5308(12)$ Å) is significant smaller than the benchmark value of 7.7 Å predicting a preferred occupation by hydrogen of the 96g site [228]. This site has a [2+2] coordination to two calcium and two rhodium atoms which form a tetrahedron. This hydrogen position is supported by the coordination surrounding of hydrogen in the β-phase.

In the orthorhombic distorted structure of β-$CaRh_2H_{3.9}$ hydrogen occupies distorted tetrahedral [Ca_2Rh_2] and trigonal bypyramidal [Ca_3Rh_2] voids. The formation of HA_2M_2 tetrahedra is well known for Laves phases, but trigonal bipyramids are more common in other hydrids, e. g., AlB_2 related hydrides such as $Be_2ZrH_{1.5}$ [229] and $ThNi_2H_{2.6}$ [230]. Fig. 5.1.1 shows the structual relation of the β-$CaRh_2H_{3.9}$ type to the cubic Laves phase. The Kagomé lattice of the β-phase is distorted and the calcium atom chains are tilted against each other, but the similarity to cubic Laves phase is clearly visible. The relation is also shown by group-subgroup relationship, however, not all of the genarated hydrogen sites are occupied. In additon, some hydrogen atoms of the β-phase occupy
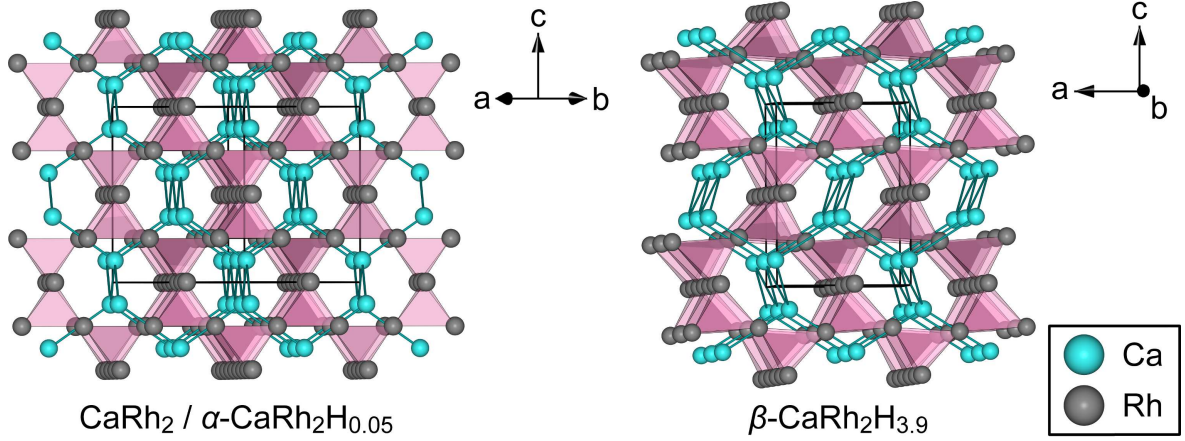
Figure 5.1.1.: Comparison of the structures of the cubic Laves phase $CaRh_2$ and the orthorhombic β-$CaRh_2H_{3.9}$ with regard to the Kagomé lattice. Hydrogen atoms are not pictured for reason of clarity.

site which are not generated from symmetry reduction from the α-phase. These intermediate site is surrounded by the distorted trigonal bipyramid and is located between two empty sites generated by the group-subgroup relationship. The hydrogen amount determined by *in situ* neutron diffraction was confirmed by hydrogen sorption experiments yielding in the formula β-$CaRh_2H_{3.8(2)}$. This content is already reached under 0.1 MPa hydrogen pressure and is stable under applied vacuum.

During dehydrogenation from the β- to the α-phase, γ-$CaRh_2H_{3.2}$ was observed crystallizing in β-$CaRh_2H_{3.9}$ type. Both phases differ in lattice parameters, hydrogen content and a miscibility gap between them is likely. This phase was not observed in the hydrogenation process and was only detected by *in situ* neutron powder diffraction.

5.2. Perovskite-type hydride CaRhH₃

The perovskite-structure is well known and attracts interest for many application. Solar cells [231,232] superconductivity [233,234] and catalysis [235] are just a few examples of applications of compounds with perovskite structure. $CaRhH_3$ crystallizes in the cubic perovskite type and is formed by decompostion of β-$CaRh_2H_{3.9}$ at 500 K and 1.0 MPa hydrogen pressure (see [8] in Chapter 15). During the formation, the hydrogen site is almost full occupied from the beginning, however, hydrogen is released by increasing temperature, e. g., yielding $CaRhD_{2.75(1)}$ at 550 K. Elementary rhodium is formed with a very small crystallite size as second phase during the decompostion of β-$CaRh_2H_{3.9}$. Estimation of the crystallite sizes by Scherrer equation result in 2 nm for rhodium (determined on (111) reflection) and 10 nm for $CaRhD_{2.93(2)}$ (determined on (200) reflection). In contrast to the border case MgRhH [141], $CaRhH_3$ is suggested to be largely a metallic hydride based on molar volume increment calculations and interatomic Rh-Rh distances ($d = 3.6512(2)$Å) [8].

6. Conclusion

The compounds within this work were obtained by hard and soft chemistry. The intermetallic compounds $M\text{Pd}_{\geq 2}$ (M = Mg, Zn, Sn, Pb, Bi) were mainly synthesized at high annealing temperatures, however the use of mineralizing agents enabled milder conditions. MgPd_3 absorbs hydrogen near ambient conditions. In contrast, BiPd_3 needed high temperatures and pressures for hydride formation. In addition, *in situ* investigations of the reaction pathways were done and unknown intermediates characterized. They show the importance of such methods to understand and improve reactions. In the case of BiPd_3, it has been shown that a neglible hydrogen absorption is sufficient to change the stacking sequence of hexagonal layers in closed packings. $[\text{Pd}_6]$ octahedra are formed as a suitable coordination surrounding for hydrogen. No intermediates were observed during its hydrogenation. The coordination surrounding also influences in the hydrogenation of MgPd_3. The interstices of MgPd_3 are not occupied simultaneously during its hydrogenation. First of all, $[\text{Pd}_6]$ and $[\text{MgPd}_5]$ octahedral voids are occupied. The consequent volume expansion increases the $[\text{Mg}_2\text{Pd}_4]$ voids which are subsequently occupied by hydrogen. This shows the preference of metallic Pd-H, but the possibility of Mg-H interactions as well. In contrast to $M\text{Pd}_2$ compounds (M = Zn, Sn), MgPd_2 absorbs hydrogen. These structures do not contain $[\text{Pd}_6]$, but strongly distorted $[M\text{Pd}_5]$ octahedral voids. During the hydrogenation of MgPd_2 the unit cell volume increases anisotropically because HMgPd_5 octahedra are formed and its level of distortion decreases. The reaction enthalpy of this hydrogenation is similar to the standard entropy of molecular hydrogen multiplied by the ambient temperature. Therefore, MgPd_2 absorbs hydrogen at mild and releases it at ambient conditions. MgPd_2H also partially releases hydrogen at hydrogen pressure and increasing temperatures forming $\text{MgPd}_2\text{H}_{0.2}$, before decomposing into cubic MgPd_3H_x and MgH_2. The introduction of magnesium in such systems increases the probability of a hydride formation. However, the stability of the hydrides decreases with increasing magnesium content. This knowledge can be used in searching for further hydrides.

It is interesting to note that most structures of palladium-rich hydrides crystallize in variants of the cubic closed packing (ccp). Furthermore, it was shown that the amount of absorbed hydrogen depends on the metal atom which is not in the first coordination sphere of hydrogen. The uptake depends more on electronic than geometric aspects of this metal atom. A hydrogen absorption is promoted if the metal has a similar electronegativity to and a greater radius than palladium. Therefore, the investigated hydrides $\text{SnPd}_3\text{H}_{0.14}$, $\text{PbPd}_3\text{H}_{0.13}$ and $\text{BiPd}_3\text{H}_{0.2}$ absorb less hydrogen than the known TlPd_3H. In addition, an increase of the valence electron concentration (VEC) by introduction of electron-rich semi-metals hinders a hydrogen absorption. The aforementioned compounds SnPd_3 and BiPd_3 are just able to form hydrides. Thus, $\text{Pd}_{11}\text{Bi}_2\text{Se}_2$ does not show a reaction towards hydrogen, but it attracts interest in catalysis. $\text{Pd}_{11}\text{Bi}_2\text{Se}_2$ exhibits a high selectivity to ethylene in the semi-hydrogenation of acetylen. However, the conversion is low and the activity starts after a long time due to a bismuth oxide layer on the surface.

Rhodium does not form a binary hydride in contrast to palladium. However, the Laves phase CaRh_2 absorbs hydrogen and forms α-$\text{CaRh}_2\text{H}_{0.05}$, β-$\text{CaRh}_2\text{H}_{3.9}$ and γ-$\text{CaRh}_2\text{H}_{3.2}$ by hydrogen incorporation in tetrahedral $[\text{Ca}_2\text{Rh}_2]$ and trigonal bipyramidal $[\text{Ca}_3\text{Rh}_2]$ voids. The Laves phase hydrides decompose kinetically controlled to the perovskite-type hydride CaRhH_3 and nano-scaled rhodium. The former is not accessible through direct synthesis of rhodium and calcium hydride. CaRhH_3 does

not form Rh-Rh bonds in contrast to the higher homologue MgPdH due to the increased ionic character of calcium. Thus, hydrides with metallic properties and covalent transition metal bonds are to be expected by the introduction of magnesium.

This work presents with the aid of simple exemplary systems, palladium-rich and calcium-rhodium hydrides that the use of magnesium or metals which are similar in electronegativity promote hydride formation whereas an increase of VEC hinders it. The latter provides an opportunity for catalytic materials.

7. Bibliography

[1] A. Götze, H. Kohlmann, Palladium hydride and hydrides of palladium-rich phases, in: Reference Module in Chemistry, Molecular Sciences and Chemical Engineering, Elsevier, 2017. `doi:10.1016/B978-0-12-409547-2.12204-8`.

[2] A. Götze, H. Auer, R. Finger, T. C. Hansen, H. Kohlmann, A sapphire single-crystal cell for *in situ* neutron powder diffraction of solid-gas reactions, Phys. B (2018) in press`doi:10.1016/j.physb.2017.11.024`.

[3] A. Götze, T. C. Hansen, H. Kohlmann, The reversible hydrogenation of $BiPd_3$ followed by *in situ* methods and the crystal structure of $PbPd_3D_{0.13(1)}$, J. Alloys Compd. 731 (2018) 1001–1008. `doi:10.1016/j.jallcom.2017.10.107`.

[4] A. Götze, N. Zapp, A. J. Peretzki, V. Pomjakushin, T. C. Hansen, H. Kohlmann, *In situ* hydrogenation and crystal chemistry studies of Co_2Si type compounds $MgPd_2$ and Pd_2Zn, Z. Anorg. Allg. Chem. 644 (2018) 367–375. `doi:10.1002/zaac.201700434`.

[5] A. Götze, J. M. Sander, H. Kohlmann, Crystal structures and hydrogenation properties of palladium-rich compounds with elements from groups 12-16, Z. Naturforsch. 71B (2016) 503–508. `doi:10.1515/znb-2016-0003`.

[6] E. Y. Zakharova, S. M. Kazakov, A. Götze, H. Kohlmann, A. N. Kuznetsov, Ternary palladium-indium-phosphorus and platinum-indium-phosphorus compounds based on the Cu_3Au-type: structure, bonding, and properties, J. Solid State Chem.

[7] A. Götze, S. Schmorl, A. N. Kuznetsov, H. Kohlmann, Vacancy ordering in $Pd_{11}Bi_2Se_2$ - Crystal structure and properties, J. Alloys Compd. 735 (2018) 1914–1920. `doi:10.1016/j.jallcom.2017.11.300`.

[8] A. Götze, J. Möllmer, H. Kohlmann, From Laves phase $CaRh_2$ to the perovskite $CaRhH_3$ - *in situ* investigation of hydrogenation intermediates $CaRh_2H_x$, Inorg. Chem. (2018) submitted.

[9] H. Cavendish, XIX. Three papers, containing experiments on factitous air, Phil Trans. R. Soc. London 56 (1766) 141–184. `doi:10.1098/rstl.1766.0019`.

[10] E. Wigner, H. B. Huntington, On the possibility of a metallic modification of hydrogen, J. Chem. Phys. 3 (1935) 764–770. `doi:10.1063/1.1749590`.

[11] J. McMinis, R. C. Clay, D. Lee, M. A. Morales, Molecular to atomic phase transition in hydrogen under high pressure, Phys. Rev. Lett. 114 (2015) 105305. `doi:10.1103/PhysRevLett.114.105305`.

[12] S. Azadi, B. Monserrat, W. M. C. Foulkes, R. J. Needs, Dissociation of high-pressure solid molecular hydrogen: A quantum Monte Carlo and anharmonic vibrational study, Phys. Rev. Lett. 112 (2014) 165501. `doi:10.1103/PhysRevLett.112.165501`.

[13] E. Brovman, Y. Kagan, A. Kholas, Structure of metallic hydrogen at zero pressure, J. Exp. Theor. Phys. 34 (1972) 1300–1315.

[14] D. Saumon, W. B. Hubbard, G. Chabrier, H. M. van Horn, The role of the molecular-metallic transition of hydrogen in the evolution of Jupiter, Saturn, and brown dwarfs, Astrophys. J. 391 (1992) 827–831. `doi:10.1086/171391`.

[15] W. B. Hubbard, T. Guillot, J. I. Lunine, A. Burrows, D. Saumon, M. S. Marley, R. S. Freedman, Liquid metallic hydrogen and the structure of brown dwarfs and giant planets, Phys. Plasmas 4 (1997) 2011–2015. `doi:10.1063/1.872570`.

[16] R. P. Dias, I. F. Silvera, Observation of the Wigner-Huntington transition to metallic hydrogen, Science 355 (2017) 715–718. `doi:10.1126/science.aal1579`.

[17] D. Castelvecchi, Hydrogen yet to prove it's metal, Nature 542 (2017) 17. `doi:10.1038/nature.2017.21379`.

[18] T. Graham, On the absorption and dialytic separation of gases by colloid septa, Philos. Trans. R. Soc. London 156 (1866) 399–439. `doi:10.1016/0016-0032(67)90260-8`.

[19] The Nobel Prize in Chemistry 2010 - Advanced information.
URL `http://www.nobelprize.org/nobel_prizes/chemistry/laureates/2010/advanced.html`

[20] J. Livage, Chimie douce: from shake-and-bake processing to wet chemistry, New J. Chem. 25 (2001) 1. `doi:10.1039/B009233I`.

[21] C. J. Brinker, G. W. Scherer, Sol-Gel Science: the physics and chemistry of sol-gel processing, Academic Press, 1990.

[22] J. Livage, M. Henry, C. Sanchez, Sol-gel chemistry of transition metal oxides, Prog. Solid State Chem. 18 (1988) 259 – 341. `doi:10.1016/0079-6786(88)90005-2`.

[23] R. Schöllhorn, Reversible topotactic redox reactions of solids by electron/ion transfer, Angew. Chem. Int. Ed. Engl. 19 (1980) 983–1003. `doi:10.1002/anie.198009831`.

[24] U. Müller, Topotactic reactions, in: Symmetry Relationships between Crystal Structures, Oxford University Press, Oxford, 2013. `doi:10.1093/acprof:oso/9780199669950.003.0016`.

[25] J. H. Westbrook, Intermetallic compounds: their past and promise, Metall. Trans. A 8 (1977) 1327–1360. `doi:10.1007/BF02642848`.

[26] K. Buschow, P. Naastepad, F. Westendorp, Preparation of $SmCo_5$ permanent magnets, J. Appl. Phys. 40 (1969) 4029–4032. `doi:10.1063/1.1657138`.

[27] E. Pina, F. Palomares, M. Garcia, F. Cebollada, A. De Hoyos, J. Romero, A. Hernando, J. Gonzalez, Coercivity in SmCo hard magnetic films for MEMS applications, J. Magn. Magn. Mater. 290 (2005) 1234–1236. `doi:10.1016/j.jmmm.2004.11.410`.

[28] H. Raisigel, O. Cugat, J. Delamare, Permanent magnet planar micro-generators, Sens. Actuators, A 130 (2006) 438–444. `doi:10.1016/j.sna.2005.10.007`.

[29] N. S. Stoloff, C. T. Liu, S. C. Deevi, Emerging applications of intermetallics, Intermetallics 8 (2000) 1313 – 1320. `doi:10.1016/S0966-9795(00)00077-7`.

[30] H. Ewe, E. W. Justi, K. Stephan, Elektrochemische Speicherung und Oxidation von Wasserstoff mit der intermetallischen Verbindung LaNi$_5$, Energy Convers. 13 (1973) 109 – 113. `doi:10.1016/0013-7480(73)90085-5`.

[31] H. A. C. M. Bruning, J. H. N. Van Vocht, F. F. Westendorp, H. Zijlstra, Battery with hydrogen absorbing material of the formula LnM$_5$, US Patent 4216274 (1980).
URL `https://www.google.com/patents/US4216274`

[32] E. Casado-Rivera, D. J. Volpe, L. Alden, C. Lind, C. Downie, T. Vázquez-Alvarez, . C. D. Angelo, F. J. DiSalvo, H. D. Abruna, Electrocatalytic activity of ordered intermetallic phases for fuel cell applications, J. Am. Chem. Soc. 126 (2004) 4043–4049. `doi:10.1021/ja038497a`.

[33] S. Yamamatsu, Shokubai 43 (2001) 549.

[34] O. Loebich, Jr., W. Wopersnow, Zur Struktur der intermetallischen Verbindung LiPd$_2$, J. Less-Common Met. 63 (1979) 83–88.

[35] O. Loebich, Jr., C. J. Raub, Das Zustandsdiagramm Lithium-Palladium und die magnetischen Eigenschaften der Li-Pd-Legierungen, J. Less-Common Met. 55 (1977) 67–76.

[36] C. Wannek, B. Harbrecht, Iod-katalysierte Herstellung von intermetallischen Verbindungen der Edelmetalle: Die Kristallstrukturen von BePd$_2$ und BePd$_3$, Z. Anorg. Allg. Chem. 628 (2002) 1597–1601. `doi:10.1002/1521-3749(200207)628:7<1597::AID-ZAAC1597>3.0.CO;2-A`.

[37] L. E. Tergenius, T. Lundström, The Crystal Structure of Pd$_2$B, J. Solid State Chem. 31 (1980) 361–367. `doi:10.1016/0022-4596(80)90100-0`.

[38] M. Beck, M. Ellner, Mittemeijer E. J., Powder diffraction data for borides Pd$_3$B and Pd$_5$B$_2$ and the formation of an amorphous boride Pd$_2$B, Powder Diffr. 16 (2001) 98–101. `doi:10.1154/1.1351156`.

[39] R. V. Gumeniuk, H. Borrmann, A. Leithe Jasper, Refinement of the crystal structures of trinickel boron, Ni$_3$B, and tripalladium boron, Pd$_3$B, Z. Kristallogr. (New Cryst. Struct.) (2006) 221–425`doi:10.1524/ncrs.2006.221.14.425`.

[40] M. Beck, M. Ellner, Mittemeijer E. J., The structure of the palladium rich boride Pd$_5$B (Pd$_{16}$B$_3$), Z. Kristallogr. 216 (2001) 591–594. `doi:10.1524/zkri.216.11.591.22480`.

[41] A. Leineweber, T. G. Berger, A. Udyansky, V. N. Bugaev, V. Duppel, The incommensurate crystal structure of the Pd$_5$B$_{1-z}$ phase; B ordering driven by elastic interaction between B atoms, Z. Kristallogr. - Cryst. Mater. 229 (2014) 353–367. `doi:10.1515/zkri-2013-1710`.

[42] T. G. Berger, A. Leineweber, Mittemeijer E. J., C. Sarbu, V. Duppel, P. Fischer, On the formation and crystal structure of the Pd$_6$B, Z. Kristallogr. 221 (2006) 450–463. `doi:10.1524/zkri.2006.221.5-7.450`.

[43] T. J. Prior, P. D. Battle, Facile synthesis of interstitial metal nitrides with the filled β-manganese structure, J. Solid State Chem. 31 (2003) 361–367. `doi:10.1016/S0022-4596(02)00171-8`.

[44] J. Kumar, R. Saxena, Formation of NaCl- and Cu$_2$O-type oxides of platinum and palladium on carbon and alumina support films, J. Less-Common Met. 147 (1989) 59–71. `doi:10.1016/0022-5088(89)90148-3`.

[45] C. Wannek, B. Harbrecht, Structure and thermal stability of the new intermetallics $MgPd_2$, $MgPd_3$, and Mg_3Pd_5 and the kinetics of the iodine-catalyzed formation of $MgPd_2$, J. Solid State Chem. 159 (2001) 113–120. `doi:10.1006/jssc.2001.9138`.

[46] H. Kohlmann, G. Renaudin, K. Yvon, C. Wannek, B. Harbrecht, Hydrogen-induced atomic rearrangement in $MgPd_3$, J. Solid State Chem. 178 (2005) 1292–1300. `doi:10.1016/j.jssc.2005.02.001`.

[47] L. E. Edshammar, Björnstjerna V., The crystal structure of Pd_2Al, Acta Chem. Scand. 17 (1963) 1803.

[48] C. Wannek, B. Harbrecht, Iodine-promoted synthesis of structurally ordered $AlPd_5$, Z. Anorg. Allg. Chem. 633 (2007) 1397–1402. `doi:10.1002/zaac.200700078`.

[49] A. Nylund, Some notes on the palladium-silicon system, Acta Chem. Scand. 20 (1966) 2381–2386.

[50] B. Aronsson, A. Nylund, The crystal structure of Pd_3Si, Acta Chem. Scand. 14 (1960) 1011–1018.

[51] Y. Andersson, The structural properties of Pd_9Si_2, Chem. Scr. 28 (1988) 125–127.

[52] T. Matković, K. Schubert, Kristallstruktur von Pd_7P_3, J. Less-Common Met. 55 (1977) 177–184. `doi:10.1016/0022-5088(77)90190-4`.

[53] L. O. Gullman, X-ray diffraction and thermo-analytical investigation of the palladium-phosphorus system, J. Less-Common Met. 11 (1966) 157–167. `doi:10.1016/0022-5088(66)90002-6`.

[54] Y. Andersson, S. Rundqvist, R. Tellgren, J. O. Thomas, T. B. Flanagan, Neutron powder diffraction investigation of pure and deuterated palladium phosphide Pd_6P, Acta Crystallogr. 37B (1981) 1965–1972. `doi:10.1107/S0567740881007784`.

[55] Y. Andersson, The crystal structure of $Pd_{15}P_2$, Acta Chem. Scand. 31 (1977) 354–358.

[56] C. Romming, E. Rost, Crystal structure of the phase $Pd_{32}S_{14}$, Acta Chem. Scand. A 30 (1976) 425–428.

[57] E. Rost, E. Vestersjo, The crystal structure of the high temperature phase Pd_3S, Acta Chem. Scand. 22 (1968) 819–826.

[58] F. Grønvold, E. Røst, The crystal structures of Pd_4Se and Pd_4S, Acta Crystallogr. 15 (1962) 11–13. `doi:10.1107/S0365110X62000031`.

[59] E. A. Wood, V. B. Compton, Laves-phase compounds of alkaline earths and noble metals, Acta Crystallogr. 11 (1958) 429–433. `doi:10.1107/S0365110X58001134`.

[60] J. Mejbar, M. Notin, A new $CaCu_5$-structure in the (Ca, Pd) system, Scr. Metall. Mater. 24 (1990) 1697–1700. `doi:10.1016/0956-716X(90)90531-K`.

[61] C. Wannek, B. Harbrecht, Phase equlibria in the palladium-rich part of the gallium-palladium system. The crystal structure of Ga_3Pd_7 and $Ga_{1-x}Pd_{2+x}$, J. Alloys Compd. 316 (2001) 99–106. `doi:10.1016/S0925-8388(00)01511-5`.

[62] K. Khalaff, K. Schubert, Kristallstruktur von Pd_5Ga_2, J. Less-Common Met. 37 (1974) 129–140. `doi:10.1016/0022-5088(74)90014-9`.

[63] C. Wannek, B. Harbrecht, Die Kristallstruktur von Ga_5Pd_{13} – eine niedersymmetrische Ordnungsvariante der kubisch dichtesten Kugelpackung, Z. Anorg. Allg. Chem. 626 (2000) 1540–1544. `doi:10.1002/1521-3749(200007)626:7<1540::AID-ZAAC1540>3.0.CO;2-T`.

[64] W. Wopersnow, K. Schubert, Nickel-palladium-germanium alloys, J. Less-Common Met. 52 (1977) 1–12. `doi:10.1016/0022-5088(77)90230-2`.

[65] T. Matković, W. Wopersnow, K. Schubert, Kristallstruktur von $Pd_{21}Ge_8$, J. Less-Common Met. 56 (1977) 69–75. `doi:10.1016/0022-5088(77)90219-3`.

[66] W. Wopersnow, K. Schubert, Kristallstruktur von $Pd_{25}Ge_9$, J. Less-Common Met. 41 (1975) 97–103. `doi:10.1016/0022-5088(75)90097-1`.

[67] T. Matković, K. Schubert, Kristallstruktur von Pd_5As und Pd_5Ge, J. Less-Common Met. 58 (1978) 1–6. `doi:10.1016/0022-5088(78)90078-4`.

[68] G. S. Saini, L. D. Calvert, R. D. Heyding, J. B. Taylor, Arsenides of the transition metals: VII. The palladium–arsenic system, Can. J. Chem. 42 (1964) 620–629. `doi:10.1139/v64-091`.

[69] U. Baelz, K. Schubert, Kristallstruktur von $Pd_2As(r)$ und Pd_2Sb, J. Less-Common Met. 19 (1969) 300–304. `doi:10.1016/0022-5088(69)90111-8`.

[70] G. S. Saini, L. D. Calvert, J. B. Taylor, Compounds of the type M_5X_2: Pd_5As_2, Ni_5Si_2, and Ni_5P_2, Can. J. Chem. 42 (1964) 1511–1517. `doi:10.1139/v64-233`.

[71] H. Kohlmann, M. Vasseur, A. Sayede, G. Lefevre, J. M. Sander, S. Doyle, Crystal structure and hydrogenation properties of Pd_5As, J. Alloys Compd. 664 (2016) 256–265. `doi:10.1016/j.jallcom.2015.12.039`.

[72] S. Sato, T. Takabatake, M. Ishikawa, Structures of superconducting palladium selenides, Pd_7Se_2 and $Pd_{34}Se_{11}$, Acta Crystallogr. C 45 (1989) 1–3. `doi:10.1107/S0108270188009825`.

[73] N. Harmsen, T. Heumann, Magnetische und röntgenographische Untersuchungen an der Legierungsreihe $SrAg_5$—$SrPd_5$, Monatsh. Chem. 102 (1971) 1442–1454. `doi:10.1007/BF00917201`.

[74] H. Kohlmann, C. Ritter, Refinement of the crystal structures of palladium rich In-Pd compounds by X-ray and neutron powder diffraction, Z. Naturforsch. 62B (2007) 929–934. `doi:10.1515/znb-2007-0709`.

[75] H. Kohlmann, C. Ritter, Reaction pathways in the formation of intermetallic $InPd_3$ polymorphs, Z. Anorg. Allg. Chem. 635 (2009) 1573–1579. `doi:10.1002/zaac.20090005`.

[76] H. Kohlmann, Hydrogenation of palladium rich compounds of aluminium, gallium and indium, J. Solid State Chem. 183 (2010) 367–372. `doi:10.1016/j.jssc.2009.11.029`.

[77] K. Page, C. S. Schade, J. Zhang, P. J. Chupas, K. W. Chapman, T. Proffen, A. K. Cheetham, R. Seshadri, Preparation and characterization of Pd_2Sn nanoparticles, Mater. Res. Bull. 42 (2007) 1969–1975. `doi:10.1016/j.materresbull.2007.05.010`.

[78] M. Ellner, Zusammenhang zwischen strukturellen und thermodynamischen Eigenschaften bei Phasen der Kupfer-Familie in T10-B4-Systemen, J. Less-Common Met. 78 (1981) 21–32. `doi:10.1016/0022-5088(81)90140-5`.

[79] L. J. Cabri, T. T. Chen, Stibiopalladinite from the type locality, Am. Mineral. 61 (1976) 1249–1254.

[80] W. Wopersnow, K. Schubert, Kristallstruktur von Pd_8Sb_3, J. Less-Common Met. 48 (1976) 79–87. `doi:10.1016/0022-5088(76)90234-4`.

[81] R. E. Marsh, The centrosymmetric-noncentrosymmetric ambiguity: some more examples, Acta Crystallogr. A 50 (1994) 450–455. `doi:10.1107/S0108767393012796`.

[82] W. Wopersnow, K. Schubert, Kristallstruktur von $Pd_{20}Sb_7$ und $Pd_{20}Te_7$, J. Less-Common Met. 51 (1977) 35–44. `doi:10.1016/0022-5088(77)90171-0`.

[83] P. Matković, K. Schubert, Kristallstruktur von Pd_9Te_4, J. Less-Common Met. 58 (1978) 39–46. `doi:10.1016/0022-5088(78)90205-9`.

[84] M. Janetzky, Palladiumreiche Telluride, Dissertation, Universität Marburg, Universität Marburg (2008).

[85] M. Janetzky, B. Harbrecht, Crystal growth, structure and properties of the palladium-rich telluride $Pd_{13}Te_3$, Z. Anorg. Allg. Chem. 632 (2006) 837–844. `doi:10.1002/zaac.200500455`.

[86] N. N. Zhuravlev, N. P. Esaulov, I. V. Rall, X-ray investigation of platinum-barium and palladium-barium alloys in the region of Pt_5Ba and Pd_5Ba compositions, Sov. Phys. Crystallogr. 15 (1970) 315–316. `doi:10.1007/BF00917201`.

[87] S. Bhan, K. Schubert, Über die Struktur von Phasen mit Kupfer Unterstruktur in einigen T-B Legierungen (T = Ni, Pd, Pt; B = Ga, In, Tl, Pb, Sb, Bi), J. Less-Common Met. 17 (1969) 73–90. `doi:/10.1016/0022-5088(69)90038-1`.

[88] N. Kurtzemann, H. Kohlmann, Crystal structure and formation of $TlPd_3$ and its new hydride $TlPd_3H$, Z. Anorg. Allg. Chem. 636 (2010) 1032–1037. `doi:10.1002/zaac.201000012`.

[89] S. Bhan, T. Gödecke, P. K. Panday, K. Schubert, Über die Mischungen Palladium-Thallium und Platin-Thallium, J. Less-Common Met. 16 (1968) 415–425. `doi:10.1016/0022-5088(68)90140-9`.

[90] N. Sarah, K. Schubert, Kristallstruktur von Pd_5Bi_2, J. Less-Common Met. 63 (1979) 75–82. `doi:10.1016/0022-5088(79)90257-1`.

[91] H. Schäfer, M. Trenkel, Der chemische Transport von Cu, Ag, Au, Ru, Rh, Pd, Os, Ir, Pt unter Mitwirkung von Gaskomplexen. Al_2Cl_6, Fe_2Cl_6 oder Al_2J_6 als Komplexbildner, Z. Anorg. Allg. Chem. 414 (1975) 137–150. `doi:10.1002/zaac.19754140205`.

[92] H.-B. Merker, H. Schäfer, B. Krebs, Neue Pd_xAl_y-Phasen und die Verbindung Pd_5AlI_2, Z. Anorg. Allg. Chem. 462 (1980) 49–56. `doi:10.1002/zaac.19804620106`.

[93] A. Götze, P. Urban, O. Oeckler, H. Kohlmann, Synthesis and crystal structure of Pd_5InSe, Z. Naturforsch. 69B (2014) 417–422. `doi:10.5560/znb.2014-3335`.

[94] H. Bönnemann, R. M. Richards, Nanoscopic metal particles - Synthetic methods and potential applications, European Journal of Inorganic Chemistry 2001 (2001) 2455–2480. `doi:10.1002/1099-0682(200109)2001:10<2455::AID-EJIC2455>3.0.CO;2-Z`.

[95] M. Heise, J.-H. Chang, R. Schönemann, T. Herrmannsdörfer, J. Wosnitza, M. Ruck, Full access to nanoscale bismuth–palladium intermetallics by low-temperature syntheses, Chem. Mater. 26 (2014) 5640–5646. `doi:10.1021/cm502315a`.

[96] C. Koenig, Self consistent band structure of ordered ScPd$_3$ and YPd$_3$, Z. Phys. B: Condens. Matter 50 (1983) 33–38. `doi:10.1007/BF01307223`.

[97] D.-H. Wu, H.-C. Wang, L.-T. Wei, R.-K. Pan, B.-Y. Tang, First-principles study of structural stability and elastic properties of MgPd$_3$ and its hydride, J. Magnesium Alloys 2 (2014) 165–174. `doi:10.1016/j.jma.2014.06.001`.

[98] E. Y. Zakharova, S. M. Kazakov, A. A. Isaeva, A. M. Abakumov, G. van Tendeloo, A. N. Kuznetsov, Pd$_5$InSe and Pd$_8$In$_2$Se - New metal-rich homological selenides with 2D palladium-indium fragments: synthesis, structure and bonding, J. Alloys Compd. 589 (2014) 48–55. `doi:10.1016/j.jallcom.2013.11.172`.

[99] J. W. Cable, E. O. Wollan, W. C. Koehler, M. K. Wilkinson, Neutron diffraction investigations of ferromagnetic palladium and iron group alloys, J. Appl. Phys. 33 (1962) 1340–1340. `doi:10.1063/1.1728719`.

[100] A. Pandey, C. Mazumdar, R. Ranganathan, Magnetic behavior of binary intermetallic compound YPd$_3$, J. Alloys Compd. 476 (2009) 14–18. `doi:10.1016/j.jallcom.2008.09.040`.

[101] T. R. Marrero, E. A. Mason, Gaseous diffusion coefficients, J. Phys. Chem. Ref. Data 1 (1972) 3–118. `doi:10.1063/1.3253094`.

[102] M. J. Assael, S. Mixafendi, W. A. Wakeham, The viscosity and thermal conductivity of normal hydrogen in the limit of zero density, J. Phys. Chem. Ref. Data 15 (1986) 1315–1322. `doi:10.1063/1.555764`.

[103] D. R. Lide (Ed.), CRC Handbook of Chemistry and Physics, Internet Version 2005, CRC Press, Boca Raton, FL, 2005.
URL `http://www.hbcpnetbase.com`

[104] M. Felderhoff, C. Weidenthaler, R. von Helmolt, U. Eberle, Hydrogen storage: the remaining scientific and technological challenges, Phys. Chem. Chem. Phys. 9 (2007) 2643–2653. `doi:10.1039/B701563C`.

[105] A. L. Allred, E. G. Rochow, A scale of electronegativity based on electrostatic force, J. Inorg. Nucl. Chem. 5 (1958) 264–268. `doi:10.1016/0022-1902(58)80003-2`.

[106] A. N. R. Bos, K. R. Westerterp, Mechanism and kinetics of the selective hydrogenation of ethyne and ethene, Chem. Eng. Process. 32 (1993) 1–7. `doi:10.1016/0255-2701(93)87001-B`.

[107] M. Baerns (Ed.), Basic Principles in Applied Catalysis, Springer Series in Chemical Physics, volume 75, Springer, Berlin, Heidelberg, 2004. `doi:10.1007/978-3-662-05981-4`.

[108] J. T. Richardson, R. Scates, M. V. Twigg, X-ray diffraction study of nickel oxide reduction by hydrogen, Appl. Catal., A 246 (2003) 137–150. `doi:10.1016/S0926-860X(02)00669-5`.

[109] K. V. Manukyan, A. G. Avetisyan, C. E. Shuck, H. A. Chatilyan, S. Rouvimov, S. L. Kharatyan, A. S. Mukasyan, Nickel oxide reduction by hydrogen: kinetics and structural transformations, J. Phys. Chem. C 119 (2015) 16131–16138. `doi:10.1021/acs.jpcc.5b04313`.

[110] F. Chen, Y. Mohassab, T. Jiang, H. Y. Sohn, Hydrogen reduction kinetics of hematite concentrate particles relevant to a novel flash ironmaking process, Metall. Mater. Trans. B 46 (2015) 1133–1145. `doi:10.1007/s11663-015-0332-z`.

[111] H. Schulz, K. Ritapal, W. Bronger, W. Klemm, Über die Reaktion von Elementen der achten Nebengruppe mit Oxiden unedler Metalle im Wasserstoffstrom, Z. Anorg. Allg. Chem. 357 (1968) 299–313. `doi:10.1002/zaac.19683570418`.

[112] C. A. Wurtz, Sur l' hydrure de cuivre, Ann. Chim 11 (1844) 250–252.

[113] H. Kohlmann, H. E. Fischer, K. Yvon, Europium palladium hydrides, Inorg. Chem. 40 (2001) 2608–2613. `doi:10.1021/ic001225d`.

[114] T. B. Flanagan, W. A. Oates, The palladium-hydrogen system, Annu. Rev. Mater. Sci. 21 (1991) 269–304.

[115] H. Wipf, Diffusion of hydrogen in metals, in: H. Wipf (Ed.), Hydrogen in Metals III, Vol. 73 of Top. Appl. Phys., Springer, Berlin, Heidelberg, 1997, pp. 51–91. `doi:10.1007/BFb0103401`.

[116] T. Skoskiewicz, Superconductivity in the palladium-hydrogen and palladium-nickel-hydrogen systems, Phys. Status Solidi A 11 (1972) K123–K126. `doi:10.1002/pssa.2210110253`.

[117] T. R. P. Gibb, Jr., J. MacMillan, R. J. Roy, The magnetic susceptibility of palladium hydride, J. Phys. Chem. 70 (1966) 3024.

[118] R. Griessen, D. G. de Groot, Effect of the anharmonicity and Debye-Waller factor on the superconductivity of PdH_x and PdD_x, Helv. Phys. Acta 55 (1982) 699–710.

[119] M. Gupta, L. Schlapbach, Electronic properties, in: L. Schlapbach (Ed.), Hydrogen in Intermetallic Compounds I, Vol. 63 of Top. Appl. Phys., Springer, Berlin, 1988, pp. 139–217. `doi:10.1007/3540183337_12`.

[120] B. M. Andreev, E. P. Magomedbekov, G. H. Sicking, Interaction of Hydrogen Isotopes with Transition Metals and Intermetalic Compounds, Springer, Berlin, 1966.

[121] J. E. Worsham, Jr., M. K. Wilkinson, C. G. Shull, Neutron-diffraction observations on the palladium-hydrogen and palladium-deuterium systems, J. Phys. Chem. Solids 3 (1957) 303–310. `doi:10.1016/0022-3697(57)90033-1`.

[122] T. B. Massalski, H. Okamoto (Eds.), Binary alloy phase diagrams, ASM International, Materials Park, Ohio, 1990.

[123] F. A. Lewis, The palladium-hydrogen system, part III: Alloy systems and hydrogen permeation, Platinum Met. Rev. 26 (1982) 121–128.

[124] C. Stanitski, J. Tanaka, Ternary hydrides of calcium and strontium with palladium, J. Solid State Chem. 4 (1972) 331–339. `doi:10.1016/0022-4596(72)90145-4`.

[125] E. Rönnebro, D. Noréus, M. Gupta, K. Kadir, B. Hauback, P. Lundqvist, The crystal and electronic structure of $CaPd_3H$, Mater. Res. Bull. 35 (2000) 315–323. `doi:10.1016/S0025-5408(00)00226-9`.

[126] H. Kohlmann, N. Kurtzemann, R. Weihrich, T. Hansen, *In situ* neutron powder diffraction on intermediate hydrides of $MgPd_3$ in a novel sapphire gas pressure cell, Z. Anorg. Allg. Chem. 635 (2009) 2399–2405. `doi:10.1002/zaac.200900336`.

[127] H. Kohlmann, A. V. Skripov, A. V. Soloninin, T. J. Udovic, The anti-perovskite type hydride InPd$_3$H$_{0.89}$, J. Solid State Chem. 183 (2010) 2461–2465. `doi:10.1016/j.jssc.2010.08.015`.

[128] S. Yamaguchi, M. Ohashi, T. Kajitani, K. Aoki, S. Ikeda, Distribution of hydrogen atoms in YPd$_3$H$_x$ studied by neutron diffraction and inelastic neutron scattering, J. Alloys Compd. 253-254 (1997) 308–312. `doi:10.1016/S0925-8388(96)02945-3`.

[129] P.-J. Ahlzén, Y. Andersson, R. Tellgren, D. Rodić, T. B. Flanagan, Y. Sakamoto, A neutron powder diffraction study of Pd$_3$MnD$_x$, Z. Phys. Chem. (Muenchen, Ger.) 163 (1989) 213–218. `doi:10.1524/zpch.1989.163.Part_1.0213`.

[130] H. Kohlmann, F. Müller, K. Stöwe, A. Zalga, H. P. Beck, Hydride formation in the intermetallic compounds CePd$_3$ and CeRh$_3$, Z. Anorg. Allg. Chem. 635 (2009) 1407–1411. `doi:10.1002/zaac.200801356`.

[131] N. Kunkel, J. Sander, N. Louis, Y. Pang, L. M. Dejon, F. Wagener, Y. N. Zang, A. Sayede, M. Bauer, S. M., H. Kohlmann, Theoretical investigation of the hydrogenation induced atomic rearrangements in palladium rich intermetallic compounds MPd$_3$ (M = Mg, In, Tl), Eur. Phys. J. 82B (2011) 1–6. `doi:10.1140/epjb/e2011-10916-5`.

[132] J. W. Turley, H. W. Rinn, Crystal structure of aluminum hydride, Inorg. Chem. 8 (1969) 18–22. `doi:10.1021/ic50071a005`.

[133] New ternary and quaternary metal hydrides with K$_2$PtCl$_6$-type structures, author=Huang, B. and Bonhomme, F. and Selvam, P. and Yvon, K. and Fischer, P., J. Less-Common Met. 171 (1991) 301–311. `doi:10.1016/0022-5088(91)90152-T`.

[134] J. J. Didisheim, P. Zolliker, K. Yvon, P. Fischer, J. Schefer, M. Gubelmann, A. F. Williams, Dimagnesium iron (II) hydride, Mg$_2$FeH$_6$, containing octahedral FeH$_6{}^{4-}$ anions, Inorg. Chem. 23 (1984) 1953–1957. `doi:10.1021/ic00181a032`.

[135] W. Bronger, M. Gehlen, G. Auffermann, Synthese und Struktur von Li$_3$RhH$_6$, einem ternären Hydrid mit isolierten [RhH$_6$]$^{3-}$-Oktaedern, Z. Anorg. Allg. Chem. 620 (1994) 1983–1985. `doi:10.1002/zaac.19946201124`.

[136] W. Bronger, M. Gehlen, G. Auffermann, Na$_3$RhH$_6$, Na$_3$IrH$_6$ und Li$_3$IrH$_6$, neue komplexe Hydride mit isolierten [RhH$_6$]$^{3-}$- und [IrH$_6$]$^{3-}$-Oktaedern, J. Alloys Compd. 176 (1991) 255–262. `doi:10.1016/0925-8388(91)90033-R`.

[137] R. O. Moyer Jr., C. Stanitski, J. Tanaka, M. I. Kay, R. Kleinberg, Ternary hydrides of calcium and strontium with iridium, rhodium and ruthenium, J. Solid State Chem. 3 (1971) 541–549. `doi:10.1016/0022-4596(71)90100-9`.

[138] R. O. Moyer Jr., B. J. Burnim, R. Lindsay, Synthesis and structures of [Sr$_{2-x}$Eu$_x$]IrH$_5$, [Sr$_{2-x}$Eu$_x$]RhH$_5$, [Ca$_{2-x}$Eu$_x$]IrH$_5$, and Eu$_2$RhH$_5$, J. Solid State Chem. 121 (1996) 56–60. `doi:10.1006/jssc.1996.0008`.

[139] W. Bronger, P. Müller, J. Kowalczyk, G. Auffermann, Synthese und Struktur von Li$_3$RhH$_4$, einem ternären Hydrid mit planaren [RhH$_4$]$^{3-}$-Baueinheiten, J. Alloys Compd. 176 (1991) 263–268. `doi:10.1016/0925-8388(91)90034-S`.

[140] F. Bonhomme, K. Yvon, P. Fischer, MgRhD$_{1-x}$, a new interstitial deuteride containing square planar [Rh$_4$D$_4$] rings with nearly linear Rh–D–Rh bridges, J. Alloys Compd. 186 (1992) 209–215. `doi:10.1016/0925-8388(92)90006-U`.

[141] J. N. Becker, J. Bauer, A. Giehr, P. I. Chu, N. Kunkel, M. Springborg, H. Kohlmann, Electronic structure of ternary rhodium hydrides with lithium and magnesium, Inorg. Chem. 53 (2013) 1135–1143. `doi:10.1021/ic402687p`.

[142] W. Bronger, Die Raumchemie des Wasserstoffs in Metallhydriden im Vergleich mit entsprechenden Fluoriden und Chloriden, Z. Anorg. Allg. Chem. 622 (1996) 9–16. `doi:10.1002/zaac.19966220103`.

[143] M. Mintz, D. Hiershler, Z. Hadari, Systematic study of the hcp $\rightleftharpoons$ fcc transitions in the heavier LnH_2-LnH_3 systems, J. Less-Common Met. 48 (1976) 241–249. `doi:10.1016/0022-5088(76)90006-0`.

[144] W. G. Bos, K. H. Gayer, The rare earth hydrides, J. Nucl. Mater. 18 (1966) 1–30. `doi:10.1016/0022-3115(66)90092-4`.

[145] H. Kohlmann, Metal Hydrides, in: R. A. Meyers,(Ed.) Encyclopaedia of Physical Sciences and Technology, vol. 9, 3rd ed, Academic Press, New York, 2002.

[146] X-Shape, Stoe & Cie GmbH, Darmstadt (Germany), 2005.

[147] X-Red32, Stoe & Cie GmbH, Darmstadt (Germany), 2005.

[148] G. M. Sheldrick, A short history of SHELX, Acta Crystallogr. A64 (2008) 112–122. `doi:10.1107/S2053229614024218`.

[149] G. M. Sheldrick, SHELX-97 Manual, Universität Göttingen, 1997.

[150] L. B. McCusker, R. B. Von Dreele, D. E. Cox, D. Louër, P. Scardi, Rietveld refinement guidelines, J. Appl. Cryst. 32 (1999) 36–50. `doi:10.1107/S0021889898009856`.

[151] V. F. Sears, Neutron scattering lengths and cross sections, Neutron News 3 (1992) 26–37. `doi:10.1080/10448639208218770`.

[152] T. C. Hansen, P. F. Henry, H. E. Fischer, J. Torregrossa, P. Convert, The D20 instrument at the ILL: a versatile high-intensity two-axis neutron diffractometer, Measurement Science and Technology 19 (2008) 034001. `doi:10.1088/0957-0233/19/3/034001`.

[153] A. Franz, A. Hoser, E9: The fine resolution powder diffractometer (FIREPOD) at BER II, Journal of large-scale research facilities JLSRF 3 (2017) A103. `doi:10.17815/jlsrf-3-127`.

[154] P. Fischer, G. Frey, M. Koch, M. Könnecke, V. Pomjakushin, J. Schefer, R. Thut, N. Schlumpf, R. Bürge, U. Greuter, S. Bondt, E. Berruyer, High-resolution powder diffractometer HRPT for thermal neutrons at SINQ, Phys. B 276-278 (2000) 146–147. `doi:10.1016/S0921-4526(99)01399-X`.

[155] H. M. Rietveld, Line profiles of neutron powder-diffraction peaks for structure refinement, Acta Crystallogr. 22 (1967) 151–152. `doi:10.1107/S0365110X67000234`.

[156] H. M. Rietveld, A profile refinement method for nuclear and magnetic structures, J. Appl. Crystallogr. 2 (1969) 65–71. `doi:10.1107/S0021889869006558`.

[157] J. Rodríguez-Carvajal, Fullprof: A program for rietveld refinement and pattern matching analysis (2012).

[158] TOPAS, Bruker AXS.
URL `www.bruker-axs.com`

7. Bibliography

[159] Crystal Impact GbR, Pearson's crystal data (2007).

[160] FIZ Karlsruhe, Inorganic crystal structure database web (2018).

[161] R. A. Young, Introduction to the Rietveld method, in: The Rietveld Method, Oxford University Press, Oxford, 1993, pp. 1–39.

[162] H. Auer, H. Kohlmann, *In situ* investigations on the formation and decomposition of $KSiH_3$ and $CsSiH_3$, Z. Anorg. Allg. Chem. 643 (2017) 945–951. `doi:10.1002/zaac.201700164`.

[163] T. C. Hansen, H. Kohlmann, Chemical reactions followed by *in situ* neutron powder diffraction, Z. Anorg. Allg. Chem. 640 (2014) 3044–3063. `doi:10.1002/zaac.201400359`.

[164] Universal Analysis 2000, TA Instruments.

[165] G. Kresse, J. Furthmüller, Vienna ab-initio simulation package (vasp).
URL `http://vasp.at`

[166] G. Kresse, J. Furthmüller, Efficiency of ab-initio total energy calculations for metals and semiconductors using a plane-wave basis set, Comput. Mater. Sci. 6 (1996) 15–50. `doi:10.1016/0927-0256(96)00008-0`.

[167] G. Kresse, J. Furthmüller, Efficient iterative schemes for ab initio total-energy calculations using a plane-wave basis set, Phys. Rev. B 54 (1996) 11169–11186. `doi:10.1103/PhysRevB.54.11169`.

[168] G. Kresse, D. Joubert, From ultrasoft pseudopotentials to the projector augmented-wave method, Phys. Rev. B 59 (1999) 1758–1775. `doi:10.1103/PhysRevB.59.1758`.

[169] P. E. Blöchl, Projector augmented-wave method, Phys. Rev. B 50 (1994) 17953–17979. `doi:10.1103/PhysRevB.50.17953`.

[170] J. P. Perdew, J. Burke, M. Ernzerhof, Generalized gradient approximation made simple, Phy. Rev. Lett. 77 (1996) 3865–3868. `doi:10.1103/PhysRevLett.77.3865`.

[171] W. Biltz, Raumchemie der festen Stoffe, L. Voss, Leipzig, 1934.

[172] R. T. Azuah, L. R. Kneller, Y. Qiu, P. L. Tregenna-Piggott, C. M. Brown, J. R. Copley, R. M. Dimeo, DAVE: a comprehensive software suite for the reduction, visualization, and analysis of low energy neutron spectroscopic data, J. Res. Natl. Inst. Stand. Technol. 114 (2009) 341–358.

[173] Y. Andersson, S. Rundqvist, R. Tellgren, J. O. Thomas, T. B. Flanagan, A neutron diffraction investigation of deuterated $Pd_3P_{0.80}$, J. Solid State Chem. 32 (1980) 321–327. `doi:10.1016/S0022-4596(80)80026-0`.

[174] Y. Andersson, S. Rundqvist, R. Tellgren, T. B. Flanagan, A neutron powder diffraction investigation of deuterated $Pd_{15}P_2$, Z. Phys. Chem. (Muenchen, Ger.) 145 (1985) 43–49. `doi:10.1524/zpch.1985.145.1_2.043`.

[175] A. C. Lawson, J. W. Conant, R. Robertson, R. K. Rohwer, V. A. Young, C. L. Talcott, Debye-Waller factors of PdD_x materials by neutron powder diffraction, J. Alloys Compd. 183 (1992) 174–180. `doi:10.1016/0925-8388(92)90742-R`.

[176] S. Yamaguchi, Z.-Q. Li, R.-T. Fu, Y. Kawazoe, Hydrogen site occupation in YPd_3 with L12 structure, Phys. Rev. B 55 (1997) 14051–14054. `doi:10.1103/PhysRevB.55.14051`.

[177] P. Önnerud, Y. Andersson, R. Tellgren, P. Nordblad, F. Bourée, G. André, The crystal and magnetic structures of ordered cubic $Pd_3MnD_{0.7}$, Solid State Commun. 101 (1997) 433–437. `doi:10.1016/S0038-1098(96)00607-2`.

[178] K. Schubert, Kristallstrukturen zweikomponentiger Phasen, Springer, Berlin, Heidelberg, 1964. `doi:10.1007/978-3-642-94904-3`.

[179] N. Novaković, J. G. Novaković, L. Matović, M. Manasijević, I. Radisavljević, B. P. Mamula, N. Ivanović, Ab initio calculations of MgH_2, MgH_2: Ti and MgH_2: Co compounds, Int. J. Hydrogen Energy 35 (2010) 598–608. `doi:10.1016/j.ijhydene.2009.11.003`.

[180] U. Häussermann, H. Blomqvist, D. Noréus, Bonding and stability of the hydrogen storage material Mg_2NiH_4, Inorg. Chem. 41 (2002) 3684–3692. `doi:10.1021/ic0201046`.

[181] P. Raybaud, F. Ropital, Process for the storage of hydrogen using a system that strikes a balance between an alloy of magnesium and palladium and the corresponding hydride, US Patent 7,547,432 (2009).
URL `https://www.google.com/patents/US7547432B2`

[182] R. Martínez-Coronado, M. Retuerto, B. Torres, M. J. Martínez-Lope, M. T. Fernández-Díaz, J. A. Alonso, High-pressure synthesis, crystal structure and cyclability of the Mg_2NiH_4 hydride, Int. J. Hydrogen Energy 38 (2013) 5738–5745. `doi:10.1016/j.ijhydene.2013.02.108`.

[183] Y. Goto, H. Kakuta, A. Kamegawa, H. Takamura, M. Okada, High-pressure synthesis of novel hydride in Mg-*M* systems (*M* = Li, Pd), J. Alloys Compd. 404 (2005) 448–452. `doi:10.1016/j.jallcom.2005.02.096`.

[184] M. Gupta, A. J. Freeman, Electronic structure and proton spin-lattice relaxation in PdH, Phys. Rev. B 17 (1978) 3029–3039. `doi:10.1103/PhysRevB.17.3029`.

[185] A. C. Switendick, Electronic structure and total energy calculations for transition metal hydrides, J. the Less-Common Met. 130 (1987) 249–259. `doi:10.1016/0022-5088(87)90116-0`.

[186] A. R. Williams, J. Kübler, C. D. Gelatt Jr., Cohesive properties of metallic compounds: Augmented-spherical-wave calculations, Phys. Rev. B 19 (1979) 6094–6118. `doi:10.1103/PhysRevB.19.6094`.

[187] K. Baba, Y. Niki, Y. Sakamoto, T. B. Flanagan, The phase transition in palladium-manganese alloys with up to 33.3 at.% Mn, J. Alloys Compd. 179 (1992) 321–331. `doi:10.1016/0925-8388(92)90231-W`.

[188] D. Rodic, P.-J. Ahlzén, Y. Andersson, T. R., B.-V. F., The crystal and magnetic structure of tetragonal Pd_3Mn, Solid State Commun. 78 (1991) 767 – 772. `doi:10.1016/0038-1098(91)90861-O`.

[189] K. Baba, Y. Niki, Y. Sakamoto, T. B. Flanagan, A. Craft, Reversibile transitions between ordered structures in the Pd_3Mn-hydrogen system, Scr. Metall. 21 (1987) 1147–1151.

[190] D. K. Saha, K. Ohshima, M. Y. Wey, R. Miida, T. Kimoto, Structure and magnetism of fcc Pd-Mn alloys, Phys. Rev. B 49 (1994) 15715. `doi:10.1103/PhysRevB.49.15715`.

[191] M. H. Rashid, D. J. Sellmyer, Spin-glass-like freezing in disordered $MnPd_3$ and $CrPd_3$ alloys, J. Appl. Phys. 55 (1984) 1735–1737. `doi:10.1063/1.333459`.

7. Bibliography

[192] P. Önnerud, Y. Andersson, R. Tellgren, P. Nordblad, The magnetic structure of ordered cubic Pd_3Mn, J. Solid State Chem. 128 (1997) 109–114. `doi:10.1006/jssc.1996.7181`.

[193] D. Rodić, P. Ahlzén, Y. Andersson, R. Tellgren, The magnetic structure of $Pd_3MnD_{0.53}$, Solid State Commun. 71 (1989) 623–626. `doi:10.1016/0038-1098(89)90549-8`.

[194] K. Schubert, S. Bhan, T. K. Biswas, K. Frank, P. K. Panday, Einige Strukturdaten intermetallischer Phasen, Naturwissenschaften 55 (1968) 542–543. `doi:10.1007/BF00660131`.

[195] S. C. Stevenson, Synthesis and hydrogenation of MPd$_3$ compounds, Placement report, Universität Leipzig, Leipzig (2017).

[196] T. B. Flanagan, S. Majchrzak, B. Baranowski, A chemical reaction strongly dependent upon the degree of order of an alloy: The absorption of hydrogen by Pd_3Fe, Philos. Mag. 25 (1972) 257–262. `doi:10.1080/14786437208229233`.

[197] P. Mélix, Berechnungen zur Wasserstoffeinlagerung in MPd$_3$-Verbindungen (M = Mg, Mn, In, Sn, Tl, Pb, Bi), Placement report, Universität Leipzig, Leipzig (2015).

[198] W. Jeitschko, The crystal structure of MoCoB and related compounds, Acta Cryst. B24 (1968) 930–934. `doi:10.1107/S0567740868003432`.

[199] W. Jeitschko, R. O. Altmeyer, Rh_2Sb with (anti-)$PbCl_2$-type structure, Z. Naturforsch. 45B (1990) 947–951. `doi:10.1515/znb-1990-0705`.

[200] B. Chevalier, Pasturel M., J.-L. Bobet, J. Etourneau, O. Isnard, J. Sanchez Marcos, J. Rodriguez Fernandez, Magnetic ordering induced by the hydrogenation of the ternary stannide CeNiSn, J. Magn. Magn. Mater. 272-276 (2004) 576–578. `doi:10.1016/j.jmmm.2003.11.222`.

[201] B. Chevalier, A. Wattiaux, J.-L. Bobet, The Doniach diagram and hydrogenation of the ternary compounds CePdIn and CePdSn, J. Phys.: Condens. Matter 18 (2006) 1743–1755. `doi:10.1088/0953-8984/18/5/026`.

[202] V. A. Yartys, R. V. Denys, O. Isnard, R. G. Delaplane, P. Svedlindh, K. H. J. Buschow, Crystal and magnetic structure of TbNiSnD studied by neutron powder diffraction, J. Magn. Magn. Mater. 311 (2007) 639–643. `doi:10.1016/j.jmmm.2006.08.043`.

[203] A. E. Dwight, Crystal structure of RENiSn and REPdSn (RE = rare earth) equiatomic compounds, J. Less-Common Met. 93 (1983) 411–413. `doi:10.1016/0022-5088(83)90195-9`.

[204] J. Murray, M. Post, J. Taylor, Thermodynamics of $LaNi_5 + H_2$ by differential heat flow calorimetry: hysteresis and entropies, in: T. N. Veziroglu (Ed.), Metal-Hydrogen Systems, Pergamon, Oxford, 1982, pp. 445–449.

[205] T. B. Flanagan, W. Luo, J. Clewley, Calorimetric enthalpies of absorption and desorption of protium and deuterium by palladium, J. Less-Common Met. 172 (1991) 42–55. `doi:10.1016/0022-5088(91)90431-3`.

[206] M. El-Boragy, S. Bhan, K. Schubert, Kristallstruktur von Pd_5Sb_2 und Ni_5As_2 und einigen Varianten, J. Less-Common Met. 22 (1970) 445–458. `doi:10.1016/0022-5088(70)90132-3`.

[207] T. Takabatake, M. Ishikawa, J. L. Jorda, Superconductivity and phase relations in the Pd-Se system, J. Less-Common Met. 134 (1987) 79–89.

[208] J. P. Neumann, A. Mikula, Y. A. Chang, Phase stability investigations of the palladium-cadmium system: Part II. structural studies, Metallurgical Transactions A 13 (1982) 1123–1126. `doi: 10.1007/BF02645492`.

[209] K. Terada, F. W. Cagle, The crystal structure of potarite (PdHg) with some comments on allopalladium, Am. Mineral. 45 (1960) 1093–1097.

[210] M. Ellner, T. Godecke, K. Schubert, Phases in the mixture Pd-Pb, Z. Metallkd. 64 (1973) 566–568.

[211] H. W. Mayer, M. Ellner, K. Schubert, Crystal structure of $Pd_{13}Pb_9$. r, J. Less-Common Met. 71 (1980) P29–P38. `doi:10.1016/0022-5088(80)90218-0`.

[212] J. N. Pratt, K. M. Myles, J. B. Darby Jr, M. H. Mueller, X-Ray studies of palladium-cadmium and palladium-antimony alloys, J. Less Common-Met. 14 (1968) 427–433. `doi: 10.1016/0022-5088(68)90166-5`.

[213] S. Geller, The crystal structure of $Pd_{17}Se_{15}$, Acta Crystallogr. 15 (1962) 713–721. `doi:10. 1107/S0365110X62001929`.

[214] H. Okamoto, The Pd-Se (palladium-selenium) system, J. Phase Equilib. 13 (1992) 69–72. `doi: 10.1007/BF02645382`.

[215] M. El-Boragy, M. Ellner, K. Schubert, On some metastable homeotypes of CuZn with Pd as majority component, Z. Metallkd. 80 (1989) 197–200.

[216] H. Zhou, X. Yang, L. Li, X. Liu, Y. Huang, X. Pan, A. Wang, J. Li, T. Zhang, PdZn intermetallic nanostructure with Pd–Zn–Pd ensembles for highly active and chemoselective semi-hydrogenation of acetylene, ACS Catal. 6 (2016) 1054–1061. `doi:10.1021/acscatal.5b01933`.

[217] M. Armbrüster, K. Konvir, M. Behrens, D. Teschner, Y. Grin, R. Schlögl, Pd-ga intermetallic compounds as highly selective semihydrogenation catalysts, J. Am. Chem. Soc. 132 (2010) 14745–14747. `doi:10.1021/ja106568t`.

[218] A. Ota, M. Armbrüster, M. Behrens, D. Rosenthal, M. Friedrich, I. Kasatkin, F. Girgsdies, W. Zhang, R. Wagner, R. Schlögl, Intermetallic compound Pd_2Ga as a selective catalyst for the semi-hydrogenation of acetylene: from model to high performance systems, J. Phys. Chem. C 115 (2011) 1368–1374. `doi:10.1021/jp109226r`.

[219] V. B. Chernogorenko, K. A. Lynchak, Production of bismuth powder by the reduction of bismuth oxide with a mixture of molecular and atomic hydrogen, Powder Metall. Met. Ceram. 12 (1973) 360–362. `doi:10.1007/BF00791258`.

[220] R. Weihrich, S. Matar, I. Anusca, F. Pielnhofer, P. Peter, F. Bachhuber, V. Eyert, Palladium site ordering and the occurrence of superconductivity in $Bi_2Pd_3Se_{2-x}S_x$, J. Solid State Chem. 184 (2011) 797 – 804. `doi:10.1016/j.jssc.2011.01.037`.

[221] S. Seidlmayer, F. Bachhuber, I. Anusca, J. Rothballer, M. Bräu, P. Peter, R. Weihrich, Half antiperovskites: V. Systematics in ordering and group-subgroup-relations for $Pb_2Pd_3Se_2$, $Bi_2Pd_3Se_2$, and $Bi_2Pd_3S_2$, Z. Kristallogr. 225 (2010) 371–381. `doi:10.1524/zkri.2010.1272`.

[222] E. Larionov, H. Li, C. Mazet, Well-defined transition metal hydrides in catalytic isomerizations, Chem. Commun. 50 (2014) 9816–9826. `doi:10.1039/C4CC02399D`.

[223] T. D. Humphries, D. A. Sheppard, C. E. Buckley, Recent advances in the 18-electron complex transition metal hydrides of Ni, Fe, Co and Ru, Coord. Chem. Rev. 342 (2017) 19–33. `doi: 10.1016/j.ccr.2017.04.001`.

[224] W. Bronger, L. Breil, Calcium-Rhodium-Hydride–Synthese und Struktur, Z. Anorg. Allg. Chem. 624 (1998) 1819–1822. `doi:10.1002/(SICI)1521-3749(1998110)624:11<1819:: AID-ZAAC1819>3.0.CO;2-L`.

[225] T. Sato, D. Noréus, H. Takeshita, U. Häussermann, Hydrides with the perovskite structure: general bonding and stability considerations and the new representative $CaNiH_3$, J. Solid State Chem. 178 (2005) 3381–3388. `doi:10.1016/j.jssc.2005.08.026`.

[226] W. Bronger, K. Jansen, P. Müller, $CaPdH_2$, ein ternäres Hydrid mit perowskitverwandter Struktur, J. Less-Common Met. 161 (1990) 299–302. `doi:10.1016/0022-5088(90)90040-Q`.

[227] W. Bronger, K. Jansen, L. Breil, $Ca_2RhD_{5.4}$ –Strukturbestimmung über Neutronenbeugungsexperimente, Z. Anorg. Allg. Chem. 624 (1998) 1477–1480. `doi:10.1002/(SICI) 1521-3749(199809)624:9<1477::AID-ZAAC1477>3.0.CO;2-I`.

[228] V. A. Somenkov, A. V. Irodova, Lattice structure and phase transition of hydrogen in intermetallic compounds, J. Less-Common Met. 101 (1984) 481–492.

[229] A. F. Andresen, K. Otnes, A. J. Maeland, Neutron scattering investigations of $Be_2ZrH_{1.5}$ and $Be_2ZrD_{1.5}$, J. Less-Common Met. 89 (1983) 201–204. `doi:10.1016/0022-5088(83)90267-9`.

[230] A. F. Andresen, H. Fjellvåg, A. J. Maeland, Formation and crystal structure of $ThNi_2D_x$, J. Less-Common Met. 103 (1984) 27–31. `doi:10.1016/0022-5088(84)90354-0`.

[231] M. A. Green, A. Ho-Baillie, H. J. Snaith, The emergence of perovskite solar cells, Nat. Photonics 8 (2014) 506–514. `doi:10.1038/nphoton.2014.134`.

[232] M. Saliba, J.-P. Correa-Baena, M. Grätzel, A. Hagfeldt, A. Abate, Perovskite solar cells: from the atomic level to film quality and device performance, Angew. Chem., Int. Ed. 57 (2018) 2554–2569. `doi:10.1002/anie.201703226`.

[233] B. Batlogg, Superconductivity in $Ba(Pb,Bi)O_3$, Physica B+C 126 (1984) 275–279.

[234] R. Cava, B. Batlogg, J. Krajewski, R. Farrow, L. W. Rupp Jr., A. White, K. Short, W. Peck, T. Kometani, Superconductivity near 30 K without copper: the $Ba_{0.6}K_{0.4}BiO_3$ perovskite, Nature 332 (1988) 814. `doi:10.1038/332814a0`.

[235] H. Tanaka, M. Misono, Advances in designing perovskite catalysts, Curr. Opin. Solid State Mater. Sci. 5 (2001) 381–387.

Part II.

Publications within this thesis

8. Palladium Hydride and Hydrides of Palladium-Rich Phases

André Götze, Holger Kohlmann

8.1. Authors' contributions

H. Kohlmann wrote the part "Palladium hydride". The part "Ternary disordered palladium-rich hydrides" was created by A. Götze and H. Kohlmann. "Ternary ordered palladium-rich hydrides $(M\mathrm{Pd}_{\geq 2})$" was written by A. Götze.

8.2. Abstract

Synthesis, crystal structure, and properties of hydrides of palladium and its intermetallic compounds are being reviewed. Focus is on crystal structure, phase diagram, interplay between hydrogen content and electronic or magnetic properties, diffusion and lattice gas behavior of hydrogen for palladium hydrides, and on synthesis and crystal chemical interpretation of hydrogenation reactions for palladium-rich compounds. Hydrogen embrittlement, heterogeneous catalysis, and isotope effects are briefly discussed. For palladium-rich compounds $M\mathrm{Pd}_3$ (M = Mg, In, Tl, Bi, Mn) hydrogen induced rearrangement between close-packed crystal structures and its crystallographic interpretation are discussed in detail.

Palladium hydride and the system Pd–H are the most studied metal hydride and metal–hydrogen phase diagram, respectively. Disordered solid solutions of palladium with other metals have also been extensively studied with respect to their behavior toward hydrogen. While these two aspects are covered in the first two chapters, the third chapter focuses on the less well investigated ternary hydrides of ordered palladium-rich compounds. Hydrides of palladium and its intermetallic compounds play an important role as model systems in condensed matter physics, for example, lattice gas, interplay of hydrogen content on electronic and magnetic properties, hydrogen storage, embrittlement of metallic materials and diffusion in metals, but they have also important application in catalysis (hydrogenation), for gas purification and isotope separation.

8.3. Remarks on nomenclature

Chemical compounds of one or more metals with hydrogen (H) are called metal hydrides. Generally H consists of the natural isotopic mixture of 99.985 % ^{1}H (protium) + 0.015 % ^{2}H (deuterium, D). If not indicated otherwise, the term metal hydride is here also used as a collective name including all isotopes, that is, protides, deuterides, and tritides. They are only differentiated explicitly in the following text in cases where isotope effects are important, for example, diffusion or neutron scattering, and in the naming of crystal structure types first determined on deuterides.

In chapters on intermetallic compounds of palladium, structural relationships, and thus crystal structure types, are of particular importance for the understanding of hydrogenation reactions and other properties. Many structure types are of one-to-three composition, like $TiAl_3$ or $AuCu_3$ types. While those two, as most structure types and names of compounds, are in line with IUPAC's rules for nomenclature based on electronegativity, some of the compounds of interest would have to be named using a three-to-one formula like Pd_3In and Pd_3Bi. For the sake of clarity and ease of recognition of structural relationships, however, in those cases IUPAC's rules are not followed; for example, they are called $InPd_3$ and $BiPd_3$.

Many palladium-rich intermetallic compounds and their hydrides derive structurally from close-packed structures, in which the hexagonal layers of close-packed atoms are usually named A, B, and C. The sequence AB … stands for the hexagonal (hcp), ABC … for the cubic-close packing (ccp). In older literature on ccp-related ordered superstructures, like $TiAl_3$ type or $ZrAl_3$ type, A and B are often used in a different way to denote the stacking sequence and are not hexagonal atomic layers. In order to avoid confusion, those layers are named A' and B' in this text.

8.4. Palladium hydride

8.4.1. History

Thomas Graham was a Scottish chemist who did a great deal of work on gas diffusion and effusion, dialysis, and colloids. In a study called "On the Absorption and Dialytic Separation of Gases by Colloid Septa" in 1866 (150 years before the publication of this article) he discovered that hydrogen not only permeates through a palladium foil at 513–538 K, but also that palladium takes up considerable amounts of hydrogen gas [1]. Palladium heated in vacuum gives off hydrogen gas and after such an activation treatment palladium is able to take in hydrogen again [1]. This can be achieved either by reaction of palladium with hydrogen gas or electrochemically by using palladium wire as a cathode in acidic aqueous solutions. The highest uptake occurs for spongy palladium, with 686 times its own volume [1], or for palladium wire with 935 times its own volume [2]. The latter corresponds to a composition $PdH_{0.74}$. It further loses 25 % of its electrical conductivity and has a reduced tenacity as compared to pristine palladium. Graham attributed the behavior to the porosity of palladium metal and assumed hydrogen to enter in a liquid state [1,2]. Because of the peculiar behavior, which was considered very unusual at that time, hydrogen was often regarded as vapor of a highly volatile metal. Palladium hydride could thus be seen as an alloy of palladium with that metal [2]. Detailed measurements like pressure–composition isotherms could later reveal composition and phase widths of palladium hydride (see later). A real breakthrough was the solution of palladium hydride and deuteride's crystal structure [3], after which the wealth of physical and chemical property data could be understood and a reasonable picture of chemical bonding be established.
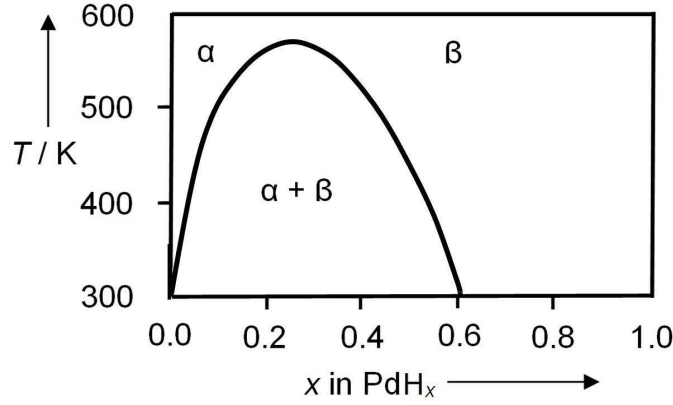
Figure 8.4.1.: Phase diagram of the system palladium–hydrogen.

8.4.2. Phase diagram and preparation

The Pd–H(D) phase diagram is very well known [4]. At room temperature, there is an α-phase PdH$_x$ with a narrow phase width of about $0 \leq x \leq 0.02$ and a β-phase with a much wider range of $0.6 \leq x \leq 1.0$ exist (Fig. 8.4.1), both with a disordered arrangement of hydrogen (deuterium) in octahedral voids of a cubic closest packing of palladium atoms. Thus, all three phases, palladium - α-palladium hydride, and β-palladium - hydride exhibit the same topology of the palladium substructure, that is, a cubic close packing, and differ only by their respective hydrogen occupation. Palladium is one of the rare examples where the crystal structure of the metal is retained upon hydrogenation except for the unit cell expansion and filling of interstitial sites by hydrogen.

At a critical temperature of 563 K and a critical pressure of 1.9 MPa for the hydride, and 556 K and 3.9 MPa for the deuteride, and a hydrogen content x = 0.257 for both, the miscibility gap vanishes and one homogeneous phase $0 < x \leq 1.0$ exists (Fig. 8.4.1); that is, pressure–composition isotherms lose their plateau above the critical temperature (Fig. 8.4.2). No critical point data for the system palladium–tritium are available.

The hydrogenation of palladium in a hydrogen atmosphere (100 kPa) yields hydrides with approximate compositions of PdH$_{0.6<x<0.7}$. In order to achieve higher hydrogen content, the chemical potential of hydrogen atoms needs to be enhanced, for example, by increase in H$_2$ gas pressure $\left(\mu_{H,g} = \frac{1}{2}(\mu^0_{H_2,g} + RT\ ln\ p_{H_2,g})\right)$ [6,7] or by RF discharge methods for enhanced dissociation of H$_2$ molecules in the gas phase [8]. The highest hydrogen contents reached so far are PdH$_{0.96}$ and PdH$_{0.98}$ [7,9].

The real structure of β-phase samples seems to depend on their history. Samples made from hydrogenation of the α-phase differ considerably with respect to their dislocation density from samples made by hydrogenation of palladium above the critical conditions and subsequent cooling under pressure. This is attributed to the abrupt volume change for the α–β-transition [4]. Confinement, for example in thin films, may lead to compressive stress of several GPa. This may be released through various mechanisms, for example, discrete stress relaxation events, formation of dislocations, plastic deformation or, if adhesion to the surface is not sufficient, film buckling [10].
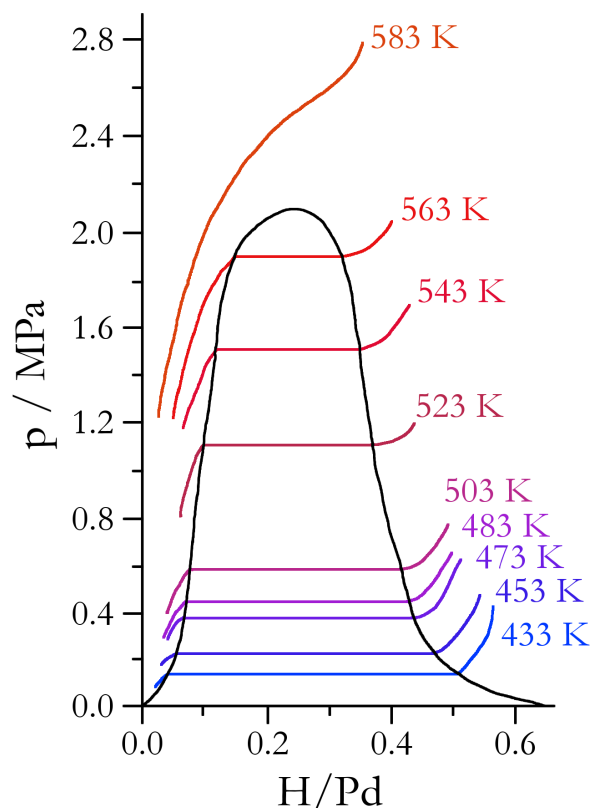
Figure 8.4.2.: Hydrogen pressure–composition isotherms of the Pd–H system (redrawn according to Ref. [5]).

8.4.3. Crystal structures

In the days before X-ray diffraction, the elucidation of crystal structures was not possible, and researchers could only speculate about the geometrical arrangement of atoms in solids. X-ray diffraction revealed that the crystal structure of palladium (ccp) is retained upon hydrogen uptake and only the unit cell expanded. There were still many speculations on the nature and position of the hydrogen within the palladium because such a weak X-ray scatterer as hydrogen could not be located by X-ray diffraction. For example, it was assumed that the properties of PdH would be close to silver (in agreement with Grimm's hydrogen shift rule [11]), and similar lattice parameters of silver and PdH were taken as an indication. Hydrogen poorer hydrides were then often interpreted as solid solutions of such PdH (and here, although not explicitly stated, only molecules could have been meant) in Pd, for example, $(PdH)_3Pd=PdH_{0.75}$ in analogy to ordered intermetallic compounds such as $AuCu_3$ [12]. Another suggestion, later shown to be wrong, was that every eighth palladium atom forms tetrahedral PdH_4 complexes, Pd_7*PdH_4 [13], a belief still pursued [14] even after the crystal structure had been determined unambiguously (see later). After the development of neutron scattering methods in the 1950s, the location of hydrogen (and even better deuterium) became possible. Due to the scattering lengths being comparable to those of most metals (in the case of hydrogen, deuterium, and palladium -3.74, 6.67, and 5.91 fm, respectively), hydrogen and deuterium atoms can easily be located with neutron in contrast to X-ray diffraction. The first neutron diffraction investigation clarified all these open questions and described the crystal structure of PdH_x and PdD_x in a defect NaCl type structure; that is, hydrogen (deuterium) atoms are located in octahedral voids of the ccp of palladium atoms, a model that is still accepted today [3]. The stoichiometric index x in PdH_x and PdD_x reflects the occupation parameter of hydrogen (deuterium) atoms, which are statistically distributed over the

H(D) octahedral   H(D) tetrahedral
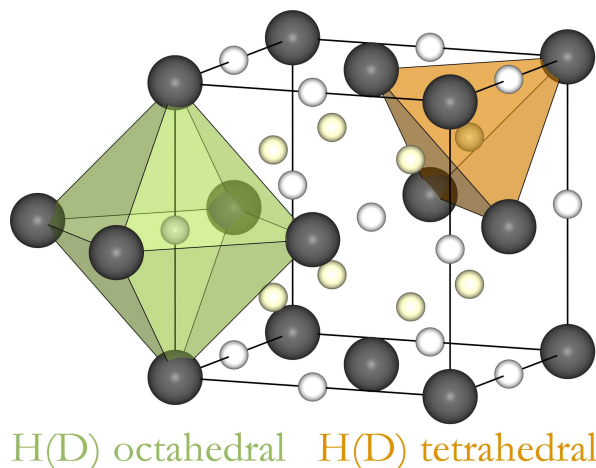
Figure 8.4.3.: Crystal structure of a cubic close packing of palladium (dark gray spheres) with possible hydrogen (deuterium) positions in octahedral (small white spheres) and tetrahedral sites (small yellow spheres). Polyhedra are shown only once for reasons of clarity. Partial filling of octahedral sites yields the accepted model for α and β palladium hydride (deuteride). Filling of tetrahedral sites occurs only for specially prepared samples (see text).

available octahedral sites (Fig. 8.4.3).

For a stoichiometric composition PdH, which has not yet been achieved (up to $PdH_{0.98}$), a lattice parameter of 409.0 pm for PdH and 408.4 pm for PdD was predicted by extrapolation [9]. Later, differences were found between samples taken through the two-phase region (Fig. 8.4.1) and those prepared above the critical point, which avoid the sudden volume changes connected to the former. The respective equations for lattice parameter versus hydrogen content x in PdH_x are given as $a = (393.80(127) + 0.1498(165)x)$ and $a = (395.34(87) + 0.1234(106)x)$ nm [15]. In the early days of neutron diffraction, hydrogen (deuterium) in the a-phase could not be located due to their low content. Modern neutron diffraction methods, however, allow the location and even the accurate determination of hydrogen (deuterium) occupation and thermal parameters as a function of temperature and gas pressure; for example, α-$PdD_{0.038(4)}$ at 390 K and 0.3 MPa deuterium gas pressure [16]. Spectroscopic techniques such as nuclear magnetic resonance and inelastic neutron scattering confirm the established structure models for α and β palladium hydride and deuteride.

In addition to the defect NaCl type α and β phase of palladium hydride and deuteride, several other phases with somewhat different crystal structures were described. When loaded with deuterium above the critical point, that is, avoiding the two-phase region in the preparation of palladium deuteride, considerable occupation of tetrahedral (up to 3.3(3) % at 6.9 MPa) in addition to the regular octahedral sites was found [17]. In this regard, it is interesting to note that other metal hydrides with occupation of both tetrahedral and octahedral voids in a close packing, for example, in lanthanide hydrides, fill the former first and then the latter, that is, in reverse order. Discontinuous changes in physical properties such as specific heat or electric conductivity at low temperature, known as the 50 K anomaly, suggested a phase transition [18]. Neutron diffraction experiments revealed that palladium does not change its topology, but that an ordering of hydrogen atoms causes the phase transition. Several ordered phases seem to exist depending on hydrogen content. Ordering by placing one in four hydrogen atoms in tetrahedral instead of octahedral sites yields a rhombohedral distortion (space group $R\bar{3}m$) [19]. A tetragonal phase was described in two different models, γ-$PdD_{0.67}$ at 50 K (space group $I4_1/amd$) with an ordered distribution of deuterium atoms [20] and $PdD_{0.76}$ at 60–70 K, where deuterium orders

in the fashion of a MoNi$_4$ type structure, that is, every fifth position is vacant, corresponding to an ideal composition of PdD$_{0.8}$ (space group $I4/m$) [21,22].

Deviations from the ideal crystal structure are observed on hydrogenation as well as on dehydrogenation due to large changes in unit cell volume upon hydrogen uptake and release. Plastic deformations manifest in dislocation density occur due to these strong volume effects. It is thus not surprising to see differences between samples hydrogenated above the critical conditions and those driven through the two-phase region of the phase diagram.

More recent studies could not confirm the rhombohedral structure, but found PdD$_{0.62}$ at 54 K in the cubic space group $Pm\bar{3}n$ with doubled lattice parameter with respect to disordered β-phase palladium deuteride [23]. For higher deuterium content, the MoNi$_4$ type ordering was confirmed in PdD$_{0.77}$ at 70 K [24], while no ordering could be observed down to 20 K for even higher deuterium content of PdD$_{\geq 0.82}$ [25]. This might be due to the fact that the limiting composition for the latter type of ordering is PdD$_{0.8}$. Palladium hydride phases with superabundant vacancies are reported when palladium was loaded at very high hydrogen gas pressures (5 GPa) around 1000 K and subsequently cooled [26]. This yields separation into PdH and phases, for which a very high vacancy concentration on the palladium sites is attributed, for example, Pd$_{3\square}$H$_4$, as based on X-ray diffraction and density measurements [26]. Since hydrogen is practically invisible to X-rays, these unusual phases need confirmation by independent methods.

For the investigation of the processes like hydrogen uptake and liberation by solids, in situ diffraction techniques are very useful. They allow for real time studies of chemical reactions or phase transitions as well as the characterization of materials under nonambient conditions [27,28]. This is particularly
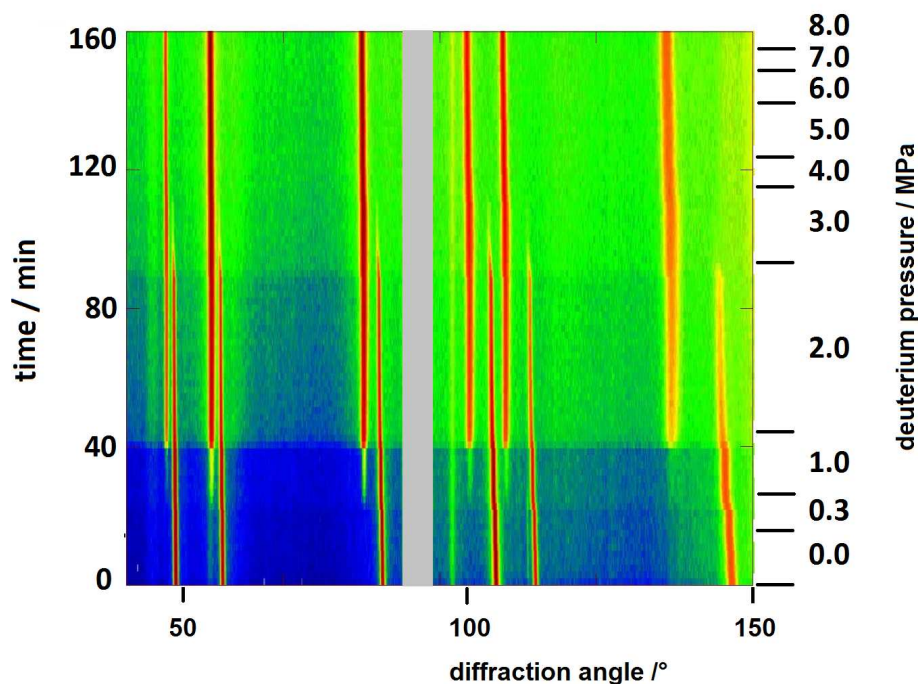
Figure 8.4.4.: Neutron powder diffraction data of palladium deuteride at $T = 446(4)$ K taken in situ on D20 (ILL, Grenoble) at $\lambda = 186.71(1)$ pm in a single crystal sapphire gas pressure cell with a time resolution of 2 min, intensities on a logarithmic scale in false color (lowest intensity, blue; highest intensity, red). The range $87° \leq 2\theta \leq 95°$ (gray shaded area) is excluded because of scattering from the sapphire single crystal.

useful in the case of metal hydrides, where phases have to be mapped as a function of gas pressure and temperature. Fig. 8.4.4 shows such a real-time study of the deuteration of palladium powder at $T = 446(4)$ K with a time resolution of 2 min by *in situ* neutron powder diffraction [29]. The graphical representation clearly shows the simultaneous occurrence of two phases, that is, α and β palladium deuteride at medium gas pressures as expected from the phase diagram.

At higher deuterium pressure and longer reaction time a is completely converted to β-phase deuteride. Rietveld analysis of the diffraction data allows for the extraction of structural data (lattice parameters, deuterium occupation and thermal displacement parameters in this case) yielding compositions in the range $0.04 \leq x \leq 0.11$ for the α-phase and $0.52 \leq x \leq 0.72$ for the β-phase at $T = 446(4)$ K and deuterium gas pressures of up to 8.0 MPa. Static (not time-resolved) *in situ* studies revealed the occupation of tetrahedral voids in palladium (Fig. 8.4.3) when the two-phase region is avoided during preparation [17]. Similar *in situ* neutron powder diffraction experiments (both static and time-resolved) turned out to be very powerful for the investigation of reaction intermediates, metastable phases, and the dependence of crystal structures on temperature and gas pressure [27,30-32]. Further *in situ* techniques like X-ray diffraction [28] and thermal analysis [33,34] yield useful additional data, completing the picture of solid–gas reactions involving hydrogen.

8.4.4. Physical properties

Given the large phase width of β-PdH$_x$, its metallic properties and simple crystal structure, it serves as an ideal test case for the influence of hydrogen incorporation into metals on their physical, chemical, and bonding properties. In the following, a few key properties are only briefly discussed, which certainly does not reflect the large body of knowledge in this field of research. The interested reader is referred to the literature given at the end of this text.

Diffusion of hydrogen

Hydrogen diffusion in solids is faster than that of any other atom, and diffusion coefficients D are often in between those typical for liquids ($D \approx 10^{-9}$ m^2 s^{-1}) and those typical for solids ($D \approx 10^{-13}$ m^2 s^{-1}). In simple metal–hydrogen systems, hydrogen in group V metals vanadium, niobium, and tantalum shows the fastest diffusion, while in palladium this is about one order of magnitude slower [35]. Einstein diffusion constants are $3.8*10^{-11}$ m^2 s^{-1} and $5.5*10^{-11}$ m^2 s^{-1} at 298 K for H and D, respectively, at small hydrogen concentrations in the a-phase. Diffusion in the β-phase was found to be faster than in the α-phase by a factor of 4.5 [4,36]. In the β-phase, jumps from octahedral to both octahedral and tetrahedral sites (Fig. 8.4.3) exist [37]. The activation energy for hydrogen jumps was determined by nuclear magnetic resonance to be 10 kJ mol^{-1} and calculated to be 14.5 kJ mol^{-1} [38]. These values are also considerably higher than the respective ones for hydrogen in platinum, indicating a weaker bonding in the latter as compared to hydrogen in palladium.

Electrical conductivity and superconductivity

There is an almost linear increase of electrical resisitivity with hydrogen content in palladium hydride [12,39], but a sharp decrease for higher H content (> 0.7) with R/R_0 down to 0.9 for the hydride and 1.1 for the deuteride when approaching stoichiometric composition [7]. Superconductivity is found both in palladium hydride and deuteride with critical temperatures T_C of 9 and 11.5 K, respectively. The occurrence of superconductivity was explained by electron–phonon coupling involving hydrogen's optic vibrations [40]. T_C increases slightly with increasing hydrogen (deuterium) content, however, with a final small decrease when approaching fully stoichiometric PdH and PdD [41].

Magnetism

The paramagnetic susceptibility decreases nearly linearly with increasing hydrogen content in palladium hydride and reaches diamagnetism at a composition of $PdH_{0.66}$. While this decrease was first used as an argument for the so-called protonic model, where electron donates its electron (leaving a proton in an interstitial site behind) to fill the d-band of the metal, it is probably due to the effect of lattice expansion instead [42].

Isotope effects

Due to the doubled mass of deuterium in comparison to protium, isotope effects are often large. This is the case, for example, for the solubility in the α-phase, which decreases in the order protium, deuterium, and tritium (i. e., equilibrium pressures are smallest for protium and largest for tritium) [4]. As expected, vibrational properties exhibit a pronounced isotope effect as well. The Einstein temperatures for α-PdH_x, α-PdD_x, β-PdH_x, β-PdD_x are 801, 540, 685, and 460 K, with θ_H/θ_D of 1.49 for both α- and β-phase. The deviation from the expected value of $\sqrt{2} \approx 1.41$ is ascribed to the anharmonicity of the vibration [4]. The critical temperature of superconductivity (see earlier) interestingly shows an inverse isotope effect with 9 K for the hydride and 11.5 K for the deuteride [43]. The anharmonicity of the H(D)–Pd potential and the large vibrational amplitude were considered to be the prime cause for this inverse isotope effect on the electron–phonon coupling and thus on T_C [44].

Electronic structure (and bonding properties)

The nature of hydrogen and the chemical bonding in palladium hydride has been under dispute for some time. Hydrogen was first considered to be protonic because migration of hydrogen to the cathode in an electric field was found; this, however, does not yield conclusive evidence, and is contradicted by other physical properties such as electrical conductivity and, additionally, is counterintuitive considering electronegativity [45]. Quantum-mechanical calculations reveal a detailed picture of the electronic structure in palladium hydride. It may serve as an archetypical example for electronic structure and chemical bonding in metallic metal hydrides and thus exhibits characteristic features found in many other metallic hydrides. This may be exemplified by comparing the calculated density of states (DOS) of pure palladium with that of palladium hydride. Far below the Fermi level, E_F, new electronic states appear which are centered at about -7 eV for PdH. They can be attributed to metal–hydrogen bonding and are formed by hybridization of H-s and Pd-s, Pd-p and Pd-d states [46]. d-states of pure palladium are further filled by introduction of hydrogen, and E_F lies in an sp-dominated band with low DOS. This results in decreased Pauli paramagnetism and decreased electronic contribution to the specific heat. The beginning of the rather flat Pd-sp-band corresponds to the Fermi level of $PdH_{0.7}$ [46]. Further filling of hydrogen into octahedral voids and consequent up-shifting E_F would not gain much energy and is, thus, not favored. This is in agreement with the experimental finding that higher hydrogen contents need enhanced chemical potential of hydrogen, for example, by high partial pressures of hydrogen gas. Another characteristic feature is the narrowing of metal d-bands due to the volume expansion upon hydrogen uptake. Most of the above mentioned features could also be verified experimentally by ultraviolet and X-ray photoelectron spectroscopy (UPS and XPS), soft X-ray emission spectroscopy (SXES), and low energy bremsstrahlung-isochromat spectroscopy (BIS) [46]. One of the largest challenges in such investigations of metal hydrides are the necessary (ultrahigh) vacuum conditions, which put severe limits due to concomitant hydrogen release.

Charge distribution on palladium hydride calculated by DFT methods and Bader charge analysis resulted in $H^{0.3-}$ for an occupation of 3.7 % in an octahedral void, reflecting the higher electronegativity

of hydrogen. The Bader charge is also negative for hydrogen in niobium palladium alloys [47].

It should be emphasized that metal hydrides are extremely versatile with respect to chemical bonding ranging from ionic to covalent and metallic; that is, palladium hydride represents only one of several types of metal hydrides with respect to their electronic structure.

8.4.5. Application

The most prominent applications of palladium and its hydride are catalysis and gas separation. The Nobel Prize in chemistry for the year 2010 was awarded to Ei-ichi Negishi, Akira Suzuki, and Richard F. Heck for their scientific work on palladium catalysis in organic chemistry. Palladium catalyzed reactions are very popular, especially in the pharmaceutical industry for the large scale production of ibuprofen. Many such reactions, however, involve palladium(II) compounds instead of palladium hydrides. Supported small palladium particles serve as hydrogenation catalysts in technical processes like the large-scale production of hydrogen peroxide or pharmaceuticals. In the course of such heterogeneous catalytic reactions, hydrogen is dissociated on the surface and, in some cases, bulk palladium hydride forms [48]. It was shown that hydrogen atoms have negative partial charge both on the surface and in the bulk [49].

Palladium may be used to separate hydrogen from other gases by diffusion through a thin membrane. It may also be used for the separation of hydrogen isotopes protium, deuterium and tritium in a kind of chromatographic column, although more efficient materials for this purpose are known [50].

8.5. Ternary disordered palladium-rich hydrides

Atomic disorder in intermetallic crystal structures is quite common, especially in case of similar electronic properties and size of the different metal atoms. Therefore mixed occupation (statistic distribution) of one or more crystallographic sites with one or more atom types can frequently be found. This may yield complete solid solution series like in the system $Pd_{1-x}Ag_x$ (Cu type structure, ccp), limited solubility as in Li_xPd_{1-x} (x $\leq$ 0.04) due to larger differences in size, limiting crystal structures and electronegativities, or to mutual occupation by only a few percent in otherwise ordered superstructures like in $MnPd_3$. Therefore, instead of a strict categorization in ordered and disordered systems, a distinction for the degree of disorder seems more appropriate in general. In case of palladium-rich intermetallic compounds, however, there is some justification to distinguish strictly. The vast majority of largely disordered structures are extended solid solutions in the Cu type (ccp) of palladium itself. Palladium atoms are successively substituted by other metals on the only crystallographic site within the crystal structure, which is the archetypical example for a solid solution. Other compounds, often with composition MPd$_3$, crystallize in ordered superstructures of a ccp, which allow an ordered distribution of M and Pd atoms and mixed occupation on these crystallographic sites could not be detected or is much less pronounced (usually > 90 % for the majority component on a site). Therefore, this contribution distinguishes between disordered and ordered palladium-rich intermetallics, but it should be emphasized that this is of course a simplification as most solid intermetallics are disordered to some extent (see earlier).

This article focuses on palladium-rich intermetallics with strong atomic disorder, of which solid solutions based on Cu type palladium are an important subset. Ordered intermetallic compounds (in the above mentioned sense) are presented in the following section. When both ordered and disordered phases of one compound are known, the more detailed discussion of both will be found in the article of ordered compounds.

8.5.1. The variety of disordered palladium-rich intermetallics

The vast majority of disordered palladium-rich intermetallics are solid solutions in the Cu type (ccp) (Table 1). Those elements surrounding palladium in the periodic system of the elements (PSE) have solubility from 0 % to 100 % in palladium. With a few metals in the PSE, the related In or AuCu types are realized, which are hard to distinguish from each other with standard X-ray diffraction. For example, both In and AuCu type were suggested for $In_{0.25}Pd_{0.75}$ [51,52]. It is remarkable that disordered compounds of palladium with half metals like germanium, arsenic, tellurium, and antimony crystallize in W or NaTl type. That is caused by the increased valence electron concentration of the compounds [53]. All mentioned W type disordered compounds are high temperature modifications. The light atoms in $PdH_{0.02}$, $PdB_{0.16}$, $PdC_{0.03}$, and $PdO_{0.24}$ were not located unambiguously and crystal structures are suggested to be either a solid solution of palladium with the nonmetal (Cu type) or of a defect NaCl type [54–57]. In view of the strong chemical differences between the non-metals and palladium, the latter seems more plausible. In the case of the hydrogen compound, this is simply a representation of α-PdH_x. Most alkaline and earth alkaline metals, as well as the elements with a higher group number in the PSE, are immiscible with palladium probably due to large electronic differences.

8.5.2. Selected palladium-rich solid solutions and their hydrogenation properties

Solid solution with a disordered arrangement of atoms in Cu type (red in Table 8.5.1) usually retain their crystal structure and incorporate hydrogen atoms in octahedral voids; that is, they form a defect NaCl-type structure similar to palladium hydride with M and Pd atoms on one site and hydrogen atoms and vacancies on the other crystallographic site. From the vast number of solid solutions with palladium (Table 8.5.1), only a few will be discussed in some detail in order to show typical examples as well as exceptions.

The system palladium–rhodium

Palladium and rhodium form a complete ccp type solid solution series, which is unique in view of its hydrogenation properties. It seems to be the only one for which the hydrogen content increases with increasing content of the substitutional metal, at least up to 10 atom-% of rhodium [60].

The system palladium–platinum

Palladium and platinum form a complete ccp type solid solution series. Hydrogenation leads to partial segregation in palladium-rich and platinum richer hydride phases. Interestingly, upon hydrogenation, the homogeneous solid solution $Pd_{1-x}Pt_x$ is reformed, that is, hydrogen induced segregation and homogenization is reversible [61].

The system palladium–copper

Within palladium-group 11 systems, copper is of special interest because, in contrast to silver or gold, substitution in palladium leads to shrinking of unit cell volumes. A distinction between geometric and electronic factors is thus possible. Relative partial molar enthalpies of hydrogen absorption are found to be a little less exothermic, and partial excess entropies of hydrogen absorption are smaller than for pure palladium [54].

Table 8.5.1.: Periodic table with binary palladium-rich solid solutions or disordered compounds from Binary Alloy Phase Diagrams [58] and Pearson Crystal Database [59] (marked with *)

Legend:
- 87.0 (red): minimum molar percentage of Pd in Cu type solid solution
- Sb: element
- 75.0 (dark blue): molar percentage of Pd in disordered compounds

1	2	3	4	5	6	7	8	9	10	11	12	13	14	15	16	17	18
H 98.0*																	He
Li 96.0	Be											B 81.4/86.0*	C 92.0/97.1*	N	O 80.6*	F	Ne
Na	Mg 75.0											Al 80.0	Si 82.0*	P	S	Cl	Ar
K	Ca	Sc 85.0	Ti 85.0	V 42.0/67.0*	Cr 51.0	Mn 69.5	Fe 0.0	Co 0.0	Ni 0.0	Cu 0.0	Zn 80.0	Ga 85.0*	Ge 97.0/84.0	As 87.0/83.3	Se	Br	Kr
Rb	Sr	Y 87.0	Zr 83.8/83.0*	Nb 70.0	Mo 56.0	Tc 72.0	Ru 82.8	Rh 0.0	Pd 0.0	Ag 0.0	Cd 74.0	In 81.0/75.0*	Sn 83.0/75.0*	Sb 75.0	Te 89.0/75.7	I	Xe
Cs	Ba	La	Hf 77.5	Ta 78.0	W 78.0	Re 84.0	Os 97.1	Ir 0.0	Pt 0.0	Au 0.0	Hg 86.2	Tl 91.0*	Pb 86.0	Bi	Po	At	Rn

Ce 83.5*	Pr 92.0*	Nd 97.0*	Pm	Sm 89.7	Eu 90.0	Gd 89.0*	Tb 88.0*	Dy 87.7	Ho 87.5	Er 87.0	Tm 88.0*	Yb 88.0	Lu 88.0*
Th 86.0*	Pa	U 83.5/89.0*	Np	Pu 86.0	Am	Cm	Bk	Cf	Es	Fm	Md	No	Lr

Red cells, Cu type; orange, In type; yellow, AuCu type; blue, W type; dark blue, NaTl type; green, crystal structure not fully established (probably defect NaCl type); no color, no palladium-rich solid solutions known yet or solubility is < 1.0 %. Elements with two colors crystallize in both structure types.

The system palladium–silver

Solid solutions of silver in palladium are examples of equilibrium pressures decreasing with increasing content of the substitutional metal, thus representing increasing temperature in p–c isotherms of palladium hydride (Fig. 8.4.1).

The system palladium–gold

$Pd_{0.81}Au_{0.19}$ is one of the rare examples where hydrogenation leads to an ordering of the metal atoms as derived from superstructure reflections in X-ray and electron diffraction patterns (crystal structure not solved yet) [62].

Conclusion on the hydrogenation behavior of palladium-rich solid solutions

The nature of the substitutional metal in palladium-rich solid solution has a distinct influence on formation and hydrogen content of hydrides, which is, however, different for a and b phases. Solid solutions with unit cell volumes smaller than that of pure palladium dissolve less, and those with larger unit cell volumes dissolve more hydrogen at low hydrogen pressures than pure palladium [4]. This results in hydrogen richer a phases and shorter plateaus in pressure–composition isotherms (representing the coexistence of both α and β phase hydrides, see also Fig. 8.4.1) for solid solutions with

larger unit cell volumes than pure palladium. Thus, those geometrical aspects, such as the size of the void on the octahedral interstices, play an important role for the α phase hydrides. In most cases, equilibrium pressures increase with increasing content of the substitutional metal, thus mimicking increasing temperature in p-c isotherms of palladium hydride (Fig. 8.4.2). In some cases, the inverse relationship holds true, for example, for the hydrogenation of $Pd_{1-x}Ag_x$. For β phase hydrides, however, only rhodium as a substitutional element in palladium increases the hydrogen content, while for all others hydrogen content is lower than in the β phase hydride of pure palladium. Critical temperatures of superconductivity sometimes exhibit two maxima, one with respect to the content of the substitutional metal and another with respect to hydrogen content. Higher values for T_C as compared to unsubstituted palladium hydride are, for example, found for hydrides of $Pd_{0.55}Cu_{0.45}$ with 17 K [60].

The order of palladium-rich intermetallic compounds of the same composition may have a profound influence on hydrogenation properties. Samples of hydrogenated $FePd_3$ with different degrees of crystallographic order show drastically different properties. More than two orders of magnitude higher hydrogen gas pressures are needed to attain the same electrical resistivity in disordered $FePd_3$ as compared to ordered $FePd_3$ (AuCu$_3$ type) [60]. The preferential occupation of crystallographic sites with a high number of palladium neighbors in ordered intermetallics lead to the suggestion that the local environment in hydrides of solid solutions is preferentially palladium-rich as well. A detailed account of ordered intermetallic compounds rich in palladium and their reactivity toward hydrogen is subject of the next chapter.

8.6. Ternary ordered palladium-rich hydrides (MPd$_{\geq 2}$)

An ordered replacement of palladium by other metals M is concomitant to a reduction of space group symmetry. This often leads to a splitting of crystallographic sites occupied by the metal atoms into independent positions, thus allowing for an ordered arrangement of M and Pd atoms, and of hydrogen filled sites. Such a decoupling of octahedral sites also enables an ordered occupation by hydrogen. The formation of different octahedral sites like [Pd$_6$], [MPd$_5$], or [M_2Pd$_4$] will influence the hydrogenation properties. Such substitution of palladium by other metals may be used either to enhance hydrogen uptake or to suppress it. The former is sought after for the formation of stable hydrides and the study of metal–hydrogen interactions (see later). The latter on the other hand attracts interest in catalysis. For example, a modification of palladium as a common highly active catalyst for the hydrogenation of acetylene to ethylene with other metals has been studied. Introducing gallium lowers the amount of interstitial hydrogen in the catalyst due to a reduction of neighboring palladium sites, but at the same time improves the selectivity of acetylene hydrogenation while maintaining high activity, which is highly desirable [63–66]. Another example is PbPd$_3$, used as a catalyst in an industrialized liquid phase process for direct production of methyl methacrylate from methacrolein, methanol, and oxygen [67]. As Lindlar catalyst (=Pd$_{1-x}$Pb$_x$ on calcium carbonate), the formation of β palladium hydride has been shown to occur [48]. This article focuses on ternary palladium-rich hydrides (molar ratio Pd to $M \geq 2$) incipient with Laves phases, followed by ccp related MPd$_3$ and the hexagonal CaPd$_3$H$_x$. The article closes with an account on hydrides of palladium-rich phosphorous compounds.

8.6.1. Hydrides of Laves phases SrPd$_2$ and EuPd$_2$

Plenty of Laves phase hydrides are known since they are renowned for absorption of considerable amount of hydrogen up to compositions of AM_2H$_7$. Well known are, for example, the hydrides of ZrV$_2$ crystallizing in the cubic MgCu$_2$ type, or in some distorted variants of it, with up to six hydrogen atoms per formula unit [68,69]. Two palladium-rich Laves phases that form hydrides are known, SrPd$_2$ and EuPd$_2$ [70,71].

Synthesis

The cubic Laves phase hydrides could be synthesized by two routes. On the first route, the intermetallic compounds are synthesized from the elements by arc melting or annealing under vacuum and subsequent hydrogenation of these intermetallics. EuPd$_2$ decomposes at hydrogen pressures over 2 MPa or further heating over 400 K at 620 kPa hydrogen pressure to the perovskite EuPdH$_3$ and the binary hydride PdH$_x$. On the second route, the hydrides were synthesized from palladium and the binary hydride SrH$_2$ or EuH$_2$ under hydrogen pressure [70,71].

Crystal structures

SrPd$_2$ and EuPd$_2$ crystallize in the cubic MgCu$_2$ type, better known as cubic Laves phases. Strontium or europium atoms form a diamond-like structure with palladium tetrahedra in the tetrahedral voids. Hydrogen probably occupies tetrahedral interstices, but the hydrogen positions were not yet experimentally determined in these cases. The hydrogen uptake results in volume expansion which is usually 5 % per hydrogen atom per formula unit on cubic Laves phase hydrides. Hence, formulae EuPd$_2$H$_x$ (x = 0.1, 1.5, 2.1) were estimated [71]. The hydrogen content of SrPd$_2$H was obtained by pyrolysis and acid hydrolysis [70].

8.6.2. Ccp related palladium-rich hydrides MPd$_3$H$_x$

The largest number of ordered palladium-rich hydrides belong to the composition MPd$_3$H$_x$ with the metal atoms M and Pd together forming ccp related structures (M: Mg, In, Tl, Sn, Pb, Bi, Sc, Y, Mn, Ce). These hydrides can be synthesized by hydrogenation of the intermetallic hydrogen free precursor compounds. Some of them show a hydrogen induced rearrangement, which will be explained in detail in this section after a short description of synthesis procedures.

Synthesis

The ordering of the structures, especially for long-range order like ZrAl$_3$ type, requires a long time of annealing because atoms have a low mobility. The compounds with thallium or tin are produced by typical solid state syntheses from elements in sealed silica tubes under inert gas atmosphere or vacuum [72,73]. MPd$_3$ (M: Mg, In, Pb, Bi) are synthesized from elements with small amounts of iodine as mineralizing agent. Iodine can be removed by mild heating (sublimation) or dissolved with half-saturated aqueous potassium iodide solution after grinding of samples [32,52,73,74]. CePd$_3$ and YPd$_3$ are prepared by arc melting [75,76], and MnPd$_3$ by high frequency induction heating [77,78]. Samples were often annealed at temperatures below the melting or decomposition point. All compounds are stable in air. The intermetallic compounds were hydrogenated in autoclaves under hydrogen or deuterium pressure (Table 8.6.1). TlPd$_3$H$_x$ could also be formed by reduction of TlPd$_3$O$_4$ in hydrogen gas atmosphere and InPd$_3$H$_x$ by the decomposition of Pd$_5$InSe or Pd$_8$In$_2$Se under high hydrogen pressure [72,73]. The grinding of MgPd$_3$ in a mortar might yield in transformation to a cubic solid solution (Cu type), that is, loss of atomic order [79].

Table 8.6.1.: Ternary palladium-rich hydrides with metal structures related to the ccp. The change of unit cell volume corresponds to the relative increase of the unit cell per formula unit upon hydrogenation

Compound (structure type)	Hydride (structure type of metal atoms without hydrogen)	Conditions of hydrogenation (deuteriation)	Change of unit cell volume/formula unit
$MgPd_3$ [a] ($ZrAl_3$)	α-$MgPd_3D_{0.79}$ ($ZrAl_3$) [79,80]	0.5 MPa D_2 / 299 K	+ 5.8 %
$MgPd_3$ [a] ($ZrAl_3$)	β-$MgPd_3H_x$ ($AuCu_3$) [79]	0.61 MPa H_2 / 750 K	+ 6.5 %
$InPd_3$ ($ZrAl_3$)	$InPd_3D_{0.89}$ ($AuCu_3$) [81]	4.5 MPa D_2 / 523 K	+ 3.5 %
$InPd_3$ ($TiAl_3$)	$InPd_3H_x$ ($AuCu_3$) [34]	2.0 MPa H_2 / 523 K	+ 3.9 %
$TlPd_3$ [b] ($ZrAl_3$)	α-$TlPd_3H_x$ ($ZrAl_3$) [72]	0.1 MPa 7.5 % H_2/Ar / 1003 K	+ 0.6 %
$TlPd_3$ [b] ($ZrAl_3$)	β-$TlPd3H$ ($AuCu_3$) [72]	0.1 MPa H_2 / 773 K	+ 3.9 %
$SnPd_3$ ($AuCu_3$)	$SnPd_3H_x$ ($AuCu_3$) [73]	5.0 MPa H_2 / 703 K	+ 0.4 %
$PbPd_3$ ($AuCu_3$)	$PbPd_3H_x$ ($AuCu_3$) [73]	5.0 MPa H_2 / 703 K	+ 0.6 %
$BiPd_3$ ($BiPd_3$)	$BiPd_3H_x$ ($ZrAl_3$) [32]		
YPd_3 ($AuCu_3$)	$YPd_3H_{0.3}$ ($AuCu_3$) [82,83]	5.0 MPa H_2 / 300–773 K	+ 0.4 %
$MnPd_3$ [a,c] ($ZrAl_3$)	$MnPd_3D_{0.61}$ [c] ($ZrAl_3$) [77]	0.1 MPa D_2 / 298 K	+ 3.5 %
$MnPd_3$ [a,c] ($ZrAl_3$)	$MnPd_3D_{0.7}$ [c] ($AuCu_3$) [77,84]	1.0 MPa D_2 / 295 K	+ 2.1 %
$CePd_3$ ($AuCu_3$)	$CePd_3H_x$ ($AuCu_3$) [85]	16 MPa H_2 / 299 K	+ 0.7 %

[a] Additional modification in $AuCu_3$ type, accessible only by hydrogenation–dehydrogenation. [79,86]

[b] Additional modification in $TiAl_3$ type structure, not yet investigated for hydrogenation properties. [72]

[c] The metal atoms of $MnPd_3$ and $MnPd_3H_x$ are slightly disordered. [77,84]

Crystal structures

MPd_3 (M = Mg, In, Tl, Sn, Pb, Sc, Y, Mn, Ce) crystallize in ordered superstructures derived from ccp (Cu type) of palladium itself by ordered substitution of palladium by metal atoms M. Dropping the F centering in a ccp leads to the well-known cubic $AuCu_3$ type structure (Fig. 8.6.1, bottom) with a splitting to two crystallographic positions in the multiplicity ratio 1:3. An infinite series of superstructures may be derived from the $AuCu_3$ type by shifting half of the layers (denoted A' in Fig. 8.6.1) by $1/2$ [110], which is equivalent to exchanging M for Pd atoms and vice versa (denoted B' in Fig. 8.6.1). A' and B' layers may now be stacked in various orders, for example, $A'B'A'B'\ldots$ in the tetragonal $TiAl_3$ type structure (twofold ccp superstructure, Fig. 8.6.1, top), $A'A'B'B'A'A'B'B'\ldots$ in the tetragonal $ZrAl_3$ type structure (fourfold ccp superstructure, Fig. 8.6.1, middle), $A'A'A'B'B'B'A'A'A'B'B'B'\ldots$ in the Tl_2PbPd_9 type structure (sixfold ccp superstructure, not shown here) and so on, while in the $AuCu_3$ only A' layers are stacked according to $A'A'\ldots$ [53,79]. Even longer stacking sequences with four, seven, or even nine like layers (18-fold superstructure), depending on annealing procedures and exact composition (x) were reported for phases $Cu_{3-x}Pd_{1+x}$ (-0.16 $\leq$ x $\leq$ 0.20) [87–89]. Complete order cannot be achieved in all cases, for example, $MnPd_3$ tends to exhibit some degree of disorder with mixed occupation of Mn and Pd atoms on some crystallographic sites [84]. All these superstructures contain octahedral voids suitable for hydrogen incorporation, which are either completely surrounded by palladium atoms, [Pd_6], by one M and five palladium atoms [MPd_5], or by two M and four palladium atoms [M_2Pd_4]. The number of [Pd_6] and [M_2Pd_4] increases in the series $TiAl_3$ type, $ZrAl_3$ type, Tl_2PbPd_9 type, ..., $AuCu_3$ type to a maximum of $1/4$ and $3/4$ of all octahedral voids in the latter, while that of [MPd_5] decrease from $1/2$ in $TiAl_3$ type to 0 in the $AuCu_3$ type.

Hydrogenation experiments show that most MPd_3 compounds take up considerable amounts of hydrogen to form hydrides MPd_3H_x (x $\leq$ 1) with a strong preference for octahedral positions surrounded exclusively by palladium, [Pd_6], for the hydrogen atoms. $AuCu_3$ type compounds (M = Sn, Pb, Sc, Y, Ce) hereby keep their structure and incorporate hydrogen in the preferred [Pd_6] octahedral sites resulting in increased unit cell volumes. The positions of the hydrogen atoms were determined
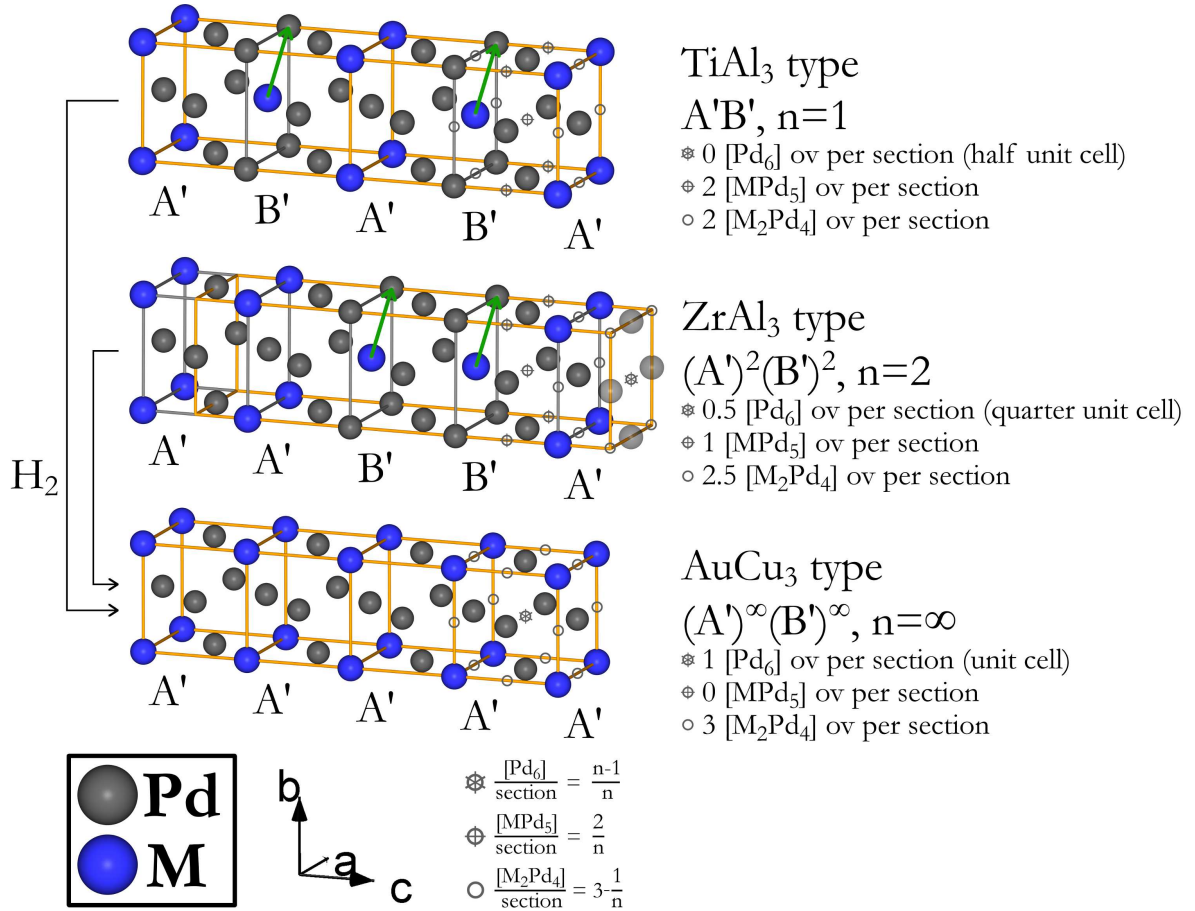
TiAl$_3$ type
A'B', n=1
✣ 0 [Pd$_6$] ov per section (half unit cell)
⊕ 2 [MPd$_5$] ov per section
○ 2 [M$_2$Pd$_4$] ov per section

ZrAl$_3$ type
(A')^2(B')^2, n=2
✣ 0.5 [Pd$_6$] ov per section (quarter unit cell)
⊕ 1 [MPd$_5$] ov per section
○ 2.5 [M$_2$Pd$_4$] ov per section

AuCu$_3$ type
(A')$^\infty$(B')$^\infty$, n=∞
✣ 1 [Pd$_6$] ov per section (unit cell)
⊕ 0 [MPd$_5$] ov per section
○ 3 [M$_2$Pd$_4$] ov per section

$$\frac{[Pd_6]}{section} = \frac{n-1}{n}$$

$$\frac{[MPd_5]}{section} = \frac{2}{n}$$

$$\frac{[M_2Pd_4]}{section} = 3-\frac{1}{n}$$

Figure 8.6.1.: Hydrogen induced rearrangement of intermetallic superstructures of MPd_3 from TiAl$_3$ type (top) and ZrAl3 type (middle) to AuCu$_3$ type (bottom) during hydrogenation by shifting half of the face diagonal of layer B' along [110] (marked by green arrows) [34]. Crystallographic unit cells are drawn in orange. The unit cell of ZrAl$_3$ type is shifted by one eighth in the c direction with respect to the other structures and the transparent palladium atoms complete the unit cell. The octahedral voids (ov) of one section (gray outline) of each structure type are shown [79].

by neutron diffraction on the deuterides and in some cases also by inelastic neutron scattering and NMR spectroscopy [72,77,79–82,85]. The crystal structure of MPd_3H_x may thus be described as a cubic anti-perovskite type.

Hydrogen in ScPd$_3$H$_x$ is assumed to occupy the [Sc$_2$Pd$_4$] octahedral voids. However, it has only been observed as a poorly crystalline secondary phase in samples of Mg$_{0.65}$Sc$_{0.35}$D$_x$ [90].

MPd_3 compounds crystallizing in ZrAl$_3$ type (M = Mg, In, Tl, Mn) incorporate hydrogen at very mild conditions; for M = Mg, Mn, even at room temperature and low hydrogen pressures (≤ 5 bar). The hydrides MPd_3H_x (x ≤ 1) are also of the cubic anti-perovskite type; that is, the MPd_3 sub-structure transforms to a AuCu$_3$-like arrangement. The driving force of this reaction is the formation of further [Pd$_6$] octahedral sites (doubling) which hydrogen occupies preferentially. This strong tendency of hydrogen to be coordinated maximally by palladium is also based on theoretical investigations [80,91]. The palladium-rich compound with manganese reacts with the same rearrangement from the tetragonal structure, which incorporates hydrogen only in [Pd$_6$] and [MnPd$_5$] octahedral sites, to the cubic structure at higher pressures [92,93]. Anti-perovskite type TlPd$_3$H shows the highest hydrogen

content with fully occupied hydrogen positions (x = 1) [72].

Due to the relationship between $ZrAl_3$ and $AuCu_3$ type structure (Fig. 8.6.1) the above mentioned structural rearrangement upon hydrogenation may formally be viewed as a shift of layers within the structure by $1/2$ [110]. While in the first place this is only a way to illustrate the structural relationships, calculations show that hydrogen placed between layers A' and B' ($[MPd_5]$ and $[M_2Pd_4]$, Fig. 8.6.1) indeed assists a gliding by $1/2$ [110] by reducing its activation energy considerably [91]. *In situ* X-ray and neutron diffraction for the hydrogenation has shown that before the rearrangement to the $AuCu_3$ type takes place $ZrAl_3$ type $MgPd_3$ incorporates hydrogen. While $[Pd_6]$ sites are preferred, $[MPd_5]$ and $[M_2Pd_4]$ voids are also occupied (Fig. 8.6.2), and may thus assist the proposed gliding operation. Further hints, that gliding by $1/2$ **[110]** may indeed take place during the reaction, at least in small domains, are the very mild reaction conditions, under which a complete reconstruction of the crystal structure seems hardly possible, and the fact that the structural transformation is irreversible (in contrast to the hydrogen uptake into the $ZrAl_3$ type structure). The $ZrAl_3$ type can only be recovered by complete removal of hydrogen (for In, Tl); however, in the cases of Mg and Mn even then the $AuCu_3$ type is retained. Thus, in the case of Mg, a hydrogenation–dehydrogenation cycle yielded a new polymorph called β-$MgPd_3$ in the $AuCu_3$ type which could not be synthesized by other means [79].

The hydrogenation of $InPd_3$ is interesting because of its four polymorphs in the $ZrAl_3$ type, the high temperature modification $TiAl_3$ type, as well as in the solid solutions of the Cu and the In type [94]. $InPd_3$ reacts in the same hydrogen induced rearrangement as $MgPd_3$, $MnPd_3$, and $TlPd_3$; however, hydrogen incorporation of tetragonal $ZrAl_3$ type has not been observed yet. The modification in the $TiAl_3$ type forms the same hydride as the one in $ZrAl_3$ type. The same gliding-like mechanism as discussed above may apply here, and calculations show the same lowering of its activation energy by hydrogen incorporation [91].

The crystal structure of $BiPd_3$ is also closely related to a close packing. The stacking sequence in this case, however, is ABAC... for the close-packed layers (not to be confused with layers A' and B' in Figs. 8.6.1 and 8.6.2, see comment above and remark on nomenclature at the beginning of this publication). This is known as double hexagonal close packing (dhcp), with lanthanum, praseodymium, and neodymium being the structural aristotypes. $BiPd_3$ itself shows a slight orthorhombic distortion hereof [95]. Another closely related structure with ABAC packing for the metal atoms is $CaPd_3H_x$, with a hydrogen filled $TiNi_3$ type structure (see later). Upon hydrogenation, $BiPd_3$ forms a hydride $BiPd_3H_{\approx 0.2}$, with a $ZrAl_3$ type for the $BiPd_3$ partial structure, and hydrogen in octahedral $[Pd_6]$ voids [32]. In order to transform the Bi/Pd substructure from its dhcp- like to a $ZrAl_3$- like arrangement,
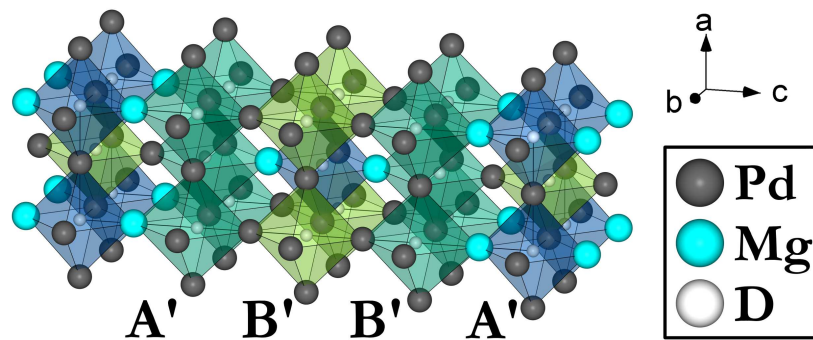

Figure 8.6.2.: Crystal structure of α-$MgPd_3D_{0.79}$ (filled $ZrAl_3$ type). The highest occupation of deuterium is on $[Pd_6]$ (light green polyhedra), followed by $[MgPd_5]$ (green polyhedra) and least occupation is on $[Mg_2Pd_4]$ octahedral voids (blue polyhedra) [80].

the stacking sequence of close-packed layers has to change to ABC as in a ccp. In addition to the hydrogen induced rearrangement described earlier, this system furthermore seems to exhibit another type of hydrogen assisted gliding operation.

Symmetry relationship

The obvious relationship of the above mentioned ccp superstructures of the metal atoms can be concisely depicted by a Bärnighausen symmetry tree illustrating the group–subgroup relationships (Fig. 8.6.3) [96]. Almost all hydrides of MPd$_3$ crystallize in the filled AuCu$_3$ type, that is, defect cubic anti-perovskite type. The AuCu$_3$ type is related to the ccp of palladium by a simple symmetry reduction step (loss of F centering). The other relevant hettotypes are on two paths starting from the AuCu type. On the right side two doublings of the c-axis by an *isomorphic* and a *klassengleiche* transition yield in the ZrAl$_3$ type, a fourfold ccp superstructure. The second path on the left hand side yields the twofold superstructure of TiAl$_3$ type by one doubling of the c-axis [94]. This structure type does not form hydrides because of missing [Pd$_6$] octahedral voids. Using these symmetry considerations, all structures of MPd$_3$ (M = Mg, In, Tl, Sn, Pb, Sc, Y, Mn, Ce) can be easily related to each other, proving that they may all be described as ordered substitutional derivatives of a cubic closest packing. The initially mentioned long-period structures of Tl$_2$PbPd$_9$ (sixfold ccp superstructure) and Cu$_3$Pd (18-fold superstructure) may also be included by adding one or two isomorphic (also called equivalent in older literature) symmetry reduction steps of index 3 (tripling the crystallographic c-axis) to the TiAl$_3$ type thus completing the picture.
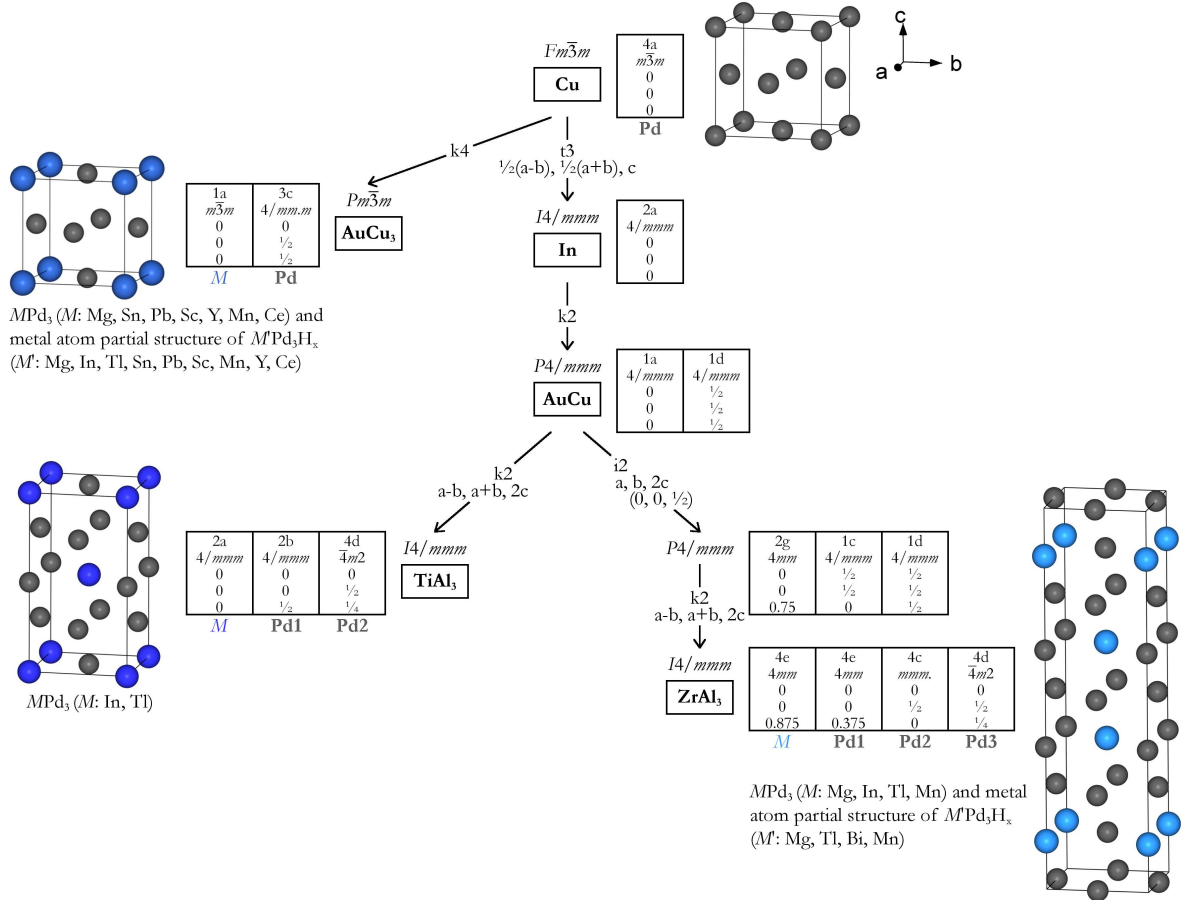

Figure 8.6.3.: Group–subgroup relationship of binary palladium-rich ccp superstructures [94]. Free positional parameters are idealized values converted from the aristotype Cu.

Electronic structure

Calculations of the DOS of the tetragonal α-MgPd$_3$ and α-MgPd$_3$H$_x$ as well as the cubic β-MgPd$_3$ and β-MgPd$_3$H$_x$ suggest metallic properties for all four compounds. The bonding states of the unhydrogenated phases are very similar and dominated by Mg-s, Mg-p, and Pd-d states. However, the cubic β-MgPd$_3$ have a higher density of Mg-s and Pd-d states just above the Fermi level being slightly less favorable than in α-MgPd$_3$. The hydrogenation of both phases lowers the energy at the Fermi levels and adds a strong H-s dominated bonding feature at lower energy, which is hybridized with Pd-d state. This hybridization is more distinct in β-MgPd$_3$H$_x$ than in α-MgPd$_3$H$_x$, implying a stronger Pd–H interaction and a higher stability. The double number of [Pd$_6$] octahedral sites in the AuCu$_3$ type compared to ZrAl$_3$ type shifts these low lying binding states slightly toward lower energy range and contributes to the higher stability of β-MgPd$_3$H$_x$ as compared to α-MgPd$_3$H$_x$ [80,97].

Magnetism of MnPd$_3$D$_x$

Manganese is the only paramagnetic atom of the metals M discussed in this article. The tetragonal and cubic modifications of MnPd$_3$ have slightly lower magnetic moments as compared to their deuterides. MnPd$_3$ and MnPd$_3$D$_x$ crystallizing in ZrAl$_3$ type show a collinear antiferromagnetism ordering in a $++--$ sequence. The main difference between the magnetic structures is the inclination angle of the magnetic moment with respect to the crystallographic c-axis (11° for MnPd$_3$ and 55° for MnPd$_{30.53}$D), which is believed to originate from differences in manganese–manganese distances [98]. The magnetic moment of manganese atoms is 4.8 μ_B in tetragonal MnPd$_3$D$_{0.53}$ and 4.1 μ_B in cubic MnPd$_3$D$_{0.67}$ [98,99]. The magnetism of cubic MnPd$_3$D$_{0.67}$ could be explained either by a noncolinear ferrimagnetic structure and a commensurate conical magnetic structure, both models fitting the neutron diffraction data equally well [99].

Hydrogen content of ccp related MPd$_3$H$_x$

It is remarkable to note that the reactivity of palladium-rich intermetallic compounds strongly depends on the crystal structure. The majority of phases with significant hydrogen uptake exhibit ccp superstructures, that is, are structurally related to the element palladium. However, not all ccp-like palladium-rich compounds incorporate hydrogen, and those that do, do so to a widely varying extent $0 < x \leq 1$ in MPd$_3$H$_x$. Electronic and geometric effects were found to be the main factors determining the hydrogen content x. The structure map shown in Fig. 8.6.4 illustrates this influence by plotting the hydrogen content x of ccp related hydrides MPd$_3$H$_x$ as a function of electronegativity and atomic radius. Metals M with electronegativity values similar to palladium show the highest hydrogen amount. Furthermore, the atomic radius has also an influence on the hydrogen content as seen for example comparing lead and manganese, which exhibit the same electronegativity, but have large differences in radii. Very pronounced similarities in electronic and geometric properties are apparently not preferable, because the solubility of these elements in palladium increases and the ordering of atoms is impeded such as in MnPd$_3$, with a sluggish order–disorder transition [84].

8.6.3. CaPd$_3$H$_x$

CaPd$_3$H$_x$ is a special case because no intermetallic precursor compound is known yet. This hydride is formed by reaction of the binary hydrides CaH$_2$ and PdH$_x$ [101]. The metal atoms of CaPd$_3$H$_x$ form the hexagonal TiNi$_3$ type, to which BiPd$_3$ is structurally related.
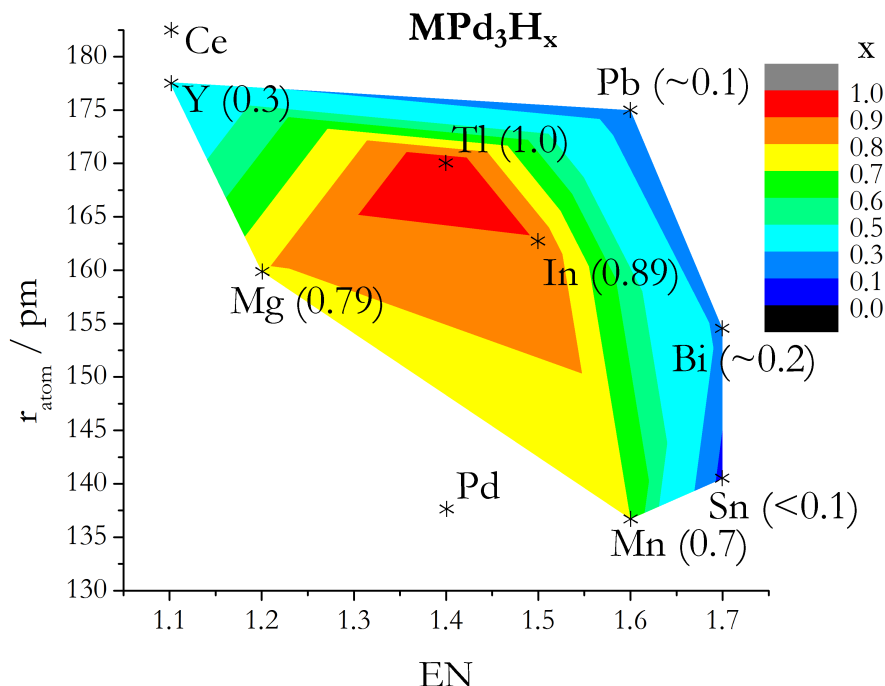
Figure 8.6.4.: Structure map for ccp related hydrides MPd$_3$H$_x$ showing the hydrogen content x as a function of electronegativity (EN by Allred and Rochow [100]) and atomic radius of M. The colored areas are meant as a guide for the eye and exact boundaries are uncertain as yet.

Synthesis

CaPd$_3$H$_x$ is synthesized by reaction of CaH$_2$ and PdH$_x$ in a ratio 1:2.4. The ground mixture reacts at 623 K under 0.5–0.8 MPa hydrogen pressure. Higher temperatures hydrogen pressures favor the formation of CaPd$_2$ and CaPdH$_2$ [101].

Crystal structure

The metal atoms of CaPd$_3$H$_x$ crystallize in the hexagonal TiNi$_3$ type structure (Fig. 8.6.5) with a double hexagonal layered sequence of ABACABAC.... [Pd$_6$] octahedra are alternately connected by faces and edges, forming short strands. Calcium is located between these strands. Octahedral voids are assumed to be fully occupied by hydrogen (Pd–H distances of 203–209 pm) [101]; however, hydrogen content and positions are not yet determined experimentally.

8.6.4. Palladium-rich hydrides with phosphorous

Three palladium-rich compounds with phosphorous are known that incorporate hydrogen or deuterium reversibly. The structures of these compounds are drastically different from Laves or MPd$_3$ phases. Pd$_3$P$_{0.8}$, Pd$_6$P, and Pd$_{15}$P$_2$ retain their crystal structure upon hydrogenation, except for an increase of unit cell volume and incorporation of hydrogen atoms in interstitial sites.

Synthesis

Palladium-rich phosphides are synthesized in high frequency induction furnaces under low argon pressure by first melting palladium and then adding phosphorous lumps, followed by multiple grinding and melting steps [102]. Pd$_{15}$P$_2$ is synthesized with an excess of palladium to prohibit the formation
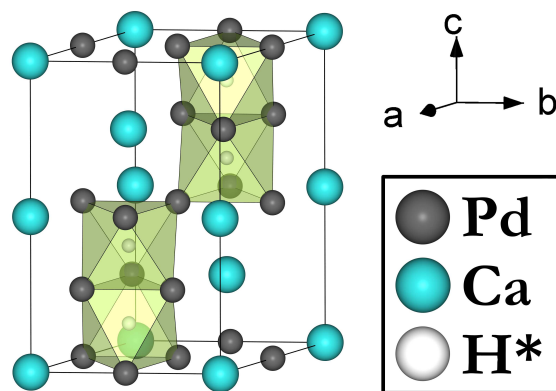
Figure 8.6.5.: Crystal structure of $CaPd_3H_x$ (filled $TiNi_3$ type). Proposed hydrogen positions in $[Pd_6]$ octahedral voids are shown in light green polyhedra [101].

of Pd_6P. The compounds are deuterated at room temperature and deuterium pressures up to 700 kPa [103–105].

Crystal structure

Pd_3P_{1-x} crystallizes in the Fe_3C type (*Pnma*) with a homogeneity range (Fig. 8.6.6). The unit cell volume of $Pd_3P_{0.8}$ increases upon deuteration. Deuterides $Pd_3P_{0.8}D_{0.14}$ were formed at 200 kPa and $Pd_3P_{0.8}D_{0.15}$ at 500 kPa deuterium pressure and contain deuterium atoms close to a vacant phosphorous site with a distorted square-pyramidal surrounding by palladium atoms [103].

Columns or triangular $[Pd_6]$ prisms running along crystallographic a direction are the dominating structural feature in the crystal structure of Pd_6P (Fig. 8.6.6). These columns are packed in the (b, c) plane. This structure is very similar to the Re_3B type (*Cmcm*). However, only every other triangular prism is filled with a phosphorous atom, and thus the orthorhombic symmetry is broken. The unit cell volume increases with increasing hydrogen content. $Pd_6PD_{0.15}$, $Pd_6PD_{0.22}$, and $Pd_6PD_{0.26}$ were formed at 200 kPa, 500 kPa, and 750 kPa deuterium pressures, respectively. Deuterium occupies some of the distorted square-pyramidal sites, linking with the empty triangular $[Pd_6]$ prisms, and some of the distorted octahedral sites linking four strands of triangular prisms [104].

The crystal structure of $Pd_{15}P_2$ (space group $R\bar{3}$, Fig. 8.6.6) may be described as an almost cubic closed packing of distorted palladium icosahedra (formed by Pd1 and Pd2) with Pd4 $(0, 0, 1/2)$ in the center. In the octahedral and tetrahedral holes of this packing, further palladium atoms (Pd3) and the phosphorous atoms are located, respectively [106]. Upon deuteration at 500 kPa deuterium pressure, the deuteride $Pd_{15}P_2D_{0.46}$ was formed with an increased unit cell volume. Deuterium occupies distorted tetrahedral $[Pd_4]$ voids in the crystal structure of $Pd_{15}P_2$ [105].

8.7. Concluding remarks

The hydrogen compounds of palladium and palladium-rich intermetallics may serve as archetypical examples for metallic hydrides with variable hydrogen content. A very detailed understanding of palladium hydride and the palladium–hydrogen phase diagram were attained in the past 150 years. It has been a very important model system for many interesting effects in the solid such as diffusion in metals, lattice gas behavior, or catalysis. A large number of palladium-rich solid solutions exist that form hydrides. The hydrogen uptake depends strongly on geometric aspects, as the size of the octahedral void in an α-phase hydride. In ordered palladium-rich intermetallic compounds we find a
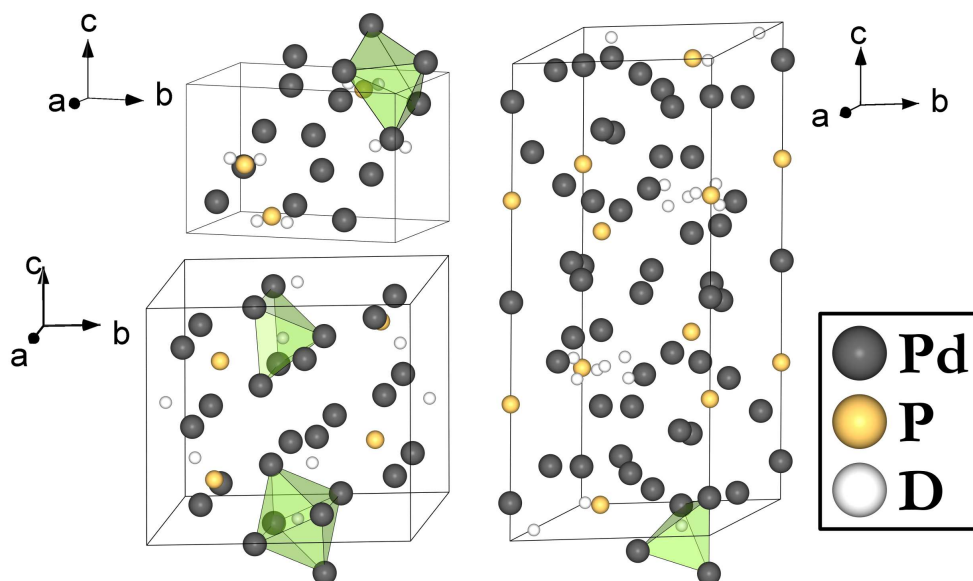
Figure 8.6.6.: Crystal structures of $Pd_3P_{0.8}D_{0.15}$ (top left) with deuterium at distorted $[Pd_5]$ square-pyramidal sites, of $Pd_6PD_{0.26}$ (bottom left) with deuterium at distorted $[Pd_6]$ octahedral and distorted $[Pd_5]$ square-pyramidal sites and $Pd_{15}P_2D_{0.46}$ (right) with deuterium at distorted $[Pd_4]$ tetrahedral sites.

very subtle interplay between hydrogen–palladium interaction and atomic order between substituting metal M and Pd atoms. It is generally deemed that hydrogen occupies preferential sites with a large number of palladium neighbors. $[Pd_6]$ octahedral voids, like in palladium itself, are primarily the most favored sites for hydrogen incorporation. Hydrogen-assisted gliding of atomic layers may be a possible mechanism for the formation of hydrides of ccp related MPd$_3$, most of which crystallize in a cubic anti-perovskite structure with hydrogen in octahedral $[Pd_6]$ voids. The hydrogenation of these ordered compounds depends in addition to geometric also on electronic aspects. New modifications of, for example, $MgPd_3$ and $MnPd_3$ ($AuCu_3$ type) could only be formed by hydrogenation and subsequent dehydrogenation; that is, by exploiting the above mentioned mechanism upon hydride formation. Furthermore, palladium-rich Laves phases, $CaPd_3H_x$ without an intermetallic precursor compound and compounds with phosphorous also form hydrides. Ordered palladium-rich compounds, which do not form hydrides, often attract interest in catalysis.

8.8. References for chapter 8

[1]   T. Graham, On the absorption and dialytic separation of gases by colloid septa, Philos. Trans. R. Soc. London 156 (1866) 399–439.

[2]   T. Graham, On the relation of hydrogen to palladium, Proc. R. Soc. London 17 (1869) 212–220.

[3]   J. E. Worsham JR., M. K. Wilkinson, C. G. Shull, Neutron-diffraction observations on the palladium-hydrogen and palladium-deuterium systems, J. Phys. Chem. Solids 3 (1957) 303–310.

[4]   T. B. Flanagan, W.A. Oates, The palladium-hydrogen system, Annu. Rev. Mater. Sci. 21 (1991) 269–304.

[5]   S. S. Shil'stein, V. P. Glazkov, A. V. Irodova, V. A. Somenkov, V. E. Antonov, E. G. Ponyatovskii, The crystal structure of high pressure hydrides, Z. Phys. Chem. 146 (1985) 129–135.

[6]   B. Baranowski, S. M. Filipek, Relative electrical resistance of Pd saturated by gaseous deuterium in a wide pressure range at 298 K, Z. Phys. Chem. 216 (2002) 699–705.

[7]   W. A. Oates, T. B. Flanagan, The reaction of hydrogen atoms with palladium and its alloys, Can. J. Chem. 53 (1975) 694–701.

[8]   J. E. Schirber, B. Morosin, Lattice constants of β-PdH$_x$ and β-PdD$_x$ with x near 1.0, Phys. Rev. B: Condens. Matter Mater. Phys. 12 (1975) 117–118.

[9]   H. Brüning, A. Sieverts, Der elektrische Widerstand wasserstoffbeladener Palladiumdrähte zwischen 160°und 310°, Z. Phys. Chem., Abt. A 163 (1933) 409–441.

[10] S. Wagner, T. Kramer, H. Uchida, P. Dobron, J. Cizek, A. Pundt, Mechanical stress and stress release channels in 10–350 nm palladium hydrogen thin films with different micro-structures, Acta Mater. 114 (2016) 116–125.

[11] H. G. Grimm, Über Bau und Grösse der Nichtmetallhydride, Z. Elektrochem. Angew. Phys. Chem. 31 (1925) 474–480.

[12] J. O. Linde, G. Borelius, Röntgenographische und elektrische Untersuchung des Systems Palladium-Wasserstoff, Ann. Phys. 84 (1927) 747–774.

[13] D. M. Nace, J. G. Aston, Palladium hydride. III. Thermodynamic study of Pd$_2$H at 303 K. Evidence for the tetrahedral PdH$_4$ structure in palladium hydride, J. Am. Chem. Soc. 79 (1957) 3627–3633.

[14] J. G. Aston, P. Mitacek JR., Structures of hydrides of palladium, Nature (London, U. K.) 195 (1962) 70–71.

[15] I. S. Balbaa, P. A. Hardy, A. San-Martin, P. G. Coulter, F. D. Manchester, The effect of lattice distortions on the X-ray measurement of lattice parameterrs for PdH$_x$: I. Empirical relationships, J. Phys. F: Met. Phys. 17 (1987) 2041–2048.

[16] M. Widenmeyer, R. Niewa, T. C. Hansen, H. Kohlmann, *In situ* neutron diffraction as a probe on formation and decomposition of nitrides and hydrides: a case study, Z. Anorg. Allg. Chem. 639 (2013) 285–295.

[17] M. P. Pitt, E. MacA Gray, Tetrahedral occupancy in the Pd-D system observed by *in situ* neutron powder diffraction, Europhys. Lett. 64 (2003) 344–350.

[18] J. G. Aston, P. Mitacek JR., Solutions of Hydrogen in Palladium, in: R. Ward (Ed.), Nonstoichiometric Compounds, American Chemical Society, Washington, D. C. (1963) pp. 111–121.

[19] G. A. Ferguson JR., A. I. Schindler, T. Tanaka, T. Morita, Neutron diffraction study of temperature-dependent properties of palladium containing absorbed hydrogen, Phys. Rev. [Sect.] A 137 (1965) 483–487.

[20] I. S. Anderson, D. K. Ross, C. J. Carlile, The structure of the γ phase of palladium deuteride, Phys. Lett. A 68 (1978) 249–251.

[21] T. E. Ellis, C. B. Satterthwaite, M. H. Mueller, T. O. Brun, Evidence for H(D) ordering in PdH$_x$ (PdD$_x$), Phys. Rev. Lett. 42 (1979) 456–458.

[22] M. H. Mueller, T. O. Brun, R. L. Hitterman, H. W. Knott, C. B. Satterthwaite, T. E. Ellis, Deuteron density modulation of D atoms in PdD$_{1-x}$, AIP Conf. Proc. 53 (1979) 391–393.

[23] S. J. Kennedy, E. Wu, E. H. Kisi, E. M. Gray, B. J. Kennedy, Ordering of deuterium in PdD$_{0.65}$ at 54 K, J. Phys.: Condens. Matter 7 (1995) L33-L40.

[24] E. Wu, S. J. Kennedy, E. MacA Gray, E. H. Kisi, The ordered structure of PdD$_{0.78}$ at 70-75 K, J. Phys.: Condens. Matter 8 (1996) 2807–2813.

[25] E. Wu, S. J. Kennedy, E. H. Kisi, E. MacA Gray, B. J. Kennedy, Neutron powder diffraction study of deuterium ordering in β phase Pd-D at low temperatures, J. Alloys Compd. 231 (1995) 108–114.

[26] Y. Fukai, Ōkuma N., Formation of superabundant vacancies in Pd hydride under high hydrogen pressure, Phys. Rev. Lett. 73 (1994) 1640–1643.

[27] T. C. Hansen, H. Kohlmann, Chemical reactions followed by *in situ* neutron powder diffraction, Z. Anorg. Allg. Chem. 640 (2014) 3044–3063.

[28] K. T. Møller, B. R. S. Hansen, A.-C. Dippel, J.-E. Jørgensen, T. R. Jensen, Characterization of gas-solid reactions using *in situ* powder X-ray diffraction, Z. Anorg. Allg. Chem. 640 (2014) 3029–3043.

[29] H. Kohlmann, N. Kurtzemann, T. C. Hansen, Metal hydride formation in palladium and palladium-rich intermetallic compounds studied by *in situ* neutron diffraction, Powder Diffr. 28 (2013) S242-S255.

[30] A. Götze, H. Kohlmann, unpublished.

[31] G. Behrendt, C. Reichert, H. Kohlmann, Hydrogenation reaction pathways in the systems Li_3N-H_2, $Li_3N-Mg-H_2$, and $Li_3N-MgH_2-H_2$ by *in situ* X-ray diffraction, *in situ* neutron diffraction, and *in situ* thermal analysis, J. Phys. Chem. C 120 (2016) 13450-13455.

[32] H. Auer, D. Wallacher, T. C. Hansen, H. Kohlmann, *In situ* hydrogenation of the Zintl phase SrGe, Inorg. Chem. 56 (2017) 1072-1079.

[33] E. Füglein, A. Léon, High-pressure DSC, in: A. Léon (Ed.), Hydrogen Technology, Springer, Berlin, Heidelberg (2008) pp. 501–521.

[34] H. Kohlmann, Hydrogenation of palladium-rich compounds of aluminium, gallium and indium, J. Solid State Chem. 183 (2010) 367–372.

[35] H. Wipf (Ed.), Hydrogen in Metals III: Properties and Applications, 1st ed., Springer, Berlin (1997).

[36] E. Storms, Formation of β-PdD containing high deuterium concentration using electrolysis of heavy-water, J. Alloys Compd. 268 (1998) 89–99.

[37] M. M. Beg, D. K. Ross, The quasielastic scattering of cold neutrons fromn the β-phase of palladium hydride, J. Phys. C: Solid State Phys. 3 (1970) 2487–2500.

[38] W. Spalthoff, Magnetische Kernresonanzuntersuchungen an Metallhydriden, Z. Phys. Chem. 29 (1961) 258–276.

[39] T. B. Flanagan, F. A. Lewis, Relationships between electrical resistance and the hydrogen content of palladium, Z. Phys. Chem. 27 (1961) 104–111.

[40] B. Stritzker, H. Wühl, Superconductivity in Metal-Hydrogen Systems, in: G. Alefeld, J. Vökl (Eds.), Hydrogen in Metals II, Springer, Berlin, Heidelberg (1978) pp. 243–272.

[41] F. A. Lewis, The palladium-hydrogen system, part II of a survey of features, Platinum Met. Rev. 26 (1982) 70–78.

[42] T. R. P. Gibb Jr., J. MacMillan, R. J. Roy, The magnetic susceptibility of palladium hydride, J. Phys. Chem. 70 (1966) 3024.

[43] B. Stritzker, W. Buckel, Superconductivity in the palladium-hydrogen and the palladium-deuterium systems, Z. Phys. 257 (1972) 1–8.

[44] R. Griessen, D. G. de Groot, Effect of the anharmonicity and Debye-Waller factor on the superconductivity of PdH_x and PdD_x, Helv. Phys. Acta 55 (1982) 699–710.

[45] T. R. P. Gibb Jr., Nonstoichiometric Hydrides, in: R. Ward (Ed.), Nonstoichiometric Compounds, American Chemical Society, Washington, D. C. (1963) pp. 99–110.

[46] M. Gupta, L. Schlapbach, Electronic Properties, in: L. Schlapbach (Ed.), Hydrogen in Intermetallic Compounds I: Electronic, Thermodynamic, and Crystallographic Properties, Preparation, Springer, Berlin (1988) pp. 139–217.

[47] S. Abound, J. Wilcox, A density functional theory study of the charge state of hydrogen in metal hydrides, J. Phys. Chem. C 114 (2010) 10978–10985.

[48] P. W. Albers, K. Möbius, C.D. Frost, S.F. Parker, Characterization of β-palladium hydride formation in the Lindlar catalyst and in carbon-supported palladium, J. Phys. Chem. C 115 (2011) 24485–24493.

[49] L. L. Jewell, B. H. Davis, Review of absorption and adsorption in the hydrogen–palladium system, Appl. Catal., A 310 (2006) 1–15.

[50] B. M. Andreev, E. P. Magomedbekov, G. H. Sicking, Interaction of Hydrogen Isotopes with Transition Metals and Intermetalic Compounds, Springer, Berlin (1966).

[51] I. R. Harris, M. Norman, A. W. Bryant, A study of some palladium-indium, platinum-indium and platinum-tin alloys, J. Less-Common Met. 16 (1968) 427–440.

[52] H. Kohlmann, C. Ritter, Refinement of the crystal structures of palladium-rich In-Pd compounds by X-ray and neutron powder diffraction, Z. Naturforsch., B: J. Chem. Sci. 62 (2007) 929–934.

[53] K. Schubert, Kristallstrukturen zweikomponentiger Phasen, Springer, Berlin, Heidelberg (1964).

[54] D. Fisher, D. M. Chisdes, T. B. Flanagan, Solution of hydrogen in palladium/copper alloys, J. Solid State Chem. 20 (1977) 149–158.

[55] T. G. Berger, A. Leineweber, E. J. Mittemeijer, C. Sarbu, V. Duppel, P. Fischer, On the formation and crystal structure of the Pd_6B, Z. Kristallogr. 221 (2006) 450–463.

[56] M. C. Cadeville, C. Lerner, On the electronic structure of interstitial transition-metal based alloys with boron and carbon impurities. Part I. Experimental study, Philos. Mag. 33 (1976) 801–824.

[57] A .G. Christy, S. M. Clar, Structural behavior of palladium(II) oxide and a palladium suboxide at high pressure: An energy-dispersive x-ray-diffraction study, Phys. Rev. B: Condens. Matter 52 (1995) 9259–9265.

[58] T. B. Massalski, H. Okamoto (Eds.), Binary alloy phase diagrams, ASM International, Materials Park, Ohio, (1990).

[59] Crystal Impact GbR, Pearson's Crystal Data, ASM International & Material Phases Data System, (2007).

[60] F. A. Lewis, The Palladium-hydrogen system, part III: Alloy systems and hydrogen permeation, Platinum Met. Rev. 26 (1982) 121–128.

[61] H. Noh, T. B. Flanagan, Y. Sakamoto, Hydrogen-induced segregation in Pd-Pt alloys, J. Alloys Compd. 231 (1995) 10–14.

[62] S.-M. Lee, H. Noh, T. B. Flanagan, S. Luo, Hydrogen-induced lattice rearrangement of a $Pd_{0.81}Au_{0.19}$ alloy,, J. Phys.: Condens. Matter 19 (2007) 326222.

[63] C. M. Pradier, M. Mazina, Y. Berthier, J. Oudar, Hydrogenation of acetylene on palladium, J. Mol. Catal. 89 (1994) 211–220.

[64] J. Osswald, R. Giedigkeit, R. Jentoft, M. Armbrüster, F. Girgdies, K. Kovnir, T. Ressler, Y. Grin, R. Schlögl, Palladium-gallium intermetallic compounds for the selective hydrogenation of acetylene Part I, J. Catal. 258 (2008) 210–218.

[65] M. Armbrüster, G. Wowsnick, M. Friedrich, M. Heggen, R. Cardoso-Gil, Synthesis and catalytic properties of nanoparticulate intermetallic Ga–Pd compounds, J. Am. Chem. Soc. 133 (2011) 9112–9118.

[66] M. Armbrüster, R. Schlögl, Y. Grin, Intermetallic compounds in heterogeneous catalysis - a quickly developing field, Sci. Technol. Adv. Mater. 15 (2014) 34803.

[67] S. Yamamatsu, Shokubai 43 (2001) 549.

[68] A. V. Irodova, I. I. Borisov, O. A. Lavrova, G. V. Laskova, L. N. Padurets, S. A. Pripadchev, Phase transitions in the ZrV2D(H) system, Sov. Phys. Solid State 25 (1983) 747–750.

[69] A.N. Bogdanova, A.V. Irodova, G. Andre, F. Bouree, The ZrV_2D_6 crystal structure, J. Alloys Compd. 356-357 (2003) 50–53.

[70] C. Stanitski, J. Tanaka, Ternary hydrides of calcium and strontium with palladium, J. Solid State Chem. 4 (1972) 331–339.

[71] H. Kohlmann, H. E. Fischer, K. Yvon, Europium palladium hydrides, Inorg. Chem. 40 (2001) 2608–2613.

[72] N. Kurtzemann, H. Kohlmann, Crystal structure and formation of $TlPd_3$ and its new Hydride $TlPd_3H$, Z. Anorg. Allg. Chem. 636 (2010) 1032–1037.

[73] A. Götze, J.M. Sander, H. Kohlmann, Crystal structures and hydrogenation properties of palladium-rich compounds with elements from groups 12-16, Z. Naturforsch. 71B (2016) 503–508.

[74] C. Wannek, B. Harbrecht, Structure and thermal stability of the new intermetallics $MgPd_2$, $MgPd_3$, and Mg_3Pd_5 and the kinetics of the iodine-catalyzed formation of $MgPd_2$, J. Solid State Chem. 159 (2001) 113–120.

[75] J. R. Thomson, The constitution of cerium-palladium alloys containing 50–100 % palladium, J. Less-Common Met. 13 (1967) 307–312.

[76] A. E. Dwight, J. W. Downey, R. A. Conner, Some AB_3 compounds of the transitiom metals, Acta Crystallogr. 14 (1961) 75–76.

[77] P.-J. Ahlzén, Y. Andersson, R. Tellgren, D. Rodic, T. B. Flanagan, Y. Sakamoto, A neutron powder diffraction study of Pd_3MnD_x, Z. Phys. Chem. (Muenchen, Ger.) 163 (1989) 213–218.

[78] T. B. Flanagan, A. P. Craft, T. Kuji, K. Baba, Y. Sakamoto, Hydrogen induced disorder-order transition in Pd_3Mn, Scr. Metall. 20 (1986) 1745–1750.

[79] H. Kohlmann, G. Renaudin, K. Yvon, C. Wannek, B. Harbrecht, Hydrogen-induced atomic rearrangement in $MgPd_3$, J. Solid State Chem. 178 (2005) 1292–1300.

[80] H. Kohlmann, N. Kurtzemann, R. Weihrich, T. Hansen, *In situ* neutron powder diffraction on intermediate hydrides of $MgPd_3$ in a novel sapphire gas pressure cell, Z. Anorg. Allg. Chem. 635 (2009) 2399–2405.

[81] H. Kohlmann, A. V. Skripov, A. V. Soloninin, T. J. Udovic, The anti-perovskite type hydride $InPd_3H_{0.89}$, J. Solid State Chem. 183 (2010) 2461–2465.

[82] S. Yamaguchi, M. Ohashi, T. Kajitani, K. Aoki, S. Ikeda, Distribution of hydrogen atoms in YPd_3H_x studied by neutron diffraction and inelastic neutron scattering, J. Alloys Compd. 253-254 (1997) 308–312.

[83] S. Yamaguchi, Z.-Q. Li, R.-T. Fu, Y. Kawazoe, Hydrogen site occupation in YPd_3 with L12 structure, Phys. Rev. B 55 (1997) 14051–14054.

[84] P. Önnerud, Y. Andersson, R. Tellgren, P. Nordblad, F. Bourée, G. André, The crystal and magnetic structures of ordered cubic $Pd_3MnD_{0.7}$, Solid State Commun. 101 (1997) 433–437.

[85] H. Kohlmann, F. Müller, K. Stöwe, A. Zalga, H. P. Beck, Hydride formation in the intermetallic compounds $CePd_3$ and $CeRh_3$, Z. Anorg. Allg. Chem. 635 (2009) 1407–1411.

[86] P.H. Andersson, O. Eriksson, L. Nordström, The effect of hydrogenation on the crystal structure and magnetic state in Pd_3Mn, J. Magn. Magn. Mater. 226-230 (2001) 1040–1041.

[87] K. Schubert, B. Kiefer, M. Wilkens, Ordnungsphasen mit großer Periode in Legierungen, Z. Naturforsch. 9A (1954) 987–988.

[88] D. Watanabe, M. Hirabayashi, S. Ogawa, On the superstructure of the alloy Cu_3Pd, Acta Crystallogr. 8 (1955) 510–512.

[89] M. Hirabayashi, S. Ogawa, On the superstructure of the ordered alloy Cu_3Pd II. X-ray diffraction study, J. Phys. Soc. Jpn 12 (1957) 259–271.

[90] M. Latroche, P. Kalisvaart, P. H. L. Notten, Crystal structure of $Mg_{0.65}Sc_{0.35}D_x$ deuterides studied by X-ray and neutron powder diffraction, J. Solid State Chem. 179 (2006) 3024–3032.

[91] N. Kunkel, J. Sander, N. Louis, Y. Pang, L.M. Dejon, F. Wagener, Y. N. Zang, A. Sayede, M. Bauer, M. Springborg, H. Kohlmann, Theoretical investigation of the hydrogenation induced atomic rearrangements in palladium-rich intermetallic compounds MPd$_3$ (M = Mg, In, Tl), Eur. Phys. J. 82B (2011) 1–6.

[92] P. Kumar, M. Hareesh, R. Balasubramaniam, Effect of hydrogen on the stabilities of ordered structures Pd$_3$Mn, J. Alloys Compd. 217 (1995) 151–156.

[93] R. Balasubramaniam, Mechanism of hydrogen induced ordering in Pd$_3$Mn, Scr. Metall. Mater. 30 (1994) 875–880.

[94] H. Kohlmann, C. Ritter, Reaction pathways in the formation of intermetallic InPd$_3$ Polymorphs, Z. Anorg. Allg. Chem. 635 (2009) 1573–1579.

[95] S. Bhan, K. Schubert, Über die Struktur von Phasen mit Kupfer Unterstruktur in einigen T-B Legierungen (T = Ni, Pd, Pt; B= Ga, In, Tl, Pb, Sb, Bi), J. Less-Common Met. 17 (1969) 73–90.

[96] H. Bärnighausen, Group-subgroup relations between space groups: a useful tool in crystal chemistry, MATCH 9 (1980) 137–175.

[97] D.-H. Wu, H.-C. Wang, L.-T. Wei, R.-K. Pan, B.-Y. Tang, First-principles study of structural stability and elastic properties of MgPd$_3$ and its hydride, J. Magnesium Alloys 2 (2014) 165–174.

[98] D. Rodić, P. Ahlzén, Y. Andersson, R. Tellgren, The magnetic structure of Pd$_3$MnD$_{0.53}$, Solid State Commun. 71 (1989) 623–626.

[99] P. Önnerud, Y. Andersson, R. Tellgren, P. Nordblad, The magnetic structure of ordered cubic Pd$_3$Mn, J. Solid State Chem. 128 (1997) 109–114.

[100] A. L. Allred, E. G. Rochow, A scale of electronegativity based on electrostatic force, J. Inorg. Nucl. Chem. 5 (1958) 264–268.

[101] E. Rönnebro, D. Noréus, M. Gupta, K. Kadir, B. Hauback, P. Lundqvist, The crystal and electronic structure of CaPd$_3$H, Mater. Res. Bull. 35 (2000) 315–323.

[102] B. Carlsson, M. Gölin, S. Rundqvist, Determination of the homogeneity range and refinement of the crystal structure of Fe$_2$P, J. Solid State Chem. 8 (1973) 57–67.

[103] Y. Andersson, S. Rundqvist, R. Tellgren, J. O. Thomas, T. B. Flanagan, A neutron diffraction investigation of deuterated Pd$_3$P$_{0.80}$, J. Solid State Chem. 32 (1980) 321–327.

[104] Y. Andersson, S. Rundqvist, R. Tellgren, J. O. Thomas, T. B. Flanagan, Neutron powder diffraction investigation of pure and deuterated palladium phosphide Pd$_6$P, Acta Crystallogr. 37B (1981) 1965–1972.

[105] Y. Andersson, S. Rundqvist, R. Tellgren, T. B. Flanagan, A neutron powder diffraction investigation of deuterated Pd$_{15}$P$_2$, Z. Phys. Chem. (Muenchen, Ger.) 145 (1985) 43–49.

[106] Y. Andersson, The crystal structure of Pd$_{15}$P$_2$, Acta Chem. Scand. 31 (1977) 354–358.

9. A Sapphire Single-Crystal Cell for *In Situ* Neutron Powder Diffraction of Solid-Gas Reactions

André Götze, Henry Auer, Raphael Finger, Thomas C. Hansen, Holger Kohlmann

9.1. Authors' contributions

This article results from a conference talk of Holger Kohlmann who assembled the manuscript. The description of the in situ neutron diffraction cell was done by R. Finger. The shown examples of hydrogenation of palladium-rich intermetallics and of Zintl phases were described by A. Götze and H. Auer, respectively. They also conducted the corresponding experiments. T. Hansen assisted during the experiments at the beamline.

9.2. Abstract

Solid-gas reactions play an important role in many technologically important processes from ore smelting to hydrogen storage and the synthesis of functional materials. *In situ* investigations are very useful for unraveling basic steps of such reactions, rationalizing them and gaining control. For investigating time-resolved solid-gas reactions, we have constructed a gas pressure cell for elastic neutron diffraction. By proper orientation of a single-crystal sapphire tube as sample holder, Bragg peaks from the container material can be completely avoided, thus yielding high-quality powder diffraction data with very clean diffraction background. This enables the extraction of high precision crystal structure data as a function of gas pressure and temperature (laser heating) in time-resolved studies. The potential of the gas pressure cell is demonstrated by *in situ* studies of the reaction of solids with hydrogen, which yielded detailed models of the reaction pathways including high quality crystal structures of reaction intermediates and products. These were used to predict successfully the existence of further metal hydrides, to explain unusual bonding properties, and to optimize the synthesis of metastable compounds.

9.3. Introduction

The importance of solid-gas reactions in science and in everyday life can hardly be overrated. They play a crucial role in many technologically important processes such as ore smelting (Fig. 9.3.1), heterogeneous catalysis, combustion of solid fuels, and the synthesis of solid materials. Solid-gas reactions are the basic step of gas storage, e. g. CO_2 sequestration or hydrogen storage, of corrosion of metals and alloys (Fig. 9.3.1) or their hardening procedures. They are thus key for the production, use and wear of many functional materials. The study of such reactions is often technically demanding due to the oftentimes harsh conditions and the difficulty to find suitable probes. This is probably the reason, why despite being subject of research for many decades, only model systems are well understood and a deeper knowledge of reaction mechanisms in solids allowing control over processes is often lacking [1–4].

Figure 9.3.1.: Ironworks in Völklingen, Germany (UNESCO World Heritage Site since 1994), as an example for two different kinds of solid-gas reactions, iron ore smelting (reaction of iron oxides with gaseous carbon monoxide; when operating $\leq$ 1986) and corrosion of steel in air (after closing in 1986); By Lokilech - Own work, CC BY-SA 3.0, `https://commons.wikimedia.org/w/index.php?curid=1331378`, download August 8, 2017.

Neutron diffraction is ideally suited to serve as a probe for such reactions because of several reasons. The gases most often used, e. g. H_2, N_2, O_2, H_2O, CO, CO_2, contain light elements, which can often be better located in crystal structures by neutron as compared to X-ray diffraction. Studying solid-gas reactions by *in situ* methods allowing control over external parameters such as pressure and temperature often requires bulky sample environment. This is easier to penetrate by neutrons than by X-rays due to the smaller absorption coefficients for most elements. Further, neutrons can probe many properties of materials, e. g. crystal structure, diffusion, magnetism, vibrational properties, and thus yield extensive information. In this contribution, we will focus on crystal structure evolvement during solid-gas reactions by elastic neutron powder diffraction. Time-resolved *in situ* investigations are very useful for unraveling basic steps of such reactions and understanding reaction pathways. This is the key to rationalize them and gain better control over reactions and processes. The potential of *in situ* neutron diffraction for the study of solid-gas reactions is intimately connected to the development of high-flux diffractometers and has increased accordingly over the past decades [5–8]. Here, we will briefly describe a single-crystal based sapphire cell and show the potential and limitations of this piece of sample environment for time-resolved *in situ* neutron powder diffraction.

9.4. Materials and methods

9.4.1. Chemical syntheses

$MgPd_3$ was synthesized by solid-state reaction of the elements (3.1 % excess of magnesium powder, 99.8 %, abcr; palladium powder, 99.95 %, $\leq$ 150 μm, Goodfellow; 25 K h^{-1} to 868 K, held for 4.5 d, quenched in air) in evacuated glass ampoules with iodine as mineralization agent (few crystals) [9]. The product was annealed for another 3 d at 868 K after regrinding and yielded α-$MgPd_3$ with about 1 % of MgO as minor phase. SrGe was prepared from the elements in sealed tantalum ampoules [10].

9.4.2. A sapphire single-crystal cell for *in situ* neutron diffraction

In situ neutron diffraction for solid-gas reaction requires dedicated sample environment. It has to hold the sample in place, give control over temperature and gas pressure, and allow neutron diffraction to be carried out. Specifically, the sample environment should fulfill the following requirements:

- chemical inertness (corrosion, hydrogen embrittlement)

- pressure stability

- temperature stability

- free optical access for the neutron beam

- low incoherent neutron scattering

- low neutron absorption

- low background

- no parasitic reflections

High-strength alloys seem to be good candidates for the material of an *in situ* cell in view of temperature and pressure stability, and are often used [11–15]. For detailed structural investigations, however, they show some disadvantages. Most severely, such materials as steel, Inconel, aluminum alloys etc.

are polycrystalline and evidently diffract the neutron beam, thus contributing to the diffraction pattern. This may lead to overlap of reflections from sample and container, especially for low-symmetry compounds in the sample, disturbing the data analysis by Rietveld refinement. Amorphous container materials (e. g. the widely used silica for high-temperature diffraction) are not an ideal choice either, because they produce a strong structured diffraction background. The degree of these problems of course scales with the neutron scattering lengths in the materials of use. Therefore, zero-scattering alloys such as $Ti_{52}Zr_{48}$ are suitable materials and are used for gas-pressure cells [16]. Due to hydrogen embrittlement, unfortunately, it cannot be used when studying hydrogenation reactions. This problem can be solved by using an inner liner, preventing hydrogen contact to the alloy. However, either pressure-temperature conditions are limited, e. g. in copper-coated vanadium cans [17] or the lining material will again produce neutron reflections.

The intrinsic flaws of amorphous and polycrystalline materials have prompted us to aim for another concept. In a powder diffraction experiment, most often the detector operates in a plane and is of limited height, i. e. measures only a thin slice of reciprocal space. Debye-Scherrer rings from a polycrystalline container material will inevitably by measured by such a detector (Fig. 9.4.1, left). In case of a single crystalline material, however, diffraction intensities are confined to small spots in reciprocal space. Having a single-crystalline container material should therefore enable a mode of operation where by proper orientation the detector in a powder diffraction experiment will measure only reciprocal space between rows of diffraction spots and therefore not see the container material (Fig. 9.4.1, right). A material available as large single crystals and fulfilling the above-mentioned requirements is synthetic α-Al_2O_3, also known as leuco-sapphire, and is thus chosen. A 10 cm long sapphire is machined to have a borehole of 6 mm inner diameter to hold the powder sample. A flange at the upper end of the single crystal in combination with an endcap machined from steel (Fig. 9.4.2) allows hermetical sealing and realization of high gas pressures. The latter also provides a free optical access of the neutron beam. Due to the design with separated endcaps, no further supports in the diffraction plane are necessary, which might disturb the diffraction experiment by neutron absorption. A similar design using a single-crystal sapphire cell was described before for inelastic scattering on gas hydrates at low temperatures [18] and inspired our development. The use of leuco-sapphire has
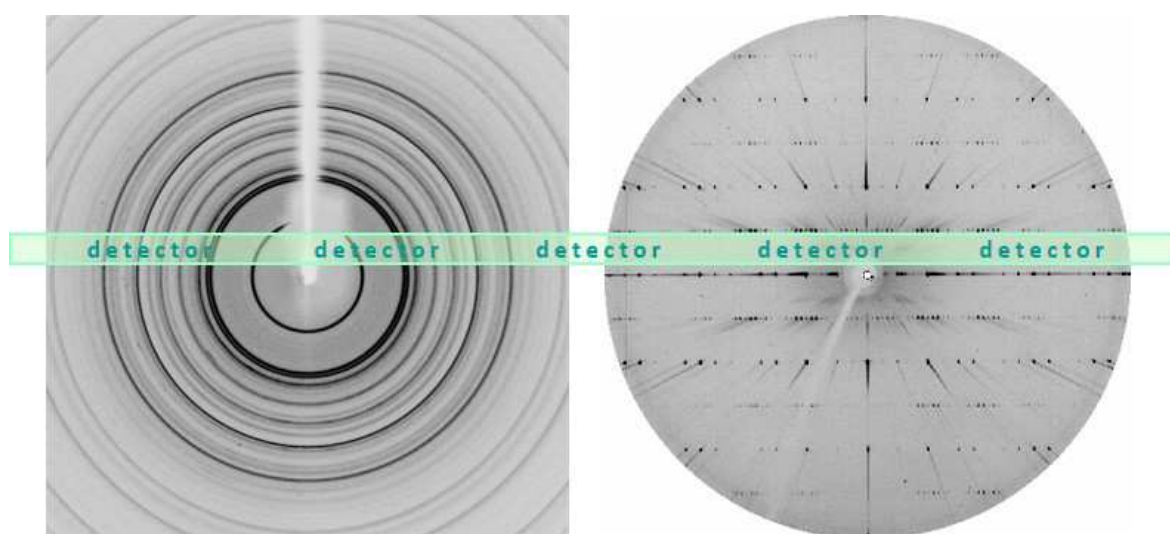

Figure 9.4.1.: Diffraction patterns of a polycrystalline material (left) and a single crystal (right) with a thin slice of reciprocal space mapped in a typical powder diffraction experiment marked in green.
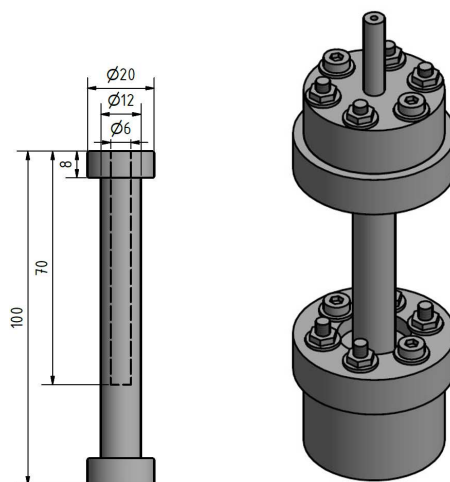
Figure 9.4.2.: Schematic drawings of the machined single-crystal sapphire (left, measures in mm, crystallographic c axis along cylinder axis or slightly inclined) and fully assembled cell (right).

the further advantage of optical transparency, which makes visual control of the reaction progress and heating by a laser possible. Neutron diffraction measurements of the empty cell and of reference samples inside the cell show that the concept of avoiding Bragg reflections from the container by using a single crystal with proper orientation with respect to the diffractometer works well. Diffraction data are comparable in quality to ex situ data due to the absence of enhanced background or parasitic reflections. In some cases incoherent scattering in the vicinity of strong single-crystal reflections of the sapphire cannot be avoided completely and a few degrees in 2θ have to be excluded [7, 19, 20].

Typical operating conditions for the sapphire single-crystal cell for *in situ* investigations of solid-gas reactions with hydrogen (deuterium) are $T \leq 700$ K, $p_{gas} \leq 16$ MPa, and time resolution of 10 s $\leq \Delta t \leq 300$ s. For avoiding mechanical failure of the flanges at the end of the container (Fig. 9.4.2), seals have to be chosen according to their hardness and assembled carefully. Due to thermal conductivity of sapphire and hydrogen gas, seals warm up, i. e. their temperature stability is also a major concern. Depending on gas pressure and temperature suitable seals consist of indium, lead or polymeric materials. For the latter O-rings of Viton GLT70 with 70 shore (15 mm outer diameter, 2 mm thickness, operating temperature according to manufacturer 293 K $\leq T \leq 493$ K, CKD-Dichtungstechnik, Germany [21]) and NBR flat seal with 65 shore (17 mm outer diameter, 9 mm inner diameter, 2 mm thickness, operating temperature according to manufacturer 243 K $\leq T \leq 373$ K, IDT-Flachdichtungen, Germany [22]) were tested successfully. Leak rates are below 1 kPa h^{-1} at room temperature for pressures up to 10 MPa. The tube attached to the upper steel cap (Fig. 9.4.2, right) is connected to a gas delivery system. This and the laser heating can be controlled remotely while the *in situ* experiment is running. It consists of two laser diode modules (LNT, 808 nm, 40 W each), 5 m long glass fibres and divergent optics to widen the beam to an area of 6*20 mm^2 at the sample inside the sapphire single-crystal cell. For safety reasons, the cell is operated inside an enclosure made from aluminum installed on the diffractometer (D20, Institut Laue-Langevon, Grenoble, France). From experience over eight years, an average lifetime of sapphire crystals is estimated to be more than five *in situ* neutron diffraction experiments. Test measurements with the empty cell and reference samples for hydrogenation have been described already [7, 19, 20]. Herein, we report on new application of in situ neutron diffraction experiments of the sapphire single-crystal cell, probing its potential and limits.

9.5. Results and Discussion

9.5.1. Hydrogenation of palladium-rich intermetallic compounds

Compounds of palladium and palladium-rich intermetallics with hydrogen are archetypical examples for metallic hydrides with variable hydrogen content. Ordered palladium-rich intermetallic compounds show a very interesting interplay between hydrogen–palladium interactions and atomic order. In MPd$_3$ (M = Mg [23], In [24,25], Tl [26], Sn, Pb [27], Bi [28]) hydrogen induces a rearrangement between different ordered variants of close packing of M and Pd atoms for which the maximization of the number of octahedral [Pd$_6$] voids plays an important role. These interstices are preferred by hydrogen and provide the highest bonding energy in their hydrides MPd$_3$H$_x$ (in general x $\leq$ 1). For M = Mg the crystal structure is retained when removing the hydrogen by gentle heating in vacuum [23]. This concept provides a soft-chemical route (chimie douce) to new polymorphs of intermetallic compounds. Some of the hydrides cannot be quenched to ambient conditions, i. e. *in situ* investigations are mandatory for their investigation. As an example, we present here a study on the hydrogen uptake of MgPd$_3$, which crystallizes in the tetragonal ZrAl$_3$ type structure (ordered variant of cubic close packing, Fig. 9.5.1, top right), at room temperature. The crystal structure exhibits three suitable interstitial sites for hydrogen (deuterium) atoms, each of them surrounded in a slightly distorted octahedral arrangement by varying numbers of magnesium and palladium atoms, [Pd$_6$], [MgPd$_5$], and [Mg$_2$Pd$_4$].

Deuterium uptake starts at room temperature when flushing the cell with deuterium gas (1 MPa, frame 1, Fig. 9.5.1). At this point, half of [Pd$_6$] and one quarter of [MgPd$_5$] are occupied while [Mg$_2$Pd$_4$] are empty. During the isothermal deuteration up to frame 17 (corresponding to 112 min) both lattice parameters increase (Δa = + 1.3 %, Δc = + 0.9 %). The development of lattice parameter a and the occupation of [MgPd$_5$] are strongly correlated as evident from the very similar dependence on time (Fig. 9.5.1). This is most probably caused by the structural arrangement of [MgPd$_5$] octahedra, which share edges and form sheets perpendicular to the crystallographic c axis (Fig. 9.5.1, top right). A volume increase by deuterium occupation in these voids will therefore be highly anisotropic and cause a larger increase in a than in c. This effect is less pronounced for [Pd$_6$] voids, which share edges with [Mg$_2$Pd$_4$] to form similar octahedral sheets. [Mg$_2$Pd$_4$] are unoccupied in the beginning of the experiment, thus working as a buffer and soothing the effect of deuterium occupation in [Pd$_6$] on the lattice parameter a. Only when the lattice and thus the size of [Mg$_2$Pd$_4$] voids has increased considerably (after 1 h, frame $\geq$ 11), they are occupied by deuterium, however, at low rates ($\leq$ 1/4) during the whole experiment. The beginning of [Mg$_2$Pd$_4$] occupation seems to mark the end of a short two-phase region. This suggests a small miscibility gap for hydrogen in α-MgPd$_3$ near the composition α-MgPd$_3$H, i. e. distinct hydride phases with and without [Mg$_2$Pd$_4$] occupation. Further investigations will be necessary, however, to confirm this hypothesis.

In order to probe the pressure dependence of deuterium occupation, it was first decreased to 0.1 MPa (frames 18 to 21) and then the cell was evacuated ($\approx$ 10 Pa, frames 22 to 35). Lattice parameters and deuterium content decrease only slightly (Fig. 9.5.1). The change to lower pressures is accompanied by a considerable decrease in reflection width. The broad reflections at higher pressure (1 MPa deuterium) indicate a wider distribution of phases, most probably differing in deuterium content, which suggests that the sample is not at thermodynamic equilibrium. By reducing the pressure, fractions with higher deuterium content apparently quickly release some deuterium. This effect is reversible as proven by broadening of reflections, increasing lattice parameters and deuterium content upon raising the pressure again to 1 MPa (frames $\geq$ 36, Fig. 9.5.1). Strain by incorporated hydrogen may also contribute somewhat to reflection width, however, it cannot explain the marked differences between
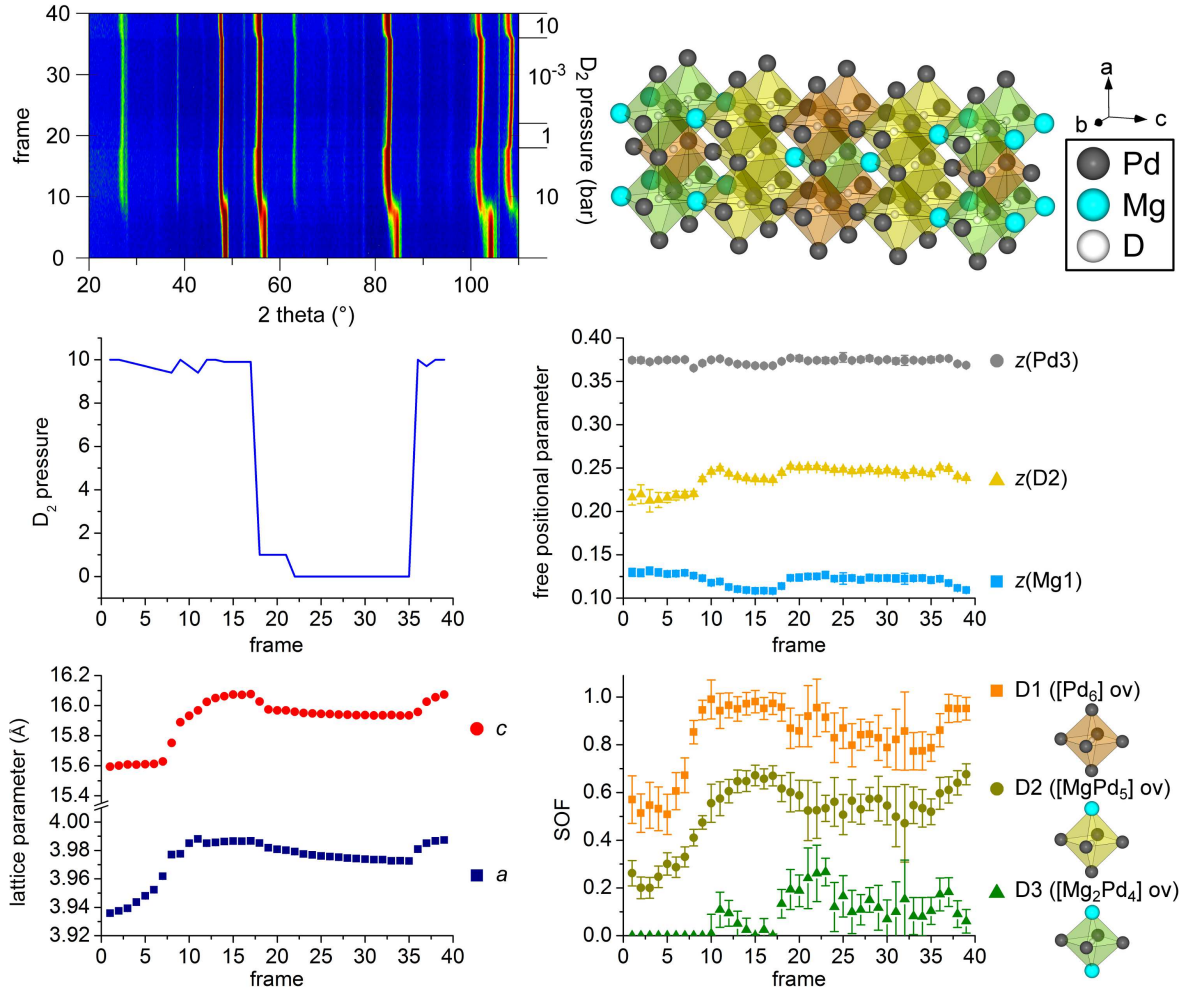
Figure 9.5.1.: *In situ* neutron powder diffraction data (top, left; intensities in false colors, each frame 6 min data collection time) of the deuteration of $MgPd_3$ (filled $ZrAl_3$ type; top right) taken on diffractometer D20 at $\lambda = 1.86786(3)$ Åin a sapphire single-crystal cell with NBR flat seal (see chapter 2.2) at $T = 297(1)$ K under various deuterium pressures (middle, left, frames 22–35: vacuum); lattice parameters (bottom, left), free positional parameters (middle right, see Table 9.5.1) and site occupation factors (SOF) of deuterium atoms (bottom right, SOF(D3) fixed to zero for frames 1 to 9) determined by sequential Rietveld refinement [31].

Table 9.5.1.: Crystal structure parameters of α-MgPd$_3$D$_{1.18(9)}$ at 1 MPa deuterium gas pressure and room temperature ($I4/mmm$, filled ZrAl$_3$ type, $a = 3.9873(4)$ Å, $c = 16.073(2)$ Å, frame 39).

atom	Wyckoff position	x	y	z	SOF	B_{iso} / Å^2
Mg1	$4e$	0	0	0.1093(9)	1	0.9(2)
Pd1	$4c$	0	1/2	0	1	0.86(9)
Pd2	$4d$	0	1/2	1/4	1	B_{iso}(Pd1)
Pd3	$4e$	0	0	0.3686(11)	1	B_{iso}(Pd1)
D1	$2b$	0	0	1/2	0.95(5)	3.1(2)
D2	$4e$	0	0	0.2386(13)	0.68(4)	B_{iso}(D1)
D3	$2a$	0	0	0	0.06(5)	B_{iso}(D1)

two states with very similar overall deuterium content. The maximum deuterium concentration is reached at the last frame of this experiment according to the formula α-MgPd$_3$D$_{1.18(9)}$ (Table 9.5.1) with full occupation of [Pd$_6$] voids (within three e.s.u.s). The free positional parameter z of Pd3 stays nearly constant through the whole *in situ* experiment. However, z(Mg1) decreases during the deuteration (vice-versa during applying vacuum) and z(D2) increases on the first deuteration and stays nearly constant afterwards. These changes in z parameters result in growing Mg1-D2-distances within the [MgPd$_5$] octahedral void (from 1.4(2) Å at frame 1 to 2.06(2) Å at frame 17). The stretching of Mg-D distances conforms to those observed before (1.901(8)-2.29(2) Å) [19] and is primarily due to the increasing deuterium uptake in [MgPd$_5$] octahedral voids.

The tetragonal α-MgPd$_3$H$_x$ phases described here are metastable intermediates of the hydrogenation reaction of ZrAl$_3$ type α-MgPd$_3$ to cubic β-MgPd$_3$H$_x$ with an anti-perovskite like structure [23]. Their characterization by *in situ* methods yields structural details needed for accurate modelling of total energies, which are indispensable for the evaluation of different reaction mechanisms such as hydrogen assisted gliding [30].

9.5.2. Hydrogenation of Zintl phases

The hydrogenation of Zintl phases leads to the formation of different types of hydrides, i. e. interstitial hydrides, where hydrogen is coordinated by the cationic partial structure or polyanionic hydrides, with hydrogen binding to the polyanion [31]. For the system SrGe-H$_2$(D$_2$) three phases are known. The hydrogen-rich γ-SrGeH$_{>1}$ shows features of both types with hydride anions tetrahedrally surrounded by four strontium atoms (interstitial type) and hydrogen covalently bound to germanium polyanions (polyanionic type) [10]. Two hydrogen poor hydrides, α- and β-SrGeH$_{>1}$, are of the interstitial type without Ge-H bonds, and cannot be quenched to ambient conditions [32]. Thus, *in situ* investigations are necessary for determination of their crystal structures, hydrogen content and hydrogen uptake and release. The reaction of SrGe at 4–5 MPa deuterium pressure and temperatures 300 K $\leq T \leq$ 620 K was followed by *in situ* neutron powder diffraction with 1 min data collection time per pattern. Fig. 9.5.2 shows a section of the 2θ range that represents the main changes during the reaction. There are four distinct phases formed during the heating and cooling cycle. The deuterium content of all phases was evaluated for all patterns by serial Rietveld refinement (FullProf [29]) using the crystal structure models described earlier [10,32].

Due to their metastable character, *in situ* diffraction was required to discover and characterize the interstitial hydrides α- and β-SrGeH$_x$. This study proves that α-, β-, and γ-hydrides of SrGe are three distinct phases, each with a more or less pronounced phase width with respect to hydrogen content.
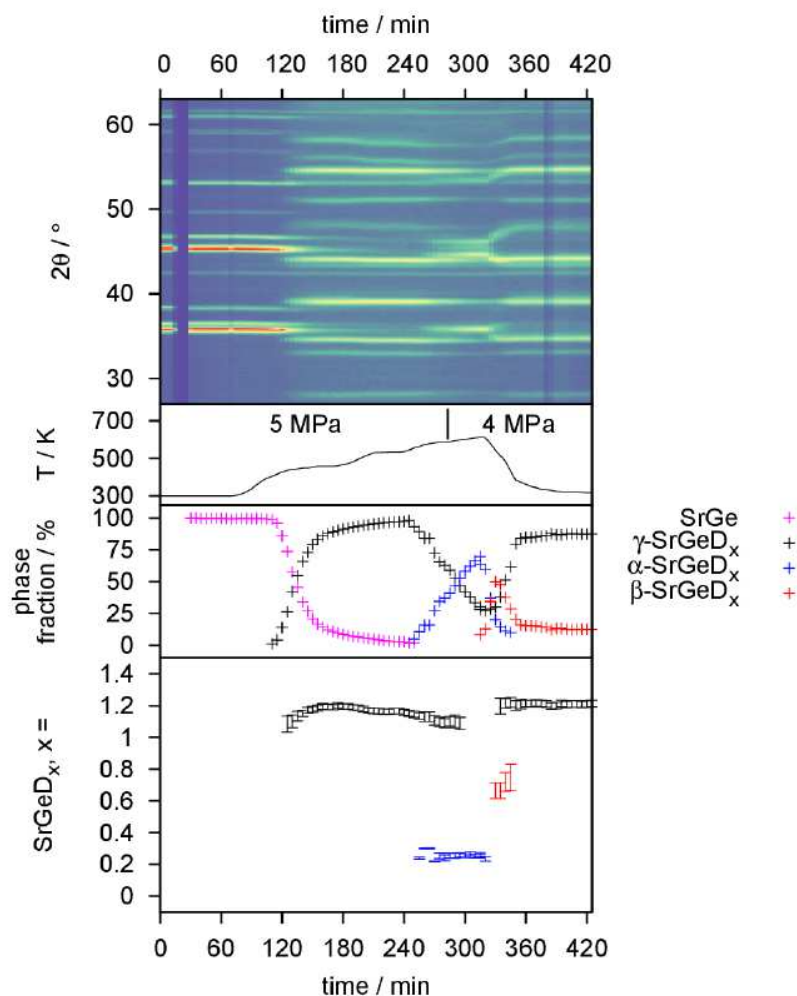
Figure 9.5.2.: *In situ* neutron powder diffraction (ILL, D20, $\lambda = 1.86832(7)$ Å) of the reaction of SrGe to γ-SrGeD$_x$ ($1.10(1) \leq x \leq 1.233(7)$) at 5.0 MPa deuterium pressure in a sapphire single-crystal cell with lead seal, the subsequent decomposition and reformation under 4.0 MPa deuterium pressure showing the additional phases α-SrGeD$_x$ ($0.23(1) \leq x \leq 0.30(2)$) and β-SrGeD$_x$ ($0.67(5) \leq x \leq 0.75(8)$).

Vacancies on hydrogen positions may be compensated for by π-bonding within the polyanionic chains [10,32]. This underlines the rich crystal chemistry of hydrides of Zintl phases with a variety of bonding situations, crystal structures and hydrogen contents. It further demonstrates the potential of *in situ* studies for these otherwise inaccessible reaction intermediates.

9.5.3. Further solid-gas reactions

The sapphire single-crystal cell described here has been used for *in situ* neutron powder diffraction studies on further systems. Zintl phases SrGa$_2$, KSi and CsSi show a single-step reaction to their hydrides SrGa$_2$H$_2$, KSiH$_3$ and CsSiH$_3$ without any noticeable phase width with respect to hydrogen content [33,34], in contrast to SrGe (see above). Various binary and ternary nitrides, imides and amides are formed by hydrogenation-dehydrogenation in the light-weight hydrogen storage material Li$_3$N-MgH$_2$[35]. Hydrogen-induced amorphization is observed for Dy$_5$Pd$_2$ [36] and SmCo$_5$ [37]. The latter is a crucial part of the widely used hydrogenation-disproportionation-desorption-recombination (HDDR) process for the production of strong permanent magnetic materials. For binary and ternary

intermetallic lithium aluminum compounds, the formation of lithium hydride is frequently observed, e. g. $LiAl + {}^x/_2 H_2 = Li_{1-x}Al + x LiH$ [38] and for the half-Heusler compound LiAlSi according to $LiAlSi + {}^1/_2 H_2 = LiH + Al + Si$ [39]. A wealth of structural data on α- and β-palladium hydride at various temperature-pressure conditions have been extracted from a single *in situ* neutron diffraction experiment [20].

9.6. Conclusion

The sapphire single-crystal cell has proven its usefulness and provides access to high-quality diffraction data and thus to accurate crystal structure information. Real-time *in situ* neutron powder diffraction of solid-gas reactions, where diffraction intensity is measured as a function of scattering angle, gas pressure, temperature and time, can efficiently be performed. The cell material has a negligible contribution to the diffraction background and the typically achievable time resolution in the order of a minute is well suited to many solid-gas reactions. The main difference to other cell designs is the use of a single crystal as sample holder, which for a proper orientation does not contribute to the diffraction pattern, because the detector does not pick up the single crystal reflections. It is thus powder diffraction in a single crystal! Its main limitation at present is the danger of mechanical failure at temperatures above 700 K. The weak point is the end of the sapphire tube where the steel caps with the seals are attached (Fig. 9.4.2). New cell designs are currently being explored in order to avoid these problems and to extend the capabilities to higher temperatures. The sapphire single-crystal cell has been applied to the study of reaction pathways of hydrogenation and dehydrogenation reactions. Their understanding has contributed to the characterization of otherwise inaccessible metastable compounds, processes of hydrogen uptake and release in hydrogen storage materials and unraveling reaction pathways in industrial processes such as HDDR. With often hundreds of data sets collected in a single *in situ* diffraction experiment, a wealth of structural information is gathered. This is particularly useful as it often characterizes functional materials at non-ambient, close to their operational conditions.

9.7. Acknowledgement

9.8. References for chapter 9

[1]   H. Schäfer, Zur Situation der präparativen Feststoffchemie, Angew. Chem. 83 (1971) 35-42.

[2]   J. Szekley, J. W. Evans, H.Y. Shon, Gas-solid Reactions, Academic Press, New York (1976).

[3]   H. Schmalzried, Solid state reactions, Solid State Phenom., 56 (1997) 13-26.

[4]   N. Pienack, W. Bensch, *In-situ*-Verfolgung der Bildung kristalliner Feststoffe, Angew. Chem., 123 (2011) 2062-2083; *In-situ* monitoring of the formation of crystalline solids, Angew. Chem. Int. Ed. 50 (2011) 2014-2034.

[5]   J. Pannetier, Time-resolved neutron powder diffraction, Chem. Scr 26A (1986) 131-139.

[6] O. Isnard, A review of *in situ* and/or time resolved neutron scattering, C. R. Phys. 8 (2007) 789-805.

[7] M. Widenmeyer, R. Niewa, T. C. Hansen, H. Kohlmann, *In situ* neutron diffraction as a probe on formation and decomposition of nitrides and hydrides: a case study, Z. Anorg. Allg. Chem. 639 (2013) 285–295.

[8] T. C. Hansen, H. Kohlmann, Chemical reactions followed by *in situ* neutron powder diffraction, Z. Anorg. Allg. Chem. 640 (2014) 3044–3063.

[9] C. Wannek, B. Harbrecht, Structure and thermal stability of the new intermetallics $MgPd_2$, $MgPd_3$, and Mg_3Pd_5 and the kinetics of the iodine-catalyzed formation of $MgPd_2$, J. Solid State Chem. 159 (2001) 113-120.

[10] H. Auer, R. Guehne, M. Bertmer, S. Weber, P. Wenderoth, T. C. Hansen, J. Haase, H. Kohlmann, Hydrides of alkaline earth-tetrel (AeTt) Zintl phases: covalent Tt-H bonds from silicon to tin, Inorg. Chem. 56 (2017) 1061-1071.

[11] I. F. Bailey, R. Done, J. W. Dreyer, E. M. Gray, A high-temperature high-pressure gas-handling cell for neutron scattering experiments, Int. J. High. Press. Res. 24 (2004) 309-315.

[12] W. F. Kuhs, E. Hensel, H. Bartels, Gas pressure cells for elastic and inelastic neutron scattering, J. Phys. Condens. Matter 17 (2005) S3009-S3015.

[13] G. N. Stepanov, A. S. Telepnev, V. G. Simkin, High-pressure gas chamber for neutron diffraction studies, Crystallogr. Rep. 52 (2007) 582-584.

[14] V. A. Yartys, R. V. Denys, J. P. Maehlen, C. J. Webb, E. Mac, A. Gray, T. Blach, A. A. Poletaev, J. K. Solberg, O. Isnard, Nanostructured metal hydrides for hydrogen storage studied by *in situ* synchrotron and neutron diffraction, Mater. Res. Soc. Symp. Proc. 1262 (2010) W04–01.

[15] S. Klotz, Techniques in High Pressure Neutron Scattering, CRC Press - Taylor and Francis (2013).

[16] K. Knorr, B. Annighöfer, W. Depmeier, A strengthened zero-scattering-alloy pressure cylinder for neutron powder diffraction, J. Appl. Crystallogr. 32 (1999) 373-374.

[17] R. Flacau, J. Bolduc, T. Bibienne, J. Huot, H. Fritzsche, Performance of Cu-coated vanadium cans for *in situ* neutron powder diffraction experiments on hydrogen storage materials, J. Appl. Crystallogr. 45 (2012) 902-905.

[18] A. J. Rondinone, C. Y. Jones, S. L. Marshall, B. C. Chakoumakos, C. J. Rawn, E. Lara-Curizo, A sapphire cell for high-pressure, low-temperature neutron-scattering experiments on gas hydrates, Can. J. Phys. 81 (2003) 381-385.

[19] H. Kohlmann, N. Kurtzemann, R. Weihrich, T. Hansen, *In situ* neutron powder diffraction on intermediate hydrides of $MgPd_3$ in a novel sapphire gas pressure cell, Z. Anorg. Allg. Chem. 635 (2009) 2399–2405.

[20] H. Kohlmann, N. Kurtzemann, T. C. Hansen, Metal hydride formation in palladium and palladium-rich intermetallic compounds studied by *in situ* neutron diffraction, Powder Diffr. 28 (2013) S242-S255.

[21] `www.ckd-dichtungstechnik.de/download/o-ringe.pdf`, August 9, 2017.

[22] `www.idt-dichtungen.de/download.php?f=02efc3d188f70b5b65212cfeff2cc0d7&fname=` `IDT_Katalog_2016_deutsch.pdf`, August 9, 2017.

[23] H. Kohlmann, G. Renaudin, K. Yvon, C. Wannek, B. Harbrecht, Hydrogen-induced atomic rearrangement in $MgPd_3$, J. Solid State Chem. 178 (2005) 1292–1300.

[24] H. Kohlmann, C. Ritter, Reaction pathways in the formation of intermetallic $InPd_3$ polymorphs, Z. Anorg. Allg. Chem. 635 (2009) 1573–1579.

[25] H. Kohlmann, A. V. Skripov, A. V. Solonimin, T. J. Udovic, The anti-perovskite type hydride $InPd_3H_{0.89}$, J. Solid State Chem. 183 (2010) 2461–2465.

[26] N. Kurtzemann, H. Kohlmann, Crystal structure and formation of $TlPd_3$ and its new hydride $TlPd_3H$, Z. Anorg. Allg. Chem. 636 (2010) 1032–1037.

[27] A. Götze, J. M. Sander, H. Kohlmann, Crystal structures and hydrogenation properties of palladium-rich compounds with elements from groups 12-16, Z. Naturforsch. 71B (2016) 503–508.

[28] A. Götze, T. C. Hansen, H. Kohlmann, The reversible hydrogenation of $BiPd_3$ followed by *in situ* methods and the crystal structure of $PbPd_3D_{0.13(1)}$, J. Alloys Compd. 731 (2018) 1001-1008.

[29] J. Rodríguez-Carvajal, FullProf: a Program for Rietveld Refinement and Pattern Matching Analysis, Insitut Laue-Langevin, Grenoble (France), 2012.

[30] N. Kunkel, J. Sander, N. Louis, Y. Pang, L. M. Dejon, F. Wagener, Y. N. Zang, A. Sayede, M. Bauer, M. Springborg, H. Kohlmann, Theoretical investigation of the hydrogenation induced atomic rearrangements in palladium-rich intermetallic compounds MPd_3 (M = Mg, In, Tl), Eur. Phys. J. B 82 (2011) 1-6.

[31] U. Häussermann, V. F. Kranak, K. Puhakainen, Hydrogenous Zintl phases: Interstitial versus polyanionic hydrides, Struct. Bond. 139 (2011) 143-161.

[32] H. Auer, D. Wallacher, T. C. Hansen, H. Kohlmann, *In situ* hydrogenation of the Zintl phase SrGe, Inorg. Chem. 56 (2017) 1072-1079.

[33] P. Wenderoth, H. Kohlmann, *In situ* neutron powder diffraction of the formation of $SrGa_2D_2$, and hydrogenation behavior of $YbGa_2$ and $EuGa_2$, Inorg. Chem. 52 (2013) 10525-10531.

[34] H. Auer, H. Kohlmann, *In situ* investigations on the formation and decomposition of $KSiH_3$ and $CsSiH_3$, Z. Anorg Allg. Chem. 643 (2017) 945-951.

[35] G. Behrendt, C. Reichert, H. Kohlmann, Hydrogenation reaction pathways in the systems Li_3N-H_2, Li_3N-Mg-H_2, and Li_3N-MgH_2-H_2 by *in situ* X-ray diffraction, *in situ* neutron diffraction, and *in situ* thermal analysis, J. Phys. Chem. C 120 (2016) 13450-13455.

[36] H. Kohlmann, E. Talik, T. C. Hansen, The hydrogenation of Dy_5Pd_2 followed by *in situ* methods, J. Solid State Chem. 187 (2012) 244-248.

[37] K. L. A. Belener, H. Kohlmann, Reaction pathways of oxide-reduction-diffusion (ORD) synthesis of $SmCo_5$ and *in situ* study of its hydrogen induced amorphization (HIA), J. Magn. Magn. Mater, 370 (2014) 134-139.

[38] C. Reichert, PhD thesis, Universität des Saarlandes, Germany (2013).

[39] N. Kunkel, C. Reichert, M. Springborg, D. Wallacher, H. Kohlmann, Hydrogenation properties of $Li_xSr_{1-x}AlSi$ studied by quantum-chemical methods ($0 \leq x \leq 1$) and in-situ neutron powder diffraction (x = 1), J. Solid State Chem. 221 (2015) 318-324.

10. The Reversible Hydrogenation of BiPd$_3$ Followed by *in Situ* Methods and the Crystal Structure of PbPd$_3$D$_{0.13(1)}$

André Götze, Thomas C. Hansen, Holger Kohlmann

10.1. Authors' contributions

The syntheses, characterizations, refinements were done and the manuscript written by A. Götze. The manuscript was revised by H. Kohlmann. A. Götze and H. Kohlmann conducted the experiment at neutron source with assitance by T. C. Hansen. M. Wagner did some preliminary investigations to this work (acknowledged).

10.2. Abstract

The hydrogenation properties of binary palladium-rich intermetallic compounds MPd$_3$ (M = Pb, Bi) were studied by X-ray powder diffraction and by *in situ* thermal analysis (DSC) under hydrogen pressure. *Ex situ* neutron powder diffraction reveals deuterium filled [Pd$_6$] octahedral voids in a cubic anti-perovskite type structure for PbPd$_3$D$_{0.13(1)}$ ($Pm\bar{3}m$, a = 404.033(6) pm, deuterium occupation = 0.13(1)) and in a ZrAl$_3$ type for BiPd$_3$D$_{0.19(1)}$ and BiPd$_3$D$_{0.23(1)}$ ($I4/mmm$, a = 404.72(1) pm, c = 1662.64(6) pm, z(Bi) = 0.1320(1), z(Pd3) = 0.3797(2), deuterium occupation = 0.46(1)). *In situ* neutron diffraction (using deuterium) reveals full reversibility of the hydrogenation and dehydrogenation reaction for BiPd$_3$ without intermediate phases and variable hydrogen content in the hydride. The relation of the crystal structures of BiPd$_3$ (akin to double-hexagonal close packing) and its hydride with filled ZrAl$_3$ type (ordered superstructure of cubic close packing) is discussed in view of a possible reaction mechanism.

10.3. Introduction

Metal hydrides can be roughly divided according to their bonding situation ranging from ionic to covalent and metallic. Palladium hydrides cover a realm from covalent semiconducting complex hydrides [1–4] to typical interstitial hydrides like palladium hydride itself. 1866 Graham observed that palladium can take up considerable amounts of hydrogen [5,6]. Since then, palladium hydride has been studied extensively concerning the Pd-H phase diagram, physical properties, crystal and electronic structures [7–12]. Several palladium-rich intermetallic compounds, in which metal atoms M substitute for palladium, e. g. MPd$_3$ (M = Mg [13,14], In [15], Tl [16], Y [17], Mn [18], Ce [19]), form hydrides as well. The hydrogenation of these intermetallics results in general in a rearrangement from one superstructure of the cubic close packing (ccp) to another ccp superstructure, e. g. from ZrAl$_3$ type or TiAl$_3$ type to AuCu$_3$ type [20]. The formation of HPd$_6$ octahedra with considerable Pd-H bond energy was shown to be the driving force behind these reactions [13,14]. In the series TiAl$_3$ type − ZrAl$_3$ type − Tl$_2$PbPd$_9$ type − AuCu$_3$ type the number of available [Pd$_6$] octahedral sites for occupation by hydrogen increases, thus, favouring the latter structures for hydride formation. The hydrogen amount in MPd$_3$H$_x$ seems to be correlated to electronic and geometric aspects of the metal atom M. The maximum hydrogen content is found for atomic radii around 165–170 pm and an electronegativity (Allred and Rochow [21]) of 1.4 [22]. SnPd$_3$ [23], PbPd$_3$ [23] and BiPd$_3$ [24,25] are good candidates to check the limits of hydride formation in ternary palladium-rich compounds, and thus the potential of predictions of hydrogen content based on electronic and geometric aspects because the substitutional metal atoms M have a high electronegativity and relatively large atomic radii. SnPd$_3$ and PbPd$_3$ crystallize in the AuCu$_3$ type (space group type $Pm\bar{3}m$), a ccp superstructure, by contrast to BiPd$_3$ that crystallizes in a superstructure of the double-hexagonal close packing (dhcp, BiPd$_3$ type, space

	group 2	group 13	group 14	group 15
3	**MgPd$_3$H$_x$** (filled ZrAl$_3$ and AuCu$_3$ type)	Al	Si	**Pd$_3$P$_{0.8}$H$_x$** **Pd$_6$PH$_x$** **Pd$_{15}$P$_2$H$_x$**
4	**CaPd$_3$H$_x$** (filled TiNi$_3$ type)	Ga	Ge	As
5	**SrPd$_2$H$_x$** (filled MgCu$_2$ type)	**InPd$_3$H$_x$** (filled AuCu$_3$ type)	**SnPd$_3$H$_x$** (filled AuCu$_3$ type)	Sb
6	Ba	**TlPd$_3$H$_x$** (filled ZrAl$_3$ and AuCu$_3$ type)	**PbPd$_3$H$_x$**[(*)] (filled AuCu$_3$ type)	**BiPd$_3$H$_x$**[(*)] (filled ZrAl$_3$ type)

Figure 10.3.1.: Hydrides of palladium-rich compounds MPd$_{\geq 2}$ with M being a main group element (MgPd$_3$H$_x$ [13,14], CaPd$_3$H$_x$ [28], SrPd$_2$H$_x$ [29], InPd$_3$H$_x$ [15], TlPd$_3$H$_x$ [16], SnPd$_3$H$_x$ [25], Pd$_3$P$_{0.8}$H$_x$ [30], Pd$_6$PH$_x$ [31], Pd$_{15}$P$_2$H$_x$ [32]). The hydrides marked with asterisks are characterized in this work.

group type *Pmma*) [22]. Furthermore, the possible extension of palladium-rich hydrides to group 15 elements (Fig. 10.3.1) gives motivation to investigate hydrogenation properties of $BiPd_3$, which is the most palladium-rich compound in the Bi-Pd system. In comparison to MPd_3 (M = Mg, In, Tl, Mn), $BiPd_3$ has a different structural relation of the starting compound to the final hydride found in the course of this study. Therefore, it was of interest to look for possible intermediates, which might give insight into mechanisms of metal hydride formation. This was done by *in situ* thermal analysis data, which often gives hints to possible intermediates and conditions of the hydrogenation process [26], and *in situ* neutron powder diffraction, by which reaction pathways may be explored in real time studies including full structural information [27].

10.4. Note on nomenclature

Hydrogen consists of the natural isotopic mixture of 99.985 % ^{1}H (protium) + 0.015 % ^{2}H (deuterium, D). If not indicated otherwise, the term metal hydride is used as a collective name including all isotopes, i. e., protides, deuterides, and tritides. They are only differentiated explicitly in the following text in cases where isotope effects are important, e. g. neutron diffraction experiments, and in the naming of crystal structure types first determined on deuterides.

Structural relationships and thus crystal structure types are of particular importance for the understanding of hydrogenation reactions of palladium-rich compounds. Many are of one-to-three composition, like the $ZrAl_3$ or $AuCu_3$ types. While those two, as most structure types and names of compounds, are in line with IUPAC's rules for nomenclature based on the position in the periodic table of the elements, some of the compounds of interest would have to be named using a three-to-one formula like Pd_3Pb and Pd_3Bi. For the sake of clarity and ease of recognition of structural relationships, however, in those cases IUPAC's rules are not followed, i. e. they are called $PbPd_3$ and $BiPd_3$.

Many palladium-rich intermetallic compounds and their hydrides derive structurally from close-packed structures, in which the hexagonal layers of close-packed atoms are usually named A, B and C. The sequence AB ... stands for the hexagonal (hcp), ABC ... stands for the cubic close packing (ccp). Literature on ccp related ordered superstructures like $TiAl_3$ type or $ZrAl_3$ type, however, sometimes uses A and B in a different way to denote the stacking sequence of MM'_3 double layers instead of hexagonal atomic layers. In order to avoid confusion, those MM'_3 double layers are named A' and B' in this text.

10.5. Experimental details

10.5.1. Synthesis of intermetallic compounds

The binary compounds MPd_3 (M = Pb, Bi) were synthesized from the elements with small amounts of iodine as mineralizing agent. Stoichiometric amounts of elements palladium powder (99.9 %, ≤ 60 μm, chemPUR and 99.95 %, ≤ 150 μm, Goodfellow), lead powder (99.95 %, -100 mesh, Alfa Aesar) and freshly ground bismuth shots (metal basis > 99 % checked with EDX) were placed in annealed silica glass ampoules under argon atmosphere. $PbPd_3$ was annealed at 1148 K for 4 h (200 K h^{-1} heating rate) and afterwards at 703 K for 35 h and $BiPd_3$ at 773 K for 7 d (30 K h^{-1} heating rate). All samples were quenched in water after annealing. The products were ground in air and iodine was dissolved in half-saturated aqueous potassium iodide solution.

Table 10.5.1.: *Ex situ* hydrogenation/deuteration conditions and diffractometer for XRPD and NPD data collection of MPd$_3$D$_\text{x}$ (M = Pb, Bi).

Compound	Conditions	Diffractometer
PbPd$_3$D$_{0.13(1)}$	5.0(2) MPa D$_2$/723(2) K/25 h	D20, ILL Grenoble
BiPd$_3$D$_{0.19(1)}$	7.0(2) MPa D$_2$/773(2) K/100 h	E9, HZB, Berlin
BiPd$_3$D$_{0.23(1)}$	12.0(2) MPa D$_2$/593(2) K/2 h	D20, ILL, Grenoble
BiPd$_3$H$_\text{x}$	20.0(2) MPa H$_2$/773(2) K/48 h	Huber G670

All binary intermetallic compounds and the powdered bismuth shots were checked by chemical analysis performed by an EDX INCA SYSTEM from Oxford Instruments mounted on a Zeiss LEO 1530 scanning electron microscope with an acceleration voltage of 20 kV and a working distance of 15 mm.

10.5.2. Hydrogenation

The powdered intermetallic samples were placed in hydrogen resistant Inconel (Böhler L718, nickel chromium alloy) crucibles in an autoclave made from the same alloy, charged with hydrogen ($\geq$ 99.9 %, Air Liquide) or deuterium (99.8 %, Air Liquide) and heated in a vertical tube furnace (Table 10.5.1). BiPd$_3$ samples for *in situ* investigations were placed in single crystal sapphire cell with a lead seal and charged with deuterium pressure or set under vacuum. These samples were heated with a contactless laser heating system.

10.5.3. X-ray powder diffraction (XRPD) and neutron powder diffraction (NPD)

Laboratory XRPD data were collected using a Huber G670 diffractometer with Guinier geometry at T = 297(2) K with either CuK$_{\alpha 1}$ or MoK$_{\alpha 1}$ radiation. Neutron powder diffraction measurements (NPD) were carried out at the Institut Laue-Langevin in Grenoble, France at the high-flux powder diffractometer D20 in high-resolution mode in the range $3° \leq 2\theta \leq 150°$ and a total data collection time of 25 min (https://doi.org/10.5291/ILL-DATA.5-21-1096, https://doi.org/10.5291/ILL-DATA.5-22-734) and at Helmholtz-Zentrum Berlin, Germany at the E9 diffractometer with a total data collection time of 8 h. Samples were enclosed in thin-walled vanadium cylinders (6 mm outer diameter). Although the intensities are represented in arbitrary units (normalized data), care has been taken to treat errors correctly. *In situ* neutron powder diffraction were also taken at diffractometer D20 under 5.2(1) MPa deuterium pressure (isotopic purity, 99.8 %) with a time resolution of 2 min per pattern. The sample was placed inside a single crystal sapphire based gas pressure cell especially designed for *in situ* neutron powder diffraction and heated by a contactless laser heating system [27]. A gas pressure controller regulated deuterium gas pressure or vacuum. The wavelengths were determined from measurements of silicon standard (NIST640b). Crystal structures were refined using the program FullProf [33]. Further details of the crystal structure investigations may be obtained from FIZ Karlsruhe, 76344 Eggenstein-Leopoldshafen, Germany (fax: (+49)7247-808-666; e-mail: crysdata@fiz-karlsruhe.de), on quoting the deposition numbers CSD-432976, -432977, and -432978.

10.5.4. *In situ* thermal analysis (DSC)

Differential scanning calorimetry (DSC) was performed *in situ* under a starting hydrogen pressure of 5.0 MPa and temperatures up to 703 K on a Q1000 DSC (TA Instruments) equipped with a gas

pressure chamber. About 20 mg of the powdered intermetallics were put in aluminium crucibles, which were closed with an aluminium lid. These were placed inside the pressure chamber, which was then purged several times with hydrogen gas before filling it to the desired hydrogen gas pressure. The samples were heated at a rate of 10 K min^{-1}, held at the final temperature for 2 h and cooled back to 300 K. Two runs were performed in order to check for reversibility of thermal effects before the hydrogen pressure was released, the sample taken out and structural characterization undertaken by XRPD.

10.6. Results and discussions

Samples MPd$_3$ (M = Pb, Bi) showed best crystallinity and phase purity, when using iodine as mineralizing agent. Based on chemical analysis of the powders, the empirical formulae Pb$_{0.97(11)}$Pd$_{3.03(11)}$ and Bi$_{0.97(5)}$Pd$_{3.03(5)}$ were determined, averaged from at least 15 energy dispersive X-ray (EDX) spectra on different particles of each sample. Samples were single phase according to X-ray powder diffraction (PbPd$_3$: $Pm\bar{3}m$, a = 403.451(9) pm; BiPd$_3$: $Pmma$, a = 939.04(4) pm, b = 574.14(4) pm, c = 496.63(8) pm, see supplement, Figs. 10.9.1 to 10.9.2), except larger samples of PbPd$_3$ used for deuterated samples for neutron diffraction. These contained 5 weight-% of the secondary phase Pd$_5$Pb$_3$. The hydrogenation of these compounds was studied by *in situ* differential scanning calorimetry (DSC) under 5.0 MPa hydrogen gas pressure. PbPd$_3$ did not show any thermal signal under these conditions. The first cycle of BiPd$_3$ showed a weak, broad exothermic signal at 580(1) K suggesting a possible reaction with hydrogen (Fig. 10.6.1). X-ray powder diffraction (XRPD) of BiPd$_3$ after the hydrogenation in the DSC experiment showed a pattern, which is different from that of the parent compound. It could be indexed to a tetragonal body-centered cell with a = 404.55(1) pm, c = 1661.98(5) pm suggesting a ZrAl$_3$-type structure. The structure model could be confirmed by Rietveld refinement, which yields a good agreement between observed and calculated powder diffraction intensities (Fig. 10.6.2). The unit cell volume of BidPd$_3$ increases during the rearrangement to the tetragonal structure by 1.6 % (5.0 MPa in DSC) and 2.1 % (20.0(2) MPa in an autoclave synthesis, see supplement, Fig. 10.9.3), respectively. No further thermal signals were recorded upon cooling and in
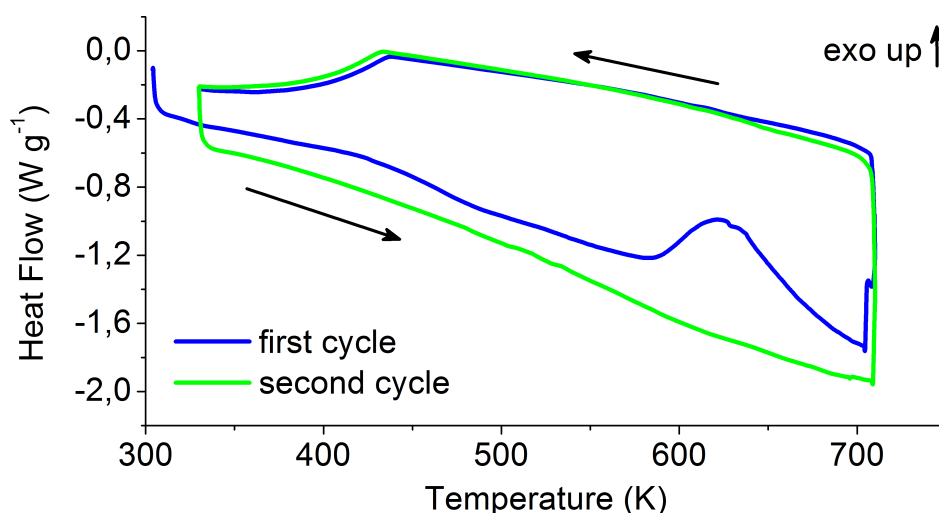

Figure 10.6.1.: *In situ* differential scanning calorimetry (DSC) of the hydrogenation of BiPd$_3$ at 5.0 MPa hydrogen pressure (starting pressure at 303 K, increasing to 7.0 MPa at the maximum temperature), showing an exothermic signal upon the first heating cycle (blue curve).
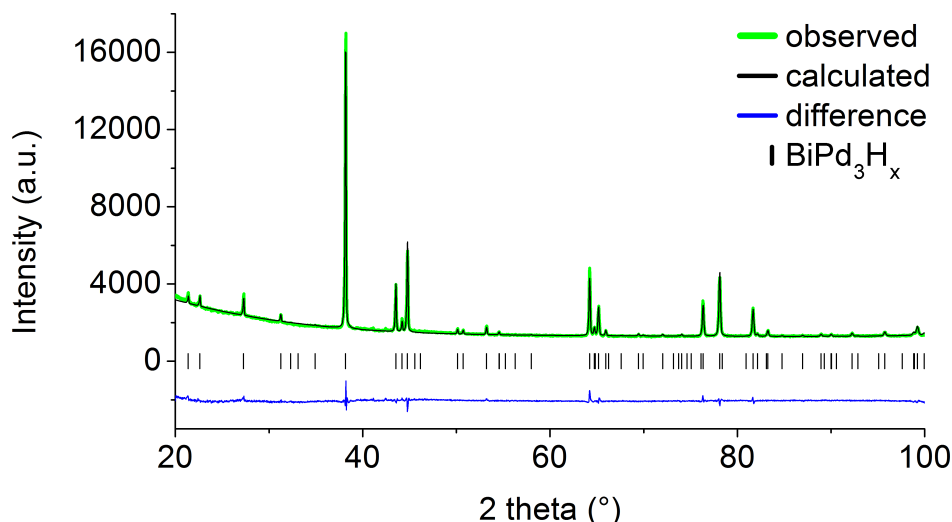
Figure 10.6.2.: Rietveld refinement of the crystal structure of tetragonal BiPd$_3$H$_x$ in the filled ZrAl$_3$ type after hydrogenation in a DSC experiment based on X-ray powder diffraction at 297(2) K (CuK$_{\alpha 1}$ radiation, λ = 154.059 pm, $I4/mmm$, a = 404.55(1) pm, c = 1661.98(5) pm, R_{wp} = 0.027, χ^2 = 1.25).

the second cycle; that is the hydrogenation reaction was not reversible under the applied conditions. In spite of the absence of observable thermal effects for PbPd$_3$, the cell volume increases by 0.6 %, as determined by X-ray powder diffraction. In contrast to BiPd$_3$, however, the structure type of the parent compound (AuCu$_3$ type in this case), is retained upon hydrogenation [34]. Thus, we expect the existence of a hydride PbPd$_3$ in a stuffed AuCu$_3$ type structure with presumably small hydrogen content.

The hydrogenation products of PbPd$_3$ and BiPd$_3$ crystallize in hydrogen filled variants of the AuCu$_3$ type and the ZrAl$_3$ type structure, respectively (Figs. 10.6.2 to 10.6.4 and 10.9.3 to 10.9.5). Both structure types may be regarded as ordered superstructures of a cubic close packing (ccp). They are members of a series formed by stacking palladium layers and mixed M/palladium layers (MM'_3 double layers, see Note on nomenclature) in an alternate fashion. The latter appears in two different kinds, named A' and B', and may be easily transformed into each other by exchanging M and Pd atoms in the mixed M/palladium layers. For the AuCu$_3$ type, only A'-type layers occur, whereas in the ZrAl$_3$ type, a sequence of $A'A'B'B'$ yields a fourfold ccp superstructure (Fig. 10.6.4) [13,35]. In many cases, hydrogenation leads to a rearrangement of a ZrAl$_3$ type to a AuCu$_3$ type in MPd$_3$ compounds, e. g. for M = Mg [19], In [35], Tl [16].

Ex situ neutron powder diffraction experiments on PbPd$_3$D$_{0.13(1)}$, BiPd$_3$D$_{0.19(1)}$ and BiPd$_3$D$_{0.23(1)}$ were carried out in order to locate hydrogen (deuterium) atoms. Deuterides instead of hydrides were used in order to avoid high background due to the large incoherent scattering of ^{1}H. They were prepared by deuteration in autoclaves at 5.0(2) MPa deuterium gas pressure and temperatures up to 723(1) K. For the deuteride of PbPd$_3$ deuterium was found to occupy exclusively octahedral voids surrounded by six palladium atoms, [Pd$_6$], as shown by difference Fourier synthesis. The good correspondence between measured and calculated diffraction data supports this structural model (Fig. 10.6.3 and Table 10.6.1). The complete crystal structure thus corresponds to the cubic anti-perovskite type like, for example, in InPd$_3$H$_x$[15]. The metal atoms of BiPd$_3$D$_x$ crystallize in the ZrAl$_3$ type like in α-MgPd$_3$D$_x$ (see Table 10.6.2) [19]. Two Fourier maxima for BiPd$_3$D$_{0.23(1)}$ correspond to the [Pd$_6$] octahedral site which is preferred also in PbPd$_3$D$_{0.13(1)}$ and to the [Bi$_2$Pd$_4$] octahedral site. Refinement of occupation parameters shows that only [Pd$_6$] octahedral sites are occupied, in agreement with
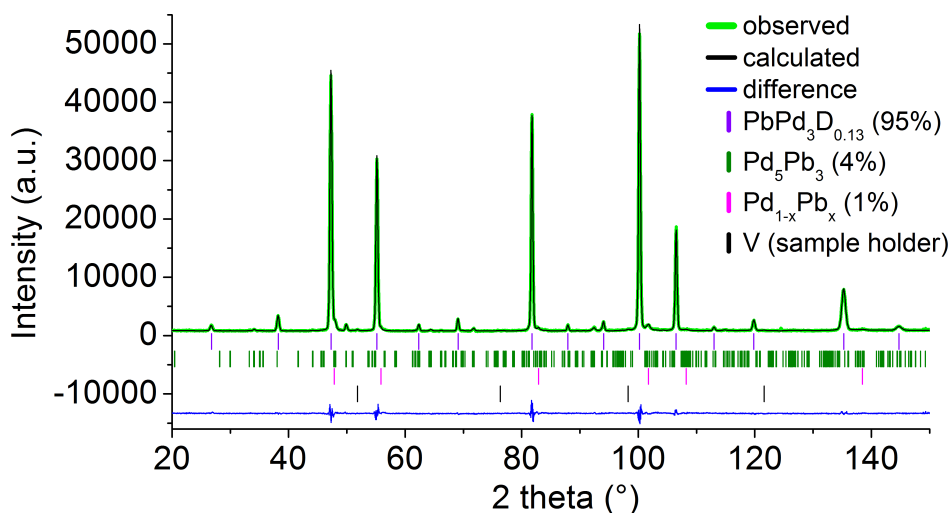
Figure 10.6.3.: Rietveld refinement of the crystal structure of cubic $PbPd_3H_{0.13(1)}$ at 298(2) K based on neutron powder diffraction ($\lambda = 186.78(5)$ pm, $Pm\bar{3}m$, $a = 404.033(6)$ pm, $R_{wp} = 0.047$, $\chi^2 = 1.25$); refinement results are summarized in Table 10.6.1.

crystal chemical arguments (Bi-D distance). For all three deuterides the octahedral $[Pd_6]$ voids are not fully occupied by deuterium and refined occupation factors lead to compositions of $PbPd_3D_{0.13(1)}$, $BiPd_3D_{0.19(1)}$ and $BiPd_3D_{0.23(1)}$. Full occupation of $[Pd_6]$ octahedral voids with hydrogen would lead to compositions of $PbPd_3H$ and $BiPd_3H_{0.5}$. The distribution of deuterium atoms is assumed to be statistical, since no sign for an ordering can be found.

The deuterium atoms in the cubic structure are surrounded by six equidistant palladium atoms, lead atoms by twelve palladium atoms forming a cuboctahedron. The palladium atoms have got
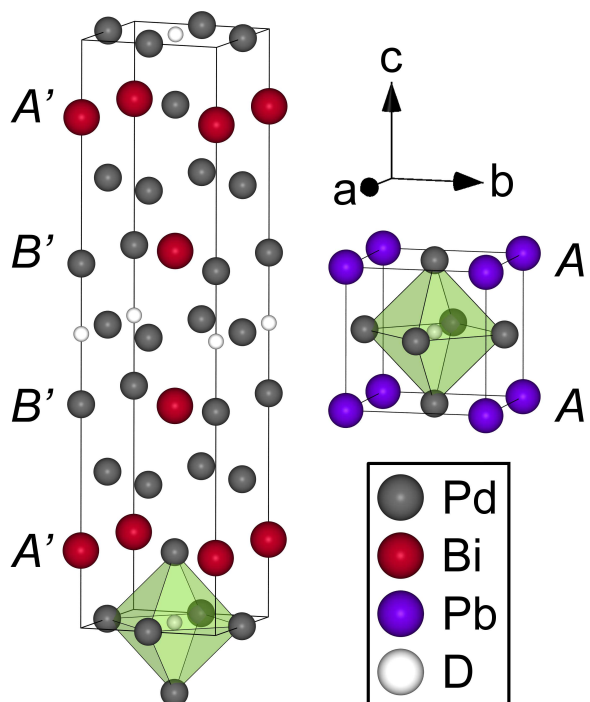
Figure 10.6.4.: Crystal structures of $BiPd_3D_{0.23(1)}$ (left) and $PbPd_3D_{0.13(1)}$ (right) with one $[DPd_6]$ octahedron for each structure shown (green).

Table 10.6.1.: Refined crystal structures of cubic PbPd$_3$D$_{0.13(1)}$ and residual values of the refinement based on neutron powder diffraction (D20, Institut Laue Langevin, Grenoble) at 298(2) K.

atom	Pb	Pd	D
Wyckoff site	$1a$	$3c$	$1b$
x	0	$^1/_2$	$^1/_2$
y	0	$^1/_2$	$^1/_2$
z	0	0	$^1/_2$
$B_{\mathrm{iso}}/10^{-4}$ pm^2	0.36(2)	0.46(2)	2.9(3)
occupation	1	1	0.13(1)

space group $Pm\bar{3}m$, $a = 404.033(6)$ pm.
$R_{\mathrm{p}} = 0.036$, $R_{\mathrm{wp}} = 0.047$, $R_{\mathrm{Bragg}} = 0.013$, $\chi^2 = 3.6$.

Table 10.6.2.: Refined crystal structures of tetragonal BiPd$_3$D$_{0.23(1)}$ at 298(2) K and 12.0(2) MPa deuterium pressure in a sapphire cell and residual values of the refinement based on neutron diffraction on D20 (Institut Laue Langevin, Grenoble).

atom	Bi	Pd1	Pd2	Pd3	D
Wyckoff site	$4e$	$4c$	$4d$	$4e$	$2b$
x	0	0	0	0	0
y	0	$^1/_2$	$^1/_2$	0	0
z	0.1320(1)	0	$^1/_4$	0.3797(2)	$^1/_2$
$B_{\mathrm{iso}}/10^{-4}$ pm^2	1.05(4)	1.00(7)	1.24(7)	1.06(5)	2.8(3)
occupation	1	1	1	1	0.46(1)

space group $I4/mmm$, $a = 404.72(1)$ pm, $c = 1662.64(6)$ pm.
$R_{\mathrm{p}} = 0.0656$, $R_{\mathrm{wp}} = 0.0887$, $R_{\mathrm{Bragg}} = 0.077$, $\chi^2 = 4.5$.

[12 + 2] coordination to four lead atoms and eight palladium atoms and are also located in the center of cuboctahedra. The two opposite Pd$_4$ squares of this polyhedron are centered by one deuterium atom each. The polyhedra of BiPd$_3$D$_x$ are comparable to those in the deuteride of PbPd$_3$, but the lower symmetry manifests itself in a small compression of the DPd$_6$ octahedra and cuboctahedra of the Bi and Pd atoms along crystallographic c. Again, the D atoms centering the square faces of the cuboctahedra around Pd1 and Pd3 complement the palladium surrounding to [12 + 2] and [12 + 1], respectively.

The interatomic D-Pd distances of the three deuterides (see Table 10.6.3) are comparable to those in α-MgPd$_3$D$_{0.79}$ (from 197(2) to 199.9(1) pm) [14], β-MgPd$_3$D$_{0.67}$ (199.10(1) pm) [13] or InPd$_3$D$_{0.89}$ (201.13 pm) [15]. In contrast to α-MgPd$_3$D$_x$, where [Pd$_6$], [MgPd$_5$] and [Mg$_2$Pd$_4$] voids are occupied by deuterium, BiPd$_3$D$_x$ incorporates deuterium only in the former; that is, it avoids those sites with Bi neighbors. D-Pd distances depend on the amount of deuterium in the structure i. e. BiPd$_3$D$_{0.19(1)}$ with less deuterium exhibits a decreased unit cell volume and therefore shorter D-Pd distances as compared to BiPd$_3$D$_{0.23(1)}$ (Table 10.6.3). The interatomic metal-metal distances are comparable to those of the hydrogen free intermetallics (d(Pb-Pd) = 285.3(1) pm [23], d(Bi-Pd) = 284.5–288.2 pm [25], d(Pd-Pd) = 281.1–289.9 pm) [22].

In contrast to PbPd$_3$, which retains its structural topology upon hydrogenation, in case of BiPd$_3$, a rearrangement from the BiPd$_3$ to the ZrAl$_3$ type occurs. In order to follow this reaction and check for possible intermediates, it was studied by *in situ* neutron powder diffraction. In order to get high

Table 10.6.3.: Interatomic distances (< 300 pm) in cubic $PbPd_3D_{0.13(1)}$, tetragonal $BiPd_3D_{0.19(1)}$ and tetragonal $BiPd_3D_{0.23(1)}$ in pm.

distance	D-Pd	M-Pd	Pd-Pd
$PbPd_3D_{0.13(1)}$	6 x 202.016(3)	12 x 285.694(3)	8 x 285.694(3)
$BiPd_3D_{0.19(1)}$	2 x 198.7(3)	4 x 282.1(2) (Pd2)	4 x 283.5(2) (Pd1-Pd3)
	4 x 202.26(1)	4 x 286.74(2) (Pd3)	4 x 286.04(1) (Pd1-Pd1), (Pd2-Pd2)
		4 x 298.0(2) (Pd1)	4 x 296.4(2) (Pd2-Pd3)
$BiPd_3D_{0.23(1)}$	2 x 200.0(3)	4 x 281.9(2) (Pd2)	4 x 284.5(2) (Pd1-Pd3)
	4 x 202.363(6)	4 x 286.84(2) (Pd3)	4 x 286.184(6) (Pd1-Pd1), (Pd2-Pd2)
		4 x 298.5(2) (Pd1)	4 x 295.7(2) (Pd2-Pd3)

quality data, a single-crystal sapphire cell was used. It consists of a sample holder made of leuco-sapphire attached to a gas delivery system and equipped with contactless laser heating. Its main advantage as compared to other *in situ* sample cells, is the low background due to the absence of Bragg peaks from the container material, when oriented appropriately [14,27,36].

An *in situ* deuteration experiment was performed on $BiPd_3$ at 5.2(1) MPa deuterium pressure with two minutes data collection time per pattern. Due to technical problems with laser heating the maximum temperature was restricted to 553(2) K and interruptions in heating occurred. The deuteration of $BiPd_3$ started after 2 h at 553(2) K, but did not complete even after 17 h (Fig. 10.6.5). No intermediates were formed during the reaction with deuterium. Rietveld refinements of the crystal structures of the starting material $BiPd_3$ and the product $BiPd_3D_x$ using the formerly derived structure models ([25], Table 10.6.2) were carried out based in the neutron powder diffraction patterns collected *in situ*. For this isothermal section of the experiment, sequential refinements yield a maximum phase content of 66 % and an increase of deuterium occupation in $BiPd_3D_x$ up to 0.15(2) (Figs. 10.6.6 and 10.9.6). This value is comparable to $BiPd_3D_{0.19(1)}$ (prepared at 7.0(2) MPa deuterium pressure, E9, BerII, Berlin) and $BiPd_3D_{0.23(1)}$ (prepared at 12.0(2) MPa deuterium pressure, see above) from *ex situ* measurements. Though, the lattice parameters and the unit cell volume stay nearly constant indicating an ideal size of the octahedral void for deuterium occupation. Both, the rearrangement of the metal atoms from the $BiPd_3$ to the $ZrAl_3$ type and the incorporation of hydrogen (deuterium) are rather slow (Figs. 10.6.5, 10.6.6 and 10.9.6). It is quite remarkable that the $ZrAl_3$ type deuteride formed at first (around 700 min, Fig. 10.6.6) contains very little deuterium (few percent occupation). This may indicate both $BiPd_3$ and $ZrAl_3$ type to be very similar in energy for $BiPd_3$. The phase fraction f of the deuteride as a function of time t may be described empirically by a square root function typical for solid gas reactions $f = 0.0278(2) * \sqrt{t/min - 563(15)} + 0.07(3)$, (graphical representation see supplement, Fig. 10.9.6).

The reversibility of the hydrogenation and the thermal stability of the hydride were checked in a second *in situ* experiment by decomposition of $BiPd_3D_{0.23(1)}$. This deuteride is stable in air and the application of vacuum at room temperature for 15 min results in the formation of $BiPd_3D_{0.20(1)}$. The back formation of $BiPd_3$ begins at about 400 K (Fig. 10.6.7) with slow decrease of the deuterium amount (Fig. 10.6.8). The volume increase of the unit cell during the decomposition is caused by the nearly linear rise of temperature. After 170 min at about 550 K, the heating rate decreases and the unit cell shrinks due to deuterium release. The phase fraction of the deuteride decreases down to 48 % (see supplement, Fig. 10.9.7) and the deuteration level converges to zero. The size of the octahedral site decreases during the decomposition in contrast to the nearly constant size during the deuteration (d(D-Pd) = 201–203(1) pm). The hydrogenation of $BiPd_3$ is fully reversible without the formation of any intermediates and with slow kinetics, as determined by both *in situ* experiments.
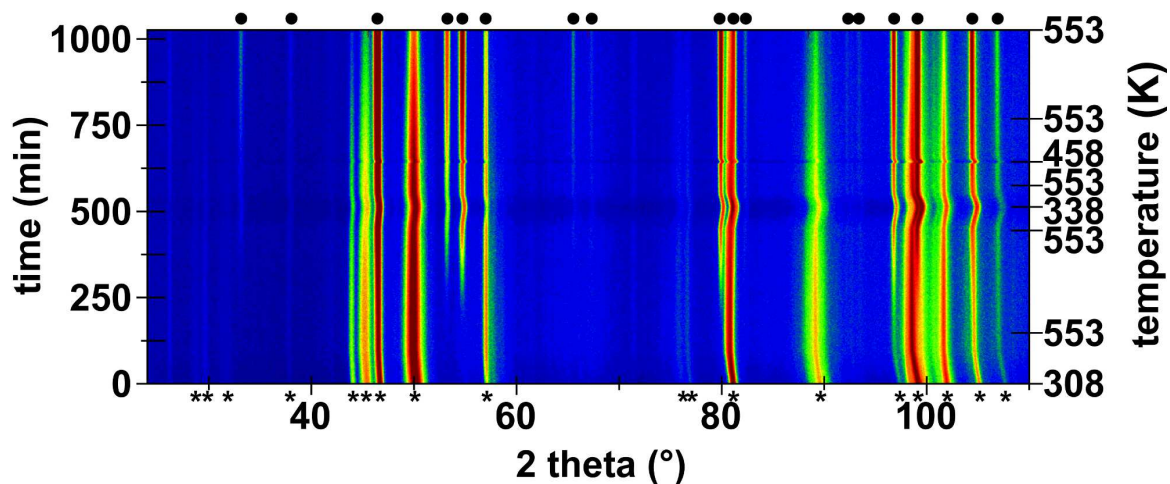
Figure 10.6.5.: *In situ* neutron powder diffraction data of the deuteration of BiPd$_3$ taken on diffractometer D20 at $\lambda = 186.78(5)$ pm in a single crystal sapphire cell under 5.2(1) MPa deuterium pressure and various temperature conditions. Intensities are in false colors. The temperature drops to 338(2) and 458(2) K are caused by the uncontrolled shutdown of the laser heating. The most intensive reflections of BiPd$_3$ are marked with asterisks and of BiPd$_3$D$_x$ with filled circles.
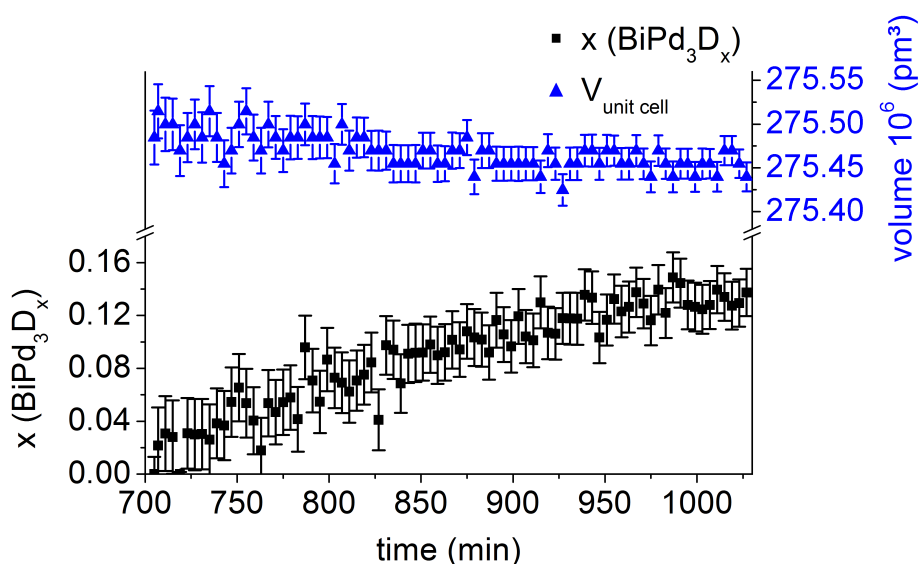

Figure 10.6.6.: Deuterium occupation and unit cell volume of BiPd$_3$D$_x$ as a function of time from Rietveld refinements based on neutron powder diffraction data at 553(3) K and deuterium pressure of 5.2(1) MPa. Error bars represent one estimated standard uncertainty and the number of data points is reduced for reasons of clarity. The amount of deuterium levels out at x = 0.15(2).
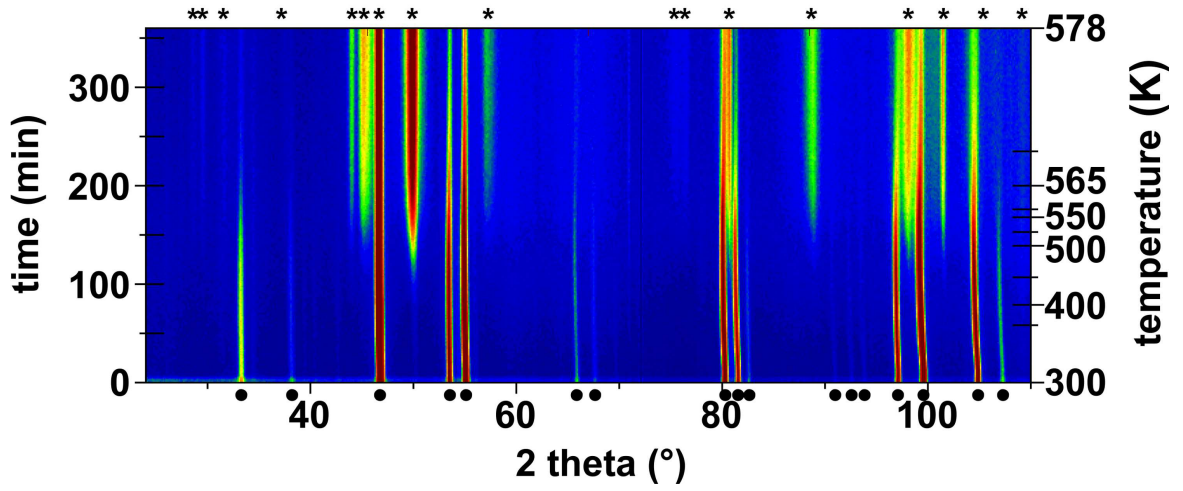
Figure 10.6.7.: Decomposition of $BiPd_3D_{0.20(1)}$ followed by *in situ* neutron powder diffraction data taken on diffractometer D20 at $\lambda = 186.62(2)$ pm in a single crystal sapphire cell under vacuum and various temperature conditions. Intensities are in false colors. The most intensive reflections of $BiPd_3D_x$ are marked with filled circles and those of $BiPd_3$ with asterisks.
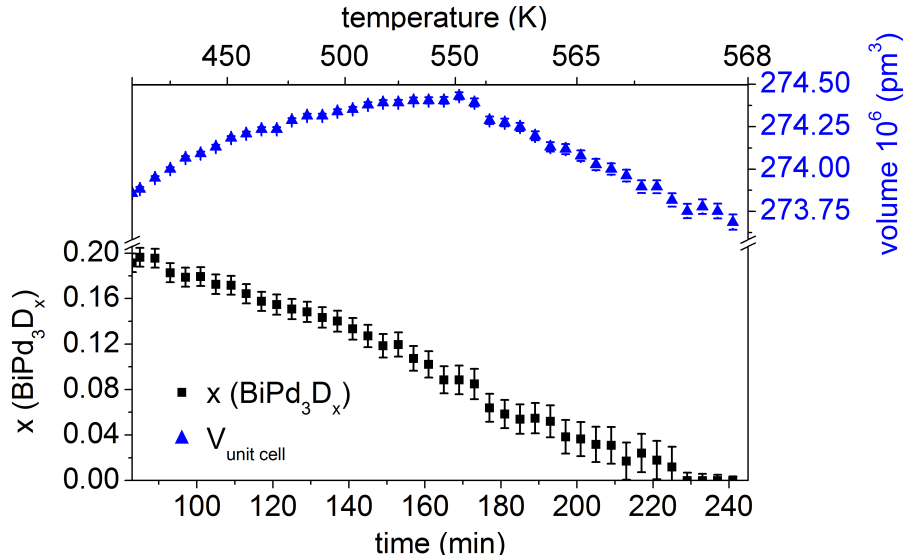
Figure 10.6.8.: Deuterium occupation (starting at x = 0.19(1)) and unit cell volume of $BiPd_3D_x$ as a function of time during decomposition from Rietveld refinements based on neutron powder diffraction under vacuum. Error bars represent one estimated standard uncertainty and the number of data points is reduced for reasons of clarity.

The hydride of BiPd$_3$ does not seem to have a closer structural relationship to BiPd$_3$. The crystal structure of BiPd$_3$ rather shows close ties to a double-hexagonal close packing (dhcp, La type) and to the TiNi$_3$ type. This can be proven by crystallographic group-subgroup relationships (Fig. 10.6.9) [37]. A *translationsgleiche* transition from the aristotype La and a *klassengleiche* transition with axes rotation result in space group *Pmma*. A further doubling of the new *b* axis finally yields the BiPd$_3$ type. The free positional atomic parameters of the BiPd$_3$ type [25] differ only little from the idealized values converted from the aristotype La. The second path on the right hand side results in the TiNi$_3$ type by an isomorphic transition with doubling of *a* and *b* axes. This may be described as a fourfold ordered superstructure of the dhcp (La type), which corresponds to metal atom positions in CaPd$_3$H$_x$ [28].

In contrast to BiPd$_3$, the filled ZrAl$_3$ type of BiPd$_3$H$_x$ is related to ccp (Cu type) [35]. A mechanism of this hydrogenation might either be a short-range diffusion of the metal atoms at these high temperatures or a gliding mechanism from dhcp (ABAC ...) of BiPd$_3$ to ccp (ABC ...) of the hydride (Fig. 10.6.10). The second mechanism is equivalent to a gliding of the hexagonal layers perpendicular to the [001] direction.

The driving force of this hydrogenation is probably the formation of [Pd$_6$] octahedral sites, regardless by which mechanism. BiPd$_3$ exhibits eight of each [BiPd$_5$] and [Bi$_2$Pd$_4$] octahedral voids per unit
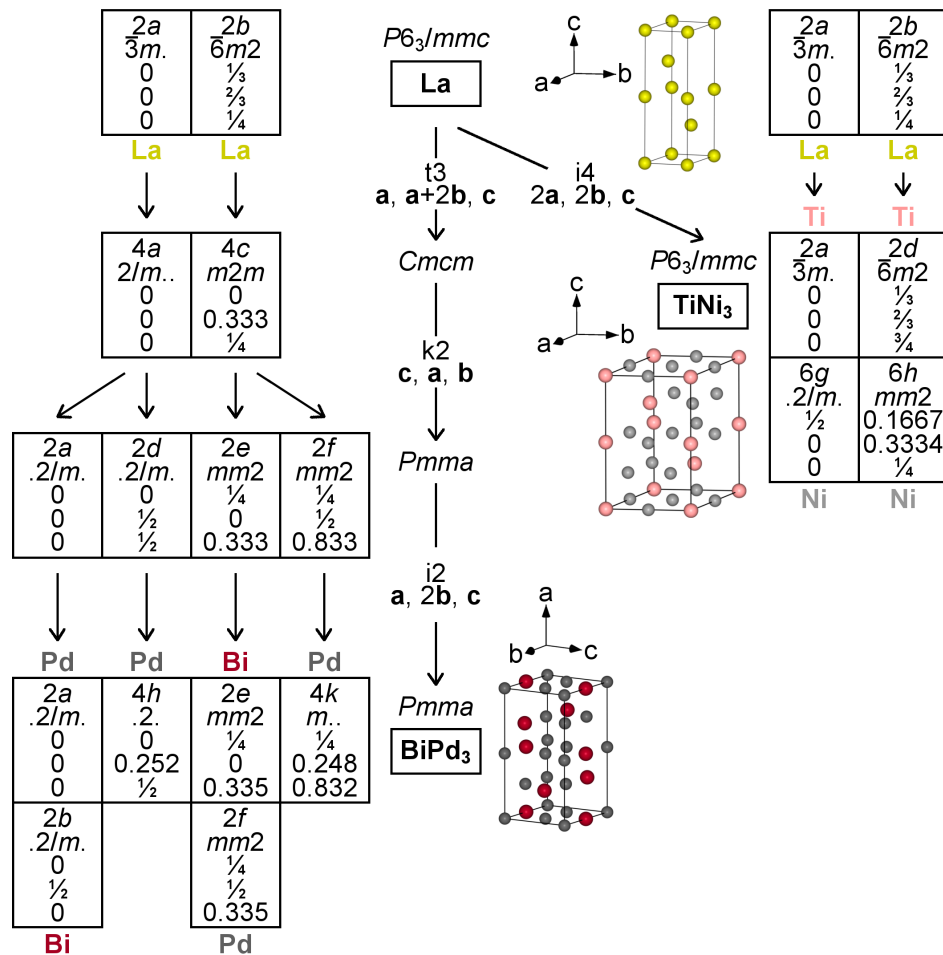
Figure 10.6.9.: Group-subgroup relationships of BiPd$_3$ and TiNi$_3$ to the aristotype La. Free positional parameters are values from the published structures. The picture shows the crystal structure of BiPd$_3$ with idealized values as transformed from the aristotype La (see text).
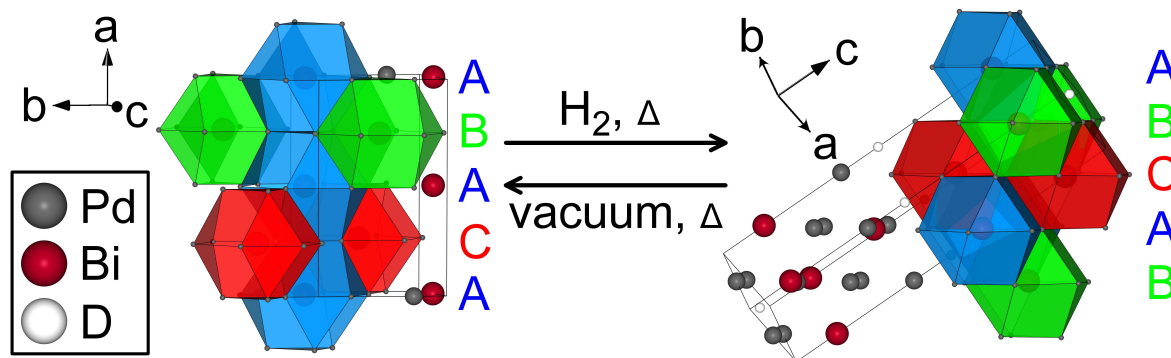
Figure 10.6.10.: Representation of the rearrangement of the crystal structure of orthorhombic $BiPd_3$ crystallizing in dhcp to tetragonal $BiPd_3D_x$ with a filled $ZrAl_3$ type structure (ccp superstructure).

cell volume (equals four formula units), but no $[Pd_6]$ voids. However, two $[Pd_6]$, further four $[BiPd_5]$ and ten $[Bi_2Pd_4]$ octahedral voids exist in $ZrAl_3$ type (per same reference of four formula units). The $AuCu_3$ type shows twice as many $[Pd_6]$ voids as compared to the $ZrAl_3$ type and no $[MPd_5]$ octahedral voids. Though, $BiPd_3$ does not form a filled $AuCu_3$ type during hydrogenation, neither at higher temperatures up to 823 K. Other MPd_3 compounds or their hydrides with such a $ZrAl_3$ type rearrange to the $AuCu_3$ type upon hydrogenation in order to maximize the fraction of $[Pd_6]$ voids (M = Mn [38], Mg [14], In [15], Tl [16]). It is an open question, whether such a reaction will occur at higher hydrogen potential, or whether there are other effects stabilizing the $ZrAl_3$ type in this case.

The formation of hydrides of $PbPd_3$ and $BiPd_3$ implies an extension of the hydrogenation of MPd_3 compounds to group 14 and 15 of the periodic table of the elements, which so far did not show any reactivity towards hydrogen [34,39]. Even though hydrogen contents are rather small, this may stimulate further work and especially draws the focus on phases structurally related to the dhcp like $TiPd_3$ or $ZrPd_3$.

10.7. Conclusion

Palladium-rich compounds MPd_3 (M = Pb, Bi) were found to take up hydrogen, thus extending this type of reaction to metals M of groups 14 and 15 of the periodic table. The crystal structures of the hydrides $PbPd_3H_{0.13(1)}$, $BiPd_3H_{0.19(1)}$ and $BiPd_3H_{0.23(1)}$ were determined by neutron powder diffraction on the deuterides. Deuterium occupies $[Pd_6]$ octahedral voids in any of these hydrides. $PbPd_3D_{0.13(1)}$ crystallizes in a cubic anti-perovskite type and the metal atoms do not change their structure ($AuCu_3$ type) during hydrogenation. In contrast, $BiPd_3$ changes from a structure related to a double-hexagonal close packing to a superstructure of the cubic close packing (hydrogen filled $ZrAl_3$ type). A short range diffusion of the metal atoms or a gliding of the hexagonal layers of $BiPd_3$ are possible mechanisms for the hydrogenation reactions. No intermediates are formed during this reversible hydrogenation followed by *in situ* DSC and *in situ* neutron powder diffraction and the hydrogenation follows a parabolic rate law, typical for solid gas reactions.

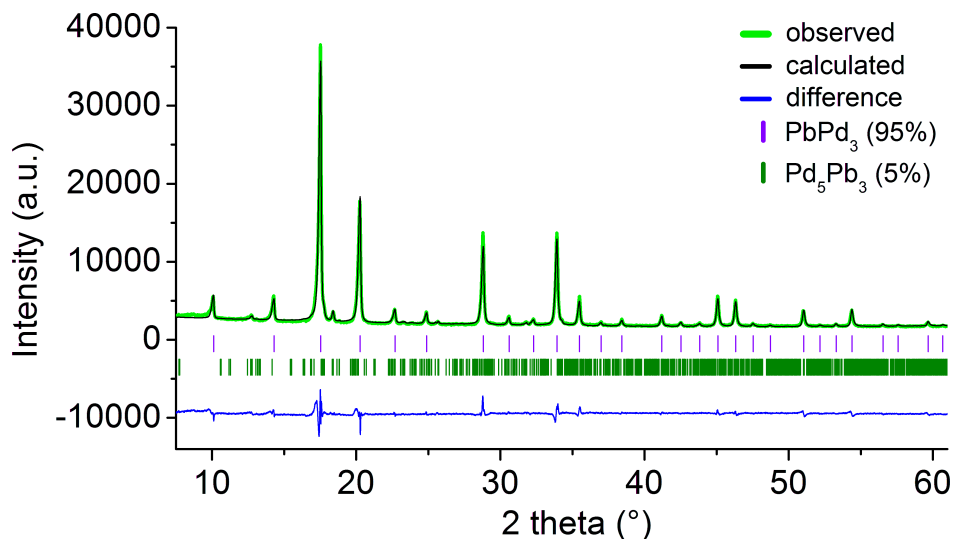## 10.8. Acknowledgement

10.9. Supplementary data

Figure 10.9.1.: Rietveld refinement of the crystal structure of cubic PbPd$_3$ at 297(2) K based on X-ray powder diffraction ($\lambda = 70.932$ pm, $Pm\bar{3}m$, $a = 403.451(9)$ pm, $R_{\text{wp}} = 0.059$, $\chi^2 = 8.9$) using FullProf [33].
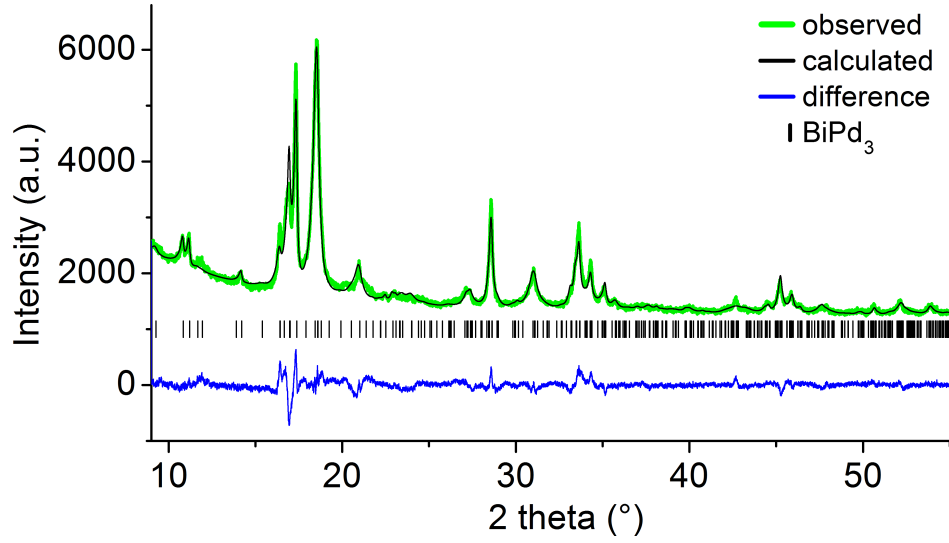
Figure 10.9.2.: Rietveld refinement of the crystal structure of orthorhombic $BiPd_3$ at 297(2) K based on X-ray powder diffraction ($\lambda = 70.926$ pm, $Pmma$, $a = 939.04(4)$ pm, $b = 574.14(4)$ pm, $c = 496.63(8)$ pm, $R_{wp} = 0.039$, $\chi^2 = 2.5$, anisotropic line broadening according to the Stephens model [40] and preferred orientation with March-Dollase model [41] in direction 100 and 010) using TOPAS [42]. Lattice parameters are in agreement with the literature [24, 25].
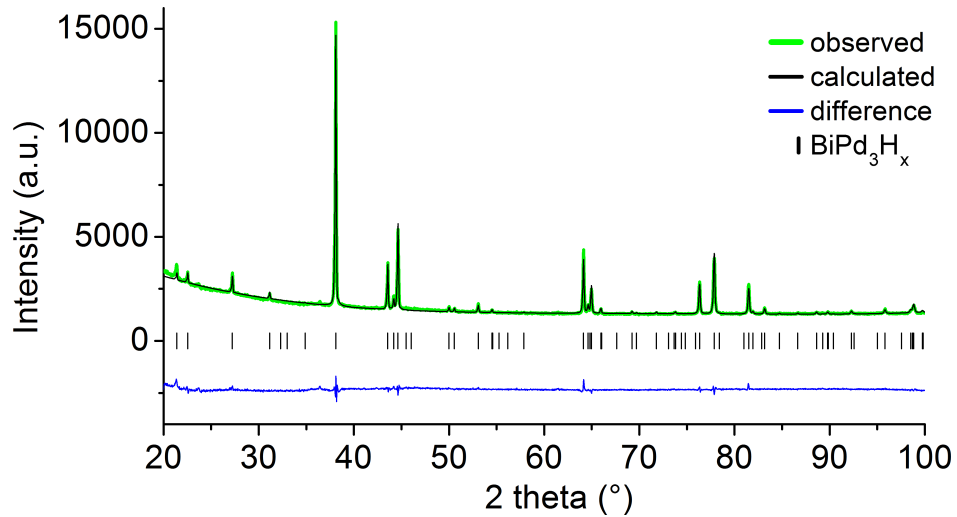
Figure 10.9.3.: Rietveld refinement of the crystal structure of tetragonal $BiPd_3H_x$ (after *ex situ* hydrogenation in an autoclave at 20.0(2) MPa hydrogen pressure and 773(2) K for 48 h) at 297(2) K based on X-ray powder diffraction ($\lambda = 154.059$ pm, $I4/mmm$, $a = 405.669(12)$ pm, $c = 1660.72(6)$ pm, $R_{wp} = 0.028$, $\chi^2 = 1.3$) using FullProf [33].
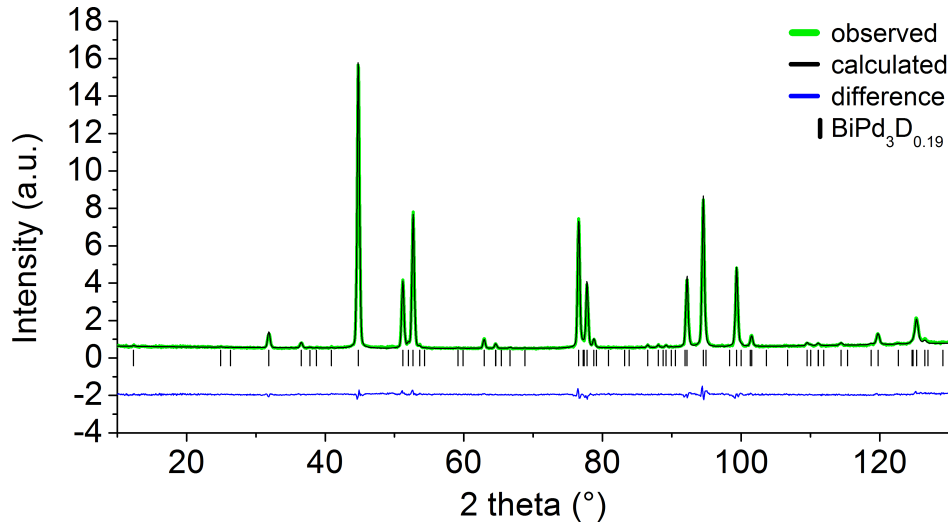
Figure 10.9.4.: Rietveld refinement of the crystal structure of tetragonal $BiPd_3D_{0.19(1)}$ at 296(2) K based on neutron powder diffraction ($\lambda = 179.725(2)$ pm, E9, HZB Berlin, $I4/mmm$, $a = 404.52(2)$ pm, $c = 1661.58(8)$ pm, $R_{wp} = 0.041$, $\chi^2 = 2.4$) using FullProf [33].
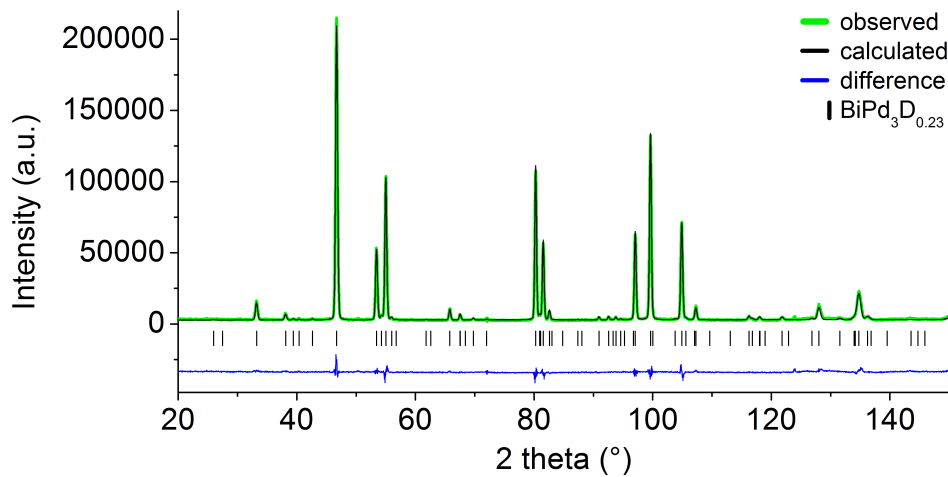

Figure 10.9.5.: Rietveld refinement of the crystal structure of tetragonal $BiPd_3D_{0.23(1)}$ at 298(2) K and 12.0(2) MPa deuterium pressure based on neutron powder diffraction ($\lambda = 186.616(2)$ pm, D20, ILL Grenoble, $I4/mmm$, $a = 404.72(1)$ pm, $c = 1662.64(6)$ pm, $R_{wp} = 0.088$, $\chi^2 = 4.5$) using FullProf [33].
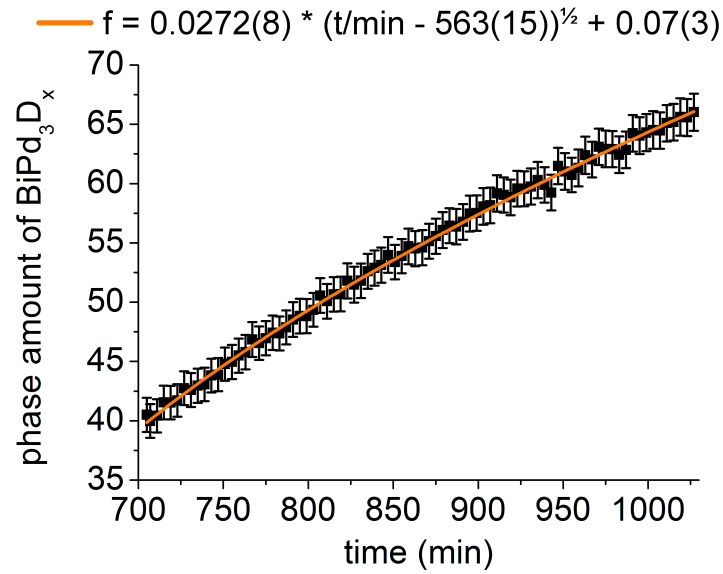
Figure 10.9.6.: Phase fraction of $BiPd_3D_x$ as a function of time (orange line: fit with square root function) during deuteration from Rietveld refinement based on neutron powder diffraction data at 553(3) K and deuterium pressure of 5.2(1) MPa. Error bars represent one estimated standard uncertainty and number of data points is reduced for better clarity.
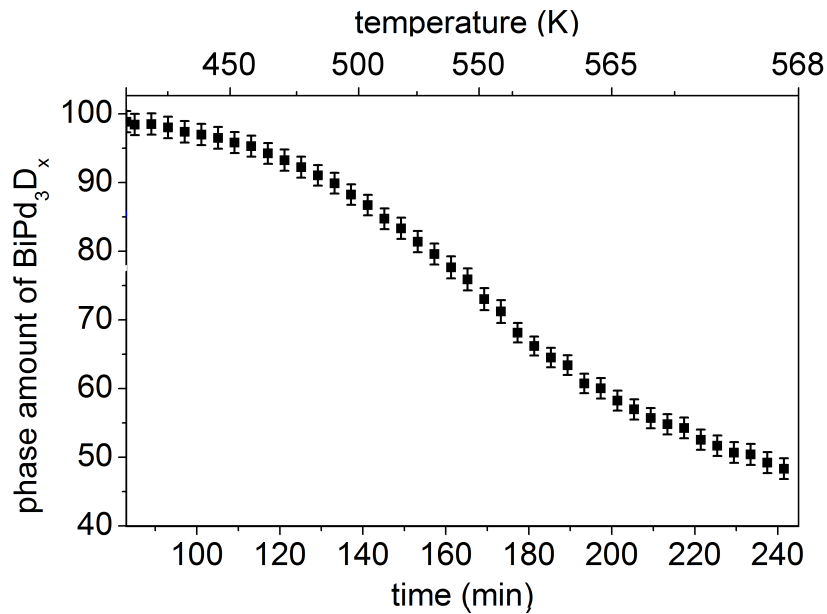

Figure 10.9.7.: Phase fraction of $BiPd_3D_x$ as a function of time during decomposition from Rietveld refinement based on neutron powder diffraction under vacuum. Error bars represent one estimated standard uncertainty and number of data points is reduced for better clarity.

10.10. References for chapter 10

[1] W. Bronger, Komplexe Übergangsmetallhydride, Angew. Chem. 103 (1991) 776–784.

[2] K. Yvon, G. Renaudin, Hydrides: solid state transition metal complexes, in: R.B. King (Ed.), Encyclopedia of Inorganic and Bioinorganic Chemistry, 3rd ed., Wiley, New York, 2005, pp. 1814–1846.

[3] H. Kohlmann, H. E. Fischer, K. Yvon, Europium palladium hydrides, Inorg. Chem. 40 (2001) 2608–2613.

[4] H. Kohlmann, Structural relationships in complex hydrides of the late transition metals, Z. Kristallogr. 224 (2009) 454–460.

[5] T. Graham, On the absorption and dialytic separation of gases by colloid septa, Philos. Trans. R. Soc. London 156 (1866) 399–439.

[6] T. Graham, On the relation of hydrogen to palladium, Proc. R. Soc. London 17 (1869) 212–220.

[7] T. B. Flanagan, W. A. Oates, The palladium-hydrogen system, Annu. Rev. Mater. Sci. 21 (1991) 269–304.

[8] E. Storms, Formation of β-PdD containing high deuterium concentration using electrolysis of heavy-water, J. Alloys Compd. 268 (1998) 89–99.

[9] B. Stritzker, H. Wühl, Superconductivity in metal-hydrogen systems, in: G. Alefeld, J. Völkl (Eds.), Hydrogen in Metals II, Springer, Berlin, Heidelberg, 1978, pp. 243–272.

[10] T. R. P. Gibb Jr., J. MacMillan, R. J. Roy, The magnetic susceptibility of palladium hydride, J. Phys. Chem. 70 (1966) 3024.

[11] J. E. Worsham JR., M. K. Wilkinson, C. G. Shull, Neutron-diffraction observations on the palladium-hydrogen and palladium-deuterium systems, J. Phys. Chem. Solids 3 (1957) 303–310.

[12] M. Gupta, L. Schlapbach, Electronic Properties, in: L. Schlapbach (Ed.), Hydrogen in Intermetallic Compounds I: Electronic, Thermodynamic, and Crystallographic Properties, Preparation, Springer, Berlin, 1988, pp. 139–217.

[13] H. Kohlmann, G. Renaudin, K. Yvon, C. Wannek, B. Harbrecht, Hydrogen-induced atomic rearrangement in MgPd$_3$, J. Solid State Chem. 178 (2005) 1292–1300.

[14] H. Kohlmann, N. Kurtzemann, R. Weihrich, T. Hansen, *In situ* neutron powder diffraction on intermediate hydrides of MgPd$_3$ in a novel sapphire gas pressure cell, Z. Anorg. Allg. Chem. 635 (2009) 2399–2405.

[15] H. Kohlmann, A. V. Skripov, A. V. Soloninin, T. J. Udovic, The anti-perovskite type hydride InPd$_3$H$_{0.89}$, J. Solid State Chem. 183 (2010) 2461–2465.

[16] N. Kurtzemann, H. Kohlmann, Crystal structure and formation of TlPd$_3$ and its new hydride TlPd$_3$H, Z. Anorg. Allg. Chem. 636 (2010) 1032–1037.

[17] S. Yamaguchi, Z.-Q. Li, R.-T. Fu, Y. Kawazoe, Hydrogen site occupation in YPd$_3$ with L12 structure, Phys. Rev. B 55 (1997) 14051–14054.

[18] K. Baba, Y. Niki, Y. Sakamoto, T. B. Flanagan, A. Craft, Reversibile Transitions between ordered structures in the Pd$_3$Mn-hydrogen system, Scr. Metall. 21 (1987) 1147–1151.

[19] H. Kohlmann, F. Müller, K. Stöwe, A. Zalga, H. P. Beck, Hydride formation in the intermetallic compounds CePd$_3$ and CeRh$_3$, Z. Anorg. Allg. Chem. 635 (2009) 1407–1411.

[20] H. Kohlmann, Hydrogenation of palladium-rich compounds of aluminium, gallium and indium, J. Solid State Chem. 183 (2010) 367–372.

[21] A. L. Allred, E. G. Rochow, A scale of electronegativity based on electrostatic force, J. Inorg. Nucl. Chem. 5 (1958) 264–268.

[22] A. Götze, H. Kohlmann, Palladium hydride and hydrides of palladium-rich phases, in: Reference Module in Chemistry, Molecular Sciences and Chemical Engineering, Elsevier, 2017.

[23] M. Ellner, Zusammenhang zwischen strukturellen und thermodynamischen Eigenschaften bei Phasen der Kupfer-Familie in T10-B4-Systemen, J. Less-Common Met. 78 (1981) 21–32.

[24] K. Schubert, S. Bhan, T. K. Biswas, K. Frank, P. K. Panday, Einige Strukturdaten intermetallischer Phasen, Naturwissenschaften 55 (1968) 542–543.

[25] S. Bhan, K. Schubert, Über die Struktur von Phasen mit Kupfer Unterstruktur in einigen T-B Legierungen (T = Ni, Pd, Pt; B = Ga, In, Tl, Pb, Sb, Bi), J. Less-Common Met. 17 (1969) 73–90.

[26] E. Füglein, A. Léon, High-pressure DSC, in: A. Léon (Ed.), Hydrogen Technology, Springer, Berlin, Heidelberg, 2008, pp. 501–521.

[27] T. C. Hansen, H. Kohlmann, Chemical reactions followed by *in situ* neutron powder diffraction, Z. Anorg. Allg. Chem. 640 (2014) 3044–3063.

[28] E. Rönnebro, D. Noréus, M. Gupta, K. Kadir, B. Hauback, P. Lundqvist, The crystal and electronic structure of $CaPd_3H$, Materials Research Bulletin 35 (2000) 315–323.

[29] C. Stanitski, J. Tanaka, Ternary hydrides of calcium and strontium with palladium, J. Solid State Chem. 4 (1972) 331–339.

[30] Y. Andersson, S. Rundqvist, R. Tellgren, J. O. Thomas, T. B. Flanagan, A Neutron diffraction investigation of deuterated $Pd_3P_{0.80}$, J. Solid State Chem. 32 (1980) 321–327.

[31] Y. Andersson, S. Rundqvist, R. Tellgren, J. O. Thomas, T. B. Flanagan, Neutron powder diffraction investigation of pure and deuterated palladium phosphide Pd_6P, Acta Crystallogr. 37B (1981) 1965–1972.

[32] Y. Andersson, S. Rundqvist, R. Tellgren, T. B. Flanagan, A neutron powder diffraction investigation of deuterated $Pd_{15}P_2$, Z. Phys. Chem. (Muenchen, Ger.) 145 (1985) 43–49.

[33] J. Rodríguez-Carvajal, FullProf: a Program for Rietveld Refinement and Pattern Matching Analysis, Insitut Laue-Langevin, Grenoble (France), 2012.

[34] A. Götze, J. M. Sander, H. Kohlmann, Crystal structures and hydrogenation properties of palladium-rich compounds with elements from groups 12-16, Z. Naturforsch. 71B (2016) 503–508.

[35] H. Kohlmann, C. Ritter, Reaction pathways in the formation of intermetallic $InPd_3$ polymorphs, Z. Anorg. Allg. Chem. 635 (2009) 1573–1579.

[36] M. Widenmeyer, R. Niewa, T. C. Hansen, H. Kohlmann, *In situ* neutron diffraction as a probe on formation and decomposition of nitrides and hydrides: a case study, Z. Anorg. Allg. Chem. 639 (2013) 285–295.

[37] H. Bärnighausen, Group-subgroup relations between space groups: a useful tool in crystal chemistry, MATCH 9 (1980) 137–175.

[38] P. H. Andersson, O. Eriksson, L. Nordström, The effect of hydrogenation on the crystal structure and magnetic state in Pd_3Mn, J. Magn. Magn. Mater. 226-230 (2001) 1040–1041.

[39] H. Kohlmann, M. Vasseur, A. Sayede, G. Lefevre, J. M. Sander, S. Doyle, Crystal structure and hydrogenation properties of Pd_5As, J. Alloys Compd. 664 (2016) 256–265.

[40] P. W. Stephens, Phenomenological model of anisotropic peak broadening in powder diffraction, J. Appl. Cryst. 32 (1999) 281-289.

[41] A. March, Mathematische Theorie der Regelung nach der Korngestalt bei affiner Deformation, Z. Kristallogr. 81 (1932) 285-297.

[42] Bruker AXS, TOPAS version 5, www.bruker-axs.com.

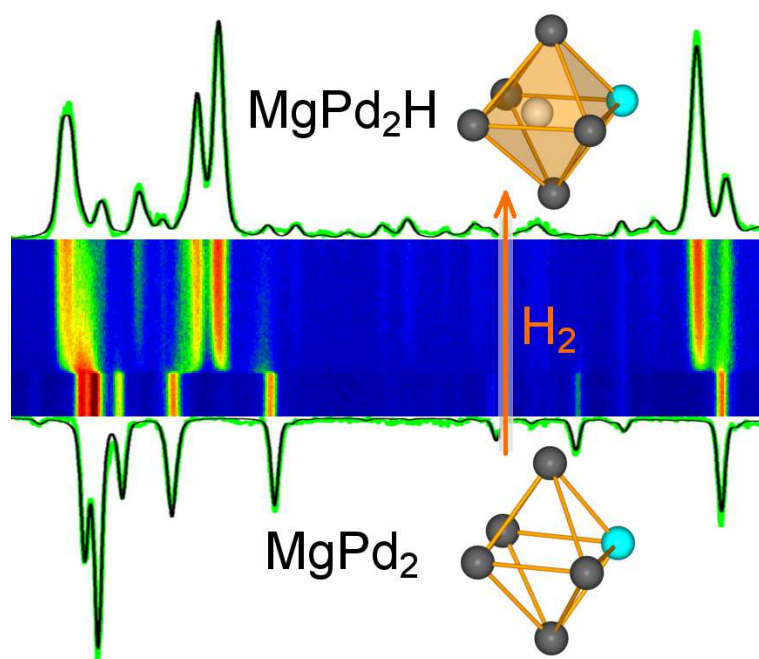# 11. *In Situ* Hydrogenation and Crystal Chemistry Studies of Co$_2$Si type compounds MgPd$_2$ and Pd$_2$Zn

André Götze, Nicolas Zapp, Andrea J. Peretzki, Vladimir Pomjakushin, Thomas C. Hansen, Holger Kohlmann

Dedicated to Professor Hartmut Bärnighausen on the Occasion of his 85th Birthday.

11.1. Authors' contributions

The syntheses, characterizations, refinements were executed by A. Götze. The quantum-mechanical calculations were done by Nicolas Zapp, who wrote also the related part "quantum-mechanical calculations". A. Götze and H. Kohlmann conducted the experiment at the neutron diffractometer D20 at the Institut Laue-Langevin with assitance by T. C. Hansen. V. Pomjakushin executed the neutron diffraction experiment at the Paul Scherrer Institut. A. J. Peretzki did preliminary investigations to this work. The manuscript was wirtten by A. Götze and revised by H. Kohlmann.

11.2. Abstract

The hydrogenation properties of the intermetallic compounds MgPd$_2$ and Pd$_2$Zn, crystallizing in the Co$_2$Si type, were studied by *in situ* thermal analysis (DSC) under hydrogen pressure. Pd$_2$Zn does not show any reaction with hydrogen while MgPd$_2$ reversibly forms the hydride MgPd$_2$H. Neutron diffraction on the deuterides reveals the compositions MgPd$_2$D$_{0.861(6)}$ (ambient) and MgPd$_2$D$_{0.97(1)}$ (308(2) K, 2.56(5) MPa deuterium) with hydrogen (deuterium) occupying distorted [MgPd$_5$] octahedral voids. Quantum-mechanical calculations support the structure models and show the hydrogenation to be exergonic for MgPd$_2$ and endergonic for Pd$_2$Zn. MgPd$_2$H releases hydrogen under normal conditions or vacuum. Heating under hydrogen pressure leads first reversibly to MgPd$_2$H$_{\approx 0.2}$ and subsequently irreversibly to MgPd$_3$H$_{\approx 1}$ and MgH$_2$. MgPd$_2$, Pd$_2$Zn and MgPd$_2$H were classified in a structure map. Trends of axial ratio changes upon hydrogenation of TiNiSi type and ZrBeSi type compounds are discussed.

11.3. Introduction

Compounds MPd$_2$ are known for all main group metals except for the alkaline earth metals Na $-$ Cs, for Pb and Bi. They crystallize in structure types typical for intermetallic compounds such as MgCu$_2$ [1], Co$_2$Si [2-4], and Zr$_2$Cu [5]. The crystal structure of LiPd$_2$ is not completely determined yet [6]. The Laves phases SrPd$_2$ and EuPd$_2$ were previously described to take up hydrogen in tetrahedral voids while retaining the cubic MgCu$_2$ type [7,8]. MPd$_2$ (M = Ga [9], In [9], Sn [10]) in the Co$_2$Si type on the other hand do not show any hydride formation. The ordered variant of this structure type (TiNiSi type) is well known for its numerous compounds reversibly taking up hydrogen, e. g. LnTSn (Ln = lanthanide; T = transition metal) [11-13]. In TiNiSi type hydrides, hydrogen atoms are tetrahedrally coordinated by metal atoms. The hydrogenation behavior of MgPd$_2$ [4] has not been studied yet. It does not seem to offer tetrahedral voids of the right size for hydrogen atoms as the before mentioned TiNiSi type intermetallic compounds, but it contains apparently well-suited octahedral voids. Such [MgPd$_5$] positions are occupied in α-MgPd$_3$H$_{0.79-0.94}$ [14]. This analogy triggered this investigation of the hydrogenation behavior of MgPd$_2$ by *in situ* thermal analysis [15] and *in situ* neutron powder diffraction [16,17], which are established methods to follow reaction pathways during hydrogenation processes. Pd$_2$Zn [18] has been included as well because of the structural similarity to MgPd$_2$.

11.4. Results and discussion

11.4.1. Synthesis and thermal analysis

The synthesis of MgPd$_2$ and Pd$_2$Zn yielded dark and light grey powders with metallic luster, respectively. According to X-ray powder diffraction (XRPD) Pd$_2$Zn was single phase, whereas MgPd$_2$ contained a small amount ($\leq$ 2 wt %) of MgO (see Figure and Table S1, Supporting Information). The refined lattice parameters are in good agreement with literature data for MgPd$_2$ (Table 11.4.1) and the first refined structural parameters in the case of Pd$_2$Zn (CSD-433793, see Figure and Table S2, Supporting Information). Based on chemical analysis of the powders, the empirical formulae Mg$_{1.06(10)}$Pd$_{1.94(10)}$ and Zn$_{1.01(8)}$Pd$_{1.99(8)}$ were determined, averaged from at least 15 energy dispersive X-ray (EDX) spectra on different particles of each sample.

The hydrogenation of these compounds was studied by *in situ* differential scanning calorimetry (DSC) under 2.5 MPa for MgPd$_2$ and 5.0 MPa hydrogen pressure for Pd$_2$Zn (Figure 1). MgPd$_2$ shows a broad exothermic signal at the beginning of the DSC experiment, an endothermic signal
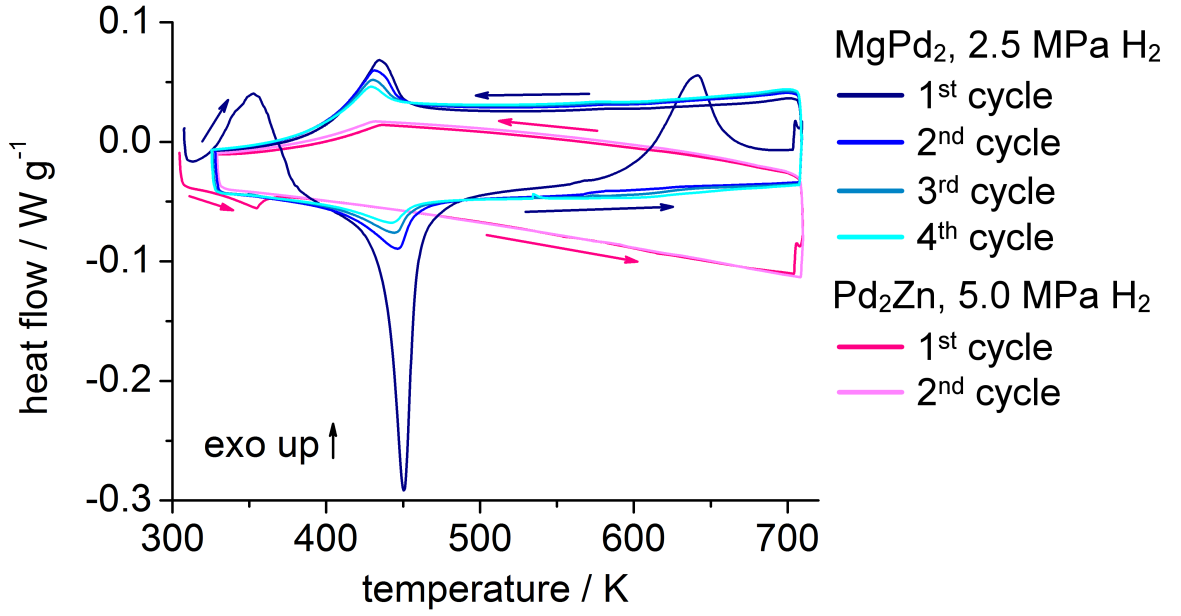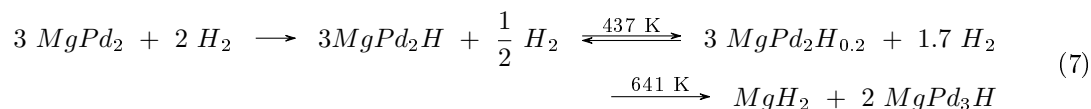
Figure 11.4.1.: *In situ* thermal analysis (DSC) of the hydrogenation of $MgPd_2$ at 2.5 MPa and of Pd_2Zn at 5.0 MPa hydrogen pressure (starting pressure at 303 K, increasing during the heating process up to 3.4 and 6.9 MPa, respectively).

at 437 K, another exothermic signal at 641 K, and an exothermic signal during the cooling process at 451 K. A subsequent DSC experiment with a maximum temperature of 363 K proved the first exothermic signal to be irreversible and belonging to the hydrogenation of $MgPd_2$. An XRPD study of $MgPd_2$ after this hydrogenation (see Figure and Table S3, Supporting Information) shows an increase of lattice parameters a and c, a decrease of b, and a unit cell volume expansion of 6.8 % compared to the starting compound (Table 11.4.1). The two thermal signals at about 440 K during the heating and cooling processes are reversible in all four cycles and decrease in heat flow with each cycle. In a similar experiment with a maximum temperature of 473 K those reversible thermal signals do not differ in heat flow. They represent the reversible hydrogen release and uptake of $MgPd_2H_{\approx 1}$ to $MgPd_2H_{\approx 0.2}$ (hydrogen content proven later) (Eq. (7)). The broad exothermic signal at 641 K, which is much weaker in the second cycle, shows the irreversible decomposition of $MgPd_2H_{\approx 0.2}$ to β-

Table 11.4.1.: Lattice parameters and unit cell volumes of $MgPd_2$ and Pd_2Zn before and after hydrogenation in a DSC experiment under hydrogen pressure and resulting unit cell volume increase according to XRPD data.

compound	a / Å	b / Å	c / Å	V / Å^3	ΔV / %
$MgPd_2$ [4]	5.4421(2)	4.1673(2)	8.0129(3)	181.72	
$MgPd_2$	5.4194(3)	4.1599(2)	7.9661(5)	179.59(2)	
$MgPd_2H_x$ [a]	5.6462(6)	4.0504(4)	8.3844(9)	191.75(4)	6.8
Pd_2Zn [18]	5.35	4.14	7.65	169.44	
Pd_2Zn	5.3291(1)	4.14427(9)	7.7366(2)	170.866(9)	
Pd_2Zn [b]	5.32927(11)	4.14397(7)	7.7367(1)	170.860(5)	0.0

[a] after hydrogenation (DSC, 2.5 MPa H_2, T_{max} = 363 K).

[b] after hydrogenation (DSC, 5.0 MPa H_2, T_{max} = 703 K).

MgPd$_3$H$_x$ (cubic anti-perovskite type) and MgH$_2$ [reacts at air to Mg(OH)$_2$, see Figure and Table S4, Supporting Information]. This decomposition explains the decrease of the reversible thermal effects with increasing number of cycles as mentioned before.

$$3\ MgPd_2\ +\ 2\ H_2\ \longrightarrow\ 3MgPd_2H\ +\ \frac{1}{2}\ H_2\ \underset{641\ K}{\overset{437\ K}{\rightleftharpoons}}\ 3\ MgPd_2H_{0.2}\ +\ 1.7\ H_2$$
$$\xrightarrow{\hspace{1cm}}\ MgH_2\ +\ 2\ MgPd_3H \tag{7}$$

Pd$_2$Zn does not show any thermal signal during hydrogenation (DSC, 5.0 MPa H$_2$, Fig. 11.4.1) and the unit cell volume does not change significantly before and after hydrogenation according to XRPD data (Table 11.4.1).

11.4.2. Crystal structure

The deuterium positions in the crystal structures were determined from neutron diffraction data. Rietveld refinements were performed based on the Co$_2$Si type of the parent intermetallic compound. Subsequent Fourier analysis revealed deuterium atoms to occupy positions surrounded by one magnesium and five palladium atoms. Rietveld refinements yielded almost complete deuterium occupation in those distorted octahedral sites [MgPd$_5$] (Fig. 11.4.2). Gravimetric determination of deuterium results in the composition MgPd$_2$D$_{1.0(1)}$ in accordance with the refined deuterium occupation. Those yield MgPd$_2$D$_{0.861(6)}$ (CSD-433792, Fig. 11.4.3 and Table 11.4.2) for a sample measured *ex situ* and MgPd$_2$D$_{0.97(1)}$ for a sample measured *in situ* [CSD-433791, 308(2) K, 2.56 MPa deuterium pressure, Fig. 11.4.4 and Table 11.4.2]. The hydrogen content of the former is lower because hydrogenated samples of MgPd$_2$ release hydrogen when stored at ambient conditions.
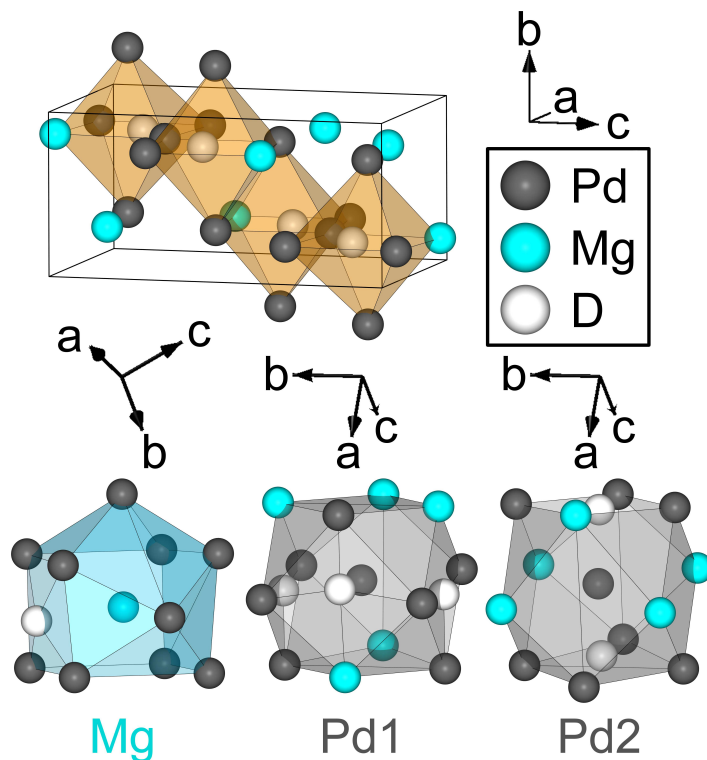

Figure 11.4.2.: Crystal structure of MgPd$_2$D$_{0.861(6)}$ with distorted DMgPd$_5$ octahedra (orange polyhedra) and the coordination sphere of the metal atoms (bottom).

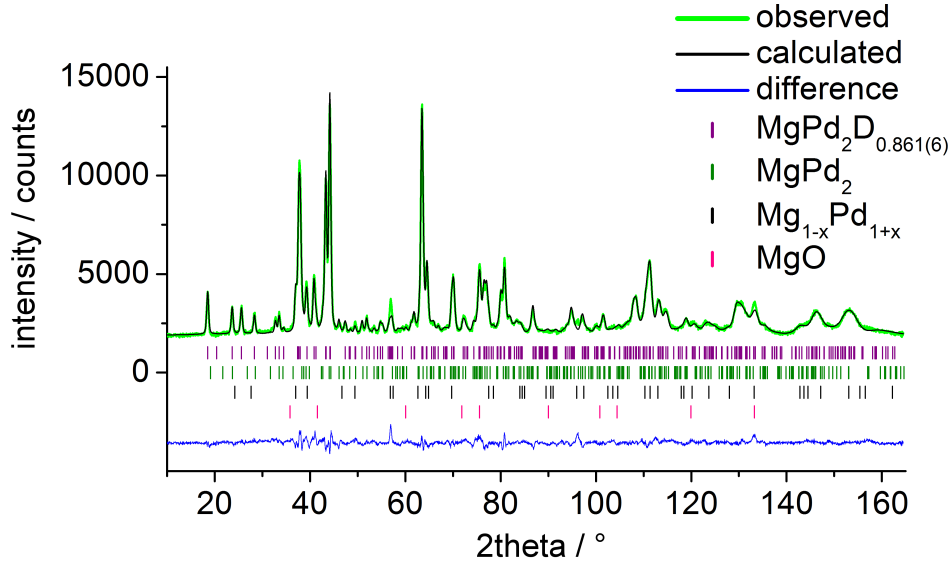Figure 11.4.3.: Rietveld refinement of the crystal structure of MgPd$_2$D$_{0.861(6)}$ [*Pnma*, $a = 5.6098(2)$ Å, $b = 4.06495(10)$ Å, $c = 8.5136(3)$ Å, 85.1(8) wt %, $R_{\text{Bragg}} = 0.047$] with the impurity phases MgPd$_2$ [*Pnma*, $a = 5.5017(9)$ Å, $b = 4.1188(6)$ Å, $c = 8.002(1)$ Å, 8.6(3) wt %, $R_{\text{Bragg}} = 0.077$], Mg$_{1-x}$Pd$_{1+x}$ [6.2(3) wt %] and MgO [0.16(2) wt %] at room temperature in a sealed vanadium cylinder based on neutron powder diffraction data ($\lambda = 1.494$ Å, HRPT, PSI, Villigen, $R_{\text{wp}} = 0.039$, $\chi^2 = 4.21$) using FullProf.[19]

The magnesium and palladium atoms have a similar coordination in MgPd$_2$H$_x$ (Fig. 11.4.2) compared to MgPd$_2$. Magnesium atoms are coordinated to ten palladium atoms forming a distorted tetragonal prism, which is capped on two neighboring faces. Hydrogen atoms are located on the Pd$_4$ tetragon neighboring both capped faces. The palladium atoms are coordinated by five magnesium and seven palladium atoms forming distorted cuboctahedra. Hydrogen atoms are located in the middle of three MgPd$_3$ tetragons in case of the Pd1 polyhedron and of MgPd$_3$ and opposite Pd$_4$ tetragons for the Pd2 polyhedron. The hydrogen atoms are surrounded by distorted octahedra of one magnesium and five palladium atoms. The distortion is less pronounced than in the hydrogen-free parent intermetallic compound (Fig. 11.4.5). The octahedra are compressed along the crystallographic b axis

Table 11.4.2.: Crystal structure parameters of MgPd$_2$D$_{0.861(6)}$ [*Pnma*, $a = 5.6098(2)$ Å, $b = 4.06495(10)$ Å, $c = 8.5136(3)$ Å] and MgPd$_2$D$_{0.97(1)}$ [*in italics, Pnma*, $a = 5.6065(5)$ Å, $b = 4.0691(3)$ Å, $c = 8.5216(7)$ Å at 308(2) K and 2.56 MPa deuterium pressure].

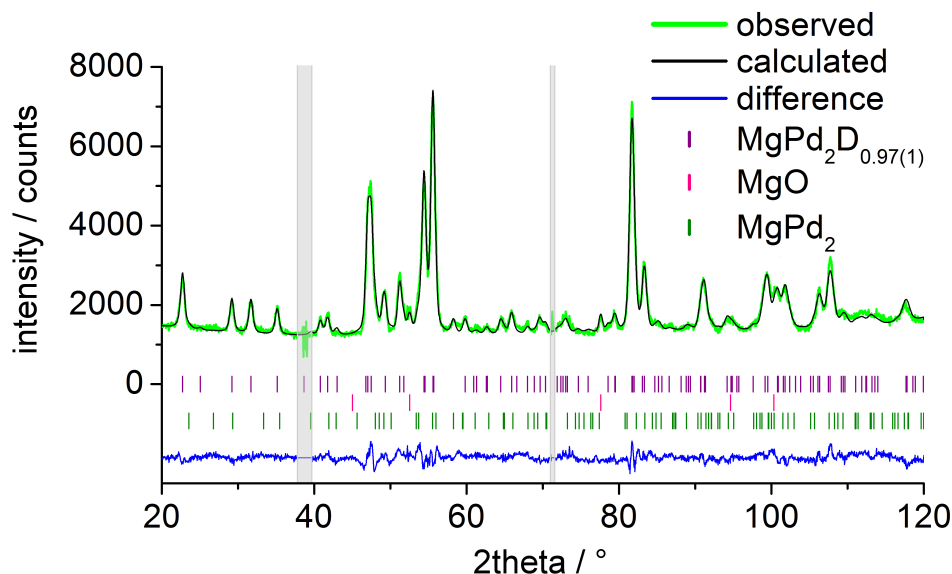| atom	site	x	y	z	B^{iso} / Å^2	SOF
Mg	4c	0.3513(5)	1/4	0.1065(5)	0.98(6)	1
		0.3487(10)		*0.1003(8)*	*2.4(1)*	
Pd1	4c	0.3627(5)	1/4	0.4304(3)	0.55(5)	1
		0.3653(8)		*0.4314(6)*	*1.1(2)*	
Pd2	4c	0.3913(6)	1/4	0.7692(3)	0.77(6)	1
		0.3902(12)		*0.7754(7)*	*2.6(2)*	
D	4c	0.6183(7)	1/4	0.6116(4)	2.60(6)	0.861(6)
		0.6127(11)		*0.6098(6)*	*4.8(1)*	*0.97(1)*

Figure 11.4.4.: Rietveld refinement of the crystal structure of $MgPd_2D_{0.97(1)}$ [*Pnma*, *tex-tita* = 5.6065(5) Å, *textitb* = 4.0691(3) Å, *textitc* = 8.5216(7) Å, 88.(1) wt %, R_{Bragg} = 0.071] with the impurity phases $MgPd_2$ [*Pnma*, *textita* = 5.490(2) Å, *textitb* = 4.119(2) Å, *textitc* = 7.988(3) Å, 11.6(4) wt %, R_{Bragg} = 0.154] and MgO [0.48(2) wt %] at 308(2) K and under 2.56(1) MPa deuterium pressure in single crystal sapphire cell based on neutron powder diffraction data (λ = 1.86786(3) Å, D20, ILL, Grenoble, NUMOR 959583, R_{wp} = 0.049, χ^2 = 4.12) using FullProf.[19]

resulting in a decreased Pd–Pd distance and stretched in the *ac* plane resulting in an increased Mg–Pd distance. This is a consequence of the change of lattice parameters upon hydrogenation. The bonding energy gained by occupation of these $MgPd_5$ octahedra is probably the driving force for the hydrogen uptake of $MgPd_2$. The same is true for the hydrogen occupation of [Pd_6] octahedral sites in other palladium-rich compounds like $MgPd_3$ and the related transition from one superstructure of the ccp to another one [14].

The Pd–Pd and Mg–Pd distances in $MgPd_2D_{0.861(6)}$ and $MgPd_2D_{0.97(1)}$ are similar to those in $MgPd_2$ (Table 3). The main difference in distances is the short Mg–Pd1 distance of 2.573(10) Å in $MgPd_2$ compared to 2.796(3) Å in $MgPd_2D_{0.861(6)}$. This is caused by the incorporation of deuterium and its space requirements. The D–Mg distances [d = 2.226(8)–2.271(5) Å] are comparable to 1.901(8)–2.29(2) Å in $MgPd_3D_x$ [14] and the D–Pd distances [d = 1.837(5)–2.106(5) Å] are typical for palladium-rich hydrides, like 1.97(2)–1.999(1) Å in $MgPd_3D_{0.79}$ [14], 2.0113(1) Å in $InPd_3D_{0.89}$ [20], or 2.000(3)–2.02363(6) Å in $BiPd_3D_{0.23}$ [21]. The interatomic deuterium–deuterium distances are greater than 3 Å and also somewhat greater than those in neighboring [$MgPd_5$] octahedral voids in $MgPd_3D_{0.94}$ (2.858 Å) [14].

Occupation of tetrahedral voids by hydrogen like [Tb_3Ni] in TbNiSnD [11], and related compounds is not observed in the hydrides of $MgPd_2$. $MgPd_2H$ is isopointal to $ScRhSi_2$ [22], but the axial ratio $(a+c)/b$ (3.474 for $MgPd_2H$ vs. 3.928 for $ScRhSi_2$), which are typical for $PbCl_2$ like structures [23,24], and the free positional parameters of both structures differ strongly, preventing a classification as isotypic. Consequently, Si2 atoms in $ScRhSi_2$ are eightfold coordinated forming a three-capped trigonal prism, whereas hydrogen atoms in $MgPd_2H$ exhibit a nearly octahedral coordination sphere. Further structure types such as $BaCdO_2$, $CuSbS_2$, $LiCaSi_2$ are also isopointal, but with even larger deviations in metrical relations. Therefore, we consider $MgPd_2H$ to be a new structure type.
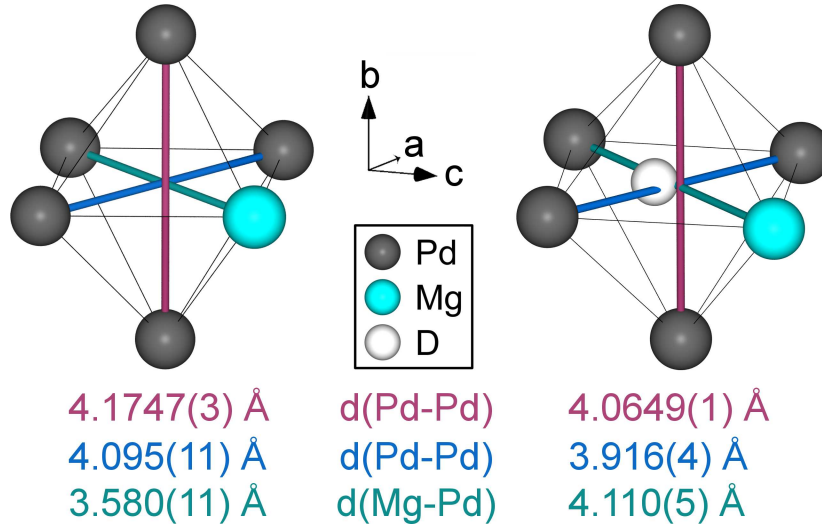
4.1747(3) Å	d(Pd-Pd)	4.0649(1) Å
4.095(11) Å	d(Pd-Pd)	3.916(4) Å
3.580(11) Å	d(Mg-Pd)	4.110(5) Å

Figure 11.4.5.: Decreasing distortion of [MgPd$_5$] octahedral site from MgPd$_2$ (left) to MgPd$_2$D$_{0.861(6)}$ (right).

Table 11.4.3.: Interatomic distances / Å (< 3.1 Å) in MgPd$_2$ (based on neutron powder diffraction, see Figure and Table S6, Supporting Information), MgPd$_2$D$_{0.861(6)}$ and MgPd$_2$D$_{0.97(1)}$ [at 308(2) K, 2.56 MPa deuterium].

compound	Mg-Pd	Pd-Pd	D-Mg	D-Pd	D-D
MgPd$_2$	2.573(10)	2 x 2.941(8)	–	–	–
	2.60(1)	2 x 2.722(10)			
	2 x 2.668(7)	2.682(10)			
	2 x 2.702(8)	2 x 2.841(7)			
	2 x 2.774(8)	2 x 2.916(7)			
	2.87(1)				
	2.871(10)				
MgPd$_2$D$_{0.861(6)}$	2 x 2.708(3)	2 x 2.812(3)	2.271(5)	1.837(5)	3.083(4)
	2.758(5)	2 x 2.824(5)		1.850(5)	
	2.759(4)	2 x 2.836(3)		2x 2.0664(8)	
	2 x 2.796(3)	2.889(4)		2.106(5)	
	2 x 2.811(3)	2 x 2.987(3)			
	2.880(5)				
	2.886(4)				
MgPd$_2$D$_{0.97(1)}$	2 x 2.721(6)	2 x 2.791(5)	2.226(8)	1.838(9)	3.039(6)
	2.724(7)	2 x 2.836(9)		1.883(8)	
	2 x 2.766(5)	2 x 2.821(6)		2.058(7)	
	2.778(9)	2.935(8)		2 x 2.068(1)	
	2.823(9)	2 x 3.021(6)			
	2 x 2.857(6)				
	2.909(7)				

11.4.3. Quantum-chemical calculations

To rationalize the hydrogenation behavior of MgPd$_2$ and Pd$_2$Zn, quantum-mechanical calculations were performed. The experimentally determined MgPd$_2$ and MgPd$_2$H structures, respectively, were used as input for the optimizations of MgPd$_2$ and Pd$_2$Zn as well as MgPd$_2$H and hypothetical Pd$_2$ZnH. The total energies derived from these optimizations are used for calculating free reaction enthalpies (see Table S7, Supporting Information) and the density of states (DOS) are calculated from the relaxed structures.

The hydrogenation of MgPd$_2$ is calculated to be thermodynamically favored (free reaction enthalpy: -152 meV mol^{-1}) in contrast to Pd$_2$Zn (+64 meV mol^{-1}). The cell parameters of MgPd$_2$, MgPd$_2$H, and Pd$_2$Zn are slightly larger than experimentally observed. The hypothetical Pd$_2$ZnH structure converges with lattice- and atomic parameters analogous to MgPd$_2$H (see Table S8 and Figure S9, Supporting Information). While the H$-M$ distance is slightly larger for MgPd$_2$H (2.334 Å) than for hypothetical Pd$_2$ZnH (2.220 Å), the H–Pd distances are similar (1.862–2.145 Å for MgPd$_2$H and 1.828–2.115 Å for Pd$_2$ZnH).
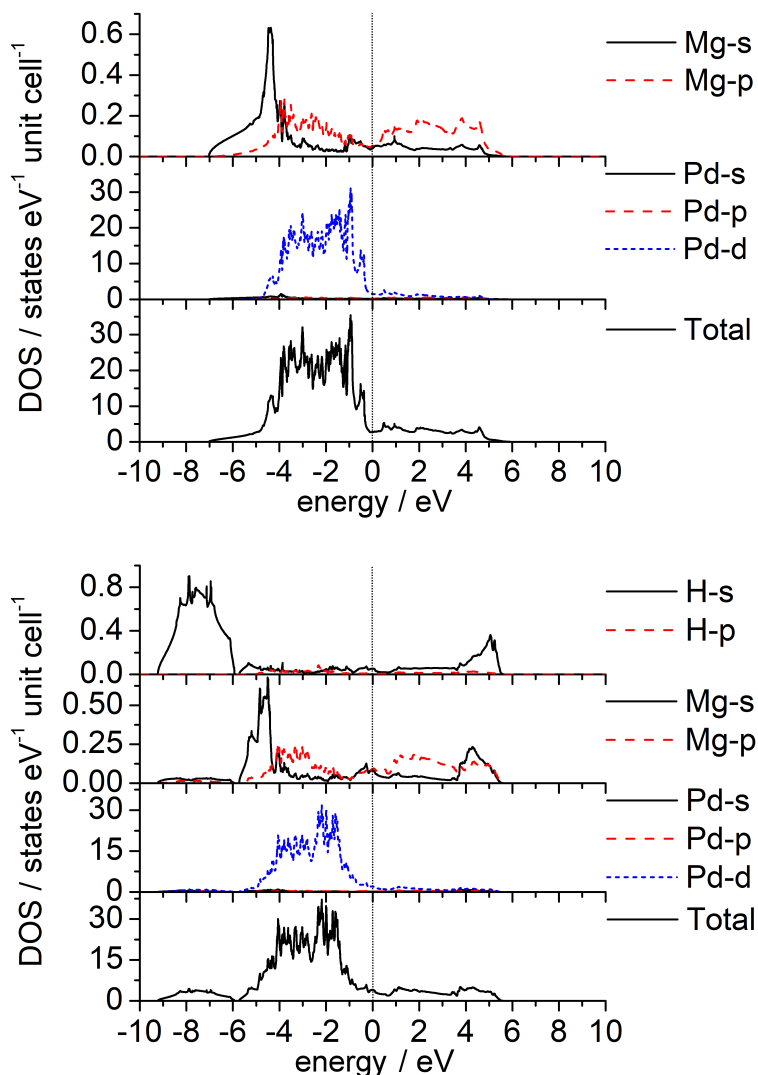

Figure 11.4.6.: Density of states (DOS) of MgPd$_2$ (top) and MgPd$_2$H (bottom). The Fermi level is set at zero. Note the different scales for the y axes.

Fig. 11.4.6 shows the DOS of $MgPd_2$ and $MgPd_2H$. The d-bands of Pd dominate the Fermi region, which has already been documented for other palladium-rich compounds, e. g. $MgPd_3$ [25], $InPd_3$ [26], and $Pd_{11}Bi_2Se_2$ [27]. The hydrogenation results in the formation of H bands from -6 to -9 eV, superimposing with Pd-d bands. The DOS at the Fermi level is increased by hydrogenation [2.6 states eV^{-1} unit $cell^{-1}$ ($MgPd_2$) or 3.7 states eV^{-1} unit $cell^{-1}$ ($MgPd_2H$), respectively], which might increase its electrical conductivity, a behavior inverse to $MgPd_3$ and $MgPd_3H$ [25]. A pseudo-gap is observed for $MgPd_2$ only.

The DOS of Pd_2Zn and Pd_2ZnH are presented in Figure S10 (Supporting Information). The above mentioned influences of hydrogenation apply here, too, the major difference to the magnesium compounds is found in the localized d-band of Zn at about -7 eV.

11.4.4. Reaction pathway by *in situ* neutron diffraction

To follow the reaction pathway of the hydrogenation of $MgPd_2$ in detail, to determine the reversible product at higher temperatures observed with *in situ* DSC, and to obtain the hydrogen content of the hydride at any reaction step, *in situ* neutron powder diffraction is the method of choice. The experiment was performed in a sapphire single crystal cell with a gas-pressure control system and a laser heating system. The *in situ* neutron powder diffraction experiment was executed to reproduce the hydrogenation experiment observed with DSC. Therefore, deuterium pressure was applied to $MgPd_2$ and subsequently the sample was heated to 437 K and afterwards cooled down to room temperature (Fig. 11.4.7). Diffraction data were binned (ten neutron diffraction patterns with 2 min data collection to one frame).

Rietveld refinements based on each frame were executed (see Figures and Tables S11–S40, Supporting Information). Selected refined parameters are displayed in Fig. 11.4.8. At beginning of this *in situ* experiment, the cell with $MgPd_2$ was flushed with deuterium gas. During this flushing process the deuteration of $MgPd_2$ already started. To check, if this deuteration at room temperature is reversible, vacuum was applied from frame two to five. Meanwhile, the phase fraction of the higher deuteride reduces to zero and at frame four to six only a phase with nearly zero deuterium content $MgPd_2D_{\approx 0}$ was included in the refinement. The lattice parameters a and c decrease and b increases, however, they do not reach the lattice parameters from the starting compound $MgPd_2$ as determined before. This might be an indication for remaining hydrogen even though the refinement of the occupation is not significantly greater than zero. From frame six to eleven, the deuterium pressure was
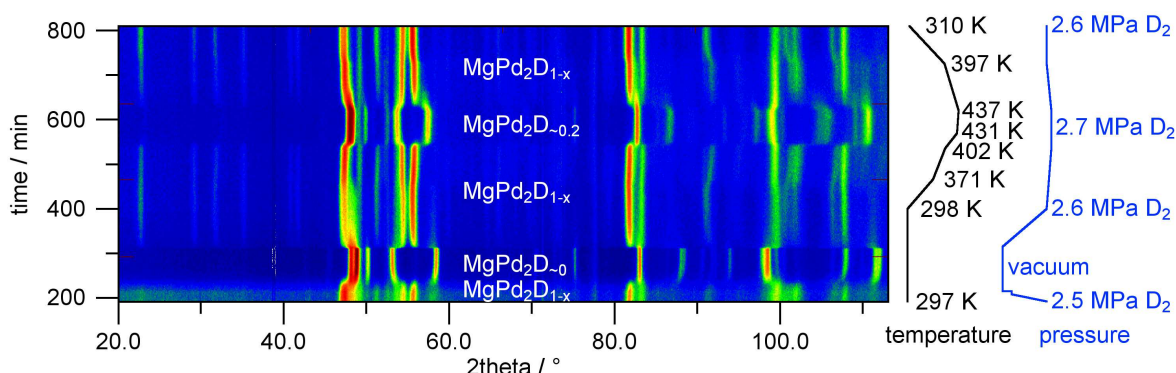

Figure 11.4.7.: *In situ* neutron powder diffraction data (NUMOR 959282–959582) of the deuteration of $MgPd_2$ taken on diffractometer D20 at $\lambda = 1.86786(3)$ Å in a single crystal sapphire cell under various temperature and deuterium pressure conditions. Intensities are in false colors.
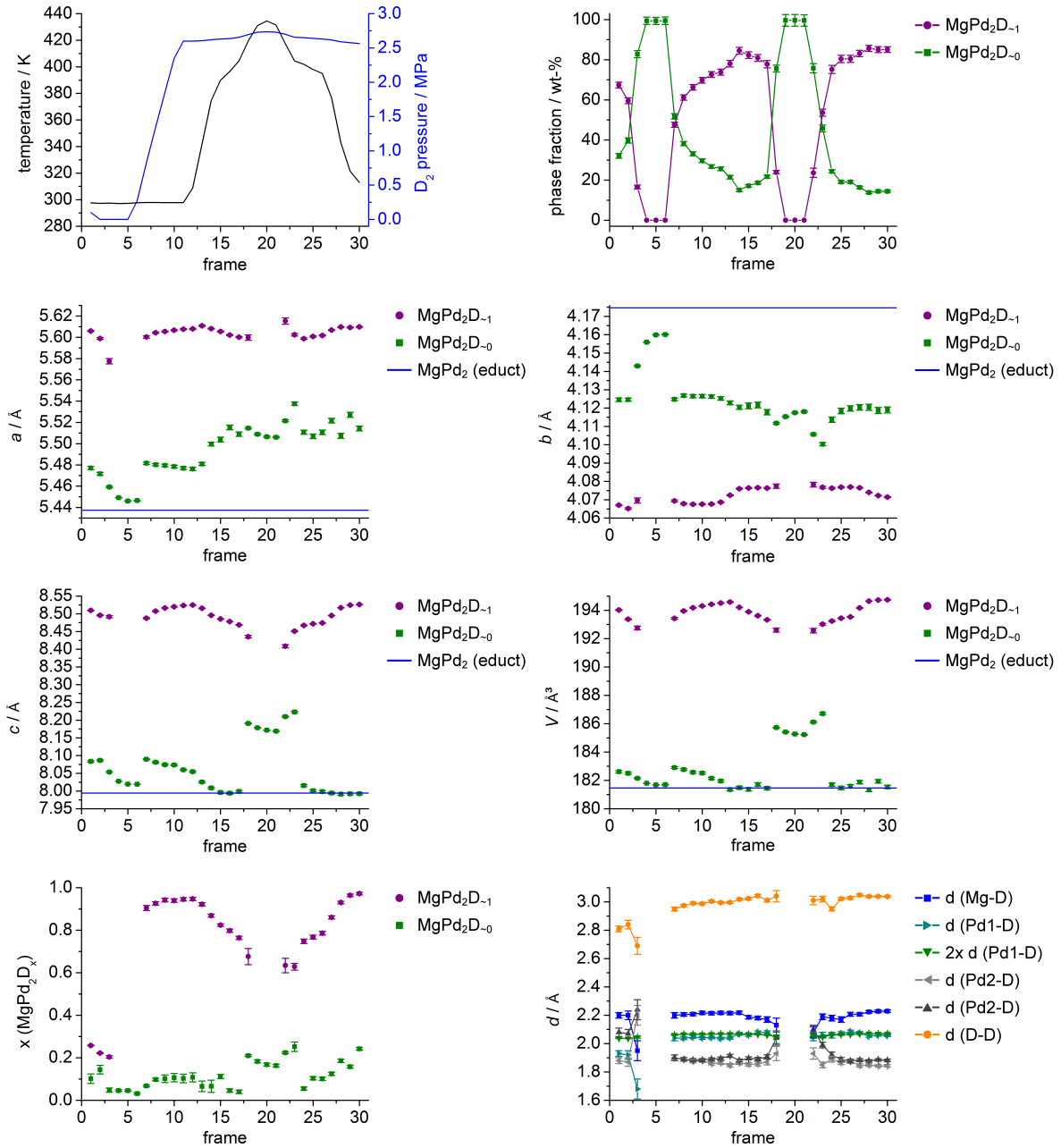
Figure 11.4.8.: Control parameters of the *in situ* deuteration of MgPd$_2$ and structural parameters refined by the Rietveld technique based on neutron diffraction data: temperatures and deuterium pressure (top, left, frames 2 - 5: vacuum), phase fraction (top, right, frames 4 - 6 and 19 - 21: no MgPd$_2$D$_{\approx 1}$ phase), lattice parameters and unit cell volume (middle), site occupation factors (SOF) of deuterium site (bottom, left) and interatomic Mg-D, Pd-D, and D-D distances (bottom right). For full crystallographic data and Rietveld plots see Figures and Tables S11-S40, Supporting Information). Error bars correspond to $\pm$ 1 estimated standard uncertainty.

increased to 2.6 MPa and kept nearly constant up to the end of the experiment. The higher hydride $MgPd_2D_{\approx1}$ forms again with steeply increasing phase fraction. The occupation of the distorted $[MgPd_5]$ octahedral site by deuterium is almost complete from the beginning of the phase formation. This occupation is easily visible by means of the increasing intensity in the neutron powder diffraction patterns for diffraction angles $20° \leq 2\theta \leq 45°$ (see Figures S16 and S17, Supporting Information). The low occupation factors of deuterium in the beginning ($0.2 < x < 0.3$ in the first frame) differ considerably from those at later stages of the experiment (e. g. $0.9 < x < 1$ at frames 6–11), although the lattice parameters are comparable. Apparently, a few hundred kPa of deuterium pressure at room temperature are enough to incorporate deuterium including a considerable unit cell volume expansion. Further increase of the deuterium amount has little influence on the lattice parameters. The sample was heated as of frame 12 and the decomposition of $MgPd_2D_{\approx1}$ started at about 413 K at frame 17. The sample releases deuterium to a composition of $MgPd_2D0.17(1)$ at temperatures up to 437 K (frames $19 - 21$). High temperatures might inhibit full deuterium occupation, however, no complete decomposition to the hydrogen-free intermetallic phase could be observed. The deuteride with a nearly full occupation started to reform during the cooling process at about 413 K (frame 22). The reaction temperatures are lower than the DSC experiment, because of significantly smaller heating and cooling rates. The D–Mg, D–Pd, and D–D distances of $MgPd_2D_{\approx1}$ stay nearly constant during the whole in situ experiment (Fig. 11.4.8).

In a further *in situ* experiment at 10.0(1) MPa deuterium pressure and temperatures up to 450 K, deuterium release could be suppressed (see Figures S41 and S42, Supporting Information). This observation is in accordance with *in situ* DSC experiments of $MgPd_2$ at 5.0 MPa hydrogen pressure, where the endothermic signal of the decomposition shifts to a higher temperature (456 K).

11.4.5. Crystal chemical discussion

The structure types discussed herein, and their relation to each other, have been extensively examined before [23,24,28]. $MgPd_2H_x$ is the first hydride crystallizing in a filled Co_2Si type. It can be classified together with other $PbCl_2$ type family members in a structure map after Jeitschko [23,24] (Fig. 11.4.9), which groups compounds according to their axial ratios a/c and $(a+c)/b$. The binary hydrides MH_2 (M = Ca [29], Sr [29], Ba [30], Eu [31], and Yb [32]) with $a/c = 0.85–0.88$ crystallize in the $PbCl_2$ type [$PbCl_2$ ratios: $a/c = 0.843$, $(a+c)/b = 3.68$] [33]. Ternary hydrides like M_2PH (M = Rb [34] and Cs [35]) crystallize in a filled anti-$PbCl_2$ type, known as filled Co_2P type [Co_2P ratios: $a/c = 0.856$, $(a+c)/b = 3.49$] [36], with an axial ratio $a/c = 0.8–0.82$. $MgPd_2$ and Pd_2Zn crystallize like other MPd_2 (M = Al [9], Mn [37], Ga [9], In [9], Sn [38], and Tl[2]) also in an anti-$PbCl_2$ type, but they are grouped with an axial a/c ratio of 0.65–0.71 to the Co_2Si type [Co_2Si ratios: $a/c = 0.692$, $(a+c)/b = 3.22$] [39].

Hydrogenation of $MgPd_2$ leads to a decrease in a/c ratio and an increase in the $(a+c)/b$ ratio due to the before mentioned dominating increase in c. CeNiSnH [13], TbNiSnD [11], and CePdSnD [12] with filled TiNiSi structure type and NdNiSnD with a filled superstructure of TiNiSi type (space group $Pna2_1$) [40] exhibit the same behavior, but with different kind of anisotropic volume increase. Lattice parameters a and b decrease, while c increases much more upon hydrogenation [12]. Compounds in TiNiSi type have a relatively large a/c ratio [TiNiSi ratios: $a/c = 0.876$, $(a+c)/b = 3.59$] [39]. The binary hydrides in $PbCl_2$ type have a shorter b axis resulting in a larger $(a+c)/b$ ratio compared to the hydrides crystallizing in the two anti-$PbCl_2$ types or rather TiNiSi type. Most TiNiSi type compounds do not incorporate hydrogen without a structural change, but form hexagonal filled ZrBeSi type hydrides with different axial ratios. To complete the discussion of the hydrides of TiNiSi type compounds, those filled ZrBeSi type hydrides are surveyed hereafter. During the hydrogenation pro-
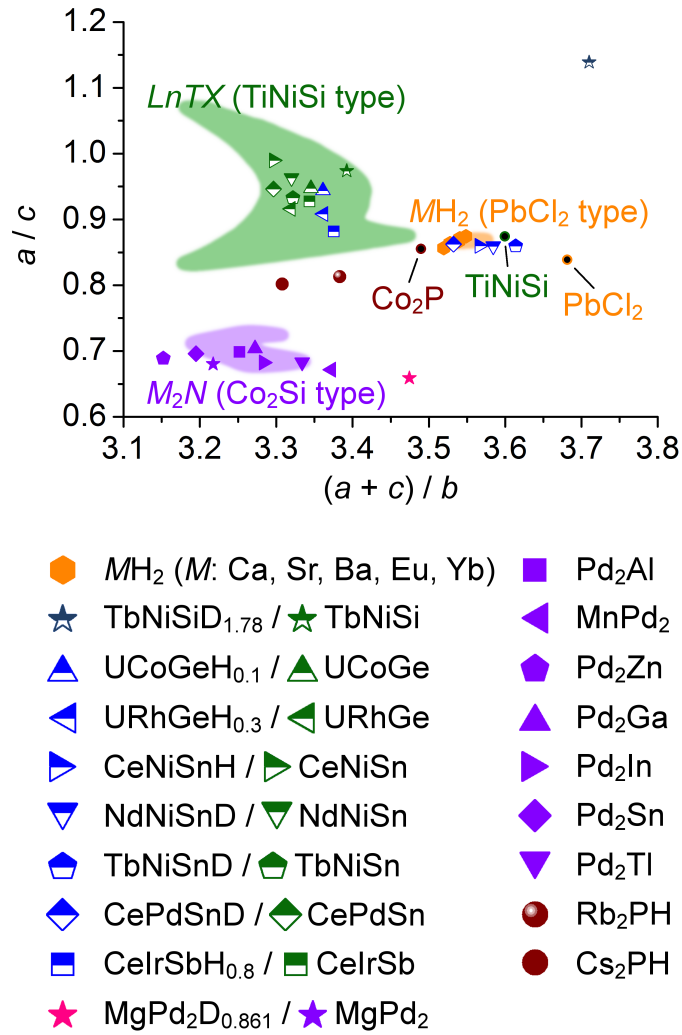
Figure 11.4.9.: Structure map after Jeitschko [23,24] with PbCl$_2$ type compounds focused on hydrides and MPd$_2$ compounds. Colored areas are redrawn [24] and compounds are ordered according to their axial ratios a/c and $(a+c)/b$. Hydrides with half-filled blue markers crystallize in filled TiNiSi type, with brown spheres in filled Co$_2$P type and with pink star in MgPd$_2$H type.

cess of CeNiSn, CeNiSnH$_1$, with filled TiNiSi type, is an intermediate of the formation of CeNiSnH$_{1.8}$ crystallizing in the filled hexagonal ZrBeSi type [13]. The maximum hydrogen amount for this type was found in LaNiSnD$_2$ (filled ZrBeSi type) with one type of [Ln$_3$Ni] tetrahedra completely occupied by hydrogen [41].

In addition to hydrides of ternary stannides, silicides form hydrides like UTSiH$_x$ (T = Co, Ni, Pd) with filled TiNiSi type (x $\approx$ 0.1) or hexagonal ZrBeSi type (x $\approx$ 1) as well [42,43]. TbNiSiD$_{1.78}$ seems to be an outlier because of very different axial ratios (see Fig. 11.4.9). Therefore, a description of a filled TiNiSi type is not recommendable. TbNiSiD$_{1.78}$ crystallizes under normal conditions in a filled ZrBeSi type [44], but shows an orthorhombic distortion below 100 K [45]. Orthogonalized lattice parameters of the hexagonal filled ZrBeSi type have similar axial ratios and would be next to TbNiSiD$_{1.78}$ with a/c ratio larger than 1.0 in Fig. 11.4.9. There are some more germanide and antimonide hydrides in filled TiNiSi type structure, e. g., UFeGeH$_{0.3}$ [46], UCoGeH$_{0.1}$ [47], URhGeH$_{0.3}$ [48], UPdGeH$_{0.1}$ [48], UIrGeH$_{0.1}$ [48], CeRhSbH$_{0.2}$ [49], and CeIrSbH$_{0.8}$ [50], however, they incor-

porate only a small hydrogen amount and two of them switch to the filled ZrBeSi type through a phase transition by higher hydrogen uptake (UFeGeH$_{1.7}$ [46] and UNiGeH$_{0.3-1.2}$ [51]). The hydrides CeNiGeH$_{1.6}$ [52], TbNiGeD$_{1.8}$ [53] and CeAuAlH$_{1.4}$ [54], that crystallize in filled ZrBeSi type, and CeCuGeH crystallizing in a threefold superstructure of the ZrBeSi type [52], are mentioned here for the sake of completeness.

11.5. Conclusions

MgPd$_2$ reversibly takes up hydrogen with 6.8 % volume increase. Lattice parameters change anisotropically upon hydrogenation. Pd$_2$Zn does not show any reaction with hydrogen. The crystal structures of MgPd$_2$D$_{0.861(6)}$ and MgPd$_2$D$_{0.97(1)}$ were determined by neutron powder diffraction data and may be described as a filled Co$_2$Si type (MgPd$_2$H type). Deuterium atoms occupy [MgPd$_5$] octahedral sites, which are less distorted in the hydride (deuteride) than in the hydrogen-free intermetallic compound. Quantum-mechanical calculations support the structure models and reaction enthalpies explain the hydrogenation properties of MgPd$_2$ (-152 meV mol^{-1}) and Pd$_2$Zn (+64 meV mol^{-1}). The reversible hydrogen uptake of MgPd$_2$ was studied by *in situ* thermal analysis (DSC) and *in situ* neutron powder diffraction under various temperatures and hydrogen (deuterium) pressures. The hydrogenation is reversible with faster kinetics during hydrogenation and slower during dehydrogenation. MgPd$_2$H$_{\approx 0.2}$ and MgPd$_2$H$_{\approx 1}$ are the first metal hydrides in filled Co$_2$Si type structure. Although hydrogen occupies different positions, they show a similar change of axial ratios [diagram after Jeitschko, plot of a/c vs. $(a+c)/b$] as TiNiSi type compounds upon hydrogenation.

11.6. Experimental section

The binary compounds MPd$_2$ (M = Mg, Zn) were synthesized from the elements with small amounts of iodine as mineralizing agent. Stoichiometric amounts of the elements palladium (powder, 99.9 %, $\leq$ 60 μm, chemPUR and 99.95 %, $\leq$ 150 μm, Goodfellow), magnesium (powder, 99.8 %, abcr, in an argon atmosphere), zinc (powder, > 98 %, $\leq$ 63 μm, Carl Roth) and 1-3 small crystals of iodine (resublimed, Merck) in silica glass ampoules sealed under vacuum. MgPd$_2$ was synthesized as described in the literature [4], though, with 5 % excess of magnesium and different annealing conditions (868 K for 10 d, 23.8 K h^{-1} heating rate). Samples of MgPd$_2$ typically contains 0.5-2 wt % MgO. Pd$_2$Zn was annealed at 1423 K for 18 h (100 K h^{-1} heating rate) and afterwards at 723 K for 10 d. All samples were quenched in water after annealing. The products were ground in air and iodine was dissolved in half-saturated aqueous potassium iodide solution. All binary intermetallic compounds were checked by chemical analysis performed with an EDX INCA SYSTEM from Oxford Instruments mounted on a Zeiss LEO 1530 scanning electron microscope with an acceleration voltage of 20 kV and a working distance of 15 mm.

For *ex situ* deuteration, the powdered MgPd$_2$ were placed in hydrogen resistant Inconel (Böhler L718, nickel chromium alloy) crucibles in an autoclave made from the same alloy and charged with deuterium (99.8 %, Air Liquide). The sample was weighted before and after deuteration for gravimetric deuterium determination. MgPd$_2$ samples for *in situ* investigations were placed in single crystal sapphire cell with a polymer seal (NBR flat seal with 65 shore, 17 mm outer diameter, 9 mm inner diameter, 2 mm thickness, IDT-Flachdichtungen, Germany) [17] and charged with deuterium pressure or set under vacuum. These samples were heated with a contactless laser heating system.

Laboratory XRPD data were collected using either a Huber G670 diffractometer with Guinier geometry at $T = 297(2)$ K with Mo-K$_{\alpha 1}$ radiation (flat transmission sample with Apiezon® grease between

two Kapton®️ foils) or a STOE STADI-P diffractometer in Debye-Scherrer setup at $T = 296(2)$ K with Cu-K$_{\alpha 1}$ radiation (glass capillary, 0.3 mm in diameter). Neutron powder diffraction measurements (NPD) were carried out at the Institut Laue-Langevin (ILL) in Grenoble, France at the high-flux powder diffractometer D20 in high-resolution mode in the range $3° \leq 2\theta \leq 150°$ and a total data collection time of 5 and 20 min [doi: 10.5291/ILL-DATA.5–24–576, NUMORS 959239 (MgPd$_2$) and 959583 (MgPd$_2$D$_{0.97(1)}$) were used for refinement] and at Paul Scherrer Instiut (PSI) in Villigen, Switzerland at the High-Resolution Powder Diffractometer for Thermal Neutrons (HRPT) in High Intensity (HI) mode [55]. Samples were enclosed in thin-walled vanadium cylinders (6 mm outer diameter). *In situ* neutron powder diffraction were taken at diffractometer D20 under various deuterium pressures (isotopic purity, 99.8 %) with a time resolution of 2 min per pattern (doi: 10.5291/ILL-DATA.5–24–576, NUMORS 959282 to 959582 and 959635 to 959667 were used for refinement, see Supporting Information). Ten patterns were binned to one frame for Rietveld refinement. The sample was placed inside a single crystal sapphire based gas pressure cell especially designed for *in situ* neutron powder diffraction with a gas pressure controller and contactless laser heating system [16]. The wavelengths were determined from measurements of silicon standard (NIST640b). Crystal structures were refined using the program FullProf [19] or TOPAS [56].

Further details of the crystal structures investigations may be obtained from the Fachinformationszentrum Karlsruhe, 76344 Eggenstein-Leopoldshafen, Germany (Fax: +49-7247-808-666; E-Mail: crysdata@fiz-karlsruhe.de, http://www.fiz-karlsruhe.de/request for deposited data.html) on quoting the depository numbers CSD-433791 (MgPd$_2$D$_{0.97(1)}$), CSD-433792 (MgPd$_2$D$_{0.861(6)}$), and CSD-433793 (Pd$_2$Zn).

Differential scanning calorimetry (DSC) was performed *in situ* under a starting hydrogen pressure of 5.0 MPa and temperatures up to 703 K on a Q1000 DSC (TA Instruments) equipped with a gas pressure chamber. About 25 mg of the powdered intermetallics were put in aluminium crucibles, which were closed with an aluminium lid. These were placed inside the pressure chamber, which was then purged several times with hydrogen gas before filling it to the desired hydrogen gas pressure. The samples were heated at a rate of 10 K min^{-1}, held at the final temperature for 2 h, and cooled back to 300 K. Two runs were performed in order to check for reversibility of thermal effects before the hydrogen pressure was released, the sample taken out and structural characterization undertaken by XRPD.

All calculations were performed with the Vienna *ab initio* simulation package (VASP) [57,58], using PAW's [59], fermi-smearing and the PBE-method [60]. The potentials were obtained from the VASP database and considered 1, 2, 12, and 10 valence electrons for H, Mg, Zn, and Pd, respectively. A cutoff energy of 600 eV was set for an automatically generated and Γ-centered k-mesh, which resolved the Brillouin zone to 0.03 Å^{-1} in structure optimizations and 0.01 Å^{-1} in density of states (DOS) calculations (e. g. 6 x 8 x 4 resp. 18 x 23 x 12 grid for MgPd$_2$). All structures were relaxed with full degrees of freedom, converging forces to 0.001 meV pm^{-1} and electronic energy to 0.01 meV. The reaction energies were calculated from total energies. The energy of molecular hydrogen was estimated from a H$_2$ molecule in a cubic box with a cell parameter of 34.5 Å, which corresponds to an ideal gas at 0.1 MPa and 293 K. The DOS were calculated on relaxed structures using the tetrahedron method with Blöchl corrections [61] and a resolution of 1 meV.

11.7. Acknowledgments

11.8. References for chapter 11

[1]   E. A. Wood, V. B. Compton, Laves-phase compounds of alkaline earths and noble metals, Acta Crystallogr. 11 (1958) 429–433.

[2]   S. Bhan, K. Schubert, Über die Struktur von Phasen mit Kupfer Unterstruktur in einigen T-B Legierungen (T = Ni, Pd, Pt; B = Ga, In, Tl, Pb, Sb, Bi), J. Less-Common Met. 17 (1969) 73–90.

[3]   K. Schubert, H. L. Lukas, H. G. Meissner, S. Bhan, Zum Aufbau der Systeme Kobalt-Gallium, Palladium-Gallium, Palladium-Zinn und verwandter Legierungen, Z. Metallkd. 50 (1959) 534–540.

[4]   C. Wannek, B. Harbrecht, Structure and thermal stability of the new intermetallics $MgPd_2$, $MgPd_3$, and Mg_3Pd_5 and the kinetics of the iodine-catalyzed formation of $MgPd_2$, J. Solid State Chem. 159 (2001) 113–120.

[5]   C. Wannek, B. Harbrecht, Iodine-catalyzed production of noble metal-rich intermetallics: the Crystal Structures of $BePd_2$ and $BePd_3$, Z. Anorg. Allg. Chem. 628 (2002) 1597–1601.

[6]   O. Loebich Jr., W. Wopersnow, Zur Struktur der intermetallischen Verbindung $LiPd_2$, J. Less-Common Met. 63 (1979) 83–88.

[7]   C. Stanitski, J. Tanaka, Ternary hydrides of calcium and strontium with palladium, J. Solid State Chem. 4 (1972) 331–339.

[8]   H. Kohlmann, H. E. Fischer, K. Yvon, Europium palladium hydrides, Inorg. Chem. 40 (2001) 2608–2613.

[9]   H. Kohlmann, Hydrogenation of palladium rich compounds of aluminium, gallium and indium, J. Solid State Chem. 183 (2010) 367–372.

[10] A. Götze, J. M. Sander, H. Kohlmann, Crystal structures and hydrogenation properties of palladium-rich compounds with elements from groups 12-16, Z. Naturforsch. 71B (2016) 503–508.

[11] V. A. Yartys, R. V. Denys, O. Isnard, R. G. Delaplane, P. Svedlindh, K. H. J. Buschow, Crystal and magnetic structure of TbNiSnD studied by neutron powder diffraction, J. Magn. Magn. Mater. 311 (2007) 639–643.

[12] B. Chevalier, A. Wattiaux, J.-L. Bobet, The Doniach diagram and hydrogenation of the ternary compounds CePdIn and CePdSn, J. Phys.: Condens. Matter 18 (2006) 1743–1755.

[13] B. Chevalier, Pasturel M., J.-L. Bobet, J. Etourneau, O. Isnard, J. Sanchez Marcos, J. Rodriguez Fernandez, Magnetic ordering induced by the hydrogenation of the ternary stannide CeNiSn, J. Magn. Magn. Mater. 272-276 (2004) 576–578.

[14] H. Kohlmann, N. Kurtzemann, R. Weihrich, T. Hansen, *In situ* neutron powder diffraction on intermediate hydrides of $MgPd_3$ in a novel sapphire gas pressure cell, Z. Anorg. Allg. Chem. 635 (2009) 2399–2405.

[15] E. Füglein, A. Léon, High-pressure DSC, in: A. Léon (Ed.), Hydrogen Technology, Springer, Berlin, Heidelberg, 2008, pp. 501–521.

[16] T.C. Hansen, H. Kohlmann, Chemical reactions followed by *in situ* neutron powder diffraction, Z. Anorg. Allg. Chem. 640 (2014) 3044–3063.

[17] A. Götze, H. Auer, R. Finger, T. C. Hansen, H. Kohlmann, A sapphire single-crystal cell for *in situ* neutron powder diffraction of solid-gas reactions, Phys. B (2017) in press.

[18] H. H. Stadelmaier, W. K. Hardy, Ternäre Kohlenstofflegierungen von Palladium und Platin mit Magnesium, Aluminium, Zink, Gallium, Germanium, Kadmium, Indium, Zinn, Quecksilber, Thallium und Blei, Z. Metallkd. 52 (1961) 391–396.

[19] J. Rodríguez-Carvajal, FullProf: A Program for Rietveld refinement and pattern matching analysis, Insitut Laue-Langevin, Grenoble (France), 2012.

[20] H. Kohlmann, A. V. Skripov, A. V. Soloninin, T. J. Udovic, The anti-perovskite type hydride InPd$_3$H$_{0.89}$, J. Solid State Chem. 183 (2010) 2461–2465.

[21] A. Götze, T. C. Hansen, H. Kohlmann, The reversible hydrogenation of BiPd$_2$ followed by *in situ* methods and the crystal structure of PbPd$_3$D$_{0.13(1)}$, J. Alloys Compd. 731 (2018) 1001–1008.

[22] B. Chabot, H. F. Braun, K. Yvon, E. Parthé, Rhodium scandium disilicide with an ordered YZn$_3$-type structure, Acta Crystallogr. 37b (1981) 668–671.

[23] W. Jeitschko, The crystal structure of MoCoB and related compounds, Acta Cryst. B24 (1968) 930–934.

[24] W. Jeitschko, R. O. Altmeyer, Rh$_2$Sb with (anti-) PbCl$_2$-type structure, Z. Naturforsch. 45b (1990) 947–951.

[25] D.-H. Wu, H.-C. Wang, L.-T. Wei, R.-K. Pan, B.-Y. Tang, First-principles study of structural stability and elastic properties of MgPd$_3$ and its hydride, J. Magnesium Alloys 2 (2014) 165–174.

[26] E. Y. Zakharova, S. M. Kazakov, A. A. Isaeva, A. M. Abakumov, G. van Tendeloo, A. N. Kuznetsov, Pd$_5$InSe and Pd$_8$In$_2$Se - New metal-rich homological selenides with 2D palladium-indium fragments: synthesis, structure and bonding, J. Alloys Compd. 589 (2014) 48–55.

[27] A. Götze, S. Schmorl, A. N. Kuznetsov, H. Kohlmann, Vacancy ordering in Pd$_{11}$Bi$_2$Se$_2$ - crystal structure and properties, J. Alloys Compd. 735 (2018) 1914–1920.

[28] R.-D. Hoffmann, R. Pöttgen, AlB$_2$ -related intermetallic compounds – a comprehensive view based on group-subgroup relations, Z. Kristallogr. 216 (2001) 127–145.

[29] M. C. Verbraeken, E. Suard, J. T. S. Irvine, Structual and electrical properties of calcium and strontium hydrides, J. Mater. Chem. 19 (2009) 2766–2770.

[30] V. P. Ting, P. F. Henry, H. Kohlmann, C. C. Wilson, M. T. Weller, Structual isotope effects in metal hydrides and deuterides, Phys. Chem. Chem. Phys. 12 (2010) 2083–2088.

[31] H. Kohlmann, K. Yvon, The crystal structures of EuH$_2$ and EuLiH$_3$ by neutron powder diffraction, J. Alloys Compd. 299 (2000) L16-L20.

[32] P. Fischer, J. Schefer, K. Tichy, R. Bischof, E. Kaldis, Crystal structure of YbD$_2$ and its temperature dependence determined by neutron powder diffraction, J. Less-Common Met. 94 (1983) 151–155.

[33] M. Lumbreas, J. Protas, S. Jebbari, G. J. Dirksen, J. Schoonman, Structure and ionic conductivity of mixed lead halides PbCl$_{2x}$Br$_{2(1-x)}$. II, Solid State Ionics 20 (1986) 295–304.

[34] M. Somer, W. Carrillo Cabrera, K. Peters, H. G. von Schnering, Crystal structure of dirubidium hydrogenphosphide, Rb$_2$[PH], Z. Kristallogr. (New Cryst. Struct.) 212 (1997) 299.

[35] H. G. von Schnering, M. Somer, K. Peters, W. Carrillo Cabrera, Y. Grin, Crystal structure of dicaesium hydrogenphosphide, Cs$_2$[PH], Z. Kristallogr. (New Cryst. Struct.) 216 (2001) 42.

[36] R. Skala, M. Drabek, The Crystal structure of Co$_2$P from X-ray powder diffraction data and its mineralogical applications, Vest. Cesk. Geol. Ustavu 76 (2001) 209–216.

[37] G. Kadar, E. Krén, M. Marton, New antiferromagnetic intermetallic compound in the Mn-Pd system: MnPd$_2$, J. Phys. Chem. Solids 33 (1972) 212–215.

[38] K. Page, C. S. Schade, J. Zhang, P. J. Chupas, K. W. Chapman, T. Proffen, A. K. Cheetham, R. Seshadri, Preparation and characterization of Pd$_2$Sn nanoparticles, Mater. Res. Bull. 42 (2007) 1969–1975.

[39] G. A. Landrum, R.-D. Hoffmann, J. Evers, H. Boysen, The TiNiSi family of compounds: structure and bonding, Inorg. Chem. 37 (1998) 5754–5763.

[40] V. A. Yartys, T. Olavesen, B. C. Hauback, H. Fjellvåg, Orthorhombic NdNiSnD with filled TiNiSi-type structure, J. Alloys Compd. 336 (2002) 181–186.

[41] V. A. Yartys, T. Olavesen, B. C. Hauback, H. Fjellvåg, H. W. Brinks, Hexagonal LaNiSnD$_2$ with a filled ZrBeSi-type structure, J. Alloys Compd. 330-332 (2002) 141–145.

[42] A. V. Kolomiets, L. Havela, A. V. Andreev, F. Wastin, J. Šebek, M. Maryško, Effect of hydrogenation on crystal structure and magnetic properties of UTSi (T = Pd, Ni) intermetallics, Phys. Rev. B 66 (2002) 144423.

[43] K. Miliyanchuk, A. V. Kolomiets, L. Havela, A. V. Andreev, UCoSiH$_{0.7}$: new representative of UTSiHx hydrides, J. Alloys Compd. 383 (2004) 103–107.

[44] H. W. Brinks, V. A. Yartys, B. C. Hauback, Crystal structure of TbNiSiD$_{1.78}$, J. Alloys Compd. 322 (2001) 106–165.

[45] H. W. Brinks, V. A. Yartys, B. C. Hauback, H. Fjellvåg, B. Ouladdiaf, The magnetic structure of TbNiSiD$_{1.78}$, J. Alloys Compd. 340 (2002) 62–66.

[46] A. M. Adamska, L. Havela, A. Błachowski, K. Ruebnbauer, J. C. Waerenborgh, N.-T. H. Kim-Ngan, A. V. Kolomiets, Hydrogen absorption and ^{57}Fe Mössbauer effect in UFeGe, J. Alloys Compd. 509 (2011) 5453–5459.

[47] A. M. Adamska, L. Havela, S. Daniš, Hydrogen induced changes in the crystal structure and magnetic properties of UCoGe, J. Phys.: Condens. Matter 23 (2011) 476002.

[48] A. M. Adamska, L. Havela, Y. Skourski, A. V. Andreev, Variations of structure and magnetic properties in UTGe hydrides (T = late transition metal), J. Alloys Compd. 515 (2012) 171–179.

[49] B. Chevalier, R. Decourt, B. Heying, F. M. Schappacher, U. C. Rodewald, R.-D. Hoffmann, R. Pöttgen, R. Eger, A. Simon, Inducing magnetism in the Kondo semiconductor CeRhSb through hydrogenation: antiferromagnetic behavior of the new hydride CeRhSbH$_{0.2}$, Chem. Mater. 19 (2007) 28–35.

[50] E. Gaudin, B. Chevalier, W. Hermes, U. C. Rodewald, R. Pöttgen, Structure, magnetic and electrical properties of CeIrSb and its hydride CeIrSbH$_{0.8}$, J. Solid State Chem. 182 (2009) 1827–1832.

[51] A. M. Adamska, L. Havela, J. Procházka, A. V. Andreev, Y. Skourski, Effects of hydrogenation on magnetism of UNiGe, J. Magn. Magn. Mater. 323 (2011) 3217–3222.

[52] B. Chevalier, M. Pasturel, J.-L. Bobet, F. Weill, J. Etourneau, The new hydrides CeNiGeH$_{1.6}$ and CeCuGeH$_{1.0}$ crystallizing in the derivative hexagonal ZrBeSi-type structure, J. Solid State Chem. 177 (2004) 752–759.

[53] H. W. Brinks, Synthesis and crystal structure of TbNiGeD$_{1.8}$, J. Alloys Compd. 379 (2004) 72–76.

[54] B. Chevalier, J.-L. Bobet, M. L. Kahn, F. Weill, J. Etourneau, Structural and magnetic properties of the new hydride CeAuAlH$_{1.4(1)}$, J. Alloys Compd. 334 (2002) 20–26.

[55] P. Fischer, G. Frey, M. Koch, M. Könnecke, V. Pomjakushin, J. Schefer, R. Thut, N. Schlumpf, R. Bürge, U. Greuter, S. Bondt, E. Berruyer, High-resolution powder diffractometer HRPT for thermal neutrons at SINQ, Phys. B 276-278 (2000) 146–147.

[56] TOPAS, Bruker AXS.

[57] G. Kresse, J. Furthmüller, Efficient iterative schemes for *ab initio* total-energy calculations using a plane-wave basis set, Phys. Rev. B 54 (1996) 11169–11186.

[58] G. Kresse, J. Furthmüller, Efficiency of ab-initio total energy calculations for metals and semiconductors using a plane-wave basis set, Comput. Mater. Sci. 6 (1996) 15–50.

[59] P. E. Blöchl, Projector augmented-wave method, Phys. Rev. B 50 (1994) 17953–17979.

[60] J. P. Perdew, J. Burke, M. Ernzerhof, Generalized gradient approximation made simple, Phy. Rev. Lett. 77 (1996) 3865–3868.

[61] P. E. Blöchl, O. Jepsen, O. K. Andersen, Improved tetrahedron method for Brillouin-zone integrations, Phys. Rev. B 1994, 49, 16223-16233.

11.9. Supporting Information

Supporting Information (see footnote on the first page of this article): Rietveld plots and refinements of the crystal structures of MgPd$_2$ and Pd$_2$Zn before and after hydrogenation based on XRPD (S1 - S5), refinement of the crystal structure of MgPd$_2$ based on neutron powder diffraction (S6), calculated energies (S7) and structural parameters (S8) for hydrogenation of MPd$_2$, crystal structure and DOS of Pd$_2$Zn and hypothetical Pd$_2$ZnH (S9, S10), Rietveld plots and refined structural parameters of MgPd$_2$D$_x$ of all frames of *in situ* neutron diffraction experiment (S11 - S40), *in situ* neutron powder diffraction data and deuterium occupation of MgPd$_2$D$_x$ at 10.0 MPa deuterium pressure (S41, S42).

In Situ Hydrogenation and Crystal Chemistry Studies of Co$_2$Si type compounds MgPd$_2$ and Pd$_2$Zn

André Götze[a], Nicolas Zapp[a], Andrea Peretzki[a], Vladimir Pomjakushin[b], Thomas C. Hansen[c] and Holger Kohlmann*[a]

Contents

X-ray powder diffraction

Figure S1. Rietveld refinement of the crystal structure of MgPd$_2$ at 297(2) K based on X-ray powder diffraction (Huber G670, MoK$_{\alpha1}$ radiation), using Topas[1].

Table S1. Refined crystal structures of MgPd$_2$ and residual values of the refinement based on XRPD (Fig. S1).

atom	Mg	Pd1	Pd2
Wyckoff site	4c	4c	4c
x	0.317(2)	0.3333(5)	0.4427(6)
y	¼	¼	¼
z	0.0919(9)	0.4270(2)	0.7658(2)
B_{iso} / Å^2	-0.1(2)	1.07(5)	1.50(7)

space group $Pnma$, a = 5.4194(3) Å, b = 4.1599(2) Å, c = 7.9661(5) Å, V = 179.59(2) Å^3

additional phase: MgO (2.0(4) %)

R_p = 0.027, R_{wp} = 0.039, R_{Bragg} = 0.010, χ^2 = 1.2
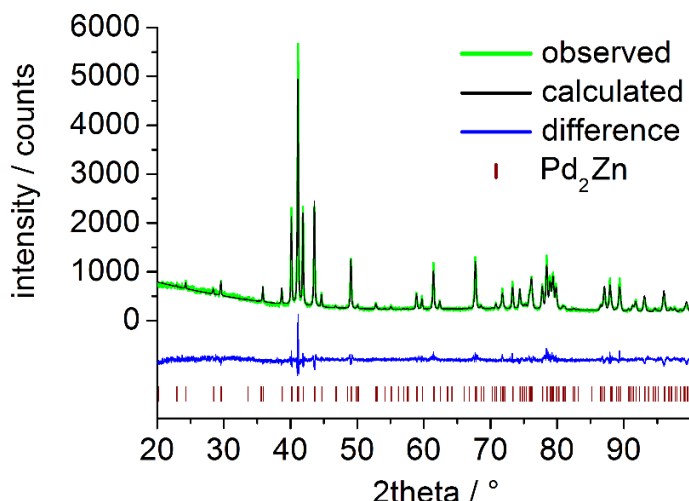
Figure S2. Rietveld refinement of the crystal structure of Pd$_2$Zn at 296(2) K based on X-ray powder diffraction (STOE STADI-P, CuK$_{\alpha1}$ radiation, 180 s exposure time, 6 summed patterns, preferred orientation with March-Dollase model[2] in direction 001 and 010), using FullProf[3].

Table S2. Refined crystal structures of Pd$_2$Zn and residual values of the refinement based on XRPD (Fig. S2).

atom	Mg	Pd1	Pd2
Wyckoff site	4c	4c	4c
x	0.3188(8)	0.3258(4)	0.4593(4)
y	¼	¼	¼
z	0.0983(4)	0.4296(2)	0.7753(2)
B_{iso} / Å^2	-4.38(7)[a]	-4.61(4)[a]	-4.74(4)[a]

space group $Pnma$, a = 5.3291(1) Å, b = 4.14427(9) Å, c = 7.7366(2) Å, V = 170.866(7) Å^3

R_p = 0.059, R_{wp} = 0.075, R_{Bragg} = 0.036, χ^2 = 2.22

[a] Negative thermal displacement parameters are not unusual in X-ray powder diffraction due to absorption and surface roughness effects.
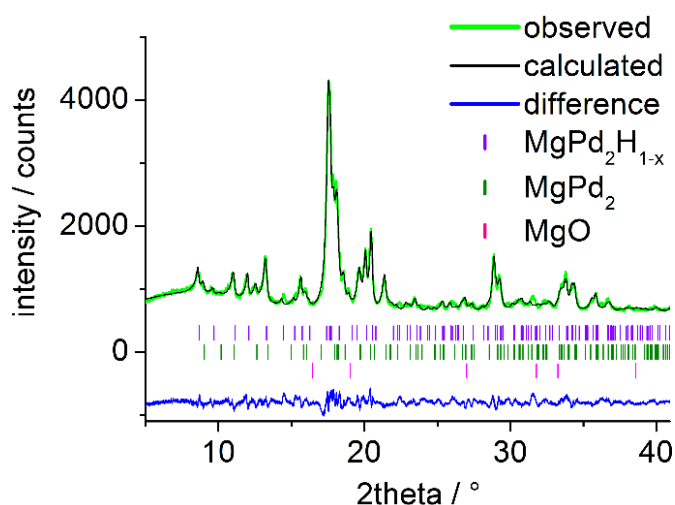
Figure S3. Rietveld refinement of the crystal structure of $MgPd_2H_x$ and $MgPd_2$ after DSC (2.5 MPa H_2, $T_{max} = 363$ K) at 297(2) K based on X-ray powder diffraction (Huber G670, MoK$_{\alpha1}$ radiation), using Topas[1].

Table S3. Refined crystal structures of $MgPd_2H_x$ and $MgPd_2$ (in italics) after DSC (2.5 MPa H_2, $T_{max} = 363$ K) and residual values of the refinement based on XRPD (Fig. S2).

atom	Mg	Pd1	Pd2
Wyckoff site	4c	4c	4c
x	0.426(3)	0.3812(7)	0.3978(11)
	0.335(4)	*0.3440(11)*	*0.4347(12)*
y	¼	¼	¼
z	0.092(2)	0.4229(5)	0.7660(4)
	0.076(3)	*0.4280(6)*	*0.7622(6)*
B_{iso} / Å^2	1.00(7)	B_{iso}(Mg)	B_{iso}(Mg)
	2.3(1)		

space group *Pnma*

$MgPd_2H_x$ (46.2(5) %): $a = 5.6462(6)$ Å, $b = 4.0504(4)$ Å, $c = 8.3844(9)$ Å, $V = 191.75(4)$ Å^3, $R_{Bragg} = 0.015$)

$MgPd_2$ (49.6(5) %): $a = 5.4418(8)$ Å, $b = 4.1339(6)$ Å, $c = 7.9891(11)$ Å, $V = 179.72(4)$ Å^3, $R_{Bragg} = 0.014$)

additional phase: MgO (4.2(4) %)

$R_p = 0.035$, $R_{wp} = 0.046$, $\chi^2 = 2.0$
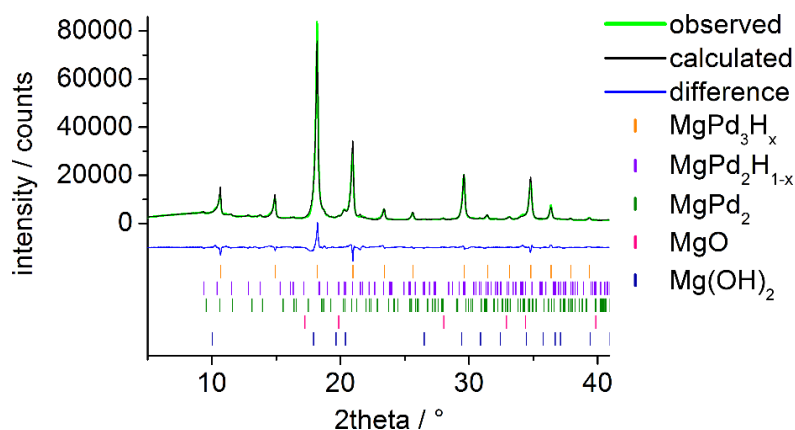
Figure S4. Rietveld refinement of the crystal structure of $MgPd_3H_x$ (filled AuCu$_3$ type) and $MgPd_2H_x$ after DSC (2.5 MPa H_2, $T_{max} = 703$ K, four cycles) at 297(2) K based on X-ray powder diffraction (Huber G670, MoK$_{\alpha1}$ radiation), using Topas[1].

Table S4. Refined crystal structure of $MgPd_3H_x$ (filled AuCu$_3$ type) after DSC (2.5 MPa H_2, $T_{max} = 703$ K) and residual values of the refinement based on XRPD (Fig. S4).

atom	Mg	Pd
Wyckoff site	1a	3c
x	0	½
y	0	½
z	0	0
B_{iso} / Å^2	0.24(10)	1.18(3)

space group $Pm\bar{3}m$

$MgPd_3H_x$ (70.0(6) %): $a = 3.985(1)$ Å, $V = 63.265(7)$ Å^3, $R_{Bragg} = 0.033$)

additional phases: $MgPd_2H_x$ (13.8(6) %, $a = 5.499(2)$ Å, $b = 4.124(1)$ Å, $c = 8.202(3)$ Å,), $MgPd_2$ 7.0(4) %, a = 5.404(4) Å, b = 4.105(3) Å, c = 8.009(6) Å), MgO (4.3(3) %), Mg(OH)$_2$ (4.9(3) %)

$R_p = 0.060$, $R_{wp} = 0.082$, $\chi^2 = 25.6$
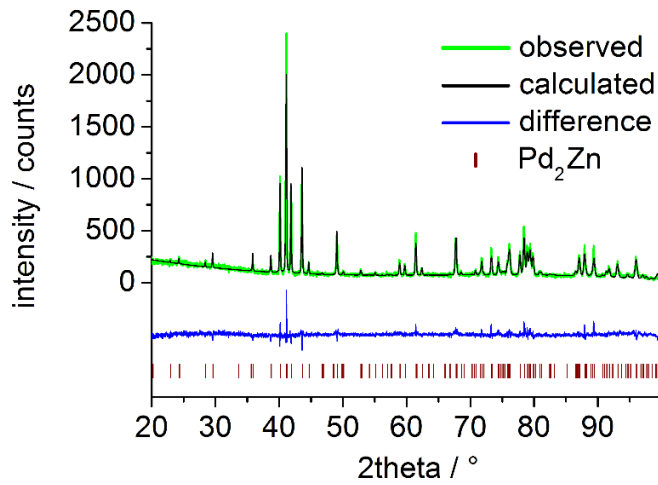
Figure S5. Rietveld refinement of the crystal structure of Pd₂Zn after DSC (5.0 MPa H₂, T_{max} = 703 K) at 296(2) K based on X-ray powder diffraction (STOE STADI-P, CuK$_{α1}$ radiation, 180 s exposure time, 2 summed patterns, preferred orientation with March-Dollase model[2] in direction 001 and 010), using Fullprof[3].

Table S5. Refined crystal structures of Pd₂Zn after DSC (50 bar H₂, T_{max} = 430 °C) and residual values of the refinement based on XRPD (Fig. S5).

atom	Mg	Pd1	Pd2
Wyckoff site	4*c*	4*c*	4*c*
x	0.3199(9)	0.3274(5)	0.4599(5)
y	¼	¼	¼
z	0.1006(5)	0.4285(3)	0.7778(3)
B_{iso} / Å²	-3.72(8)[a]	-3.87(5)[a]	-3.82(5)[a]

space group *Pnma*, *a* = 5.32927(11) Å, *b* = 4.14397(7) Å, *c* = 7.7367(1) Å, *V* = 170.860(5) Å³

R_p = 0.091, R_{wp} = 0.122, R_{Bragg} = 0.059, $χ^2$ = 1.82

[a] Negative thermal displacement parameters are not unusual in X-ray powder diffraction due to absorption and surface roughness effects.

Ex-situ neutron powder diffraction
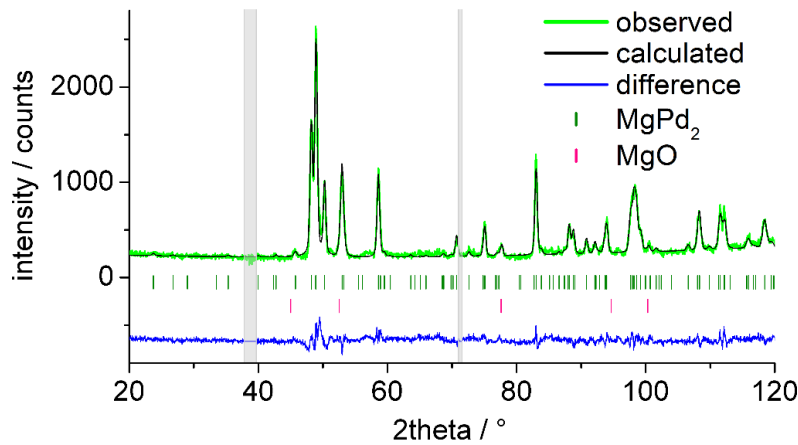
Figure S6. Rietveld refinement of MgPd₂ at air in single crystal sapphire cell based on neutron powder diffraction data (λ = 1.86786(3) Å, D20, ILL, Grenoble, NUMOR 959239), using FullProf[3].

Table S6. Refined crystal structures of MgPd₂ and residual values of the refinement based on NPD (Fig. S6).

atom	Mg	Pd1	Pd2
Wyckoff site	4*c*	4*c*	4*c*
x	0.316(2)	0.340(2)	0.437(1)
y	¼	¼	¼
z	0.1079(9)	0.4293(8)	0.7583(9)
B_{iso} / Å²	3.9(3)	1.5(2)	1.2(2)

space group *Pnma*, *a* = 5.4374(3) Å, *b* = 4.1747(3) Å, *c* = 7.9942(4) Å, *V* = 181.47(2) Å³

additional phase: MgO (0.48(4) %)

R_p = 0.069, R_{wp} = 0.090, R_{Bragg} = 0.108, $χ^2$ = 2.67

Quantum chemical calculations

Table S7. Calculated energies and reaction enthalpies per formula units of $M\text{Pd}_2 + \frac{1}{2}\,H_2 \rightarrow M\text{Pd}_2H$.

compound	M = Mg	M = Zn
H_2	-6.696 eV	
$M\text{Pd}_2$	-12.420 eV	-10.464 eV
$M\text{Pd}_2H$	-15.920 eV	-13.750 eV
	-0.152 eV	+0.064 eV

Table S8. Comparison of structural parameters of $M\text{Pd}_2$ and $M\text{Pd}_2H$ from diffraction experiment (exp) with those from calculation (calc).

parameter	MgPd$_2$	MgPd$_2$H	Pd$_2$Zn	Pd$_2$ZnH
a_{exp}	5.4374(3) Å[a]	5.6065(5) Å[b]	5.3291(1) Å[c]	-
a_{calc}	5.5282 Å	5.6843 Å	5.4114 Å	5.6058 Å
deviation of a	1.7 %	1.4 %	1.5 %	-
b_{exp}	4.1747(3) Å[a]	4.0691(3) Å[b]	4.14427(9) Å[c]	-
b_{calc}	4.2015 Å	4.0888 Å	4.2001 Å	4.0761 Å
deviation of b	0.6 %	0.5 %	1.3 %	-
c_{exp}	7.9942(4) Å[a]	8.5216(7) Å[b]	7.7366(2) Å[c]	-
c_{calc}	8.1475 Å	8.6749 Å	7.8556 Å	8.3590 Å
deviation of c	1.9 %	1.8 %	1.5 %	-
V_{exp}	181.47(2) Å³[a]	194.41(3) Å³[b]	170.866(7) Å³[c]	-
V_{calc}	189.24 Å³	201.62 Å³	178.55 Å³	191.00 Å³
deviation of V	4.3 %	3.7 %	4.5 %	-
$x(M)_{exp}$	0.316(2)[a]	0.3487(10)[b]	0.3188(8)[c]	-
$x(M)_{calc}$	0.3288	0.3538	0.3161	0.3397
$z(M)_{exp}$	0.1079(9)[a]	0.1003(8)[b]	0.0983(4)[c]	-
$z(M)_{calc}$	0.0984	0.1060	0.0996	0.1104
$x(\text{Pd1})_{exp}$	0.340(2)[a]	0.3653(8)[b]	0.3258(4)[c]	-
$x(\text{Pd1})_{calc}$	0.3391	0.3624	0.3285	0.3495
$z(\text{Pd1})_{exp}$	0.4293(8)[a]	0.4314(6)[b]	0.4296(2)[c]	-
$z(\text{Pd1})_{calc}$	0.4280	0.4269	0.4309	0.4323
$x(\text{Pd2})_{exp}$	0.437(1)[a]	0.3902(12)[b]	0.4593(4)[c]	-
$x(\text{Pd2})_{calc}$	0.4371	0.3894	0.4586	0.4159
$z(\text{Pd2})_{exp}$	0.7583(9)[a]	0.7754(7)[b]	0.7753(2)[c]	-
$z(\text{Pd2})_{calc}$	0.7655	0.7689	0.7760	0.7812
$x(\text{D})_{exp}$		0.6127(11)[b]		-
$x(\text{H})_{calc}$		0.6129		0.6183
$z(\text{D})_{exp}$		0.6098(6)[b]		-
$z(\text{H})_{calc}$		0.6119		0.6098

[a] Parameters of MgPd$_2$ yield from Rietveld refinement based on neutron powder diffraction (Table S6) [b] Parameters of MgPd$_2$D$_{0.97(1)}$ yield from Rietveld refinement based on neutron powder diffraction (Table 2) [c] Parameters of Pd$_2$Zn yield from Rietveld refinement based on XRPD (Table S2)
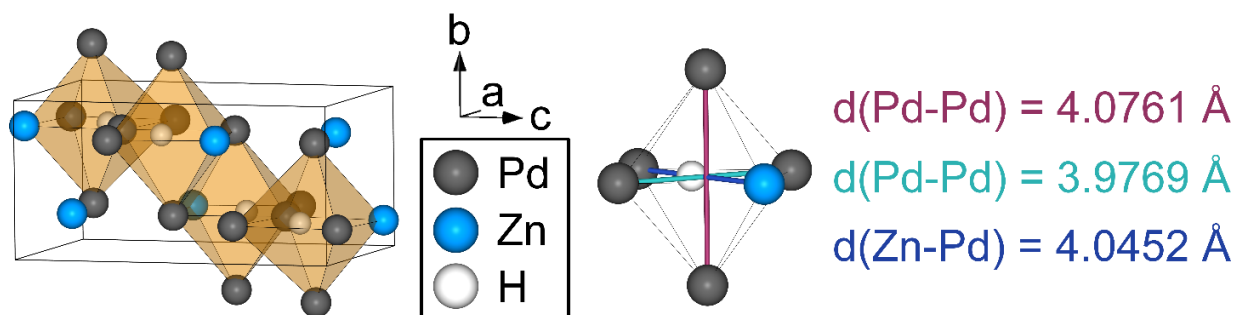
Figure S9. Crystal Structure (left) and coordination polyhedra of hydrogen (right) of hypothetical Pd₂ZnH based on quantum mechanical calculations.
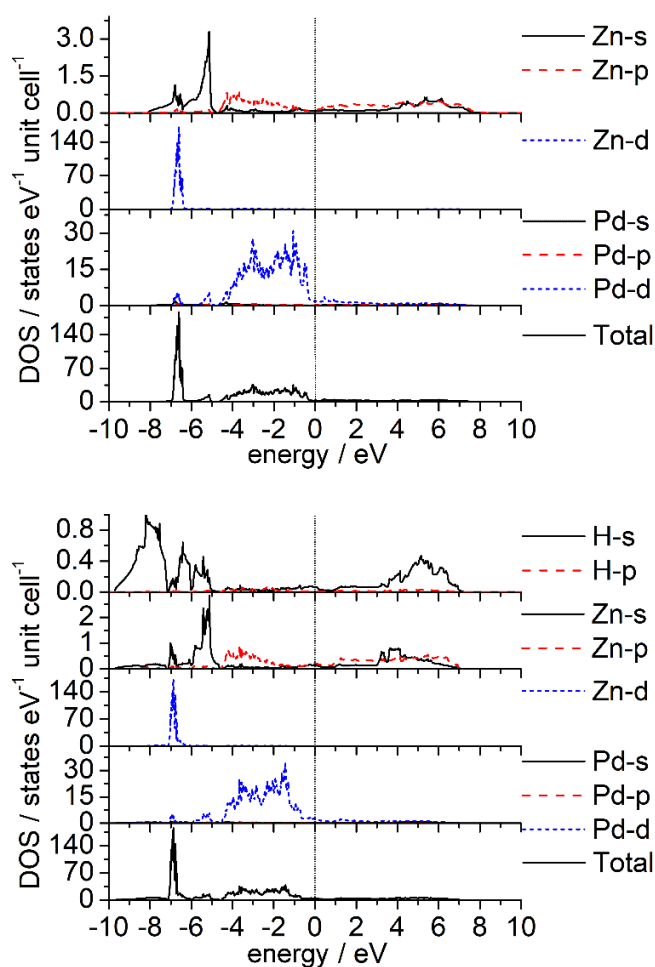
Figure S10. Density of states (DOS) of Pd₂Zn (top) and hypothetical Pd₂ZnH (bottom). The Fermi-level is set to zero. Note the different scales for the y axis.

In-situ neutron powder diffraction
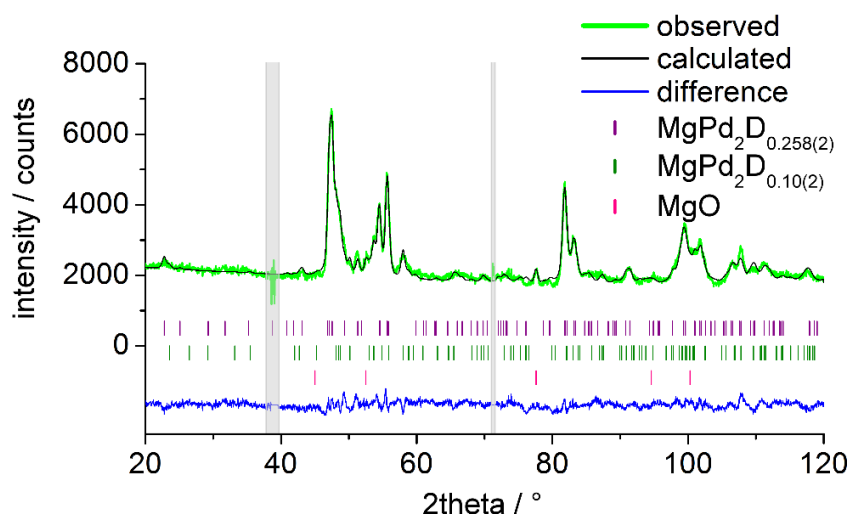
Figure S11. Rietveld refinement of frame 1 at 298(1) K in single crystal sapphire cell under 0.10(5) MPa D_2 pressure based on neutron powder diffraction data (λ = 1.86786(3) Å, D20, ILL, Grenoble, NUMORS 959282-959291), using FullProf[3].

Table S11. Refined crystal structures of $MgPd_2D_{0.258(2)}$ and $MgPd_2D_{0.10(2)}$ (in italics) of frame 1 (0.10(5) MPa D_2, 298(1) K) and residual values of the refinement based on NPD (Fig. S11).

atom	Mg	Pd1	Pd2	D
Wyckoff site	*4c*	*4c*	*4c*	*4c*
x	0.339(1)	0.3734(11)	0.401(1)	0.610(5)
	0.344(2)	*0.353(2)*	*0.432(2)*	*0.651[b]*
y	¼	¼	¼	¼
z	0.1215(6)	0.4240(6)	0.7611(6)	0.587(2)
	0.1278(10)	*0.4430(9)*	*0.7365(10)*	*0.576[b]*
SOF	1	1	1	0.258(2)
				0.10(2)

space group *Pnma*

$MgPd_2D_{0.258(2)}$ (67(1) %): a = 5.6059(7) Å, b = 4.0671(4) Å, c = 8.5096(10) Å, V = 194.02(4) Å³, B_{iso}(overall)[a] = -0.88(9) Å², R_{Bragg} = 0.112)

$MgPd_2D_{0.10(2)}$ (32.1(12) %): a = 5.4418(8) Å, b = 4.1339(6) Å, c = 7.9891(11) Å, V = 182.61(8) Å³, B_{iso}(overall)[b] = 0.2(2) Å², R_{Bragg} = 0.141)

additional phase: MgO (0.57(5) %)

R_p = 0.035, R_{wp} = 0.044, χ^2 = 4.3

[a] Displacement parameters are fixed to the values of refinement of $MgPd_2D_{0.97(1)}$ (see Table 2). [b] Positional and displacement parameters are fixed to the values of refinement of frame 4 (see Table S14).

Figure S12. Rietveld refinement of frame 2 at 297(1) K in single crystal sapphire cell under vacuum based on neutron powder diffraction data (λ = 1.86786(3) Å, D20, ILL, Grenoble, NUMORS 959292-959301), using FullProf[3].

Table S12. Refined crystal structures of $MgPd_2D_{0.222(2)}$ and $MgPd_2D_{0.14(2)}$ (in italics) of frame 2 (vacuum, 297(1) K) and residual values of the refinement based on NPD (Fig. S12).

atom	Mg	Pd1	Pd2	D
Wyckoff site	*4c*	*4c*	*4c*	*4c*
x	0.337(1)	0.377(1)	0.405(1)	0.614(6)
	0.341(1)	*0.3167(11)*	*0.4097(11)*	*0.651[b]*
y	¼	¼	¼	¼
z	0.1236(6)	0.4251(6)	0.7603(6)	0.589(2)
	0.0902(11)	*0.4296(8)*	*0.7880(9)*	*0.576[b]*
SOF	1	1	1	0.222(2)
				0.14(2)

space group *Pnma*

$MgPd_2D_{0.222(2)}$ (60(1) %): a = 5.5989(8) Å, b = 4.0652(5) Å, c = 8.4957(12) Å, V = 193.37(5) Å³, B_{iso}(overall)[a] = -0.72(11) Å², R_{Bragg} = 0.104)

$MgPd_2D_{0.14(2)}$ (40(1) %): a = 5.472(1) Å, b = 4.1246(8) Å, c = 8.087(2) Å, V = 182.50(7) Å³, B_{iso}(overall)[b] = 0.3(2) Å², R_{Bragg} = 0.113

additional phase: MgO (0.65(5) %)

R_p = 0.039, R_{wp} = 0.049, χ^2 = 5.0

[a] Displacement parameters are fixed to the values of refinement of $MgPd_2D_{0.97(1)}$ (see Table 2). [b] Positional and displacement parameters are fixed to the values of refinement of frame 4 (see Table S14).

Figure S13. Rietveld refinement of frame 3 at 297(1) K in single crystal sapphire cell under vacuum based on neutron powder diffraction data (λ = 1.86786(3) Å, D20, ILL, Grenoble, NUMORS 959302-959311), using FullProf[3].

Table S13. Refined crystal structures of $MgPd_2D_{0.204(6)}$ and $MgPd_2D_{0.05(1)}$ (in italics) of frame 3 (vacuum, 297(1) K) and residual values of the refinement based on NPD (Fig. S13).

atom	Mg	Pd1	Pd2	D
Wyckoff site	4c	4c	4c	4c
x	0.324(3)	0.390(3)	0.395(4)	0.64(1)
	0.3396(9)	*0.3228(7)*	*0.4205(6)*	*0.651[b]*
y	¼	¼	¼	¼
z	0.149(2)	0.437(2)	0.750(2)	0.547(7)
	0.1026(6)	*0.4257(5)*	*0.7692(6)*	*0.576[b]*
SOF	1	1	1	0.204(6)
				0.05(1)

space group *Pnma*

$MgPd_2D_{0.204(6)}$ (16.6(9) %): a = 5.578(3) Å, b = 4.070(1) Å, c = 8.492(3) Å,
V = 192.8(1) Å³, B_{iso}(overall)[a] = -0.9(3) Å², R_{Bragg} = 0.179)

$MgPd_2D_{0.05(1)}$ (83(2) %): a = 5.4592(6) Å, b = 4.1430(4) Å, c = 8.0535(7) Å,
V = 182.15(3) Å³, B_{iso}(overall)[b] = 0.21(8) Å², R_{Bragg} = 0.078)

additional phase: MgO (0.61(4) %)

R_p = 0.046, R_{wp} = 0.059, χ^2 = 5.7

[a] Displacement parameters are fixed to the values of refinement of $MgPd_2D_{0.97(1)}$ (see Table 2). [b] Positional and displacement parameters are fixed to the values of refinement of frame 4 (see Table S14).
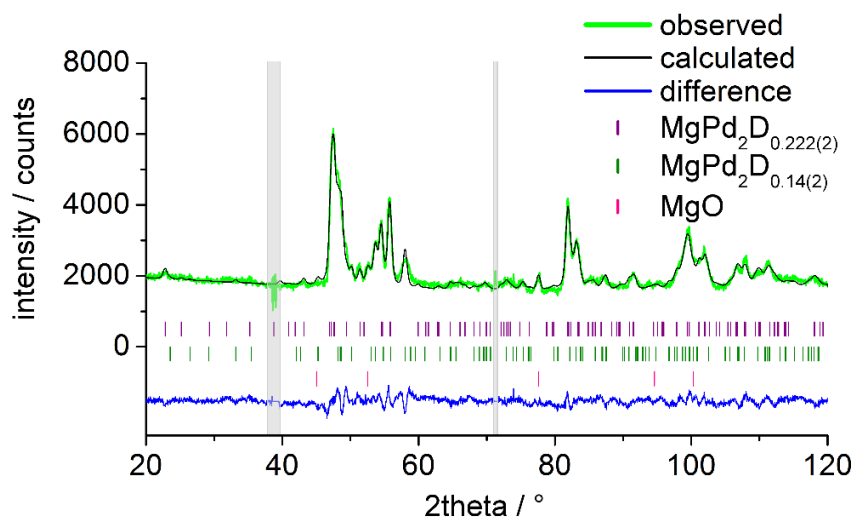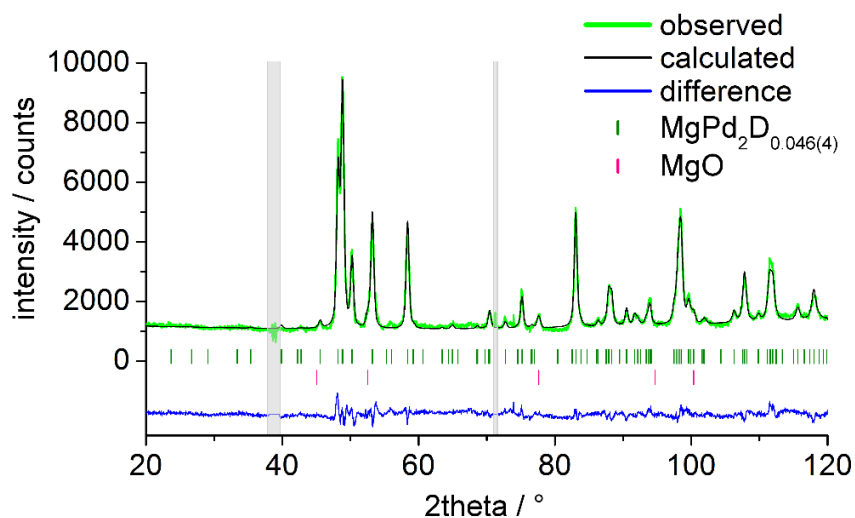
Figure S14. Rietveld refinement of frame 4 at 297(1) K in single crystal sapphire cell under vacuum based on neutron powder diffraction data (λ = 1.86786(3) Å, D20, ILL, Grenoble, NUMORS 959312-959321), using FullProf[3].

Table S14. Refined crystal structures of MgPd$_2$D$_{0.046(4)}$ of frame 4 (vacuum, 297(1) K) and residual values of the refinement based on NPD (Fig. S14).

atom	Mg	Pd1	Pd2	D
Wyckoff site	4c	4c	4c	4c
x	0.331(2)	0.330(2)	0.431(1)	0.651(11)
y	¼	¼	¼	¼
z	0.1018(7)	0.4287(8)	0.7634(11)	0.576(10)
B_{iso} / Å²	1.3(2)	0.8(1)	1.4(2)	4.797[a]
SOF	1	1	1	0.046(4)

space group *Pnma*

MgPd$_2$D$_{0.046(4)}$ (99(2) %): a = 5.4493(3) Å, b = 4.1559(2) Å, c = 8.0276(3) Å, V = 181.80(2) Å³, R_{Bragg} = 0.102)

additional phase: MgO (0.60(4) %)

R_p = 0.047, R_{wp} = 0.060, χ^2 = 5.3

[a] Displacement parameter of D is fixed to the value of refinement of MgPd$_2$D$_{0.97(1)}$ (see Table 2).
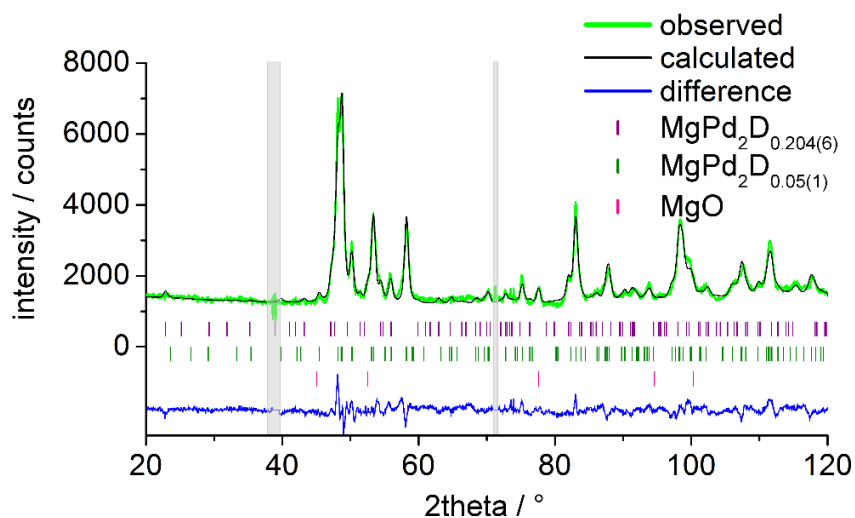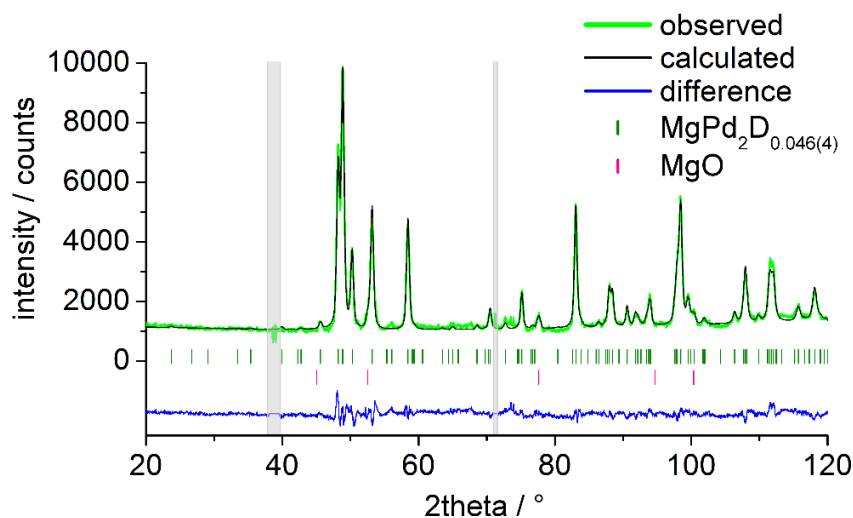
Figure S15. Rietveld refinement of frame 5 at 297(1) K in single crystal sapphire cell under vacuum based on neutron powder diffraction data (λ = 1.86786(3) Å, D20, ILL, Grenoble, NUMORS 959322-959331), using FullProf[3].

Table S15. Refined crystal structures of $MgPd_2D_{0.046(4)}$ of frame 5 (vacuum, 297(1) K) and residual values of the refinement based on NPD (Fig. S15).

atom	Mg	Pd1	Pd2	D
Wyckoff site	4c	4c	4c	4c
x	0.323(2)	0.337(1)	0.4336(11)	0.665(11)
y	¼	¼	¼	¼
z	0.1011(6)	0.4311(7)	0.7607(9)	0.579(9)
B_{iso} / Å²	1.6(2)	0.66(12)	1.4(2)	4.797[a]
SOF	1	1	1	0.046(4)

space group *Pnma*

$MgPd_2D_{0.046(4)}$ (99(2) %): a = 5.4461(3) Å, b = 4.1599(2) Å,

c = 8.0195(3) Å, V = 181.68(1) Å³, R_{Bragg} = 0.094)

additional phase: MgO (0.62(4) %)

R_p = 0.047, R_{wp} = 0.060, χ^2 = 5.4

[a] Displacement parameter of D is fixed to the value of refinement of $MgPd_2D_{0.97(1)}$ (see Table 2).

Figure S16. Rietveld refinement of frame 6 at 298(1) K in single crystal sapphire cell under D_2 pressure range from vacuum to 0.60(5) MPa based on neutron powder diffraction data ($\lambda = 1.86786(3)$ Å, D20, ILL, Grenoble, NUMORS 959332-959341), using FullProf[3].

Table S16. Refined crystal structures of $MgPd_2D_{0.032(4)}$ of frame 6 (0.3(3) MPa D_2, 298(1) K) and residual values of the refinement based on NPD (Fig. S16).

atom	Mg	Pd1	Pd2	D
Wyckoff site	$4c$	$4c$	$4c$	$4c$
x	0.324(2)	0.339(1)	0.433(1)	0.66(2)
y	¼	¼	¼	¼
z	0.1019(7)	0.4326(7)	0.7570(10)	0.575(1)
B_{iso} / Å²	1.6(2)	0.66(12)	1.4(2)	4.797[a]
SOF	1	1	1	0.032(4)

space group *Pnma*

$MgPd_2D_{0.032(4)}$ (99(2) %): $a = 5.4465(3)$ Å, $b = 4.1601(2)$ Å, $c = 8.0194(4)$ Å, $V = 181.70(2)$ Å³, $R_{Bragg} = 0.102$)

additional phase: MgO (0.54(4) %)

$R_p = 0.049$, $R_{wp} = 0.062$, $\chi^2 = 5.8$

[a] Displacement parameter of D is fixed to the value of refinement of $MgPd_2D_{0.97(1)}$ (see Table 2).

Figure S17. Rietveld refinement of frame 7 at 298(1) K in single crystal sapphire cell under D_2 pressure range from 0.55(5) to 1.10(5) MPa based on neutron powder diffraction data (λ = 1.86786(3) Å, D20, ILL, Grenoble, NUMORS 959342-959351), using FullProf[3].

Table S17. Refined crystal structures of $MgPd_2D_{0.904(12)}$ and $MgPd_2D_{0.068(4)}$ (in italics) of frame 7 (0.8(3) MPa D_2, 298(1) K) and residual values of the refinement based on NPD (Fig. S17).

atom	Mg	Pd1	Pd2	D
Wyckoff site	4*c*	4*c*	4*c*	4*c*
x	0.345(2)	0.355(2)	0.396(2)	0.611(3)
	0.342(3)	*0.350(3)*	*0.428(3)*	*0.694[b]*
y	¼	¼	¼	¼
z	0.106(2)	0.4308(12)	0.776(1)	0.602(1)
	0.1026(6)	*0.4257(5)*	*0.7692(6)*	*0.581[b]*
SOF	1	1	1	0.904(12)
				0.068(4)

space group *Pnma*

$MgPd_2D_{0.904(12)}$ (48(1) %): a = 5.6003(11) Å, b = 4.0694(5) Å, c = 8.487(2) Å, V = 193.43(6) Å³, B_{iso}(overall)[a] = -0.59(12) Å², R_{Bragg} = 0.112)

$MgPd_2D_{0.068(4)}$ (52(1) %): a = 5.4816(11) Å, b = 4.1248(7) Å, c = 8.089(2) Å, V = 182.91(6) Å³, B_{iso}(overall)[c] = 0.26(12) Å², R_{Bragg} = 0.084)

additional phase: MgO (0.60(4) %)

R_p = 0.048, R_{wp} = 0.060, χ^2 = 5.8

[a] Displacement parameters are fixed to the values of refinement of $MgPd_2D_{0.97(1)}$ (see Table 2). [b] Positional parameters were fixed during refinement for stability. [c] Displacement parameters are fixed to the values of refinement of frame 4 (see Table S14).
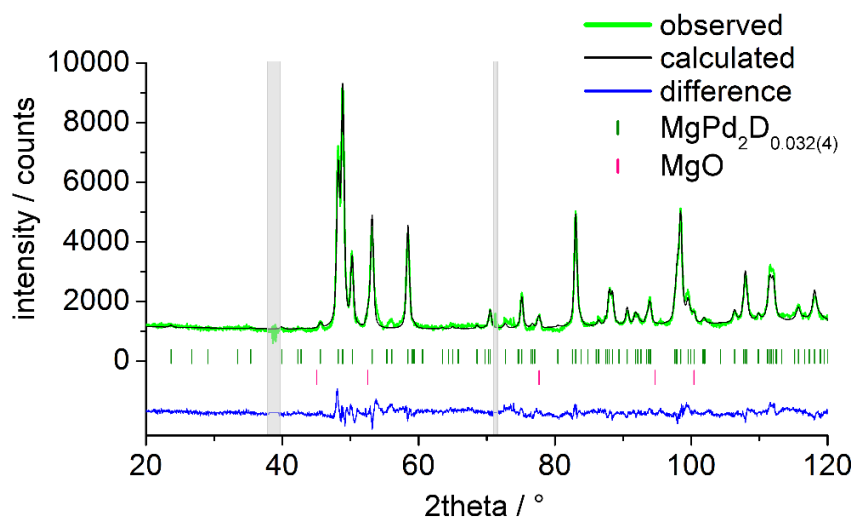
Figure S18. Rietveld refinement of frame 8 at 298(1) K in single crystal sapphire cell under D$_2$ pressure range from 1.10(5) to 1.60(5) MPa based on neutron powder diffraction data (λ = 1.86786(3) Å, D20, ILL, Grenoble, NUMORS 959352-959361), using FullProf[3].

Table S18. Refined crystal structures of MgPd$_2$D$_{0.926(8)}$ and MgPd$_2$D$_{0.098(6)}$ (in italics) of frame 8 (1.3(3) MPa D$_2$, 298(1) K) and residual values of the refinement based on NPD (Fig. S18).

atom	Mg	Pd1	Pd2	D
Wyckoff site	4c	4c	4c	4c
x	0.349(2)	0.3584(12)	0.395(2)	0.608(2)
	0.349(3)	*0.353(3)*	*0.431(3)*	*0.695(7)*
y	¼	¼	¼	¼
z	0.122(2)	0.440(1)	0.740(2)	0.6056(9)
	0.1026(6)	*0.4257(5)*	*0.7692(6)*	*0.580(5)*
SOF	1	1	1	0.926(8)
				0.098(6)

space group *Pnma*

MgPd$_2$D$_{0.926(8)}$ (61(1) %): a = 5.6043(7) Å, b = 4.0678(4) Å, c = 8.5075(10) Å, V = 193.95(4) Å³, B_{iso}(overall)[a] = -0.38(9) Å², R_{Bragg} = 0.103)

MgPd$_2$D$_{0.098(6)}$ (38.2(10) %): a = 5.4802(11) Å, b = 4.1268(8) Å, c = 8.081(2) Å, V = 182.76(6) Å³, B_{iso}(overall)[b] = 0.2(1) Å², R_{Bragg} = 0.088)

additional phase: MgO (0.60(4) %)

R_p = 0.043, R_{wp} = 0.055, χ^2 = 5.0

[a] Displacement parameters are fixed to the values of refinement of MgPd$_2$D$_{0.97(1)}$ (see Table 2). [b] Displacement parameters are fixed to the values of refinement of frame 4 (see Table S14).
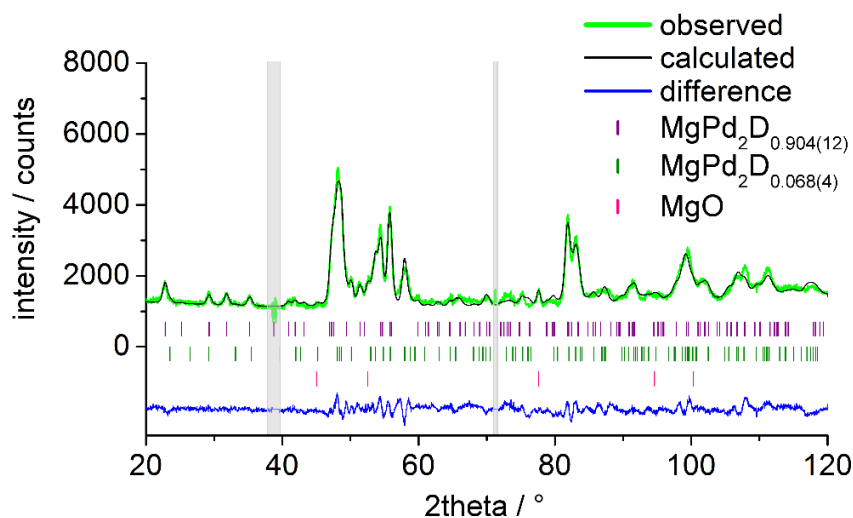
Figure S19. Rietveld refinement of frame 9 at 298(1) K in single crystal sapphire cell under D_2 pressure range from 1.60(5) to 2.10(5) MPa based on neutron powder diffraction data (λ = 1.86786(3) Å, D20, ILL, Grenoble, NUMORS 959362-959371), using FullProf[3].

Table S19. Refined crystal structures of $MgPd_2D_{0.942(9)}$ and $MgPd_2D_{0.10(2)}$ (in italics) of frame 9 (1.9(3) MPa D_2, 298(1) K) and residual values of the refinement based on NPD (Fig. S19).

atom	Mg	Pd1	Pd2	D
Wyckoff site	4c	4c	4c	4c
x	0.349(1)	0.3596(11)	0.393(2)	0.609(2)
	0.353(3)	*0.361(3)*	*0.436(2)*	*0.649[b]*
y	¼	¼	¼	¼
z	0.0985(10)	0.4314(7)	0.7761(8)	0.6069(8)
	0.122(2)	*0.440(2)*	*0.741(2)*	*0.593[b]*
SOF	1	1	1	0.942(9)
				0.10(2)

space group *Pnma*

$MgPd_2D_{0.942(9)}$ (66(1) %): a = 5.6054(6) Å, b = 4.0676(3) Å, c = 8.5163(9) Å, V = 194.18(3) Å³, B_{iso}(overall)[a] = -0.34(8) Å², R_{Bragg} = 0.094)

$MgPd_2D_{0.10(2)}$ (33.1(10) %): a = 5.4795(12) Å, b = 4.1264(8) Å, c = 8.074(2) Å, V = 182.57(7) Å³, B_{iso}(overall)[c] = 0.2(1) Å², R_{Bragg} = 0.092

additional phase: MgO (0.60(4) %)

R_p = 0.043, R_{wp} = 0.054, χ^2 = 4.9

[a] Displacement parameters are fixed to the values of refinement of $MgPd_2D_{0.97(1)}$ (see Table 2). [b] Positional parameters were fixed during refinement for stability. [c] Displacement parameters are fixed to the values of refinement of frame 4 (see Table S14).
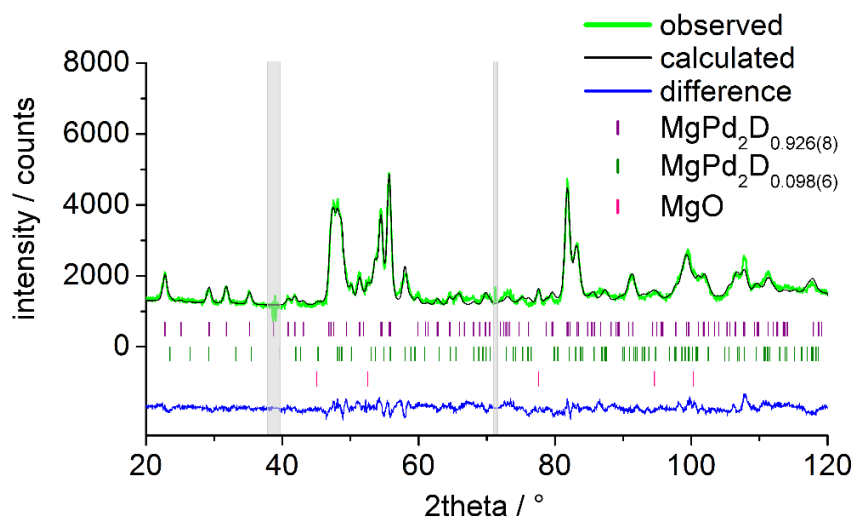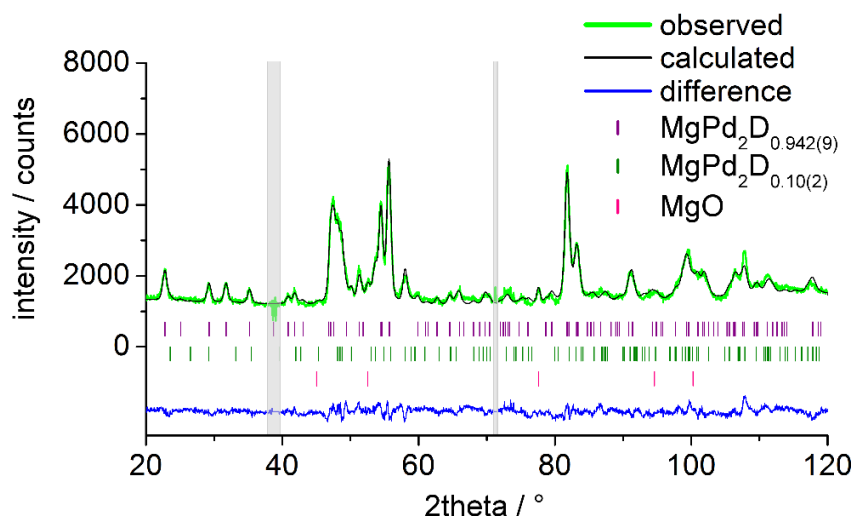
Figure S20. Rietveld refinement of frame 10 at 298(1) K in single crystal sapphire cell under D$_2$ pressure range from 2.10(5) to 2.60(5) MPa based on neutron powder diffraction data (λ = 1.86786(3) Å, D20, ILL, Grenoble, NUMORS 959372-959381), using FullProf[3].

Table S20. Refined crystal structures of MgPd$_2$D$_{0.939(8)}$ and MgPd$_2$D$_{0.11(2)}$ (in italics) of frame 10 (2.4(3) MPa D$_2$, 298(1) K) and residual values of the refinement based on NPD (Fig. S20).

atom	Mg	Pd1	Pd2	D
Wyckoff site	4*c*	4*c*	4*c*	4*c*
x	0.349(1)	0.3609(11)	0.393(2)	0.609(2)
	0.352(3)	*0.363(3)*	*0.435(3)*	*0.649[b]*
y	¼	¼	¼	¼
z	0.1001(10)	0.4312(7)	0.7760(8)	0.6066(8)
	0.122(2)	*0.440(2)*	*0.740(2)*	*0.593[b]*
SOF	1	1	1	0.939(8)
				0.11(2)

space group *Pnma*

MgPd$_2$D$_{0.939(8)}$ (70(1) %): *a* = 5.6067(5) Å, *b* = 4.0676(3) Å,

c = 8.5200(8) Å, *V* = 194.30(3) Å^3, *B*$_{iso}$(overall)[a] = -0.32(8) Å^2,

R$_{Bragg}$ = 0.093)

MgPd$_2$D$_{0.11(2)}$ (29.7(9) %): a = 5.478(1) Å, b = 4.1265(9) Å, c = 8.074(2) Å,

V = 182.51(7) Å^3, B$_{iso}$(overall)[c] = 0.3(2) Å^2, R$_{Bragg}$ = 0.091)

additional phase: MgO (0.54(4) %)

R$_p$ = 0.042, *R*$_{wp}$ = 0.053, χ^2 = 4.8

[a] Displacement parameters are fixed to the values of refinement of MgPd$_2$D$_{0.97(1)}$ (see Table 2). [b] Positional parameters are fixed to them of frame 9 (see Table S19) for sequential refinement (frame 9-14). [c] Displacement parameters are fixed to the values of refinement of frame 4 (see Table S14).

Figure S21. Rietveld refinement of frame 11 at 298(1) K in single crystal sapphire cell under 2.60(5) MPa D_2 pressure based on neutron powder diffraction data (λ = 1.86786(3) Å, D20, ILL, Grenoble, NUMORS 959382-959391), using FullProf[3].

Table S21. Refined crystal structures of $MgPd_2D_{0.945(8)}$ and $MgPd_2D_{0.10(2)}$ (in italics) of frame 11 (2.60(5) MPa D_2, 298(1) K) and residual values of the refinement based on NPD (Fig. S21).

atom	Mg	Pd1	Pd2	D
Wyckoff site	*4c*	*4c*	*4c*	*4c*
x	0.350(1)	0.3619(10)	0.391(2)	0.610(2)
	0.359(3)	*0.370(3)*	*0.439(2)*	*0.649[b]*
y	¼	¼	¼	¼
z	0.0988(9)	0.4321(6)	0.7759(7)	0.6076(8)
	0.123(2)	*0.440(2)*	*0.739(2)*	*0.593[b]*
SOF	1	1	1	0.945(8)
				0.10(2)

space group *Pnma*

$MgPd_2D_{0.945(8)}$ (73(1) %): a = 5.6076(5) Å, b = 4.0677(3) Å,

c = 8.5235(8) Å, V = 194.42(3) Å³, B_{iso}(overall)[a] = -0.28(8) Å²,

R_{Bragg} = 0.080)

$MgPd_2D_{0.10(2)}$ (26.8(9) %): a = 5.477(1) Å, b = 4.1262(9) Å, c = 8.060(2) Å,

V = 182.14(7) Å³, B_{iso}(overall)[c] = 0.0(1) Å², R_{Bragg} = 0.097)

additional phase: MgO (0.56(4) %)

R_p = 0.041, R_{wp} = 0.052, χ^2 = 4.6

[a] Displacement parameters are fixed to the values of refinement of $MgPd_2D_{0.97(1)}$ (see Table 2). [b] Positional parameters are fixed to them of frame 9 (see Table S19) for sequential refinement (frame 9-14). [c] Displacement parameters are fixed to the values of refinement of frame 4 (see Table S14).

Figure S22. Rietveld refinement of frame 12 at temperature range from 298(1) to 316(1) K in single crystal sapphire cell under 2.60(5) MPa D_2 pressure based on neutron powder diffraction data (λ = 1.86786(3) Å, D20, ILL, Grenoble, NUMORS 959392-959401), using FullProf[3].

Table S22. Refined crystal structures of $MgPd_2D_{0.947(8)}$ and $MgPd_2D_{0.11(2)}$ (in italics) of frame 12 (2.60(5) MPa D_2, 307(9) K) and residual values of the refinement based on NPD (Fig. S22).

atom	Mg	Pd1	Pd2	D
Wyckoff site	4*c*	4*c*	4*c*	4*c*
x	0.350(1)	0.3619(10)	0.391(2)	0.610(2)
	0.352(3)	*0.400(3)*	*0.431(2)*	*0.649[b]*
y	¼	¼	¼	¼
z	0.0997(9)	0.4321(6)	0.7764(8)	0.6069(8)
	0.136(2)	*0.427(2)*	*0.752(2)*	*0.593[b]*
SOF	1	1	1	0.947(8)
				0.11(2)

space group *Pnma*

$MgPd_2D_{0.947(8)}$ (74(2) %): a = 5.6079(5) Å, b = 4.0687(3) Å, c = 8.5248(8) Å, V = 194.51(3) Å³, B_{iso}(overall)[a] = -0.18(8) Å², R_{Bragg} = 0.070)

$MgPd_2D_{0.11(2)}$ (25.7(9) %): a = 5.476(1) Å, b = 4.1253(10) Å, c = 8.055(2) Å, V = 181.96(8) Å³, B_{iso}(overall)[c] = 0.00(8) Å², R_{Bragg} = 0.108)

additional phase: MgO (0.51(4) %)

R_p = 0.042, R_{wp} = 0.053, χ^2 = 4.9

[a] Displacement parameters are fixed to the values of refinement of $MgPd_2D_{0.97(1)}$ (see Table 2). [b] Positional parameters are fixed to them of frame 9 (see Table S19) for sequential refinement (frame 9-14). [c] Displacement parameters are fixed to the values of refinement of frame 4 (see Table S14).
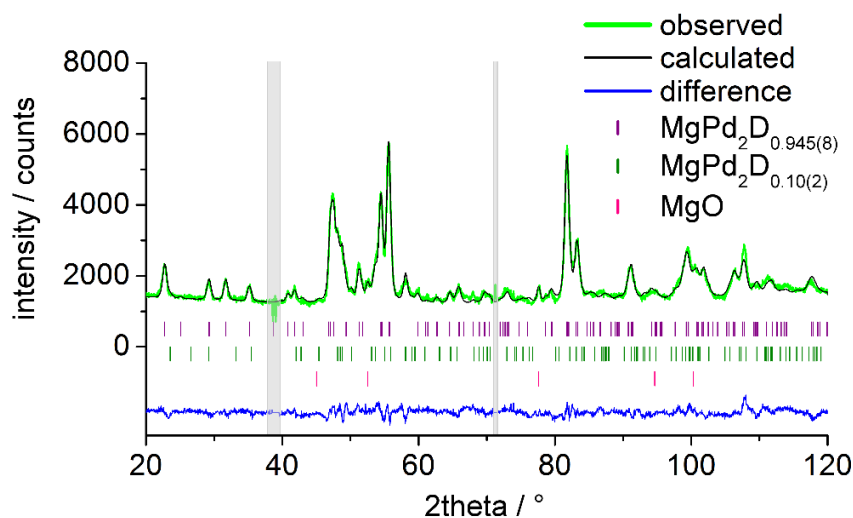
Figure S23. Rietveld refinement of frame 13 at temperature range from 320(1) to 358(1) K in single crystal sapphire cell under D_2 pressure range from 2.60(5) to 2.61(5) MPa based on neutron powder diffraction data (λ = 1.86786(3) Å, D20, ILL, Grenoble, NUMORS 959402-959411), using FullProf[3].

Table S23. Refined crystal structures of $MgPd_2D_{0.922(8)}$ and $MgPd_2D_{0.07(2)}$ (in italics) of frame 13 (2.61(5) MPa D_2, 339(19) K) and residual values of the refinement based on NPD (Fig. S23).

atom	Mg	Pd1	Pd2	D
Wyckoff site	*4c*	*4c*	*4c*	*4c*
x	0.351(1)	0.3616(11)	0.388(2)	0.611(2)
	0.359(3)	*0.408(3)*	*0.421(2)*	*0.649[b]*
y	¼	¼	¼	¼
z	0.1003(10)	0.4318(7)	0.7766(8)	0.6063(8)
	0.147(2)	*0.427(2)*	*0.751(2)*	*0.593[b]*
SOF	1	1	1	0.922(8)
				0.07(2)

space group *Pnma*

$MgPd_2D_{0.922(8)}$ (78(2) %):   a = 5.6108(5) Å,   b = 4.0725(3) Å, c = 8.5155(8) Å,   V = 194.58(3) Å³, B_{iso}(overall)[a] = 0.14(8) Å², R_{Bragg} = 0.072)

$MgPd_2D_{0.07(2)}$ (21.5(9) %): a = 5.481(1) Å, b = 4.1228(11) Å, c = 8.026(2) Å, V = 181.36(8) Å³, B_{iso}(overall)[c] = -0.5(2) Å², R_{Bragg} = 0.125)

additional phase: MgO (0.47(4) %)

R_p = 0.043, R_{wp} = 0.054, χ^2 = 5.1

[a] Displacement parameters are fixed to the values of refinement of $MgPd_2D_{0.97(1)}$ (see Table 2). [b] Positional parameters are fixed to them of frame 9 (see Table S19) for sequential refinement (frame 9-14). [c] Displacement parameters are fixed to the values of refinement of frame 4 (see Table S14).
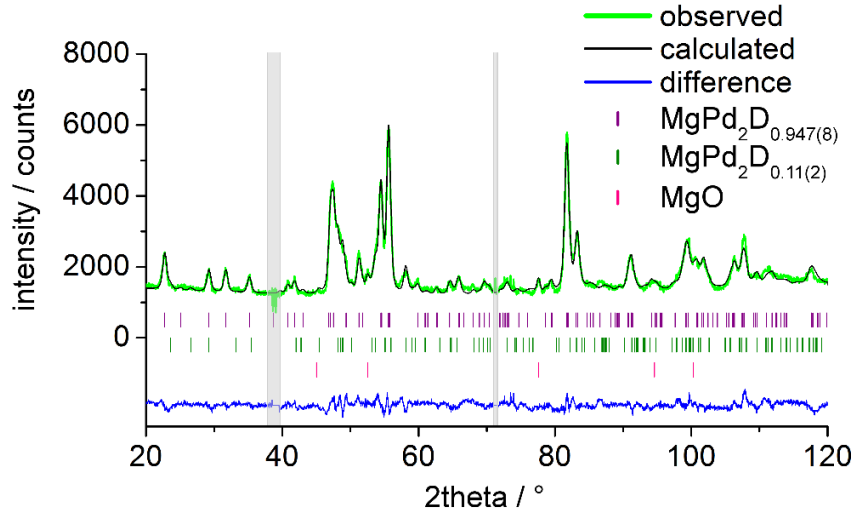
Figure S24. Rietveld refinement of frame 14 at temperature range from 363(1) to 384(1) K in single crystal sapphire cell under D$_2$ pressure range from 2.61(5) to 2.63(5) MPa based on neutron powder diffraction data (λ = 1.86786(3) Å, D20, ILL, Grenoble, NUMORS 959412-959421), using FullProf[3].

Table S24. Refined crystal structures of MgPd$_2$D$_{0.868(7)}$ and MgPd$_2$D$_{0.07(3)}$ (in italics) of frame 14 (2.62(5) MPa D$_2$, 374(11) K) and residual values of the refinement based on NPD (Fig. S24).

atom	Mg	Pd1	Pd2	D
Wyckoff site	4*c*	4*c*	4*c*	4*c*
x	0.349(1)	0.3596(10)	0.394(1)	0.614(2)
	0.348(4)	*0.427(3)*	*0.416(4)*	*0.649[b]*
y	¼	¼	¼	¼
z	0.1030(10)	0.4309(6)	0.7740(8)	0.6072(8)
	0.145(2)	*0.428(2)*	*0.748(2)*	*0.593[b]*
SOF	1	1	1	0.868(7)
				0.07(3)

space group *Pnma*

MgPd$_2$D$_{0.868(7)}$ (84(2) %):   *a* = 5.6081(4) Å,   *b* = 4.0760(3) Å, *c* = 8.4958(7) Å,   *V* = 194.20(2) Å³,   *B*$_{iso}$(overall)[a] = 0.12(8) Å², *R*$_{Bragg}$ = 0.081)

MgPd$_2$D$_{0.07(3)}$ (15.0(8) %): a = 5.500(2) Å, b = 4.1204(12) Å, c = 8.009(2) Å, V = 181.49(9) Å³, B$_{iso}$(overall)[c] = -1.5(2) Å², R$_{Bragg}$ = 0.141)

additional phase: MgO (0.48(4) %)

R$_p$ = 0.041, *R*$_{wp}$ = 0.052, *χ^2* = 4.8

[a] Displacement parameters are fixed to the values of refinement of MgPd$_2$D$_{0.97(1)}$ (see Table 2). [b] Positional parameters are fixed to them of frame 9 (see Table S19) for sequential refinement (frame 9-14). [c] Displacement parameters are fixed to the values of refinement of frame 4 (see Table S14).
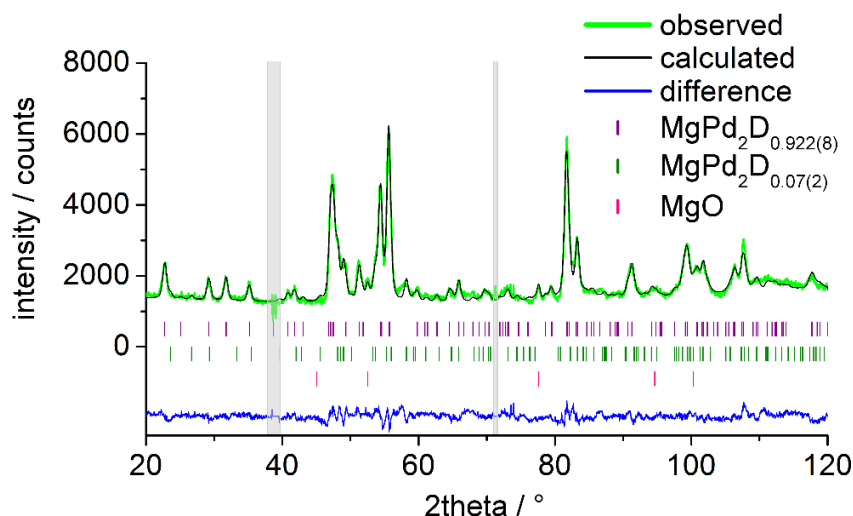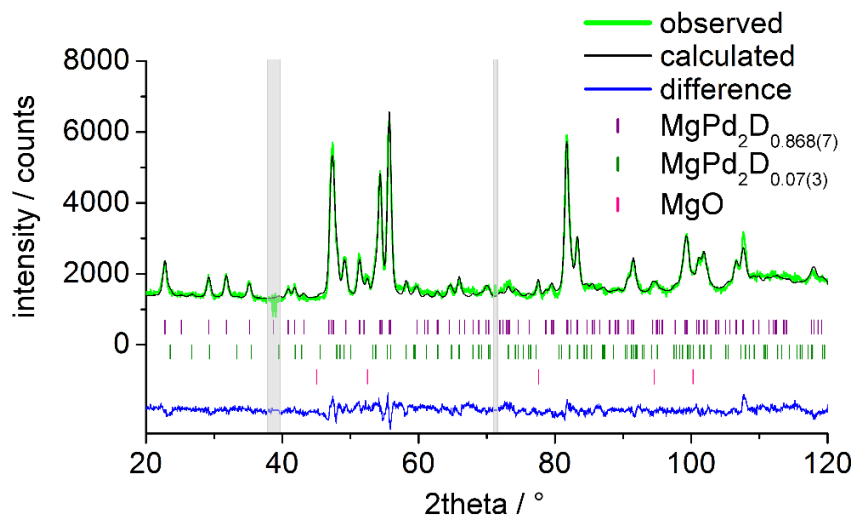
Figure S25. Rietveld refinement of frame 15 at temperature range from 386(1) to 393(1) K in single crystal sapphire cell under 2.63(5) MPa D_2 pressure based on neutron powder diffraction data (λ = 1.86786(3) Å, D20, ILL, Grenoble, NUMORS 959422-959431), using FullProf[3].

Table S25. Refined crystal structures of $MgPd_2D_{0.824(6)}$ and $MgPd_2D_{0.11(1)}$ (in italics) of frame 15 (2.63(5) MPa D_2, 390(4) K) and residual values of the refinement based on NPD (Fig. S25).

atom	Mg	Pd1	Pd2	D
Wyckoff site	4*c*	4*c*	4*c*	4*c*
x	0.348(1)	0.3613(11)	0.395(1)	0.617(2)
	0.342(5)	*0.428(4)*	*0.422(5)*	*0.649[b]*
y	¼	¼	¼	¼
z	0.1011(10)	0.4317(7)	0.7749(8)	0.6065(9)
	0.138(3)	*0.424(4)*	*0.746(3)*	*0.593[b]*
SOF	1	1	1	0.824(6)
				0.11(1)

space group *Pnma*

$MgPd_2D_{0.824(6)}$ (82(2) %): *a* = 5.6054(5) Å, *b* = 4.0764(3) Å, *c* = 8.4853(7) Å, *V* = 193.89(3) Å³, B_{iso}(overall)[a] = 0.06(8) Å², R_{Bragg} = 0.100)

$MgPd_2D_{0.11(1)}$ (17.2(6) %): a = 5.504(2) Å, b = 4.121(2) Å, c = 7.996(3) Å, V = 181.37(12) Å³, B_{iso}(overall)[c] = 0.35 Å², R_{Bragg} = 0.158)

additional phase: MgO (0.50(4) %)

R_p = 0.044, R_{wp} = 0.055, χ^2 = 5.6

[a] Displacement parameters are fixed to the values of refinement of $MgPd_2D_{0.97(1)}$ (see Table 2). [b] Positional parameters are fixed to them of frame 9 (see Table S19). [c] Displacement parameters are fixed to the values of refinement of frame 4 (see Table S14) and B_{iso}(overall) was fixed during refinement for stability.

Figure S26. Rietveld refinement of frame 16 at temperature range from 394(1) to 397(1) K in single crystal sapphire cell under D$_2$ pressure range from 2.63(5) to 2.64(5) MPa based on neutron powder diffraction data (λ = 1.86786(3) Å, D20, ILL, Grenoble, NUMORS 959432-959441), using FullProf[3].

Table S26. Refined crystal structures of MgPd$_2$D$_{0.798(8)}$ and MgPd$_2$D$_{0.046(8)}$ (in italics) of frame 16 (2.64(5) MPa D$_2$, 396(2) K) and residual values of the refinement based on NPD (Fig. S26).

atom	Mg	Pd1	Pd2	D
Wyckoff site	4*c*	4*c*	4*c*	4*c*
x	0.348(2)	0.3614(12)	0.399(2)	0.622(2)
	0.338(5)	*0.437(3)*	*0.408(5)*	*0.649[b]*
y	¼	¼	¼	¼
z	0.1034(12)	0.4315(7)	0.7733(9)	0.6061(9)
	0.141(3)	*0.425(4)*	*0.743(3)*	*0.593[b]*
SOF	1	1	1	0.798(8)
				0.046(8)

space group *Pnma*

MgPd$_2$D$_{0.798(8)}$ (81(2) %): a = 5.6021(5) Å, b = 4.0766(3) Å, c = 8.4780(7) Å, V = 193.61(3) Å³, B_{iso}(overall)[a] = 0.02(8) Å², R_{Bragg} = 0.100)

MgPd$_2$D$_{0.046(8)}$ (18.6(6) %): a = 5.515(2) Å, b = 4.122(2) Å, c = 7.994(3) Å, V = 181.72(12) Å³, B$_{iso}$(overall)[c] = 0.35 Å², R$_{Bragg}$ = 0.158)

additional phase: MgO (0.50(4) %)

R_p = 0.045, R_{wp} = 0.056, χ^2 = 5.8

[a] Displacement parameters are fixed to the values of refinement of MgPd$_2$D$_{0.97(1)}$ (see Table 2). [b] Positional parameters are fixed to them of frame 9 (see Table S19). [c] Displacement parameters are fixed to the values of refinement of frame 4 (see Table S14) and B_{iso}(overall) is fixed to value of refinement of frame 15 (see Table S25).
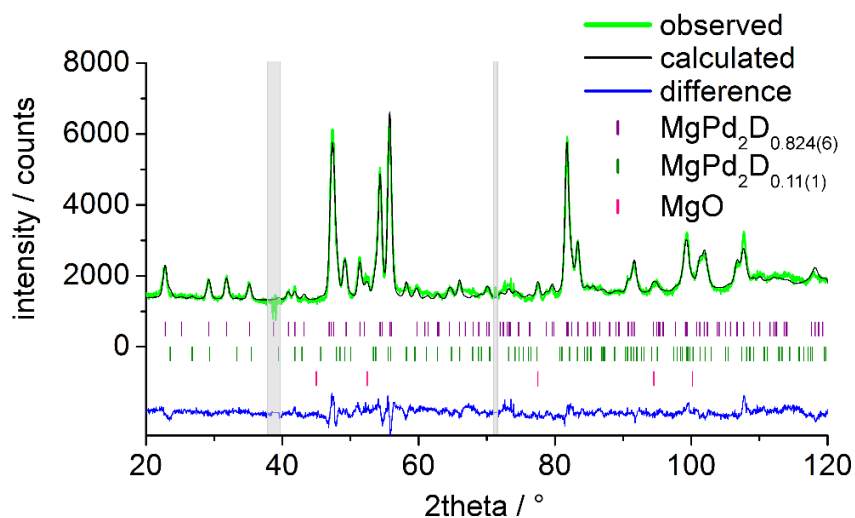
Figure S27. Rietveld refinement of frame 17 at temperature range from 397(1) to 407(1) K in single crystal sapphire cell under D_2 pressure range from 2.65(5) to 2.66(5) MPa based on neutron powder diffraction data (λ = 1.86786(3) Å, D20, ILL, Grenoble, NUMORS 959442-959451), using FullProf[3].

Table S27. Refined crystal structures of $MgPd_2D_{0.764(8)}$ and $MgPd_2D_{0.040(8)}$ (in italics) of frame 17 (2.66(5) MPa D_2, 402(5) K) and residual values of the refinement based on NPD (Fig. S27).

atom	Mg	Pd1	Pd2	D
Wyckoff site	4*c*	4*c*	4*c*	4*c*
x	0.348(2)	0.359(1)	0.398(2)	0.622(2)
	0.354(5)	*0.421(4)*	*0.415(4)*	*0.649[b]*
y	¼	¼	¼	¼
z	0.106(2)	0.4299(9)	0.7728(11)	0.6030(12)
	0.152(2)	*0.430(3)*	*0.746(2)*	*0.593[b]*
SOF	1	1	1	0.764(8)
				0.040(8)

space group *Pnma*

$MgPd_2D_{0.764(8)}$ (78(2) %): *a* = 5.6001(6) Å, *b* = 4.0763(3) Å, *c* = 8.4688(9) Å, *V* = 193.33(3) Å³, B_{iso}(overall)[a] = 0.13(10) Å², R_{Bragg} = 0.109)

$MgPd_2D_{0.040(8)}$ (21.7(7) %): a = 5.509(2) Å, b = 4.118(2) Å, c = 7.999(3) Å, V = 181.45(11) Å³, B_{iso}(overall)[c] = 0.35 Å², R_{Bragg} = 0.152)

additional phase: MgO (0.48(4) %)

R_p = 0.048, R_{wp} = 0.061, χ^2 = 6.8

[a] Displacement parameters are fixed to the values of refinement of $MgPd_2D_{0.97(1)}$ (see Table 2). [b] Positional parameters are fixed to them of frame 9 (see Table S19). [c] Displacement parameters are fixed to the values of refinement of frame 4 (see Table S14) and B_{iso}(overall) is fixed to value of refinement of frame 15 (see Table S25).
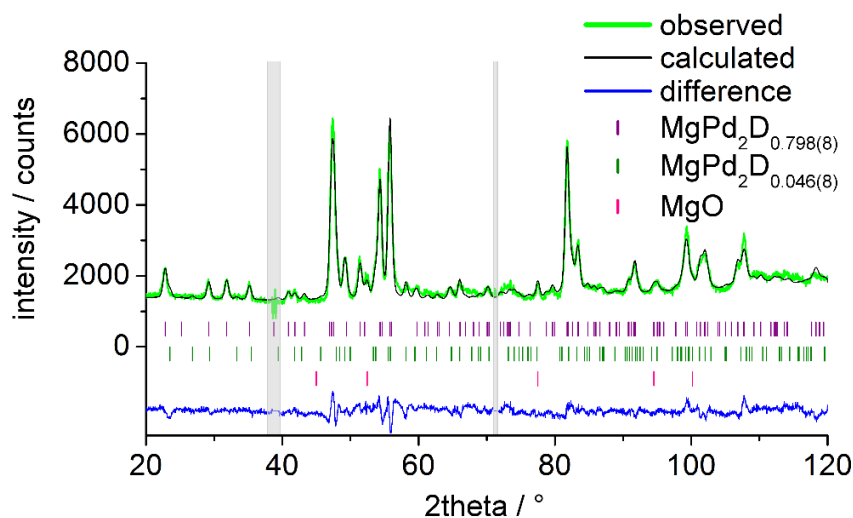
Figure S28. Rietveld refinement of frame 18 at temperature range from 410(1) to 428(1) K in single crystal sapphire cell under D$_2$ pressure range from 2.67(5) to 2.72(5) MPa based on neutron powder diffraction data (λ = 1.86786(3) Å, D20, ILL, Grenoble, NUMORS 959452-959461), using FullProf[3].

Table S28. Refined crystal structures of MgPd$_2$D$_{0.68(4)}$ and MgPd$_2$D$_{0.210(4)}$ (in italics) of frame 18 (2.70(5) MPa D$_2$, 419(9) K) and residual values of the refinement based on NPD (Fig. S28).

atom	Mg	Pd1	Pd2	D
Wyckoff site	4*c*	4*c*	4*c*	4*c*
x	0.308(5)	0.380(4)	0.431(5)	0.657(6)
	0.348(2)	*0.350(2)*	*0.426(2)*	*0.691(2)*
y	¼	¼	¼	¼
z	0.148(4)	0.427(3)	0.757(3)	0.584(5)
	0.1250(12)	*0.4343(12)*	*0.747(11)*	*0.613(1)*
SOF	1	1	1	0.68(4)
				0.210(4)

space group *Pnma*

MgPd$_2$D$_{0.68(4)}$ (24.0(9) %): *a* = 5.600(3) Å, *b* = 4.0774(12) Å, *c* = 8.436(4) Å,

V = 192.6(1) Å³, *B*$_{iso}$(overall)[a] = 0.30 Å², *R*$_{Bragg}$ = 0.209)

MgPd$_2$D$_{0.210(4)}$ (76(2) %): a = 5.5146(7) Å, b = 4.1118(4) Å, c = 8.1909(11) Å,

V = 185.73(4) Å³, B$_{iso}$(overall)[b] = 0.13(9) Å², R$_{Bragg}$ = 0.080)

additional phase: MgO (0.41(6) %)

R$_p$ = 0.051, *R*$_{wp}$ = 0.065, χ^2 = 7.5

[a] Displacement parameters are fixed to the values of refinement of MgPd$_2$D$_{0.97(1)}$ (see Table 2) and *B*$_{iso}$(overall) was fixed during refinement for stability. [b] Displacement parameters are fixed to the values of refinement of frame 19 (see Table S29).
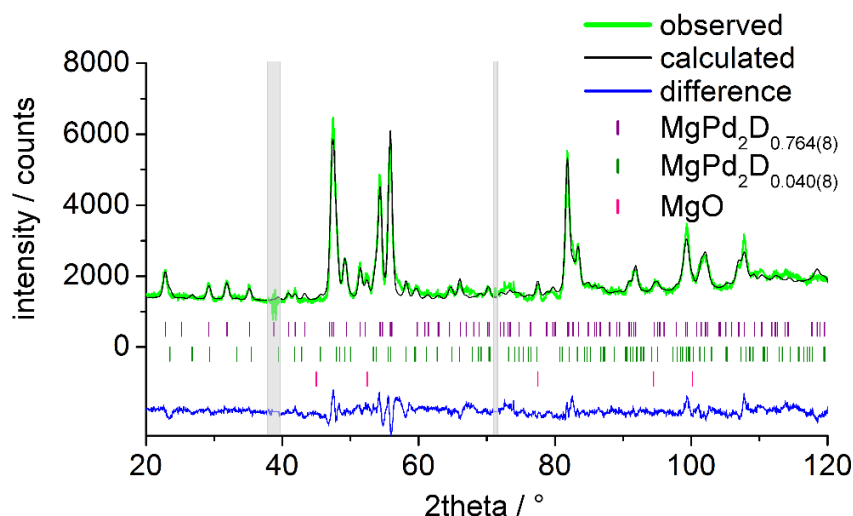
Figure S29. Rietveld refinement of frame 19 at temperature range from 428(1) to 433(1) K in single crystal sapphire cell under D_2 pressure range from 2.72(5) to 2.73(5) MPa based on neutron powder diffraction data (λ = 1.86786(3) Å, D20, ILL, Grenoble, NUMORS 959462-959471), using FullProf[3].

Table S29. Refined crystal structures of $MgPd_2D_{0.183(6)}$ of frame 19 (2.73(5) MPa, 431(3) K) and residual values of the refinement based on NPD (Fig. S29).

atom	Mg	Pd1	Pd2	D
Wyckoff site	*4c*	*4c*	*4c*	*4c*
x	0.340(2)	0.356(2)	0.428(2)	0.667(4)
y	¼	¼	¼	¼
z	0.1177(12)	0.4364(11)	0.7509(10)	0.610(3)
B_{iso} / Å²	2.3(3)	1.1(2)	0.4(2)	4.797[a]
SOF	1	1	1	0.183(6)

space group *Pnma*

$MgPd_2D_{0.183(6)}$ (100(3) %): *a* = 5.5088(6) Å, *b* = 4.1153(3) Å, *c* = 8.1785(9) Å, *V* = 185.41(3) Å³, R_{Bragg} = 0.127)

additional phase: MgO (0.37(6) %)

R_p = 0.057, R_{wp} = 0.072, χ^2 = 9.0

[a] Displacement parameter of D is fixed to the value of refinement of $MgPd_2D_{0.97(1)}$ (see Table 2).

Figure S30. Rietveld refinement of frame 20 at temperature range from 433(1) to 435(1) K in single crystal sapphire cell under D$_2$ pressure range from 2.73(5) to 2.74(5) MPa based on neutron powder diffraction data (λ = 1.86786(3) Å, D20, ILL, Grenoble, NUMORS 959472-959481), using FullProf[3].

Table S30. Refined crystal structures of MgPd$_2$D$_{0.168(7)}$ of frame 20 (2.74(5) MPa, 434(1) K) and residual values of the refinement based on NPD (Fig. S30).

atom	Mg	Pd1	Pd2	D
Wyckoff site	4c	4c	4c	4c
x	0.340(2)	0.357(2)	0.430(1)	0.669(5)
y	¼	¼	¼	¼
z	0.116(1)	0.4370(10)	0.7508(10)	0.608(3)
B_{iso} / Å²	2.4(3)	0.7(2)	0.2(2)	4.797[a]
SOF	1	1	1	0.168(7)

space group *Pnma*

MgPd$_2$D$_{0.168(7)}$ (100(3) %): *a* = 5.5065(6) Å, *b* = 4.1174(3) Å, *c* = 8.1717(9) Å, *V* = 185.27(3) Å³, R_{Bragg} = 0.126)

additional phase: MgO (0.39(6) %)

R_p = 0.056, R_{wp} = 0.072, χ^2 = 9.1

[a] Displacement parameter of D is fixed to the value of refinement of MgPd$_2$D$_{0.97(1)}$ (see Table 2).
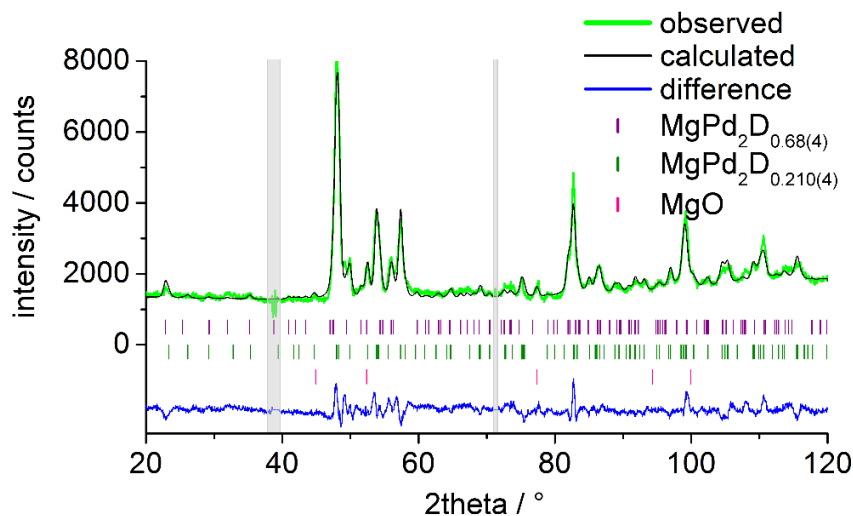
Figure S31. Rietveld refinement of frame 21 at temperature range from 437(1) to 430(1) K in single crystal sapphire cell under D_2 pressure range from 2.74(5) to 2.73(5) MPa based on neutron powder diffraction data (λ = 1.86786(3) Å, D20, ILL, Grenoble, NUMORS 959483-959492), using FullProf[3].

Table S31. Refined crystal structures of $MgPd_2D_{0.163(7)}$ of frame 21 (2.73(5) MPa, 433(4) K) and residual values of the refinement based on NPD (Fig. S31).

atom	Mg	Pd1	Pd2	D
Wyckoff site	4c	4c	4c	4c
x	0.339(2)	0.356(2)	0.430(1)	0.667(5)
y	¼	¼	¼	¼
z	0.113(1)	0.4377(10)	0.7507(10)	0.607(3)
B_{iso} / Å²	2.3(3)	0.7(2)	0.4(2)	4.797[a]
SOF	1	1	1	0.163(7)

space group *Pnma*

$MgPd_2D_{0.163(7)}$ (100(3) %): a = 5.5061(6) Å, b = 4.1181(3) Å, c = 8.1691(9) Å, V = 185.23(3) Å³, R_{Bragg} = 0.129

additional phase: MgO (0.43(6) %)

R_p = 0.057, R_{wp} = 0.073, χ^2 = 9.2

[a] Displacement parameter of D is fixed to the value of refinement of $MgPd_2D_{0.97(1)}$ (see Table 2).
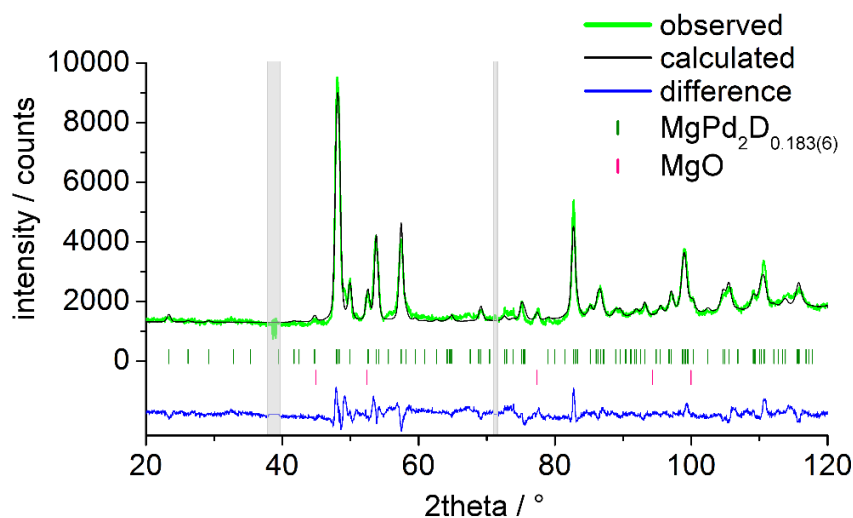
Figure S32. Rietveld refinement of frame 22 at temperature range from 427(1) to 409(1) K in single crystal sapphire cell under D$_2$ pressure range from 2.72(5) to 2.68(5) MPa based on neutron powder diffraction data (λ = 1.86786(3) Å, D20, ILL, Grenoble, NUMORS 959493-959502), using FullProf[3].

Table S32. Refined crystal structures of MgPd$_2$D$_{0.63(3)}$ and MgPd$_2$D$_{0.224(4)}$ (in italics) of frame 22 (2.70(5) MPa D$_2$, 418(9) K) and residual values of the refinement based on NPD (Fig. S32).

atom	Mg	Pd1	Pd2	D
Wyckoff site	4*c*	4*c*	4*c*	4*c*
x	0.302(3)	0.378(3)	0.441(3)	0.657(5)
	0.348(3)	*0.348(2)*	*0.423(2)*	*0.696(3)*
y	¼	¼	¼	¼
z	0.149(3)	0.422(2)	0.758(2)	0.579(4)
	0.1275(12)	*0.430(1)*	*0.747(1)*	*0.613(1)*
SOF	1	1	1	0.63(3)
				0.224(4)

space group *Pnma*

MgPd$_2$D$_{0.63(3)}$ (24(2) %): *a* = 5.615(3) Å, *b* = 4.078(1) Å, *c* = 8.409(4) Å,

V = 192.6(1) Å³, *B*$_{iso}$(overall)[a] = -1.8(4) Å², *R*$_{Bragg}$ = 0.160)

MgPd$_2$D$_{0.224(4)}$ (76(3) %): a = 5.5215(8) Å, b = 4.1057(5) Å, c = 8.210(1) Å,

V = 186.12(5) Å³, B$_{iso}$(overall)[b] = 0.1(1) Å², R$_{Bragg}$ = 0.076)

additional phase: MgO (0.57(7) %)

R$_p$ = 0.051, *R*$_{wp}$ = 0.065, χ^2 = 7.6

[a] Displacement parameters are fixed to the values of refinement of MgPd$_2$D$_{0.97(1)}$ (see Table 2). [b] Displacement parameters are fixed to the values of refinement of frame 19 (see Table S29).
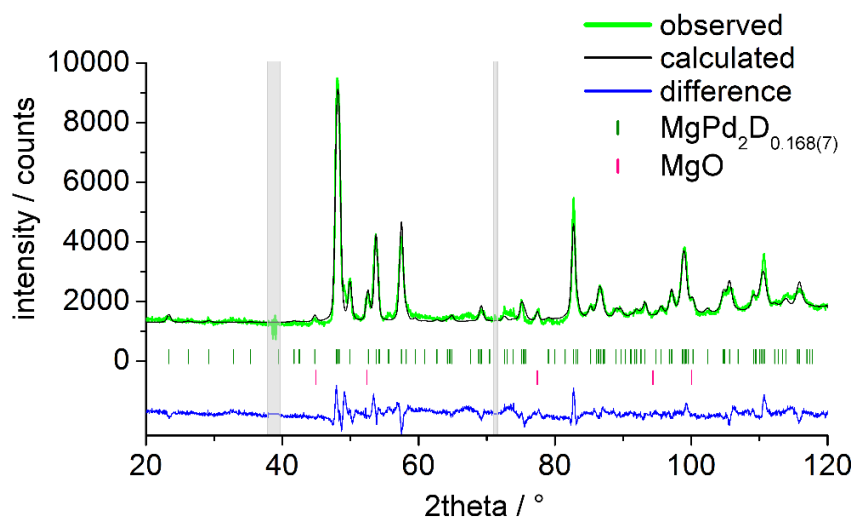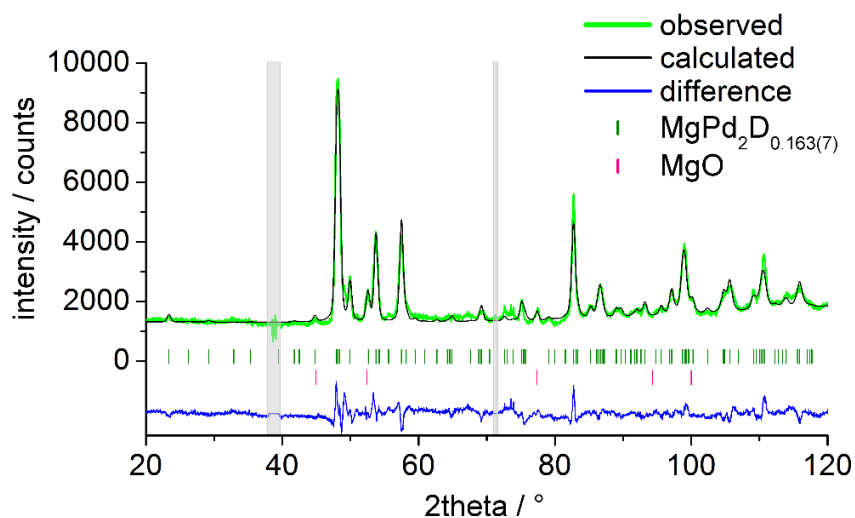
Figure S33. Rietveld refinement of frame 23 at temperature range from 408(1) to 402(1) K in single crystal sapphire cell under D_2 pressure range from 2.68(5) to 2.65(5) MPa based on neutron powder diffraction data (λ = 1.86786(3) Å, D20, ILL, Grenoble, NUMORS 959503-959512), using FullProf[3].

Table S33. Refined crystal structures of $MgPd_2D_{0.63(2)}$ and $MgPd_2D_{0.25(2)}$ (in italics) of frame 23 (2.66(5) MPa D_2, 405(3) K) and residual values of the refinement based on NPD (Fig. S33).

atom	Mg	Pd1	Pd2	D
Wyckoff site	4c	4c	4c	4c
x	0.328(2)	0.373(2)	0.417(2)	0.636(4)
	0.353(4)	*0.348(3)*	*0.424(3)*	*0.687[b]*
y	¼	¼	¼	¼
z	0.130(2)	0.4249(12)	0.760(1)	0.596(2)
	0.137(2)	*0.431(2)*	*0.743(2)*	*0.611[b]*
SOF	1	1	1	0.63(2)
				0.25(2)

space group *Pnma*

$MgPd_2D_{0.63(2)}$ (54(2) %): a = 5.6024(11) Å, b = 4.0768(5) Å, c = 8.451(2) Å, V = 193.02(6) Å³, B_{iso}(overall)[a] = -0.8(1) Å², R_{Bragg} = 0.131)

$MgPd_2D_{0.25(2)}$ (46(2) %): a = 5.538(2) Å, b = 4.1003(8) Å, c = 8.223(2) Å, V = 186.71(8) Å³, B_{iso}(overall)[c] = 0.1(2) Å², R_{Bragg} = 0.088)

additional phase: MgO (0.59(7) %)

R_p = 0.050, R_{wp} = 0.065, χ^2 = 7.6

[a] Displacement parameters are fixed to the values of refinement of $MgPd_2D_{0.97(1)}$ (see Table 2). [b] Positional parameters were fixed during refinement for stability. [c] Displacement parameters are fixed to the values of refinement of frame 19 (see Table S29).

Figure S34. Rietveld refinement of frame 24 at temperature range from 401(1) to 400(1) K in single crystal sapphire cell under 2.65(5) MPa D$_2$ pressure based on neutron powder diffraction data (λ = 1.86786(3) Å, D20, ILL, Grenoble, NUMORS 959513-959522), using FullProf[3].

Table S34. Refined crystal structures of MgPd$_2$D$_{0.748(11)}$ and MgPd$_2$D$_{0.055(7)}$ (in italics) of frame 24 (2.65(5) MPa D$_2$, 400(1) K) and residual values of the refinement based on NPD (Fig. S34).

atom	Mg	Pd1	Pd2	D
Wyckoff site	4c	4c	4c	4c
x	0.348(2)	0.354(1)	0.397(2)	0.614(3)
	0.356(5)	*0.411(4)*	*0.414(4)*	*0.687[b]*
y	¼	¼	¼	¼
z	0.105(2)	0.4293(10)	0.7762(11)	0.601(1)
	0.159(2)	*0.433(2)*	*0.748(2)*	*0.611[b]*
SOF	1	1	1	0.748(11)
				0.055(7)

space group *Pnma*

MgPd$_2$D$_{0.748(11)}$ (75(2) %): a = 5.5987(7) Å, b = 4.0763(4) Å, c = 8.4671(11) Å,

V = 193.23(4) Å³, B_{iso}(overall)[a] = 0.000(10) Å², R_{Bragg} = 0.108)

MgPd$_2$D$_{0.055(7)}$ (24.4(8) %): a = 5.511(2) Å, b = 4.114(1) Å, c = 8.015(3) Å,

V = 181.70(11) Å³, B_{iso}(overall)[c] = 0 Å², R_{Bragg} = 0.142)

additional phase: MgO (0.47(4) %)

R_p = 0.051, R_{wp} = 0.067, χ^2 = 8.2

[a] Displacement parameters are fixed to the values of refinement of MgPd$_2$D$_{0.97(1)}$ (see Table 2). [b] Positional parameters are fixed to them of frame 23 (see Table S33) for sequential refinement (frame 24-27). [c] Displacement parameters are fixed to the values of refinement of frame 19 (see Table S29) and B_{iso}(overall) is not refined for stability.
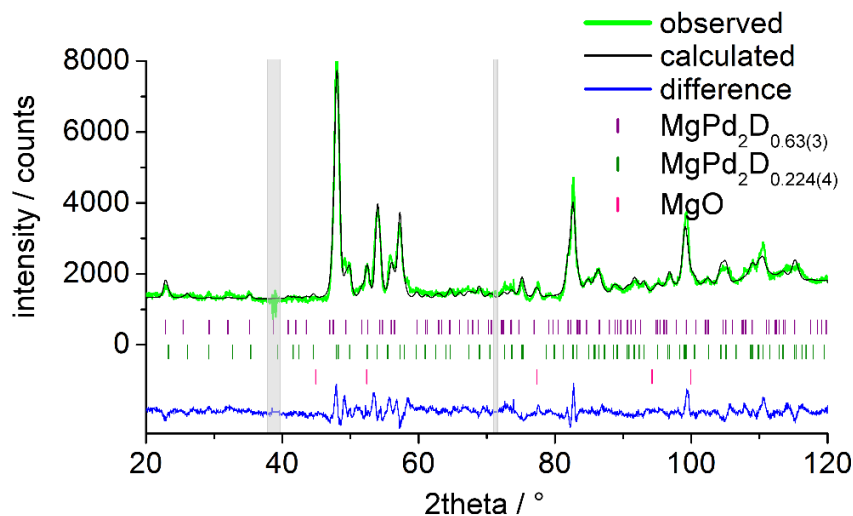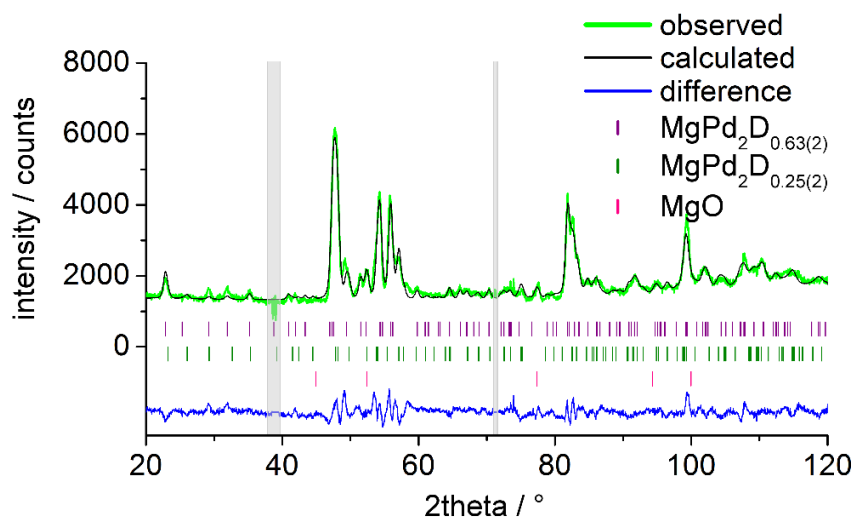
Figure S35. Rietveld refinement of frame 25 at temperature range from 399(1) to 398(1) K in single crystal sapphire cell under D_2 pressure range from 2.65(5) to 2.64(5) MPa based on neutron powder diffraction data (λ = 1.86786(3) Å, D20, ILL, Grenoble, NUMORS 959523-959532), using FullProf[3].

Table S35. Refined crystal structures of $MgPd_2D_{0.768(9)}$ and $MgPd_2D_{0.104(8)}$ (in italics) of frame 25 (2.64(5) MPa D_2, 398(1) K) and residual values of the refinement based on NPD (Fig. S35).

atom	Mg	Pd1	Pd2	D
Wyckoff site	4*c*	4*c*	4*c*	4*c*
x	0.345(2)	0.360(1)	0.397(2)	0.620(2)
	0.356(5)	*0.417(4)*	*0.422(4)*	*0.687[b]*
y	¼	¼	¼	¼
z	0.104(1)	0.4312(9)	0.7726(10)	0.6051(11)
	0.145(3)	*0.428(3)*	*0.745(3)*	*0.611[b]*
SOF	1	1	1	0.768(9)
				0.104(8)

space group *Pnma*

$MgPd_2D_{0.768(9)}$ (80(2) %): *a* = 5.6007(6) Å, *b* = 4.0768(3) Å, *c* = 8.4717(9) Å,

V = 193.44(3) Å³, B_{iso}(overall)[a] = 0.14(10) Å², R_{Bragg} = 0.104)

$MgPd_2D_{0.104(8)}$ (19.1(6) %): a = 5.507(2) Å, b = 4.118(2) Å, c = 8.001(3) Å,

V = 181.46(12) Å³, B_{iso}(overall)[c] = 0 Å², R_{Bragg} = 0.143)

additional phase: MgO (0.51(4) %)

R_p = 0.048, R_{wp} = 0.061, χ^2 = 6.8

[a] Displacement parameters are fixed to the values of refinement of $MgPd_2D_{0.97(1)}$ (see Table 2). [b] Positional parameters are fixed to them of frame 23 (see Table S33) for sequential refinement (frame 24-27). [c] Displacement parameters are fixed to the values of refinement of frame 19 (see Table S29) and B_{iso}(overall) is not refined for stability.
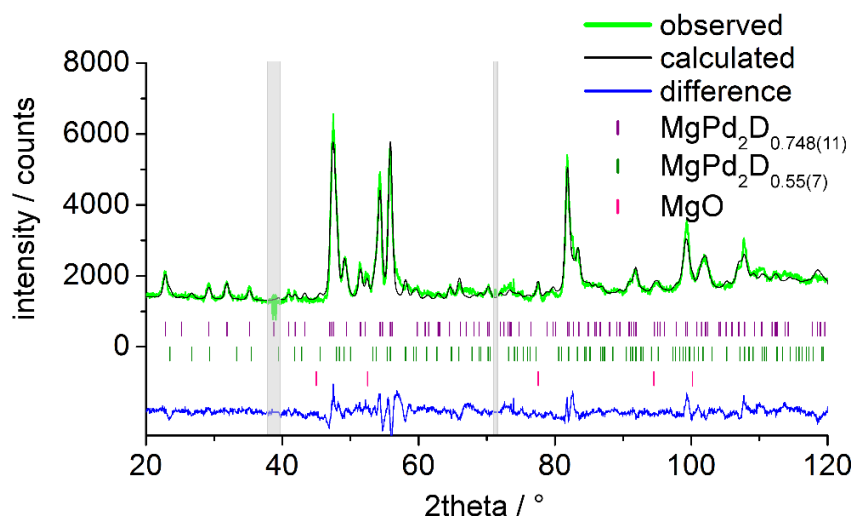
Figure S36. Rietveld refinement of frame 26 at temperature range from 397(1) to 396(1) K in single crystal sapphire cell under D_2 pressure range from 2.64(5) to 2.63(5) MPa based on neutron powder diffraction data (λ = 1.86786(3) Å, D20, ILL, Grenoble, NUMORS 959533-959542), using FullProf[3].

Table S36. Refined crystal structures of $MgPd_2D_{0.786(9)}$ and $MgPd_2D_{0.101(8)}$ (in italics) of frame 26 (2.63(5) MPa D_2, 396(1) K) and residual values of the refinement based on NPD (Fig. S36).

atom	Mg	Pd1	Pd2	D
Wyckoff site	4*c*	4*c*	4*c*	4*c*
x	0.347(2)	0.360(1)	0.399(2)	0.620(2)
	0.352(4)	*0.428(4)*	*0.416(4)*	*0.687[b]*
y	¼	¼	¼	¼
z	0.107(1)	0.4299(8)	0.7720(10)	0.6056(10)
	0.147(3)	*0.428(3)*	*0.746(2)*	*0.611[b]*
SOF	1	1	1	0.786(9)
				0.101(8)

space group *Pnma*

$MgPd_2D_{0.786(9)}$ (80(2) %): *a* = 5.6017(5) Å, *b* = 4.0769(3) Å, *c* = 8.4742(8) Å,

V = 193.53(3) Å³, B_{iso}(overall)[a] = 0.00(2) Å², R_{Bragg} = 0.098)

$MgPd_2D_{0.101(8)}$ (19.1(6) %): a = 5.511(2) Å, b = 4.120(2) Å, c = 7.999(3) Å,

V = 181.59(12) Å³, B_{iso}(overall)[c] = 0 Å², R_{Bragg} = 0.144)

additional phase: MgO (0.48(4) %)

R_p = 0.046, R_{wp} = 0.059, χ^2 = 6.3

[a] Displacement parameters are fixed to the values of refinement of $MgPd_2D_{0.97(1)}$ (see Table 2). [b] Positional parameters are fixed to them of frame 23 (see Table S33) for sequential refinement (frame 24-27). [c] Displacement parameters are fixed to the values of refinement of frame 19 (see Table S29) and B_{iso}(overall) is not refined for stability.
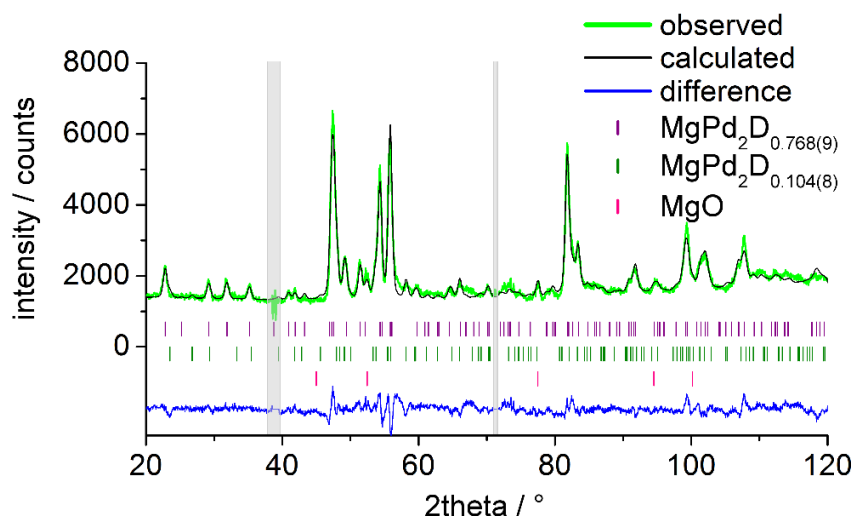
Figure S37. Rietveld refinement of frame 27 at temperature range from 394(1) to 361(1) K in single crystal sapphire cell under D_2 pressure range from 2.63(5) to 2.60(5) MPa based on neutron powder diffraction data (λ = 1.86786(3) Å, D20, ILL, Grenoble, NUMORS 959543-959552), using FullProf[3].

Table S37. Refined crystal structures of $MgPd_2D_{0.860(8)}$ and $MgPd_2D_{0.125(7)}$ (in italics) of frame 27 (2.62(5) MPa D_2, 377(17) K) and residual values of the refinement based on NPD (Fig. S37).

atom	Mg	Pd1	Pd2	D
Wyckoff site	*4c*	*4c*	*4c*	*4c*
x	0.348(1)	0.3629(11)	0.395(1)	0.618(2)
	0.325(4)	*0.441(3)*	*0.407(5)*	*0.687[b]*
y	¼	¼	¼	¼
z	0.1026(10)	0.4314(6)	0.7739(8)	0.6082(8)
	0.131(3)	*0.423(4)*	*0.743(3)*	*0.611[b]*
SOF	1	1	1	0.860(8)
				0.125(7)

space group *Pnma*

$MgPd_2D_{0.860(8)}$ (83(2) %): a = 5.6068(4) Å, b = 4.0765(3) Å, c = 8.4951(7) Å,

V = 194.16(2) Å³, B_{iso}(overall)[a] = -0.06(8) Å², R_{Bragg} = 0.091)

$MgPd_2D_{0.125(7)}$ (16.3(5) %): a = 5.522(2) Å, b = 4.120(2) Å, c = 7.994(3) Å,

V = 181.88(12) Å³, B_{iso}(overall)[c] = 0 Å², R_{Bragg} = 0.145)

additional phase: MgO (0.52(4) %)

R_p = 0.043, R_{wp} = 0.054, χ^2 = 5.3

[a] Displacement parameters are fixed to the values of refinement of $MgPd_2D_{0.97(1)}$ (see Table 2). [b] Positional parameters are fixed to them of frame 23 (see Table S33) for sequential refinement (frame 24-27). [c] Displacement parameters are fixed to the values of refinement of frame 19 (see Table S29) and B_{iso}(overall) is not refined for stability.
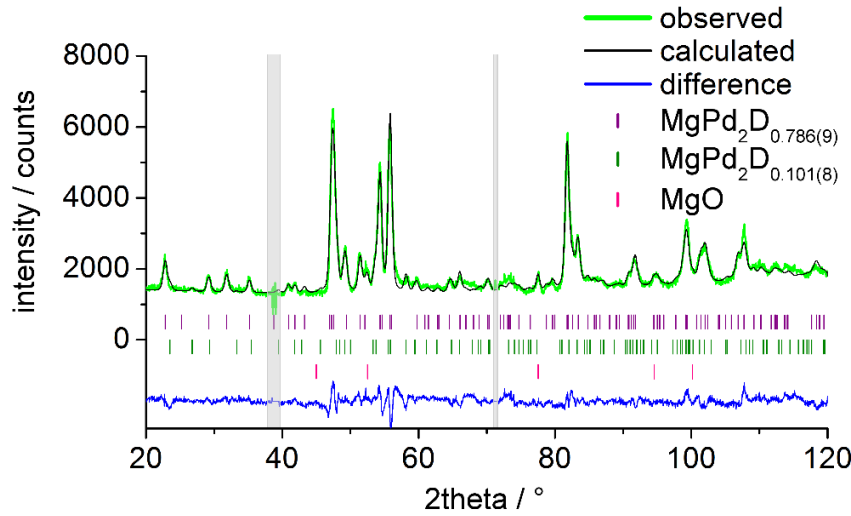
Figure S38. Rietveld refinement of frame 28 at temperature range from 359(1) to 327(1) K in single crystal sapphire cell under D$_2$ pressure range from 2.60(5) to 2.58(5) MPa based on neutron powder diffraction data (λ = 1.86786(3) Å, D20, ILL, Grenoble, NUMORS 959553-959562), using FullProf[3].

Table S38. Refined crystal structures of MgPd$_2$D$_{0.930(6)}$ and MgPd$_2$D$_{0.186(8)}$ (in italics) of frame 28 (2.59(5) MPa D$_2$, 343(16) K) and residual values of the refinement based on NPD (Fig. S38).

atom	Mg	Pd1	Pd2	D
Wyckoff site	4c	4c	4c	4c
x	0.3492(12)	0.3642(9)	0.392(1)	0.614(1)
	0.313(4)	*0.437(3)*	*0.414(6)*	*0.687[b]*
y	¼	¼	¼	¼
z	0.1007(8)	0.4328(5)	0.7743(7)	0.6092(6)
	0.123(3)	*0.419(4)*	*0.749(3)*	*0.611[b]*
SOF	1	1	1	0.930(6)
				0.186(8)

space group *Pnma*

MgPd$_2$D$_{0.930(6)}$ (86(1) %): a = 5.6097(4) Å, b = 4.0740(2) Å, c = 8.5170(6) Å,

V = 194.65(2) Å³, B_{iso}(overall)[a] = -0.14(7) Å², R_{Bragg} = 0.080)

MgPd$_2$D$_{0.186(8)}$ (13.8(5) %): a = 5.507(2) Å, b = 4.120(2) Å, c = 7.991(3) Å,

V = 181.3(1) Å³, B_{iso}(overall)[c] = 0 Å², R_{Bragg} = 0.150)

additional phase: MgO (0.54(4) %)

R_p = 0.041, R_{wp} = 0.051, χ^2 = 4.7

[a] Displacement parameters are fixed to the values of refinement of MgPd$_2$D$_{0.97(1)}$ (see Table 2). [b] Positional parameters are fixed to them of frame 23 (see Table S33). [c] Displacement parameters are fixed to the values of refinement of frame 4 (see Table S14) and B_{iso}(overall) is not refined for stability.
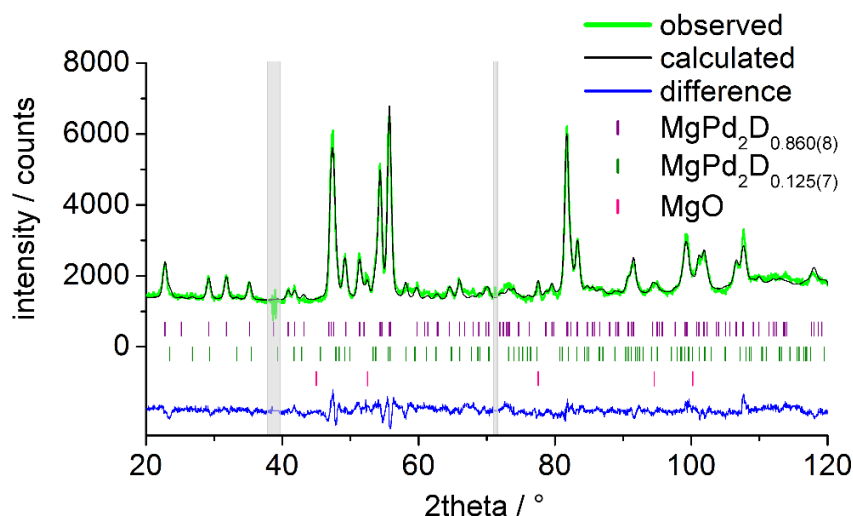
Figure S39. Rietveld refinement of frame 29 at temperature range from 325(1) to 317(1) K in single crystal sapphire cell under D_2 pressure range from 2.58(5) to 2.57(5) MPa based on neutron powder diffraction data (λ = 1.86786(3) Å, D20, ILL, Grenoble, NUMORS 959563-959572), using FullProf[3].

Table S39. Refined crystal structures of $MgPd_2D_{0.964(6)}$ and $MgPd_2D_{0.158(6)}$ (in italics) of frame 29 (2.58(5) MPa D_2, 321(4) K) and residual values of the refinement based on NPD (Fig. S39).

atom	Mg	Pd1	Pd2	D
Wyckoff site	*4c*	*4c*	*4c*	*4c*
x	0.3500(11)	0.3630(9)	0.3911(12)	0.6135(12)
	0.315(4)	*0.445(3)*	*0.410(5)*	*0.687[b]*
y	¼	¼	¼	¼
z	0.1008(8)	0.4323(5)	0.7751(6)	0.6092(6)
	0.124(3)	*0.420(4)*	*0.746(3)*	*0.611[b]*
SOF	1	1	1	0.964(6)
				0.158(6)

space group *Pnma*

$MgPd_2D_{0.964(6)}$ (85(1) %): *a* = 5.6092(4) Å, *b* = 4.0722(2) Å, *c* = 8.5245(6) Å,

V = 194.72(2) Å³, B_{iso}(overall)[a] = -0.34(6) Å², R_{Bragg} = 0.075)

$MgPd_2D_{0.158(6)}$ (14.4(5) %): a = 5.527(2) Å, b = 4.119(2) Å, c = 7.992(3) Å,

V = 181.9(1) Å³, B_{iso}(overall)[c] = 0 Å², R_{Bragg} = 0.130)

additional phase: MgO (0.54(4) %)

R_p = 0.041, R_{wp} = 0.051, χ^2 = 4.6

---

[a] Displacement parameters are fixed to the values of refinement of $MgPd_2D_{0.97(1)}$ (see Table 2). [b] Positional parameters are fixed to them of frame 23 (see Table S33). [c] Displacement parameters are fixed to the values of refinement of frame 4 (see Table S14) and B_{iso}(overall) is not refined for stability.
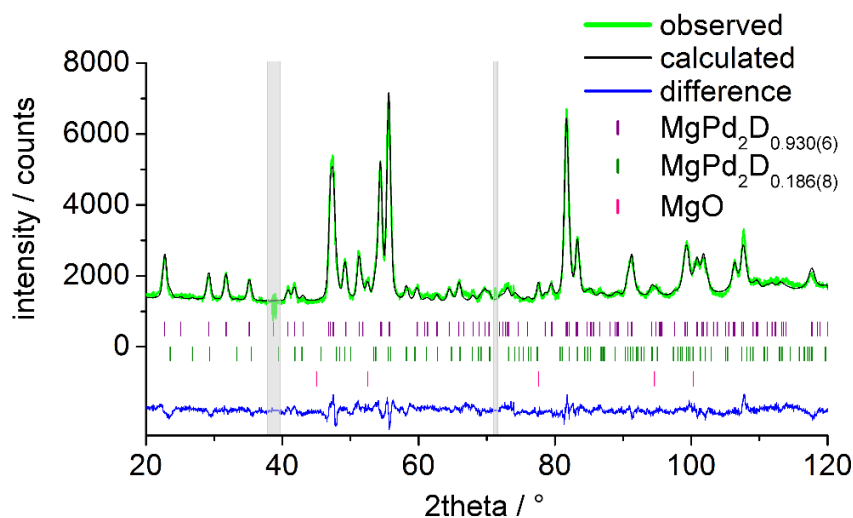
Figure S40. Rietveld refinement of frame 30 at temperature range from 316(1) to 310(1) K in single crystal sapphire cell under D$_2$ pressure range from 2.57(5) to 2.56(5) MPa based on neutron powder diffraction data (λ = 1.86786(3) Å, D20, ILL, Grenoble, NUMORS 959573-959582), using FullProf[3].

Table S40. Refined crystal structures of MgPd$_2$D$_{0.972(6)}$ and MgPd$_2$D$_{0.242(6)}$ (in italics) of frame 30 (2.57(5) MPa D$_2$, 313(3) K) and residual values of the refinement based on NPD (Fig. S40).

atom	Mg	Pd1	Pd2	D
Wyckoff site	4c	4c	4c	4c
x	0.3501(11)	0.3634(8)	0.3905(12)	0.6130(12)
	0.314(4)	*0.438(3)*	*0.422(6)*	*0.687[b]*
y	¼	¼	¼	¼
z	0.1004(7)	0.4326(5)	0.7746(6)	0.6094(6)
	0.124(3)	*0.418(4)*	*0.747(3)*	*0.611[b]*
SOF	1	1	1	0.972(6)
				0.242(6)

space group *Pnma*

MgPd$_2$D$_{0.972(6)}$ (85(1) %): a = 5.6098(4) Å, b = 4.0714(2) Å, c = 8.5262(6) Å,

V = 194.74(2) Å³, B_{iso}(overall)[a] = -0.39(6) Å², R_{Bragg} = 0.071)

MgPd$_2$D$_{0.242(6)}$ (14.4(5) %): a = 5.514(2) Å, b = 4.119(2) Å, c = 7.993(3) Å,

V = 181.54(12) Å³, B_{iso}(overall)[c] = 0 Å², R_{Bragg} = 0.136)

additional phase: MgO (0.49(3) %)

R_p = 0.040, R_{wp} = 0.051, χ^2 = 4.5

[a] Displacement parameters are fixed to the values of refinement of MgPd$_2$D$_{0.97(1)}$ (see Table 2). [b] Positional parameters are fixed to them of frame 23 (see Table S33). [c] Displacement parameters are fixed to the values of refinement of frame 4 (see Table S14) and B_{iso}(overall) is not refined for stability.
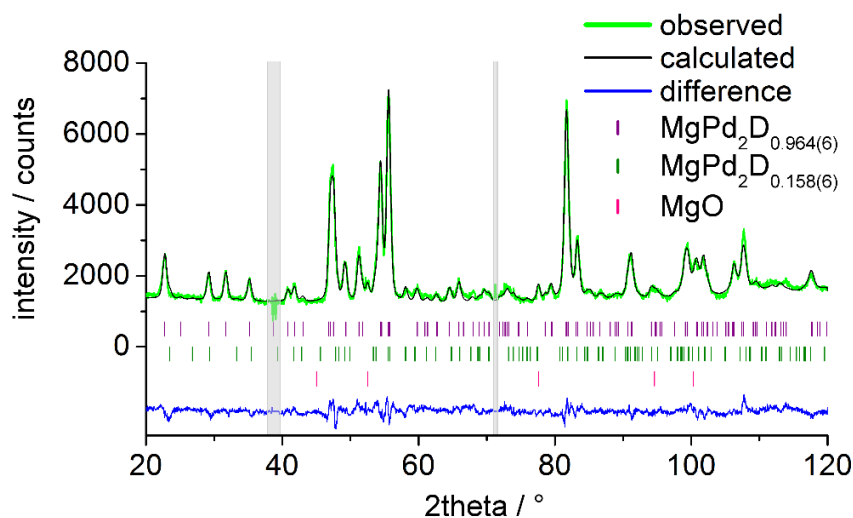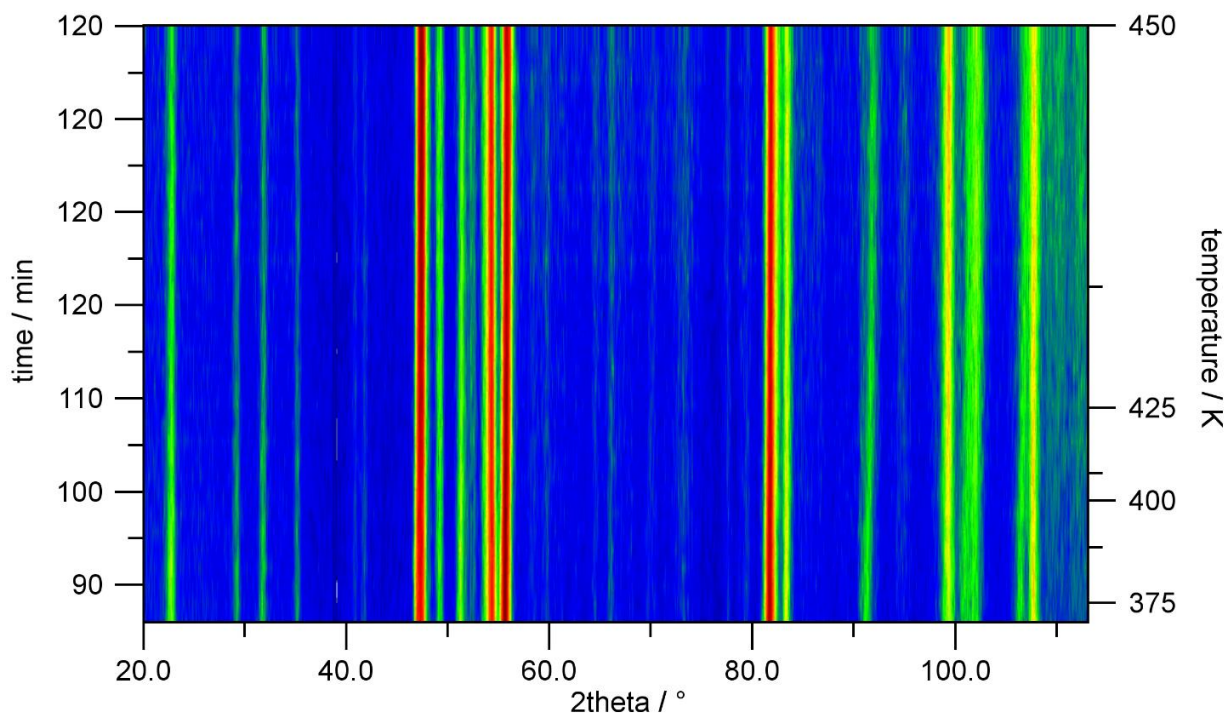
Figure S41. *In situ* neutron powder diffraction data of MgPd$_2$D$_{1-x}$ (NUMORS 959635-959667) during increasing temperatures (367(1) – 450(1) K) taken on diffractometer D20 at λ = 1.86786(3) Å in a single crystal sapphire cell under 10.0(1) MPa deuterium pressure. Intensities are in false colors.
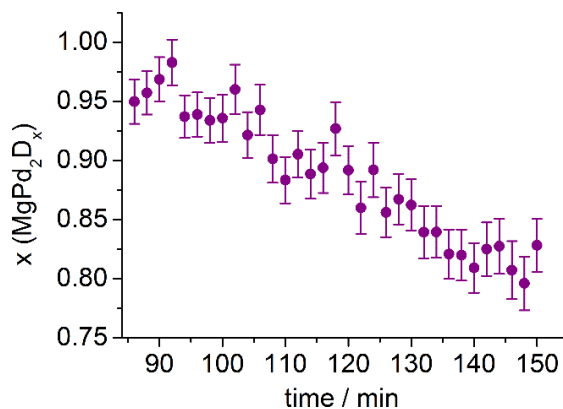
Figure S42. Deuterium occupation of MgPd$_2$D$_x$ as a function of time during increasing temperatures (367(1) – 450(1) K) from sequential Rietveld refinement based on neutron powder diffraction data under 10.0 MPa deuterium pressure (see figure S41). Error bars represent one estimated standard uncertainty

References

[1]   TOPAS version 5; Bruker AXS, www.bruker-axs.com.

[2]   A. March, Z. Kristallogr. 81 (1932) 285-297.

[3]   J. Rodríguez-Carvajal, FullProf: A Program for Rietveld Refinement and Pattern Matching Analysis (version 5.30); Insitut Laue-Langevin, Grenoble (France), 2012.

12. Crystal Structures and Hydrogenation Properties of Palladium-Rich Compounds with Elements from Groups 12-16

André Götze, Jonas M. Sander, Holger Kohlmann

Dedicated to Prof. Dr. Wolfgang Jeitschko on the Occasion of His 80th Birthday.

12.1. Authors' contributions

J. M. Sander did the syntheses and experiments on Pd_3As, $Pd_{20}Sb_7$, Pd_5Sb, Pd_8Sb_3 PdSb and Pd_5TlAs. He wrote the part "Binary palladium-rich compounds with element of group 15". The compounds $Pd_{0.75}Zn_{0.25}$, PdCd, PdHg, Pd_2Sn, $SnPd_3$, Pd_5Pb_3 $Pd_{13}Pb_9$ $PbPd_3$ Pd_5Bi_2, $Pd_{17}Se_{15}$, Pd_4Se, Pd_5CdSe, Pd_5HgSe, Pd_5InSe, Pd_8In_2Se, $Pd_3Bi_2Se_2$ Pd_5CdAs, Pd_5InAs were synthesized and investigated by A. Götze. The parts "Binary palladium-rich compounds with element of group 12", "- 14" and "- 16" as well as "Ternary palladium-rich compounds with Pd_5TlAs type and related structures" and "The half-antiperovskite $Pd_3Bi_2Se_2$" were written by A. Götze. The manuscript was revised by H. Kohlmann.

12.2. Abstract

We report on crystal structure data and hydrogenation properties of 24 palladium-rich intermetallic compounds with elements from groups 12–16 of the Periodic Table. Refined crystal structures based on X-ray powder diffraction data are presented for Pd_3As (Fe_3P type structure) and several members of the Pd_5TlAs type structure family. Hydrogenation was studied *in situ* by differential scanning calorimetry (DSC) under 5.0 MPa hydrogen pressure up to 430 ℃. $Pd_{0.75}Zn_{0.25}$, PdCd, PdHg, Pd_2Sn, Pd_5Pb_3, $Pd_{13}Pb_9$, Pd_3As, $Pd_{20}Sb_7$, Pd_8Sb_3, Pd_5Sb_2, PdSb, Pd_5Bi_2, $Pd_{17}Se_{15}$, Pd_4Se, Pd_5TlAs, Pd_5CdSe, Pd_5CdAs, Pd_5HgSe, Pd_5InAs, Pd_8In_2Se and $Pd_3Bi_2Se_2$ do not show any sign of hydrogen uptake according to DSC and X-ray diffraction. For Pd_3Sn and Pd_3Pb a significant hydrogen uptake with unit cell volume increases of 0.4 and 0.6 %, respectively, with a retained structure type of the parent intermetallic was observed. Hydrogenation of Pd_5InSe yields $Pd_3InH_{\approx 0.9}$ and a mixture of palladium selenides. Thermal analysis experiments in helium and in hydrogen atmosphere show that this is a multistep reaction with a decomposition of Pd_5InSe to Pd_3In and a liquid phase and subsequent hydrogenation of Pd_3In.

12.3. Introduction

Palladium can take up large amounts of hydrogen to form solid solutions PdH_{1-x} [1,2]. Palladium-rich phases, where some of the palladium atoms have been substituted by other metals in an ordered fashion, either show reduced hydrogen capacity as compared to pure palladium, e.g. MPd$_3$ phases (M = Mg [3], Ca [4], In [5], Tl [6], Y [7], Mn [8], Ce [9]), or no reactivity towards hydrogen like for Pd_2Al, Pd_3Al, Pd_2Ga, $Pd_{13}Ga_5$, Pd_5In_3, Pd_2In and Pd_5As [10,11]. In some cases the hydrogenation reactions in MPd$_3$ phases are accompanied by transformation of one superstructure of the cubic close packing (ccp, Cu type) to another ccp superstructure, e.g. from $ZrAl_3$ type $MgPd_3$ to an $AuCu_3$ type arrangement. This interesting rearrangement can formally be seen as a gliding of layers within the intermetallic structures, and through a hydrogenation-rearrangement-dehydrogenation cycle it produces metastable compounds not accessible via other synthesis routes [3,12]. In order to shed more light on this phenomenon we aim at a systematic investigation of the hydrogenation behavior of palladium-rich compounds. Especially, we would like to understand the prerequisites for hydrogen uptake and the hydrogen induced rearrangement as a function of the substitute M. Choosing a variety of elements M from groups 12–16 of the Periodic Table may help to distinguish between size and electronic effects, which both may play a role for hydrogenation and atomic rearrangement in palladium-rich intermetallic compounds. To the best of our knowledge, hydrogenation reactions were not reported for any of these compounds as yet.

12.4. Results and discussion

Twenty-four binary and ternary palladium-rich compounds with elements from groups 12–16 of the Periodic Table were synthesized from the elements. In order to monitor their reactivity towards hydrogen *in situ* thermal analysis experiments (differential scanning calorimetry, DSC) were performed on powder samples under 5.0 MPa hydrogen pressure up to 430 ℃ (see Experimental Section). In such experiments hydrogen uptake is often easily detected by exothermic signals [10]. In addition X-Ray powder diffraction (XRPD) data were taken before and after the hydrogenation DSC experiments. Rietveld analysis was used to accurately determine unit cell volumes (Table 12.4.1), because an increase often indicates a possible hydrogen uptake. A change of more than 0.2 % was considered significant in the following.

Table 12.4.1.: Structural properties of palladium-rich intermetallic compounds before and after hydrogenation according to Rietveld refinement on the basis of XRPD data (hydrogenation conditions in *in situ* DSC see Experimental section).

compound	unit cell volume increase (%)	secondary phases (XRD)	space group (structure type)	a (Å)	b (Å)	c (Å)	β (°)	unit cell volume V (Å^3)
$Pd_{0.75}Zn_{0.25}$		–	$Fm\bar{3}m$ (Cu type)	3.8680(6)				57.87(1)
	0.2	–	$Fm\bar{3}m$ (Cu type)	3.8708(1)				57.996(4)
PdCd		–	$P4/mmm$ (AuCu type)	3.0318(2)		3.6234(3)		33.309(4)
	−0.2	–	$P4/mmm$ (AuCu type)	3.0263(2)		3.6310(3)		33.254(5)
PdHg		–	$P4/mmm$ (AuCu type)	3.02697(5)		3.6967(1)		33.867(1)
	0	–	$P4/mmm$ (AuCu type)	3.02812(7)		3.6943(1)		33.875(2)
Pd_2Sn		18 % Pd_3Sn	$Pnma$ (Co$_2$Si type)	5.6424(2)	4.3072(1)	8.0899(3)		196.61(1)
	0	20 % Pd_3Sn	$Pnma$ (Co$_2$Si type)	5.64352(6)	4.30708(4)	8.08942(8)		196.630(3)
Pd_3Sn		5 % Pd_2Sn	$Pm\bar{3}m$ (AuCu$_3$ type)	3.9779(1)				62.947(4)
	0.4	5 % Pd_2Sn	$Pm\bar{3}m$ (AuCu$_3$ type)	3.9808(6)				63.084(2)
Pd_5Pb_3		2 % Pd_3Pb	$C2$ (Ni$_5$Ge$_3$ type)	13.3202(6)	7.6611(3)	7.2602(6)	52.231(6)	585.66(8)
	−0.3	7 % Pd_3Pb	$C2$ (Ni$_5$Ge$_3$ type)	13.2978(4)	7.6582(2)	7.2398(2)	52.384(2)	584.02(3)
$Pd_{13}Pb_9$		31 % Pd_5Pb_3	$C2/c$ (Pd$_{13}$Pb$_9$ type)	15.6057(3)	9.0577(2)	13.9238(4)	55.797(3)	1627.77(9)
	−0.1	32 % Pd_5Pb_3	$C2/c$ (Pd$_{13}$Pb$_9$ type)	15.6048(4)	9.0491(3)	13.9237(5)	55.806(3)	1626.3(1)
Pd_3Pb		–	$Pm\bar{3}m$ (AuCu$_3$ type)	4.03068(9)				65.484(3)
	0.6	–	$Pm\bar{3}m$ (AuCu$_3$ type)	4.03809(6)				65.846(2)
Pd_3As		–	$I\bar{4}$ (Ni$_3$P type)	9.9762(2)		4.82209(8)		479.92(1)
	0.2	–	$I\bar{4}$ (Ni$_3$P type)	9.988(1)		4.8216(6)		481.0(1)
$Pd_{20}Sb_7$		28 % Pd_8Sb_3	$R\bar{3}$ (Pd$_{20}$Sb$_7$ type)	11.7259(2)		11.0173(2)		1311.89(5)
Pd_5Sb_2		–	$P6_3cm$ (Pd$_5$Sb$_2$ type)	7.6154(2)		13.8835(4)		697.29(3)
	0.2		$P6_3cm$ (Pd$_5$Sb$_2$ type)	7.6205(5)		13.896(1)		689.8(1)
Pd_8Sb_3			$R\bar{3}c$ (Yb$_8$In$_3$ type)	7.6059(2)		42.999(2)		2154.1(2)
PdSb		–	$P6_3mmc$ (NiAs type)	4.07457(6)		5.5873(1)		80.333(2)
	0.2	–	$P6_3mmc$ (NiAs type)	4.0774(1)		5.5927(2)		80.522(4)
Pd_5Bi_2		–	$C2/m$ (Pd$_5$Bi$_2$ type)	14.3914(2)	5.76875(7)	6.73909(9)		489.13(1)
	0.2	–	$C2/m$ (Pd$_5$Bi$_2$ type)	14.3994(3)	5.7719(1)	6.74366(2)		490.03(2)
$Pd_{17}Se_{15}$		–	$Pm\bar{3}m$ (Pd$_{17}$Se$_{15}$ type)	10.6051(2)				1192.73(6)
	−0.2	–	$Pm\bar{3}m$ (Pd$_{17}$Se$_{15}$ type)	10.5983(2)				1190.45(5)
Pd_4Se		10 % Pd_7Se_2	$P\bar{4}2_1c$ (Pd$_4$Se type)	5.23037(6)		5.6439(1)		154.398(5)
	−0.3	–	$P\bar{4}2_1c$ (Pd$_4$Se type)	5.2246(6)		5.63807(6)		153.900(3)
Pd_5CdSe		20 % $Pd_{34}Se_{11}$	$P4/mmm$ (Pd$_5$TlAs type)	4.00638(4)		7.0052(1)		112.440(3)
	−0.1	15 % $Pd_{34}Se_{11}$	$P4/mmm$ (Pd$_5$TlAs type)	4.00496(8)		7.0036(2)		112.335(5)
Pd_5HgSe		–	$P4/mmm$ (Pd$_5$TlAs type)	4.01305(3)		7.03851(7)		113.352(2)
	0	–	$P4/mmm$ (Pd$_5$TlAs type)	4.01365(2)		7.03873(5)		113.390(1)
Pd_5InSe		–	$P4/mmm$ (Pd$_5$TlAs type)	4.0269(4)		6.9829(8)		113.23(2)
	–	Reaction to mixture of 63 % Pd$_3$InH$_x$ + 23 % Pd$_8$In$_2$Se + 14 % Pd$_{34}$Se$_{11}$						
Pd_8In_2Se		27 % Pd_5InSe	$P4/mmm$ (Pd$_8$In$_2$Se type)	4.0067(1)		10.9451(6)		175.71(1)
	–	Reaction to mixture of 68 % Pd$_3$InH$_x$ + 11 % Pd$_8$In$_2$Se + 9 % Pd$_{34}$Se$_{11}$ + 9 % Pd$_7$Se$_4$ + 3 % Pd$_{17}$Se$_{15}$						
$Pd_3Bi_2Se_2$		–	$C2/m$ (Ni$_3$Bi$_2$S$_2$ type)	11.7081(5)	8.4083(4)	8.3927(5)	113.845(3)	595.89(5)
	0	–	$C2/m$ (Ni$_3$Bi$_2$S$_2$ type)	11.712(1)	8.4094(9)	8.397(1)	113.893(6)	596.0(1)
Pd_5CdAs		9 % CdPd + 7% Pd_2As	$P4/mmm$ (Pd$_5$TlAs type)	3.97566(5)		6.9867(2)		110.431(4)
	0.1	10 % Pd_2As	$P4/mmm$ (Pd$_5$TlAs type)	3.97709(3)		6.9887(1)		110.542(3)
Pd_5InAs		11 % $Pd_{1-x}In_x$	$P4/mmm$ (Pd$_5$TlAs type)	3.9861(1)		6.9814(2)		110.925(5)
	0	11 % $Pd_{1-x}In_x$	$P4/mmm$ (Pd$_5$TlAs type)	3.98639(8)		6.9816(2)		110.946(5)
Pd_5TlAs		12 % $Pd_{13}Tl_9$	$P4/mmm$ (Pd$_5$TlAs type)	4.00146(9)		7.0427(2)		112.765(5)

12.4.1. Binary palladium-rich compounds with elements of group 12

The compounds PdCd, PdHg (both AuCu type) and $Pd_{0.75}Zn_{0.25}$ (solid solution of Cu type) were synthesized from the elements. The latter was formed in an attempt to prepare an ordered phase Pd_3Zn via mineralization by iodine within 3 months. Crystal structures refined on the basis of XRPD data (Table 12.4.1) are in good agreement with the literature [14–16]. No reaction with hydrogen is observed for any of the three compounds under given terms (Table 12.4.1).

12.4.2. Binary palladium-rich compounds with elements of group 14

The compounds Pd_2Sn (Co_2Si type), Pd_5Pb_3 (Ni_5Ge_3 type), and $Pd_{13}Pb_9$ ($Pd_{13}Pb_9$ type) do not show any reaction with hydrogen according to DSC experiments and by comparing XRPD data before and after the hydrogenation experiment. Refined crystal structures (Table 12.4.1) agree well with those from the literature [17–19]. The structures of Pd_3Sn and Pd_3Pb are also in accordance with literature [20]. However, an increase of the unit cell volume by up to 0.4 and 0.6 % upon hydrogenation, respectively, indicates a possible hydrogen uptake. $[Pd_6]$ octahedral sites, which are preferred by hydrogen [5], are present in their structures ($AuCu_3$ type). Several hydrides MPd_3H_x with occupation of these interstices, resulting in a cubic anti-perovskite type structure, are known already ($M =$ Mg [3], In [5], Tl [6], Y [7], Mn [8], Ce [9]). However, no significant thermal signal during the *in situ* DSC experiment could be observed. This may be assigned to low hydrogen content and small bonding energy of hydrogen in these compounds.

12.4.3. Binary palladium-rich compounds with elements of group 15

From the wide range of Pd–As compounds known [11,21–33] only for $PdAs_2$ and Pd_5As high quality crystal structure data are available [33,11]. For Pd_3As [26] only a structure type was assigned, but no crystal structure was refined. This prompted us to reinvestigate the crystal structure of Pd_3As and perform a Rietveld refinement based on XRPD data. The results (Table 12.4.2 and Fig. 12.4.1) confirm the assignment of the Fe_3P structure type ($D0_e$) and provide the first refined structure data for Pd_3As.

XRPD data confirm the NiAs structure type for PdSb and the refined lattice parameters (Table 12.4.1) are in good agreement with literature [34,35]. The correspondence of refined lattice parameters for Pd_5Sb_2, Pd_8Sb_3, $Pd_{20}Sb_7$, and Pd_5Bi_2 with those from literature [36–38] is also reasonable. According to the absence of thermal effects in DSC experiments and the absence of significant unit cell volume changes (no XRD for $Pd_{20}Sb_7$ and Pd_8Sb_3 after hydrogenation), none of the Pd–As, Pd–Sb and Pd–Bi phases investigated shows any signs for hydrogen uptake.

Table 12.4.2.: Crystal structure data for Pd_3As from Rietveld refinement based on X-ray powder diffraction data; Rietveld plot see Fig. 12.4.1

atom	Wyckoff site	symmetry	x	y	z	B_{iso} ($Å^2$)
Pd1	$8g$	1	0.0797(3)	0.1092(3)	0.257(1)	0.53(6)
Pd2	$8g$	1	0.1349(3)	0.4688(3)	0.0180(9)	0.25(6)
Pd3	$8g$	1	0.3290(3)	0.2775(3)	0.254(1)	0.18(6)
As	$8g$	1	0.2824(4)	0.0399(4)	0.019(1)	0.62(8)

space group $I\bar{4}$, $a = 9.9761(1)$ Å, $c = 4.82191(8)$ Å.

$R_p = 0.029$; $R_{wp} = 0.037$; $\chi^2 = 2.45$; $R_{Bragg} = 0.138$.
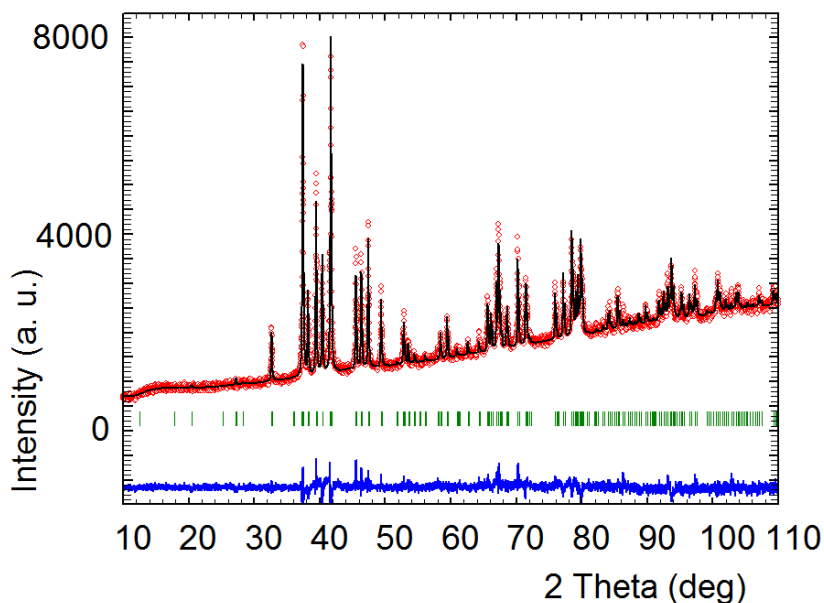
Figure 12.4.1.: Rietveld refinement of the crystal structure of Pd_3As based on X-ray powder diffraction data (CuK_α radiation); refined crystal structure data and residual values in Table 12.4.2. Further details of the crystal structure investigation may be obtained from Fachinformationszentrum Karlsruhe, 76344 Eggenstein-Leopoldshafen, Germany ((+49)7247-808-666; e-mail: crysdata@fiz-karlsruhe.de) on quoting the deposition number CSD-430924.

12.4.4. Binary palladium-rich compounds with elements of group 16

Pd_4Se and $Pd_{17}Se_{15}$ were synthesized and their structure are in good accord with literature data [39,40]. The unit cell volumes of both compounds decrease slightly during the hydrogenation experiment, which might be connected to the reaction of the side product in case of Pd_4Se (Table 12.4.1). DSC and XRPD experiments suggest the absence of significant hydrogen incorporation.

12.4.5. Ternary palladium-rich compounds with Pd_5TlAs type and related structures

The structure type of Pd_5TlAs may be described as an intergrowth structure with $AuCu_3$ like and CsCl like slabs [41]. It may also be derived from a cubic close packing by doubling of one lattice parameter, i. e. a cubic-tetragonal transition, and ordering the eight atomic positions in a 5:1:1:1 fashion with five palladium, one thallium, one arsenic atom and one vacancy. It thus represents one of many ordered intermetallic compounds related to the cubic close packing by crystallographic group–subgroup relationships [42–44]. This structure type exhibits many octahedral sites, which seem to be attractive for incorporation of hydrogen. Compounds with this type of structure thus seem to be good candidates for hydrogenation. The refined structures of Pd_5InAs, Pd_5HgSe and Pd_5InSe are in good agreement with literature [43,45–47]. For all other compounds listed in Tables 12.4.1 and 12.4.3 these are the first refined crystal structure data. The only free positional parameter, $z(Pd2)$ is higher for the compounds with arsenic than for those with selenium resulting in shorter Pd–As as compared to Pd–Se distances as expected from atomic sizes (Table 12.4.3). The c/a ratio of the Pd_5TlAs type

Table 12.4.3.: Crystal structure data of Pd_5TlAs type compounds ($P4/mmm$, Tl in $1c$ $^1/_2$ $^1/_2$ 0, As in $1b$ 0 0 $^1/_2$, Pd1 in $1a$ 0 0 0, Pd2 in $4i$ 0 $^1/_2$ z, refined lattice parameters see Table 12.4.1) as refined from XRPD data.

compound	$z(Pd2)$	c/a
Pd_5CdSe	0.2814(2)	1.7485
Pd_5HgSe	0.2891(2)	1.7539
Pd_5InSe	0.28111(8) [43]	1.7341
Pd_5CdAs	0.2921(1)	1.7572
Pd_5InAs	0.2929(3)	1.7514
Pd_5TlAs	0.2922(2)	1.76

structure is always considerably smaller than two. That means that the smaller selenium or arsenic atoms are packed closer along the crystallographic c direction than the larger cadmium, mercury, indium or thallium atoms.

From all compounds listed above only Pd_5InSe exhibits reactivity towards hydrogen (Table 12.4.1). The distorted $[Pd_4M_2]$ (M = Cd, Hg, In) and $[Pd_5X]$ (X = As, Se) octahedral sites in Pd_5MX are two possible hydrogen positons in this structure. Occupation by hydrogen would lead to distances between 1.96 and 2.06 Å, which are comparable with palladium-hydrogen d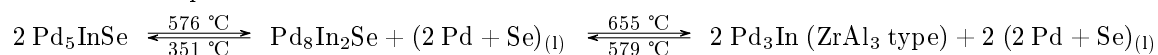istances in $Pd_3InH_{0.89}$ (2.01 Å [5]). However, unreasonably short distances As–H, Se–H, Cd–H, Hg–H, In–H, Tl–H would result, which probably prevents hydrogen from entering the structures.

Pd_5InSe and Pd_8In_2Se [46] form Pd_3InH_x during the hydrogenation experiment. Differential thermal analysis (DTA) of Pd_5InSe in helium atmosphere was executed and the results have shown two reversible thermal signals with a hysteresis (Fig. 12.4.2, top). X-ray powder diffraction after the DTA confirmed that the reaction is fully reversible. To investigate the intermediates, a temperature-resolved XRPD experiment was carried out. The false color plot (Fig. 12.4.2, bottom) shows the formation of Pd_8In_2Se at about 525 ℃. Upon further heating Pd_8In_2Se decomposed at about 625 ℃ and Pd_3In ($ZrAl_3$ type) was formed. On cooling (not shown here) Pd_5InSe returned. We suggest the following reactions to take place:

$$2\,Pd_5InSe \xrightleftharpoons[351\,℃]{576\,℃} Pd_8In_2Se + (2\,Pd + Se)_{(l)} \xrightleftharpoons[579\,℃]{655\,℃} 2\,Pd_3In\,(ZrAl_3\ type) + 2\,(2\,Pd + Se)_{(l)}$$

For the proposed liquid phase we have indirect evidence from annealing experiments. Pd_5InSe samples were annealed at 600 and 800 ℃, i. e. after the first and second thermal signal in the DTA, respectively, and the silica glass ampoules were quenched in water. The main phases were Pd_8In_2Se at 600 ℃ and Pd_5In at 800 ℃ with secondary phases $Pd_{34}Se_{11}$, Pd_7Se_4 and $Pd_{17}Se_{15}$. The latter forms from the liquid (2 Pd + Se) by quenching according to the phase diagram [48] of the system Pd–Se. Thus, hydrogen plays a role in the reactions (Table 12.4.1) only insofar that it reacts with Pd_3In formed by thermal decomposition of Pd_5InSe.

12.4.6. The half-antiperovskite $Pd_3Bi_2Se_2$

The half-antiperovskite $Pd_3Bi_2Se_2$ ($Ni_3Bi_2S_2$ type) [49] was investigated for its hydrogenation properties. $[Pd_6]$ octahedral sites in its crystal structure, albeit strongly distorted, suggested this structure family to be a good hydrogenation candidate from geometric reasons. However, neither *in situ* DSC nor comparison of unit cell volumes before and after the hydrogenation experiment hint towards any hydrogen uptake.
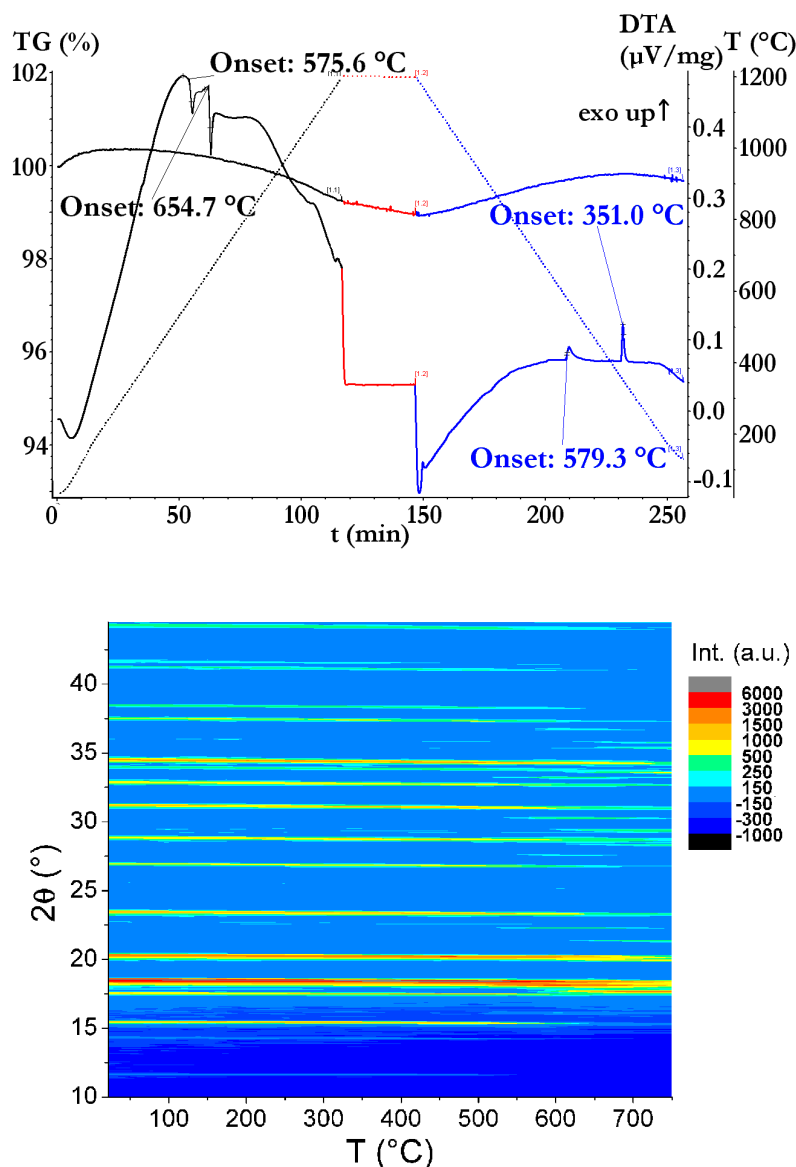
Figure 12.4.2.: Differential thermal analysis (top) and temperature-resolved XRPD (Mo$K_{\alpha 1}$ radiation; bottom) of Pd$_5$InSe.

12.5. Conclusion

Twenty-four palladium-rich intermetallic compounds were synthesized, their crystal structures refined by the Rietveld method and their hydrogenation behavior investigated. For Pd$_3$As, Pd$_5$CdSe, Pd$_5$CdAs, Pd$_5$TlAs, the refined crystal structure data are presented for the first time. From all investigated compounds, only Pd$_3$Sn and Pd$_3$Pb show signs of significant hydrogen uptake while retaining the structure type of the parent intermetallic compound. No hydrogen uptake could be observed for any compound containing an element of groups 15 or 16. This seems to confirm the assumption that electronic effects are more important than geometric effects in palladium-rich intermetallic compounds [50]. Pd$_5$InSe decomposes to Pd$_3$In and palladium selenides, the former reacting with hydrogen to yield Pd$_3$InH$_{\approx 0.9}$.

12.6. Experimental section

12.6.1. Synthesis of intermetallic compounds

Intermetallic compounds were synthesized from stoichiometric mixtures of the elements in evacuated silica tubes. Temperature treatment is given in the following as final temperature, holding time and heating rate, e. g. 875 ℃ 24 h 1 ℃ min^{-1} describes a temperature treatment of heating with 1 ℃ min^{-1} to 875 ℃, holding this temperature for 24 h and cooling with the natural cooling rate of the furnace. In some cases a few mg of iodine was added (chemical vapor transport reaction), denoted by "I$_2$".

$Pd_{0.75}Zn_{0.25}$: 1000 ℃ 4 d

PdCd: 770 ℃ 3 h, 280 ℃ 14 d

PdHg: I$_2$, 400 ℃ 9 d 1 ℃ min^{-1}

Pd_2Sn: I$_2$, 720 ℃ 5 d 1 ℃ min^{-1}

Pd_3Sn: 720 ℃ 72 h 1 ℃ min^{-1}

Pd_5Pb_3: 1200 ℃ 2 h 1.5 ℃ min^{-1} quenched at 900 ℃, ground in mortar, 370 ℃ 11 d 1 ℃ min^{-1}

$Pd_{13}Pb_9$: 1200 ℃ 2 h 1.5 ℃ min^{-1} quenched at 900 ℃, ground in mortar, 520 ℃ 9 d 1 ℃ min^{-1}

Pd_3Pb: I$_2$, 875 ℃ 24 h 1 ℃ min^{-1}, 430 ℃ 7 d

Pd_3As: 650 ℃ 2 h 3.5 ℃ min^{-1}, 1000 ℃ 72 h 2 ℃ min^{-1}

$Pd_{20}Sb_7$: 900 ℃ 168 h 2.1 ℃ min^{-1}, 25 ℃ 1.2 ℃ min^{-1}

Pd_8Sb_3: 1000 ℃ 120 h 1.8 ℃ min^{-1}

Pd_5Sb_2: 1000 ℃ 168 h 1.3 ℃ min^{-1}

PdSb: 850 ℃ 6 h 2 ℃ min^{-1}, 750 ℃ 48 h 1.7 ℃ min^{-1}

Pd_5Bi_2: I$_2$, 450 ℃ 4 d 0.5 ℃ min^{-1}

$Pd_{17}Se_{15}$: 430 ℃ 7 d 1 ℃ min^{-1}

Pd_4Se: 700 ℃ 2 h 1 ℃ min^{-1}, 375 ℃ 7 d

Pd_5TlAs: 650 ℃ 2 h 3.4 ℃ min^{-1}, 1000 ℃ 30 h 1.9 ℃ min^{-1}

Pd_5CdSe, Pd5CdAs: 750 ℃ 6 d 1 ℃ min^{-1}

Pd_5HgSe I$_2$, 400 ℃ 10 d

Pd_5InSe, Pd5InAs: I2, 950 ℃ 4 h; 700 ℃ 7 d

Pd_8In_2Se 950 ℃ 4 h; 750 ℃ 6 d

$Pd_3Bi_2Se_2$: 1200 ℃ 1 h 3 ℃ min^{-1}; 500 ℃ 500 h

Products were obtained as gray powders, some of them with a silvery luster.

12.6.2. X-ray powder diffraction

XRPD data were collected using flat reflection samples on a Panalytical X'Pert at $T = 23(1)$ ℃ with CuK_α radiation or using flat transmission samples on a Huber Guinier G670 camera with an image plate system using either Cu$K_{\alpha 1}$ or Mo$K_{\alpha 1}$ radiation. Rietveld refinements were carried out with the program FullProf [13] and pseudo-Voigt as profile function. Absorption effects were modelled with a fixed overall thermal displacement parameter of -1.8 Å^2 in the refinement of the crystal structure of Pd_3As.

12.6.3. Thermal analysis (*in situ* DSC and *ex situ* DTA)

Differential scanning calorimetry was performed *in situ* under hydrogen pressures on a Q1000 DSC (TA Instruments) equipped with a gas pressure chamber. Twenty to thirty milligrams of the powdered intermetallics was put in aluminum crucibles, which were closed with an aluminum lid. These were placed inside the pressure chamber, which was then purged several times with hydrogen gas before filling it to the final hydrogen gas pressure of 5.0 MPa. Samples were heated to 430 ℃ with 10 ℃ min^{-1}, held at that temperature for a minimum of 1 h, and cooled to 27 ℃ with 10 ℃ min^{-1}. Usually, two or three such runs were performed, before the hydrogen pressure was released, the sample taken out and structural characterization undertaken. After releasing the gas pressure, the products were characterized *ex situ* by XRPD. The difference thermal analysis (DTA) of Pd_5InSe in helium atmosphere was carried out on a Netzsch F1 Jupiter device using sintered alumina crucibles and a heating rate of 10 ℃ min^{-1}.

12.7. References for chapter 12

[1] T. Graham, On the absorption and dialytic separation of gases by colloid septa, Philos. Trans. R. Soc. London 156 (1866) 399–439.

[2] T. B. Flanagan, W.A. Oates, The palladium-hydrogen system, Annu. Rev. Mater. Sci. 21 (1991) 269–304.

[3] H. Kohlmann, N. Kurtzemann, R. Weihrich, T. Hansen, *In situ* neutron powder diffraction on intermediate hydrides of $MgPd_3$ in a novel sapphire gas pressure cell, Z. Anorg. Allg. Chem. 635 (2009) 2399–2405.

[4] E. Rönnebro, D. Noréus, M. Gupta, K. Kadir, B. Hauback, P. Lundqvist, The crystal and electronic structure of $CaPd_3H$, Mater. Res. Bull. 35 (2000) 315–323.

[5] H. Kohlmann, A. V. Skripov, A. V. Soloninin, T. J. Udovic, The anti-perovskite type hydride $InPd_3H_{0.89}$, J. Solid State Chem. 183 (2010) 2461–2465.

[6] N. Kurtzemann, H. Kohlmann, Crystal structure and formation of $TlPd_3$ and its new hydride $TlPd_3H$, Z. Anorg. Allg. Chem. 636 (2010) 1032–1037.

[7] S. Yamaguchi, M. Ohashi, T. Kajitani, K. Aoki, S. Ikeda, Distribution of hydrogen atoms in YPd_3H_x studied by neutron diffraction and inelastic neutron scattering, J. Alloys Compd. 253-254 (1997) 308–312.

[8] K. Baba, Y. Niki, Y. Sakamoto, T. B. Flanagan, A. Craft, Reversibile Transitions between ordered structures in the Pd_3Mn-hydrogen system, Scr. Metall. 21 (1987) 1147–1151.

[9] H. Kohlmann, F. Müller, K. Stöwe, A. Zalga, H. P. Beck, Hydride formation in the intermetallic compounds $CePd_3$ and $CeRh_3$, Z. Anorg. Allg. Chem. 635 (2009) 1407–1411.

[10] H. Kohlmann, Hydrogenation of palladium-rich compounds of aluminium, gallium and indium, J. Solid State Chem. 183 (2010) 367–372.

[11] H. Kohlmann, M. Vasseur, A. Sayede, G. Lefevre, J. M. Sander, S. Doyle, Crystal structure and hydrogenation properties of Pd_5As, J. Alloys Compd. 664 (2016) 256–265.

[12] N. Kunkel, J. Sander, N. Louis, Y. Pang, L.M. Dejon, F. Wagener, Y. N. Zang, A. Sayede, M. Bauer, M. Springborg, H. Kohlmann, Theoretical investigation of the hydrogenation induced atomic rearrangements in palladium-rich intermetallic compounds MPd_3 (M = Mg, In, Tl), Eur. Phys. J. 82B (2011) 1–6.

[13] J. Rodríguez-Carvajal, FullProf: a Program for Rietveld Refinement and Pattern Matching Analysis, Insitut Laue-Langevin, Grenoble (France), 2012.

[14] K. Terada, F. W. Cagle, Jr., The crystal structure of potarite (PdHg) with some comments on allopalladium, Am. Miner. 45 (1960) 1093-1097.

[15] J. P. Neumann, A. Mikula, Y. A. Chang, Phase stability investigations of the palladium-cadmium system: Part II. structural studies, Metall. Trans. A 13 (1982) 1123-1126.

[16] H. N. Nowotny, E. Bauer, A. Stempfl, Ein Beitrag zum System Palladium-Zink, Monatsh. Chem. 82 (1951) 1086-1093.

[17] K. Page, C. S. Schade, J. Zhang, P. J. Chupas, K. W. Chapman, T. Proffen, A. K. Cheetham, R. Seshadri, Preparation and characterization of Pd_2Sn nanoparticles, Mater. Res. Bull. 42 (2007) 1969-1975.

[18] M. Ellner, T. Gödecke, K. Schubert, Phases in the mixture Pd-Pb, Z. Metallkd. 64 (1973) 566-568.

[19] H. W. Mayer, M. Ellner, K. Schubert, Crystal structure of $Pd_{13}Pb_9$.r J. Less-Common Met. 71 (1980) P29-P38.

[20] M. Ellner, Zusammenhang zwischen strukturellen und thermodynamischen Eigenschaften bei Phasen der Kupfer-Familie in T10-B4-Systemen, J. Less-Common Met. 78 (1981) 21–32.

[21] L. Thomassen, Über Kristallstrukturen einiger binärer Verbindungen der Platinmetalle II, Z. Phys. Chem., Abt. B 4 (1929) 277-287.

[22] G .F. Claringbull, M. H. Hey, Mineral. Soc., Notice No. 94 (1954) 1004.

[23] S. Geller, B. T. Matthias, Superconductivity in the Ni-Pd-As system, J. Phys. Chem. Solids 4 (1958) 156-157.

[24] K. Schubert, S. Bhan, W. Burkhardt, R. Gohle, H. G. Meissner, M. Pötzschke, E. Stolz, Einige strukturelle Ergebnisse an metallischen Phasen (5), Naturwissenschaften 47 (1960) 303.

[25] C. J. Raub, G. W. Webb, An investigation of the phase-diagram palladium-arsenic in connection with superconductivity, J. Less-Common Met. 5 (1963) 271-277.

[26] G. S. Saini, L. D. Calvert, R. D. Heyding, J. B. Taylor, Arsenides of the transition metals: VII. The palladium–arsenic system, Can J. Chem. 42 (1964) 620-629.

[27] G. S. Saini, L. D. Calvert, J. B. Taylor, Compounds of the type M_5X_2: Pd_5As_2, Ni_5Si_2, and Ni_5P_2, Can J. Chem. 42 (1964) 1511-1517.

[28] U. Bälz, K. Schubert, Kristallstruktur von Pd_2As (r) und Pd_2Sb, J. Less-Common Met. 19 (1969) 300-304.

[29] L. J. Cabri, J. H. G. LaFlamme, J. M. Stewart, J. F. Rowland, T. T. Chen, New data on some palladium arsenides and antimonides, Can. Mineral. 13 (1975) 321-335.

[30] T. Matkovic, K. Schubert, Kristallstruktur von Pd_5As und Pd_5Ge, J. Less-Common Met. 58 (1978) P1-P6.

[31] M. Ellner, On the crystal chemical parameters of metastable intermetallic compounds, Z. Metallkd. 76 (1985) 372-377.

[32] H. Okamoto, As-Pd (arsenic-palladium), J. Phase Equilib. 13 (1992) 572-573.

[33] N. E. Brese, H. G. von Schnering, Bonding trends in pyrites and a reinvestigation of the structures of $PdAs_2$, $PdSb_2$, $PtSb_2$ and $PtBi_2$, Z. Anorg. Allg. Chem. 620 (1994) 393-404.

[34] J. N. Pratt, K. M. Myles, J. B. Darby, Jr., M. H. Mueller, X-Ray studies of palladium-cadmium and palladium-antimony alloys, J. Less-Common Met. 14 (1968) 427-433.

[35] W. S. Kim, G. Y. Chao, Phase relations in the system Pd-Sb-Te, Can. Mineral. 29 (1991) 401-409.

[36] M. El-Boragy, S. Bhan, K. Schubert, Kristallstruktur von Pd_5Sb_2 und Ni_5As_2 und einigen Varianten, J. Less-Common Met. 22 (1970) 445-458.

[37] M. Ellner, M. El-Boragy, Über die eisenhaltigen Vertreter des Strukturtyps Pd_5Sb_2, J. Alloys Compd. 184 (1992) 131-138.

[38] N. Sarah, K. Schubert, Kristallstruktur von Pd_5Bi_2, J. Less-Common Met. 63 (1979) P75-P82.

[39] T. Takabatake, M. Ishikawa, J. L. Jorda, Superconductivity and phase relations in the Pd-Se system, J. Less-Common Met. 134 (1987) 79-89.

[40] S. Geller, The crystal structure of $Pd_{17}Se_{15}$, Acta Crystallogr. 15 (1962) 713-721.

[41] W. B. Pearson, The similarities of the populous Cu_2Sb and $TlAsPd_5$ structures: Analysis of the building principles and formula of the $TlAsPd_5$ structure, Z. Kristallogr. 175 (1986) 187-193.

[42] H. Kohlmann, C. Ritter, Reaction pathways in the formation of intermetallic $InPd_3$ Polymorphs, Z. Anorg. Allg. Chem. 635 (2009) 1573–1579.

[43] A. Götze, P. Urban, O. Oeckler, H. Kohlmann, Synthesis and Crystal Structure of Pd_5InSe, Z. Naturforsch. 69b (2014) 417-422.

[44] R. Pöttgen, Coloring, distortions, and puckering in selected intermetallic structures from the perspective of group-subgroup relations, Z. Anorg. Allg. Chem. 640 (2014) 869-891.

[45] F. Laufek, A. Vymazalová, M. Drábek, J. Navrátil, T. Plrchácek, J. Drahokoupil, Crystal structure and transport properties of Pd_5HgSe, Solid State Sci. 14 (2012) 1476-1479.

[46] E. Y. Zakharova, S. M. Kazakov, A. A. Isaeva, A. M. Abakumov, G. Van Tendeloo, A. N. Kuznetsov, Pd_5InSe and Pd_8In_2Se – New metal-rich homological selenides with 2D palladium–indium fragments: Synthesis, structure and bonding, J. Alloys Compd. 589 (2014) 48-55.

[47] E. Y. Zakharova, N. A. Andreeva, S. M. Kazakov, A. N. Kuznetsov, Ternary arsenides based on platinum–indium and palladium–indium fragments of the Cu_3Au-type: Crystal structures and chemical bonding, J. Alloys Compd. 621 (2015) 307-313.

[48] H. Okamoto, The Pd-Se (palladium-selenium) system, J. Phase Equilib. 13 (1992) 69-72.

[49] R. Weihrich, S. F. Matar, I. Anusca, F. Pielnhofer, P. Peter, F. Bachhuber, V. Eyert, Palladium site ordering and the occurrence of superconductivity in $Bi_2Pd_3Se_{2-x}S_x$, J. Solid State Chem. 184 (2011) 797-804.

[50] X. Ke, G. J. Kramer, O. M. Løvvik, The influence of electronic structure on hydrogen absorption in palladium alloys J. Phys.: Condens. Matter 16 (2004) 6267-6277.

13. Ternary Palladium-Indium-Phosphorus and Platinum-Indium-Phosphorus Compounds Based on the Cu₃Au-type: Structure, Bonding, and Properties

Elena Y. Zakharova, Sergey M. Kazakov, André Götze, Holger Kohlmann, Alexey N. Kuznetsov

This manuscript is accepted.
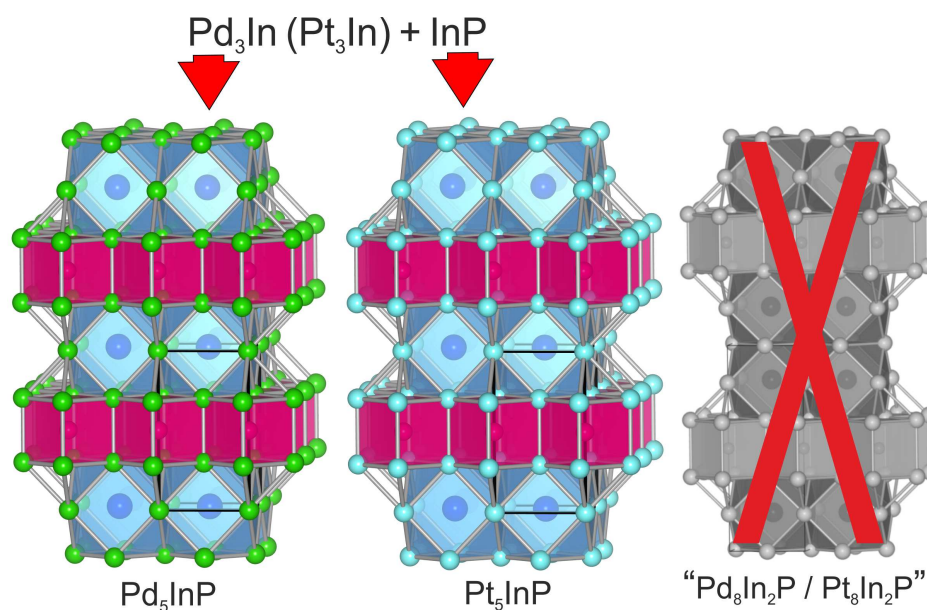
13.1. Authors' contributions

E.Y. Zakharova, S. M. Kazakov and A. N. Kuznetsov did the synthesis, crystal structure analysis, DFT calculations and wrote the manuscript. A. Götze and H. Kohlmann performed the hydrogenation studies.

13.2. Abstract

Two metal-rich palladium-indium and platinum-indium phosphorus-containing compounds, Pd_5InP and Pt_5InP, were synthesized as phase-pure powders using a high-temperature ampoule technique. Their crystal structures were determined from Rietveld analysis of powder diffraction data. Both compounds crystallize in tetragonal system with $P4/mmm$ space group (Pd_5InP: $a = 3.9303(5)$ Å, $c = 6.9269(1)$ Å, $Z = 1$, $R_p = 0.029$; $R_b = 0.004$; Pt_5InP: $a = 3.9500(1)$ Å, $c = 6.9814(3)$ Å, $Z = 1$, $R_p = 0.034$, $R_b = 0.005$). Both compounds belong to the rare Pd_5TlAs structure type, with their main structural units being indium-centered $[TM_{12}In]$ cuboctahedra (TM = Pd, Pt) of the Cu_3Au type, single-stacked along the c axis, alternating with $[TM_8P]$ rectangular prisms of the $PtHg_2$ type. DFT electronic structure calculations predict both compounds to be 3D metallic conductors and to show diamagnetic behavior. The latter was confirmed by magnetic measurements. Charge density analysis shows that both compounds are intermetallic in nature. According to the bonding analysis based on the electron localizability indicator topology, both compounds feature four-centered interactions of the $3TM+$In type between the transition metal and indium atoms in their heterometallic fragments. Additionally, essentially pairwise interactions between platinum atoms are also observed, indicating a somewhat more localized bonding in the case of platinum-based compounds. Both compounds do not show any significant hydrogen uptake up to pressures of ca. 7 MPa and temperatures of 700 K.

13.3. Introduction

Ordered intermetallic compounds are a fascinating object of studies, featuring both wide variety of structures and a range of convoluted bonding patterns, often accompanied by interesting and potentially useful physical properties. When such metallic system is diluted with a typical non-metal, the situation with both structure and bonding becomes even less straightforward. In our work, we are particularly interested in obtaining new structural arrangements based on well-established intermetallic fragments, one of which is a cubic Cu_3Au structure type based on the copper structure. Applying this approach to the palladium-indium and platinum-indium intermetallics of the Cu_3Au type and its derivatives, and introducing such typical non-metals as selenium and arsenic into a heterometallic matrix, we have recently characterized several new mixed palladium-indium and platinum-indium selenides and arsenides, such as Pd_5InSe [1,2], Pd_8In_2Se [1], $Pd_{17}In_4Se_4$ [3], Pd_5InAs, Pt_5InAs, and Pt_8In_2As [4], all of which feature cuboctahedral $[Pd_{12}In]$ fragments that are encountered in binary intermetallics of the Cu_3Au structure type. The compounds with 5:1:1 atomic ratios belong to the Pd_5TlAs structure type, a relatively uncommon type that was established in early 1970s by EL-BORAGY and SCHUBERT [5] and until recently included only a few structurally characterized palladium- and platinum-based compounds, e. g. Pt_5MgP [5] and Pd_5HgSe [6]. The compounds with 8:2:1 atomic ratio belong to the Pd_8In_2Se-type [1], that features double-stacked along the c axis $[Pd_{12}In]$ fragments, separated by the same type of rectangular prisms of the $PtHg_2$ type as in Pd_5InSe, and thus is essentially a second homologue to the Pd_5TlAs type of structure.

It must be noted that although several other palladium and platinum ternary pnictides, silicides and selenides, belonging to the Pd_5TlAs type, were suggested in the same paper [5], no structural data was provided and the compositions were not established properly, and in many cases the assignment to the structure type was made based on the poly-phase samples containing up to 50 % impurities. And, surprisingly, the structures of most of the suggested compounds were never studied since then, let alone their properties. Here we report the results of our purposeful synthesis of the compounds of the Pd_5TlAs- and Pd_8In_2Se-type in Pd-In-P and Pt-In-P systems, their crystal and electronic structures, bonding analysis, as well as magnetic properties and the response to hydrogenation.

13.4. Material and methods

13.4.1. Synthetic and analytical procedures

Two synthetic routes were used during the sample preparation. Palladium (foil, 99.98 %) and platinum (powder, 99.8 %), indium (shot, 99.999 %), and red phosphorus (98 %, purified by treating with alkaline solution, rinsed with distilled water, and thoroughly dried in vacuum dissicator) were used for initial synthetic attempts. Stoichiometric mixtures of the elements (ca. 0.4–0.8 g in total per sample) were put into dried silica ampoules, sealed under vacuum (ca. 3 Pa), and annealed at 873 K for 48 h, then cooled down. The products were then thoroughly ground and pressed into pellets, put back into evacuated silica ampoules and annealed twice for 360 h at 873 K with intermediate homogenization, then cooled down naturally. According to the XRPD data (Stoe Theta/Theta, CuK_α radiation), all samples contained large amounts of impurities. Phase-pure samples of both Pd_5InP and Pt_5InP were obtained by using high puritygrade InP (> 99.99 %) rather than elemental indium and phosphorus as starting substances. That second synthetic route implied using stoichiometric amounts of palladium and platinum metals along with InP, that were put into evacuated silica ampoules and annealed at 873 K for 180 h, then re-ground, pressed into pellets and annealed at the same temperature for another 300 h, then cooled down naturally. The resulting products did not contain any impurities detectable by the XRRD. Attempts were made to synthesize 8:2:1 compositions using transition metals, indium, and indium phosphide, following the same synthetic procedure as for phase-pure 5:1:1 compositions. However, XRD data showed that only 5:1:1 compounds and respective binary intermetallics were present in the samples after annealing.

13.4.2. Crystal structure determination

X-ray powder diffraction patterns were recorded using a Bruker D8 Advance diffractometer ($CuK_{\alpha 1}$-radiation, Ge(111) monochromator, reflection geometry, LynxEye strip detector). Crystal structures of both compounds were refined using the Rietveld method as implemented in the TOPAS package [7]. Rietveld refinements were performed using the fundamental parameter approach for the peak shape description. The starting structural model was derived from the published data for Pd_5InSe [1] and Pt_5InAs [4]. The preferred orientation was corrected using a spherical harmonics approach implemented in TOPAS.

13.4.3. Computational details

Band structure calculations for Pd_5InP and Pt_5InP were performed on a density-functional theory (DFT) level utilizing the all-electron full-potential linearized augmented plane wave method (FP-LAPW) as implemented in the ELK code [8], as well as using the PAW pseudopotential approach as implemented in the VASP code [9, 10]. In all-electron calculations, the Brillouin zone sampling was performed using 11 x 11 x 7 k-point grid (84 irreducible k-points), the muffin-tin sphere radii for the respective atoms were (Bohr): 2.60 (In), 2.55 (Pt), 2.44 (Pd), 2.00 (P), and the maximum moduli for the reciprocal vectors k_{max} were chosen so that $R_{MT}k_{max} = 10.0$. In the pseudopotential approach, a Monckhorst-Pack k-point mesh of 14 x 14 x 10 (140 irreducible k-points) was employed, and the energy cutoff was set at 500 eV. The PBESol exchange-correlation functional [11] of the GGA-type was used in all calculations. The convergence of the total energy with respect to the k-point sets was checked. Atomic charges were analyzed according to Bader's QTAIM approach [12]. The electron localizability indicator (ELID) was calculated according to [13] using DGrid package [14]. The calculations were performed using the Intel Core-i7-based laboratory cluster and the MSU Lomonosov

supercomputer [15]. Structure visualization and topological analysis of the electron localization indicator were performed using VESTA [16] and ParaView [17] packages, respectively. The Crystal Orbital Hamilton Population (COHP) analysis, based on the VASP calculations, was performed according to [18-20] using the Lobster 2.2.1 software package [21]. The hypothetical structure of Pt_8In_2P compound was obtained by unconstrained structure optimization using the VASP package and Pt_8In_2As (tetragonal, $P4/mmm$) unit cell as starting model. The Pt_8In_2P cell metrics converged to the values of $a = 3.9566$ Å, $c = 11.0239$ Å, which is naturally smaller than those of Pt_8In_2As ($a = 3.9872$ Å, $c = 11.1129$ Å). The COHP plots were done using wxDragon package [22].

13.4.4. Magnetic measurements

Magnetic measurements on the bulk samples were performed on a Quantum Design PPMS-9 magnetometer in the temperature range of 4–300 K in the magnetic field of 5 kOe. Corrections for the diamagnetic contribution of a probe holder were made. Both Pd_5InP and Pt_5InP were found to be diamagnetic.

13.4.5. Hydrogen uptake measurements

Differential scanning calorimetry (DSC) was performed in situ under hydrogen pressure on a Q1000 device (TA Instruments) equipped with a gas pressure chamber. Ca. 20 mg of the powdered sample was put into an aluminum crucible, sealed with an aluminum lid and placed inside the pressure chamber, which was then purged several times with hydrogen gas, before filling it to the starting hydrogen gas pressure of 5.0 MPa at 308 K. The sample was then heated to 700 K at a rate of 10 K per min, held at that temperature for a minimum of 1 h, and cooled down to 300 K. During the heating cycle, the pressure increases up to 7.1 MPa. Two runs were performed; then the hydrogen pressure was released, the sample taken out and characterization undertaken by XRPD.

13.5. Results and discussion

13.5.1. Remarks on the synthetic procedures

In both palladium- and platinum-based systems, we have attempted to produce both first and second homologues, i. e. TM_5InP and TM_8In_2P (TM = Pd, Pt) types of compounds, analogous to the previously obtained palladium-indium selenides [1] and platinum-indium arsenides [4], with the synthetic conditions chosen accordingly. XRPD data from both systems have shown that only the first homologue, TM_5InP, is obtained in each case in the form of phase-pure samples, while the ones with the TM_8In_2P target composition contained mixtures of TM_5InP and TM_3In. Therefore we have to conclude that the second homologues in either system cannot be produced under equilibrium conditions. It also has to be noted that the synthesis of phase-pure TM_5InP fails if performed from the elements, even after several annealings of pressed pellets for considerable amount of time with mechanical homogenization in-between. The most likely reason for such difficulties is extreme difference in melting points of the components, making the reaction media heterogeneous and severely reducing the interface areas. This problem was also encountered in the synthesis of palladium-indium selenium- and arsenic-containing compounds [1,4]. In the case of phosphorus-containing ones, however, it can be rectified by the use of InP as a precursor, which allows to obtain phase-pure samples using reasonable annealing times and the same temperatures as synthesis from the elements.
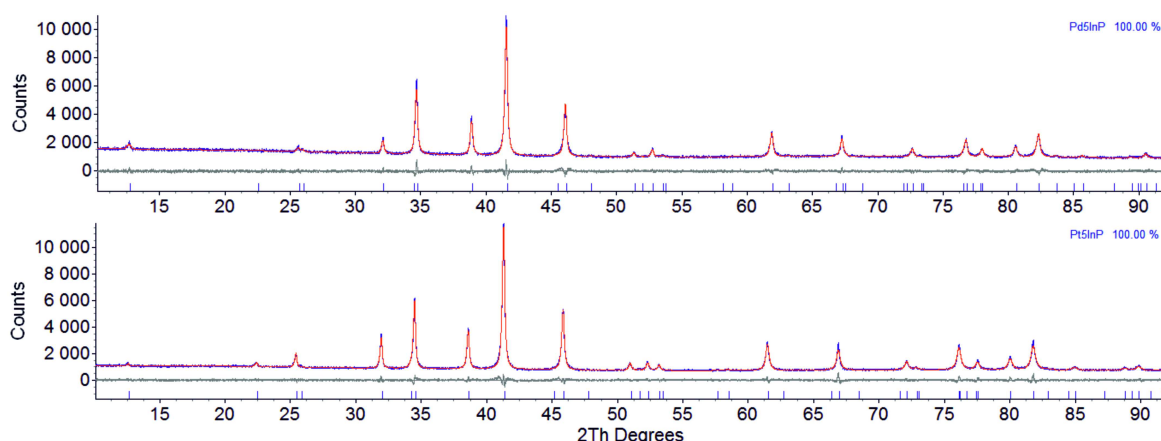
13.5.2. Crystal structure description

Figure 13.5.1.: Observed, calculated, and difference Rietveld plots for the Pd_5InP (top) and Pt_5InP (bottom) samples.

Crystallographic data, atomic coordinates and selected bond distances for Pd_5InP and Pt_5InP are given in Tables 13.5.1 to 13.5.3. Final Rietveld refinement plots are given in Fig. 13.5.1. The crystal structures of the new compounds are depicted in Figs. 13.5.2 and 13.5.3. According to the Rietveld refinement data, Pd_5InP and Pt_5InP are fully isotypic with the Pd_5InSe compound [1] and represent the Pd_5TlAs structure type. Neither the Rietveld analysis, nor the fact that the samples with exact 5:1:1 ratio between palladium/platinum, indium, and phosphorus are found to be phase-pure, support the compositions of '$Pd_{72}In_{14}P_{14}$' and '$Pt_{72}In_{14}P_{14}$', suggested in [5], that imply small excess of palladium or platinum, respectively, present in the structures with respect to 5:1:1 ratio. These structures are rather densely packed and hardly can accommodate extra palladium or platinum atoms. Also, when in our attempts to produce Pt_8In_2P compound we have obtained samples containing only the first homologue and binary intermetallics, we have performed Rietveld refinement, according to which the sample consisted of 50.64 % Pt_5InP and 49.36 % Pt_3In. Unit cell parameters of the former compound were: $a = 3.9380(1)$ Å, and $c = 6.9857(2)$ Å, which agrees well with the parameters of the pure Pt_5InP sample and proves that the compound has no discernible homogeneity range with respect to the platinum content increase. Apparently, the palladium and platinum content of the compounds was slightly overestimated in [5].

Similarly to the other compounds of this type, the structures are built from indiumcentered $[Pd_{12}In]$ or $[Pt_{12}In]$ cuboctahedra, joined via common faces along the (001) plane to form heterometallic layers, alternating along the c axis with the layers of rectangular prisms $[Pd_8P]$ or $[Pt_8P]$ of the $PtHg_2$ structure type joined via common edges. Cuboctahedra and prisms are connected in the c-direction via common $TM(2)$-$TM(2)$ edges. To estimate the degree of distortion of the polyhedra, comprising the structures of ternary compounds, along the c axis, we use the height-to-width ratio for cuboctahedra and square prisms that we have established for selenides in [1]. Evidently, for a cubic Pt_3In [23] this parameter is precisely 1, as for any undistorted cuboctahedron. For Pd_3In ($TiAl_3$ type) [23, 24], which can be regarded as a parent intermetallic for Pd_5InP, this ratio is 0.91, showing that cuboctahedra are significantly compressed in a vertical direction. For Pd_5InP, this ratio is found to be 1.050, and for Pt_5InP it is 1.048, indicating very similar small degree of elongation of cuboctahedra along the c axis. This is pretty close to the original Pd_5TlAs, featuring height-to-width ratio for cuboctahedra of 1.06. Interestingly, while both ternary palladium-indium selenides have this parameter at 0.97 [1], palladium-indium and platinum-indium arsenides show a slightest degree of elongation, height-
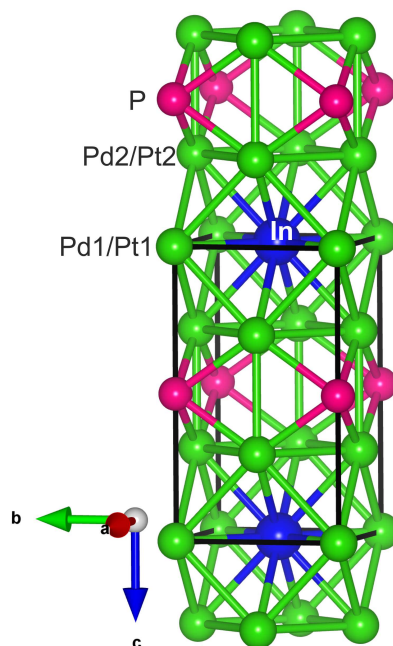
Figure 13.5.2.: Atomic positions in the unit cells of Pd$_5$InP and Pt$_5$InP.

to-width of 1.01 [4]. Thus, phosphides and selenides are at the opposite poles on the cuboctahedron distortion scale. As far as $[TM_8\mathrm{P}]$ prisms are concerned, in Pd$_5$InP the height-to-width ratio is 1.005, almost perfect 1, and in Pt$_5$InP it is only slightly larger, 1.018. This degree of elongation is relatively low in comparison with that observed in Pd$_5$InAs (1.05), Pt$_5$InAs (1.07), and Pt$_8$In$_2$As (1.08), and, once again, closely resembles that in the Pd$_5$TlAs compound, where [Pd$_8$As] polyhedra are almost perfectly cubic, with height-to-width ratio being 0.995, although the directions of the distortion are opposite here.

The distances between palladium or platinum atoms (Table 13.5.3) in ternary phosphides are slightly longer than in respective metals and are very close to those in their parent intermetallics Pd$_3$In (2.77-

Table 13.5.1.: Data collection and Rietveld analysis parameters, and final residuals for Pd$_5$InP and Pt$_5$InP.

compound	Pd$_5$InP	Pt$_5$InP
data collection	Bruker D8 Advance	
radiation type source	X-ray, CuK$_{\alpha1}$	
data collection temperature / K	295	
range in 2θ, step size / °	7-94, 0.02	7-98, 0.02
space group	$P4/mmm$ (No. 123)	
Z	1	
a / Å	3.9303(5)	3.9500(1)
c / Å	6.9269(1)	6.9814(3)
V / Å^3	107.004(3)	108.926(9)
R_p, R_wp	0.030, 0.038	0.034, 0.043
R_Bragg	0.004	0.005
GOF	1.36	1.36

Table 13.5.2.: Refined coordinates, occupancies, and isotropic displacement parameters for Pd_5InP and Pt_5InP (in italics).

atom	Wyckoff position	x	y	z	B_{iso} / $Å^2$
Pd1	$1a$	0	0	0	1.0(2)
Pt1					*0.4(2)*
Pd2	$4i$	0	1/2	0.2983(1)	B_{iso}(Pd1)
Pt2				*0.29642(9)*	B_{iso}(Pt1)
In	$1c$	1/2	1/2	0	0.9(2)
					1.0(2)
P	$1b$	0	0	1/2	0.7(2)
					0.4(3)

Table 13.5.3.: Selected interatomic distances for the Pd_5InP and Pt_5InP structures.

atoms	distance / Å	atoms	distance / Å	atoms	distance / Å
		Pd_5InP			
Pd1-Pd2	2.8521(8) Å	Pd1-In	2.7792(8) Å	Pd2-P	2.4109(6) Å
Pd2-Pd2	2.7792(8) Å	Pd1-In	2.8521(8) Å		
		Pt_5InP			
Pt1-Pt2	2.8606(5) Å	Pt1-In	2.7930(5) Å	Pt2-P	2.4332(4) Å
Pt2-Pt2	2.7930(5) Å	Pt2-In	2.8606(5) Å		

2.89 Å [23,24]) and Pt_3In (2.82 Å [23]) , and also to those in Pd_5HgSe (2.84-2.85 Å [6]). Transition metal to indium distances in phosphorus-containing compounds are also very similar to the ones found in ternary selenium- and arsenic-containing analogues (2.80-2.86 Å [1,4]) and binary intermetallics Pd3In and Pt3In (2.76-2.87 Å and 2.82 Å, respectively). Palladium-phosphorus distances (2.41 Å) are ca. 0.1-0.2 Å longer than in PdP_2 (2.33-2.34 Å) [25] or Pd_3P (2.22-2.37 Å) [26], and platinum-phosphorus distances in square prisms (2.43 Å) are just ca 0.03 Å longer than in PtP_2 (2.40 Å [27]).

13.5.3. Electronic structure and bonding

Electronic structures of Pd_5InP and Pt_5InP were evaluated based on the DFT calculations. Total and projected densities of states (DOS) near the Fermi level for both compounds are shown in Fig. 13.5.4. As can be seen from the DOS plots, the main features for both compounds are essentially the same. Main contributions near the Fermi level arise from the transition metal dstates, which are almost completely filled and close to the d^{10}-configuration. The contributions from phosphorus 3p-states and indium 5s- and 5p-states reside in a significantly lower energy range, between ca. -4 and -10 eV). Indium 5p-states also show a contribution to a region above the Fermi level. This picture is very typical for Cu_3Au-based compounds of palladium and platinum and has been observed previously for a number of binary and ternary compounds ($Pd_{7-\delta}SnTe_2$ [28], $Pd_{17}In_4Se_4$ [2], Pd_3In, Pd_5InSe, Pd_8In_2Se [1], Pt_5InAs, and Pt_8In_2As [4]). Relatively low yet non-zero DOS at the Fermi level indicates 3D metallic conductivity. The fact that the DOS for ternary compounds are so similar to those of their parent intermetallics indicates that the heterometallic fragments are largely responsible for the main features and peculiarities of electronic structures of ternary compounds. The only significant observed difference between DOS of palladium- and platinum-indium binaries as compared to respective ternary phases is that in the latter compounds the Fermi level falls directly into a pseudo-gap, while in the
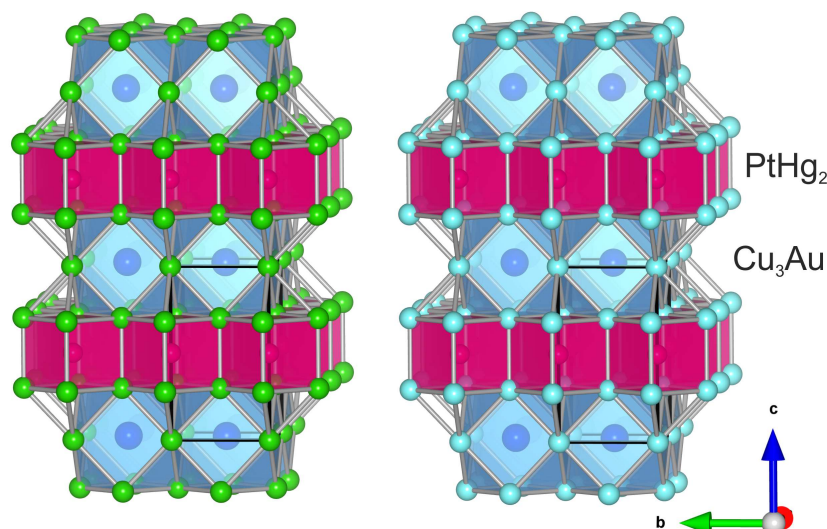
Figure 13.5.3.: Polyhedral representation of the crystal structures of Pd_5InP (left) and Pt_5InP (right). Palladium atoms are shown as green, platinum as cyan, indium as blue, and phosphorus as purple spheres. The unit cell is delineated by black lines.

former it does not [1,4]. Calculated magnetic moments on palladium and platinum atoms are very close to zero, and spin-polarized calculations show no energy gain of magnetic configurations over non-magnetic, which indicates probable diamagnetic behavior of the compounds. This hypothesis is confirmed by the results of magnetic measurements, showing diamagnetism for both compounds.

Band structures of Pd_5InP and Pt_5InP (Fig. 13.5.5) are also consistent with 3D metallic behavior. A slight spatial anisotropy in the band dispersion might be deduced based on unequal band density near the Fermi level along different directions in the k-space. However, the only direction where bands do not cross the Fermi level is X-M, and the only direction where the flatness of the bands, often indicative of a 2D-structure, is observed is Γ-X direction. Given that those are orthogonal, we can take this as an additional indication of somewhat anisotropic structure arising from layers of Cu_3Au-type cuboctahedra; yet, this effect does not appear to be too pronounced, and the number of bands crossing the Fermi level along the k-path is too big to treat the structure other than essentially 3D.

Charge density for all compounds was calculated and analyzed within the framework of R. Bader's QTAIM approach [12]. Atomic charges obtained from calculated charge density are: Pd_5InP, -0.32 (Pd1), -0.16 (Pd2), +0.78 (In), +0.10 (P); Pt5InP, -0.42 (Pt1), -0.24 (Pt), +1.05 (In), +0.35 (P). As seen from the data, there is a noticeable charge transfer from indium atoms centering the cuboctahedra towards transition metal atoms, particularly pronounced in the case of platinum, pointing out towards a polar transition metal - indium interactions. Phosphorus atoms also carry a partial positive charge, albeit comparably small, which nevertheless points out towards possible degree of polarity of the transition metal-phosphorus interactions at least in the case of platinum. It has to be noted that in the Cu_3Au-based palladium-indium selenides no significant charge transfer was observed between selenium and palladium atoms [1,3], which might be taken as an indication of higher polarity of platinum and palladium bonds with phosphorus as compared to selenium. Nevertheless, as with other compounds of the type, charge density distribution clearly indicates that both compounds are essentially intermetallic and can only be formally and traditionally called 'phosphides', as they do not, in fact, contain negatively charged phosphorus atoms.

It must be noted that charge density partitioning according to Bader's scheme, while very useful
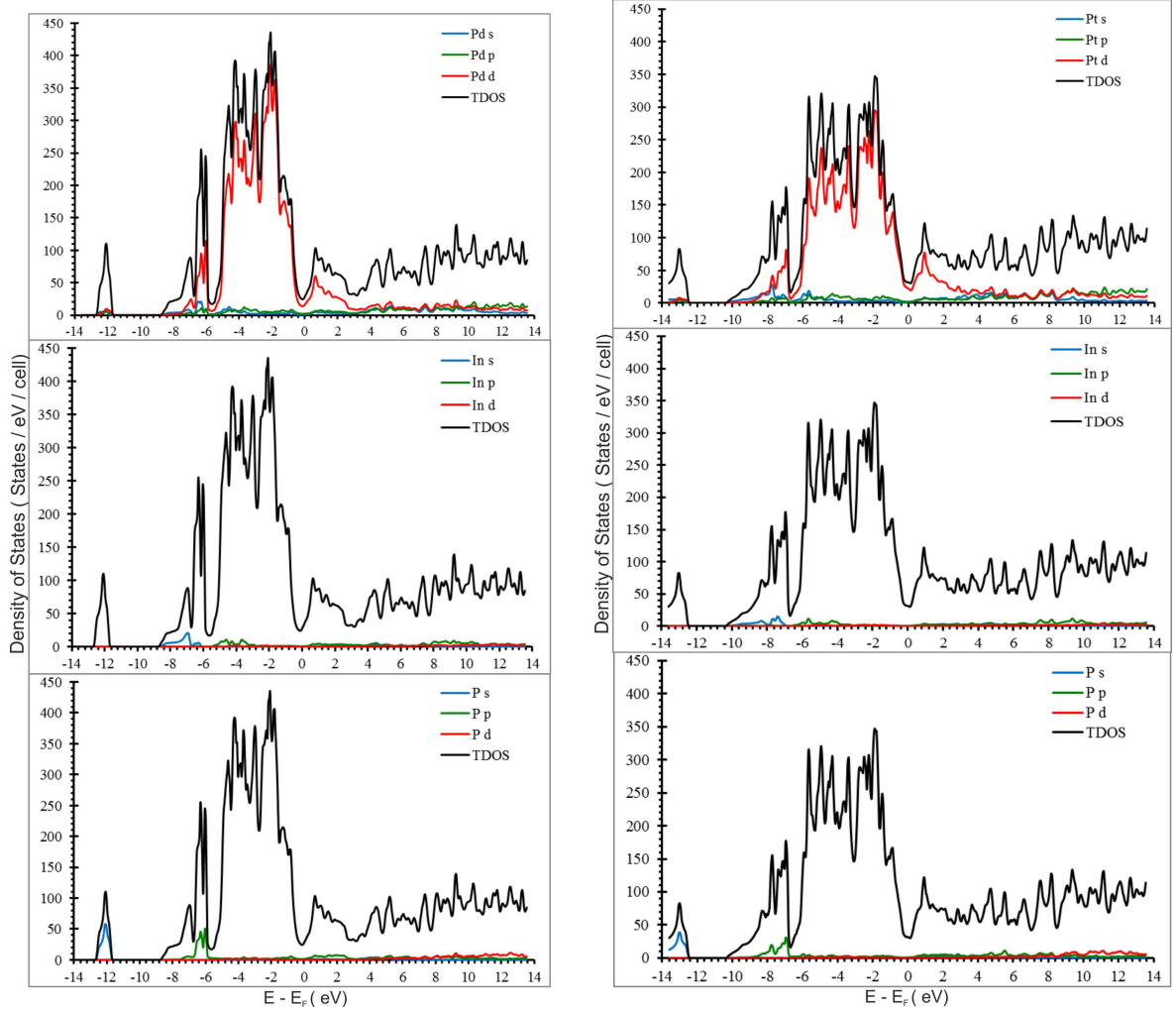
Figure 13.5.4.: Total (TDOS) and projected (PDOS) *l*-resolved densities of states near the Fermi level for Pd_5InP (left) and Pt_5InP (right), top to bottom: *TM*, In, P. Fermi level is at zero.

when analyzing ionic structures and charge redistribution in molecular objects, can only provide limited information in cases of complex bonding patterns, particularly in solid state, since charge density has only atomic attractors and is thus not very well-suited for the detailed description of covalent or metallic interactions. In order to gain more insight into the chemical bonding in the compounds in question, we have performed topological analysis of the electron localizability indicator (ELI-D) [13], which has a benefit of featuring bonds and lone pairs as attractors in addition to the nuclei. The basis of the ELI-D analysis is the study of its topology while going down from higher values of localization parameter (Y) and the observation and assignment of arising features. ELI-D can also be partitioned, in the spirit of the QTAIM, into space-filling basins of the respective attractors (atoms, lone pairs, or bonds), the integration of charge density over which can provide more quantitative bonding description. The ELI-D isosurfaces for Pd_5InP and Pt_5InP are shown in Figs. 13.5.6 and 13.5.7, respectively.

Typically for compounds based on d-metals, at high and medium values of Y we only observe atomic shells for both compounds. Other features start to appear below Y 0.95 in the intermetallic part of the structures. Fig. 13.5.6 shows the ELI-D topology at $Y = 0.915$, where we can clearly see eight non-atomic attractors tetrahedral in shape (labelled Ω1) that are positioned around indium atoms. These maxima correspond to the tetrasynaptic ELI-D basins of the fourcentered 3Pd+In bonding
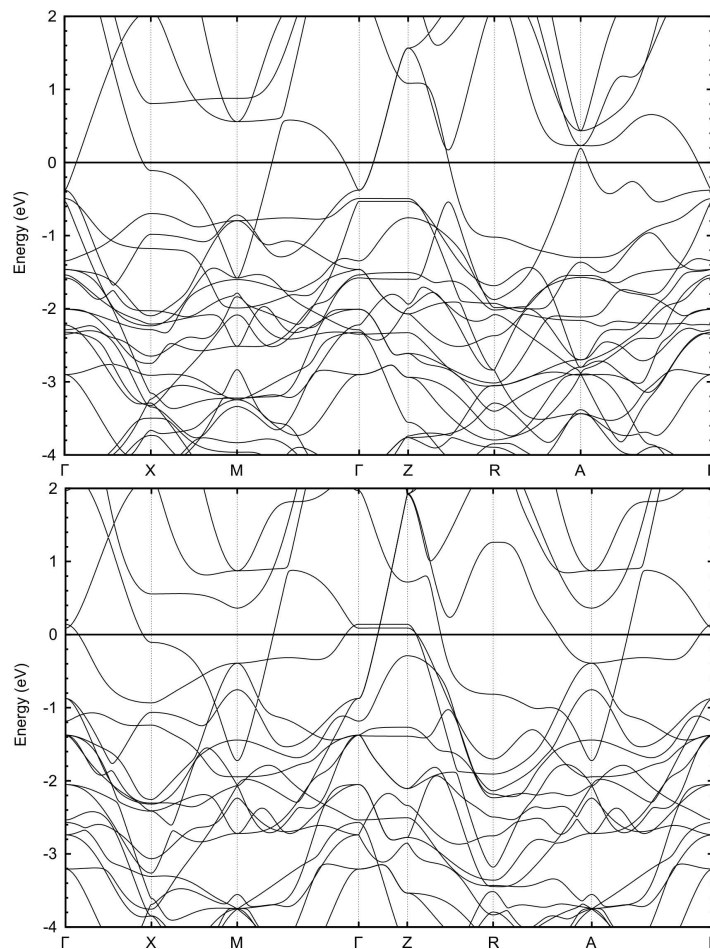
Figure 13.5.5.: Band structures near the Fermi level for Pd_5InP (top) and Pt_5InP (bottom) from DFT calculations.
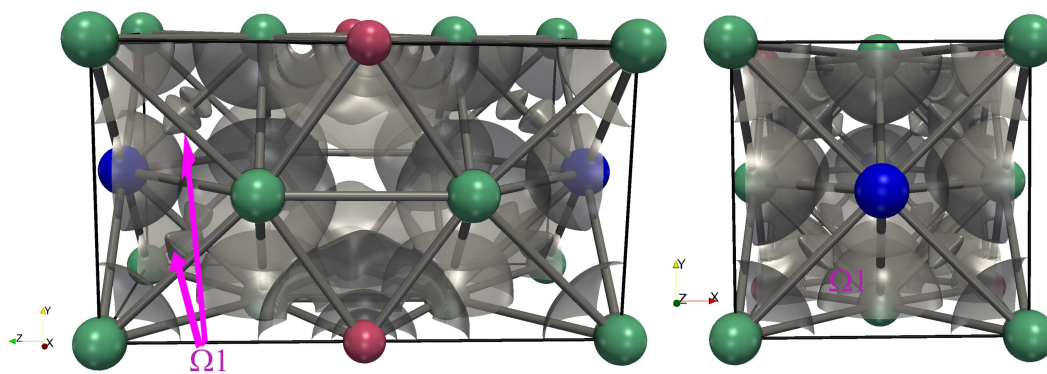
Figure 13.5.6.: ELI-D isosurfaces ($Y = 0.915$) for Pd_5InP. For the explanation of $\Omega1$ see the text.

interactions. Similar basins were observed in the bonding patterns of palladium-indium selenides and arsenides, as well as palladium-indium intermetallics [1,3,4]. The integration of electron density over each tetrasynaptic basin results in ca. 0.7 electrons (e), which is slightly less than 0.9 e in Pd_5InAs [4]. Fig. 13.5.7 displays ELI-D isosurfaces for Pt_5InP at $Y = 0.940$ and $Y = 0.925$. As evident from the figure, bonding pattern is not quite the same in the palladium- and platinum-based compounds. In the ELI-D topology of the latter, we also observe these tetrasynaptic basins ($\Omega1$) corresponding to multi-centered metal-metal bonding, however, they are not the first features to appear in the ELI-D

after the atomic shells. For Pt_5InP below $Y = 0.950$ we first observe the appearance of disynaptic basins ($\Omega2$) that, based on their location, correspond to the pairwise Pt-Pt interactions, and only at lower localization parameter values ($Y = 0.925$) we see the domains of the $\Omega1$ type appearing. This pattern exactly mirrors the one observed for Pt_5InAs and Pt_3In [4] and confirms that the presence of pairwise Pt-Pt interactions is what distinguishes the bonding in platinum-based compounds of 5:1:1 and 8:2:1 type from palladium-based ones. The integration of the charge density over the bonding basins for platinum-based compounds gives us the following results: 0.8 e ($\Omega1$), 0.4 e ($\Omega2$). Once again, these values are lower than those calculated for Pt_5InAs (1.6 and 0.6 e, respectively). As we can see from these data, despite pairwise interactions appearing before the four-centered ones in the ELI-D topology, the number of electrons involved in the latter is still greater, so the multicentered metallic bonding is still the prevailing effect in the heterometallic fragments here, as it was found to be in the case of palladium-based compounds. Nevertheless, pairwise Pt-Pt interactions, even though featuring smaller number of electrons involved, might provide extra stability for the structure.

In addition to the direct-space bonding analysis, we have also employed orbital space bonding description based on the Crystal Orbital Hamilton Population analysis [18-20]. The underlying idea here is, despite having an electronic structure description employing plane waves, the orbitals can be reconstructed by using projections of plane-wave wavefunctions onto an arbitrary basis of local orbitals. And studying projected COHP near the Fermi level for specific interactions we can assign bonding, anti-bonding or non-bonding character to them. The COHP plots for Pd_5InP and Pt_5InP are shown in Fig. 13.5.8. We see that, moving up the energy scale, bonding character of *TM*-*TM* and *TM*-In interactions changes to anti-bonding closer to the Fermi level; however, at the Fermi level itself there are no anti-bonding contributions (apart from very small Pd-P ones), so the structures are
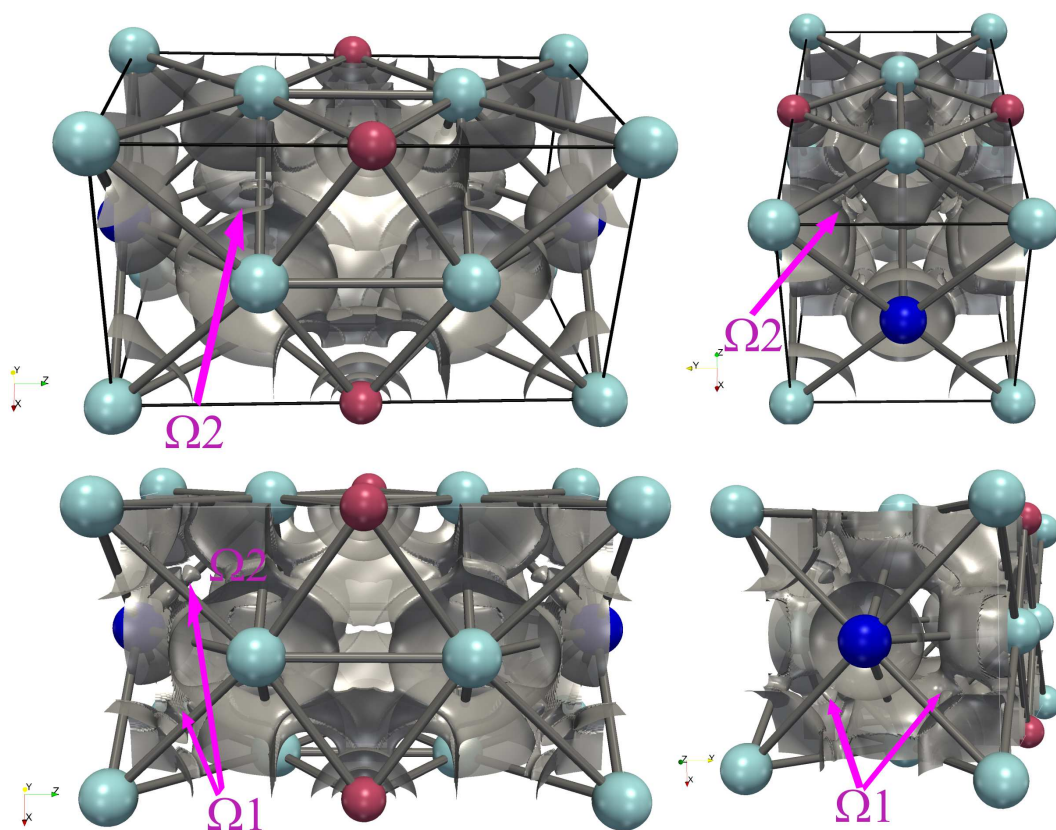

Figure 13.5.7.: ELI-D isosurfaces (top row - $Y = 0.940$; bottom row - $Y = 0.925$) for Pt_5InP. For the explanation of $\Omega1$ and $\Omega2$ see the text.

stabilized. Above the Fermi level, anti-bonding character prevails. If we compare this picture to the one observed for the second homologues (with double-stacked cuboctahedral fragments), Pt_8In_2As [4] and hypothetical optimized Pt_8In_2P, we will see stronger anti-bonding character of Pt-Pt and Pt-In interactions at the Fermi level for both structures, particularly in the former one. It appears that the bonding in double-stacked structures is not optimized, which might account for their relative scarcity as compared to the first homologues.

In order to study the possibility of altering structural and electronic properties of the title compounds by hydrogen intercalation, we have performed hydrogenation experiments on both samples up to the hydrogen pressure of ca. 7 MPa and the temperature of 700 K. No indication of possible hydrogen uptake was observed neither by thermal analysis, nor by XRPD of the products. This is quite similar to the other already investigated Pt_5TlAs type compounds, with the exception of Pd_5InSe, that forms Pd_3InH_x by decomposition [29]. The reason for this behavior is, most likely, the lack of [Pd_6] octahedral voids in the structures, which appear to be preferred for hydrogen incorporation. Apparently, their absence inhibits a hydrogen uptake. So far, of this class of compounds, binary palladium-rich intermetallics like Pd_3In appear to exhibit the best hydrogenation properties [30,31].

13.6. Conclusion

Using the high-temperature ampoule technique, we have synthesized two ternary metal-rich compounds with linear intergrowth structures, Pd_5InP and Pt_5InP, and determined their crystal structures from XRRD data. All compounds are built from cuboctahedral [$TM_{12}In$] fragments (TM = Pd, Pt) of tetragonally distorted Cu_3Au-type fragments, alternating along the c axis with [TM_8P] rectangular
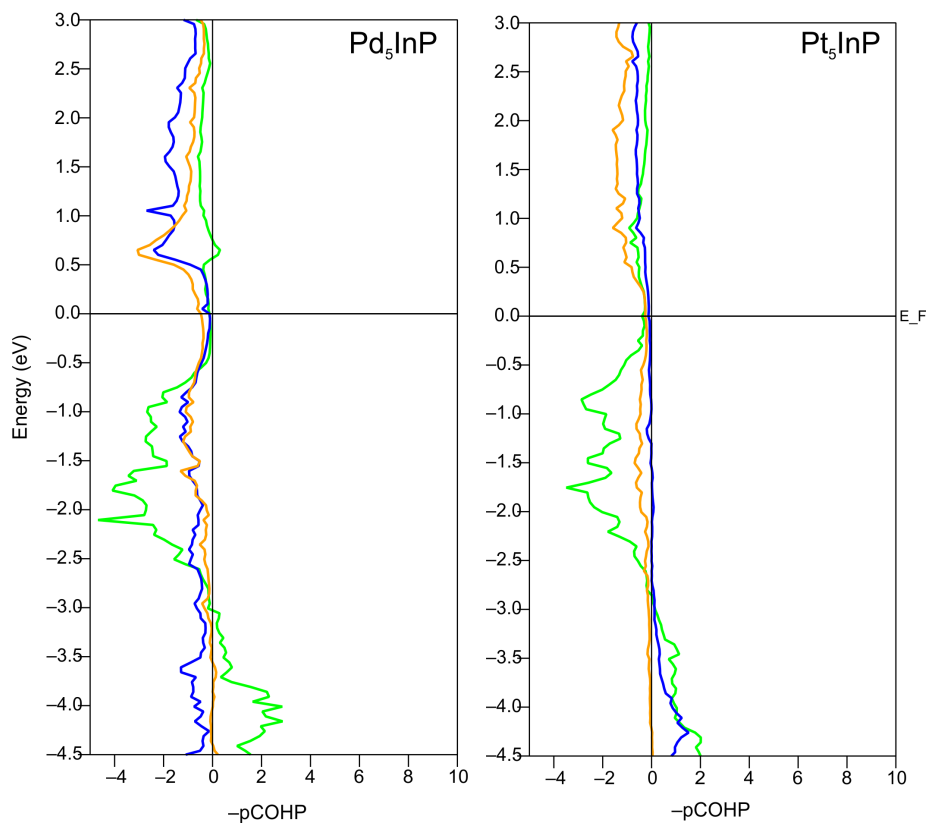

Figure 13.5.8.: COHP plots for Pd_5InP and Pt_5InP. Pd-Pd and Pt-Pt interactions are shown in green, Pd-In and Pt-In − in blue, and Pd-P and Pt-P − in brown.
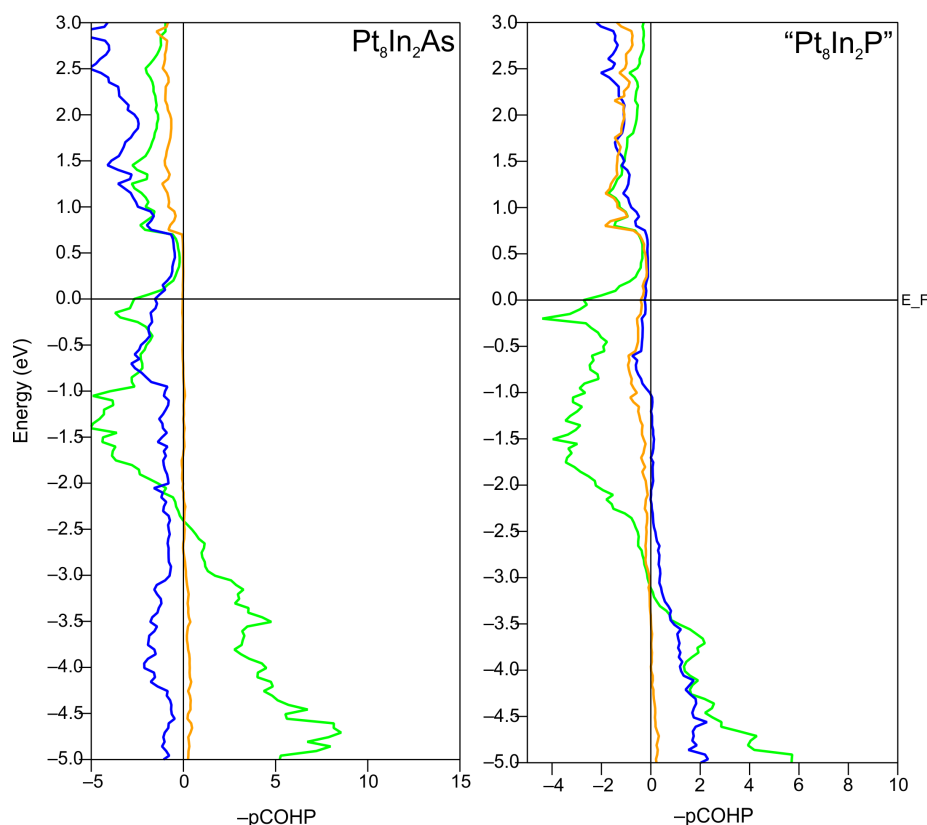
Figure 13.5.9.: COHP plots for Pt_8In_2As and hypothetical optimized structure of Pt_8In_2P. Pt-Pt interactions are shown in green, Pt-In – in blue, and Pt-P and Pt-As – in brown.

prisms with $PtHg_2$ structure. The compounds were found to be fully isotypic and to belong to the rare Pd_5TlAs structure type [5]. DFT calculations predict all compounds to be 3D metallic conductors and to exhibit diamagnetic behavior. The latter was confirmed by the magnetic measurement data. According to the bonding analysis based on the ELI-D topologies and Bader's QTAIM approach, both compounds are essentially intermetallic and feature multi-centered transition metal - indium interactions in their heterometallic fragments and show significant charge transfer from indium to transition metal atoms, indicating the polarity of bonding, particularly in the case of platinum-based compounds. The distinguishing feature of the latter compounds is the additional pairwise Pt-Pt bonding within heterometallic fragments, that was not observed in the cases of palladium-based compounds and might account for the differences in the stability between the two groups. Both compounds were tested with respect to the possibility of hydrogen uptake up to 7 MPa and 700 K, but no measurable effect was observed.

13.7. Acknowledgments

13.8. References for chapter 13

[1] E. Y. Zakharova, S. M. Kazakov, A. A. Isaeva, A. M. Abakumov, G. Van Tendeloo, A. N. Kuznetsov, Pd_5InSe and Pd_8In_2Se - new metal-rich homological selenides with 2D palladium - indium fragments: Synthesis, structure and bonding, J. Alloys Compd. 589 (2014) 48-55.

[2] A. Götze, P. Urban, O. Oeckler, H. Kohlmann, Synthesis and crystal structure of Pd_5InSe, Z. Naturforsch. 69B (2014) 417–422.

[3] E. Y. Zakharova, A. V. Churakov, T. Doert, A. N. Kuznetsov, $Pd_{17}In_4Se_4$, a metal-rich palladium–indium selenide with an open-framework structure, Eur. J. Inorg. Chem. (2013) 6164–6169.

[4] E. Y. Zakharova, N. A. Andreeva, S. M. Kazakov, A. N. Kuznetsov, Ternary arsenides based on platinum–indium and palladium–indium fragments of the Cu_3Au-type: crystal structures and chemical bonding, J. Alloys Compd. 621 (2015) 307–313.

[5] M. El-Boragy, K. Schubert, Distorted close-packed structure containing constitutional vacancies, Z. Metallkde. 61 (1970) 579-584.

[6] F. Laufek, A. Vymazalová, M. Drábek, J. Navrátil, T. Plecháček, J. Drahokoupil, Crystal structure and transport properties of Pd_5HgSe, Solid State Sci. 14 (2012) 1476-1479.

[7] TOPAS V3, General profile and structure analysis software for powder diffraction data, User's Manual, Bruker AXS, Karlsruhe, Germany, 2003.

[8] ELK, an all-electron full-potential linearised augmented-plane wave (FP-LAPW) code, ver. 3.1.12. http://elk.sourceforge.net.

[9] G. Kresse, D. Joubert, From ultrasoft pseudopotentials to the projector augmented-wave method, Phys. Rev. B 59 (1999) 1758–1775.

[10] G. Kresse, J. Furthmüller, Vienna Ab-initio Simulation Package (VASP), v.5.4.4, http://vasp.at.

[11] J. P. Perdew, A. Ruzsinszky, G. I. Csonka, O. A. Vydrov, G. E. Scuseria, L. A. Constantin, X. Zhou, K. Burke, Restoring the density-gradient expansion for exchange in solids and surfaces, Phys. Rev. Lett. 100 (2008) 136406.

[12] R. F. W. Bader, Atoms in Molecules: A Quantum Theory, Oxford University Press, Oxford, 1990.

[13] a) M. Kohout, A measure of electron localizability, Int. J. Quantum Chem. 97 (2004) 651-658; b) M. Kohout, Bonding indicators from electron pair density functionals, Faraday Discuss. 135 (2007) 43–54; c) M. Kohout, K. Pernal, F. R. Wagner, Y. Grin, Electron localizability indicator for correlated wavefunctions. I. Parallel-spin pairs, Theor. Chem. Acc. 112 (2004) 453–459.

[14] M. Kohout, DGrid, ver. 4.6, Radebeul, 2011.

[15] V. Sadovnichy, A. Tikhonravov, V. Voevodin, and V. Opanasenko, From petascale toward exascale; In: Contemporary High Performance Computing: (Chapman & Hall/CRC Computational Science), CRC Press, Boca Raton, USA, 2013, 283-307.

[16] K. Momma, F. Izumi, VESTA 3 for three-dimensional visualization of crystal, volumetric and morphology data, J. Appl. Crystallogr. 44 (2011) 1272-1276.

[17] ParaView 5.2.0. Open Source Scientific Visualization. http://www.paraview.org.

[18] R. Dronskowski, P. E. Blöchl, Crystal orbital Hamilton populations (COHP): energy-resolved visualization of chemical bonding in solids based on density-functional calculations, J. Phys. Chem. 97 (1993) 8617–8624.

[19] V. L. Deringer, A. L. Tchougréeff, R. Dronskowski, Crystal orbital Hamilton population (COHP) analysis as projected from plane-wave basis sets, J. Phys. Chem. A 115 (2011) 5461-5466.

[20] S. Maintz, V. L. Deringer, A. L. Tchougréeff, R. Dronskowski, Analytic projection from plane-wave and PAW wavefunctions and application to chemical-bonding analysis in solids, J. Comput. Chem. 34 (2013) 2557–2567.

[21] S. Maintz, V. L. Deringer, A. L. Tchougréeff, R. Dronskowski, LOBSTER: A tool to extract chemical bonding from plane-wave based DFT, J. Comput. Chem. 37 (2016) 1030–1035.

[22] wxDragon 2.1.3. http://www.wxdragon.de

[23] S. Bhan, K. Schubert, Über die Struktur von Phasen mit Kupfer Unterstruktur in einigen T-B Legierungen (T = Ni, Pd, Pt; B = Ga, In, Tl, Pb, Sb, Bi) J. Less-Common Met. 17 (1969) 73–90.

[24] a) H. Kohlmann, C. Ritter, Refinement of the crystal structures of palladium-rich In-Pd compounds by X-ray and neutron powder diffraction, Z. Naturforsch. 62B (2007) 929–934; b) H. Kohlmann, C. Ritter, Reaction pathways in the formation of intermetallic $InPd_3$ polymorphs, Z. Anorg. Allg. Chem. 635 (2009) 1573–1579.

[25] W. H. Zachariasen, The crystal structure of palladium diphosphide, Acta Crystallogr. 16 (1963) 1253-1255.

[26] Y. Andersson, S. Rundqvist, R. Tellgren, J. O. Thomas, T. B. Flanagan, A neutron diffraction investigation of deuterated $Pd_3P_{0.8}$, J. Solid State Chem. 32 (1980) 321-327.

[27] S. Furuseth, K. Selte, A. Kjekshus, Redetermined crystal structures of $PdAs_2$, $PdSb_2$, PtP_2, $PtAs_2$, $PtSb_2$, α-$PtBi_2$, and $AuSb_2$, Acta Chem. Scand. 19 (1965) 735-741.

[28] S. V. Savilov, A. N. Kuznetsov, B. A. Popovkin, V. N. Khrustalev, P. Simon, J. Getzschmann, T. Doert, M. Ruck, Synthesis, crystal structure and electronic structure of modulated $Pd_{7-\delta}SnTe_2$, Z. Anorg. Allg. Chem. 631 (2005) 293-301.

[29] A. Götze, J. M. Sander, H. Kohlmann, Crystal structures and hydrogenation properties of palladium-rich compounds with elements from groups 12-16, Z. Naturforsch. 71B (2016) 503–508.

[30] A. Götze, H. Kohlmann, Palladium Hydride and Hydrides of Palladium-Rich Phases, in: Reference Module in Chemistry, Molecular Sciences and Chemical Engineering, Elsevier, 2017.

[31] H. Kohlmann, A. V. Skripov, A. V. Soloninin, T. J. Udovic, The anti-perovskite type hydride $InPd_3H_{0.89}$, J. Solid State Chem. 183 (2010) 2461-2465.

14. Vacancy Ordering in $Pd_{11}Bi_2Se_2$ - Crystal Structure and Properties

André Götze, Sara Schmorl, Alexey N. Kuznetsov, Holger Kohlmann

14.1. Authors' contributions

The syntheses, EDX and XRPD measurements as well as the structure solution and refinements were done by A. Götze. Peter Schulz and Markus Nentwig executed the single crstal diffraction experiments (acknowledged). S. Schmorl did the magnetic measurements. A. N. Kuznetsov performed the DFT-calculations and wrote the part "Electronic structure of $Pd_{11}Bi_2Se_2$". The manuscript was written by A. Götze and revised by H. Kohlmann.

14.2. Abstract

The crystal structure of $Pd_{11}Bi_2Se_2$ was determined and refined from X-ray single crystal data (space group $Fd\bar{3}m$, $a = 12.4879(14)$ Å, $Z = 8$). In contrast to the earlier reported $Pd_3(Bi_{0.6}Se_{0.4})$, the title compound crystallizes in a 2 x 2 x 2 superstructure of the BiF_3 type with ordered bismuth and selenium distribution and an ordered vacancy according to $Pd_{11}\square Bi_2Se_2$. The vacancy is located at the center of a palladium tetrahedron capped with a bismuth tetrahedron (stella quadrangula). $Pd_{11}Bi_2Se_2$ is isopointal to $Li_{13}In_3$ but shows different ordering of the minority components. $Pd_{11}Bi_2Se_2$ is inert to water, organic solvents and concentrated hydrochloric acid and its melting point is 905(1) K. It exhibits a very small effective magnetic moment of $\mu_{\text{eff}} = 0.0114(2)$ μ_B per palladium atom. $Pd_{11}Bi_2Se_2$ does not take up hydrogen up to 7.2(2) MPa hydrogen pressure and temperatures up to 703 K. In the electronic structure, the region near the Fermi level is dominated by almost filled Pd 4d-states. Low yet non-zero density of states and a pseudo-gap at the Fermi level might indicate $Pd_{11}Bi_2Se_2$ to be a poor metal.

14.3. Introduction

Intermetallic palladium-rich compounds with an ordered arrangement of the atoms often crystallize in superstructures of the cubic close packing (ccp, Cu type) [1]. Binary compounds like MPd$_3$ (M = Mg [2,3], Mn [4], In [5], Tl [6]) usually show stacking variants of AuCu$_3$-like blocks, e. g. TiAl$_3$ type (twofold ccp superstructure), ZrAl$_3$ type (fourfold ccp superstructure) or Pd$_9$Tl$_2$Pb type (sixfold ccp superstructure). While AuCu$_3$ type compounds, e. g. CePd$_3$ and Pd$_3$Pb take up hydrogen preserving the crystal structure of the parent intermetallic [7,8], those with ccp superstructures undergo a hydrogen induced transition to the AuCu$_3$ type [9]. This rearrangement may be described by a gliding mechanism of layers within these intermetallics [10], driven by increasing the number of [Pd$_6$] octahedral voids, which are preferred for hydrogen occupation [11].

Pd$_3$Bi crystallizes in a superstructure of the double hexagonal closed packing (dhcp, La type) and shows a hydrogen induced transition to a ccp related structure (filled ZrAl$_3$ type) [8,12]. Ternary palladium-rich compounds like Pd$_5$$MY$ (M: Cd, In; Y: As, Se) are also related to the ccp with an ordered vacancy Pd$_5\square MY$, but do not incorporate hydrogen [13-16]. The absence of hydride formation in palladium-rich compounds is of importance for increasing the selectivity of heterogeneous catalysts [17,18], like the Lindlar catalyst (Pd$_{1-x}$Pb$_x$) [19], or Ga-Pd compounds for selective hydrogenation of acetylene [17,20,21]. InPd$_2$ shows a high catalytic activity and selectivity for the semi-hydrogenation of ethyne and high stability towards ethene [22]. Therefore, it is of great importance to derive rules for the ability of palladium-rich intermetallics to form bulk hydride phases. The hydrogen uptake of MPd$_3$ compounds seems to be correlated with electronic and geometric aspects of the metal atom M [12]. Data available on hydrogenation properties of palladium-rich intermetallic compounds known so far suggest that high valence electron concentrations (VEC) inhibit hydrogen incorporation. The exact VEC limit for hydrogen uptake is not yet known.

To shed more light on the hydrogenation behavior of palladium-rich compounds and to understand the influence of these geometric and electronic effects in more detail, we aim at studying hydrogenation properties of compounds with an increased valence electron concentration (VEC). This might be achieved by starting at Pd$_3$Bi with the highest VEC for hydride forming compounds MPd$_3$ known so far, and substituting group 16 elements for bismuth. Therefore, Pd$_3$(Bi$_{0.6}$Se$_{0.4}$) [23], which is related to the W type, is a good candidate. It was reported to crystallize in the BiF$_3$ type with a mixed occupation of bismuth and selenium atoms on one crystallographic site [23]. In this contribution, we reinvestigated the synthesis and the X-ray crystal structure and report on magnetic properties, electronic structure, and chemical properties of the obtained compound Pd$_{11}$Bi$_2$Se$_2$.

14.4. Material and methods

14.4.1. Synthesis, stability and EDX analysis of Pd$_{11}$Bi$_2$Se$_2$

The title compound was synthesized from stoichiometric amounts of palladium powder (99.9 %, $\leq$ 60 μm, Chempur and 99.95 %, $\leq$ 150 μm, Goodfellow), bismuth shots (metal basis > 99 % checked with EDX) and selenium drops (VEB Laborchemie, Apolda), in sealed silica glass ampoules under argon atmosphere. The mixtures were heated to 1473 K for 2 h and further annealed at 773 K for one week. The products were ground in a mortar after cooling. Typical sample size was from 0.25 g to 1.5 g. The stability of the products were tested by additional X-ray powder diffraction after a month in air. Chemical analysis was performed by an EDX INCA SYSTEM from Oxford Instruments, mounted on a Zeiss LEO 1530 scanning electron microscope, with an acceleration voltage of 20 kV, and a working distance of 15 mm.

14.4.2. X-ray diffraction

Single-crystal data were measured on an IPDS-I diffractometer (Stoe & Cie GmbH, Darmstadt, Germany) equipped with an image plate detector using AgK_α radiation ($\lambda = 0.56086$ Å, graphite monochromator). A numerical absorption correction was performed with X-Red [24]. Crystal faces were optimized with the program X-Shape [25]. The structure was solved by direct methods, and refined with SHELX-2013 [26].

Further details of the crystal structure investigation may be obtained from Fachinformationszentrum Karlsruhe, 76344 Eggenstein-Leopoldshafen, Germany (fax: +49-7247-808-666; e-mail: crysdata@fiz-karlsruhe.de) on quoting the deposition number CSD-433594.

X-ray powder diffraction data was collected using flat transmission samples (powder in apiezon grease between two kapton sheets) on an image plate Guinier powder diffractometer (Huber Guinier camera G670 at $T = 296$ K with $CuK_{\alpha 1}$ radiation, $\lambda = 1.54056$ Å, Ge(111) monochromator). Rietveld refinements were carried out with the program FullProf [27], and the Pseudo Voigt function was used to model diffraction peak shapes.

14.4.3. Magnetism

Temperature dependent magnetic susceptibility measurements were carried out using an MPMS 7XL SQUID magnetometer (QUANTUM DESIGN) at an applied magnetic field of 0.02 T in the temperature range from 2 to 330 K. The diamagnetic correction was performed by the program package DAVE [28], and the magnetic parameters were calculated by a linear regression according to the Curie-Weiss-law with the program OriginPro8G.

14.4.4. Thermal analysis

Differential scanning calorimetry (DSC) was performed *in situ* under hydrogen pressure on a Q1000 (TA Instruments) equipped with a gas pressure chamber. 20 mg of the powdered sample was put in an aluminium crucible, which was closed with an aluminium lid. This was placed inside the pressure chamber, which was then purged several times with hydrogen gas, before filling it to the final hydrogen gas pressure of 5.0 MPa. The sample was heated to 703 K with 10 K min^{-1}, held at that temperature for a minimum of 1 h, and cooled to 300 K. Two runs were performed; then the hydrogen pressure was released, the sample taken out and structural characterization undertaken by XRPD. The differential thermal analysis (DTA) of $Pd_{11}Bi_2Se_2$ in helium atmosphere was carried out on a Netzsch F1 Jupiter device using sintered alumina crucibles and a heating rate of 10 K min^{-1}.

14.4.5. Computational details

The electronic structure of $Pd_{11}Bi_2Se_2$ was calculated on the density-functional theory (DFT) level utilizing two approaches. Obtained crystallographic data were used for the modeling in both approaches. In the first one, we used the all-electron full-potential linearized augmented plane wave method (FP-LAPW) for the band structure calculations as implemented in the ELK code [29] with relativistic effects, including spin-orbit coupling, taken into account. The Brillouin zone sampling was performed using 4 x 4 x 4 k-point mesh. The Perdew-Burke-Ernzerhof exchange-correlation functional PBE [30] of the GGA-type was used in the calculations. The muffin-tin sphere radii for the respective atoms are (Bohr): 2.70 (Bi), 2.20 (Pd), 2.00 (Se). The maximum moduli for the reciprocal vectors k_{max} were chosen so that $R_{MT}k_{max} = 7.5$. The convergence criteria for the procedure were set as RMS change in Kohn-Sham potential $< 10^{-5}$ eV, absolute change in total energy $< 6 \times 10^{-5}$ eV. In the second approach, we performed the scalar-relativistic calculations using Vienna Ab-initio Simulation

Package (VASP) [31] employing the same PBE functional as in FP-LAPW calculations, and PAW pseudopotentials [32]. The energy cut-off was set at 450 eV with a 12 x 12 x 12 Monckhorst-Pack [33] k-point mesh. Absolute change in total energy for convergence was taken as $\Delta E < 10^{-5}$ eV. The calculations were performed using the MSU Lomonosov supercomputer [34].

14.5. Results and discussion

14.5.1. Synthesis, chemical and physical properties of Pd$_{11}$Bi$_2$Se$_2$

The intermetallic compound Pd$_{11}$Bi$_2$Se$_2$ was synthesized from the elements and yielded a grey powder with a metallic luster, and crystals of several hundred micrometers in size. Based on chemical analysis of the powder and the single crystal, the empirical formulae Pd$_{11.15(11)}$)Bi$_{1.88(7)}$Se$_{2.0(1)}$ and Pd$_{11.2(2)}$Bi$_{1.81(3)}$Se$_{2.0(2)}$ were determined, averaged from a least sixteen energy dispersive X-ray (EDX) spectra of each. The product is stable in air, and does not dissolve in water, acetone, ethanol or concentrated hydrochloric acid. It dissolves slowly in concentrated nitric acid or concentrated nitrohydrochloric acid. Pd$_{11}$Bi$_2$Se$_2$ melts at 905(1) K as determined by thermal analysis (DTA). A small hysteresis is observed upon cooling, where the solidification takes place at 892(1) K. The compound does not show any reaction with hydrogen under 7.2(2) MPa hydrogen pressure and temperatures up to 703 K. The unit cell volumes before and after the experiment do not differ significantly. The absence of bulk hydride formation could be interesting for hydrogenation catalysis, e. g. to improve selectivity compared to pure palladium like in Ag-Pd or Ga-Pd catalysts [18,35]. The values of the magnetic susceptibility are very close to zero. The Curie-Weiss model at 0.02 T yields $C = 2.249(3)\ 10^{-9}\ \mathrm{m}^3$ K mol^{-1}, $\theta_\mathrm{C} = 2.0(3)$ K which leads to an effective magnetic moment of $\mu_\mathrm{eff} = 0.0114(2)\ \mu_\mathrm{B}$ per palladium atom. Such small magnetic moments are known to occur in palladium-rich compounds, e. g. 0.0926(1) μ_B in Pd$_{13}$Te$_3$ [36] and 0.129 μ_B in YPd$_3$ [37] and might result from paramagnetic impurities (see Fig. 14.5.1).
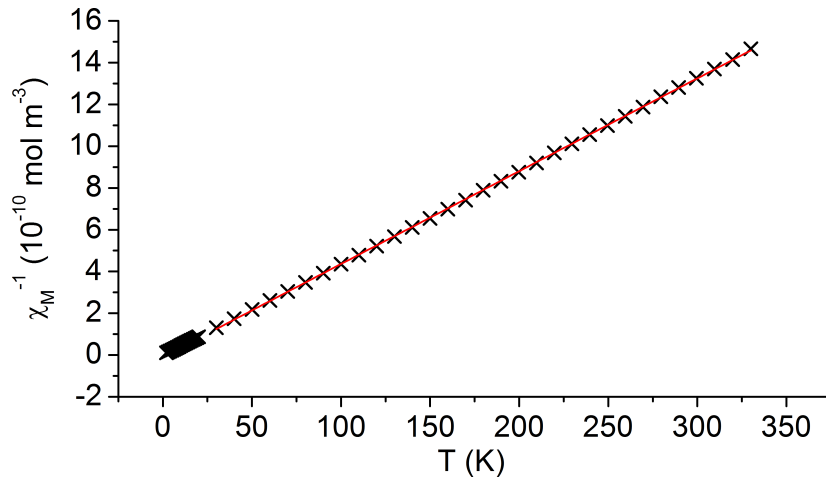
Figure 14.5.1.: Determination of the Curie constant ($C = {}^1\!/\mathrm{b} = 2.249(3)\ 10^{-9}\ \mathrm{m}^3$ K mol^{-1}) and the Curie temperature ($T_\mathrm{C} = -\ {}^\mathrm{a}\!/\mathrm{b} = 2.0(3)$ K) by linear regression ($\chi_\mathrm{M}^{-1} = \mathrm{a} + \mathrm{b}T$, with a = -8.8(13) 10^8 mol m^{-3}, b = 4.446(6) 10^8 mol m^{-3} K^{-1}) at 0.02 T after the diamagnetic correction.
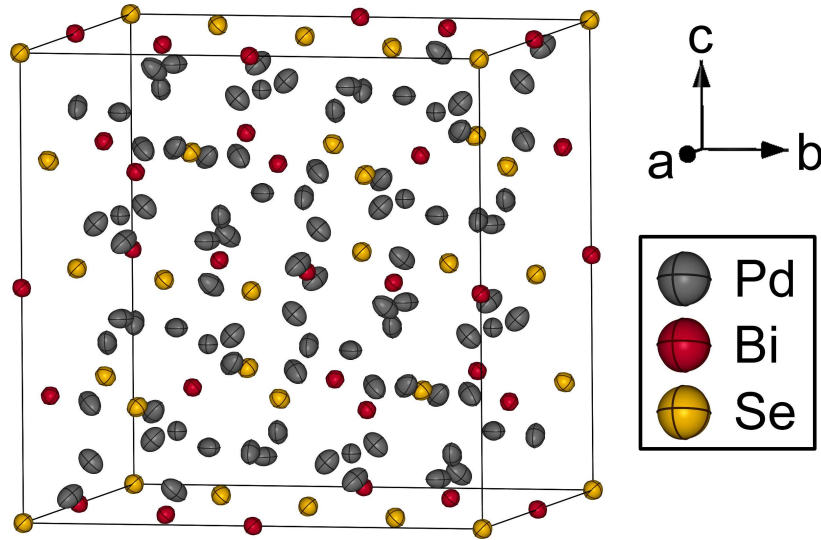
Figure 14.5.2.: Crystal structure of $Pd_{11}Bi_2Se_2$. Thermal displacement ellipsoids are shown at the 99 % probability level.

14.5.2. Crystal structure of $Pd_{11}Bi_2Se_2$

The crystal structure of $Pd_{11}Bi_2Se_2$ was solved and refined from X-ray single crystal data (Fig. 14.5.2 and Tables 14.5.1 and 14.5.2). It crystallizes in space group $Fd\bar{3}m$ with eight formula units per unit cell and two free positional parameters. The sample is single phase according to powder diffraction data (Fig. 14.5.3). The structure parameters from Rietveld refinement based on X-ray powder diffraction (Fig. 14.5.3) show a good accordance with those from single crystal diffraction (Table 14.5.1).

The bismuth atoms are coordinated by twelve palladium atoms, forming distorted icosahedra, which are face-linked with each other (Fig. 14.5.4). This coordination sphere of bismuth is not unusual and occurs e. g. in $Ho_{12}Co_5Bi$ [38]. The selenium atoms have [6 + 2] coordination by palladium atoms, forming a distorted cube. A similar coordination is observed in Pd_5InSe, in which the selenium atoms are located in the center of a tetragonal prism of palladium atoms, and ordered in planes [13,15]. The selenium atoms in this structure are ordered in channels, and their polyhedra are edge-linked to each other. Pd1 (Wyckoff position 48*f*, see Table 14.5.1) has a [4 + 2 + 2 + 1] coordination of five palladium, two bismuth and two selenium atoms, forming a mono-capped rectangular prism Fig. 14.5.4). Pd2 (Wyckoff position 8*a*) is coordinated by six palladium atoms forming an octahedron, which is capped by four selenium atoms forming a tetrahedron. The bismuth atoms also form a tetrahedron enclosing the void (Wyckoff position 8*b*) according to $Pd_{11}\square Bi_2Se_2$ (Fig. 14.5.4). The distances of the Bi atoms to the void are short (d(Bi-$\square$) = 2.7037(3) Å) compared to d(Bi-Pd) = 2.85 − 2.88 Å in Pd_3Bi [39], though similar to d(Bi-Pd) = 2.595 − 2.913 Å) in Pd_8Bi_3 [40]. Furthermore, the voids are surrounded

Table 14.5.1.: Crystal structure parameters of $Pd_{11}Bi_2Se_2$ ($Fd\bar{3}m$, a = 12.4879(14) Å, $U_{eq} = {}^1/_3\,(U_{11} + U_{22} + U_{33})$).

atom	Wyck.	x	y	z	U_{eq} / Å^2	U_{11} / Å^2	$U_{22} = U_{33}$ / Å^2	U_{23} / Å^2	$U_{13} = U_{12}$ / Å^2
Bi	16*d*	$^1/_2$	$^1/_2$	$^1/_2$	0.0056(2)	0.0056(2)	U_{11}(Bi)	-0.00029(8)	U_{23}(Bi)
Se	16*c*	0	0	0	0.0061(3)	0.0061(3)	U_{11}(Se)	0.0001(2)	U_{23}(Se)
Pd1	48*f*	0.34466(6)	$^1/_8$	$^1/_8$	0.0083(2)	0.0061(3)	0.0094(2)	0.0020(2)	0
Pd2	8*a*	$^1/_8$	$^1/_8$	$^1/_8$	0.0060(3)	0.0060(3)	U_{11}(Pd2)	0	U_{23}(Pd2)
Pd3	32*e*	0.28373(4)	x(Pd3)	x(Pd3)	0.0095(2)	0.0095(2)	U_{11}(Pd3)	0.0024(2)	U_{23}(Pd3)

by four additional Pd3 atoms forming a second tetrahedron, and these palladium atoms are closer to the void center ($d(\text{Pd3-}\square) = 1.9741(3)$ Å). This prohibits an occupation of the void by palladium, because the shortest yet known Pd-Pd distances of intermetallics with full occupation of both Pd sites are e. g. $d(\text{Pd-Pd}) = 2.227$ Å in UPd_2Sn [41] or $d(\text{Pd-Pd}) = 2.251$ Å in β-$NbPd_3$[42]. The Pd3 atom (Wyckoff position $32e$) has a [6 + 3] coordination of bismuth and palladium atoms forming a strongly distorted, tri-capped trigonal prism (Fig. 14.5.4). The bond lengths in $Pd_{11}Bi_2Se_2$ are shown in Table 14.5.3. The shortest interatomic distances between two palladium atoms are similar to the distances in palladium (2.75 Å) [43,44], and the distances up to 2.9 Å are comparable with Pd-Pd distances in Pd_3Bi (2.85 − 2.90 Å) [39], or in Pd_4Se (2.76 − 2.93 Å) [45]. The Bi-Pd bond length is consistent with those observed in Pd_3Bi (2.85 − 2.88 Å) [39]. The shorter distance of 2.77 Å results from Pd3 atoms that are close to the above mentioned void in the bismuth tetrahedron, which is also seen in a somewhat larger atomic displacement parameter for Pd3 (Table 14.5.1). The short Pd-Se bond length also agrees with that in Pd_5InSe (2.50 Å) [13,15], or in Pd_4Se (2.46 − 2.49 Å) [45], and the longer bond of 2.70 Å is within the range of Pd-Se bond lengths in $Pd_{34}Se_{11}$ (2.40 − 2.79 Å) [46].

Table 14.5.2.: Crystallographic data and structure refinement of $Pd_{11}Bi_2Se_2$.

|	
emperical formula	$Pd_{11}Bi_2Se_2$
formula mass	1746.28 g mol^{-1}
crystal system	cubic
space group	$Fd\bar{3}m$ (No. 227, origin choice 2)
cell parameters	$a = 12.4879(14)$ Å
cell volume	1947.5(7) Å^3
formula units per unit cell	$Z = 8$
X-ray density	11.912 g cm$_{-3}$
absorption coefficient	34.071 mm^{-1}
$F(000)$	5920
diffractometer	Stoe IPDS I
radiation	Ag K_α (0.56086 Å)
2θ range	$12.6° < 2\theta < 60.3°$
absorption correction	numerical [24,25]
measured reflections	10306
independent data	145 (140 with $I > 2\ \sigma(I)$)
parameters	14
weighting scheme	$w = 1 / [\sigma^2 F_o{}^2 + (0.0228P)^2]$
	with $P = [F_c{}^2 + \text{Max}(F_o{}^2,0)] / 3$
extinction coefficient	$x = 0.00013(2)$
extinction expression	$F_c{}^* = kF_c[1 + 0.001xF_c{}^2\lambda^3 / \sin(2\theta)]^{-1/4}$
	with the overall scale factor k
refinement	full-matrix least-squares on F^2
R_{int}	0.0508
R_σ	0.0170
$R1\ [I > 2\ \sigma(I)]\ /\ wR2\ [I > 2\ \sigma(I)]$	0.0142 / 0.0339
$R1$ (all data) / $wR2$ (all data)	0.0155 / 0.0343
GooF (all data)	1.176
$\Delta\rho_{\text{min}}\ /\ \Delta\rho_{\text{max}}$, e Å^{-3}	-0.925 / 1.289
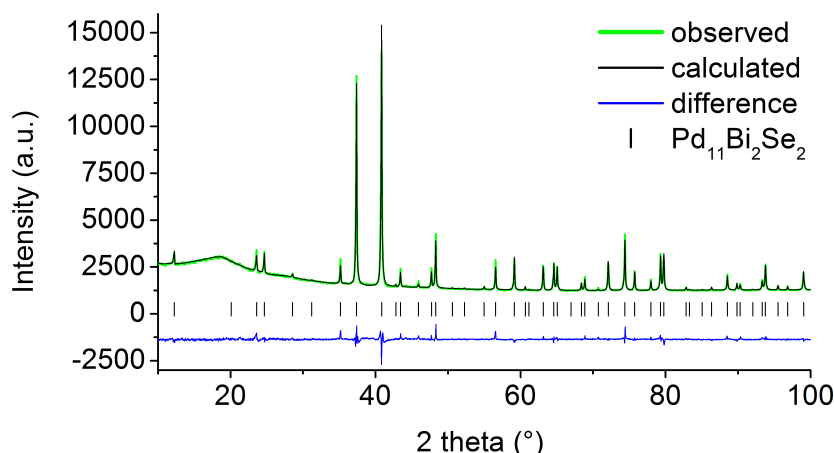
Figure 14.5.3.: Rietveld refinement of the crystal structure of $Pd_{11}Bi_2Se_2$ (λ = 1.54056 Å, R_p(background corrected) = 0.245; R_{wp}(background corrected) = 0.142; χ^2 = 1.39; R_{Bragg} = 0.0955; $Fd\bar{3}m$ (Origin2), a = 12.4833(3) Å, x(Pd1) = 0.3421(2), x(Pd3) = 0.2856(1)).

14.5.3. Crystal structure relationships

Many palladium-rich ternary compounds like Pd_5MY (M: Cd, In, Tl; Y: As, Se) are related to the cubic closed packed (ccp) Cu type [13-16] as proven by a group-subgroup relationships, according to Bärnighausen [47]. In $Pd_{11}Bi_2Se_2$, however, the valence electron concentration (VEC) is increased to $^{22}/_{15}$ = 1.47, and this is a typical value for intermetallics with crystal structures related to the cubic W type [1], e. g. $Pd_{20-x}Te_7$ [36]. $Pd_{11}Bi_2Se_2$ is isopointal to $Li_{13}In_3$, which is a 64-fold superstructure of the W type [48]. They are not isotypic because the minority components are ordered differently (In atoms in $Li_{13}In_3$ on sites $8b$ and $16c$ and Bi and Se atoms in $Pd_{11}Bi_2Se_2$ on sites $16d$ and $16c$). Another difference concerns the void in $Pd_{11}Bi_2Se_2$ resulting in some relaxation of the crystal structure and free positional parameters (x(Pd3) = 0.28373(4) and x(Pd1) = 0.34466(6)). They differ more from the ideal values (0.25 and 0.375, respectively, as generated from the group-subgroup relationships) compared to those in $Li_{13}In_3$ (x(Li3) = 0.240(2) and x(Li4) = 0.375(2)) [49].

The structure of $Pd_{11}Bi_2Se_2$ is very similar to the BiF_3 type that was proposed for $Pd_3(Bi_{0.6}Se_{0.4})$ [23]. The ratio of Pd atoms to Bi/Se atoms are very similar for both, being $^{11}/_4$ for $Pd_{11}Bi_2Se_2$ and $^{12}/_4$ for $Pd_3(Bi_{0.6}Se_{0.4})$. The Bi and Se atoms of $Pd_3(Bi_{0.6}Se_{0.4})$ are proposed to be statistically distributed and form a ccp with occupied octahedral and tetrahedral voids by Pd atoms. The Bi and Se atoms in $Pd_{11}Bi_2Se_2$ are ordered and form a ccp related substructure as well (see Fig. 14.5.5a). Their octahedral voids are occupied by Pd3 atoms and only five eighths of tetrahedral voids are filled

Table 14.5.3.: Selected interatomic distances (< 3 Å) in $Pd_{11}Bi_2Se_2$.

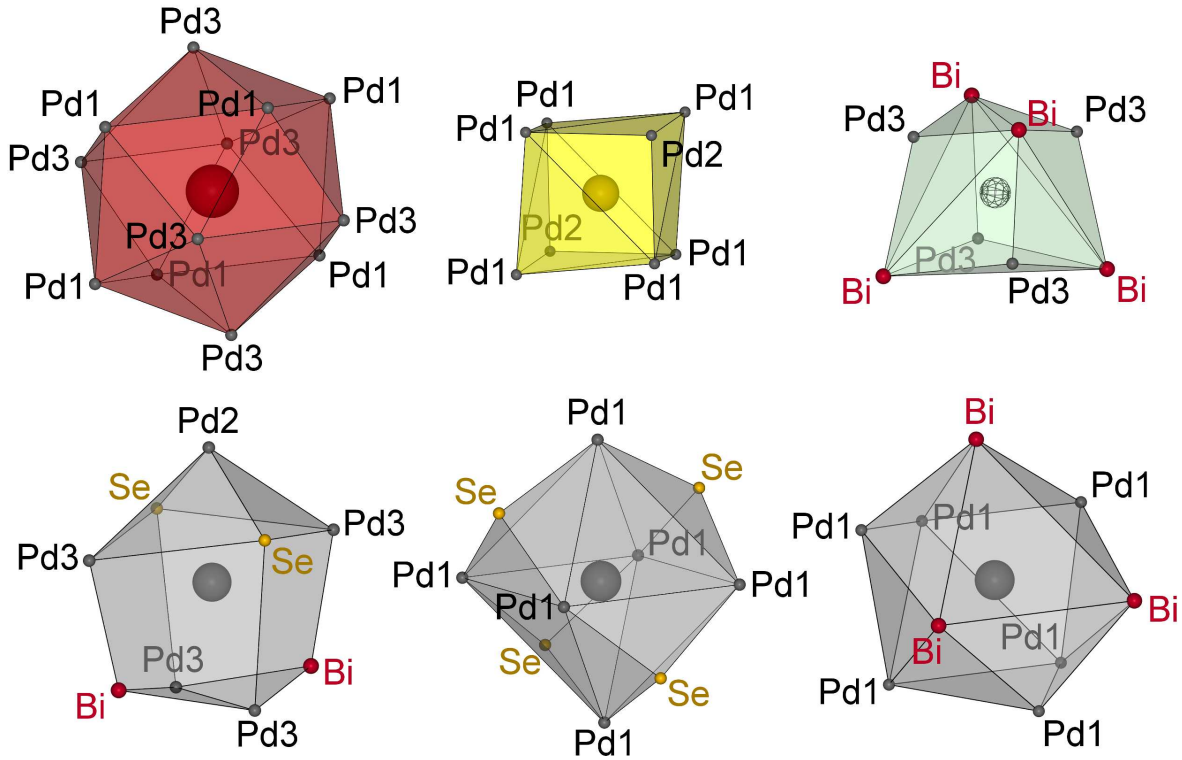| atom		d / Å	atom		d / Å
Pd1	2x Se	2.5041(4)	Pd3	3x Bi	2.7656(4)
	1x Pd2	2.7430(8)		3x Pd1	2.8589(7)
	2x Pd3	2.8589(7)		3x Pd1	2.9047(6)
	2x Pd3	2.9047(6)	Bi	6x Pd3	2.7656(4)
	2x Bi	2.9388(6)		6x Pd1	2.9388(6)
Pd2	4x Se	2.7037(3)	Se	6x Pd1	2.5041(4)
	6x Pd1	2.7430(8)		2x Pd2	2.7037(3)

Figure 14.5.4.: Coordination polyhedra of Bi (top, left), Se (top, center), void (top, right), Pd1 (bottom, left), Pd2 (bottom, center) and Pd3 (bottom, right) atoms in $Pd_{11}Bi_2Se_2$.

with Pd1 and Pd2 atoms. The remaining eighth of tetrahedral voids remain empty according to the crystal chemical formula $(Pd3)[o]_4(Pd1)[t]_6(Pd2)[t]\square[t]Bi_2Se_2$. In view of such pronounced similarities and rather subtle differences, which are easily overlooked in the evaluation of X-ray diffraction data, we assume that the proposed $Pd_3(Bi_{0.6}Se_{0.4})$ [23] is in fact identical to $Pd_{11}Bi_2Se_2$. Due to the improvement of X-ray powder diffractometers we could now observe the superstructure reflections for that compound and derive the true composition and crystal structure.

The structure of $Pd_{11}Bi_2Se_2$ may alternatively be described through substructures. A cubic Laves phase type of $(Pd2)Bi_2$ (Fig. 14.5.5b) and of $\square Se_2$, which additionally form a spinel type $(\square Se_2(Pd3)_4$, see Fig. 14.5.5c) are shifted by $\frac{1}{2} \frac{1}{2} \frac{1}{2}$ with respect to each other. Pd1 atoms $(48f)$ are occupying $[Bi_2Se_2]$ tetrahedra, located between Bi and Se tetrahedra of both mentioned Laves-phase like substructures (Fig. 14.5.5d).

14.5.4. Electronic structure of $Pd_{11}Bi_2Se_2$

Since $Pd_{11}Bi_2Se_2$ has a relatively large unit cell that includes 120 atoms in total, all of them being rather heavy, we have utilized two approaches to the electronic structure calculations. In the first one, we have employed full-potential linearized augmented plane wave method (FP-LAPW) and relativistic corrections, but due to the approach being extremely resource-heavy, the trade-off included a rather coarse k-point mesh (see Section 14.4.5). In the second one, we used PAW pseudopotentials rather than an all-electron approach, which due to the less resource-demanding nature of the method allowed us to use finer k-point mesh and tighter convergence criteria, however, at the cost of expected somewhat less strict relativistic corrections. However, the results from both methods have provided very similar pictures of the electronic structure, with only relatively small quantitative differences. Therefore, we will base our discussion mainly on the FP-LAPW results. Calculated total (TDOS) and projected
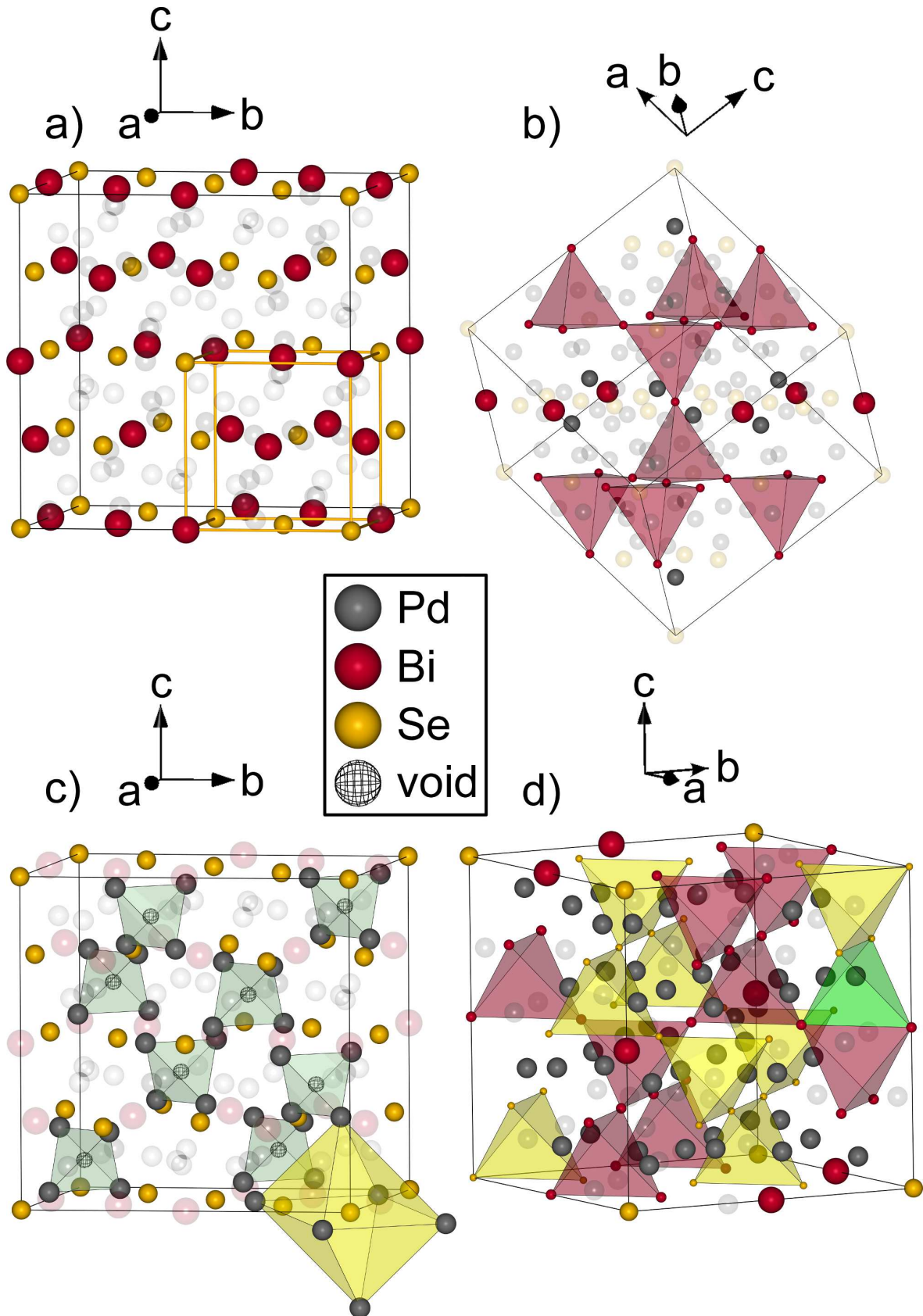
Figure 14.5.5.: Substructures of Pd$_{11}$Bi$_2$Se$_2$: a) ccp of Bi and Se atoms, b) cubic Laves phase type for (Pd2)Bi$_2$, c) spinel type for □Se$_2$(Pd3)$_4$, d) two Laves phases types ((Pd2)Bi$_2$ and □Se$_2$) shifted by $^1/_2$ $^1/_2$ $^1/_2$ and connected by Pd1 centered tetrahedra (exemplary one green tetrahedral shown). Atoms, which are not part of the substructure, are transparent for reason of clarity.

(PDOS) densities of states near the Fermi level are shown in Fig. 14.5.6. (DOS plots from VASP calculations are presented in the Supplementary section).

As seen from Fig. 14.5.6, the region near the Fermi level is dominated by the Pd 4d-states, that are almost filled. This is quite typical for palladium-based intermetallic compounds, like Pd_3In [15] and palladium-rich chalcogenides [15,50]. Non-zero DOS at the Fermi level points out towards the metallic conductivity for the compound, also typical for ternary group 10 metal-rich chalcogenides. The almost filled nature of the d-states and a pseudo-gap at the Fermi level (slightly more pronounced in the pseudopotential calculations) might indicate relatively poor metallic behavior. Compared to the palladium d-states, the contributions from Bi and Se p-states appear rather low, which is partially due to the number of the respective atoms in the unit cell. Fig. 14.5.7 shows the scaled up contributions from bismuth and selenium, and it is clearly seen that both the Bi 6p-states and Se 4p-states fall exactly into the same energy range of ca. -7 eV - 3 eV, where they mix with the majority of the Pd 4d-states. This might be tentatively taken as an indication of a covalent nature of the Pd-Se and Pd-Bi interactions. The 6s-states of bismuth are well-localized far below the Fermi level, between -11 and -12 eV (see Fig. 7) and most likely represent a lone pair, not participating in the bonding with other atoms.

We have also performed a charge density analysis within the framework of Bader's QTAIM theory [51,52]. Calculated atomic charges are: Bi +0.91; Se -0.10; Pd1 -0.09; Pd2 +0.12; Pd3 -0.29. As seen from these charges, there is a certain amount of electron density transferred from the bismuth atom to palladium and selenium. Different charges of three crystallographically unique palladium sites are in perfect agreement with the differences in their coordination. The most negatively charged palladium atom, Pd3, has three bismuth and six palladium atoms surrounding it, so it has three atoms transferring electrons to it. Relatively low, but still negatively charged Pd1 is coordinated by five palladium, two bismuth and two selenium atoms. Bismuth atoms provide electron density and selenium atoms attract it, hence the low negative charge on both Pd1 and Se. Lastly, Pd2 carries a low positive charge of +0.12 since it is coordinated by six palladium and four selenium atoms, the latter acting as attractors of electron density. However, since electronegativities of palladium and selenium are quite close, relative charges on palladium and selenium are rather low. This confirms the essentially covalent nature of Pd-Se bonding assumed from the DOS plots. As for Pd-Bi interactions, there is certain polarity to it based on the charge density redistribution, however, bismuth atomic charge being under +1 is still indicative of the presence of strong covalency, which also agrees with the conclusions based on the DOS analysis.
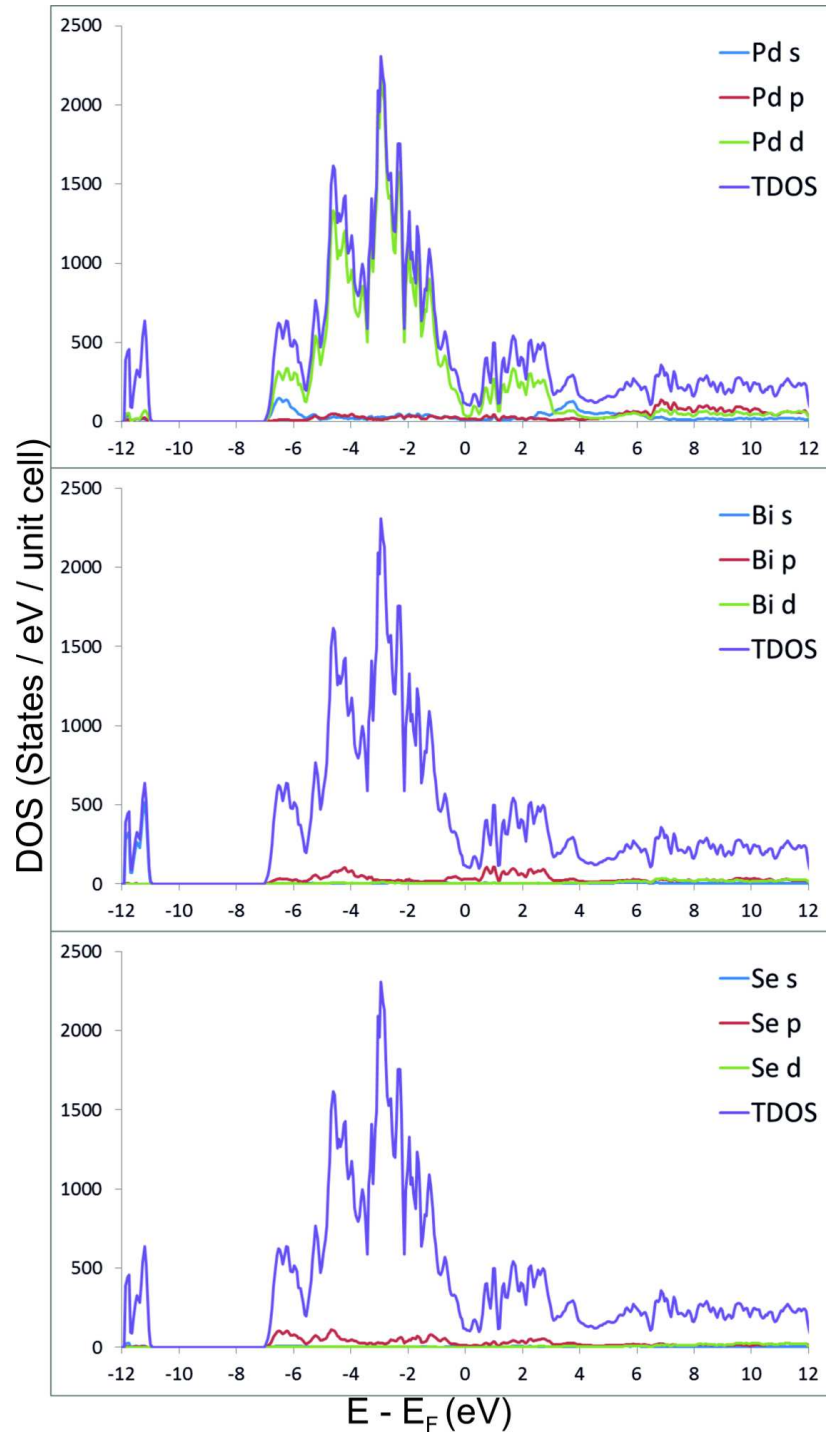
Figure 14.5.6.: Calculated total and l-resolved projected DOS for $Pd_{11}Bi_2Se_2$ (top to bottom): Pd, Bi, and Se projections (Fermi level is at zero).
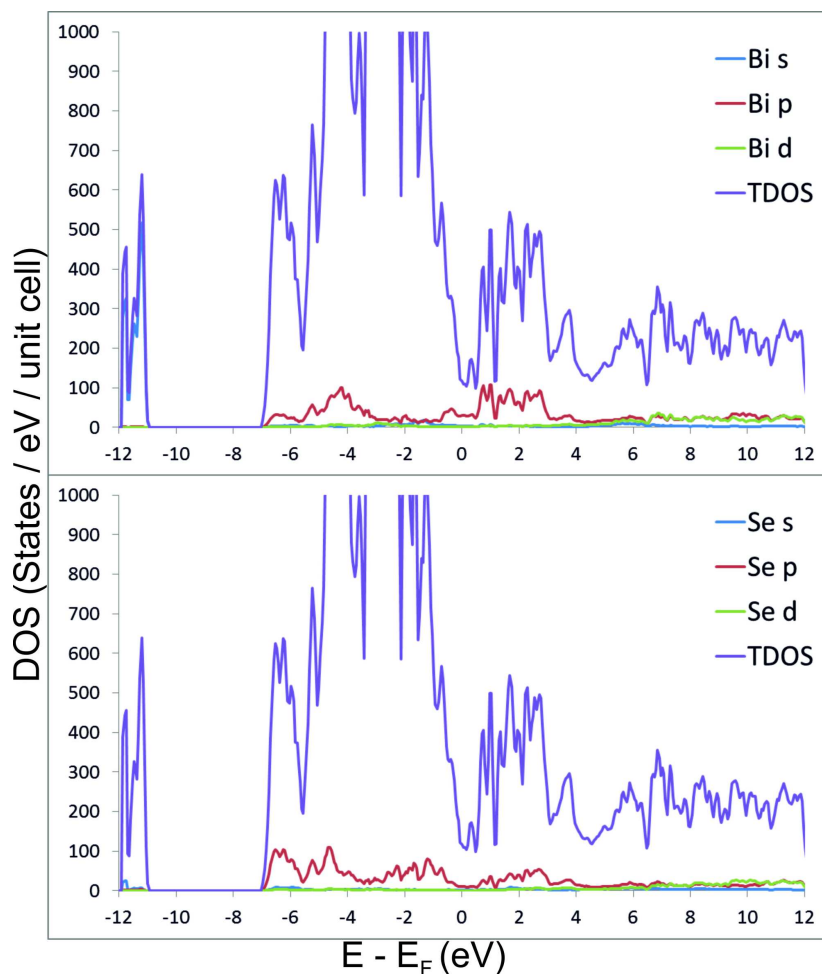
Figure 14.5.7.: Enlarged l-resolved Bi (top) and Se (bottom) projected DOS for $Pd_{11}Bi_2Se_2$ (Fermi level is at zero).

14.6. Conclusions

The crystal structure of $Pd_{11}Bi_2Se_2$ was solved and refined from X-ray single crystal data. It crystallizes isopointal to $Li_{13}In_3$, a 4 x 4 x 4 superstructure of the W type, with ordered occupation and an ordered vacancy according to $Pd_{11}\square Bi_2Se_2$. It is most probably identical to the earlier reported $Pd_3(Bi_{0.6}Se_{0.4})$, claimed to crystallize in BiF_3 type, a 2 x 2 x 2 superstructure of the W type, with mixed occupation of palladium and selenium atoms and no ordered vacancy. The structure of $Pd_{11}Bi_2Se_2$ can be described alternatively as substructures of a cubic Laves phase type for $(Pd2)Bi_2$ shifted by $^1/_2$ $^1/_2$ $^1/_2$ to a spinel type for $\square Se_2(Pd3)_4$ with Pd1 occupying tetrahedra connecting both substructures. $Pd_{11}Bi_2Se_2$ is stable in air and inert to many solvents, even to concentrated hydrochloric acid. The magnetic moment is minute with 0.0114(2) μ_B per palladium atom. No hydrogen uptake could be observed for $Pd_{11}Bi_2Se_2$, which might attract interest for catalysis. In the electronic structure, the region near the Fermi level is dominated by almost filled Pd 4d-states. Low yet non-zero DOS at the Fermi level predicts the compound to be a metallic conductor, while a pseudo-gap in the density of states might indicate $Pd_{11}Bi_2Se_2$ to be a poor metal.

14.7. Acknowledgements

14.8. Supplementary data
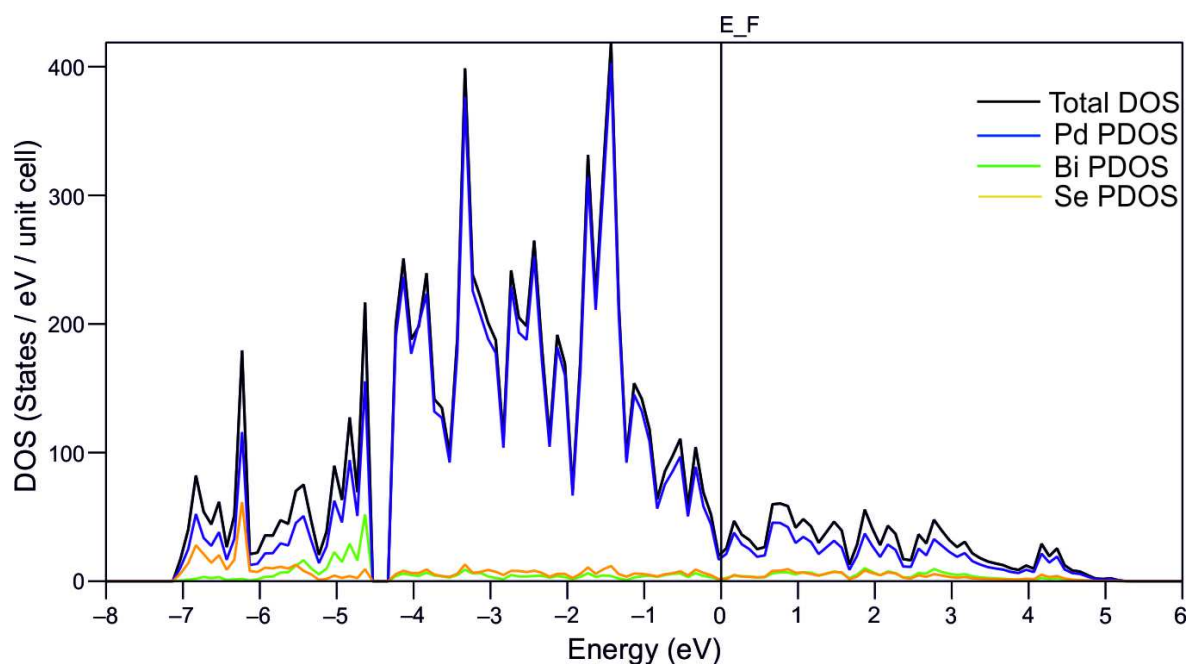
Figure 14.8.1.: Total and projected densities of states near the Fermi level for $Pd_{11}Bi_2Se_2$ obtained from VASP calculations.

14.9. References for chapter 14

[1]   K. Schubert, Kristallstrukturen zweikomponentiger Phasen, Springer, Berlin, Heidelberg (1964).

[2]   H. Kohlmann, N. Kurtzemann, R. Weihrich, T. Hansen, *In situ* neutron powder diffraction on intermediate hydrides of $MgPd_3$ in a novel sapphire gas pressure cell, Z. Anorg. Allg. Chem. 635 (2009) 2399–2405.

[3]   H. Kohlmann, G. Renaudin, K. Yvon, C. Wannek, B. Harbrecht, Hydrogen-induced atomic rearrangement in $MgPd_3$, J. Solid State Chem. 178 (2005) 1292–1300.

[4]   K. Baba, Y. Niki, Y. Sakamoto, T. B. Flanagan, A. Craft, Reversibile transitions between ordered structures in the Pd_3Mn-hydrogen system, Scr. Metall. 21 (1987) 1147–1151.

[5]   H. Kohlmann, A. V. Skripov, A. V. Soloninin, T.J. Udovic, The anti-perovskite type hydride $InPd_3H_{0.89}$, J. Solid State Chem. 183 (2010) 2461–2465.

[6]   N. Kurtzemann, H. Kohlmann, Crystal structure and formation of $TlPd_3$ and its new hydride $TlPd_3H$, Z. Anorg. Allg. Chem. 636 (2010) 1032–1037.

[7]   H. Kohlmann, F. Müller, K. Stöwe, A. Zalga, H. P. Beck, Hydride formation in the intermetallic compounds $CePd_3$ and $CeRh_3$, Z. Anorg. Allg. Chem. 635 (2009) 1407–1411.

[8] A. Götze, T. C. Hansen, H. Kohlmann, The reversible hydrogenation of $BiPd_3$ followed by *in situ* methods and the crystal structure of $PbPd_3D_{0.13(1)}$, J. Alloy. Compd. 731 (2018) 1001–1008.

[9] H. Kohlmann, Hydrogenation of palladium-rich compounds of aluminium, gallium and indium, J. Solid State Chem. 183 (2010) 367–372.

[10] H. Kohlmann, C. Ritter, Reaction pathways in the formation of intermetallic $InPd_3$ polymorphs, Z. Anorg. Allg. Chem. 635 (2009) 1573–1579.

[11] N. Kunkel, J. Sander, N. Louis, Y. Pang, L. M. Dejon, F. Wagener, Y. N. Zang, A. Sayede, M. Bauer, M. Springborg, H. Kohlmann, Theoretical investigation of the hydrogenation induced atomic rearrangements in palladium-rich intermetallic compounds MPd_3 (M = Mg, In, Tl), Eur. Phys. J. B 82 (2011) 1–6.

[12] A. Götze, H. Kohlmann, Palladium hydride and hydrides of palladium-rich phases, in: Reference Module in Chemistry, Molecular Sciences and Chemical Engineering, Elsevier (2017).

[13] A. Götze, P. Urban, O. Oeckler, H. Kohlmann, Synthesis and crystal structure of Pd_5InSe, Z. Naturforsch. 69B (2014) 417–422.

[14] A. Götze, J. M. Sander, H. Kohlmann, Crystal structures and hydrogenation properties of palladium-rich compounds with elements from groups 12-16, Z. Naturforsch. 71B (2016) 503–508.

[15] E. Y. Zakharova, S. M. Kazakov, A. A. Isaeva, A. M. Abakumov, G. van Tendeloo, A. N. Kuznetsov, Pd_5InSe and Pd_8In_2Se - new metal-rich homological selenides with 2D palladium-indium fragments: synthesis, structure and bonding, J. Alloy. Compd. 589 (2014) 48–55.

[16] E. Y. Zakharova, N. A. Andreeva, S. M. Kazakov, A. N. Kuznetsov, Ternary arsenides based on platinum–indium and palladium–indium fragments of the Cu_3Au-type: crystal structures and chemical bonding, J. Alloy. Compd. 621 (2015) 307–313.

[17] J. Osswald, R. Giedigkeit, R. Jentoft, M. Armbrüster, F. Girgdies, K. Kovnir, T. Ressler, Y. Grin, R. Schlögl, Palladium-gallium intermetallic compounds for the selective hydrogenation of acetylene Part I, J. Catal. 258 (2008) 210–218.

[18] Q. W. Zhang, J. Li, X. X. Liu, Q. M. Zhu, Synergetic effect of Pd and Ag dispersed on Al_2O_3 in the selective hydrogenation of acetylene, Appl. Catal. A 197 (2000) 221–228.

[19] P. W. Albers, K. Möbius, C. D. Frost, S. F. Parker, Characterization of β-palladium hydride formation in the lindlar catalyst and in carbon-supported palladium, J. Phys. Chem. C 115 (2011) 24485–24493.

[20] M. Armbrüster, G. Wowsnick, M. Friedrich, M. Heggen, R. Cardoso-Gil, Synthesis and catalytic properties of nanoparticulate intermetallic Ga–Pd compounds, J. Am. Chem. Soc. 133 (2011) 9112–9118.

[21] M. Armbrüster, R. Schlögl, Y. Grin, Intermetallic compounds in heterogeneous catalysis - a quickly developing field, Sci. Technol. Adv. Mater. 15 (2014) 34803.

[22] Y. Luo, A. V. Villaseca, M. Friedrich, D. Teschner, A. Knop-Gericke, M. Armbrüster, Addressing electronic effects in the semi-hydrogenation of ethyne by $InPd_2$ and intermetallic Ga-Pd compounds, J. Catal. 338 (2016) 265–272.

[23] M. El Boragy, M. Ellner, K. Schubert, On some metastable homeotypes of CuZn with Pd as majority component, Z. Metallkd. 80 (1989) 197–200.

[24] X-Red32, Stoe & Cie GmbH (2005) Darmstadt (Germany).

[25] X-Shape, Stoe & Cie GmbH (2005) Darmstadt (Germany).

[26] G. M. Sheldrick, A short history of SHELX, Acta Crystallogr. A 64 (2008) 112–122.

[27] J. Rodríguez-Carvajal, FullProf: a Program for Rietveld Refinement and Pattern Matching Analysis, Insitut Laue-Langevin, Grenoble (France) (2012).

[28] R. T. Azuah, L. R. Kneller, Y. Qiu, P. L. Tregenna-Piggott, C. M. Brown, J. R. Copley, R. M. Dimeo, DAVE: a comprehensive software suite for the reduction, visualization, and analysis of low energy neutron spectroscopic data, J. Res. Natl. Inst. Stand. Technol. 114 (2009) 341–358.

[29] ELK: An all-electron full-potential linearised augmented-plane wave (FP-LAPW) code.

[30] J. P. Perdew, J. Burke, M. Ernzerhof, Generalized gradient approximation made simple, Phys. Rev. Lett. 77 (1996) 3865–3868.

[31] G. Kresse, J. Furthmüller, Vienna ab-initio simulation package (VASP).

[32] G. Kresse, D. Joubert, From ultrasoft pseudopotentials to the projector augmented-wave method, Phys. Rev. B 59 (1999) 1758–1775.

[33] H. J. Monkhorst, J. D. Pack, Special points for Brillonin-zone integrations, Phys. Rev. B 13 (1976) 5188–5192.

[34] V. Sadovnichy, A. Tikhonravov, V. Voevodin, V. Opanasenko, in: J. S. Vetter (Ed.), Contemporary High Performance Computing: from Petascale toward Exascale, CRC Press, Boca Raton, USA (2013) 283–307.

[35] M. Armbrüster, K. Konvir, M. Behrens, D. Teschner, Y. Grin, R. Schlögl, Pd-Ga intermetallic compounds as highly selective semihydrogenation catalysts, J. Am. Chem. Soc. 132 (2010) 14745–14747.

[36] M. Janetzky, Palladiumreiche Telluride, Dissertation Universität Marburg (2008).

[37] A. Pandey, C. Mazumdar, R. Ranganathan, Magnetic behavior of binary intermetallic compound YPd_3, J. Alloy. Compd. 476 (2009) 14–18.

[38] A. V. Tkachuk, A. Mar, Structure and physical properties of ternary rare-earth cobalt bismuth intermetallics $(RE)_{12}Co_5Bi$ (RE = Y, Gd, Tb, Dy, Ho, Er, Tm), Inorg. Chem. 44 (2005) 2272–2281.

[39] S. Bhan, K. Schubert, Über die Struktur von Phasen mit Kupfer Unterstruktur in einigen T-B Legierungen (T = Ni, Pd, Pt; B = Ga, In, Tl, Pb, Sb, Bi), J. Less-Common Met. 17 (1969) 73–90.

[40] N. Sarah, K. Schubert, Kristallstruktur von Pd_5Bi_2 J. Less-Common Met. 63 (1979) 75–82.

[41] I. Maksimov, F. J. Litterst, H. Rechenberg, M. A. C. de Melo, R. Feyerherm, R. W. A. Hendrikx, T. J. Gortenmulder, J. A. Mydosh, S. Süllow, Effect of disorder on the magnetic and transport properties of $UPd_{2-x}Sn$, Phys. Rev. B 67 (2003) 104405.

[42] B. C. Giessen, N. J. Grant, New intermediate phases in system of Nb or Ta with Rh, Ir, Pd, or Pt, Acta Crystallogr. 17 (1964) 615–616.

[43] R. H. Schroeder, N. Schmitz-Pranghe, R. Kohlhaas, Experimentelle Bestimmung der Gitterparameter der Platinmetalle im Temperaturbereich -190 bis 1709 ℃, Z. Metallkd. 63 (1972) 12–16.

[44] H. E. Swanson, E. Tatge, Standard X-ray diffraction powder patterns I, Natl. Bur. Stand. Circular 539 (1953) 1–95.

[45] T. Takabatake, M. Ishikawa, J. L. Jorda, Superconductivity and phase relations in the Pd-Se system, J. Less-Common Met. 134 (1987) 79–89.

[46] S. Sato, T. Takabatake, M. Ishikawa, Structures of superconducting palladium selenides, Pd_7Se_2 and $Pd_{34}Se_{11}$, Acta Crystallogr. C 45 (1989) 1–3.

[47] H. Bärnighausen, Group-subgroup relations between space groups: a useful tool in crystal chemistry, MATCH 9 (1980) 137–175.

[48] M. Janetzky, B. Harbrecht, Crystal growth, structure and properties of the palladium-rich telluride $Pd_{13}Te_3$, Z. Anorg. Allg. Chem. 632 (2006) 837–844.

[49] J. Stöhr, W. Müller, H. Schäfer, Darstellung und Kristallstruktur von Li$_2$In und Li$_{13}$In$_3$, Z. Naturforsch. **33B** (1978) 1434–1437.

[50] E. Y. Zakharova, A. V. Churakov, T. Doert, A. N. Kuznetsov, Pd$_{17}$In$_4$Se$_4$, a metal-rich palladium–indium selenide with an open-framework structure, Eur. J. Inorg. Chem. (2013) 6164–6169.

[51] M. Yu, D. R. Trinkle, Accurate and efficient algorithm for Bader charge intergration, J. Chem. Phys. **134** (2011) 64111.

[52] R. F. W. Bader, Atoms in Molecules: a Quantum Theory, Oxford University Press, Oxford (1990).

15. From the Laves Phase CaRh$_2$ to the Perovskite CaRhH$_3$ - *In Situ* Investigation of the Hydrogenation Intermediates CaRh$_2$H$_x$

André Götze, Jens Möllmer, Holger Kohlmann

$$CaRh_2 \longrightarrow \alpha\text{-}CaRh_2H_{0.05} \longrightarrow \beta\text{-}CaRh_2H_{3.9} \longrightarrow CaRhH_3 + Rh$$

γ-CaRh$_2$H$_{3.2}$

kinetically hindered
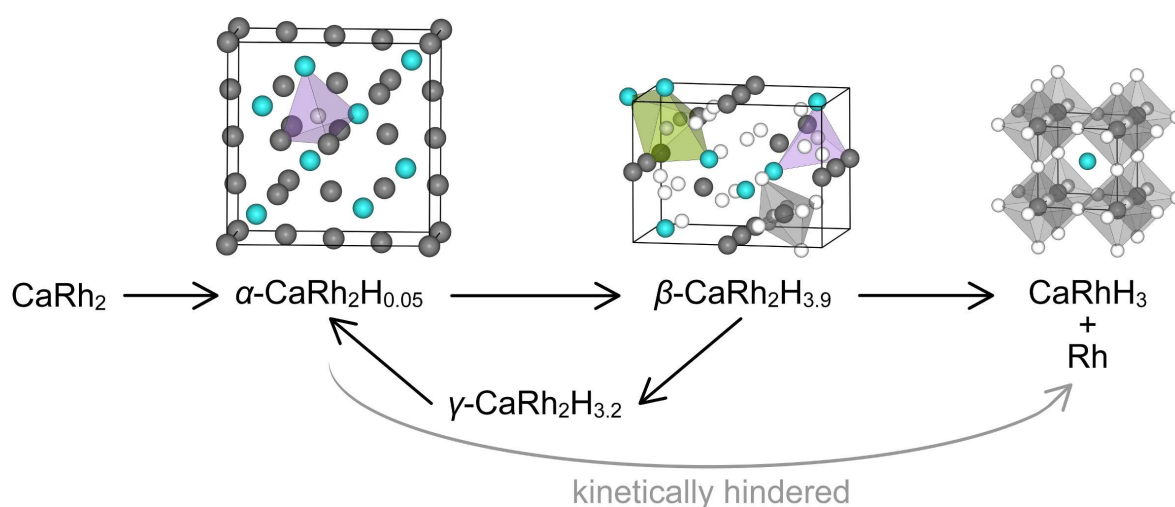
15.1. Authors' contributions

The syntheses, chemical analysis, powder diffraction, thermal analysis and structure solution and refinements were done by A. Götze. J. Möllmer conducted the hydrogen soprtion experiments. The manuscript was written by A. Götze and revised by H. Kohlmann.

15.2. Abstract

The hydrogenation properties of the cubic Laves phase $CaRh_2$ and the formation of the perovskite $CaRhH_3$ were studied by *in situ* thermal analysis (DSC), sorption experiments, and *in situ* neutron powder diffraction. Three Laves phase hydrides are formed successively at room temperature and hydrogen gas pressures up to 5 MPa. Cubic α-$CaRh_2H_{0.05}$ is a stuffed cubic Laves phase with statistically distributed hydrogen atoms in tetrahedral $[Ca_2Rh_2]$ voids ($ZrCr_2H_{3.08}$ type, $Fd\bar{3}m$, $a = 7.5308(12)$ Å). Orthorhombic β-$CaRh_2D_{3.93(5)}$ (own structure type, *Pnma*, $a = 6.0028(3)$ Å, $b = 5.6065(3)$ Å, $c = 8.1589(5)$ Å) and γ-$CaRh_2D_{3.20(10)}$ (β-$CaRh_2H_{3.9}$ type, *Pnma*, $a = 5.9601(10)$ Å, $b = 5.4912(2)$ Å, $c = 8.0730(11)$ Å) are low-symmetry variants thereof with hydrogen occupying distorted tetrahedral $[Ca_2Rh_2]$ and trigonal bipyramidal $[Ca_3Rh_2]$ voids. Hydrogen sorption experiments shows the hydrogenation to take place already at 0.1 MPa and to yielded in β-$CaRh_2H_{3.8(2)}$. At 560 K and 5 MPa hydrogen pressure the Laves phase hydride decomposes kinetically controlled to nano-crystalline rhodium and $CaRhD_{2.93(2)}$ ($CaTiO_3$ type, $Pm\bar{3}m$, $a = 3.6512(2)$ Å). The hydrogenation of $CaRh_2$ provides a synthesis route to otherwise not accessible perovskite-type $CaRhH_3$.

15.3. Introduction

Complex transition metal hydrides have attracted renewed interest recently in the search for hydrogen-rich compounds, high T_C superconductors, as hydrogen storage materials and in catalysis [1–4]. Ternary hydrides of the late transition metals often show a transition from mainly ionic and covalent to more pronounced metallic bonding with increasing transition metal or decreasing hydrogen content. This may be illustrated by ternary alkaline and alkaline earth rhodium hydrides. While rhodium does not form a binary hydride, several ternary hydrides are known, e. g. typical semi-conducting 18-electron complex hydrides A_3RhH_6 (A = Li [5], Na [6]) with isolated RhH_6 octahedra. Li_3RhH_4 with reduced hydrogen content might be regarded at first sight as a typical 16 valence electron complex hydride. However, weak rhodium-rhodium interactions are noticed between the stacked square planar RhH_4 units [7]. Stronger metal-metal bonding is found in $MgRhH_{1-x}$, where Rh-H and significant Rh-Rh interactions prevail [8,9]. The latter might be weakened by exchanging magnesium by the higher homologue calcium due to the higher space requirement as suggested by DFT calculations [9]. This opportunity to influence the type of chemical bonding in hypothetical hydrides CaRhHx has not been explored yet.

The effect of increasing rhodium content on chemical bonding is also seen in the calcium rhodium hydrides known so far. M_2RhH_{5+x} (M = Ca [10,11], Sr [10,12], Eu [13]) crystallize in the well-known K_2PtCl_6 type with isolated RhH_6 octahedra (disordered RhH_{5+x}) as central structural unit. Increasing the rhodium content leads to $Ca_8Rh_5H_{25}$ and $Ca_8Rh_6H_{24}$ with enhanced metallic bonding. This is accompanied by an increasing connectivity of RhH_6 (corner-sharing) [11,14]. The maximum connection by corners would be reached in the perovskite structure. This is not known yet in the Ca-Rh-H system, despite synthesis approaches in the molar ratio from 3:1 to 1:3 of calcium hydride and rhodium [14]. Perovskite type calcium hydrides are reported for other transition metals like $CaNiH_3$ [15] and $CaPdH_2$ [16].

In this work, a synthetic access to the perovskite-type hydride $CaRhH_3$ by a different synthesis route through the Laves phase $CaRh_2$ is reported. Furthermore, the hydrogenation properties of $CaRh_2$ and the reaction pathway to the perovskite was investigated by *in situ* thermal analysis [17] and *in situ* neutron powder diffraction [18].

15.4. Experimental section

15.4.1. Synthesis and chemical analysis

The binary compound $CaRh_2$ in typical quantities of 0.5 g was synthesized from the elements. Rhodium (powder fine, 99.95+ %, Chempur) and calcium (shot, redistilled, 99.5 %, Alpha Aesar, ≤ 10 mm, under argon atmosphere) with an excess of 14.2 mol-% were sealed in niobium ampoules (9 mm internal diameter, 0.5 mm wall thickness, 100 mm length), heated under vacuum in a tube furnace to 1423 K with a heating rate of 50 K h^{-1} and held at this temperature for 48 h. Samples contain typically 1 to 8 wt-% of unreacted rhodium and in some cases up to 5.5 wt-% CaO. For *ex situ* hydrogenation (deuteration), well-ground samples were placed in hydrogen resistant Inconel (Böhler L718, nickel-chromium alloy) crucibles and reacted with hydrogen (99.9 %, Air liquide) or deuterium gas (99.8 %, Air liquide) in autoclaves made from the same alloy. $CaRh_2H(D)_x$ samples were synthesized at 295 K under 5.0 MPa hydrogen (deuterium) pressure and $CaRhH(D)_3$ at 703 K for 48 h (50 K h^{-1} heating rate) under 5.0 MPa hydrogen (deuterium) pressure.

Chemical analyses were performed by an EDX INCA SYSTEM from Oxford Instruments mounted on a Zeiss LEO 1530 scanning electron microscope with an acceleration voltage of 20 kV and a working distance of 15 mm.

15.4.2. Powder diffraction

Laboratory X-ray powder diffraction (XRPD) data were collected using a STOE STADI-P diffractometer in Debye-Scherrer geometry at $T = 296(2)$ K with $CuK_{\alpha 1}$ radiation (glass capillary, 0.2 mm in diameter). In situ XRPD data were taken at a Huber G670 diffractometer with Guinier geometry with $MoK_{\alpha 1}$ radiation in silica glass capillary (0.3 mm in diameter) attached to a gas supply system19 under isothermal conditions at 723 K and various hydrogen pressures.

In situ neutron powder diffraction were taken at the diffractometer D20 (ILL, Grenoble, France) under various deuterium pressures (isotopic purity, 99.8 %) with a time resolution of 2 min per pattern (doi: 10.5291/ILL-DATA.5-24-605, NUMORs 974037 to 974686 were used for refinement, see Supplement; NUMOR is used in ILL's internal numbering system for experimental data sets). The sample was placed inside a single crystal sapphire based gas pressure cell especially designed for in situ neutron powder diffraction with a gas pressure controller and contactless laser heating system [18]. The wavelengths were determined from measurements of a silicon standard (NIST640b).

The XRD patterns were indexed with the help of the computer program TOPAS [20] and crystal structures were refined using the program FullProf [21]. For Rietveld refinement, nine patterns were binned to one frame, which is named after the first NUMOR. Displayed difference plots of refinements are calculated by the difference of observed and calculated intensities. Besides the commonly used R_p and R_{wp} values the background corrected R'_p and R'_{wp} values are also listed. The unusual background of in situ neutron powder diffraction data, resulting mainly from phonon scattering of the sapphire cell and diffuse scattering on deuterium gas, were fitted by manually set background points on patterns with low numbers of reflections. In order to avoid correlation of parameters, background points were refined only in the final cycles. The isotropic thermal displacement parameters B_{iso} of Rietveld refinements based on neutron powder diffraction were corrected by 0.323 Å^2 calculated by the difference of $B_{iso}(Rh)_{exp}$ (Supplement, Figure S2) and $B_{iso}(Rh)_{lit}$ (0.068 Å^2) [22]. The scale factors of $CaRhD_{3-x}$ and Rh (nano-crystalline) of *in situ* neutron diffraction were constraint by the factor 4.5252 (Eq. (8)), which represents a stoichiometric formation of both compounds during the decomposition of $CaRh_2D_x$. The ratio of the scale factors (S) of $CaRhD_{3-x}$ and Rh (nano-crystalline) were calculated from molecular weight times formula unit per cell (ATZ) and unit cell volume (V).

$$S_{\text{CaRhD}_{3\text{-x}}} = \frac{1}{\beta_{\text{Rh (nano)}}} = \frac{ATZ_{\text{Rh (nano)}}V_{\text{Rh (nano)}}}{ATZ_{\text{CaRhD}_{3\text{-x}}}V_{\text{CaRhD}_{3\text{-x}}}} = 4.5252 \tag{8}$$

Further details of the crystal structure investigations may be obtained from FIZ Karlsruhe, 76344 Eggenstein-Leopoldshafen, Germany (fax: (+49) 7247-808-666; e-mail: crysdata@fiz-karlsruhe.de, on quoting the deposition numbers CSD-434620 (CaRhD$_{2.93(2)}$), CSD-434621 (α-CaRh$_2$D$_{0.05}$), CSD-434622 (*beta*-CaRh$_2$D$_{3.93(5)}$), CSD-434623 (*gamma*-CaRh$_2$D$_{3.20(10)}$).

15.4.3. Thermal analysis

Differential scanning calorimetry (DSC) was performed *in situ* under a starting hydrogen pressure of 5.0 MPa and temperatures up to 703 K on a Q1000 DSC (TA Instruments) equipped with a gas pressure chamber. About 20-50 mg of the powdered intermetallics were put in aluminum crucibles, which were closed with an aluminum lid. These were placed inside the pressure chamber, which was then purged several times with hydrogen gas before filling it to the desired hydrogen gas pressure. The samples were heated at a rate of 10 K min^{-1}, held at the final temperature for 2 h and cooled back to 300 K. Two runs were performed in order to check for reversibility of thermal effects before the hydrogen pressure was released, the sample taken out and structural characterization undertaken by XRPD.

15.4.4. Hydrogen sorption experiments

The sorption isotherms of the pure hydrogen were measured with the volumetric sorption analyzer AUTOSORB-iQ (Quantachrome GmbH & Co KG, Germany) at 313 K. The measuring cell (outer diameter 6 mm, inner diameter 4 mm, length 250 mm) as well as the receiving vessel/ reservoir were used in a stainless steel version. The connections were made as Swagelok®-VCR adapter to avoid leakages of the openable components. The temperature control during the measurement was done externally. For this purpose, a temperature control unit consisting of a thermostat Julabo F12-ED (JULABO GmbH, Germany) with connected double wall vessel was used. Water was chosen as the temperature control medium, which served both in the temperature control circuit and as a medium for direct transmission (within the double wall vessel). The temperature was measured directly (with the connected external thermocouple) at the level of the sample within the temperature control medium.

Before starting the measurement, about 200 mg of CaRh$_2$ was transferred to the measuring cell and then pretreated for 8 h at 393 K (heating rate 5 K min^{-1}) and a final vacuum of < 10-2 Pa. Subsequently, the sample was weighed again, the activated sample amount was determined and the measurement started. The measurement begins with the determination of the void volume with helium (Air Products, Purity 5.2; 99.9992 %) at measurement temperature (313 K). Then vacuum is drawn again for approx. 30 min and the actual measurement with hydrogen (Air Products, Purity 5.2; 99.9992 %) is started. The equilibration times were chosen so that a measurement point was taken if within 300 s the pressure did not change more than 0.3 % of the final value. The generated measurement data are automatically output to a volume-based loading of hydrogen per gram of activated CaRh$_2$ as a function of the detected absolute pressure at the constant temperature of 313 K. After finishing the first sorption isotherm the measurement on elevated sample was repeated three times by increasing activation temperature from 313 K and 393 K to 573 K.

15.5. Results and discussion

15.5.1. Synthesis, thermal analysis and sorption experiments

The synthesis of $CaRh_2$ yields a grey powder with metallic luster. An excess of calcium (see experimental part) is needed because of reaction with the container material (niobium). However, samples contain small amounts of Rh (1-8 wt-%) and CaO (0-5.5 wt-%) according to XRPD. An alternative synthesis by arc-melting did not yield reproducible results, as calcium evaporates before rhodium melts. Based on chemical analysis of the powder, the empirical formula $Ca_{1.03(4)}Rh_{1.97(4)}$ was determined and the refined lattice parameter of $CaRh_2$ (Supplement, Figures S1, S2) are in good agreement with the literature data [23].

The hydrogenation of $CaRh_2$ was studied by *in situ* differential scanning calorimetry (DSC) under 5.0 MPa starting hydrogen pressure (Fig. 15.5.1). Two irreversible exothermic signals, can be observed. The first signal at the beginning shows the hydrogen uptake of the Laves phase $CaRh_2$ and the second at 480 K the decomposition to $CaRhH_3$ and Rh proven by an XRPD study of the product. Upon cooling and in the complete second cycle no further signals are observed. This suggests $CaRhH_3$ to be stable under 5.0 MPa hydrogen pressure and at $298\ K \leq T \leq 700\ K$. Both hydrides were also formed *ex situ* in an autoclave at room temperature and 703 K, respectively, under 5.0 MPa deuterium pressure.

The intermediate will be called β-$CaRh_2H(D)_x$, because *in situ* neutron powder diffraction experiments (see below) show that the cubic Laves phase also takes up hydrogen (α-$CaRh_2H(D)_x$). An additional hydride of $CaRh_2$ (γ-$CaRh_2H(D)_x$) containing less hydrogen than β-phase is also implicated. Trials of direct synthesis of the hydrides by calcium hydride and rhodium under hydrogen pressure were not successful as they did not react under tested conditions ($T_{max} = 853$ K, $p(H_2) = 1.0$ MPa). The hydrides α-, β-$CaRh_2H_x$ and $CaRhH_3$ are stable at ambient conditions and release hydrogen at air, whereby the α-phase is formed back from the β-phase.

Hydrogen sorption measurements show that 7.63 mmol hydrogen gas per gram $CaRh_2$ are sorbed (Fig. 15.5.2). The hydride β-$CaRh_2H_{3.8(2)}$ is formed assuming that all hydrogen is absorbed. The
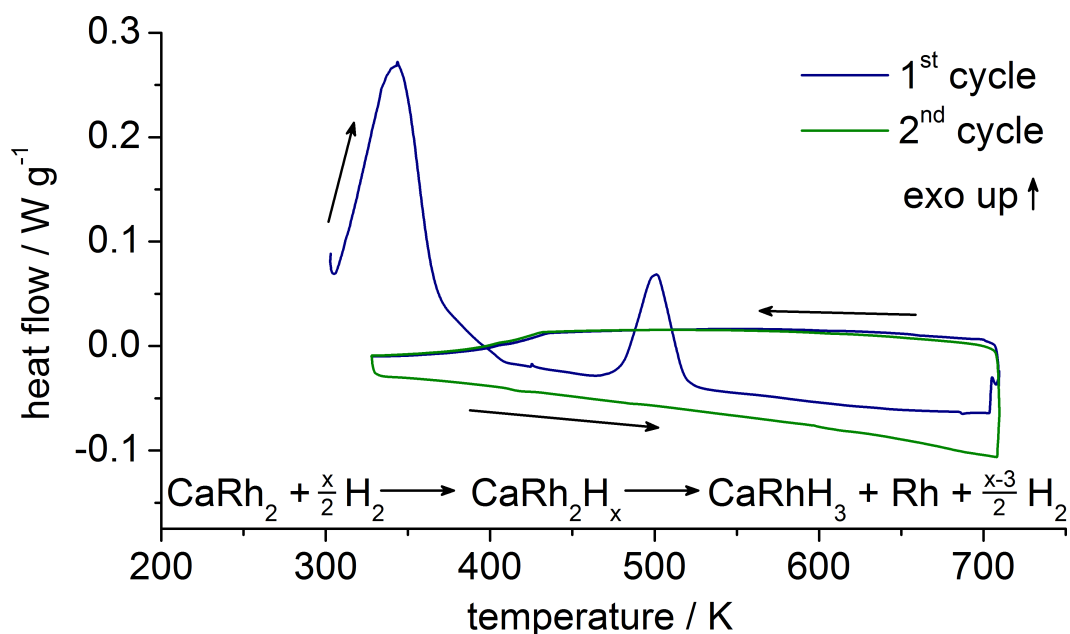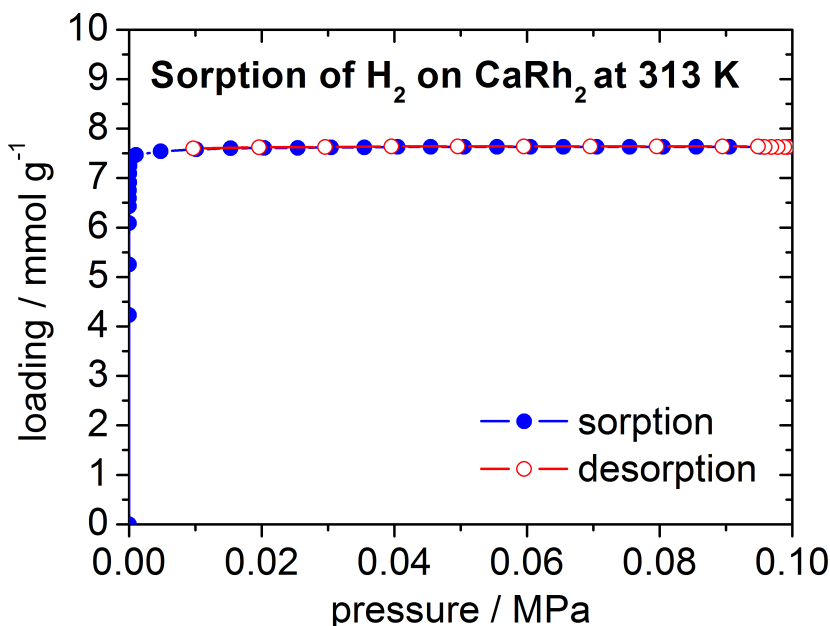

Figure 15.5.1.: *In situ* thermal analysis (DSC) of the hydrogenation of $CaRh_2$ at 5.0 MPa hydrogen pressure (starting pressure at 303 K, increasing during heating process up to 7.0 MPa).

Figure 15.5.2.: Sorption and desorption isotherm of hydrogen on CaRh$_2$ at 313 K.

maximum hydrogen content is already reached under 0.1 MPa hydrogen pressure. The hydride releases no hydrogen during the desorption process and even activation under applied vacuum and temperatures up to 573 K does not remove the complete hydrogen. Therefore, subsequent volumetric sorption experiments resulted in lower loadings (Supplement, Figure S3).

15.5.2. Crystal Structures

The crystal structures of the metal atoms of the hydrides were determined by XRPD and the complete structure determination were based on *in situ* neutron diffraction of the deuterides in a single crystal sapphire cell (Fig. 15.5.3). For the Laves phase, three different deuteride-phases, a disordered cubic α-phase with statistically distributed deuterium atoms and orthorhombic β- and γ-phases with different deuterium contents, could be identified.

The formation of α-CaRh$_2$H$_x$ was observed by reflection shifts and thus a lattice parameter increase based on *in situ* XRPD under isothermal conditions at 723(5) K (Supplement, Figure S4). The metal atoms of α-CaRh$_2$H$_x$ retain the cubic MgCu$_2$-type arrangement from the educt Laves phase. At room temperature, the maximum increase of the unit cell volume from CaRh$_2$ to α-CaRh$_2$D$_x$ is 0.25 % (Supplement, Figure S5). Assuming a typical volume expansion for Laves phase hydrides of 5 % per hydrogen atom per formula unit [24], a composition α-CaRh$_2$D$_{0.05}$ (CSD-434621) is estimated. Deuterium atoms could not be located by difference Fourier analysis, however, an occupation of [Ca$_2$Rh$_2$] tetrahedral voids is most likely, due to the occupation in the β-phase (see below). In addition, the lattice parameters of the α-phase are significantly smaller than 7.7 Å, i. e. a preference of hydrogen atoms to occupy 96g sites (here: Ca$_2$Rh$_2$ tetrahedra) may be expected [25]. Under these assumptions α-CaRh$_2$H$_x$ crystallizes in ZrCr$_2$H$_{3.08}$ type [26] with approximately 0.4 % occupation of H atoms. The Ca atoms are surrounded by 24 H sites and Rh by 12 H sites forming a distorted hexagonal prism.

The XRD pattern of β-CaRh$_2$H$_x$ was indexed to an orthorhombic unit cell and subsequently refined to $a = 5.9542(3)$ Å, $b = 5.6032(3)$ Å, $c = 8.1305(5)$ Å(Supplement, Figure S6). The structure type of ZrV$_2$H$_6$ ($T = 10$ K) [27] was found to be a suitable starting model for structure refinements. A

refinement of the deuterium positions, however, did not fit with the neutron powder diffraction data well. Therefore, all eleven [Rh$_4$], [CaRh$_3$] and [Ca$_2$Rh$_2$] tetrahedral sites were considered as possible deuterium sites. Their positions were generated by crystallographic group-subgroup relationship (Fig. 15.5.4). The deuterium positions were tested with initial occupations of 0.01 by alternating refinements of the deuterium occupation or positions, removing of deuterium sites with negative site occupancy factors (SOF) and subsequent difference Fourier analyses. This lead to a satisfactory model with deuterium situated in two [Ca$_2$Rh$_2$] tetrahedra, which is typical for Laves phases, and two distorted [Ca$_3$Rh$_2$] trigonal bipyramids between two [Ca$_2$Rh$_2$] tetrahedra (Table 15.5.1 and Figs. 15.5.3 and 15.5.5). This structure model yields a composition of β-CaRh$_2$D$_{3.93(5)}$ (CSD-434622) and a good correspondence between measured and calculated neutron diffraction patterns (Fig. 15.5.5). The metal
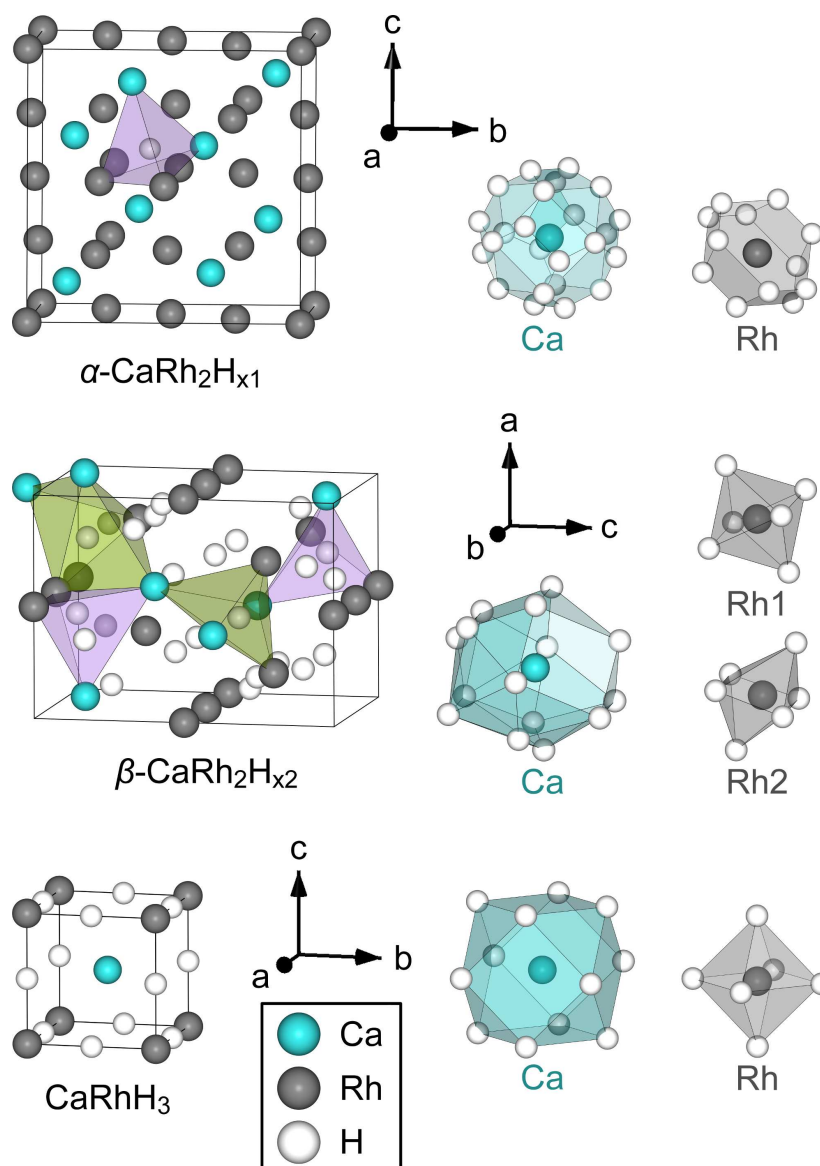
Figure 15.5.3.: Crystal structures of α-CaRh$_2$H$_{x1}$ with one representative H site shown (top, ZrCr$_2$H$_{3.08}$ type, HCa$_2$Rh$_2$ tetrahedron in lavender), β-CaRh$_2$H$_{x2}$ (middle, β-CaRh$_2$H$_{3.9}$ type, HCa$_2$Rh$_2$ tetrahedra (H1 left, H2 right) in lavender, HCa$_3$Rh$_2$ trigonal bipyramids (H3 right, H4 left)) in lime color and CaRhH$_3$ (bottom, cubic perovskite). Polyhedra around Ca and Rh atoms are shown at the right side.

atoms of β-CaRh$_2$H$_x$ deviate from these initial positions (Fig. 15.5.4) by 38.1 and 32.9 pm along the direction [100] and 8.0 and 8.8 pm along [001] (Supplement, Table S6).

Trigonal bipyramids are unusual coordination polyhedra in Laves phase hydrides, but common in ZrTH$_3$ (T = Co [30], Ni [31]), LnNi$_3$H$_{2-x}$ (Ln = Ho [32], Er [33]), the ternary alkaline earth metal hydride Ca$_4$Mg$_3$H$_{14}$ [34], the Zintl phase hydride Nd$_2$Ga$_2$D$_{3.32}$ [35] and hydrides of the AlB$_2$ type, e. g., ThNi$_2$D$_{2.6}$ [36] and Be$_2$ZrD$_{1.5}$ [37]. The hydrogen positions of β-CaRh$_2$H$_x$ are closely related to those of the α-phase (Fig. 15.5.6). The hydrogen atoms H1 and H2 occupying tetrahedral voids in the β-phase are derived from H23 and H24 in α-CaRh$_2$D$_x$ (Figs. 15.5.3 and 15.5.6). H3 (β) is located halfway between two H21 atoms and H4 halfway between H25 and H27. This marks the transition from exclusive occupation of tetrahedral voids to the extension to distorted trigonal bipyramids. The remaining sites of H22 and H26 in the α-phase are too close to H1 and H2 and thus not occupied in the β-phase. The calcium atoms in β-CaRh$_2$H$_x$ are coordinated by 13 H atoms forming a septi-capped trigonal prism. Rh1 and Rh2 are surrounded by six H atoms forming strongly distorted octahedra (Fig. 15.5.3, middle right). The group-subgroup relationship (Fig. 15.5.4) proves the close structural relationship between the cubic (α) and orthorhombic (β) hydride of CaRh$_2$. This is commonly found in Laves phase hydrides [38–42].

$Fd\bar{3}m$ — ZrCr$_2$H$_{3.08}$

8a	16d	96g
$\bar{4}3m$	.3m	..m
1/8	1/2	0.315
1/8	1/2	0.315
1/8	1/2	0.132
Zr	Cr	H

t3
1/2(a-b), 1/2(a+b), c
(1/4, 1/4, 0)

$I4_1/amd$ — ZrV$_2$H$_{2.18}$

4a	8d	16h	32i
$\bar{4}m2$	.2/m.	.m.	1
0	0	0	0.817
3/4	1/2	0.130	0.947
1/8	1/2	0.132	0.315
Zr	V	H1	H2

t2

$Imma$

4e	4b	8h	8i	16j	16j
mm2	.2/m.	m..	.m.	1	1
0	0	0	0.120	0.817	0.303
3/4	1/2	0.130	3/4	0.947	0.567
0.125	1/2	0.132	0.382	0.315	0.565
	4c	H11	H12	H13	H14
	.2/m.				
	3/4				
	3/4				
	3/4				

k2

$Pnma$

Ca	Rh1	H21	H22	H24	H26
4c	4b	8d	4c	8d	8d
.m.	$\bar{1}$	1	.m.	1	1
0.000	0	0.000	0.120	0.817	0.303
3/4	1/2	0.130	3/4	0.947	0.567
0.125	1/2	0.132	0.382	0.315	0.565
4c	4b		4c	8d	8d
.m.			.m.	1	1
0.75			0.880	0.183	0.697
3/4			3/4	0.553	0.933
0.75			0.382	0.315	0.565
	Rh2		H23	H25	H27

Figure 15.5.4.: Transformation of α-CaRh$_2$H$_x$ (ZrCr$_2$H$_{3.08}$ type) with H occupying only [Ca$_2$Rh$_2$] sites to *Pnma* by group-subgroup relationship [28]. ZrV$_2$H$_{2.18}$ (190 K) [29] is a hettotype of ZrCr$_2$H$_{3.08}$.
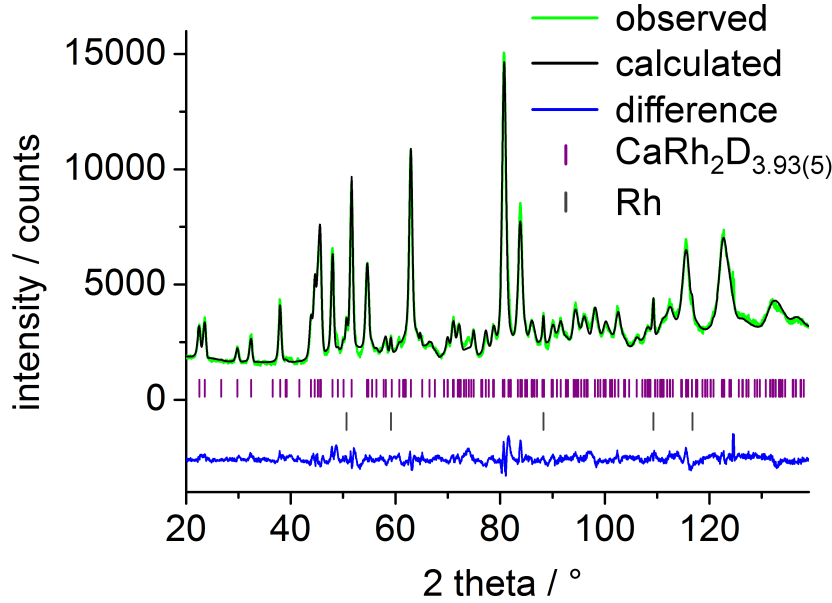
Figure 15.5.5.: Rietveld refinement of the crystal structure of β-CaRh$_2$D$_{3.93(5)}$ (96(2) wt-%, $Pnma$, $a = 6.0028(3)$ Å, $b = 5.6065(3)$ Å, $c = 8.1589(5)$ Å, $R_{\mathrm{Bragg}} = 0.048$, for further details see Table 15.5.1) and Rh (4.4(2) wt-%, $Fm\bar{3}m$, $a = 3.8031(2)$ Å, $R_{\mathrm{Bragg}} = 0.075$) at 296(1) K and 0.1 MPa deuterium pressure in single crystal sapphire cell based on neutron powder diffraction ($\lambda = 1.8676(3)$ Å, D20, ILL, Grenoble, NUMORs 974184-974192, $R_{\mathrm{p}} = 0.037$, $R'_{\mathrm{p}} = 0.111$, $R_{\mathrm{wp}} = 0.048$, $R'_{\mathrm{wp}} = 0.121$, $\chi^2 = 7.51$).

During the *in situ* experiment, an additional deuteride of CaRh$_2$, called γ-phase, was found containing less deuterium than the β-phase, e. g. γ-CaRh$_2$D$_{3.20(10)}$ (CSD-434623, see Supplement Figure and Table S7) at 465(12) K and under vacuum. This phase was only observed as side product during the dehydrogenation of the β-phase at high temperatures (406-630 K) and applied vacuum. Despite of the higher temperatures, the lattice parameters of the γ-phase are smaller compared to β-phase. This unit cell compression results from the lower hydrogen content especially from barely occupied tetrahedral voids which reflects the strong decrease of b (Fig. 15.5.6). Consequently, the interatomic distances decrease more in crystallographic b than in c direction and stay almost constant in a.

Table 15.5.1.: Crystal structure parameters of *beta*-CaRh$_2$D$_{3.93(5)}$ ($Pnma$, $a = 6.0028(3)$ Å, $b = 5.6065(3)$ Å, $c = 8.1589(5)$ Å) based on neutron powder diffraction (see Fig. 15.5.5) at 296(1) K and under 0.1 MPa deuterium pressure.

atom	Wyckoff position	x	y	z	B_{iso} / Å^2	SOF
Ca	$4c$	0.0711(10)	$^3/_4$	0.1340(7)	0.5(1)	1
Rh1	$4b$	0	$^1/_2$	$^1/_2$	0.34(8)	1
Rh2	$4c$	0.6977(9)	$^3/_4$	0.7380(5)	0.59(10)	1
D1 [a]	$4c$	0.0581(8)	$^1/_4$	0.6079(7)	0.83(4)	0.737(9)
D2 [a]	$8d$	0.143(2)	0.015(3)	0.667(2)	B_{iso}(D1)	0.203(5)
D3 [b]	$4c$	0.0576(9)	$^1/_4$	0.1468(6)	B_{iso}(D1)	0.949(9)
D4	$8d$	0.7538(5)	0.9906(6)	0.6039(3)	B_{iso}(D1)	0.921(9)

[a] D occupying [Ca$_2$Rh$_2$] tetrahedron, [b] D occupying [Ca$_3$Rh$_2$] trigonal bipyramid
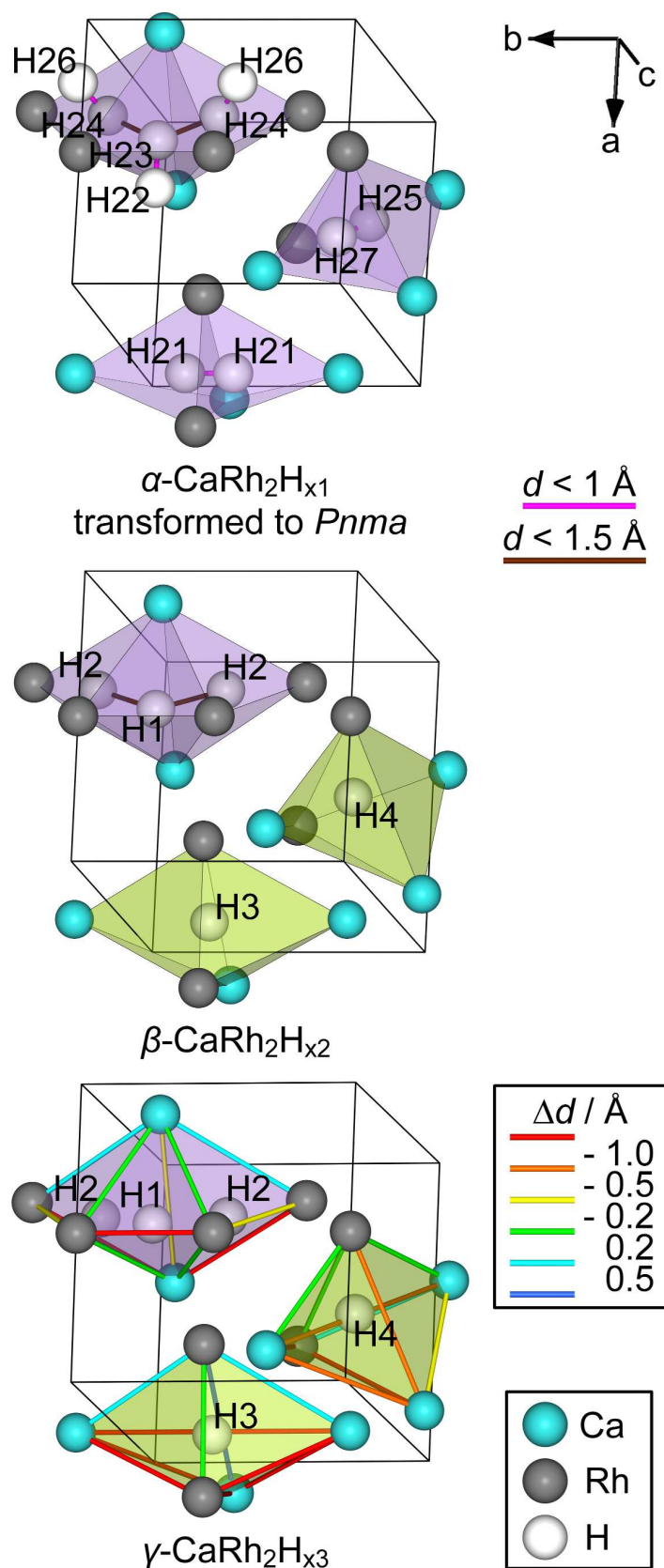
Figure 15.5.6.: Comparison of the hydrogen sites of β-CaRh$_2$H$_{x2}$ (middle) with α-CaRh$_2$H$_{x1}$ (left, unit cell transformed to *Pnma*, see Fig. 15.5.4) and γ-CaRh$_2$H$_{x3}$ (right) (x1 < x3 < x2). Short H-H distances are marked with pink and brown lines. The difference in metal atom distances $\Delta d = d_\gamma - d_\beta$ are indicated by a color code (inset).
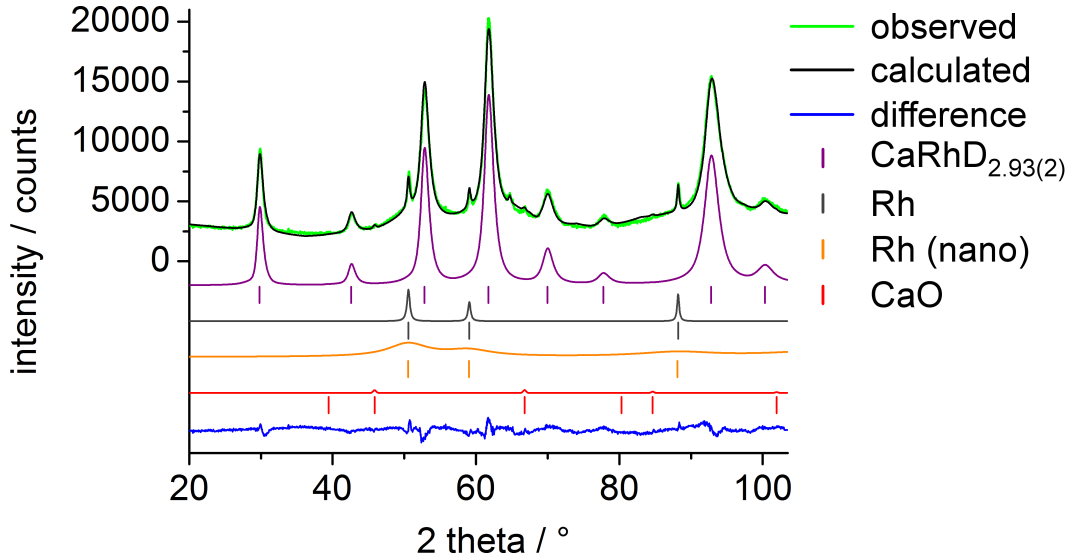
Figure 15.5.7.: Rietveld refinement of the crystal structure of $CaRhD_{2.93(2)}$ (51.6(8) wt-%, $Pm\bar{3}m$, $CaTiO_3$ type, $a = 3.6512(2)$ Å, $R_{Bragg} = 0.014$, for further details see Table 15.5.2), Rh (7.0(5) wt-%, $Fm\bar{3}m$, $a = 3.8006(2)$ Å, $R_{Bragg} = 0.060$), Rh (41.3(9) wt-%, nano-crystalline) and CaO (0.18 wt-%, scale factor is fixed) at 306(2) K and under 0.1 MPa deuterium pressure in a single crystal sapphire cell based on neutron powder diffraction ($\lambda = 1.8676(3)$ Å, D20, ILL, Grenoble, NUMORs 974681-974686, $R_p = 0.036$, $R'_p = 0.089$; $R_{wp} = 0.045$, $R'_{wp} = 0.094$; $\chi^2 = 6.50$).

$CaRhH_3$ (after DSC) was found to be cubic with $a = 3.64727(9)$ Å and the metal atoms are arranged in the CsCl type (Supplement, Figure S8), which is an indication of a perovskite formation. The perovskite $CaRhD_{2.93(2)}$ (CSD-434620) and elementary rhodium as decomposition products of $CaRh_2D_x$ were confirmed by neutron powder diffraction data (Fig. 15.5.7). The deuterium site is nearly fully occupied with a deviation of four estimated standard uncertainties (e.s.u.s) (Table 15.5.2). Broad reflections indicate very small rhodium crystallites. The rhodium atoms in $CaRhH_3$ are surrounded by six hydrogen atoms forming octahedra, which was also observed in β- and γ-$CaRh_2H_x$ in a strongly distorted form (Fig. 15.5.3).

The interatomic Ca-D and D-D distances of $CaRhD_{2.93(2)}$ (Table 15.5.2) are between 2.506 and 2.607 Å of the perovskites $CaNiD_3$ [15] and $CaPdD_2$ [16], respectively. The Rh-D distance is also located between the T-D distances of these perovskites (d(Ni-D) = 1.772 Å in $CaNiD_3$ [15] and d(Pd-D) = 1.843 Å in $CaPdD_2$ [16]). From a geometrical point of view, this is expected as the atomic radius of rhodium is between those of nickel and palladium. The distances of α-$CaRh_2D_x$ are comparable to those of the parent Laves phase $CaRh_2$ because of the very small volume expansion. The Ca-Rh

Table 15.5.2.: Crystal structure parameters and selected interatomic deuterium distances of perovskite-type $CaRhD_{2.93(2)}$ ($Pm\bar{3}m$, $a = 3.6512(2)$ Å) based on neutron powder diffraction (Fig. 15.5.7) at 306(2) K and under 0.1 MPa deuterium pressure.

atom	Wyckoff position	x	y	z	B_{iso} / Å^2	SOF
Ca	$1b$	$1/2$	$1/2$	$1/2$	0.95(7)	1
Rh	$1a$	0	0	0	0.87(5)	1
D	$3d$	0	0	$1/2$	1.68(3)	0.976(6)

d(Ca-D) = 2.58178(10) Å, d(Rh-D) = 1.82559(10) Å, d(D-D) = 2.58178(10) Å

Table 15.5.3.: Interatomic distances (< 3 Å) in β-$CaRh_2D_{3.93(5)}$ (see Table 15.5.1 and Fig. 15.5.5) and γ-$CaRh_2D_{3.20(10)}$ (see Supplement, Table and Figure S7) based on neutron powder diffraction.

distance / Å		β-phase	γ-phase	distance / Å		β-phase	γ-phase
Rh1	2x Rh1	2.8033(2)	2.7456(3)	D3	1x Ca	2.417(8)	2.34(2)
	2x Rh2	2.818(4)	2.796(9)		2x Ca	2.8064(4)	2.7477(10)
D1	1x Ca	2.236(8)	2.30(6)		1x Rh2	1.704(7)	1.55(2)
	1x Ca	2.245(8)	2.39(7)		1x Rh2	1.743(7)	1.91(2)
	2x Rh1	1.692(3)	1.57(3)		2x D4	2.332(5)	2.29(2)
	2x D2	1.49(2)	1.70(6)		2x D4	2.690(5)	2.67(2)
	2x D2	2.95(2)	3.02(6)		2x D4	2.772(5)	2.74(2)
	2x D4	2.335(5)	2.29(4)	D4	1x Ca	2.445(6)	2.37(2)
	2x D4	2.466(5)	2.33(5)		1x Ca	2.605(6)	2.56(2)
D2	1x Ca	2.18(2)	2.05(4)		1x Ca	2.792(6)	2.79(2)
	1x Ca	2.45(2)	2.40(4)		1x Rh1	1.705(3)	1.692(7)
	1x Rh1	1.61(1)	1.88(3)		1x Rh2	1.769(4)	1.753(12)
	1x Rh2	1.71(2)	1.59(4)		1x D4	2.698(5)	2.69(2)
	1x D2	2.64(2)	2.55(5)		1x D4	2.909(5)	2.80(2)
	1x D2	2.97(2)	2.94(5)				
	1x D3	2.34(2)	2.10(4)				
	1x D3	2.44(2)	2.55(4)				
	1x D4	1.99(1)	1.69(3)				
	1x D4	2.30(1)	2.35(3)				

distances of β- (3.128(7) - 3.931(7) Å) and γ-$CaRh_2D_x$ (2.99(2) - 4.01(2) Å) are increased compared to $CaRh_2$ (3.1195(2) Å). The same tendency is also observed for Rh-Rh, 2.8033(2) - 3.008(8) Å in the β-phase and 2.7456(3) - 3.00(2) Å in the γ-phase compared to 2.6603(2) Å in $CaRh_2$, and Ca-Ca distances, 3.549(8) - 3.655(5) Å in the β-phase and 3.53(3) - 3.58(2) Å in the γ-phase compared to 3.2582(2) Å in $CaRh_2$. The interatomic Ca-D and Rh-D distances of β- and γ-$CaRh_2D_x$ (Table 15.5.3) are slightly shorter than 2.3562 - 2.584 Å or 1.709 - 1.927 Å in $Ca_8Rh_5D_{23}$ [14], but they are in the range of 2.018 - 2.838 Å in $CaNi_5D_{4.8}$ [43] and $1.559 - 1.647$ Å in Li_3RhD_6 [5]. Furthermore, the Ca-D distances are comparable to the binary deuteride CaD_2 (2.239 - 2.631 Å) [44]. The smallest D-D distance between D1 and D2 of β- (1.49(2) Å) and γ-$CaRh_2D_x$ (1.70(6) Å) is smaller than the blocking radius of $r_B \approx 2$ Å[25], i. e. a simultaneous occupation of neighboring H1 and H2 sites is excluded. The sum of SOF(H1) and SOF(H2) must therefore not be greater than 1. This means, that a maximum hydrogen occupation will give the formula $CaRh_2H_5$.

15.5.3. Crystal Chemical Analysis

Hydrides (deuterides) in the Ca-Rh-H system show a transition from mostly covalent to metallic bonding in the series from CaH_2 to $CaRh_2H_x$ with increasing rhodium content (Table 15.5.4). The valence electron concentration (VEC, [45]) decreases, whereas the molar volume increment of deuterium increases. These reflect the bonding properties with small values indicating metallic and high values indicating ionic bonding [46]. $Ca_2RhD_{5.4}$ is close to a typical ionic-covalent 18-electron complex, which is shown by the high volume increment of deuterium. Increasing Rh-Rh interactions and metallic properties are apparent in $Ca_8Rh_5D_{23}$ and $Ca_8Rh_6D_{24}$ with accordingly smaller deuterium

Table 15.5.4.: Valence electron concentration (*VEC*) after [45], volume increment of deuterium $V_{(D)}$ [46] and selected distances of deuterides in the Ca-Rh system.

deuteride	*VEC*	$V_{(D)}$ / cm^3 mol^{-1} [a]	d(D-Rh) / Å	d(D-Rh) / Å
CaD$_2$ [44]	1.33	7.58		
Ca$_2$RhD$_{5.4}$ [11]	1.12	6.03	1.752	5.129
Ca$_8$Rh$_5$D$_{23}$ [14]	1.08	5.75	1.701-1.869	3.636
Ca$_8$Rh$_6$D$_{24}$ [14]	1.05	5.45	1.732-1.821	3.641
CaRhD$_{2.93(2)}$	1	4.84	1.8256(1)	3.6512(2)
β-CaRh$_2$D$_{3.93(5)}$	0.86	3.04	1.61(1)-1.769(4)	2.8033(2)
γ-CaRh$_2$D$_{3.2(1)}$	0.84	2.78	1.55(2)-1.91(2)	2.7456(3)

[a] calculated with $V_{(Ca^{2+})}$ = 6.5 cm^3 mol^{-1} [47] and $V_{(Rh)}$ = 8.3 cm^3 mol^{-1} [46]

volume increments. The perovskite CaRhD$_{2.93(2)}$ completes the transition from the K$_2$PtCl$_6$ type to the cubic perovskite type [14]. The orthorhombic β- and γ-CaRh$_2$D$_x$ continue this series with further decreased volume increments for deuterium, indicating typical metallic interstitial type hydrides (Table 15.5.4).

15.5.4. *In situ* Diffraction

The reaction pathway of the hydrogenation of CaRh$_2$ was observed with *in situ* neutron powder diffraction in a single crystal sapphire cell (Fig. 15.5.8). The structure of both the β- and the γ-phase were solved from the neutron diffraction data (vide supra). The full crystal structures including the hydrogen content were refined by the Rietveld technique (Fig. 15.5.9). The *in situ* experiment started under vacuum at room temperature (NUMOR 974038). Already at 0.02 MPa a deuterium sorption by CaRh$_2$ was noted, leading to a unit cell volume expansion up to 0.25 %. In addition to this deuteride, called α-CaRh$_2$D$_x$ thereafter, the formation of β-CaRh$_2$D$_x$ was observed. Then the deuterium pressure was increased further up to 5.0 MPa, in order to complete the formation of the β-phase. The deuterium content of the β-phase is constant at about 4 deuterium atoms per formula unit from the beginning of its formation. However, the unit cell parameters increase anisotropic with increasing deuterium pressure. The expansion is more pronounced in crystallographic *a* and *c* than in *b*, because the occupation of D2 increases with increasing deuterium pressure (Fig. 10.6.8). This can be explained by repulsive interaction of the deuterium atoms (see short D-D distances in Table 15.5.3). The deuterium pressure was decreased and vacuum applied to check the reversibility of the β-phase formation. β-CaRh$_2$D$_x$ is stable under vacuum and latter trends of lattice parameters and deuterium occupation are reversible. Upon heating under vacuum, γ-CaRh$_2$D$_x$ was formed. A miscibility gap between β- and γ-phase is presumed as both phases are observed simultaneously and γ-CaRh$_2$D$_x$ has a sharp decrease of about 0.5 deuterium atoms per formula unit. The structural differences of β- and γ-CaRh$_2$D$_x$ are discussed in detail in the section crystal structures (vide supra). The educt CaRh$_2$ is formed back completely at 512(3) K (NUMOR 974388). The second deuteration reaction was carried out almost isothermally (500 K $\leq$ *T* $\leq$ 560 K). In the first deuteration step, the maximum volume expansion is 1.2 % at a temperature of 506(3) K and the formula α-CaRh$_2$D$_{0.24}$ can be estimated based on the typically volume expansion for Laves phase hydrides [24]. The formation of β-CaRh$_2$D$_x$ from the α-phase begins subsequently, before the decomposition to CaRhD$_{3-x}$ and rhodium takes place. The lattice parameters of β-CaRh$_2$D$_x$ and CaRhD$_{3-x}$ increase with increasing deuterium pressure, but the deuterium contents of both compounds are almost constant (β-CaRh$_2$D$_{3.7(2)}$ and CaRhD$_{2.84(11)}$). During the formation of CaRhD$_{3-x}$, β-CaRh$_2$D$_x$ is an intermediate, which decomposes
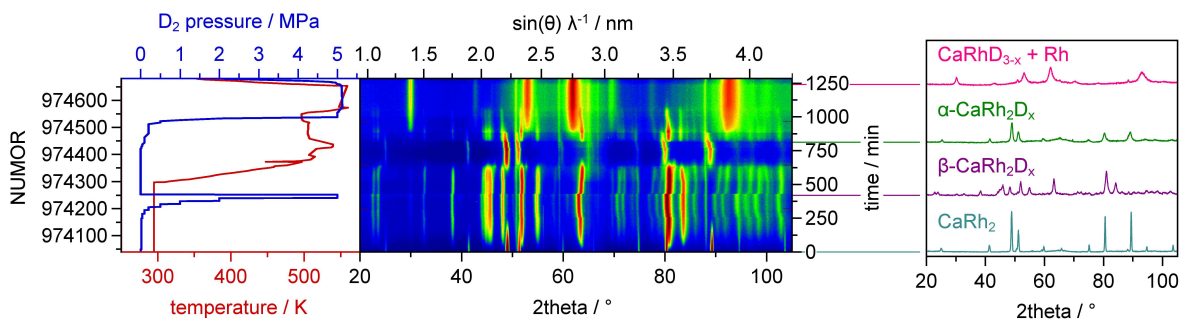
Figure 15.5.8.: *In situ* neutron powder diffraction data (NUMORs 974038-974680) of the deuteration of CaRh$_2$ taken on diffractometer D20 (ILL, Grenoble, $\lambda = 1.8676(3)$ Å) in a single crystal sapphire cell under various temperature and deuterium pressure conditions. The temperature drop to 448(2) K (NUMOR 974373) is caused by the uncontrolled shutdown of the laser heating. Intensities are in false colors.

also to perovskite and rhodium. At the end of the *in situ* experiment, the decomposition is complete. There are two distinct rhodium fractions. One yields sharp reflections in the diffraction experiments and represents the secondary phase from the synthesis of CaRh$_2$, while the second one features very broad diffraction lines (Fig. 15.5.7). This second fraction is the rhodium formed by decomposition of CaRh$_2$H$_{\approx 3.9}$ to CaRhH$_{\approx 3}$ + Rh. Using the Scherrer equation, its crystallite size is estimated to be below 1.8 nm (determined on (111) reflection), i. e. nano-crystalline rhodium is produced.

15.6. Conclusion

The cubic Laves phase CaRh$_2$ takes up hydrogen and forms first a cubic α-phase with low hydrogen content, followed by an orthorhombic β-phase with a higher hydrogen content. The hydrogenation is reversible under vacuum and temperatures about 450 K with the formation of γ-CaRh$_2$H$_x$ as intermediate. The Laves phase hydrides decompose at 480 K and a hydrogen pressure of 5.0 MPa to the perovskite CaRhH$_3$ and nano-crystalline rhodium. This formation of perovskite-type CaRhH$_3$ is exothermic determined by *in situ* DSC and thus kinetically controlled as a lower hydrogen content arises at higher hydrogen pressures. A direct synthesis of this perovskite hydride from the binary hydride CaH$_2$ and rhodium was not successful. The intermediate Laves phase hydrides are only visible by *in situ* methods and the crystal structures of β-CaRh$_2$D$_{3.93(5)}$, and γ-CaRh$_2$D$_{3.20(10)}$ and CaRhD$_{2.93(2)}$ were determined from *in situ* neutron powder diffraction data. Volumetric sorption measurements of β-phase result in the composition of β-CaRh$_2$H$_{3.8(2)}$, which supports the hydrogen content of the refined structures based on neutron diffraction. Hydrogen occupies distorted tetragonal [Ca$_2$Rh$_2$] and trigonal bipyramidal [Ca$_3$Rh$_2$] sites in the orthorhombic CaRh$_2$ hydrides. The latter coordination is unusual for Laves phase hydrides. γ-CaRh$_2$H$_x$ is only observed during the dehydrogenation of the β-phase. Deuterium positions in the perovskite-type CaRhH$_3$ are nearly fully occupied. Perovskite-type CaRhH$_3$, α-, β-, and γ-CaRh$_2$H$_x$ extend the range of hydrides in the calcium-rhodium system to higher rhodium content. Metallic bonding is suggested by the crystal structures and molar volume increments.
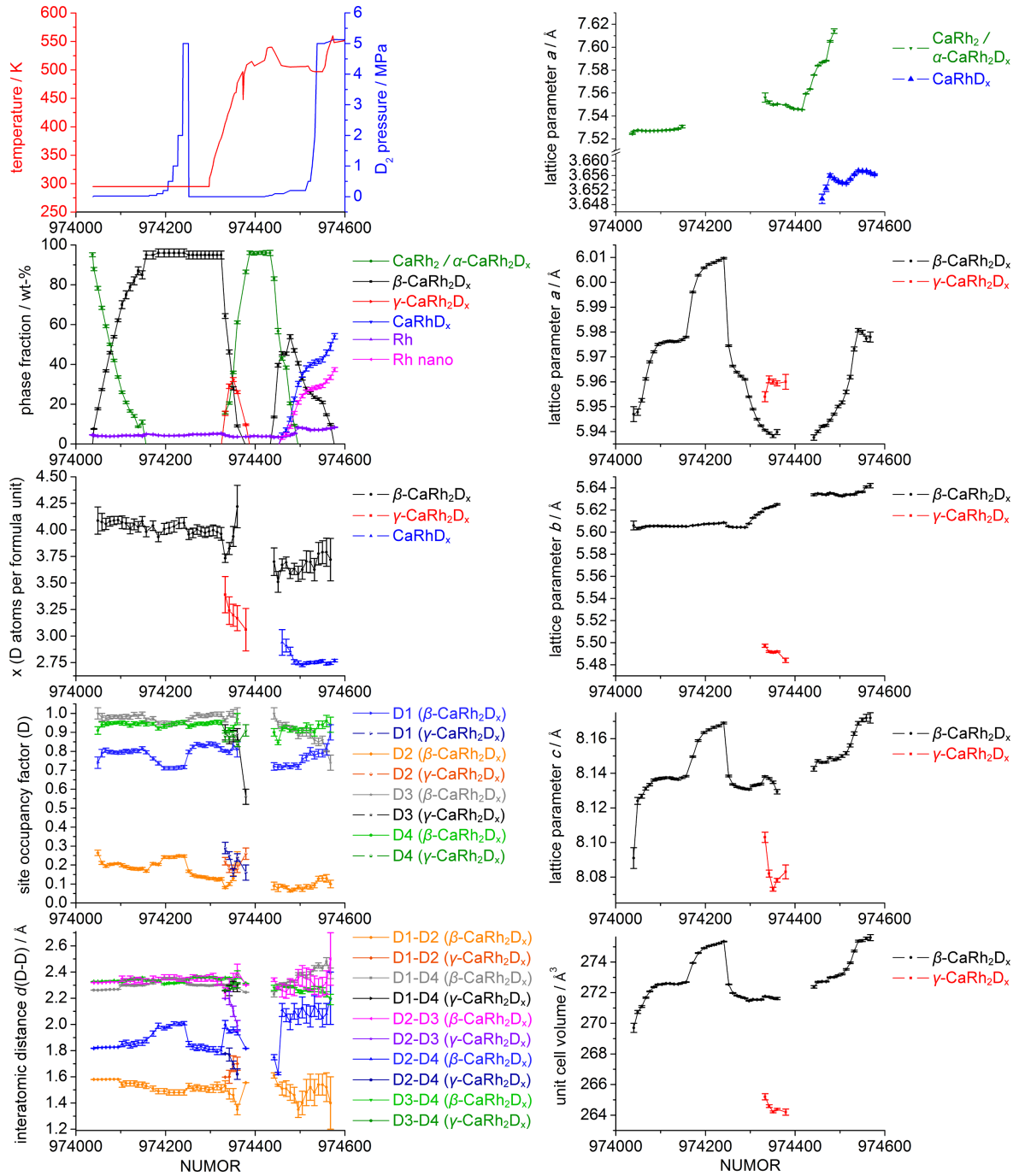
Figure 15.5.9.: Control parameters of the *in situ* deuteration of CaRh$_2$ and refined structural parameters based on neutron powder diffraction data: temperatures and deuterium pressure, phase fractions, deuterium content per formula unit, *SOF* of deuterium sites, minimum interatomic D-D distances (all left, from top to bottom), lattice parameters and unit cell volume (right). Error bars represent $\pm\sigma$. Each NUMOR 2 min.

15.7. Acknowledgment

15.8. References for chapter 15

[1]   T. D. Humphries, D. A. Sheppard, C. E.Buckley, Recent advances in the 18-electron complex transition metal hydrides of Ni, Fe, Co and Ru. Coord. Chem. Rev. 342 (2017) 19–33.

[2]   S. Takagi, Y. Iijima, T. Sato, H. Saitoh, K. Ikeda, T. Otomo, K. Miwa, T. Ikeshoji, S.-I. Orimo, Formation of novel transition metal hydride complexes with ninefold hydrogen coordination. Sci. Rep. 7 (2017) 44253.

[3]   K. M. Waldie, F. M. Brunner, C. P. Kubiak, Transition metal hydride catalysts for sustainable interconversion of CO$_2$ and formate: thermodynamic and mechanistic considerations. ACS Sustainable Chem. Eng. 6 (2018) 6841–6848.

[4]   K. Spektor, W.A. Crichton, S. Konar, S. Filippov, J. Klarbring, S.I. Simak, U. Häussermann, Unraveling hidden Mg-Mn-H phase relations at high pressures and temperatures by *in situ* synchrotron diffraction, Inorg. Chem. 57 (2018) 1614–1622.

[5]   W. Bronger, M. Gehlen, G. Auffermann, Synthese und Struktur von Li$_3$RhH$_6$, einem ternären Hydrid mit isolierten [RhH$_6$]$^{3-}$-Oktaedern, Z. Anorg. Allg. Chem. 620 (1994) 1983–1985.

[6]   W. Bronger, M. Gehlen, G. Auffermann, Na$_3$RhH$_6$, Na$_3$IrH$_6$ und Li$_3$IrH$_6$, neue komplexe Hydride mit isolierten [RhH$_6$]$^{3-}$- und [IrH$_6$]$^{3-}$-Oktaedern, J. Alloys Compd. 176 (1991) 255–262.

[7]   W. Bronger, P. Müller, J. Kowalczyk, G. Auffermann, Synthese und Struktur von Li$_3$RhH$_4$, einem ternären Hydrid mit planaren [RhH$_4$]$^{3-}$-Baueinheiten, J. Alloys Compd. 176 (1991) 263–268.

[8]   F. Bonhomme, K. Yvon, P. Fischer, MgRhD$_{1-x}$, a new interstitial deuteride containing square planar [Rh$_4$D$_4$] rings with nearly linear Rh–D–Rh bridges, J. Alloys Compd. 186 (1992) 209–215.

[9]   J.N. Becker, J. Bauer, A. Giehr, P.I. Chu, N. Kunkel, M. Springborg, H. Kohlmann, Electronic structure of ternary rhodium hydrides with lithium and magnesium, Inorg. Chem. 53 (2014) 1135–1143.

[10] W. Bronger, K. Jansen, L. Breil, Ca$_2$RhD$_{5.4}$–Strukturbestimmung über Neutronenbeugungsexperimente, Z. Anorg. Allg. Chem. 624 (1998) 1477–1480.

[11] R. O. Moyer, C. Stanitski, J. Tanaka, M. I. Kay, R. Kleinberg, Ternary hydrides of calcium and strontium with iridium, rhodium and ruthenium, J. Solid State Chem. 3 (1971) 541–549.

[12] W. Bronger, R. Beißmann, G. Ridder, Ternäre Strontium-Rhodium-Hydride, J. Alloys Compd. 203 (1994) 91–96.

[13] R. O. Moyer Jr., B. J. Burnim, R. Lindsay, Synthesis and structures of [Sr$_{2-x}$Eu$_x$]IrH$_5$,[Sr$_{2-x}$Eu$_x$]RhH$_5$,[Ca$_{2-x}$Eu$_x$]IrH$_5$, and Eu$_2$RhH$_5$, J. Solid State Chem. 121 (1996) 56–60.

[14] W. Bronger, L. Breil, Calcium-Rhodium-Hydride - Synthese und Struktur, Z. Anorg. Allg. Chem. 624 (1998) 1819–1822.

[15] T. Sato, D. Noréus, H. Takeshita, U. Häussermann, Hydrides with the perovskite structure: General bonding and stability considerations and the new representative CaNiH$_3$, J. Solid State Chem. 178 (2005) 3381–3388.

[16]   W. Bronger, K. Jansen, P. Müller, CaPdH$_2$, ein ternäres Hydrid mit perowskitverwandter Struktur, J. Less-Common Met. 161 (1990) 299–302.

[17]   E. Füglein, A. Léon, High-pressure DSC, in: A. Léon (Ed.), Hydrogen Technology, Springer, Berlin, Heidelberg, 2008, pp. 501–521.

[18]   T. C. Hansen, H. Kohlmann, Chemical reactions followed by *in situ* neutron powder diffraction, Z. Anorg. Allg. Chem. 640 (2014) 3044–3063.

[19]   H. Auer, H. Kohlmann, *In situ* investigations on the formation and decomposition of KSiH$_3$ and CsSiH$_3$, Z. Anorg. Allg. Chem. 643 (2017) 945–951.

[20]   TOPAS, Bruker AXS.

[21]   J. Rodríguez-Carvajal, FullProf: A program for Rietveld refinement and pattern matching analysis, Insitut Laue-Langevin, Grenoble (France), 2012.

[22]   E. G. Moshopoulou, R. M. Ibberson, J. L. Sarrao, J. D. Thompson, Z. Fisk, Structure of Ce$_2$RhIn$_8$: an example of complementary use of high-resolution neutron powder diffraction and reciprocal-space mapping to study complex materials, Acta Crystallogr. B 62 (2006) 173–189.

[23]   E. A. Wood, V. B. Compton, Laves-phase compounds of alkaline earths and noble metals, Acta Crystallogr. 11 (1958) 429–433.

[24]   H. Kohlmann, H. E. Fischer, K. Yvon, Europium Palladium Hydrides, Inorg. Chem. 40 (2001) 2608–2613.

[25]   V. A. Somenkov, A. V. Irodova, Lattice structure and phase transition of hydrogen in intermetallic compounds, J. Less-Common Met. 101 (1984) 481–492.

[26]   D. Fruchart, A. Rouault, C. B. Shoemaker, D. P. Shoemaker, Neutron diffraction studies of ZrCr$_2$D$_x$ and ZrV$_2$D$_x$(H$_x$), Phys. Status Solidi A 57 (1980) K119-K122.

[27]   A. N. Bogdanova, A. V. Irodova, G. André, F. Bourée, The ZrV$_2$D$_6$ crystal structure, J. Alloys Compd. 356-357 (2003) 50–53.

[28]   H. Bärnighausen, Group-subgroup relations between space groups: a useful tool in crystal chemistry, MATCH 9 (1980) 139–175.

[29]   A. V. Irodova, G. André, F. Bourée, Hydrogen redistribution in the solid solutions ZrV$_2$D$_x$, $2.2 \leq x \leq 2.7$.: II. Structure of the intermediate phase: 'Lattice liquid crystal'. A neutron-diffraction study, J. Alloys Compd. 350 (2003) 196–204.

[30]   A. V. Irodova, V. A. Somenkov, S. S. Shil'stein, L. N. Padurets, A. A. Chertkov, Structure of CoZrD$_3$, Kristallografiya 23 (1978) 1044–1045.

[31]   S. W. Peterson, V. N. Sadana, W. L. Korst, Neutron diffraction study of nickel zirconium hydride, J. Phys. France 25 (1964) 451–453.

[32]   Y.E. Filinchuk, D. Sheptyakov, K. Yvon, Directional metal-hydrogen bonding in interstitial hydrides: II. Structural study of HoNi$_3$D$_x$ (x = 0, 1.3, 1.8), J. Alloys Compd. 413 (2006) 106–113.

[33]   Y. E. Filinchuk, K. Yvon, Directional metal–hydrogen bonding in interstitial hydrides. III. Structural study of ErCo$_3$D$_x$ ($0 \leq x \leq 4.3$), J. Solid State Chem. 179 (2006) 1041–1052.

[34]   F. Gingl, F. Bonhomme, K. Yvon, P. Fischer, Tetracalcium trimagnesium tetradecahydride, Ca$_4$Mg$_3$H$_{14}$: The first ternary alkaline earth hydride, J. Alloys Compd. 185 (1992) 273–278.

[35]   J. Ångström, R. Johansson, T. Sarkar, M. H. Sørby, C. Zlotea, M. S. Andersson, P. Nordblad, R. H. Scheicher, U. Häussermann, M. Sahlberg, Hydrogenation-induced structure and property changes in the rare-earth metal gallide NdGa: Evolution of a [GaH]$_2$- polyanion containing Peierls-like Ga-H chains, Inorg. Chem. 55 (2016) 345–352.

[36]   A. F. Andresen, H. Fjellvåg, A. J. Maeland, Formation and crystal structure of ThNi$_2$D$_x$, J. Less-Common Met. 103 (1984) 27–31.

[37] A. F. Andresen, K. Otnes, A. J. Maeland, Neutron scattering investigations of Be$_2$ZrH$_{1.5}$ and Be$_2$ZrD$_{1.5}$, J. Less-Common Met. 89 (1983) 201–204.

[38] J. Ropka, R. Černý, V. Paul-Boncour, T. Proffen, Deuterium ordering in Laves-phase deuteride YFe$_2$D$_{4.2}$, J. Solid State Chem. 182 (2009) 1907–1912.

[39] W. Sikora, J. Malinowski, H. Figiel, Symmetry analysis of hydrogen related structural transformations in Laves phase intermetallic compounds, J. Alloys Compd. 446-447 (2007) 423–428.

[40] A. Werwein, F. Maaß, L. Y. Dorsch, O. Janka, R. Pöttgen, T. C. Hansen, J. Kimpton, H. Kohlmann, Hydrogenation Properties of Laves Phases *Ln*Mg$_2$ (*Ln* = La, Ce, Pr, Nd, Sm, Eu, Gd, Tb, Ho, Er, Tm, Yb), Inorg. Chem. 56 (2017) 15006–15014.

[41] H. Kohlmann, F. Fauth, P. Fischer, A. V. Skripov, V. N. Kozhanov, K. Yvon, Low-temperature deuterium ordering in the cubic Laves phase derivative α-ZrCr$_2$D$_{0.66}$, J. Alloys Compd. 327 (2001) L4-L9.

[42] H. Kohlmann, K. Yvon, Revision of the low-temperature structures of rhombohedral ZrCr$_2$D$_x$ (x $\sim$ 3.8), and monoclinic ZrV$_2$D$_x$ (1.1 < x < 2.3) and HfV$_2$D$_x$ (x $\sim$ 1.9), J. Alloys Compd. 309 (2000) 123–126.

[43] A. Yoshikawa, Y. Uyenishi, H. Iizumi, T. Matsumoto, N. Takano, F. Terasaki, Determination of the position and occupancy of deuterium in CaNi$_5$ deuterides by neutron diffraction, J. Alloys Compd. 280 (1998) 204–208.

[44] A. F. Andresen, A. J. Maeland, D. Slotfeldt-Ellingsen, Calcium hydride and deuteride studied by neutron diffraction and NMR, J. Solid State Chem. 20 (1977) 93–101.

[45] K. Schubert, Kristallstrukturen zweikomponentiger Phasen, Springer, Berlin, Heidelberg, 1964.

[46] W. Bronger, Die Raumchemie des Wasserstoffs in Metallhydriden im Vergleich mit entsprechenden Fluoriden und Chloriden, Z. Anorg. Allg. Chem. 622 (1996) 9–16.

[47] W. Biltz, Raumchemie der festen Stoffe, L. Voss, Leipzig, 1934.

15.9. Supporting information

The Supporting Information is available free of charge on the Journal of Inorganic Chemistry Publications website. The supplement.pdf contains further results such as Rietveld refinement plots of the educt CaRh$_2$ (Figures S1, S2), the intermediate Laves phase hydrides (Figures S 5-7) and of the perovskite CaRhH$_3$ (Figure S8); isotherms of the hydrogenation of CaRh$_2$ (Figure S3) and *in situ* XRPD data of the hydrogenation of CaRh$_2$ at 723 K. The in_situ_refinement.zip file contains all relevant data of the Rietveld refinements based on *in situ* neutron powder diffraction and an info_file.pdf, which explains how to handle the refined data.

Supplement to:

From the Laves phase CaRh$_2$ to the perovskite CaRhH$_3$ – *in situ* investigation of hydrogenation intermediates CaRh$_2$H$_x$

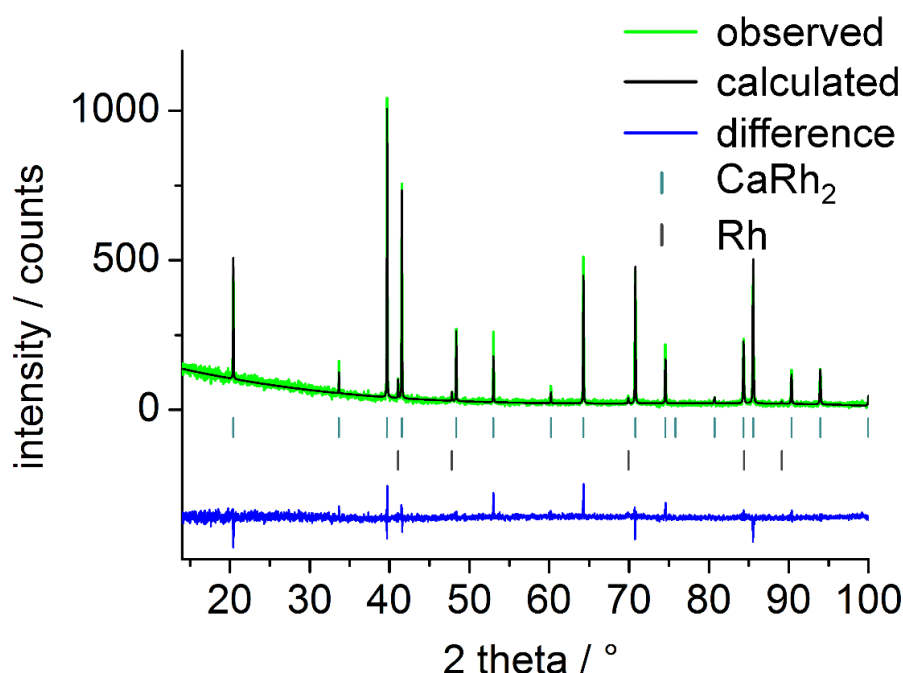André Götze[†], Jens Möllmer[‡] and Holger Kohlmann[†*]

Contents

Supplement

Figure S1. Rietveld refinement of the crystal structure of CaRh$_2$ (96(3) wt-%, $Fd\bar{3}m$, MgCu$_2$ type, a = 7.52419(12) Å, B_{iso}(Ca) = -4.3(2) Å², B_{iso}(Rh) = -4.01(8) Å², R_{Bragg} = 0.127) and Rh (4.4(8) wt-%, $Fm\bar{3}m$, a = 3.8029(3) Å, R_{Bragg} = 0.343) based on XRPD (STOE STADI-P, CuK$_{\alpha1}$ radiation, R_p = 0.130, R_p' = 0.386, R_{wp} = 0.168, R_{wp}'= 0.324; χ^2 = 1.20), using FullProf [1]. Negative thermal displacement parameters are not unusual in X-ray powder diffraction due to absorption and surface roughness effects.
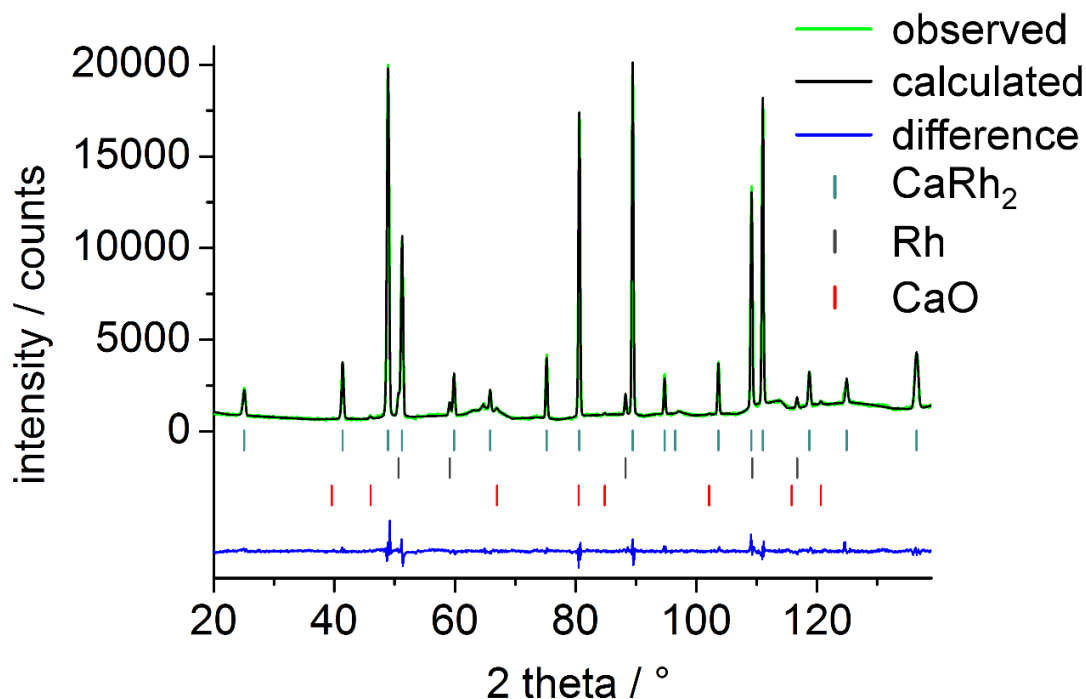
Figure S2. Rietveld refinement of the crystal structure of $CaRh_2$ (95.1(10) wt-%, $Fd\bar{3}m$, $MgCu_2$ type, a = 7.5245(6) Å, $B_{iso}(Ca)$ = 0.23(4) Å², $B_{iso}(Rh)$ = 0.08(2) Å², R_{Bragg} = 0.031), Rh (4.65(10) wt-%, $Fm\bar{3}m$, a = 3.8030(3) Å, B_{iso} = 0.068 Å² [2], R_{Bragg} = 0.064) and CaO (0.23(3) wt-%) at 296(1) K and air in single crystal sapphire cell based on NPD (λ = 1.8676(3) Å, D20, ILL, Grenoble, NUMOR 974037, R_p = 0.035, R_p' = 0.124, R_{wp} = 0.046, R_{wp}' = 0.097, χ^2 = 2.99), using FullProf [1].
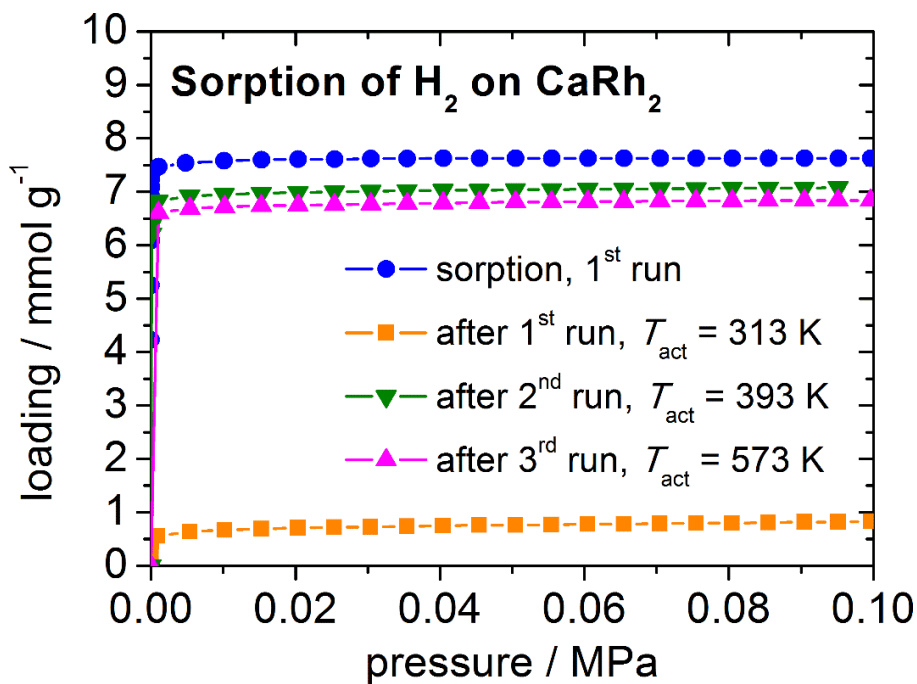
Figure S3. Sorption isotherms of hydrogen on $CaRh_2$ at 313 K after activation at various temperatures.
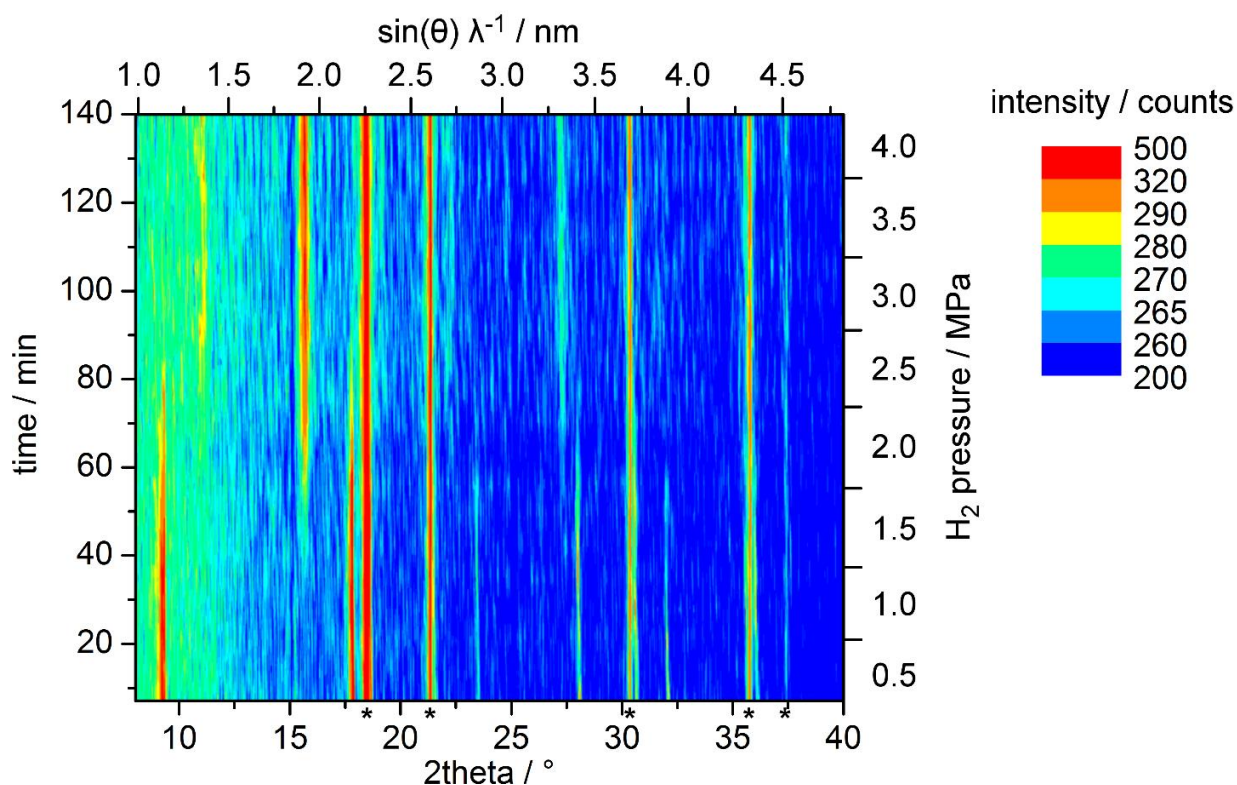
Figure S4. *In situ* X-ray powder diffraction (XRPD) data of the hydrogenation of CaRh$_2$ taken on diffractometer Huber G670 (MoK$_{\alpha1}$ radiation) in a silica glass capillary at 723 K and under various hydrogen pressure conditions. CaRh$_2$ takes up hydrogen and forms α-CaRh$_2$H$_x$ (bottom, reflections shift to lower 2θ angles) and subsequent CaRhH$_{3-x}$ (top) under hydrogen pressures from about 2.0 MPa. Reflections of rhodium are marked with asterisks. Intensities are in false colors.
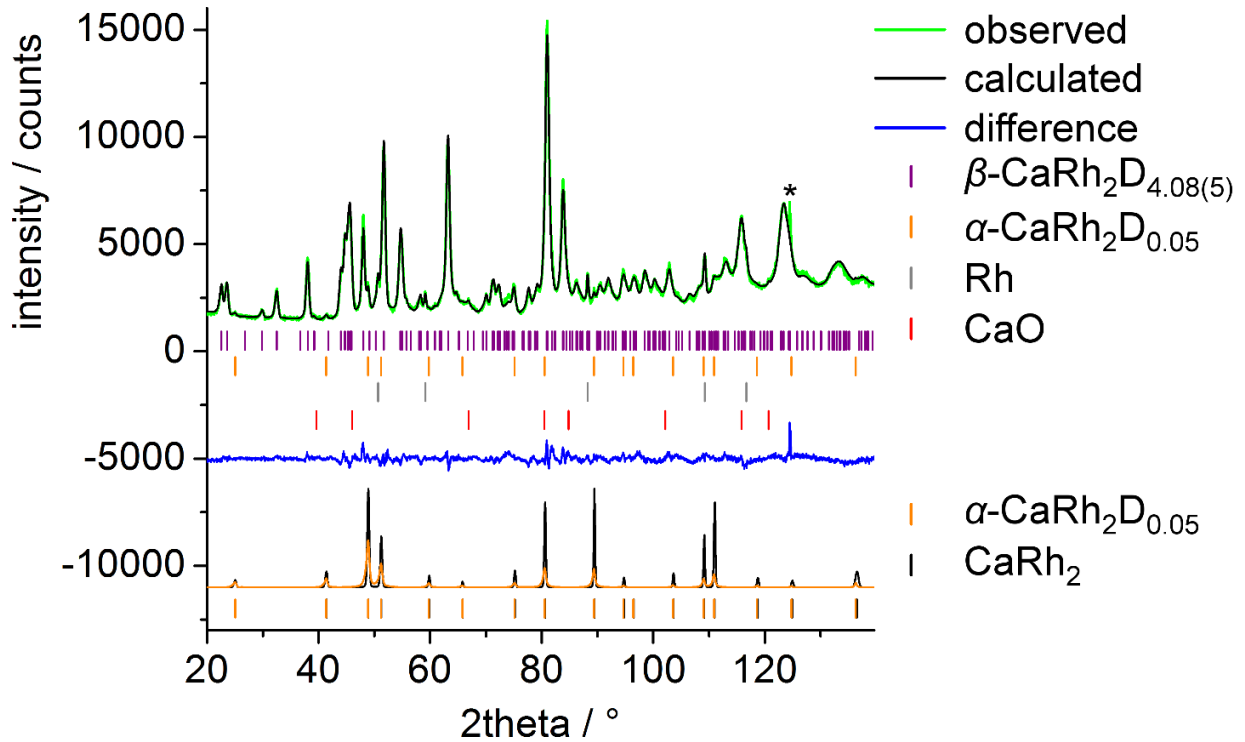
Figure S5. Rietveld refinement of the crystal structure of β-CaRh$_2$D$_{4.08(5)}$ (85(2) wt-%, *Pnma*, a = 5.9769(3) Å, b = 5.6054(2) Å, c = 8.1374(4) Å, R_{Bragg} = 0.045, for further details see Table S5), α-CaRh$_2$D$_{0.05}$ (11.0(10) wt-%, *Fd$\bar{3}$m*, a = 7.5308(12) Å, R_{Bragg} = 0.037), Rh (4.0(1) wt-%, *Fm$\bar{3}$m*, a = 3.8032(2) Å, B_{iso} = 0.068 Å^2 [2], R_{Bragg} = 0.042) and CaO (0.1 wt-%) at 295(1) K and 0.02 MPa deuterium pressure based on NPD (λ = 1.8676(3) Å, D20, ILL, Grenoble, NUMORs 974148-974156, R_p = 0.032, R_p' = 0.091, R_{wp} = 0.041, R_{wp}' = 0.101, χ^2 = 5.40), using FullProf [1] and a comparison (bottom) of α-CaRh$_2$D$_{0.05}$ (V = 427.09(12) Å^3) with CaRh$_2$ (Figure S2, V = 426.02(6) Å, NUMOR 974037, intensities of CaRh$_2$ are multiplied by factor 0.12 to compensate the phase fraction and the exposure time of both patterns). The asterisk marks a reflection from the sapphire cell.

Table S5. Crystal structure parameters of β-CaRh$_2$D$_{4.08(5)}$ based on NPD (NUMORs 974148-974156, see Figure S5) at 295(1) K and 0.02 MPa deuterium pressure.

atom	Wyckoff position	x	y	z	B_{iso} / Å^2	SOF
Ca	4*c*	0.0592(12)	¾	0.1328(7)	0.59(11)	1
Rh1	4*b*	0	½	½	0.71(7)	1
Rh2	4*c*	0.6946(9)	¾	0.7398(5)	B_{iso}(Rh2)	1
D1 [a]	4*c*	0.0533(8)	¼	0.6069(6)	1.44(6)	0.816(8)
D2 [a]	8*d*	0.142(3)	0.016(4)	0.683(2)	B_{iso}(D1)	0.181(6)
D3 [b]	4*c*	0.0631(9)	¼	0.1461(6)	B_{iso}(D1)	0.998(9)
D4 [b]	8*d*	0.7541(6)	0.9922(6)	0.6047(3)	B_{iso}(D1)	0.953(8)

[a] D occupying [Ca₂Rh₂] tetrahedron, [b] D occupying [Ca₃Rh₂] trigonal bipyramid
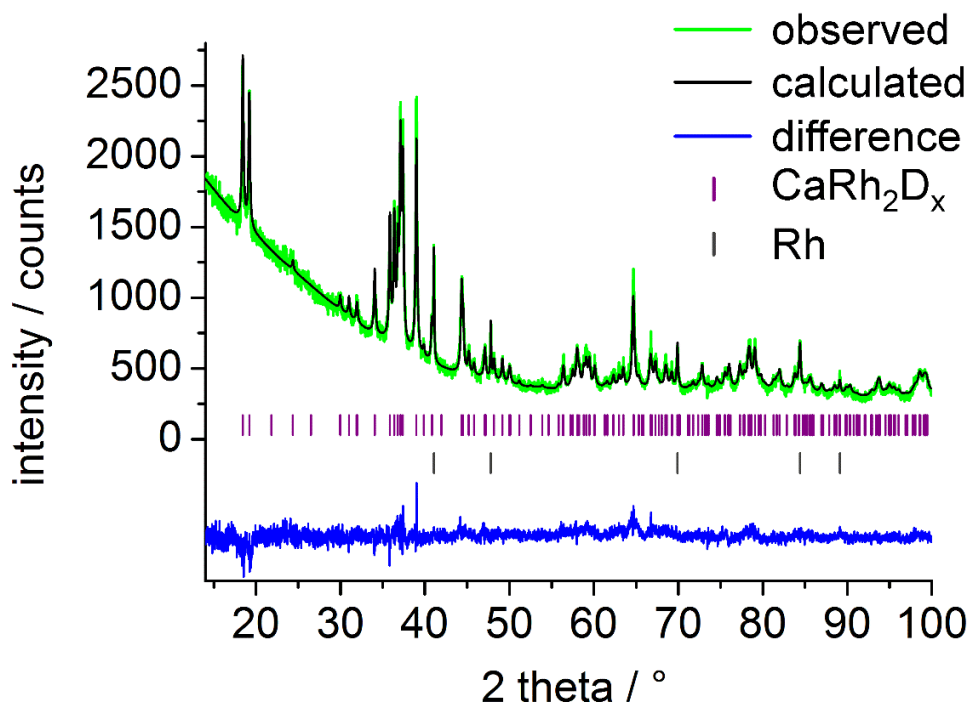
Figure S6. Rietveld refinement of the crystal structure of *β*-CaRh$_2$D$_x$ (95.3(9) wt-%, *Pnma*, *a* = 5.9542(3) Å, *b* = 5.6032(3) Å, *c* = 8.1305(5) Å, R_{Bragg} = 0.176, , for further details see Table S6) and Rh (4.8(2) wt-%, *Fm$\bar{3}$m*, *a* = 3.8024(2) Å, R_{Bragg} = 0.024) based on XRPD (STOE STADI-P, CuK$_{α1}$ radiation, R_p = 0.040, R_p' = 0.329, R_{wp} = 0.054, R_{wp}'= 0.254; $χ^2$ = 1.94), using FullProf [1].

Table S6. Crystal structure parameters of metal atoms of *β*-CaRh$_2$D$_x$ (*Pnma*, *a* = 5.9542(3) Å, *b* = 5.6032(3) Å, *c* = 8.1305(5) Å) based on XRPD (see Figure S6) compared to initial parameters (in italics) generated from MgCu$_2$ type (Figure 3).

atom	Wyckoff position	x	y	z	B_{iso} / Å²
Ca	4*c*	0.064(1) *0.0*	¾	0.1349(8) *0.125*	-1.5(1) [a]
Rh1	4*b*	0	½	½	-2.04(5) [a]
Rh2	4*c*	0.6947(5) *0.75*	¾	0.7392(5) *0.75*	-1.57(6) [a]

[a] Negative thermal displacement parameters are not unusual in X-ray powder diffraction due to absorption and surface roughness effects.
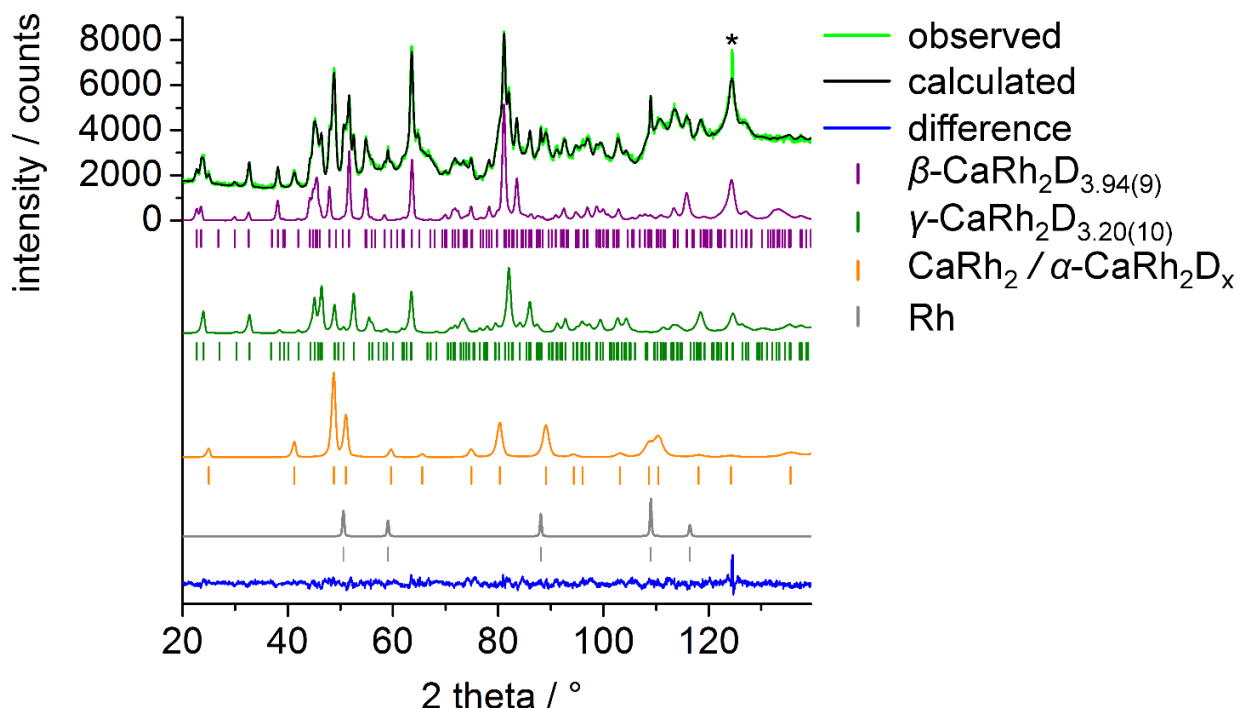
Figure S7. Rietveld refinement of the crystal structure of β-CaRh$_2$D$_{3.94(9)}$ (28.0(8) wt-%, *Pnma*, a = 5.9382(6) Å, b = 5.6234(4) Å, c = 8.1348(7) Å, R_{Bragg} = 0.044, for further details see Table S7), γ-CaRh$_2$D$_{3.20(10)}$ (32.4(10) wt-%, *Pnma*, a = 5.9601(10) Å, b = 5.4912(2) Å, c = 8.0730(11) Å, R_{Bragg} = 0.040, for further details see Table S7), CaRh$_2$ (36.0(6) wt-%, MgCu$_2$ type, a =3.5499(6) Å), Rh (3.6(1) wt-%, *Fm$\overline{3}$m*, a = 3.8092(2) Å, R_{Bragg} = 0.024) and CaO (0.1 wt-%, not displayed) at 465(12) K and vacuum based on NPD (λ = 1.8676(3) Å, D20, ILL, Grenoble, NUMORs 974351-974359, R_p = 0.026, R_p' = 0.103, R_{wp} = 0.033, R_{wp}'= 0.109, χ^2 = 3.49), using FullProf [1]. The asterisk marks a reflection from the sapphire cell.

Table S7. Crystal structure parameters of β-CaRh$_2$D$_{3.94(9)}$ and γ-CaRh$_2$D$_{3.20(10)}$ (in italics) based on NPD (NUMORs 974351-974359, see Figure S7) at 465(12) K and under applied vacuum. Displacement parameters are fixed to the refinement of NUMORs 974301-974309.

atom	Wyckoff position	x	y	z	SOF
Ca	4c	0.053(2)	¾	0.126(2)	1
		0.067(3)		*0.134(2)*	
Rh1	4b	0	½	½	1
Rh2	4c	0.707(2)	¾	0.7494(12)	1
		0.678(2)		*0.728(1)*	
D1 [a]	4c	0.058(2)	¼	0.609(2)	0.83(2)
		0.053(9)		*0.585(8)*	*0.16(2)*
D2 [a]	8d	0.146(8)	0.024(10)	0.66807 [c]	0.13(1) [c]
		0.111(5)	*0.018(7)*	*0.718(4)*	*0.19(1)*
D3 [b]	4c	0.059(2)	¼	0.149(2)	1.00(2)
		0.054(3)		*0.142(2)*	*0.88(3)*
D4 [b]	8d	0.758(1)	0.9861(12)	0.6068(9)	0.92(1)
		0.751(1)	*0.995(2)*	*0.5999(8)*	*0.89(1)*

[a] D occupying [Ca$_2$Rh$_2$] tetrahedron, [b] D occupying [Ca$_3$Rh$_2$] trigonal bipyramid
[c] parameters were refined alternating
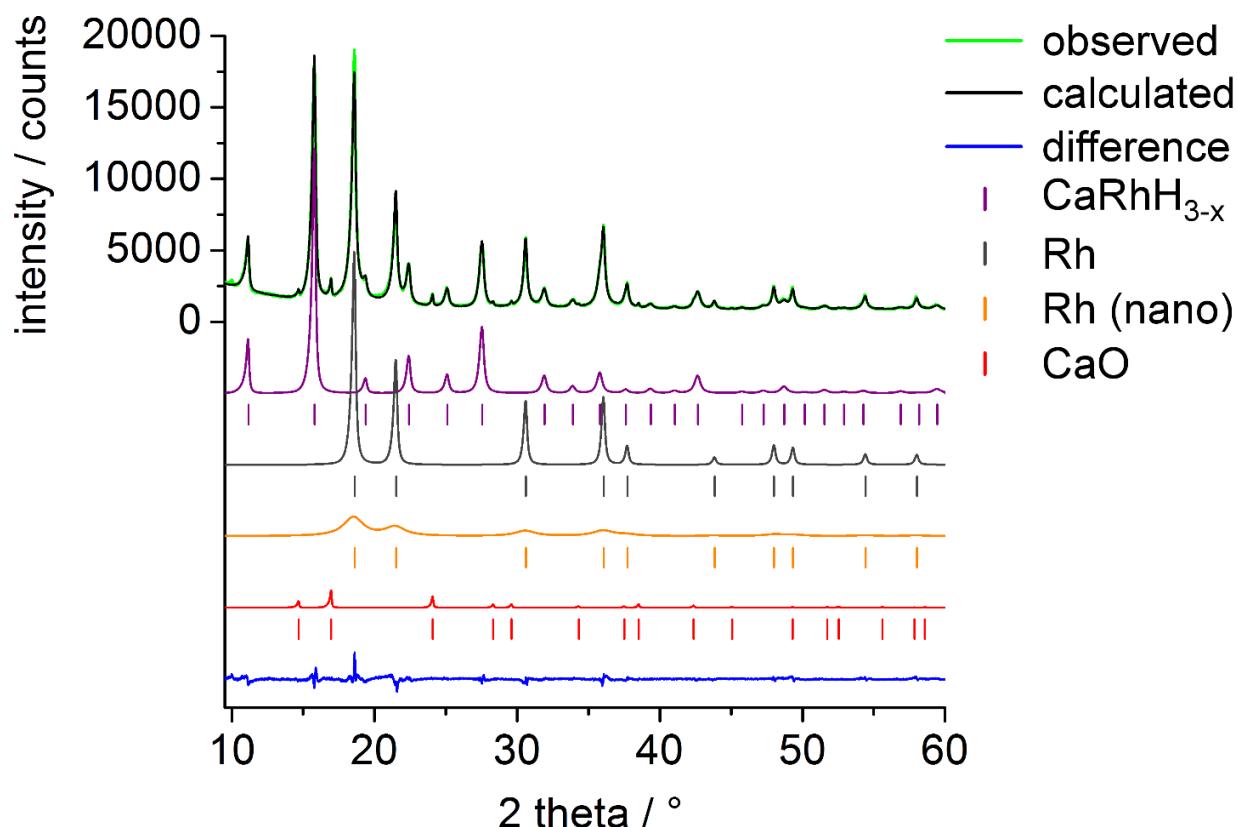
Figure S8. Rietveld refinement of the crystal structure of CaRhH$_{3-x}$ (40.2(1) wt-%, $Pm\bar{3}m$, metal atoms: CsCl type, a = 3.64727(9) Å, B_{iso}(Ca) = 0.85(2) Å², B_{iso}(Rh) = 0.54(2) Å², R_{Bragg} = 0.007), Rh (36.1(1) wt-%, $Fm\bar{3}m$, a = 3.79972(7) Å, R_{Bragg} = 0.019), Rh (18.3(2) wt-%, nano crystalline) and CaO (5.44(10) wt-%) based on XRPD (Huber G670, MoK$_{\alpha1}$ radiation, R_p = 0.029, R_p' = 0.068, R_{wp} = 0.037, R_{wp}' = 0.068, χ^2 = 2.56), using TOPAS [3].

References

[1]   J. Rodríguez-Carvajal, FullProf: A Program for Rietveld Refinement and Pattern Matching Analysis (version 5.30); Insitut Laue-Langevin, Grenoble (France), 2012.

[2]   E. G Moshopoulou, R. M. Ibberson, J. L. Sarrao, J. D. Thompson, Z. Fisk, Structure of Ce$_2$RhIn$_8$: an example of complementary use of high-resolution neutron powder diffraction and reciprocal-space mapping to study complex materials. *Acta Crystallog*r. B 62 (2006) 173-189.

[3]   *TOPAS*, version 5; Bruker AXS, www.bruker-axs.com.

Part III.

Unpublished results within this thesis

16. Quantum-Mechanical Calculations of MPd$_3$ and MPd$_3$H (M = Mg, Zr, Sc) and Crystal Structure of SnPd$_3$D$_{0.138(7)}$

16.1. Authors' contributions

The syntheses and hydrogenation experiments of SnPd$_3$ were done by Siobhan C. Stevenson. The quantum-mechanical calculations of MPd$_3$ (M = Mg, Zr, Sc) were done by Nicolas Zapp. The text was written and Rietveld refinement of the structure of SnPd$_3$D$_{0.138(7)}$ based on neutron diffraction done by André Götze. This text is not approved by Siobhan C. Stevenson.

16.2. Introduction

MPd$_3$ compounds are known to form hydrides. The hydrogen uptake depends on the metal M. For main group elements the hydrogen amount is correlated to electronic and geometric aspects [1]. SnPd$_3$ is assumed to absorb little hydrogen. Hydrogenation investigations on SnPd$_3$ show a volume expansion (0.4 %) [2], however, the hydrogen position and occupation was not determined, yet. Therefore, a neutron powder diffraction study was conducted.

MgPd$_3$H$_{0.7}$ (anti-perovskite type) is another example for hydride formation [3]. Although, scandium and zirconium are similar in electronegativity and radius compared to magnesium, ScPd$_3$ and ZrPd$_3$ do not show a significant hydrogen uptake [4]. Density functional theory (DFT) calculations were conducted to compare the thermodynamical stability of MPd$_3$H (M = Mg, Sc, Zr).

16.3. Crystal structure of SnPd$_3$D$_{0.138(7)}$ based on neutron powder diffraction

SnPd$_3$ was synthesized by a solid state reaction in a sealed silica glass ampoule. Selenium was added as mineralizing agent. A grey powder was yielded with impurities of Pd$_2$Sn and Pd$_3$Sn$_{0.8}$Se$_{0.2}$ [4]. SnPd$_3$ was deuterated at 703 K under 5.0 MPa hydrogen pressure for 48 h. The structure of SnPd$_3$D$_{0.138(7)}$ was refined based on neutron powder diffraction (Fig. 16.3.1 and Table 16.3.1). It crystallizes in a defect anti-perovskite type. Hydrogen occupies the [Pd$_6$] octahedral voids. The hydrogen absorption of SnPd$_3$ is comparble to PbPd$_3$ (0.13 hydrogen per formula unit) [5]. The interatomic Pd-D distances of both hydrides are also similar (SnPd$_3$D$_{0.138(7)}$: d(Pd-D) = 1.99169(6) Å, PbPd$_3$D$_{0.13(1)}$: d(Pd-D) = 2.02016(3) Å [5]).
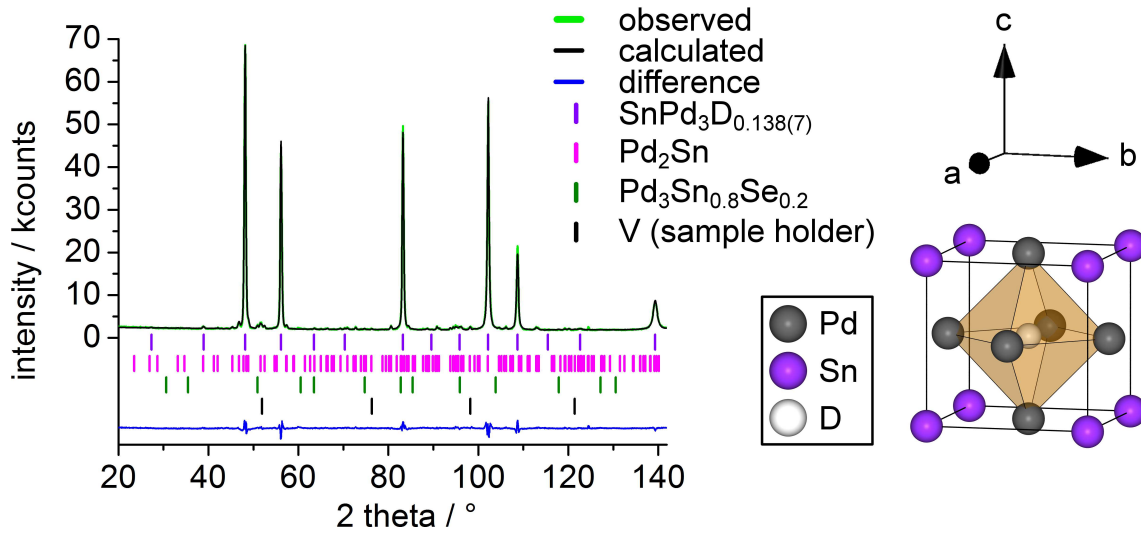
Figure 16.3.1.: Rietveld refinement of the crystal structure of cubic $SnPd_3D_{0.138(7)}$ (92(1) wt-%, $Pm\bar{3}m$, $a = 3.98338(11)$ Å, $R_{\text{Bragg}} = 0.021$, for furter details see Table 16.3.1), Pd_2Sn (7.2(1) wt-%, Co_2Si type, $Pnma$, $a = 5.6491(7)$ Å, $b = 4.3111(5)$ Å, $c = 8.0986(11)$ Å, $R_{\text{Bragg}} = 0.18$), $Pd_3(Sn_{0.8}Se_{0.2})$ (0.50(2) wt-%) at 296(1) K based on neutron powder diffraction (D20, ILL, Grenoble, $\lambda = 1.8673(2)$ Å, $R_p = 0.034$, $R'_p = 0.092$, $R_{\text{wp}} = 0.044$, $R'_{\text{wp}} = 0.082$, $\chi^2 = 6.21$). Crystal structure of $SnPd_3D_{0.138(7)}$ with one DPd_6 octahedron is shown (green polyhedra).

Table 16.3.1.: Refined crystal structure and selected interatomic distances of cubic $SnPd_3D_{0.138(7)}$ based on neutron powder diffraction (Fig. 16.3.1) at 296(1) K.

atom	Sn	Pd	D
Wyckoff position	$1a$	$3c$	$1b$
x	0	½	½
y	0	½	½
z	0	0	½
B_{iso} / Å²	0.76(7)	0.63(3)	1.8(4)
SOF	1	1	0.138(7)
$d(\text{Pd-D}) = 1.99169(6)$ Å, $d(\text{Sn-D}) = 3.44971(6)$ Å			

16.4. *Ab initio* calculations of the hydrogenation of *M*Pd$_3$ (*M* = Mg, Zr, Sc)

The hydrogenation properties of *M*Pd$_3$ (*M* = Mg, Zr, Sc) were investgated by DFT calculations which were performed with the Vienna *ab initio* simulation package (VASP) [6,7] using PAW's [8], Fermi-smearing and the PBE-method [9]. A cutoff energy of 600 eV was set for an automatically generated and Γ-centered *k*-mesh, which resolved the Brillouin zone to 0.03 Å^{-1} in structure optimizations. All structures were relaxed with full degrees of freedom, converging forces to 0.001 meV pm^{-1} and electronic energy to 0.01 meV. If experimentally determined structures exist, they were used for structure optimization. Initial parameters for the unknown hydrides were taken from the intermetallics and hydrogen was assumed to occupy [Pd$_6$] octahedral voids. The structures of the hydrides were also relaxed. The parameters of ScPd$_3$ were used for the nonexistent ZrPd$_3$ crystallizing in AuCu$_3$ type. All initial structures are summerized in Table 16.4.1.

Table 16.4.1.: Used initial structures for the structure optimization.

compound	structure type	initial parameters of
MgPd$_3$	AuCu$_3$	MgPd$_3$ [3]
MgPd$_3$H	anti-perovskite	MgPd$_3$H$_{0.7}$ [3]
ScPd$_3$	AuCu$_3$	ScPd$_3$ [10]
ScPd$_3$H	anti-perovskite	ScPd$_3$ [10] [a]
ZrPd$_3$	AuCu$_3$	ScPd$_3$ [10]
ZrPd$_3$H	anti-perovskite	ScPd$_3$ [10] [a]
ZrPd$_3$	TiNi$_3$	ZrPd$_3$ [4]
ZrPd$_3$	anti-BaMnO$_3$	ZrPd$_3$H [4] [a]

[a] H is assumed to occupy [Pd$_6$] octahedral voids

The reaction energies were calculated from total energies of the optimizations (Table 16.4.2). The energy of molecular hydrogen was estimated from a H$_2$ molecule in a cubic box with a cell parameter of 34.5 Å, which corresponds to an ideal gas at 0.1 MPa and 293 K. The hydrogenation of MgPd$_3$ is thermodynamically favored compared to ScPd$_3$ or ZrPd$_3$.

Table 16.4.2.: Calculated energies and reaction enthalpies of the hydrogenation of *M*Pd$_3$ (*M*Pd$_3$ + 1/2 H$_2$ → *M*Pd$_3$H), E(H$_2$) = -6.696 eV (formula unit)$^{-1}$.

M	Mg	Sc	Zr	Zr
stucture type of *M*Pd$_3$ [a]	AuCu$_3$	AuCu$_3$	AuCu$_3$	TiNi$_3$
space group	$Pm\bar{3}m$	$Pm\bar{3}m$	$Pm\bar{3}m$	$P6_3/mmc$
E(*M*Pd$_3$) / eV (formula unit)$^{-1}$	-17.072 eV	-22.343	-24.189	-24.283
E(*M*Pd$_3$H) / eV (formula unit)$^{-1}$	-20.815	-25.779	-26.472	-26.906
ΔH / kJ mol^{-1} (formula unit)$^{-1}$	-38.106	-8.490	+102.743	+69.942

[a] H occupies [Pd$_6$] octahedral voids resulting in anti-perovskite type (filled AuCu$_3$ type) and anti-BaMnO$_3$ type (filled TiNi$_3$ type)

16.5. Conclusion

The crystal structure of SnPd$_3$D$_{0.138(7)}$ was determined by neutron powder diffraction. Deuterium occupies the [Pd$_6$] octahedral sites. SnPd$_3$D$_{0.138(7)}$ crystallizes in the cubic anti-perovskite type. Quantum-mechanical calculations support the different hydrogenation properties of MgPd$_3$ (-38.1 kJ mol^{-1} (formula unit)$^{-1}$), ScPd$_3$ (-8.5 kJ mol^{-1} (formula unit)$^{-1}$) and ZrPd$_3$ (+102.7 for cubic and +69.9 kJ mol^{-1} (formula unit)$^{-1}$ for hexagonal structure).

16.6. References for chapter 16

[1] A. Götze, H. Kohlmann, Palladium hydride and hydrides of palladium-rich phases, in: Reference Module in Chemistry, Molecular Science and Chemical Engineering, Elsevier, 2017.

[2] A. Götze, J. M Sander, H. Kohlmann, Crystal structures and hydrogenation properties of palladium-rich compounds with elements from group 12-16, Z. Naturforsch. 71B (2016), 503-508.

[3] H. Kohlmann, G. Renaudin, K. Yvon, C. Wannek, B. Harbrecht, Hydrogen-induced atomic rearrangement in MgPd$_3$, J. Solid State Chem. 178 (2005) 1292-1300.

[4] S. C. Stevenson, Synthesis and hydrogenation of MPd$_3$ compounds, Placement report, Universität Leipzig, Leipzig (2017).

[5] A. Götze, T. C. Hansen, H. Kohlmann, The reversible hydrogenation of BiPd$_3$ followed by *in situ* methods and the crystal structure of PbPd$_3$D$_{0.13(1)}$, J. Alloys Compd. 731 (2018) 1001-1008.

[6] G. Kresse, J. Furthmüller, Efficient iterative schemes for *ab initio* total-energy calculations using a plane-wave basis set, Phys. Rev. B 54 (1996) 11169–11186.

[7] G. Kresse, J. Furthmüller, Efficiency of ab-initio total energy calculations for metals and semiconductors using a plane-wave basis set, Comput. Mater. Sci. 6 (1996) 15–50.

[8] P. E. Blöchl, Projector augmented-wave method, Phys. Rev. B 50 (1994) 17953–17979.

[9] J. P. Perdew, J. Burke, M. Ernzerhof, Generalized gradient approximation made simple, Phy. Rev. Lett. 77 (1996) 3865–3868.

[10] B. Erdmann, C. Keller, Actinide(lanthanide)-noble metal alloy phases, preparation and properties, J. Solid State Chem. 7 (1973) 40-48.

17. Hydrogen Sorption Measurements of MgPd$_2$

17.1. Authors' contributions

The sorption measurements and analysis were done by Jens Möllmer (Institute of Non-Classical Chemistry at Leipzig University, Germany). The synthesis of MgPd$_2$, the graphics and text were prepared by André Götze. The text was not approved by Jens Möllmer.

17.2. Introduction

MgPd$_2$ takes up hydrogen at room temperature and under hydrogen pressure of several hundred kPa. Furthermore, the formed hydride releases hydrogen under ambient conditions (see [4] in [1]). Therefore, a sorption enthalpy of MgPd$_2$ near to the benchmark value of -38.9 kJ (mol H$_2$)$^{-1}$ can be expected. This value can be calculated by the equation for the Gibbs energy with the point, that the change in entropy is equal with the standard entropy of molecular hydrogen. For determination of the sorption enthalpy isotherms at different temperatures (283, 298 and 313 K) were measured and additional sorption experiments were executed to check the hydrogen content in MgPd$_2$H$_x$ determined by *in situ* neutron powder diffraction data.

17.3. Hydrogen sorption experiments

The sorption isotherms of hydrogen of MgPd$_2$ show a loading of 1.75(9) for volumetric (Fig. 17.3.1, left, p(H$_2$)$_{max}$ = 0.1 MPa) and 1.86 mmol hydrogen per gram MgPd$_2$ for gravimetric sorption experiments (Fig. 17.3.2, left, p(H$_2$)$_{max}$ = 2.48 MPa). The maximum hydrogen loading within one standard deviation is reached at about 250, 500 and 800 kPa at 283, 298 and 313 K, respectively. The hydrogen sorption enthalpy was calculated at a loading of 0.85 (mmol H$_2$) g^{-1} that is approximately the inflection point of the isotherms. The calculations were done by a linear regression of the natural logarithm of the pressure and the reciprocal temperature (Fig. 17.3.1, right) and results in -37.3 kJ (mol H$_2$)$^{-1}$. This value is near to the benchmark value of -38.9 kJ (mol H$_2$)$^{-1}$ as assumed and is probably by accident similar to the reaction enthalpy of elementary palladium with hydrogen (-38.2 kJ (mol H$_2$)$^{-1}$) [2]. In disordered Mn$_x$Pd$_{1-x}$ the reaction enthalpy increases with increasing x to -37.0 kJ (mol H$_2$)$^{-1}$) for Mn$_{0.075}$Pd$_{0.925}$ [3] and the ordered MnPd$_3$ has a decreased enthalpy (approximatly -66.9 kJ (mol H$_2$)$^{-1}$) [4] which demonstrate a higher stability of the ordered hydride. The entropy (ΔS = -110.7 J (mol H$_2$)$^{-1}$ K^{-1}) was calculated from the intercept of the linear regression (Fig. 17.3.1, right).

A hysteresis in the absorbtion and desorption isotherms was observed, which is well known for intermetallic compound-hydrogen systems [5]. Therefore the desorption enthalpy and entropy are different to those of the sorption process. A desorption enthalpy of 41.8 kJ (mol H$_2$)$^{-1}$ and an entropy of 123.2 J (mol H$_2$)$^{-1}$ K^{-1} were determined in the same way as for the sorption process. The enthalpy
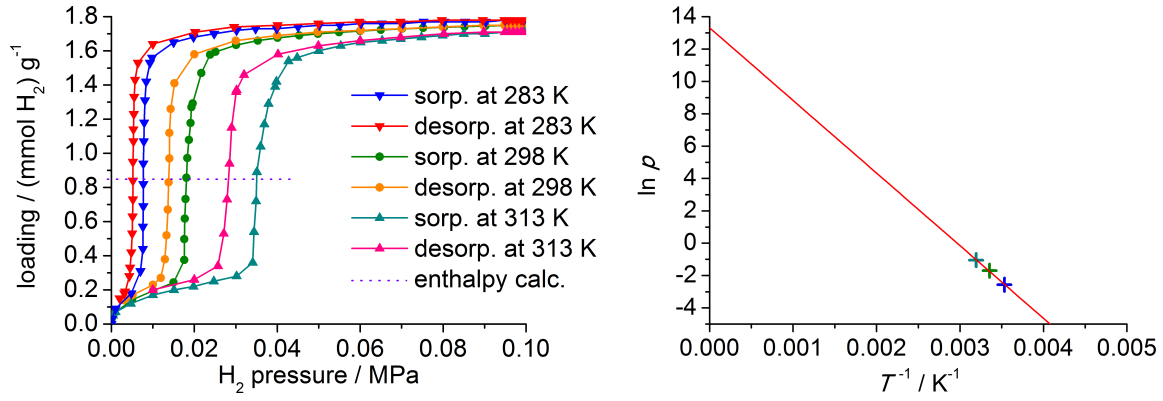
Figure 17.3.1.: Sorption and desorption isotherms of hydrogen on MgPd$_2$ at different temperatures (left) and determination of the sorption enthalpy ($\Delta H =$ b R = -37.3 kJ (mol H$_2$)$^{-1}$) and entropy ($\Delta S =$ -a R = -110.7 J (mol H$_2$)$^{-1}$ K^{-1}) by linear regression (ln $p =$ a + b T^{-1}, a = 13.3(8), b = -4.5(2) 10^3 K) at a loading of 0.85 (mol H$_2$) g^{-1} (right).

of the desorption process is larger than the absolute enthaply of the sorption process ($\Delta H_{\mathrm{desorb}} = \Delta H_{\mathrm{sorb}} +$ 4.5 kJ (mol H$_2$)$^{-1}$).

The hydrogen content of the hydrides MgPd$_2$ determined by *in situ* neutron diffraction were confirmed by gravimetric sorption experiments at similar conditions (Fig. 17.3.2). A comparison of both methods shows similar hydrogen contents whereby those of the sorption measurements are slightly smaller. The hydrogen content determined by neutron diffraction under isothermal conditions increases only after a deuterium pressure of 0.5 MPa due to a relativ constant pressure increase over time without paying attention to reach the equilibrium.
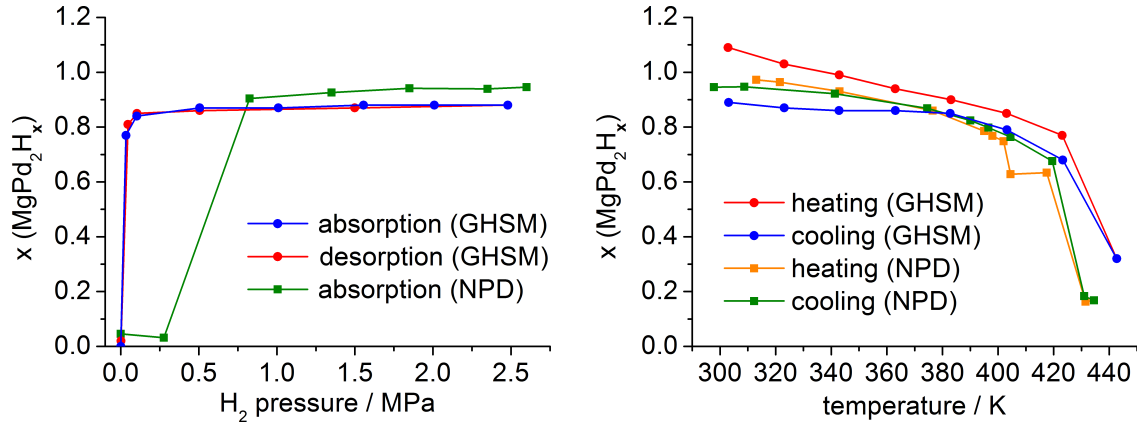
Figure 17.3.2.: Sorption and desorption isotherms (left) and isobar (right) of hydrogen on MgPd$_2$ determined by gravimetric hydrogen sorption measurements (GHSM) compared to neuton powder diffraction (NPD).

17.4. Conclusion

Sorption and desorption enthalpies and entropies were determined by measured sorption isotherms. Results for the enthalpies of the hydride formation and deformation of MgPd$_2$ are -37.3 and 41.8 kJ (mol H$_2$)$^{-1}$, respectively. The magnitudes of entropies are -110.7 for sorption and 123.2 J (mol H$_2$)$^{-1}$ K^{-1} for desorption process. A hystersis in pressure-composition (*p-c*) isotherm was observed. Furthermore,

the hydrogen content of $MgPd_2H_x$ under isothermal and isobaric conditions determined by sorption experiments are consitent with those determined by *in situ* neutron diffraction. Therefore, sorption experiments are not only a good method to verify the hydrogen content from neutron diffraction, but give insight into thermodynamics.

17.5. References for chapter 17

[1] A. Götze, N. Zapp, A. J. Peretzki, V. Pomjakushin, T. C. Hansen, H. Kohlmann, *In situ* hydrogenation and crystal chemistry studies of Co_2Si type compounds $MgPd_2$ and Pd_2Zn, Z. Anorg. Allg. Chem. 644 (2018) 367-375.

[2] T. B. Flanagan, W. Luo, J. D. Clewley, Calorimetric enthalpies of absorption and desorption of protium and deuterium by palladium, J. Less-Common Met. 172-174 (1991) 42-55.

[3] T. B. Flanagan, S. Luo, Thermodynamics of hydrogen solution and hydride formation in Pd-Mn alloys. 1. Disordered alloys and a correlation effect, J. Phys. Chem. 110 (2006) 8080-8086.

[4] T. B. Flanagan, D. Wang, Solubility and diffusion of H in ordered ($L1_2$) and disordered Pd_3Mn, J. Phys. Chem. Solids 75 (2014) 651-655.

[5] J. Murray, M. Post, J. Taylor, Thermodynamics of $LaNi_5 + H_2$ by differential heat flow calorimetry: hysteresis and entropies, in T. N. Veziroglu (ed.), Metal-Hydrogen Systems, Pergamon, Oxford (1982) 445-449.

18. Catalytic Measurements of the Semi-Hydrogenation of Acetylene with $Pd_{11}Bi_2Se_2$

18.1. Authors' contributions

The catalytic measurements, and graphical analysis were done by Toni Keilhauer, Ioannis Aviziotis and Marc Armbrüster (Institute of Chemistry, TU Chemnitz, Germany) and the XPS measurements by Thomas Seyller (Institute of Physics, TU Chemnitz, Germany). The synthesis of $Pd_{11}Bi_2Se_2$ and the text were prepared by André Götze. The text was not approved by Toni Keilhauer, Ioannis Aviziotis, Marc Armbrüster and Thomas Seyller.

18.2. Introduction

$Pd_{11}Bi_2Se_2$ with a high palladium amount of 73 % does not form a hydride. A phase pure synthesis without additives like iodine has been shown (see Chapter 14 in [1]). These are good preconditions for the compound as hydrogenation catalyst. The selective hydrogenation of acetylene to ethylene is an important reaction for the preperation of polyethylene. However, the formation of ethane should be inhibited within this process and a high-selective catalyst is necessary. Catalytical properites of $Pd_{11}Bi_2Se_2$ with regards to conversion and selectivity to ethylene were investigated.

18.3. Catalytic measurement of the semi-hydrogenation of acetyle

The catalytic measurements were executed in a feed of 0.5 % C_2H_2, 5 % H_2 and 50 % C_2H_4 in helium gas (total flow of 30 ml min^{-1}) at 437 K. The investigation results in a high selectivity to ethylene (90 to 95 %) and low selectivities to ethane (< 10 %) and to C_4H_x (< 5 %) (Fig. 18.3.1). The conversion started only after 7.5 h and reaches a maximum conversion of 46 %. This phenomenon was understood by X-ray photoelectron spectroscopy (XPS) measurements of $Pd_{11}Bi_2Se_2$ before and after the catalytic experiment. The determined values of selectivity are comparable with those of PdZn as catalyst material, however, the conversion is far below that of PdZn [2].

XPS measurement of Bi 4f before catalysis shows sharp Bi signals at 157 and 163 eV and broad signals at 158 and 164 eV which are assigned to the oxide state of bismuth and indicate the presence bismuth oxide on the surface of the material. After the catalysis the broad signals are absent and only the sharp signals of metallic bismuth remain.
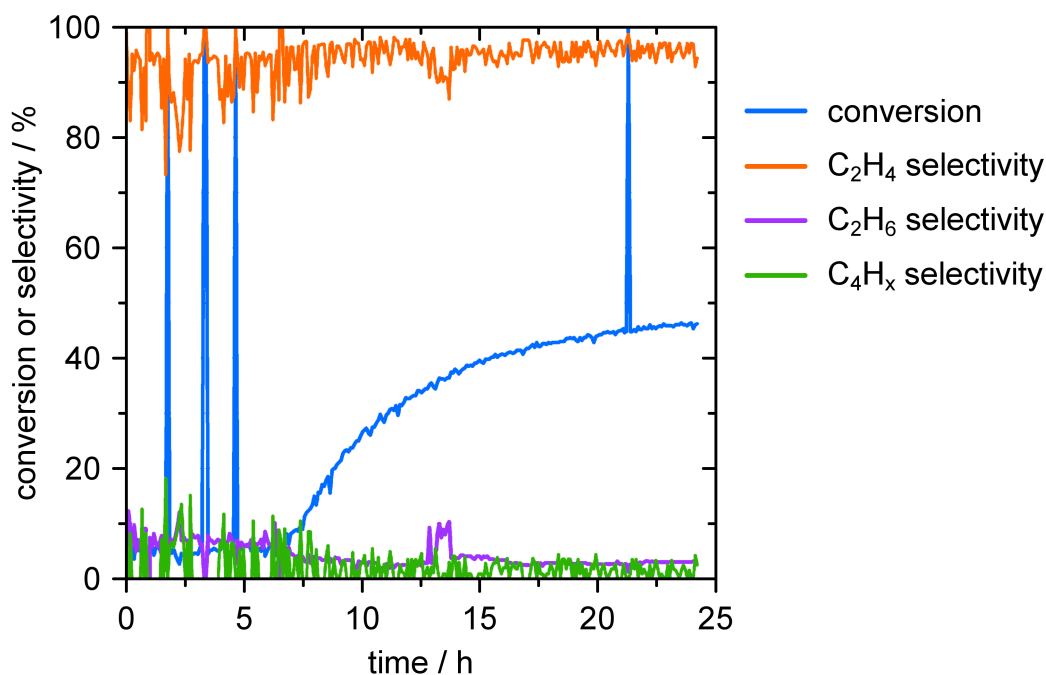
Figure 18.3.1.: Acetylene conversion and selectivity to ethylene of the semi-hydrogenation of acetylene with $Pd_{11}Bi_2Se_2$ as catalyst are plotted against time. The sharp peaks in conversion are artifacts.

18.4. Conclusion

$Pd_{11}Bi_2Se_2$ was found to be a highly selective catalyst for the semi-hydrogenation of acetylene with a low conversion. The catalytst is active afer a long duration time due to the reduction of bismuth oxid on the surface.

18.5. References for chapter 18

[1] A. Götze, S. Schmorl, A. N. Kuznetsov, H. Kohlmann, Vacancy ordering in $Pd_{11}Bi_2Se_2$ - crystal structure and properties, J. Alloys Compd. 735 (2018) 1914-1920.

[2] H. Zhou, X. Yang, L. Li, X. Liu, Y. Huang, X. Pan, A. Wang, J. Li, T. Zhang, PdZn intermetallic nanostructure with Pd–Zn–Pd ensembles for highly active and chemoselective semi-hydrogenation of acetylene, ACS Catal. 6 (2016) 1054-1061.

Part IV.

Curriculum Vitae

Curriculum Vitae

André Götze

08.03.1989	geboren in Eilenburg
2007	allgemeine Hochschulreife (Abitur), Martin-Rinckart Gymnasium Eilenburg, Haus Albert Schweitzer Bad Düben
07/2007 - 04/2008	Wehrdienst
10/2008 - 11/2011	Studium: Bachelor of Science Chemie an der Universität Leipzig
10/11/2011	Bachelor of Science (Chemie) Bachelorarbeit am Insitut für Anorganische Chemie der Universität Leipzig im Arbeitskreis von Prof. Dr. Harald Krautscheid mit dem Titel: "Synthese und Charakterisierung von binären Aluminium-Schwefel-Verbindungen"
10/2011 - 12/2013	Studium: Master of Science Chemie an der Universität Leipzig
10/12/2013	Master of Science (Chemie) Masterarbeit am Insitut für Anorganische Chemie der Universität Leipzig im Arbeitskreis von Prof. Dr. Holger Kohlmann mit dem Titel: "Synthese und Strukturen von ternären palladiumreichen Phasen mit Indium und Quecksilber"
seit 03/2014	Doktorand am Insitut für Anorganische Chemie der Universität Leipzig im Arbeitskreis von Prof. Dr. Holger Kohlmann

Auslandsaufenthalte

10/2014, 07/2015, 12/2015, 11/2016, 03/2018	Institut Laue-Langevin, Grenoble, Frankreich, Messzeiten an der Neutronenquelle
09/2017	Lomonossow-Universität Moskau, Vortragseinladung und Kooperationstreffen

Publikationen

9   André Götze, Jens Möllmer, Holger Kohlmann
From Laves phase $CaRh_2$ to the perovskite $CaRhH_3$ - *in situ* investigation of hydrogenation intermediates $CaRh_2H_x$
Inorg. Chem. **2018**, submitted.

8   Elena Y. Zakharova, Sergey M Kazakov, André Götze, Holger Kohlmann, Alexey N. Kuznetsov
Ternary palladium-indium-phosphorus and platinum-indium-phosphorus compounds based on the Cu_3Au-type: structure, bonding, and properties
J. Solid State Chem. **2018**, accepted.

7   André Götze, Nicolas Zapp, Andrea J. Peretzki, Vladimir Pomjakushin, Thomas C. Hansen, Holger Kohlmann
In situ hydrogenation and crystal chemistry studies of Co_2Si type compounds $MgPd_2$ and Pd_2Zn
Z. Anorg. Allg. Chem. **2018**, *644*, 367-375.

6   André Götze, Sara Schmorl, Alexey N. Kuznetsov, Holger Kohlmann
Vacancy ordering in $Pd_{11}Bi_2Se_2$ - Crystal structure and properties
J. Alloys Compd. **2018**, *735*, 1914-1920.

5   André Götze, Thomas C. Hansen, Holger Kohlmann
The reversible hydrogenation of $BiPd_3$ followed by *in situ* methods and the crystal structure of $PbPd_3D_{0.13(1)}$
J. Alloys Compd. **2018**, *731*, 1001–1008.

4   André Götze, Henry Auer, Raphael Finger, Thomas C. Hansen, Holger Kohlmann
A sapphire single-crystal cell for *in situ* neutron powder diffraction of solid-gas reactions
Phys. B **2018**, in press.

3	André Götze, Holger Kohlmann
	Palladium Hydride and Hydrides of Palladium-Rich Phases
	In: *Reference Module in Chemistry, Molecular Sciences and Chemical Engineering*, Elsevier **2017**.

2	André Götze, Jonas M. Sander, Holger Kohlmann
	Crystal structures and hydrogenation properties of palladium-rich compounds with elements from groups 12-16
	Z. Naturforsch. **2016**, *71B*, 503-508.

1	André Götze, Philipp Urban, Oliver Oeckler, Holger Kohlmann
	Synthesis and crystal structure of Pd_5InSe
	Z. Naturforsch. **2014**, *69B*, 417-422.

Tagungsbeiträge

11	Reaction Pathways of the Hydrogenation of MPd$_3$ and Crystal Structures of Their Hydrides
	André Götze, Siobhan C. Stevenson, Holger Kohlmann
	16th European Conference on Solid State Chemistry, Glasgow (Vereinigtes Königreich), **2017**, Poster.

10	Hydrogenation Properties of $MgPd_2$
	André Götze, Holger Kohlmann
	43. Hirschegg-Seminar Festkörperchemie, Hirschegg (Österreich), **2017**, Vortrag.

9	Hydrogenation Properties of the Binary Palladium Rich Compounds $MgPd_2$ and MPd$_3$ (M: Sn, Pb, Bi)
	André Götze, Andrea Peretzki, Holger Kohlmann
	24rd Annual Conference of the German Crystallographic Society, Stuttgart, **2016**, Poster.

8	Hydrogen - A "Conductor" for Palladium Rich Intermetallic Structure Rearrangement in MPd$_3$
	André Götze, Holger Kohlmann
	GDCH Wissenschaftsforum Chemie, Dresden, **2015**, Poster.

7	Hydride Formation in the Intermetallic Compound $BiPd_3$
	André Götze, Holger Kohlmann
	41. Hirschegg-Seminar Festkörperchemie, Hirschegg (Österreich), **2015**, Vortrag.

6   Hydrogenation Properties of $BiPd_3$ and Related Selenium Substituted Compounds
André Götze, Holger Kohlmann
23rd Annual Conference of the German Crystallographic Society, Göttingen, **2015**, Vortrag.

5   Crystal Structure of Isotypic Compounds of Pd_5TlAs-type Structure
André Götze, Holger Kohlmann
17. Vortragstagung der Fachgruppe Festkörperchemie und Materialforschung der GDCH, Dresden, **2014**, Poster.

4   Synthesis, Structural and Morphological Study of $SmCo_xCr_{1-x}O_3$ (x = 0.33, 0.5, 0.67 and 1) Perovskites
S. Aleksovska, S. Dimitrovska-Lazova, A. Götze, M. Marinšek, H. Kohlmann, E. Hey-Hawkins
XXIII Congress, Society of Chemists and Technologists of Macedonia, Ohrid (Mazedonien), **2014**, Poster.

3   Synthesis and Investigation of Some Structural and Catalytic Characteristics of $PrCr_xNi_{1-x}O_3$ (x = 0.33, 0.5, 0.67 and 1) Perovskites
S. Dimitrovska-Lazova, M. Gjorgievska, A. Götze, H. Kohlmann, E. Hey-Hawkins, V. Mirčeski, S. Aleksovska
XXIII Congress, Society of Chemists and Technologists of Macedonia, Ohrid (Mazedonien), **2014**, Poster.

2   Strukturen und Hydriereigenschaften von palladiumreichen Phasen des Pd_5TlAs-Strukturtyps
André Götze, Holger Kohlmann
12. Mitteldeutsches Anorganiker Nachwuchssymposium, Freiberg, **2014**, Vortrag.

1   Crystal structures of palladium rich intermetallic compounds of Pd_5TlAs-type structure
André Götze, Holger Kohlmann
34th Berlin School on Neutron Scattering, Berlin, **2014**, Poster.

Kurzfassung der wissenschaftlichen Ergebnisse

zur Dissertation

Structure-Directing Influence of Hydrogen on the Formation of Hydrides of Palladium

and Rhodium Compounds Based on *In Situ* Studies

Der Fakultät für Chemie und Mineralogie der Universität Leipzig

vorgelegt von

M. Sc. André Götze

im Juni 2018

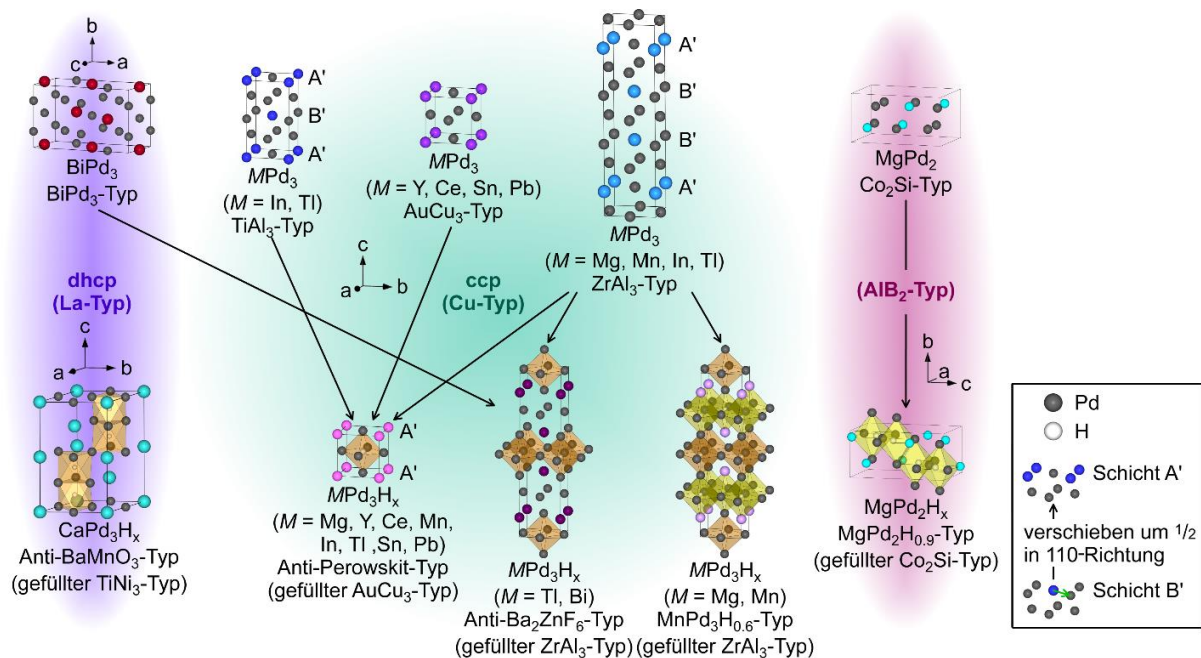angefertigt im Institut für Anorganische Chemie

Abbildung 1: Strukturdirigierender Einfluss von Wasserstoff bei der Bildung von palladiumreichen Hydriden.

Einleitung und Motivation

Interstitielle Hydride sind Wasserstoffverbindungen mit metallischem Charakter, bei denen Wasserstoff meist Tetraeder- oder Oktaederlücken von intermetallischen Verbindungen besetzt. Häufig werden diese Hydride von Edelmetallverbindungen gebildet. Einige palladiumreiche Verbindungen $M\text{Pd}_3$ sind dafür bekannt, in verwandten Strukturen der kubisch-dichtesten Packung (ccp, Cu-Strukturtyp) zu kristallisieren. Bei der Hydrierung wird oft eine Umlagerung von einer Überstruktur der ccp zu einer anderen beobachtet. Die treibende Kraft dieser Umlagerung ist die Generierung von $[\text{Pd}_6]$-Oktaederlücken, die von Wasserstoff bevorzugt besetzt werden. InPd_3 und TlPd_3 bilden die Hydride $\text{InPd}_3\text{H}_{0.89}$ und TlPd_3H. Bei den leichteren homologen Verbindungen des Aluminiums und Galliums wurde hingegen noch keine Wasserstoffabsorption beobachtet. Daraus lässt sich schließen, dass die Minoritätskomponente einen wesentlichen Einfluss auf die Wasserstoffaufnahme hat. Es ergeben sich die Kernfragen, welche elektronischen und geometrischen Eigenschaften das Element M haben muss, um eine Hydridbildung zu fördern und wie der Hydrierungsprozess abläuft. In dieser Arbeit wurden weitere binäre palladiumreiche Verbindungen synthetisiert und auf deren Hydriereigenschaften getestet, um an diesem einfachen System exemplarisch die Hydridbildung zu verstehen. *In situ*-Methoden, wie Pulverneutronenbeugung, wurden genutzt, um den Reaktionsverlauf dieser Festkörper-Gas-Reaktionen zu analysieren. Mögliche Intermediatbildungen können beobachtet und erhaltene Erkenntnisse für Syntheseoptimierung genutzt werden. Die Untersuchungen wurden auf ternäre Systeme mit Halbmetallen erweitert, um den Einfluss einer höheren Valenzelektronenkonzentration (*VEC*) zu beleuchten. Die untersuchten Systeme sind aufgrund ihres hohen Palladiumgehalts auch für die Katalyse interessant.

Der Übergang von metallischen zu kovalenten Hydriden ist nahtlos. Die meisten Hydride lassen sich aber dennoch grob zu einer Gruppe zuordnen. Bei einigen ternären Rhodium-Hydriden wurde gezeigt, dass sie metallische Eigenschaften haben, jedoch auch kovalente Rh-Rh-Bindungen ausbilden. Diese Verbindungen lassen sich nicht als metallische Hydride klassifizieren. Deshalb wurde untersucht, ob es im Calcium-Rhodium-System ein Hydrid mit der Zusammensetzung CaRhH_x gibt, und ob dieses ebenfalls direkte Rh-Rh-Bindungen ausbildet.

Materialien und Methoden

Die Verbindungen wurden durch typische Festkörperreaktionen bei hohen Temperaturen in abgeschmolzenen Quarzglasampullen durchgeführt. In manchen Fällen wurde Iod als Mineralisator hinzugefügt, um die Kristallinität und Reinheit zu erhöhen. Die Synthese der Hydride und Deuteride erfolgte in Autoklaven bei bis zu 20 MPa Wasserstoffdruck und 823 K. Die Reinheit der Verbindungen wurde mittels Röntgenpulverbeugung (XRPD) und Energiedispersiver Röntgenspektroskopie (EDX) untersucht. Die Position und die Besetzung der Wasserstoffatome in der Kristallstruktur der Hydride wurde mit Neutronenpulverbeugung bestimmt. Diese wurde an deuterierten Proben durchgeführt, weil Deuterium, verglichen mit Wasserstoff, einen kleineren inkohärenten Streubeitrag besitzt. Hydrierungsreaktionen wurden mittels dynamischer Differenzkalorimetrie (DSC) untersucht. Die Messungen wurden in einer integrierten Druckgaskammer bei bis zu 5 MPa Wasserstoffdruck und einer Maximaltemperatur von 703 K durchgeführt. Mehrere Zyklen wurden gemessen, um die Reaktionen auf Reversibilität zu überprüfen. Die beobachteten Reaktionen wurden mit *in situ*-XRPD und -Neutronenbeugung reproduziert. Die Hydrierungsreaktionen wurden direkt auf dem Neutronendiffraktometer in einer Leukosaphireinkristallzelle am Institut Laue-Langevin in Grenoble durchgeführt. Auf die Zelle wurde bis zu 12 MPa Wasserstoffdruck gegeben und die Probe mit einer Laserheizung bis zu 573 K geheizt. Gravimetrische und volumetrische Wasserstoffsorptionsmessungen wurden in Kooperation mit dem Institut für Nichtklassische Chemie an der Universität Leipzig durchgeführt. Katalytische Messungen zur Semihydrierung von Acetylen wurden in Kooperation mit dem Institut für Chemie der Technischen Universität Chemnitz gemessen. Quantenmechanische Rechnungen wurden in Kooperation mit der Lomonossow-Universität Moskau durchgeführt. Zusätzlich wurden Charakterisierungsmethoden wie Röntgeneinkristallstrukturanalyse, magnetische Messungen und Stabilitätsuntersuchungen (thermische Stabilität, Luftstabilität) verwendet.

Ergebnisse

Hydrierungen palladiumreicher Verbindungen

Der Schwerpunkt dieser Arbeit liegt in der Untersuchung von Hydriereigenschaften palladiumreicher Verbindungen. Geordnete binäre Verbindungen werden gebildet, wenn deren Minoritätselement ausreichend verschieden in Elektronegativität und Geometrie ist. Die meisten MPd$_3$-Verbindungen kristallisieren in einer Überstruktur der kubisch-dichtesten Packung (ccp) (*Abbildung 1*). Die kubischen Verbindungen SnPd$_3$ und PbPd$_3$ nehmen Wasserstoff unter Volumenzunahme auf und bilden die Hydride SnPd$_3$H$_{0.14}$ und PbPd$_3$H$_{0.13}$. Wasserstoff besetzt die bevorzugten [Pd$_6$]-Oktaederlücken und der Anti-Perowskit-Typ wird gebildet. Tetragonales MgPd$_3$ ist ebenfalls dafür bekannt, Wasserstoff aufzunehmen. *In situ*-Untersuchungen ergaben, dass zuerst [Pd$_6$] und [MgPd$_5$]-Oktaederlücken besetzt werden. Die [Mg$_2$Pd$_4$]-Lücken werden erst mit Wasserstoff besetzt, wenn sie durch die Volumenzunahme der vorausgegangenen Wasserstoffabsorption groß genug sind. BiPd$_3$ mit einer größeren Valenzelektronenkonzentration (*VEC*) als die vorangegangenen MPd$_3$ Verbindungen, kristallisiert in einer orthorhombischen Struktur, die mit der doppelt-hexagonal-dichtesten Packung (dhcp) verwandt ist. Eine geringe Wasserstoffaufnahme reicht aus, um eine wasserstoffinduzierte Umlagerung zur kubisch-dichtesten Packung zu erwirken (*Abbildung 2*). Die Reaktion verläuft ohne die Bildung von Intermediaten ab. Mögliche Mechanismen für die Umlagerung sind kurzwegige Atomdiffusionen oder Gleitungen der hexagonalen Schichten. Auf Grund der hohen Temperatur (> 550 K) ist der erstgenannte wahrscheinlicher. Bezogen auf die Elektronegativität, bilden die Zinn-, Blei- und Bismutverbindungen die Grenze für Hydierbarkeit von MPd$_3$. Eine
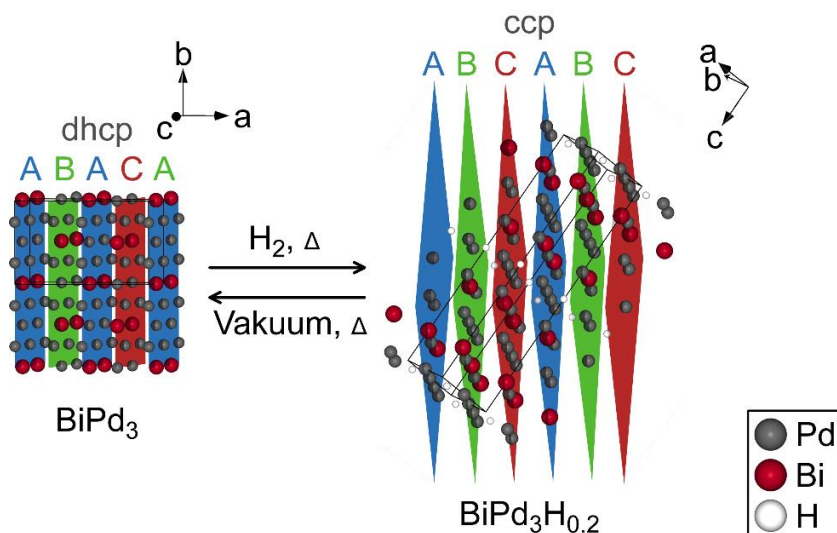

Abbildung 2: Darstellung der wasserstoffinduzierten Umlagerung vom orthorhombischen BiPd$_3$ (dhcp-Überstruktur) zum tetragonalen BiPd$_3$H$_{0.2}$ (ccp-Überstruktur).

4

$$3\ MgPd_2 + 2\ H_2 \longrightarrow 3\ MgPd_2H + \tfrac{1}{2}\ H_2 \xrightleftharpoons{437\ K} 3\ MgPd_2H_{0.2} + 1.7\ H_2 \xrightarrow{641\ K} MgH_2 + 2\ MgPd_3H$$
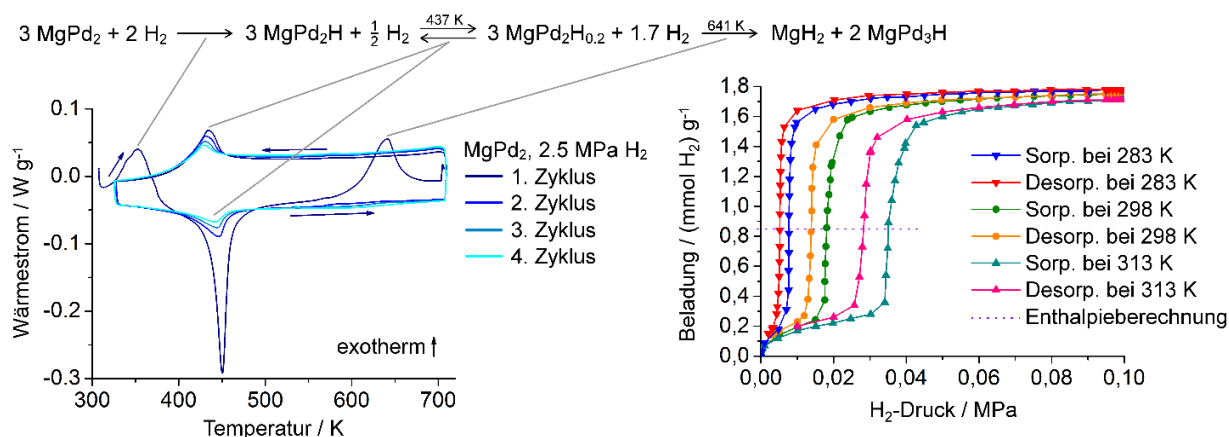
Abbildung 3: Reaktionsverlauf (oben), beobachtet mit *in situ*-DSC (links), und Isothermen (rechts) von der Hydrierung von MgPd$_2$

weitere Erhöhung der *VEC* führt zu anderen Strukturen und Verbindungen. Palladiumreiche Verbindungen, wie zum Beispiel Pd$_3$As und Pd$_{20}$Sb$_7$, nehmen keinen Wasserstoff auf.

Palladiumreiche Verbindungen mit einem Verhältnis von zwei Anteilen Palladium zu einem Anteil Metal *M* kristallisieren im Co$_2$Si-Typ, der verwandt mit dem AlB$_2$-Typ ist. Die Strukturen von *M*Pd$_2$-Verbindungen enthalten keine [Pd$_6$]-, sondern nur stark verzerrte [*M*Pd$_5$]-Oktaederlücken. MgPd$_2$ ist die einzige *M*Pd$_2$-Verbindung (*M* = Mg, Zn, Sn, Pb), die Wasserstoff aufnimmt. Während der Hydrierung von MgPd$_2$ dehnt sich dessen Elementarzelle anisotrop aus, weil Wasserstoff [MgPd$_5$]-Oktaederlücken besetzt, deren Grad der Verzerrung abnimmt. Die Hydrierung zu MgPd$_3$H findet mit einer schnelleren Kinetik statt als die Dehydrierung. Die aus Isothermen bestimmte Reaktionsenthalpie ist ähnlich groß wie die Standardentropie von molekularem Wasserstoff multipliziert mit der Raumtemperatur. Dadurch absorbiert MgPd$_2$ Wasserstoff unter milden Bedingungen und gibt ihn bei Normalbedingungen wieder ab. MgPd$_2$H desorbiert Wasserstoff auch reversibel bei Temperaturerhöhung und bildet MgPd$_2$H$_{0.2}$. Bei weiterer Temperaturerhöhung zersetzt sich das Hydrid irreversibel zu kubischem MgPd$_3$H$_x$ und Magnesiumhydrid (*Abbildung 3*).

Neben den binären palladiumreichen Verbindungen, wurden auch einige ternäre Verbindungen, wie zum Beispiel isotype Verbindungen des Pt$_5$TlAs-Strukturtyps, synthetisiert und auf Hydridbildung untersucht. Auch hier verhindert die Erhöhung der *VEC*, durch Einbringen von elektronenreichen Halbmetallen, eine signifikante Wasserstoffaufnahme. Pd$_5$InSe als Vorläuferverbindung zeigt hingegen eine Wasserstoffaufnahme. Bei hohen

5

Temperaturen zersetzt es sich über Pd_8In_2Se zu $InPd_3$ und Palladiumseleniden. Das gebildete $InPd_3$ nimmt anschließend Wasserstoff auf. $Pd_{11}Bi_2Se_2$ reagiert ebenfalls nicht mit Wasserstoff. Es kristallisiert in einer 4 x 4 x 4 -Überstruktur des W-Strukturtyps. Die Struktur enthält Lücken mit einer geordneten Verteilung, die jedoch nicht für Wassserstoffeinbau geeignet sind. Die Verbindung wurde zuvor irrtümlich als $Pd_3Bi_{0.6}Se_{0.4}$ veröffentlicht [1], das im BiF_3-Strukturtyp kristallisiert und in dem Bismut- und Selenatome mischbesetzt sind. In $Pd_{11}Bi_2Se_2$ sind diese Atome ausgeordnet und ein etwas geringer Palladiumgehalt ist vorhanden. Diese Verbindung wurde bei der Semihydrierung von Acetylen als Katalysatormaterial getestet (*Abbildung 4*). Es zeigt eine sehr hohe Selektivität zum Ethylen bei einem niedrigen Umsatz. Die Katalyse beginnt aufgrund einer passivierenden Bismutoxidschicht auf der Oberfläche von $Pd_{11}Bi_2Se_2$ erst nach einigen Stunden.

Hydride des Calcium-Rhodium-Systems

Im Calcium-Rhodium-System waren bisher nur Verbindungen mit einem größeren Calciumanteil als Rhodium bekannt. Ein Hydrid mit der Zusammensetzung $CaRhH_x$ war noch nicht bekannt trotz der Versuche, es aus Calciumhydrid und Rhodium zu synthetisieren [2]. Das Perowskit-Typ-Hydrid $CaRhH_3$ kann durch die Hydrierung der Laves-Phase $CaRh_2$ erhalten werden (*Abbildung 5*). Durch *in situ*-Neutronenbeugungsexperimente wurde der Hydrierungsweg analysiert. $CaRh_2$ bildet kubisches α-$CaRh_2H_{0.05}$ unter Wasserstoffaufnahme in $[Ca_2Rh_2]$-Tetraederlücken. Durch weitere Wasserstoffaufnahme wird die orthorhombisch verzerrte Laves-Phase β-$CaRh_2H_{3.9}$ gebildet. Sorptionsmessungen
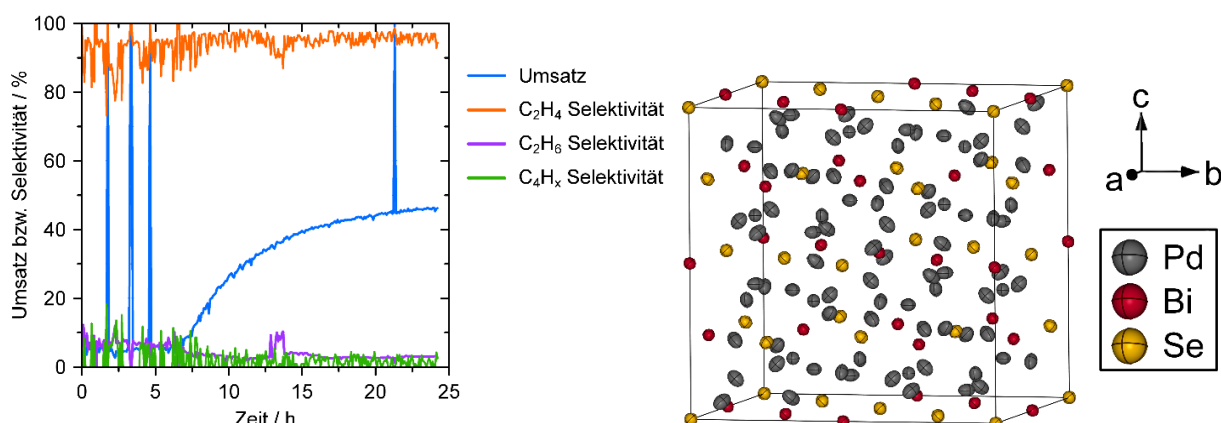

Abbildung 4: Umsatz und Selektivitäten von der Semihydrierung von Acetylen (links) mit $Pd_{11}Bi_2Se_2$ (Kristallstruktur rechts) als Katalysatormaterial. Die Ausschläge im Umsatz sind Artefakte.
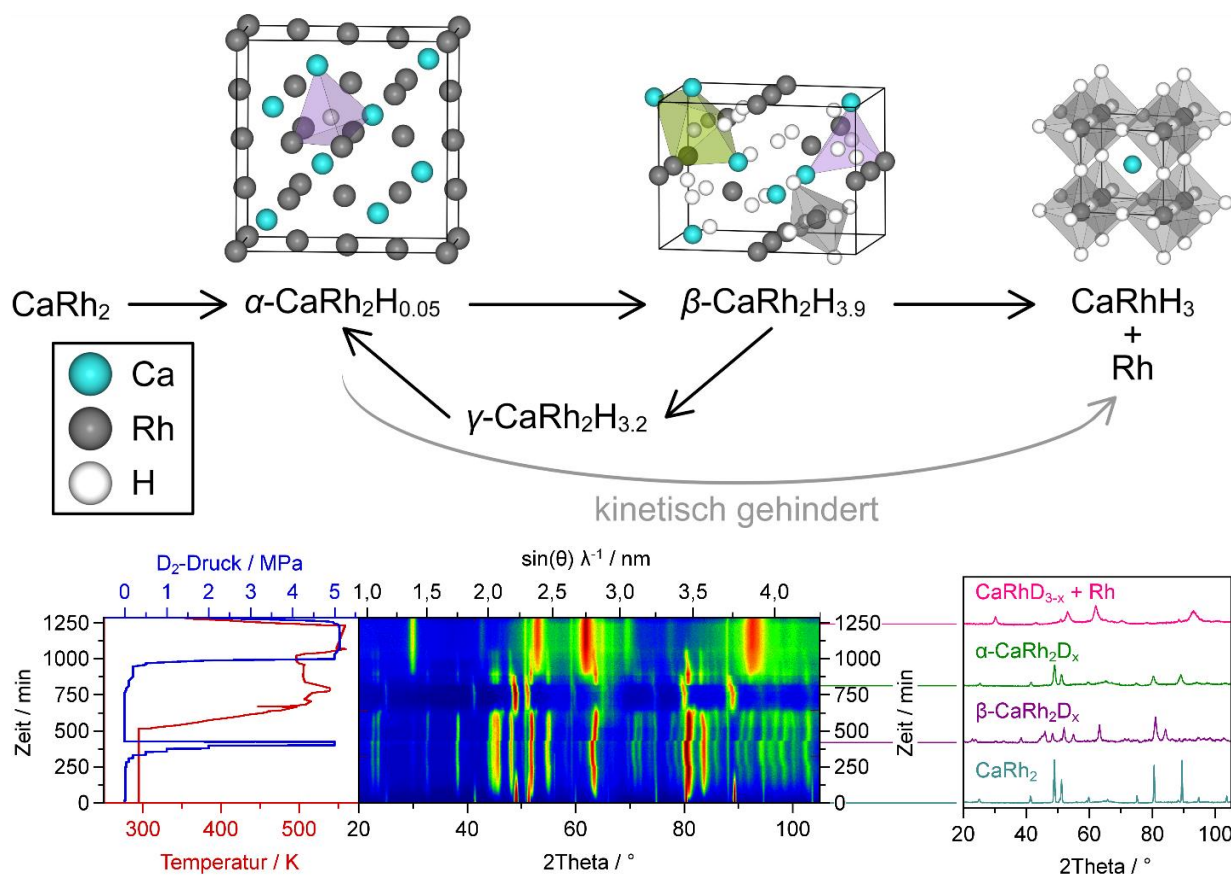
Abbildung 5: Reaktionsweg der Hydrierung des Laves-Phasen-Hydrids CaRh$_2$ (oben) untersucht mit *in situ*-Neutronenpulverbeugung am Institut Laue-Langevin in Grenoble (unten).

bestätigen diesen Wasserstoffgehalt. Wasserstoff besetzt dabei für Laves-Phasen ungewöhnliche trigonal-bipyramidale [Ca$_3$Rh$_2$]-Lücken, die zwischen zwei unbesetzten [Ca$_2$Rh$_2$]-Tetraederlücken liegen. Bei der Dehydrierung bildet sich ein zur β-Phase isotypes γ-CaRh$_2$H$_{3.2}$. Dieses wird nicht bei der Hydrierung beobachtet und besitzt wahrscheinlich eine Mischungslücke zum β-Hydrid. Die Laves-Phasen-Hydride können durch Temperaturerhöhung unter Wasserstoffdruck zum Perowskit CaRhH$_3$ und nano-kristallinem Rhodium zersetzt werden. Ein anderer Zugang zu dieser Verbindung ist bisher nicht bekannt und ist zum Beispiel über Direktsynthese nicht möglich. CaRhH$_3$ hat hauptsächlich metallischen Charakter und bildet keine direkten Rh-Rh-Bindungen aus. Damit unterscheidet sich es vom leichteren Homologen MgRhH, das schwache Rh-Rh-Bindungen ausbildet.

Fazit

In dem exemplarischen System der palladiumreichen intermetallischen Verbindungen, konnte gezeigt werden, dass deren Wasserstoffaufnahme mehr von elektronischen als geometrischen Aspekten abhängt. Die Wasserstoffabsorption wird gefördert, wenn die Minoritätskomponente eine ähnliche Elektronegativität wie Palladium, jedoch einen größeren Atomradius besitzt. $SnPd_3$ absorbiert deshalb weniger Wasserstoff als $InPd_3$. Eine Erhöhung der Valenzkonzentration durch Einbau von Halbmetallen hemmt außerdem die Wasserstoffaufnahme. So absorbieren die Grenzverbindungen $BiPd_3$ und $SnPd_3$ noch signifikant Wasserstoff, Verbindungen mit Halbmetallen wie zum Beispiel $Pd_{11}Bi_2Se_2$ hingegen nicht. Diese Verbindungen sind jedoch interessant für die Katalyse. So zeigt $Pd_{11}Bi_2Se_2$ eine hohe Selektivität zu Ethylen bei der Semihydrierung von Acetylen. Die Einbringung von Magnesium in palladiumreichen Systemen erhöht die Wahrscheinlichkeit einer Hydridbildung, denn $MgPd_2$ nimmt im Gegensatz zu anderen $M$$Pd_2$ Verbindungen (M = Zn, Sn) Wasserstoff auf. Diese Erkenntnisse können auf andere unbekannte Systeme übertragen werden, um Vorhersagen über Wasserstoffabsorption zu treffen.

In situ-Methoden, wie Pulverneutronenbeugungen, haben sich in dieser Arbeit als das Mittel der Wahl bewährt, um Festkörper-Gas-Reaktionen zu analysieren. So konnte gezeigt werden, dass geringe Wasserstoffaufnahmen im Fall von $BiPd_3$ ausreichen, um durch Änderungen in der Schichtfolge der Kugelpackungen, geeignete Wasserstoffkoordinationsumgebungen, $[Pd_6]$-Oktaeder, zu bilden. Intermediate konnten bei dieser Hydrierung nicht beobachtet werden. Im Gegensatz dazu, wurden bei $CaRh_2$ die Intermediat-Hydride $CaRh_2H_x$ entdeckt und der Reaktionsweg zum $CaRhH_3$ aufgedeckt. $CaRhH_3$ bildet, verglichen zum höheren Homologen $MgPdH$, keine Rh-Rh-Bindungen auf Grund des etwas stärker ionischen Charakters des Calciums aus. Hydride mit metallischen Eigenschaften und kovalenten Übergangsmetallbindungen sollten folglich mit Elementen wie Magnesium zu erwarten sein.

Literatur

[1] M. El-Boragy, M. Ellner, K. Schubert, On some metastable homeotypes of CuZn with Pd as majority component, Z. Metallkd. **1989**, *80*, 197-200.

[2] W. Bronger, L. Breil, Calcium-Rhodium-Hydride – Synthese und Struktur, *Z. Anorg. Allg. Chem.* **1998**, *624*, 1819-1822.

Publikationen zum Promotionsthema

o   A. Götze, J. Möllmer, H. Kohlmann
    From Laves phase $CaRh_2$ to the perovskite $CaRhH_3$ - *in situ* investigation of hydrogenation intermediates $CaRh_2H_x$
    Inorg. Chem. **2018**, submitted.

o   E. Y. Zakharova, S. M. Kazakov, A. Götze, H. Kohlmann, A. N. Kuznetsov
    Ternary palladium-indium-phosphorus and platinumindium-phosphorus compounds based on the Cu_3Au-type: structure, bonding, and properties
    J. Solid State Chem. **2018**, accepted.

o   A. Götze, N. Zapp, A. J. Peretzki, V. Pomjakushin, T. C. Hansen, H. Kohlmann
    In situ hydrogenation and crystal chemistry studies of Co_2Si type compounds $MgPd_2$ and Pd_2Zn
    Z. Anorg. Allg. Chem. **2018**, *644*, 367-375.

o   A. Götze, S. Schmorl, A. N. Kuznetsov, H. Kohlmann
    Vacancy ordering in $Pd_{11}Bi_2Se_2$ - Crystal structure and properties
    J. Alloys Compd. **2018**, *735*, 1914-1920.

o   A. Götze, T. C. Hansen, H. Kohlmann
    The reversible hydrogenation of $BiPd_3$ followed by *in situ* methods and the crystal structure of $PbPd_3D_{0.13(1)}$
    J. Alloys Compd. **2018**, *731*, 1001–1008.

o   A. Götze, H. Auer, R. Finger, T. C. Hansen, H. Kohlmann
    A sapphire single-crystal cell for *in situ* neutron powder diffraction of solid-gas reactions
    Phys. B **2018**, in press.

o   A. Götze, H. Kohlmann
    Palladium Hydride and Hydrides of Palladium-Rich Phases
    In: *Reference Module in Chemistry, Molecular Sciences and Chemical Engineering*, Elsevier **2017**.

o   A. Götze, J. M. Sander, H. Kohlmann
    Crystal structures and hydrogenation properties of palladium-rich compounds with elements from groups 12-16
    Z. Naturforsch. **2016**, *71B*, 503-508.

Weitere Publikationen

- A. Götze, P. Urban, O. Oeckler, H. Kohlmann
  Synthesis and crystal structure of Pd_5InSe
  Z. Naturforsch. **2014**, *69B*, 417-422.